

REPORT DOCUMENTATION PAGE

0482

Public reporting burden for this collection of information is estimated to average 1 hour per response, including the time for reviewing data needed, and completing and reviewing this collection of information. Send comments regarding this burden estimate or any other aspect of this collection of information, including suggestions for reducing this burden, to Washington Headquarters Services, Directorate for Information Operations and Reports (0704-4302). Respondents should be aware that notwithstanding any other provision of law, no person shall be subject to any penalty for failing to comply with a collection of information if it does not display a valid OMB control number. **PLEASE DO NOT RETURN YOUR FORM TO THE ABOVE ADDRESS.**

1. REPORT DATE (DD-MM-YYYY) 20-09-2005		2. REPORT TYPE Final		3. DATES COVERED (From - To) 01-10-2001 to 30-06-2005	
4. TITLE AND SUBTITLE Active Aeroelastic Tailoring of High-aspect-ratio Composite Wings				5a. CONTRACT NUMBER	
				5b. GRANT NUMBER F49620-02-1-0425	
				5c. PROGRAM ELEMENT NUMBER	
6. AUTHOR(S) Cesnik, Carlos E. S.				5d. PROJECT NUMBER	
				5e. TASK NUMBER	
				5f. WORK UNIT NUMBER	
7. PERFORMING ORGANIZATION NAME(S) AND ADDRESS(ES) The University of Michigan Department of Aerospace Engineering 1320 Beal Avenue 3024 FXB Ann Arbor, Michigan 48109-2140				8. PERFORMING ORGANIZATION REPORT NUMBER CESC-F005639-Final	
9. SPONSORING / MONITORING AGENCY NAME(S) AND ADDRESS(ES) AFOSR/NA 801 N. Randolph Street Room 942 Arlington, Virginia 22203-1997				10. SPONSOR/MONITOR'S ACRONYM(S)	
				11. SPONSOR/MONITOR'S REPORT NUMBER(S)	
12. DISTRIBUTION / AVAILABILITY STATEMENT Approved for public release; distribution unlimited					
13. SUPPLEMENTARY NOTES The views and conclusions contained herein are those of the author and should not be interpreted as necessarily representing the official policies or endorsement, either expressed or implied, of AFOSR or the U.S. Government.					
14. ABSTRACT Nonlinear aeroelastic modeling and the fundamental mechanisms of active aeroelastic tailoring of high-aspect-ratio composite wings for High-altitude Long-endurance (HALE) aircraft is presented. To investigate the effects of distributed anisotropic strain actuation and their synergism with the passive aeroelastic tailored composite structure, a new framework was developed for analysis and design of high aspect ratio active flexible wings. The formulation is capable of modeling the nonlinear large deflection behavior of slender wings and other structural members, deformation due to applied voltages on the active plies in the skin of the wing, and the unsteady subsonic aerodynamic forces acting on the wing. Because HALE wings are long and slender, they can be well modeled as beams undergoing three dimensional displacements and rotations. The cross sectional stiffness, inertia, and actuation properties of the wing are calculated along the span, and then a nonlinear beam model is constructed. A novel beam representation was developed and it was based entirely on the beam strains, resulting in a computationally efficient low-order model suitable for preliminary structural design and control synthesis. The formulation was then extended to analyze different beam configurations, particularly in the presence of joints and splits. With that, the entire vehicle can be modeled and non-conventional wing configurations such as the joined wing could be analyzed. Finally, different aircraft configurations such as the ones being considered for the new Air Force Sensor Craft vehicle were studied.					
15. SUBJECT TERMS Nonlinear aeroelasticity, active tailoring, Sensorcraft, piezocomposite actuators, HALE aeroelasticity					
16. SECURITY CLASSIFICATION OF:			17. LIMITATION OF ABSTRACT UU	18. NUMBER OF PAGES 319	19a. NAME OF RESPONSIBLE PERSON
a. REPORT U	b. ABSTRACT U	c. THIS PAGE U			19b. TELEPHONE NUMBER (include area code)

FINAL REPORT

GRANT NUMBER F49620-02-1-0425

**ACTIVE AEROELASTIC TAILORING OF HIGH-ASPECT-RATIO COMPOSITE
WINGS**

PRINCIPAL INVESTIGATOR:

CARLOS E. S. CESNIK, Ph.D.
ASSOCIATE PROFESSOR OF AEROSPACE ENGINEERING
THE UNIVERSITY OF MICHIGAN
1320 BEAL AVENUE 3024 FXB
ANN ARBOR, MICHIGAN 48109-2140

PROGRAM MANAGER:

CAPT. CLARK ALLRED, Ph.D.
AFOSR/NA
PROGRAM MANAGER, STRUCTURAL MECHANICS
801 N. RANDOLPH STREET ROOM 942
ARLINGTON, VIRGINIA 22203-1997
TELEPHONE: (703) 696-7259
FAX: (703) 696-8451

Abstract

This report summarizes the work done and the accomplishments under Grant No. F49620-02-1-0425. The study addressed nonlinear aeroelastic modeling and the fundamental mechanisms of active aeroelastic tailoring of high-aspect-ratio composite wings for High-altitude Long-endurance (HALE) aircraft. The primary source of nonlinearity came from the structural dynamics. The geometry of this class of vehicles allows for large deformations while maintaining small local strains. The emphasis was on actively exploring structural flexibility to enhance flight performance and reduce structural weight, while controlling aeroelastic instabilities. To investigate the effects of distributed anisotropic strain actuation and their synergism with the passive aeroelastic tailored composite structure, a suitable nonlinear active aeroelastic framework was required. Therefore, an analysis and design tool was developed for high aspect ratio active flexible wings. The formulation is capable of modeling the nonlinear large deflection behavior of slender wings and other structural members, deformation due to applied voltages on the active plies in the skin of the wing, and the unsteady subsonic aerodynamic forces acting on the wing. Because HALE wings are long and slender, they can be well modeled as beams undergoing three dimensional displacements and rotations. The cross sectional stiffness, inertia, and actuation properties of the wing are calculated along the span, and then a 1-D nonlinear beam model is constructed. A novel beam representation was developed and it was based entirely on the beam strains, resulting in a computationally efficient low-order model suitable for preliminary structural design and control synthesis. The formulation was then extended to analyze different beam configurations, particularly in the presence of joints and splits. With that, the entire vehicle can be modeled and non-conventional wing configurations such as the joined wing could be analyzed. Finally, different aircraft configurations such as the ones being considered for the new Air Force Sensor Craft vehicle were studied.

20051114 015

Content

Introduction	3
Summary of the Accomplishments	3
Development of NAST—Nonlinear Aeroelastic Simulation Toolbox [2],[10]	3
Element Description	4
Member and Inter-Member Equations	6
Equations of Motion	6
Utilizing APA for Wing Warping [2], [3], [9]	7
Baseline Vehicles	8
Vehicle Deformation During Unsymmetric Maneuver	10
Roll Response	10
Concluding Remarks	11
Acknowledgements	12
References	13

Appendix A: Brown, E. L., "Integrated Strain Actuation in Aircraft with Highly Flexible Composite Wings," Ph.D. Thesis, Massachusetts Institute of Technology, Cambridge, Massachusetts, June 2003.

Appendix B: Cesnik, C. E. S. and Brown, E. L., "Active Warping Control of a Joined Wing Airplane Configuration," *Proceedings of the 44th Structures, Structural Dynamics, and Material Conference*, Hampton, Virginia, April 7—10, 2003.

Appendix C: Cesnik, C. E. S. and Brown, E., "Modeling of High Aspect Ratio Active Flexible Wings for Roll Control," *Proceedings of the 43rd Structures, Structural Dynamics, and Material Conference*, Denver, Colorado, April 22—25, 2002, AIAA Paper 2002-1719.

Appendix D: Cesnik, C. E. S. and Brown, E., "Active Warping Control of a Joined Wing Aircraft," *International Forum on Aeroelasticity and Structural Dynamics*, Amsterdam, The Netherlands, June 4—6, 2003.

Appendix E: Cesnik, C. E. S. and Su, W., "Nonlinear Aeroelastic Modeling and Analysis of Fully Flexible Aircraft," *Proceedings of the 46th AIAA/ASME/ASCE/AHS/ASC Structural, Structural Dynamics and Materials Conference*, Austin, Texas, April 18—21, 2005, AIAA-2005-2169.

Appendix F: Cesnik, C. E. S. and Su, W., "Nonlinear Aeroelastic Behavior of Fully Flexible Slender Vehicles," *International Forum on Aeroelasticity and Structural Dynamics*, Munich, Germany, June 28—July 1, 2005.

Introduction

The first successful powered heavier-than-air flight took place about 100 years ago. The Wright Flier used the motion of the pilot's hips to control the warping of the wing and, therefore, the vehicle roll. Historically, the relatively soft-in-torsion wings were replaced by stiffer designs with the increase in vehicle flying speeds. The lack of authority to twist the stiffer wings resulted in replacing wing warping with discrete aileron control. Within this concept, maneuver loads are generated at discrete movable parts of the wings in contrast to its reshaping.

Two decades ago, the concept of active aeroelastic wing (AAW) was introduced. There, instead of generating maneuver loads from a set of control surfaces and fight the flexibility of the wing, the control surfaces are used to induce deformation on the wing so that the reshape of the wing is responsible for generating such loads. Different numerical studies have been pursued, showing promises of achieving different objectives while reducing overall systems weight^[5]. A modified F/A-18A with a relatively flexible wing was constructed as a testbed for this concept and has been flight tested at NASA Dryden successfully.

More recently, with the advancement of active materials and the development of anisotropic piezo-composite actuators (APA)^{[1],[6]}, one may be able to once again implement wing warping for maneuver load generation. Through APA embedded as an integral load-bearing component of the wing structure, local strains can be induced at certain areas of the wing structure and in certain directions. Those strains are controlled externally by applied electric field to the actuators. By properly designing the active structure, a single physical structural realization can achieve several different aeroservoelastic objectives, presenting itself as a truly active aeroelastic tailoring mechanism. Moreover, this could bring the AAW concept to its fulfillment, and represents a fundamental step towards the development of a more generic morphing aircraft.

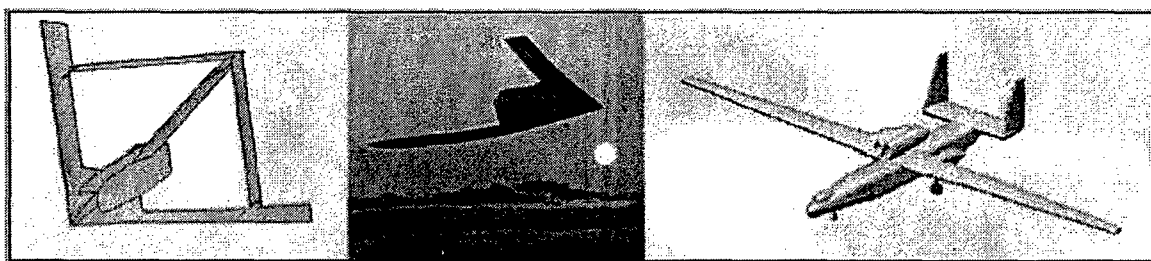


Figure 2. ISR Sensor Craft platform concepts

Among the types of aircraft that could take advantage of such concept, high-altitude long-endurance ones are the most likely candidates. Figure 1 shows some of the concepts being considered for the new USAF Sensor Craft. Due to mission requirements, those vehicles present high-aspect-ratio wings that result in relatively flexible structures. If the conventional design paradigm is to be used, the wing flexibility has to be counteracted by additional structural reinforcements that will result in extra mass penalty. Some basic studies exploring APA for active aeroelastic tailoring of such vehicles^[4] show that multiple objectives can be achieved by the same wing realization. Studies were conducted for flutter boundary enhancement and gust load response. It is worthwhile mentioning here that the wing's high flexibility results in nonlinear structural motions. This adds another degree of complexity to this already reach domain in which the structural dynamics of the flexible vehicle must be modeled accordingly.

Summary of the Accomplishments

A series of accomplishments were obtained under this grant. Detailed description of them is given in the Appendices.

Development of NAST—Nonlinear Aeroelastic Simulation Toolbox [2],[1 0]

A key contribution from this grant was the development of the active-flexible-wing analysis formulation including the ability to handle fully-flexible joined-wing vehicles. This is a fundamental component for the investigation of the effects of embedded anisotropic actuation on the aeroelastic response of high-aspect-ratio composite wings, particularly for vehicles like the Sensor Craft. The nonlinear beam problem was solved by solely tracking beam

curvatures without ever having to introduce displacement or rotation variables. This approach allowed for effective and computationally efficient analysis of active wings. However, this choice of unknown field makes the application of displacement constraints (i.e., joint of wings, wing-tail-fuselage, etc.) somewhat difficult. This has been overcome in a clever way and it is described below.

For the present study, the vehicle is allowed six rigid body degrees of freedom as well as flexible degrees of freedom. The wings are allowed fully coupled three-dimensional bending, twisting, and extensional deformation. Flaps and ailerons may be included for comparison purposes and for the study of hybrid vehicle control. Inclusion of flexible fuselage and vertical tail complete the formulation. A finite-state unsteady airloads model is integrated into the system equations, with the exception of the fuselage. The model allows for a low order set of nonlinear equations that can be put into state-space form to facilitate control design. All this has been coded into Matlab, and the resulting code is the so-called NAST—Nonlinear Aeroelastic Simulation Toolbox. Its basic features are summarized in Figure 2.

The analysis formulation has been developed and implemented in Matlab to effectively study generic high-aspect-ratio wing aircraft. Sensitivity analysis has been under development for optimum design.

Basic features:

- Nonlinear aeroelastic steady state deformation
- Linearized aeroelastic response
- Fully nonlinear time-marching aeroelastic simulation
- Recovery of ply stress/strain, evaluation of ply failure
- Evaluation of flutter instability boundary, limit cycle oscillations
- Simulation of free flight of fully flexible vehicle
- Structure and aeroelastic modes, natural frequencies
- Closed-loop aeroelastic simulation

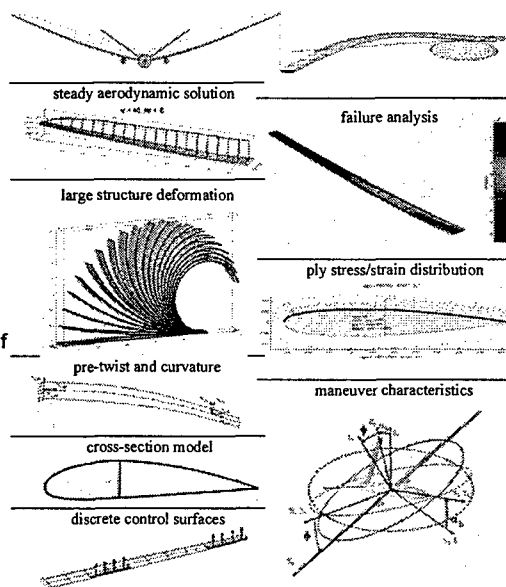


Figure 2. Summary of NAST basic capabilities

Element Description

Specialized beam elements were created that have four local strain degrees-of-freedom: extension, twist, and two bending ones. Figure 3 exemplifies the deformations of constant-strain elements.



Figure 3. Deformations of a typical constant-strain element

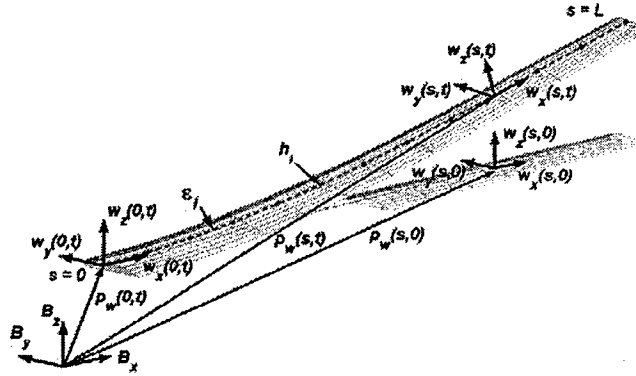


Figure 4. Wing coordinates

Each node along the beam is determined by a vector consisting of 12 components. Suppose the beam reference frame is w , which is a function of the natural beam coordinate s , the 12-component vector is denoted as,

$$h(s)^T = [p_w(s)^T, w_x(s)^T, w_y(s)^T, w_z(s)^T] \quad (1)$$

where, p_w is the position of frame w in the body coordinate, w_x , w_y , and w_z are the direction vectors pointing along the beam axis, toward the leading edge, and normal to the airfoil, respectively. As discussed in [2], the governing equation, which relates the dependent displacements to the independent strains, is,

$$\frac{\partial h(s)}{\partial s} = A(s)h(s) \quad (2)$$

where, A is a matrix function of the strains. The solution of (2) can be given by

$$h(s) = e^{G(s)} h_0 \quad (3)$$

where h_0 is the beam boundary conditions.

Member and Inter-Member Equations

In the model of highly flexible joined-wing aircraft, the fuselage and the vertical tail are both modeled as slender beams, similarly to the wings. Therefore, it is necessary to model a split beam system as illustrated in Figure 5. For simplicity, consider three members in this beam system. Member 1 consists of two elements and members 2 and 3 each consist of one element only. A modification to the original kinematics of [2] to allow the analysis of split beams is presented in [10].

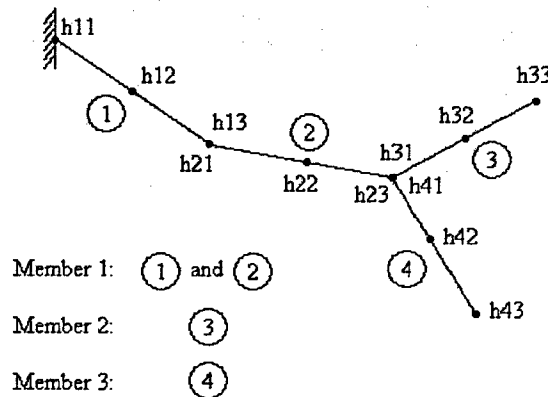


Figure 5. A split (or bifurcated) beam system

The kinematics for these members is obtained by marching the elemental kinematics from the boundary node to the end nodes at each branch, which could be written as follows:

Element 1			Element 2		
Node 1	Node 2	Node 3	Node 1	Node 2	Node 3
$h_{11} = h_0$	$h_{12} = e^{G_1} h_{11}$	$h_{13} = e^{G_1} h_{12}$	$h_{21} = D_{21} h_{13}$	$h_{22} = e^{G_2} h_{21}$	$h_{23} = e^{G_2} h_{22}$
Element 3			Element 4		
Node 1	Node 2	Node 3	Node 1	Node 2	Node 3
$h_{31} = D_{32} h_{23}$	$h_{32} = e^{G_3} h_{31}$	$h_{33} = e^{G_3} h_{32}$	$h_{41} = D_{42} h_{23}$	$h_{42} = e^{G_4} h_{41}$	$h_{43} = e^{G_4} h_{42}$

where h_{ij} is the displacement of the j th node of the i th element. D_{ij} contains the direction cosines, accounting for the different directions of different elements at the connection. These equations can be written into a matrix form,

$$\begin{bmatrix}
 I & & & & & & & & & & \\
 -e^{G_1} & I & & & & & & & & & \\
 & -e^{G_1} & I & & & & & & & & \\
 & & -D_{21} & I & & & & & & & \\
 & & & -e^{G_2} & I & & & & & & \\
 & & & & -e^{G_2} & I & & & & & \\
 & & & & & -D_{32} & I & & & & \\
 & & & & & & -e^{G_3} & I & & & \\
 & & & & & & & -e^{G_3} & I & & \\
 & & & & & & & & -D_{42} & I & \\
 & & & & & & & & & -e^{G_4} & I \\
 & & & & & & & & & & -e^{G_4} & I
 \end{bmatrix}
 \begin{Bmatrix}
 h_{11} \\ h_{12} \\ h_{13} \\ h_{21} \\ h_{22} \\ h_{23} \\ h_{31} \\ h_{32} \\ h_{33} \\ h_{41} \\ h_{42} \\ h_{43}
 \end{Bmatrix}
 =
 \begin{Bmatrix}
 h_0 \\ 0 \\ 0 \\ 0 \\ 0 \\ 0 \\ 0 \\ 0 \\ 0 \\ 0 \\ 0 \\ 0
 \end{Bmatrix} \quad (4)$$

Note that, the location of D_{42} reflects the relation between members 2 and 4.

The other parts of the current framework, such as the construction of stiffness matrix, mass matrix, equation of motion, and the solution procedure are basically left unchanged, except for some modifications to make them compatible with the new kinematics relation added into the existing framework. This framework is now enhanced with the ability to model the highly flexible aircraft with flexible fuselage and vertical tail. Figure 6 shows a built-up model. The point of CG is the root of the beam systems

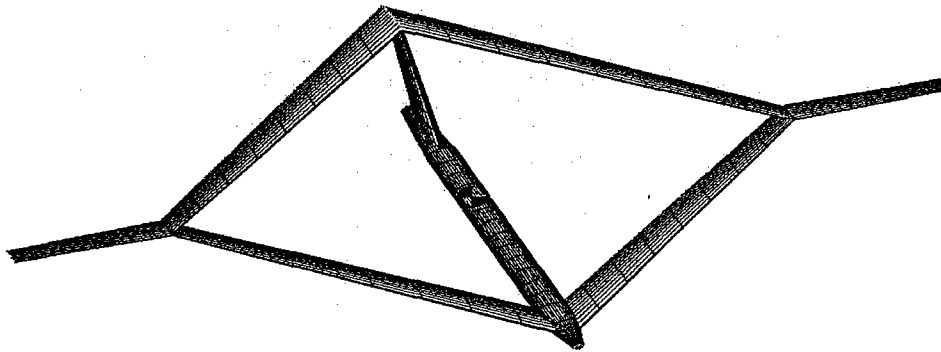


Figure 6. Illustration of a built-up joined wing aircraft with flexible fuselage and vertical tail

Equations of Motion

With the six rigid body degrees of freedom, the system structural degrees of freedom are represented by the column matrix q , where

$$\dot{q} = [\dot{\varepsilon}_1^T, \dot{\varepsilon}_2^T, \dots, \dot{\varepsilon}_n^T, V_B^T, \omega_B^T]^T \quad (5)$$

and ε_i contains the strain variables for wing member i , V_B and ω_B are the linear velocity and angular velocity of the vehicle, respectively, represented in the body frame, B . The dependent variables for the entire vehicle are put into the column matrix H ,

$$\dot{H} = [\dot{h}_1^T, \dot{h}_2^T, \dots, \dot{h}_n^T, V_B^T, \omega_B^T]^T \quad (6)$$

The dependent degrees of freedom are related to the independent degrees of freedom through a Jacobian matrix relation

$$H = f(q), \quad dH = \left[\frac{\partial H}{\partial q} \right] dq = [J_H(q)] dq \quad (7)$$

The expression for virtual work on the vehicle is now given by

$$\delta W = \delta q^T (-\bar{M}\ddot{q} - \bar{C}\dot{q} - \bar{K}q + \bar{N}g + \bar{B}_V V + \bar{B}_{F1} F^{dst} + \bar{B}_{F2} F^{pt} + \bar{B}_{M1} M^{dst} + \bar{B}_{M2} M^{pt} + B_{q0} q_0 + B_H H) \quad (8)$$

The principle of virtual work requires that the total virtual work done on the system be equal to zero, leading to the equations of motion,

$$\bar{M}\ddot{q} + \bar{C}\dot{q} + \bar{K}q = B_V V + B_{F1} F^{dst} + B_{F2} F^{pt} + B_{M1} M^{dst} + B_{M2} M^{pt} + \bar{N}g + B_{q0} q_0 + B_H H \quad (9)$$

The distributed loads are divided into aerodynamic loads and user supplied loads. The aerodynamic loads evaluated at the current state have the incremental form

$$\begin{aligned} F^{aero}(t) &= F^{aero}(t_0 + \Delta t) \approx F_0(q_0, \dot{q}_0, \lambda_0) + F_{\ddot{q}} \ddot{q} + F_{\dot{q}} \Delta \dot{q} + F_q \Delta q + F_{\lambda} \Delta \lambda \\ M^{aero}(t) &= M^{aero}(t_0 + \Delta t) \approx M_0(q_0, \dot{q}_0, \lambda_0) + M_{\ddot{q}} \ddot{q} + M_{\dot{q}} \Delta \dot{q} + M_q \Delta q + M_{\lambda} \Delta \lambda \end{aligned} \quad (10)$$

here λ is column matrix of induced flow states as described in [7]. The induced flow states are governed by a differential equation of the form

$$\dot{\lambda} = L_1 \lambda + L_2 \ddot{q} + L_3 \dot{q} \quad (11)$$

The aeroelastic equations of motion are obtained by moving the state dependent aerodynamic loads over to the left hand side of Eq. (9) and augmenting the structure states with the induced flow states, which can be represented in state space form as

$$\dot{x} = A(x)x + B(x)u(x, t) \quad (12)$$

where the state vector is now given by

$$x = [\dot{q}^T, q^T, \lambda^T]^T \quad (13)$$

Utilizing APA for Wing Warping [2], [3], [9]

As part of this grant, an in-depth investigation^[2] was conducted of the effects of using APA in three classes of Uninhabited Aerial Vehicles (UAV): small (e.g., Pointer), medium (e.g., Predator), and large (e.g., Global Hawk). The three classes of UAVs were studied for both wing warping and aileron controls. Different objectives included: roll controllability, flutter enhancement, and gust load alleviation and response. Also, an assessment of the structural weight penalty incurred for using current technology APA was conducted. Although the final decision has to be made at the system's level (including mission effectiveness, survivability, etc.) and a formal numerical optimization study is still needed, results from [2] show that wing warping is possible today by employing APA as part of the composite wing construction. Basic performance results of the active wing are comparable with the ones from a wing with ailerons.

Similar numerical investigations as in [2] but on a joined-wing Sensorcraft configuration can be found in [3] and [9]. This is part of a new high-altitude long-endurance ISR platform being considered by the USAF to carry a variety of sensors. Due to the unusual shapes of joined-wing airplane configurations, the effects of structural deformation on the static aerodynamic and aeroelastic behavior are difficult to intuit and predict. Deformation of the structure at a certain location may produce large changes in angle of attack in the lifting surfaces at other locations. Efforts to minimize structural weight may create aeroelastic instabilities that are not encountered in conventional aircraft design. For joined-wing aircraft, the first sign of failure may be in the buckling of the aft members as the structure is softened. Flutter and divergence may also become a problem in these members due to the reduction in structural frequency as they go into compression. As the aircraft becomes more flexible, the nature of the geometric structural nonlinearities become more important and the lift distribution on the aircraft may be adversely affected.

Active distributed control using embedded piezocomposites in the wing structure may be able to improve the performance in several ways, and also may allow for lighter designs by actively offsetting critical instabilities. Warping the structure in order to change the aerodynamic force distribution across the vehicle may be a means of eliminating or reducing unwanted structural couplings due to deformation. The degrading effects of in-plane loads on the aft members may be dealt with through the use of active/passive internal structural couplings. Passive structure design may be incapable of dealing with the global structural load transfers at all flight conditions. By embedding active materials in large areas of the vehicle, the global behavior of the structure may be enhanced. Actuators embedded in the forward wings will be able to respond to stresses measured in the aft wings. Actuators anywhere in the structure can respond to measurements taken everywhere over the structure. This may allow for global modal behavior to be adjusted by timing and shaping the internal stresses in the structure.

Passive composite structural design can exploit structural couplings to prevent aeroelastic instabilities. While this may work for certain instabilities at certain flight conditions, it may have a negative effect on other aeroelastic characteristics at other flight conditions. The ability to actively adjust the structural couplings would have obvious benefits.

For the numerical study, a sample of the results presented in [3], [9]-[11] (and included in the Appendices) is presented here. Baseline vehicles (Fig. 7) were created with to represent two different concepts of achieving roll maneuverability: wing warping (active) and classic aileron (passive) concepts. For both cases, controllable changes in aerodynamic loads only occur in the outer wing. The active wing contains anisotropic piezocomposite actuators (APAs) that can produce 1350 μ strain of free strain amplitude and are distributed along the entire outer wing. The passive wing contains a 50%-span/20%-chord aileron that is allowed 30° of amplitude deflection.

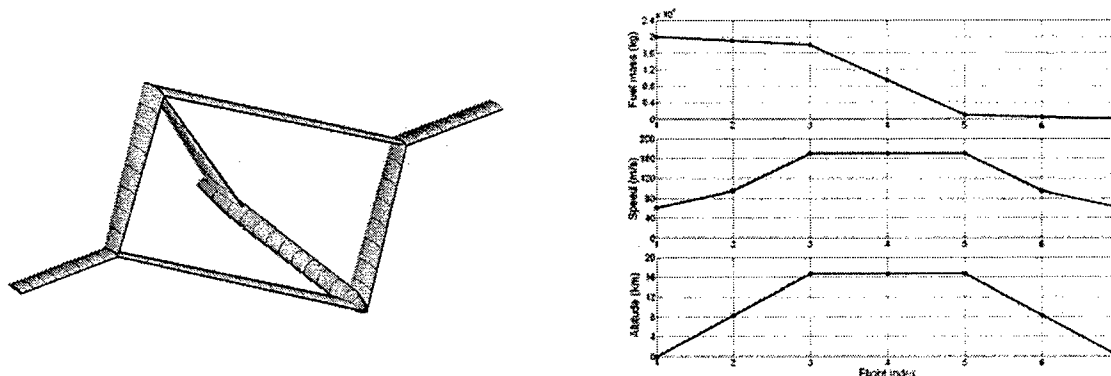


Figure 7. Baseline joined-wing Sensorcraft vehicle with unswept outer wings (where APA actuators or ailerons are present) and its basic mission profile.

Baseline Vehicles

Three sets of constraints were defined to help guide the baseline designs: laminate strength (based on first-ply failure) at 2.5-g load, laminate strength based on gust loads, and minimum linearized flutter margin. For both vehicles, the 2.5-g load factor was shown to be the critical constraint and the wing structural thickness distribution was sized so that maximum strain was reached along the span. All the results related to the baseline designs can be found in [3].

Seven flight index points represent the nominal mission profile, as also indicated in Fig. 7. At each index point, the altitude, fuel mass, and nominal flight velocity are specified. The index points represent: (1) takeoff, (2) climb, (3) cruise ingress, (4) cruise/loiter/cruise, (5) cruise egress, (6) decent, and (7) landing. The fuel burn determines the duration of each flight segment. The nominal flight speed at each index point is based on the cruise speed (input parameter), and is computed such that the dynamic pressure is constant (constant indicated air speed). The trim body angle is also obtained at each index point for a set of equally spaced increasing flight speeds, up to 200% of the nominal speed at that flight index. At each flight index point, the vehicle is trimmed for equilibrium in horizontal flight at a given flight speed.

From top view, the vehicle shape is symmetric (although one may want to vary the forward/aft location of the joint). The wings are denoted right forward inboard, left forward inboard, right rear inboard, left rear inboard, right outboard, and left outboard. Right and left are determined as in Fig. 8 (as viewed from top with nose pointing up). Each of the six wing members is divided into four regions for definition of cross-section layup and ply thickness distribution. The forward and rear members are identical in construction, and the material distribution will follow the numbering convention as indicated in Fig. 6.

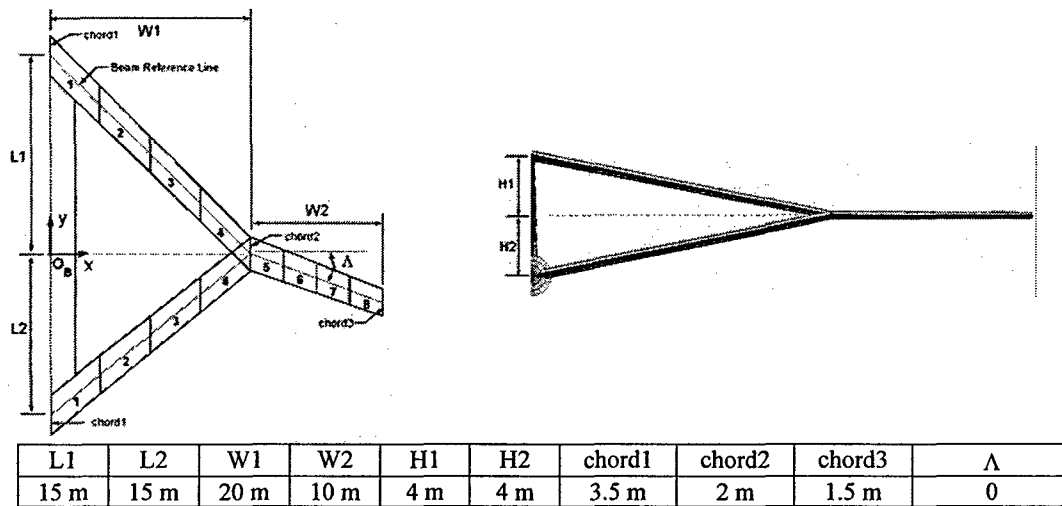


Figure 8. Baseline joined-wing Sensorcraft vehicle geometry.

Vehicle Mass Breakdown. The vehicle mass breakdown is given in Table 1. The fuel is assumed to be distributed evenly throughout the inner and outer wings, independent of the total amount of fuel on board. The fuselage contains no fuel.

Table 1: Vehicle Mass Distribution.

Cruise altitude	16,700 m
Cruise speed	170 m/s
Fuselage structure + payload + engine mass	4,000 kg
Fuel mass	20,000 kg
Active vehicle total wing structure mass	11,191 kg
Passive vehicle total wing structure mass	10,459 kg
Added mass for aileron mounts/wing	58.9 kg

Wing Cross Section. For simplicity, NACA 4415 was chosen as the airfoil and it is kept constant throughout the wing members. A single spar is used at 45% chord. For the final wing layup, the top and bottom skins have ply groups composed of [0/45/-45/0] and the web with ply groups of [0₄]. For the active outer wing, the “45” and “-45” ply groups are APA. Everything else is S-glass. Material properties and thickness distributions can be found in [3]. The maximum induced tip twist angle generated by the APA is 5.5°.

Vehicle Deformation During Unsymmetric Maneuver

To exemplify the effects of the completely flexible vehicle, consider the case in which the aircraft is flying at 100 m/s at sea level. The body angle of attack is zero. The right outer wing is actuated to be twisted to generate a roll moment. Fig. 9 shows the vehicle during the maneuver. As it can be seen, the vertical tail deflects with the rest of the vehicle, and although the intent is to generate roll, a potentially severe yaw is also generated. This will impact the vehicle trim and the set of maneuver loads needed to follow a certain trajectory. Furthermore, these extra deformations are expected to impact the vehicle stability and response to gust as well.

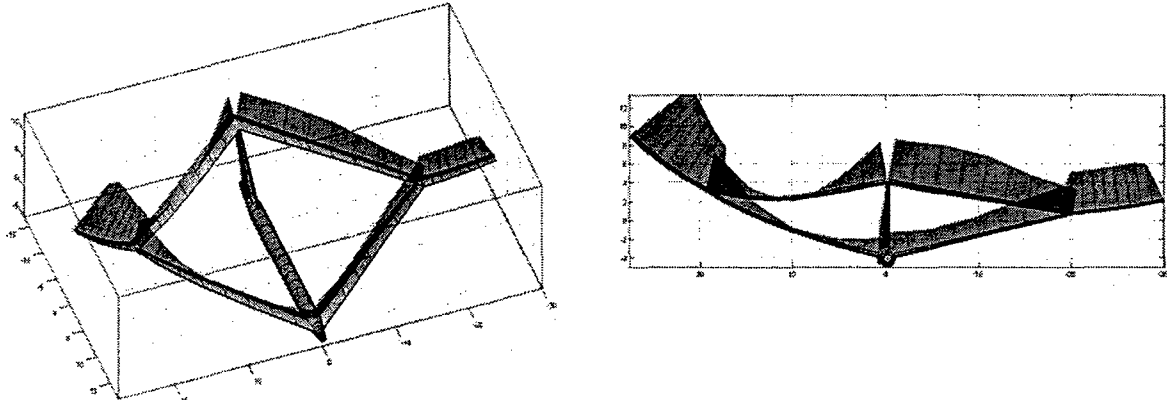


Figure 9. Deformation at level flight with non-symmetric actuation (two views of the same case)

Roll Response

In the study of roll response, the selected flight condition is 16.7 km altitude, and 195 m/s. The body angle of attack is zero. To achieve the roll motion, antisymmetric twist actuation is employed. As a comparison, both linearized and non-linear approaches are implemented [3] here. In linearized approach, the aircraft is firstly brought to its nonlinear steady state with roll motion locked. Both the roll moment and roll damping are calculated based on this deformed structure. The roll responses are then calculated based on these quantities. This approach has the advantage of being computationally efficient, which is very desirable for preliminary studies. On the other hand in the non-linear approach, the deformed shape of the aircraft is updated at each time step, and all the aerodynamic loads are calculated according to the updated deformed shapes. Although more time consuming, this presents the most accurate representation of the maneuver.

To assess the effects of the flexibility and rigidity of different parts of the vehicle on its roll response, six different models are considered here, which are listed in Table 2.

Table 2. Different levels of flexibility to be considered in the present study

	Fuselage	Vertical Tail	Inner Wing	Outer Wing	Joint
Model 1	rigid	rigid	rigid	flexible	flexible
Model 2	rigid	rigid	flexible	flexible	flexible
Model 3	rigid	flexible	flexible	flexible	flexible
Model 4	flexible	flexible	flexible	flexible	flexible
Model 5	flexible	flexible	flexible	flexible	rigid

To exemplify part of what is planned for the final paper, Figs. 10 and 11 show the roll response of models 1 to 3. As it can be seen from Fig. 10, the additional vehicle flexibility brings more complexity to the roll response as it starts developing. Also the maximum roll rate that the vehicle can reach is actually lower than what the semi-rigid model can predict. This supports the need to include the flexibility of the fuselage and vertical tail when analyzing such flexible vehicles.

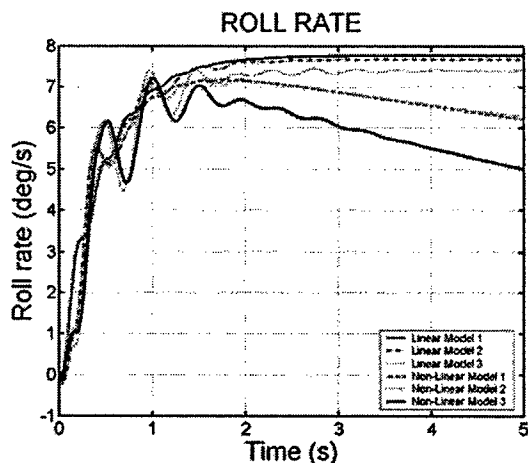


Figure 10. Roll rate, Models 1 to 3

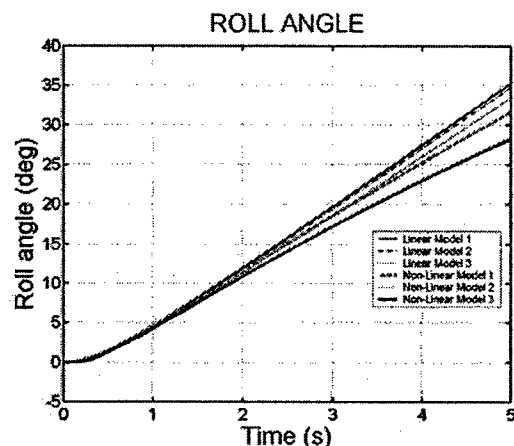


Figure 11. Roll angle, Models 1 to 3

Concluding Remarks

This grant studied some of the unique aeroelastic characteristics of the joined-wing Sensorcraft, with emphasis on the concept of wing warping actuation for maneuver load generation. The study employed the newly developed framework for the analysis, design, and simulation of high-flexible multi-segmented wing vehicles, also developed under this grant.

From the results of the numerical studies, it is clear that joined-wing configurations present much richer and complex aeroelastic characteristics than single-wing ones. As for the linearized flutter speed, flexible fuselage and vertical tail both reduces the flutter speed of joined-wing configuration, whereas the flexibility of the fuselage and tail of the single-wing configuration does not significantly impacts the wing flutter (unless the wing flutters first). Although the linearized flutter speed can be easily obtained, the actual (nonlinear) flutter speed can be higher or lower than that, depending on a series of parameters. Therefore, one must use the nonlinear flutter speed calculation to determine the stability boundary of flexible vehicles like the ones studied here. Regarding the unique problem of loss of stiffness in the aft wing in the joined-wing configuration, preliminary results indicated that the added flexible fuselage decreases "buckling" speed, while adding the flexibility of the vertical tail increases it. More studies are needed to better understand those relative effects.

While the proposed framework has been created to handle any structural configuration made of slender (active) composite components (wing, tail, fuselage), in its current form it cannot naturally handle the flexibility of the body in a wing-body (flying wing) configuration (Northrop-Grumman Sensorcraft concept). Separate effort is under way to extend the framework to bring non-slender flexible bodies to be coupled with the present nonlinear aeroelastic formulation.

When analyzing the joined-wing concepts, the importance of wing flexibility and the availability of a geometrically nonlinear structural dynamics solver were demonstrated. Of particular interest for the joined-wing configuration is the criticality of the sudden rear wing loss of stiffness (buckling) that compromises the vehicle integrity. This can be alleviated by proper twist control of the forward inboard wing. While in this study this was demonstrated using wing warping induced by APA, in principle similar effect could be achieved using ailerons in the forward inboard wing. For the roll response, it was shown that the wing-warping design based on current APA technology presents a terminal roll rate which is three-times smaller than the aileron concept due to limited twist authority. This could be overcome with an APA of similar mechanical properties as used in this study but with 3.75-times greater maximum free strain. This is within range of the promises of single-crystal fiber composites.

Even though numerical design optimization will improve the baseline vehicle designs and should be employed to support navigating such reach design space, the relative results obtained here represent the order of response expected from each concept for the joined-wing Sensorcraft configuration. Again, the concepts are based on current technology material properties and construction practices. The active concept uses APA properties that are achievable with today's technology and the model includes all the fundamental static and dynamic effects on the aeroelastic responses. The aileron design contains significant idealizations, and represents the performance upper bound for the concept. No surface control inertia or aerodynamic losses with high deflection angles have been

included in the model, or any control flexibility that comes with very large control surfaces. In fact, the chosen size of the aileron was based on the maximum practical size surface that can be fitted within such wing without being concerned with mechanical fixtures and actuator systems.

Another important aspect of the vehicles' designs presented here is that they are driven by strength consideration, which penalized the wing-warping concept and favored the aileron-actuated one. Stiffness constraints got automatically satisfied once the layups were thickened enough to sustain the high loads. If a reduced maximum load factor is chosen, other constraints may become active, particularly related to aileron reversal and gust loads (as was seen for the latter in some of the design studies conducted in [2]). In fact, the overall system/mission requirements, including performance and survivability considerations, will certainly impact the design solution, potentially changing the importance of roll performance as assumed here.

Acknowledgements

This research was supported by the Air Force Office of Scientific Research, USAF, under grant (Dr. Daniel Segalman, Dr. Dean Mook, and Capt. Clark Allred, Ph.D., were the technical monitors). The views and conclusions contained herein are those of the author and should not be interpreted as necessarily representing the official policies or endorsement, either expressed or implied, of AFOSR or the U.S. Government.

References

- [1] Bent, A. A., "Active Fiber Composite Material Systems for Structural Control Applications," In *Proceedings of the SPIE's 6th International Symposium on Smart Structures and Materials*, Newport Beach, California, March 1999.
- [2] Brown, E. L., "Integrated Strain Actuation in Aircraft with Highly Flexible Composite Wings," Ph.D. Thesis, Massachusetts Institute of Technology, Cambridge, Massachusetts, June 2003. (Appendix A)
- [3] Cesnik, C. E. S. and Brown, E. L., "Active Warping Control of a Joined Wing Airplane Configuration," *Proceedings of the 44th Structures, Structural Dynamics, and Material Conference*, Hampton, Virginia, April 7—10, 2003. (Appendix B)
- [4] Cesnik, C. E. S. and Ortega-Morales, M., "Active Aeroelastic Tailoring of Slender Flexible Wings," *International Forum on Aeroelasticity and Structural Dynamics*, Madrid, Spain, June 5—7, 2001.
- [5] Pendleton, E. W., Griffin, K. E., Kehoe, M., and Perry, B., "A Flight Research Program for the Active Aeroelastic Wing Concept," In *Proceedings of the 37th AIAA/ASME/AHS/ASC Structures, Structural Dynamics and Materials Conference*, Salt Lake City, Utah, April 1996.
- [6] Wilkie, W.K., Bryant, R.G., High, J.W., Fox, R.L., Hellbaum, R.F., Jalink, A., Little, B.D., and Mirick, P.H., "Low-cost piezocomposite actuator for structural control applications," In *Proceedings of the SPIE 7th Symposium on Smart Structures and Materials*, Newport Beach, California, March 2000. pp. 323-334.
- [7] Peters, D.A. and Johnson, M.J., "Finite-State Airloads for Deformable Airfoils on Fixed and Rotating Wings", Symposium on Aeroelasticity and Fluid/Structure Interaction, Proceedings of the Winter Annual Meeting, ASME, Nov 6-11, 1994.
- [8] Cesnik, C. E. S. and Brown, E., "Modeling of High Aspect Ratio Active Flexible Wings for Roll Control," *Proceedings of the 43rd Structures, Structural Dynamics, and Material Conference*, Denver, Colorado, April 22—25, 2002, AIAA Paper 2002-1719. (Appendix C)
- [9] Cesnik, C. E. S. and Brown, E., "Active Warping Control of a Joined Wing Aircraft," *International Forum on Aeroelasticity and Structural Dynamics*, Amsterdam, The Netherlands, June 4—6, 2003. (Appendix D)
- [10] Cesnik, C. E. S. and Su, W., "Nonlinear Aeroelastic Modeling and Analysis of Fully Flexible Aircraft," *Proceedings of the 46th AIAA/ASME/ASCE/AHS/ASC Structural, Structural Dynamics and Materials Conference*, Austin, Texas, April 18—21, 2005, AIAA-2005-2169. (Appendix E)
- [11] Cesnik, C. E. S. and Su, W., "Nonlinear Aeroelastic Behavior of Fully Flexible Slender Vehicles," *International Forum on Aeroelasticity and Structural Dynamics*, Munich, Germany, June 28—July 1, 2005. (Appendix F)

Appendix A:

Brown, E. L., "Integrated Strain Actuation in Aircraft with Highly Flexible Composite Wings," Ph.D. Thesis, Massachusetts Institute of Technology, Cambridge, Massachusetts, June 2003.

Integrated Strain Actuation In Aircraft With Highly Flexible Composite Wings

by

Eric L. Brown

B.S., Mechanical Engineering
Massachusetts Institute of Technology, 1993

M.S., Mechanical Engineering
The University of Michigan, 1995

Submitted to the Department of Mechanical Engineering
in Partial Fulfillment of the Requirements for the Degree of
Doctor of Science in Mechanical Engineering

at the

Massachusetts Institute of Technology

June 2003

Copyright © 2003 by Eric Brown. All Rights Reserved.

The author hereby grants to MIT permission to reproduce and to distribute publicly
paper and electronic copies of this thesis document in whole or in part.

Signature of Author _____
Department of Mechanical Engineering

Certified by _____
Carlos E. S. Cesnik
Visiting Associate Professor of Aeronautics and Astronautics
Thesis Supervisor

Certified by _____
Ahmed Ghoniem
Professor of Mechanical Engineering
Committee Chairman

Accepted by _____
Ain Sonin
Chairman, Department Committee on Graduate Students

Integrated Strain Actuation In Aircraft With Highly Flexible Composite Wings

by

Eric L. Brown

Submitted to the Department of Mechanical Engineering
on February 21, 2003 in Partial Fulfillment of the Requirements
for the Degree of Doctor of Science in Mechanical
Engineering

ABSTRACT

The purpose of this thesis is to provide a framework for the study of wing warping as a means of achieving multiple aeroelastic goals. Shape change is achieved by integrating anisotropic piezoelectric composites (APC) within the passive composite wing skin. The goals include the ability of integrated strain actuation (ISA) to provide sufficient wing deformation for roll maneuver, gust load alleviation, flutter suppression, and redistribution of maneuver loads.

A nonlinear analysis tool was constructed to study the behavior of aircraft with highly flexible active wings undergoing large deformation. It combines a new large displacement, strain-based finite element beam formulation with a finite-state unsteady aerodynamics model and a thin-wall active beam cross section model. The tool was created with the flexibility to model different aircraft configurations, including unconventional ones such as joined wing designs. The effects of sweep and dihedral, as well as large deformations are taken into account in the calculation of aerodynamic loads. The strain-based finite element formulation allows for a simplified control design because the flexible degrees of freedom are easily accessible by strain gages.

To support the evaluation of ISA performance, and to study the impact of vehicle size on performance, three representative conventional vehicles using aileron control are modeled. The vehicles are based on fielded unmanned aerial vehicles (UAV), representing low, medium, and high altitude classes. The ISA wings are modeled by replacing some of the passive composite plies in with APC. The active and passive vehicles are compared based on the goals stated above. The impact of the piezoelectric composite material properties on weight and performance is discussed. The required property values are determined for making ISA a viable method for primary roll control and wing stability.

Numerical results show that roll control without ailerons is possible using present actuator technology. Integrated strain actuation is also shown to significantly alleviate gust loading and increase the flutter speed. Peak maneuver stresses are significantly reduced through active lift redistribution.

Thesis Supervisor: Carlos E. S. Cesnik, Visiting Associate Professor of Aeronautics and Astronautics
Thesis Chairperson: Ahmed Ghoniem, Professor of Mechanical Engineering

Acknowledgements

I would like to acknowledge and give special thanks to my thesis advisor, Professor Carlos E. S. Cesnik. He has worked tirelessly to give advice and support to all of his students. When he left MIT to take a faculty position at the University of Michigan midway through the development of my thesis, I thought that it would be very difficult to communicate and exchange ideas. However, our dialogue was never interrupted and continued up to the completion of my work. Observing the work ethic and professional qualities of Carlos has been a great source of inspiration.

I would also like to thank my thesis committee, Profs. Ahmed Ghoniem, John Dugundji, Rudrapatna Ramnath, and Dr. Ken Kaiser, for stimulating conversations and the exchange of ideas during thesis reviews.

My friends and family were very forgiving when I missed important events in order to work on this thesis and are very appreciated. I would like to thank my good friend Marc, who helped me get through rough times, and Alice, who was there for me during the most demanding phase of the thesis, and, of course, my parents, who have always been supportive of me.

The fellowship for graduate study was provided by The Charles Stark Draper Laboratory, Inc., under the sponsorship of Internal Company IR&D. Many people at Draper provided moral support during my thesis work. I would like to especially thank Peter Sebelius for his confidence in me.

Funding for this work was provided by the Air Force Office of Scientific Research, under grant F49620-02-1-0425, and monitored by Drs. Daniel J. Segalman and Dean Mook. Such support does not constitute an endorsement by AFOSR of the views expressed herein.

Publication of this thesis does not constitute approval by Draper or the sponsoring agency of the findings or conclusions contained herein. It is published for the exchange and stimulation of ideas.

Table of Contents

ACKNOWLEDGMENTS	5
TABLE OF CONTENTS	7
LIST OF FIGURES	11
LIST OF TABLES	17
1. INTRODUCTION	19
1.1 Motivation	19
1.2 Previous Work	22
1.2.1 Design of Highly Flexible Aircraft	22
1.2.2 Nonlinear Aeroelasticity	23
1.2.3 Actuators	23
1.2.4 Active Aeroelasticity	25
1.2.5 Aeroservoelasticity	27
1.2.6 Summary Remarks	28
1.3 Overview of Present Work	28
2. THEORETICAL FORMULATION	31
2.1 Vehicle Model Description	32
2.2 Formulation of the Equations of Motion	33
2.2.1 Rigid Body Motion	34
2.2.2 Member Equations	36
2.2.3 Global Structural Equations of Motion	56
2.2.4 Aerodynamics	56
2.2.5 Aeroelastic System Equations	59
2.3 Solution of the Aeroelastic System	60

2.3.1 Steady State Solution	61
2.3.2 Trim Solution	62
2.3.3 Stability Analysis	63
2.3.4 Time stepping solution	63
3. NUMERICAL IMPLEMENTATION	65
3.1 Introduction Data	65
3.2 Processing Vehicle Configuration Data	66
3.2.1 Cross Section Layup Specification	70
3.3 Initializing the Vehicle Geometric Variables	71
3.4 Construction of the Finite Element Matrices	74
3.5 Kinematics Solver	75
3.6 Aerodynamics Module	76
3.7 Obtaining the Aeroelastic System Matrices	77
3.8 Steady State Solution Module	78
3.9 Roll Response Solver	80
4. NUMERICAL VALIDATION OF FORMULATION	82
4.1 Static and Dynamic Cantilevered Beam Tests	83
4.1.1 Test Case 1 - Concentrated Tip Force	84
4.1.2 Test Case 2 - Concentrated Tip Moment	86
4.1.3 Test Case 3 - Multiple Point Forces	87
4.1.4 Test Case 4 - Dynamic Response	89
4.2 Multiple Constraint Deflection Testing	91
4.2.1 Test Case 1 - Fixed-Fixed, Vertical Distributed Load	91
4.2.2 Test Case 2 - Fixed-Fixed, Vertical Point Load	92
4.2.3 Test Case 3 - Fixed-Fixed, Axial Point Load	93
4.2.4 Test Case 4 - Fixed-Pinned in Center, Vertical Point Tip Load	94
4.2.5 Test Case 5 - Fixed-Pinned in Center, Multi-Axial Point Load	95
4.3 Joined Member Static Deflection Testing	97
4.3.1 Test Case 1 - Simple Point Load at Joint	98

4.3.2	Test Case 2 - Multi-Axis Point Load at Joint	98
4.3.3	Test Case 3 - Complex Load Case	99
4.4	Aeroelastic Test Cases	101
4.4.1	Goland Wing	101
4.4.2	Highly Flexible, Slender Wing	102
4.4.3	Aileron Lift and Moment	103
4.5	Cross Sectional Properties	104
5.	NUMERICAL STUDIES	108
5.1	Introduction	108
5.2	Guidelines for Creating the Numerical Models	110
5.2.1	Flight Plan Construction	110
5.2.2	Fuselage	111
5.2.3	Fuel Storage	111
5.2.4	General Wing Properties	111
5.2.5	Ailerons	111
5.2.6	Passive Wing Layup and Thickness Distribution	112
5.2.7	Active Wing Layup and Thickness Distribution	112
5.2.8	Material Properties	112
5.3	Baseline Vehicle Data	113
5.3.1	Static Twist Response	118
5.3.2	Effects of Active Material Properties on Wing Twist	118
5.4	Roll Performance - Wing Warping vs. Aileron	120
5.4.1	Transient Roll Response	120
5.4.2	Roll Actuation Frequency Response	124
5.5	Wing Stabilization Using Active Control	135
5.5.1	Turbulence Gust Alleviation Performance	137
5.5.2	Flutter Suppression	152
5.6	Maneuver Loads Reduction	154
6.	CONCLUDING REMARKS	158

6.1 Summary.....	158
6.2 Conclusions from Numerical Studies.....	160
6.3 Thesis Key Contributions.....	164
6.4 Recommendations for Future Work.....	165
BIBLIOGRAPHY	167
APPENDIX A - Aerodynamic Loads Formulation	172
APPENDIX B - Properties of the Test Wings.....	178
APPENDIX C - Controller Design	197
APPENDIX D - Member Kinematics	201

List of Figures

- 1.1 Active Fiber Composite (AFC) actuator components and schematic.
- 1.2 Langley Macro-Fiber Composite (MFC) actuator components.
- 1.3 Deformation of an AFC actuator patch.

- 2.1 A generic vehicle analysis model
- 2.2 A vehicle model showing static aerodynamic loading distributions
- 2.3 A joined wing vehicle model
- 2.4 Fuselage position and orientation with respect to an inertial frame
- 2.5 Illustration of a single undeformed member
- 2.6 Wing geometry variables
- 2.7 Auxiliary reference frames
- 2.8 Deformations represented by a single element with constant strain distribution
- 2.9 Differential beam element
- 2.10 Engines and other non-structural masses are modeled as additional rigid bodies.
- 2.11 Example of a nodal constraint
- 2.12 Example of inter-member constraint
- 2.13 Airfoil motion definition
- 2.14 Net forces represented in the body frame

- 3.1 Information flow in present implementation
- 3.2 Vehicle configuration parameters
- 3.3 Vehicle configuration solver block diagram
- 3.4 Wing model with varying airfoil from root to tip
- 3.5 Member construction
- 3.6 Input/output relationship for aeroelastic system update
- 3.7 Block diagram for steady state aeroelastic solution

- 4.1 Load condition for test case 1
- 4.2 Comparison of tip position along the x axis for test case 1

- 4.3 Comparison of tip position along the z axis for test case 1
- 4.4 Load condition for test case 2
- 4.5 Comparison of tip position along the x axis for test case 2
- 4.6 Comparison of tip position along the z axis for test case 2
- 4.7 Load condition for test case 3
- 4.8 Comparison of tip position along the x axis for test case 3
- 4.9 Comparison of tip position along the z axis for test case 3
- 4.10 Beam model for the dynamic response test
- 4.11 Tip displacement comparison for $F=10\sin 20t$
- 4.12 Tip displacement comparison for $F=10\sin 50t$
- 4.13 Tip displacement comparison for $F=5\sin 55.6t$
- 4.14 Load condition for test case 1
- 4.15 Displacement comparison for test case 1
- 4.16 Load condition for test case 2
- 4.17 Displacement comparison for test case 2
- 4.18 Load condition for test case 3
- 4.19 Displacement comparison for test case 3
- 4.20 Load condition for test case 4
- 4.21 Displacement comparison for test case 4
- 4.22 Load condition and resulting deformation for test case 5
- 4.23 Beam deflections along the y axis for test case 5
- 4.24 Beam deflections along the z axis for test case 5
- 4.25 Dimensions and boundary condition for the test model
- 4.26 Loading condition for test case 1
- 4.27 Deflection results for test case 1
- 4.28 Loading condition for test case 2
- 4.29 Deflection results for test case 2
- 4.30 Loading condition for test case 3
- 4.31 Deflection results for test case 3
- 4.32 Limit cycle oscillations in the Goland wing flying at 12% over flutter speed

- 5.1 Basic vehicle geometry for numerical studies
- 5.2 Unmanned aircraft used as baselines for creating the numerical cases studied here
- 5.3 Aileron configuration for roll comparison results
- 5.4 Cross section layup for the aileron design
- 5.5 Active cross section layup
- 5.6 Wing geometry for the small class vehicle
- 5.7 Wing geometry for the medium class vehicle
- 5.8 Wing geometry for the large class vehicle
- 5.9 Nominal mission profile for the small class vehicle
- 5.10 Nominal mission profile for the medium class vehicle
- 5.11 Nominal mission profile for the large class vehicle
- 5.12 Wing tip twist angle due to maximum actuation for the three ISA1 wing classes
- 5.13 Wing tip twist angle due to maximum actuation for the three ISA2 wing classes
- 5.14 The effect of active ply properties on tip twist
- 5.15 Control input for roll response
- 5.16 Roll rate response of the small class vehicle
- 5.17 Roll rate response of the medium class vehicle
- 5.18 Roll rate response of the large class vehicle
- 5.19 Roll angle response of the small class vehicle
- 5.20 Roll angle response of the medium class vehicle
- 5.21 Roll angle response of the large class vehicle
- 5.22 Frequency response from roll actuation input to roll angle, small vehicle
- 5.23 Frequency response from roll actuation input to roll angle, small vehicle
- 5.24 Frequency response from roll actuation input to roll angle, small vehicle
- 5.25 Frequency response from roll actuation input to roll rate, small vehicle
- 5.26 Frequency response from roll actuation input to roll rate, small vehicle
- 5.27 Frequency response from roll actuation input to roll rate, small vehicle
- 5.28 Frequency response from roll actuation input to tip twist, small vehicle
- 5.29 Frequency response from roll actuation input to tip twist, medium vehicle
- 5.30 Frequency response from roll actuation input to tip twist, large vehicle
- 5.31 Frequency response from roll actuation input to tip deflection, small vehicle

- 5.32 Frequency response from roll actuation input to tip deflection, medium vehicle
- 5.33 Frequency response from roll actuation input to tip deflection, large vehicle
- 5.34 Frequency response from roll actuation input to roll angle, large vehicle (Mach 0.4, sea level)
- 5.35 Frequency response from roll actuation input to roll rate, large vehicle (Mach 0.4, sea level)
- 5.36 Frequency response from roll actuation input to tip twist, large vehicle (Mach 0.4, sea level)
- 5.37 Frequency response from roll actuation input to tip deflection, large vehicle (Mach 0.4, sea level)
- 5.38 Roll moment due to aileron deflection for varying flight speed and thickness of the $\pm 45^\circ$ graphite epoxy plies (large class vehicle wing).
- 5.39 Roll moment at Mach 0.5 due to aileron deflection for varying thickness of the $\pm 45^\circ$ graphite epoxy plies (large class vehicle wing).
- 5.40 Model representation for stability and gust alleviation control
- 5.41 Closed loop plant representation
- 5.42 Comparison of the linearized and nonlinear responses to 5 m/s "1-cos gust" disturbance
- 5.43 Vertical turbulence gust disturbance based on the Dryden model⁴⁷.
- 5.44 Tip bending displacement response due to turbulence, small vehicle, Test Case 1
- 5.45 Tip bending displacement response due to turbulence, small vehicle, Test Case 2
- 5.46 Tip bending displacement response due to turbulence, small vehicle, Test Case 3
- 5.47 Tip bending displacement response due to turbulence, medium vehicle, Test Case 1
- 5.48 Tip bending displacement response due to turbulence, medium vehicle, Test Case 2
- 5.49 Tip bending displacement response due to turbulence, medium vehicle, Test Case 3
- 5.50 Tip bending displacement response due to turbulence, large vehicle, Test Case 1
- 5.51 Tip bending displacement response due to turbulence, large vehicle, Test Case 2
- 5.52 Tip bending displacement response due to turbulence, large vehicle, Test Case 3
- 5.53 Tip rotation response due to turbulence, small vehicle, Test Case 1
- 5.54 Tip rotation response due to turbulence, small vehicle, Test Case 2
- 5.55 Tip rotation response due to turbulence, small vehicle, Test Case 3
- 5.56 Tip rotation response due to turbulence, medium vehicle, Test Case 1
- 5.57 Tip rotation response due to turbulence, medium vehicle, Test Case 2

- 5.58 Tip rotation response due to turbulence, medium vehicle, Test Case 3
- 5.59 Tip rotation response due to turbulence, large vehicle, Test Case 1
- 5.60 Tip rotation response due to turbulence, large vehicle, Test Case 2
- 5.61 Tip rotation response due to turbulence, large vehicle, Test Case 3
- 5.62 Aileron and warping responses, small vehicle, Test Case 1
- 5.63 Aileron and warping responses, small vehicle, Test Case 2
- 5.64 Aileron and warping responses, small vehicle, Test Case 3
- 5.65 Aileron and warping responses, medium vehicle, Test Case 1
- 5.66 Aileron and warping responses, medium vehicle, Test Case 2
- 5.67 Aileron and warping responses, medium vehicle, Test Case 3
- 5.68 Aileron and warping responses, large vehicle, Test Case 1
- 5.69 Aileron and warping responses, large vehicle, Test Case 2
- 5.70 Aileron and warping responses, large vehicle, Test Case 3
- 5.71 Root locus of unstable aeroelastic mode vs. flight speed, with vertical rigid body motion.
- 5.72 Open loop tip bending and tip angle responses at 167 m/s and sea level
- 5.73 Closed loop tip bending and tip angle responses at 167 m/s and sea level
- 5.74 Vehicle under load factor 4 condition, with (bottom) and without (top) active load redistribution, maximum twist actuation applied
- 5.75 Normalized bending moment during a 4-g maneuver
- 5.76 Longitudinal ply strains at the root station with and without load redistribution
- 5.77 Transverse ply strains at the root station with and without load redistribution
- 5.78 Shear ply strains at the root station with and without load redistribution

- A.1 Airfoil motion definition.
- A.2 Example of finite span correction distribution.

- C.1 Closed loop plant representation
- C.2 Tip response of the analytical model to a random gust disturbance, ('closed loop 1' refers to the realizable LQR gains and 'closed loop 2' refers to the full state LQR gains).
- C.3 Tip angle of attack response of the open and closed loop system to a random gust disturbance

C.4 Twist moment response of the closed loop system to a random gust disturbance

C.5 Bending moment response of the closed loop system to a random gust disturbance

D.1 Independent and dependent beam variables

List of Tables

- 3.1 Description of data that defines a flexible member.
- 3.2 Data for defining the thin-wall cross-section layup.
- 3.3 Flexible member finite element data.
- 3.4 Fuselage finite element data.
- 3.5 Kinematics data and derivatives, functions of the current strain values.
- 3.6 Data returned by the aerodynamics module.
- 3.7 Control input format for roll response solver

- 4.1 Properties of the test beam.
- 4.2 Properties of the beam for multiple constraint deflection test.
- 4.3 Stiffness properties of the beam for inter-member constraint test.
- 4.4 Properties of the Goland wing.
- 4.5 Flutter results for the Goland wing.
- 4.6 Highly flexible wing properties of Ref. [14].
- 4.7 Natural frequencies of the highly flexible wing (rad/s).
- 4.8 Flutter results for the highly flexible wing.
- 4.9 Parameters for aileron lift and moment comparison.
- 4.10 Material properties used in the ATR prototype blade cross-sectional analysis.
- 4.11 Non-zero stiffness and inertia results for the ATR prototype blade.
- 4.12 Actuation results for the ATR prototype blade.

- 5.1 Basic vehicle characteristics for numerical studies
- 5.2 Material properties
- 5.3 Physical properties of the baseline small class vehicle
- 5.4 Physical properties of the baseline medium class vehicle
- 5.5 Physical properties of the baseline large class vehicle
- 5.6 Wing natural frequencies for the small class vehicle (Hz)
- 5.7 Wing natural frequencies for the medium class vehicle (Hz)

- 5.8 Wing natural frequencies for the large class vehicle (Hz)
- 5.9 Simulation data for Test Case 1
- 5.10 Simulation data for Test Case 2
- 5.11 Simulation data for Test Case 3
- 5.12 RMS open and closed loop tip response for the small class vehicle
- 5.13 RMS open and closed loop tip response for the medium class vehicle
- 5.14 RMS open and closed loop tip response for the large class vehicle
- 5.15 Percentage change in ply strains due to load redistribution (root station)

Chapter 1

Introduction

1.1 Motivation

In 1903, the Wright Flyer made its maiden flight at Kitty Hawk. Its primary means of lateral control was by warping the wings, which was inspired by observing the wing tips of a hawk in flight. The pilot shifted his hips from side to side to simultaneously deform the wings and control the rudder. These wings were very flexible, but did not pose serious aeroelastic problems at the low flight speed which they were flown.

Aircraft design has come a long way since then. High performance aircraft feature relatively stiff wings with multiple, complex control surfaces. To fly faster and perform high-load maneuvers, wings have been stiffened to guarantee aeroelastic stability, structural integrity, and the prevention of performance degrading wing twist. At high speeds, wing flexibility makes it impossible for the ailerons to provide specified roll rates, due to loss of control effectiveness and subsequent aileron reversal. Today's most advanced aircraft and commercial airliners feature very stiff wings compared to those of

earlier airplanes, in order to minimize aeroelastic warping of the wings. The cost has been an effective increase in wing structural weight.

High-altitude long-endurance (HALE) aircraft feature thin, light wings with a high aspect ratio. Long, slender wings, by their very nature, provide good lift and drag characteristics. However, by virtue of dimensional and structural requirements, these wings generally experience significant amounts of wing deformation. A common approach to counteracting this is to use composite materials to stiffen the wings.

A basic question remains: *Is the flexibility of the wings necessarily a bad thing?* Modern, "stiff" wing aircraft can do many things that the birds cannot. But the contrary is also the case. Nature is not in the business of building hinged, hydraulically actuated ailerons and flaps. But it knows wing flexibility better than any airplane engineer. Birds represent the ultimate in morphing aircraft design. By subtle adjustments in wing camber, some birds can control the unsteadiness of the flow around it, and use it to their advantage. A hawk can fully extend its wings in order to glide, and then retract them into a tucked position, perform a high-speed dive, and swoop up its prey. A morphing airplane would be able to fly in a low-drag configuration to travel long distances to its target, then change to a high-speed configuration to carry out another segment of its mission. The trend towards stiffer wings was partially due to the inability to deal with the aeroelastic repercussions of wing flexibility.

Highly morphing aircraft may be a long way off. But the technology exists today to alter a wing's twist and camber. If the flaps and ailerons were removed from the wing, then a perfectly smooth surface could be achieved, eliminating flow disturbances due to control surface deflection. Wing twist could be the sole means of achieving roll control, and the airplane industry would have come full circle to its very beginnings. The basic technological ingredients to do this are recently coming together. Computational fluid dynamics and the modeling of fluid-structure interactions have advanced greatly in the past two decades. Active materials are now finding applications within every engineering discipline, and are steadily improving in their ability to directionally deform a structure. Nonlinear finite element methods and computer processing speeds have advanced to a degree where design cycles can be greatly reduced. Modern control design is relatively mature in its development.

Active materials that can provide directional authority and high bandwidth could make wing warping control a reality. Designing the wings with conformable surfaces that have active materials integrated within the wing skin and internal structure may lead to lighter designs for several reasons:

1. The active materials are integrated into the structure and contribute to its overall stiffness, eliminating the extra weight associated with hydraulic lines and actuators.
2. Closed-loop wing warping control may extend the flutter and divergence boundaries, increasing the feasible design space.
3. The ability to tailor the spanwise lift distribution based on flight condition may lead to drag reduction, reducing the amount of fuel required for the mission.
4. Twisting the wings to redistribute aerodynamic maneuver loads can reduce peak root stresses in the wings, allowing for a lighter structure.

Structural design of aircraft wings is an inherently iterative process. With highly flexible wings, this is complicated by the fact that the aerodynamic loads depend on the deformed shape of the wing, which in turn depends on the aerodynamic loads. For wing designs using integrated strain actuation (ISA), knowledge of how the active and passive composite constructions affect the overall aeroelastic behavior of the vehicle is critical for a successful design. For wings with embedded strain actuation, the active materials influence significantly the dynamics of the structure, contributing to both stiffness and inertia.

Active wings may have the potential to exploit aeroelastic tailoring concepts to the limit, using wing flexibility to improve performance rather than degrade it. At high dynamic pressure, flaps and ailerons may experience control reversal, due to the aerodynamic twisting moment experienced by the wing when they are deflected. High frequency control surface actuation may excite structural or aeroelastic modes of the complete aircraft, or may produce no effect at all. Wings with embedded strain actuators may have the potential to overcome some of these problems. However, the techniques for the modeling, analysis, and design of such wings have not been brought together into a single framework. A methodology must exist which allows for the aerodynamics,

active flexible structure, and control problems to be considered simultaneously. A framework which ties these sub-disciplines together, in a form suitable for preliminary design, would be very valuable in the evaluation of wing warping control as a viable new aircraft technology.

1.2 Previous Work

There have been several studies in the literature associated with active aeroelastic tailoring, nonlinear aeroelasticity in highly-flexible wings, and aeroservoelastic design optimization, and they are summarized next. A good recent overview of aeroelasticity is presented by Friedmann⁴³. Therein, he discusses the role that the field of aeroelasticity continues to play in modern day aircraft, covering a broad range of topics including nonlinear aeroelasticity, aeroservoelasticity, and the role of new technologies in this field.

1.2.1 Design of Highly Flexible Aircraft

Jones and co-workers have worked on HALE vehicle design during the last decade (e.g., Refs. [1, 2]). They describe some of the design challenges associated with these vehicles. Among other things, they show that standard aircraft design techniques are not applicable for these wings as the altitude and aspect ratio increase. This is because these vehicles tend to be unique in configuration, and therefore the required empirical data needed for these methods is unavailable.

In Ref. [27], Drela modeled the complete flexible aircraft as an assemblage of joined nonlinear beams and applied aerodynamic strip theory. The resulting nonlinear equation set is solved by a full Newton method. Through simplifications of the model, the computational size is made small enough for interactive preliminary design.

Pendaries presents the flight dynamics equations of a free-flexible high-aspect-ratio aircraft with full coupling between rigid and flexible modes implemented in the software *Super Flutty*⁴⁶. A particular instability observed was a coupling between the rigid modes and the first bending mode, which resulted in a flapping-like motion. Propulsion by this flapping motion was then studied as an alternative to propellers.

1.2.2 Nonlinear Aeroelasticity

Patil and co-workers have studied the nonlinear behavior of flexible wings undergoing large deflections. In Ref. [3], the necessity for including higher-order nonlinear effects to accurately model the aeroelastic behavior is detailed. In particular, a linear aeroelastic analysis based on the undeformed geometry will lead to erroneous results when the wings are highly flexible. To accurately model the behavior, the wings must be brought to their nonlinear equilibrium condition before the analysis can proceed. From there, a stability analysis can be performed on the linearized model. It was found that the flutter speed tends to decrease when the wing tip displacements increase. This effect can only be obtained if the wings are first brought to the nonlinear static equilibrium through an iterative process. The main reasons for the changes in aeroelastic behavior as the wings deform are that both the structural modes and the influence of aerodynamic forces onto the structure change considerably as the deformation increases. The first chordwise bending mode of the straight wing, for instance, will tend towards a "rocking" mode as the tip deflection increases, and may coalesce with the first torsion mode. An important result of Ref. [7] is that the total lift predicted from a linear model will generally be higher than the actual lift. As the wing deforms, the local lift forces rotate with the wing, reducing the net lift on the vehicle.

1.2.3 Actuators

Several types of smart materials have been used as actuators in aircraft applications. Giurgiutiu presents a good overview of recent smart materials applications in helicopter and fixed wing aircraft⁴⁴. He reviews induced strain actuator applications and experimental results for both discrete actuation of control surfaces and for distributed induced-strain actuation for deforming the lifting surface. Among other things, the use of PZT-fiber composites as a means of producing twist in helicopter blades is discussed.

Bent and Hagood⁸ were the originators of the work that led to the development of Active Fiber Composites (AFC). These consist of individually fabricated PZT fibers, embedded in an epoxy layer between two layers of interdigitated electrodes (Fig. 1.1). The electrodes are used both for poling and to achieve electric field alignment along the

longitudinally oriented and poled PZT fibers. These actuators achieve a high actuation energy density by exploiting the d_{33} performance of fibers versus the d_{31} actuation of monolithic piezoceramic materials. Rogers and Hagood⁹ applied AFCs to a Mach-scale CH-47D helicopter blade for the experimental study of individual blade control (IBC) applications. A more comprehensive study using AFCs for IBC in a Mach and Froude-scale rotor has been performed under the NASA/Army/MIT Active Twist Rotor program.⁴⁸ Successful forward flight wind-tunnel tests of a four bladed fully active rotor system demonstrated up to 40 dB vibration reduction in closed-loop using integral twist of the blade.

Wilkie et al. describe the design, manufacture and testing of Macro-Fiber Composites (MFC) developed at NASA Langley.⁴⁵ These are similar to AFCs in their basic design and operation. The most significant difference is in the manufacture of the fibers themselves. Whereas the AFC fibers are extruded individually, the MFC fibers (Fig. 1.2) are cut from PZT plates, allowing for a low-cost alternative. Present actuator technology achieves free strains greater than 2000 μ strain peak-to-peak.

Both AFCs and MFCs are high conformable and may be applied to large surfaces. The deformation of an AFC actuator patch is shown in Figure 1.3.

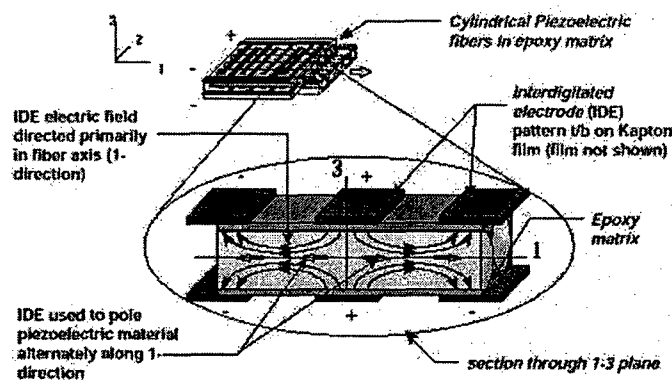


Figure 1.1: Active Fiber Composite (AFC) actuator components and schematic.

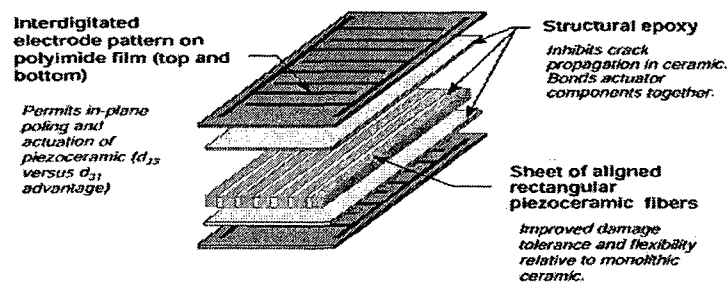


Figure 1.2: Langley Macro-Fiber Composite (MFC) actuator components.



Figure 1.3: Deformation of an AFC actuator patch.

1.2.4 Active Aeroelasticity

One of the first piezoelectric-based active aeroelastic wing studies was conducted by Crawley and co-workers^{4,5,6}. In Ref. [6], a typical section analysis is employed to provide an understanding of the fundamental mechanisms and limitations involved in performing aeroelastic control. Both discrete control surface and induced strain actuation are modeled and examined in various combinations. In Ref. [4] the dominant issues in the preliminary design of a strain actuated aeroelastic wing were examined. Scaling parameters were used to characterize the authority and effectiveness of the piezoelectric actuation. They studied the effects of composite fiber angle and sweep with isotropic piezoelectric wafers to exploit bending-twist couplings for producing wing twist. The resulting active wing hardware was studied at NASA Langley under the PARTI wing program³⁵.

Librescu and co-workers have studied the use of adaptive materials to control the effects of pressure pulse loading on wings⁷. In this study, the wings were modeled as geometrically linear, single-cell, doubly tapered thin walled beams, taking into account the effects of transverse shear, warping restraint, material anisotropy, and the effects of piezoactuators distributed over the surface. The results detail the effects of wing

parameters, such as ply angles, tapering, and actuator size and placement, on the response due to various excitations. A control methodology is implemented which is based on the simultaneous application of an optimal feedback control and a tailoring technique. The devised control scheme augments the performance index with a term that takes into account the time-dependent external load and is basically designed to regulate a desired final state. The electric current, and thus, power required for vibration suppression is derived. Concurrent sensing and actuation of the piezoelectric elements is assumed.

The Active Aeroelastic Wing^{10,39} (AAW) is a joint research effort involving the Navy, Air Force Research Lab, NASA Dryden, and Boeing Phantom Works. The technology integrates aerodynamics, active controls, and structural aeroelastic behavior to maximize aircraft performance. It is basically a Navy F/A-18 with its wings modified to reduce torsional stiffness. Multiple leading and trailing edge control surfaces promote favorable wing twist at high dynamic pressure, eliminating the potential for aileron reversal. The control forces for producing roll come from the deformed wing shape. Results from this benchmark flight program are intended to provide guidance for future wing warping aircraft designs.

Khot has done extensive work in the areas of flexible fighter-type wings, active structures, and multi-criteria optimal structure and controller design, (e.g. Refs. [23-26,36-38]). He and co-workers have explored the AAW concept by using elastic twist and camber deformation in a fighter-type wing (e.g., Ref. [36]). The goal was to enhance roll maneuver performance at high dynamic pressures. Therein, a full-scale conventional wing construction was considered for the assessment of the strain energy required to produce the antisymmetric twist and camber deformation needed for a given roll performance. The actuators that would generate the deformation were not defined in the study and therefore their effects on the aeroelastic characteristics of the wing could not be assessed.

Cesnik and Sahoo⁴⁹ numerically studied the use of high-authority anisotropic piezocomposite actuators applied to the skin of an Uninhabited Combat Aerial Vehicle (UCAV) model. The actuator authority was treated as a design variable and the model was optimized for weight. The results showed that the current state-of-the-art actuators, such as AFC, do not have the authority needed for wing warping roll control for this type

of aircraft. A three to four-fold increase in authority would be needed. The expected properties of actuators under development were determined to have sufficient authority for wing warping control.

Cesnik and Ortega-Morales present a framework for studying the effects of combined bending and twisting actuation on the aeroelastic performance of highly-flexible active composite wings^{32,33}. Therein, the nonlinear active aeroelastic analysis consists of an asymptotically correct active cross-section formulation, geometrically-exact mixed formulation for dynamics of moving beams, and a finite-state unsteady aerodynamics model. LQG controllers were designed to alleviate gust loads and to extend the flutter boundary.

1.2.5 Aeroservoelasticity

Karpel has done extensive work in the areas of aeroelasticity and structural dynamics, interaction with control systems, and analytical and optimization methods (e.g. Refs. [28,29,30,31]). In Ref. [31], an integrated framework is presented which ties the structural and control system design of flight vehicles. An interaction module facilitates the transfer of models during simultaneous structure and control optimization. The control module is constructed so that most general control laws can be incorporated into the aeroservoelastic loop.

Rogers³⁴ studied the nonlinear control of a wing with torsional nonlinearity. Therein, he presents an alternative approach to dynamics cancellation, which requires an accurate model of the actual system. A two degree-of-freedom airfoil with torsional nonlinearity and control surface is modeled. A parameter optimal control, using nonlinear combinations of system states with each nonlinear product term multiplied by a constant coefficient, is evaluated. He shows that the nonlinear parameter optimal control implementation exhibits reduced sensitivity to system variations compared to the partial feedback linearization pitch control design.

1.2.6 Summary Remarks

While different topics have been investigated in the areas of active and/or highly flexible wings, there are still fundamental issues to be addressed. To know whether the integral strain actuated wing concept is viable for high-aspect-ratio configurations, a systematic study with the appropriate modeling capabilities is required. A computational environment must be developed with the required modeling and analysis capabilities, and more detailed studies must be conducted to determine the ability of embedded anisotropic piezocomposite materials to improve the overall performance of the aircraft.

1.3 Present Work

The goal of the present work is to numerically explore the use of anisotropic piezoelectric composite materials (APC) embedded in a flexible composite wing structure as a means of enhancing aeroelastic performance and providing sufficient wing warping control for vehicle maneuvering. The development of a numerical framework to accurately model active flexible wings and their effects on vehicle performance will support this goal. For the purpose of optimal design studies, the numerical design environment must allow for parametric representation of the vehicle geometry and structure. It must also capture the important nonlinear structural and aeroelastic behavior with suitable accuracy for preliminary design. To further support the objective, the effectiveness of integral twist actuation for roll maneuver is compared against conventional aileron control. The effects of wing flexibility and actuator material properties on the aeroelastic behavior are also addressed.

Due to the nature of the problem, this thesis relies heavily on the construction of a numerical environment with the required modeling capabilities. Since no commercial software product exists that combines the required multi-disciplinary capabilities to address this problem (i.e., large nonlinear deflections, aeroelasticity, integral strain actuation, and control design), the numerical environment is constructed from the bottom up. The two major steps in this thesis are the construction of this numerical environment and the use of it to study the behavior of aircraft with flexible active wings and identify ways to improve aircraft performance using integrated strain actuation. The numerical

design environment to study these aircraft was developed in MATLAB¹⁴. The formulation allows for the six rigid degrees of freedom as well as the flexible wing and tail degrees of freedom. A new strain-based finite element formulation for active beams undergoing large three-dimensional deformation was developed in support to this study. The representation leads to a convenient form of the equations of motion and achieves fast convergence of the nonlinear numerical solution. Numerical validation of this new structural formulation is performed against commercial nonlinear finite element codes with good agreement. To model unusual vehicle configurations, such as joined wing aircraft, a method was developed to enforce inter-member constraints while retaining the convergence qualities of the strain-based element approach. These constraints impose an energy penalty on violation of the initial joint geometry.

Chapter 2 presents the theoretical formulation. A description of the vehicle modeling requirements is first presented. The structural equations of motion are then developed. The formulation is sufficiently general to allow for a wide variety of vehicle configurations to be modeled. Obtaining the cross-sectional stiffness and actuation constants is discussed. The kinematics relations for the new strain-based formulation are introduced. Special considerations are made for complex geometries. The finite-state unsteady aerodynamics equations are described and the aeroelastic equations of motion are presented. Different methods of solution of the aeroelastic equations are then described in detail. The detailed derivation of the aerodynamic forces and moments, as well as the induced-flow dynamics is given in Appendix A. A more detailed derivation of the kinematics relations is given in Appendix D.

Chapter 3 details various aspects of the numerical procedure and the layout of the numerical environment. The data for defining the vehicle and the flow of information is discussed. The processing of vehicle data into a form compatible with the strain based finite element formulation is presented. Finally, details of several of the solution algorithms are given.

Chapter 4 is devoted to the basic numerical validation of the new structural formulation and overall numerical implementation. The nonlinear structural model is evaluated for accuracy for both static and dynamic loading. Comparisons are made with previously published data and with commercial finite element packages. The aeroelastic

capabilities are evaluated by considering previously obtained flutter results for both a stiff and a highly flexible wing. Natural frequencies of the highly flexible wing using the present implementation are also compared with previous results and an analytical solution.

Chapter 5 presents the numerical studies. It looks at three representative vehicles for each of three different size/altitude scales. The study is designed to determine the performance of integrated strain actuation in realistic vehicles. A vehicle model using aileron control is first constructed for each vehicle class, based on fielded UAVs with high-aspect-ratio wings. The model design is based on strength and stability requirements and is considered to be a realistic model representation. Two active wing models are then constructed for each vehicle class by modifying the aileron-based design. One design uses standard thickness actuators while the other uses reduced thickness actuators in order to achieve an equal weight design as the aileron wing. Vehicle performance is then evaluated and compared in several areas, including transient and frequency roll response, gust load alleviation, and flutter stabilization. Some of the effects of varying actuator material properties on actuator twist authority are presented. Finally, the ability of the active wing designs to reduce maneuver stresses through load redistribution is examined. The cross-section properties of the wing models are listed in Appendix B. In Appendix C, a more detailed description of the controller design is given.

Finally, Chapter 6 presents an overall summary of this thesis, its main conclusions, and recommendations for future work in this field.

Chapter 2

Theoretical Formulation

This chapter begins with an overview of the vehicle modeling capabilities and basic modeling assumptions. The generic nature of the formulation allows for arbitrary vehicle configurations. The equations of motion for a rigid body with multiple highly flexible appendages (beams) are derived by applying the Principle of Virtual Work. The newly developed strain-based approach for representing large three-dimensional deformations of a beam is presented. A thin-wall multi-cell formulation¹³ for the analysis of composite beam cross-sections is used to obtain the cross-sectional stiffness and actuation constants. This formulation takes into account the effects of anisotropic piezoelectric composites embedded within the passive composite outer surface and spar. The aerodynamics model is presented and combined with the structural system to arrive at the aeroelastic equations of motion for the vehicle. Finally, different solution methods are presented.

2.1 Vehicle Model Description

The capability to model the complete vehicle is needed so one can investigate the effects of large wing deformations, nonlinear aeroelastic behavior, and the impact of wing flexibility on the vehicle stability derivatives. The structures model must accurately capture the low- to mid-frequency range dynamic behavior of the wings, e.g., the first eight to ten modes, since those are generally the most important ones for the wing's aeroelastic behavior. The wings and tails are modeled as nonlinear beams, and may have dihedral, sweep, and pre-twist. The wing surfaces and spar may consist of several layers of active and passive composite materials. Cross-sectional mass, stiffness, and actuation properties are computed at various stations along the wing, based on the airfoil section and layup. A finite state unsteady aerodynamics model is incorporated, which is capable of representing the aerodynamic forces and moments on a lifting surface undergoing large deformations.

The developed framework allows for several vehicle configurations to be modeled, depending on the requirements of the analysis. A conventional vehicle model is shown in Figure 2.1. The fuselage is always modeled as a rigid body.

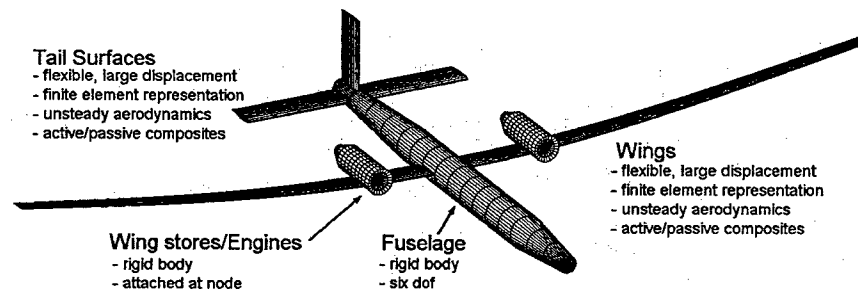


Figure 2.1: A generic vehicle analysis model.

An example of static aerodynamic loads is depicted in Figure 2.2. The aerodynamic force distribution can be tailored so that the forces at the wing tips are zero to approximate the true spanwise distribution. Roll, pitch, and yaw moments may be obtained to determine flight stability derivatives. Flutter stability may be determined by considering the small perturbation response about some nonlinear equilibrium point.

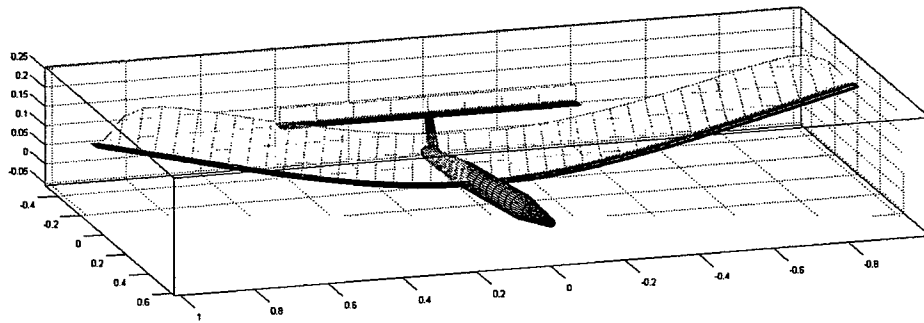


Figure 2.2: A vehicle model showing static aerodynamic loading distributions.

More unusual vehicle designs may also be considered, such as the joined wing vehicle configuration shown in Figure 2.3. Due to the nature of the finite element representation, this type of vehicle requires special attention. As discussed below, since the finite elements are strain-based (the beam strains are the independent degrees of freedom), a method must be employed to impose displacement and rotation compatibility at the joint where the wing members meet.

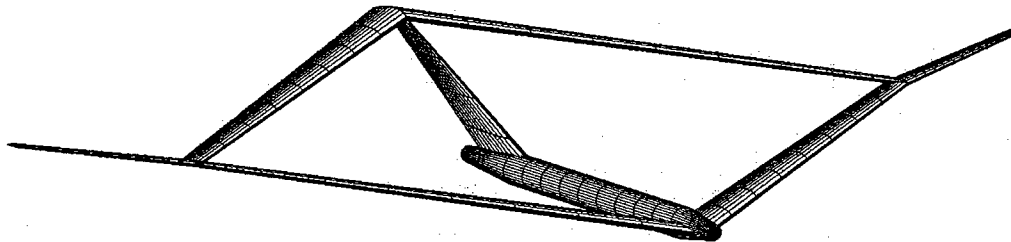


Figure 2.3: A joined wing vehicle model.

2.2 Formulation of the Equations of Motion

The equations of motion are derived by systematically accounting for the work done by all internal and external generalized forces against the corresponding displacements of the system degrees of freedom. The generalized forces contributing to the transfer of work include gravitational, inertial, internal elastic and damping, piezoelectric, aerodynamic, and distributed and point forces and moments. The work contributed by each of the generalized forces is equal to the magnitude of the force times

the corresponding displacement. The work due to distributed forces and moments is integrated over each element based on the assumed displacement functions for the finite element.

The constitutive work relations are first written in terms of the fundamental displacement variables, and then converted to the set of independent vehicle degrees of freedom. Application of the Principle of Virtual Work leads to the final form of the system equations.

2.2.1 Rigid Body Motion

Consider the fuselage as shown in Figure 2.4. Depending on the type of analysis, the tail surfaces may be treated as part of the fuselage, or may be modeled as flexible members attached to the fuselage, and treated in the same way as the wings. The body coordinate system, B , is fixed to the fuselage. The position of the body, P_B , is defined in the global coordinate system, G , which is considered an inertial frame.

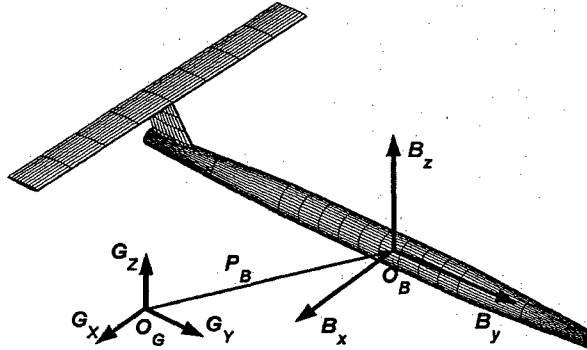


Figure 2.4: Fuselage position and orientation with respect to an inertial frame.

Let the motion of the fuselage be resolved in frame B . Then the virtual work due to inertial forces acting on the body is given by

$$\delta W = -\delta \beta^T M_B \ddot{\beta} \quad (2.1)$$

where

$$\beta = \int \begin{bmatrix} v_B \\ \omega_B \end{bmatrix} dt \quad (2.2)$$

and

$$M_B = \left[\begin{array}{c|c} m_B & -m_B r_{cg}^\times \\ \hline m_B r_{cg}^\times & I_B - m_B r_{cg}^\times r_{cg}^\times \end{array} \right] \quad (2.3)$$

The quantities v_B and ω_B are the linear and angular velocity of the body, resolved in frame B , m_B and I_B are the fuselage mass and inertia matrices, respectively, r_{cg} is the position of the center of gravity of the fuselage, with respect to coordinate system B , and $\delta\beta$ contains virtual displacements and rotations of the body. The matrix $[r_{cg}^\times]$ is given by

$$r_{cg}^\times = \begin{bmatrix} 0 & -r_z & r_y \\ r_z & 0 & -r_x \\ -r_y & r_x & 0 \end{bmatrix} \quad (2.4)$$

Similarly, the virtual work due to gravitational forces acting on the body is given by

$$\delta W = -\delta\beta^T N_B g^B \quad (2.5)$$

where

$$N_B = \left[\begin{array}{c} m_B \\ m_B r_{cg}^\times \end{array} \right] \quad (2.6)$$

and g^B is the gravity vector, resolved in frame B .

The 12x1 position/orientation vector, h_B , establishes the position and orientation of the body with respect to the global coordinate system,

$$h_B = \begin{bmatrix} P_B \\ \vec{B}_x \\ \vec{B}_y \\ \vec{B}_z \end{bmatrix}_{12 \times 1} \quad (2.7)$$

The present method was chosen over Euler angles and quaternions for describing the body position and orientation, allowing for the relationship between the incremental motions, $d\beta$, and the position vector, h_B , to be derived in a form convenient to the present formulation,

$$\frac{d}{dt} h_B = A(v_B, \omega_B) h_B \quad (2.8)$$

where

$$A = \begin{bmatrix} 0 & v_x & v_y & v_z \\ 0 & 0 & \omega_z & -\omega_y \\ 0 & -\omega_z & 0 & \omega_x \\ 0 & \omega_y & -\omega_x & 0 \end{bmatrix} \quad (2.9)$$

Here the components of the A matrix are 3x3 diagonal sub-matrices containing the linear and angular velocity components, resolved in the body frame. An incremental change in body position and orientation is solved by

$$h_B(t + \Delta t) = e^{A\Delta t} h_B(t) \quad (2.10)$$

2.2.2 Member Equations

Because of the general nature of the implementation, the wings and tails are considered to be independent members attached at the root to the fuselage. Each member is an assemblage of elements and may include slope discontinuities in the beam reference line at the node between elements as well as variation in the level of discretization, as shown in Figure 2.5.

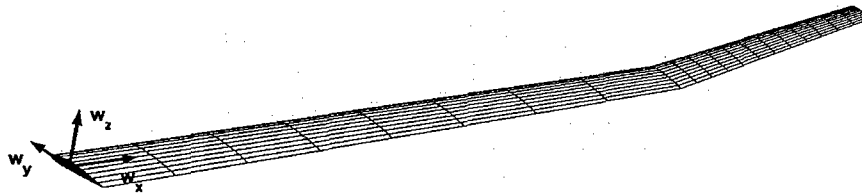


Figure 2.5: Illustration of a single undeformed member.

In the present implementation of the formulation, each member must be rigidly attached at the root to the fuselage. Because of this, the vertical stabilizers shown in Figures. 2.2 and 2.3 cannot be modeled as flexible lifting surfaces. However, all of the lifting surfaces in Figure 2.1 may be modeled as flexible lifting surfaces. This limitation may be overcome through small modification to the formulation, and further modification to the code, but was not pursued in the present work.

A more detailed representation of the wing variables is given in Figure 2.6. The position, p , and coordinate system, w , are functions of the beam coordinate, s , and are defined in the body coordinate system, B .

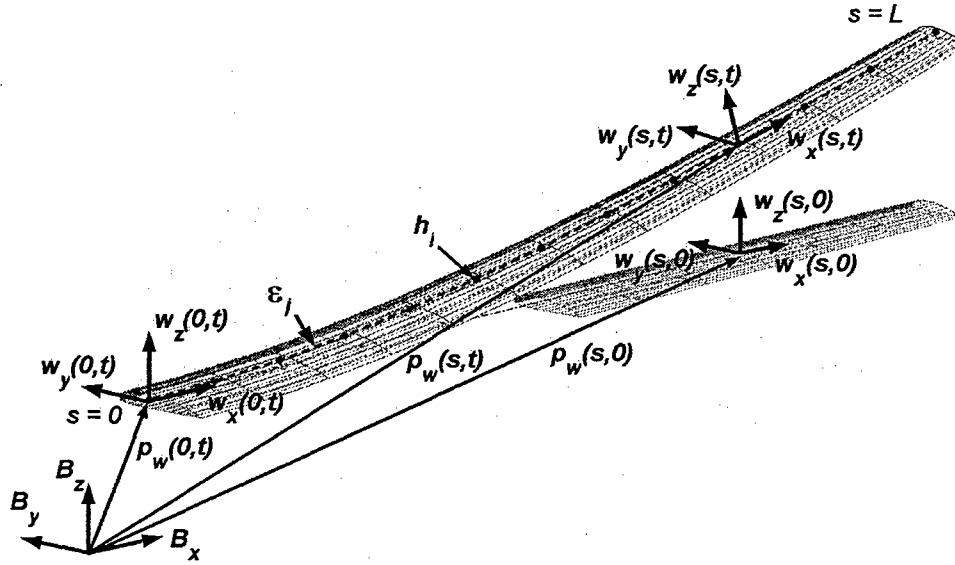


Figure 2.6: Wing geometry variables.

Three auxiliary reference frames are used to aid in the beam reference line definition, as shown in Figure 2.7. Reference frame a defines the orientation of the airfoil. If the wing is swept, then frame a and frame w are not aligned. For the undeformed vehicle, axis a_y lies in the body y - z plane. When the dihedral angle is zero, the axis a_x is parallel to B_x . Frame $a0$ differs from frame a if the zero-lift angle of the airfoil, α_0 , is nonzero, in which case $a0$ is rotated about a_x by $-\alpha_0$. Frame b is aligned with the body frame, B , when the vehicle is undeformed. This reference frame is used to define the orientation of engines and wing stores mounted to the wing, which are generally aligned with the fuselage. All of these reference frames are aligned when the wing is straight (no dihedral, sweep, or twist) and the root angle of attack as well as the airfoil zero-lift angle are equal to zero.

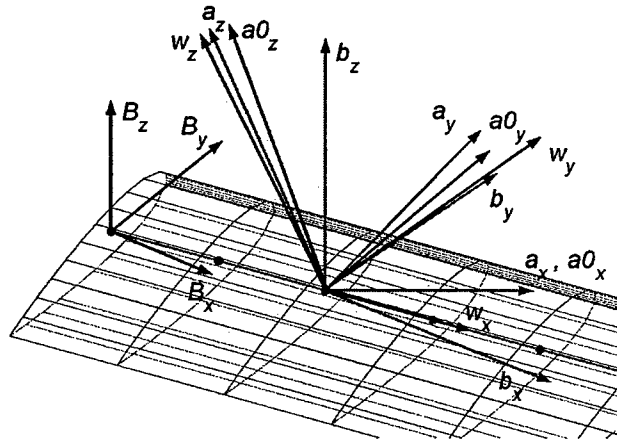


Figure 2.7: Auxiliary reference frames.

Element Description

A new nonlinear beam element was developed for this work, each having four strain degrees of freedom, representing extension, twist, and two bending strains of the beam reference line. The deformations of this element are exemplified in Figure 2.8.



Figure 2.8: Deformations represented by a single element with constant strain distribution.

The strain vector for an element is denoted ε , with its components given by

$$\varepsilon = [\varepsilon_x, \kappa_x, \kappa_y, \kappa_z]^T \quad (2.11)$$

where ε_x is the extensional strain and κ_x , κ_y , and κ_z , represent twisting of the beam reference line, bending about the beam y axis and bending about the beam z axis, respectively. As can be seen, a constant strain distribution over the element can result in a wide range of highly geometrically nonlinear shapes. A single element, for example, can be deformed into a circle or spiral.

The kinematics of the element are described as follows. The beam reference frame, $w(s)$, is a function of the beam coordinate, s . The position and orientation of a point on the reference line are described by the 12x1 vector h , where

$$h(s) = \begin{bmatrix} p(s) \\ w_x(s) \\ w_y(s) \\ w_z(s) \end{bmatrix}_{12 \times 1} \quad (2.12)$$

where p is the position of frame w in the body coordinate system and w_x , w_y , and w_z are the unit direction vectors pointing along the beam axis, toward the leading edge, and normal to the airfoil, respectively, resolved in the body frame. The dependent vector h is related to the independent strain variables through a set of partial differential equations,

$$\frac{\partial}{\partial s} h(s) = A(s)h(s) \quad (2.13)$$

where

$$A(s) = \begin{bmatrix} 0 & 1 + \varepsilon_x(s) & 0 & 0 \\ 0 & 0 & \kappa_z(s) & -\kappa_y(s) \\ 0 & -\kappa_z(s) & 0 & \kappa_x(s) \\ 0 & \kappa_y(s) & -\kappa_x(s) & 0 \end{bmatrix} \quad (2.14)$$

where the blocks are all 3x3 diagonal matrices. Assuming constant strain over the element, the position and orientation of the beam reference line can be obtained given the boundary condition. These are given by

$$h(s) = e^{A(s-s_0)} h_0 = e^{G(s)} h_0 \quad (2.15)$$

where h_0 is the element boundary condition and s_0 is the associated beam coordinate. In the present formulation, each element has three equally spaced nodes where $h(s)$ is evaluated. The solution at the three nodes is given by

$$h_{i,1} = h_0, \quad h_{i,2} = e^{G_i} h_{i,1}, \quad h_{i,3} = e^{G_i} h_{i,2} \quad (2.16)$$

$$G_i = \frac{1}{2} A_i \Delta s_i \quad (2.17)$$

where Δs_i is length of element i .

In the formulation of the finite element matrices, several functions of the beam coordinate must be integrated over the length of the element and are assumed to vary linearly between each of the nodes of the three noded element. Let $\eta(s)$ represent some function of the beam coordinate, s , which may be a physical property, distributed force, or displacement variable. Assuming a linear distribution between each node, $\eta(s)$ can be represented by its value at the three beam coordinates (s_1, s_2, s_3) by

$$\eta(s) = [z_1(s) \ z_2(s) \ z_3(s)] \begin{bmatrix} \eta_1 \\ \eta_2 \\ \eta_3 \end{bmatrix} \quad (2.18)$$

where

$$\begin{aligned} z_1(s) &= \frac{s_2 - s}{s_2 - s_1}, \quad z_2(s) = \frac{s - s_1}{s_2 - s_1}, \quad z_3(s) = 0 & (s_1 \leq s \leq s_2) \\ z_1(s) &= 0, \quad z_2(s) = \frac{s_3 - s}{s_3 - s_2}, \quad z_3(s) = \frac{s - s_2}{s_3 - s_2} & (s_2 \leq s \leq s_3) \end{aligned} \quad (2.19)$$

and the z_i are zero everywhere outside of $[s_1, s_3]$.

Calculation of Cross-Sectional Properties

In the present implementation, the solution for cross-sectional properties is based on Ref. [13], with modifications for compatibility with the present implementation. The formulation presents an asymptotically correct solution for multi-cell, thin-wall beams consisting of active and passive anisotropic composite materials, and accounts for the effects of three-dimensional warping. The solution provides both the cross-sectional stiffness and actuation constants. For the present work, only the formulation for a two-cell beam was implemented based on Ref. [13]. The general form of the constitutive relation can be written as

$$\begin{Bmatrix} F_x \\ M_x \\ M_y \\ M_z \end{Bmatrix} = \begin{bmatrix} K_{11} & K_{12} & K_{13} & K_{14} \\ K_{21} & K_{22} & K_{23} & K_{24} \\ K_{31} & K_{32} & K_{33} & K_{34} \\ K_{41} & K_{42} & K_{43} & K_{44} \end{bmatrix} \begin{Bmatrix} \varepsilon_x \\ \kappa_x \\ \kappa_y \\ \kappa_z \end{Bmatrix} - \begin{Bmatrix} F_x^{(a)} \\ M_x^{(a)} \\ M_y^{(a)} \\ M_z^{(a)} \end{Bmatrix} \quad (2.20)$$

where F_x is the extensional force, M_x , M_y , and M_z are moments about the local x , y and z axes, respectively. The superscript (a) refers to the contribution due the active plies in the cross section. A detailed description of the derivation can be found in [13]. The expression for the internal active forces and moments can be written as

$$\begin{Bmatrix} F_x^{(a)} \\ M_x^{(a)} \\ M_y^{(a)} \\ M_z^{(a)} \end{Bmatrix} = \begin{bmatrix} B_{11} & B_{12} & \cdots & B_{1m} \\ B_{21} & B_{22} & \cdots & B_{2m} \\ B_{31} & B_{32} & \cdots & B_{3m} \\ B_{41} & B_{42} & \cdots & B_{4m} \end{bmatrix} \begin{Bmatrix} v_1 \\ v_2 \\ \vdots \\ v_m \end{Bmatrix} = B_E v \quad (2.21)$$

where v_i is the voltage applied to the i th actuator patch, and m is the total number of actuators in the cross section.

The strain distribution in a given ply in a cross section can be reconstructed, given the beam strains and the applied voltages on the actuator (if the ply is active), and is given by the relation

$$\underline{\varepsilon}_i^{(m)} = \underline{\varepsilon}_i^{(t)} - \underline{\varepsilon}_i^{(a)} \quad (i=1,2,3) \quad (2.22)$$

where $\underline{\varepsilon}_i^{(t)}$, $\underline{\varepsilon}_i^{(a)}$, and $\underline{\varepsilon}_i^{(m)}$ are the total strain, piezoelectric strain, and mechanical stain, respectively, at finely discretized points in the cross section, and i represents the strain direction with respect to the local fiber axes (1-longitudinal, 2-transverse, 3-shear). The total and piezoelectric strains are given by

$$\underline{\varepsilon}_i^{(t)} = E_i \varepsilon \quad (2.23)$$

$$\underline{\varepsilon}_1^{(a)} = \frac{d_{11}}{t} v, \quad \underline{\varepsilon}_2^{(a)} = \frac{d_{12}}{t} v, \quad \underline{\varepsilon}_3^{(a)} = \frac{d_{13}}{t} v \quad (2.24)$$

where ε contains the beam reference line strains for the element, v is the applied voltage, d_{11} , d_{12} , and d_{13} are piezoelectric constants, and t is a characteristic electrode spacing.

The matrices E_i are based on the derivation in [13]. If the ply is a passive composite material, then the piezoelectric components of strain are equal to zero. Given the ply strains, the ply stresses can be evaluated using the constitutive stress-strain relations for the thin-wall model. Ply failure criteria can also be evaluated.

In general, any method capable of returning accurate cross-section properties may be used in the present framework. A more advanced finite element solver, such as VABS¹⁷, would be desirable. It provides a higher level of accuracy when the wall thickness increases and can solve for the properties of any general cross section with limited restrictions. An attempt was made to implement an early version of VABS as the cross section solver for the present work, but because of computational efficiency, that approach was abandoned. An updated version such as UM/VABS¹⁸ has overcome this limitation.

Element Virtual Work

The total virtual work done on an element due to all internal and external forces and moments can be written as

$$\delta W = -\delta h^T \ddot{M} \dot{h} - \delta \epsilon^T K \epsilon + \delta \epsilon^T B_v v - \delta h^T N g + \delta p^T B_F F^{ds} + \delta \theta^T B_M M^{ds} + \delta p^T F^{pt} + \delta \theta^T B_M M^{pt} \quad (2.25)$$

where the terms involved, including the effects of inertial, gravitational, internal strain, piezoelectric, distributed, and point forces and moments, are described below.

Elastic Virtual Work on Element

The total virtual work done on an element of length Δs due to internal elastic strains is given by

$$\delta W = - \int_{s=0}^{\Delta s} \delta \epsilon(s)^T K_E(s) \epsilon(s) ds = -\delta \epsilon^T K \epsilon \quad (2.26)$$

where the element stiffness matrix, K , is found by integrating the cross-section stiffness, $K_E(s)$, over the length of the element. The cross-section stiffness matrix is evaluated at the middle of each element, based on the composite layup and airfoil section, and is

assumed to be constant over the length of the element. Since the element strains are also assumed to be constant, the element stiffness matrix is given by

$$K = K_E \Delta s \quad (2.27)$$

Piezoelectric Virtual Work on Element

The total virtual work done on an element of length Δs due to internal piezoelectric actuation is given by

$$\delta W = \int_{s=0}^{\Delta s} \delta \epsilon(s)^T B_E(s) v(s) ds = \delta \epsilon^T B_v v \quad (2.28)$$

where the $4 \times m$ matrix $B_E(s)$ is the cross-section actuation matrix, which is calculated during cross section analysis, B_v is its integral over the length of the element, and m is the number of independent active plies in the element cross section. Like the element stiffness, the actuation constants are evaluated at the center of the element, and assumed to be constant over the length of the element. The element actuation matrix is given by

$$B_v = B_E \Delta s \quad (2.29)$$

Inertial Virtual Work on a Differential Cross Section Element, ds

A differential wing section of length ds is shown in Figure 2.9. The wing cross section is assumed to maintain its shape while undergoing translations and rotations.

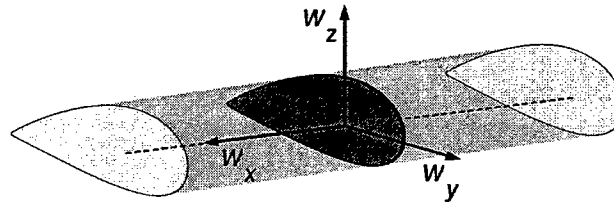


Figure 2.9: Differential beam element.

Let p be the position of a point on the beam reference line with respect to the body coordinate system. Then the position and acceleration of a point, a , in the cross section can be given by

$$\begin{aligned} p_a &= p + xw_x + yw_y + zw_z \\ \ddot{p}_a &= \ddot{p} + x\ddot{w}_x + y\ddot{w}_y + z\ddot{w}_z \end{aligned} \quad (2.30)$$

where $\{x,y,z\}$ is the position of point a in the local coordinate system, $w(s)$. The inertial force acting on a differential volume element, $dA ds$, located at a is given by

$$dF_a = -\rho(\ddot{p} + x\ddot{w}_x + y\ddot{w}_y + z\ddot{w}_z)dA ds \quad (2.31)$$

The virtual work done by inertial forces on the differential volume element is given by

$$\delta W_a = \delta p_a^T dF_a = -\rho(\delta p^T + x\delta w_x^T + y\delta w_y^T + z\delta w_z^T)(\ddot{p} + x\ddot{w}_x + y\ddot{w}_y + z\ddot{w}_z)dA ds \quad (2.32)$$

Integrating over the cross section, the total virtual work done on the beam element due to inertia forces is given by

$$\delta W(s) = -\begin{bmatrix} \delta p^T & \delta w_x^T & \delta w_y^T & \delta w_z^T \end{bmatrix} \begin{bmatrix} m & mr_x & mr_y & mr_z \\ mr_x & A_{xx} & A_{xy} & A_{xz} \\ mr_y & A_{yx} & A_{yy} & A_{yz} \\ mr_z & A_{zx} & A_{zy} & A_{zz} \end{bmatrix} \begin{bmatrix} \ddot{p} \\ \ddot{w}_x \\ \ddot{w}_y \\ \ddot{w}_z \end{bmatrix} = -\delta h(s)^T M(s) \ddot{h}(s) ds \quad (2.33)$$

where $m(s)$ is the cross-sectional mass per unit length, $r(s) = [r_x \ r_y \ r_z]^T$ is the center of gravity position in the local coordinate system, and $A_{ij}(s)$ are related to the components of the cross-sectional inertia matrix by

$$\begin{bmatrix} A_{xx} = \frac{1}{2}(I_{yy} + I_{zz} - I_{xx}) & A_{xy} = I_{xy} & A_{xz} = I_{xz} \\ A_{yx} = I_{yx} & A_{yy} = \frac{1}{2}(I_{xx} + I_{zz} - I_{yy}) & A_{yz} = I_{yz} \\ A_{zx} = I_{zx} & A_{zy} = I_{zy} & A_{zz} = \frac{1}{2}(I_{xx} + I_{yy} - I_{zz}) \end{bmatrix} \quad (2.34)$$

where $I_{ij}(s)$ are the inertia matrix components of the cross section element about p and with respect to the local coordinate system.

Inertial Virtual Work on Element

The total virtual work due to inertial loads on an element of length Δs is found by integrating the cross-sectional virtual work over the length of the element. The vector of position and orientation variables, $h(s)$, and the cross-sectional mass matrix, $M(s)$, are assumed to vary linearly between each of the nodes of the three noded element. The total virtual work on an element due to inertia forces is given by

$$\delta W = - \int_{s=0}^{\Delta s} \delta h(s)^T M(s) \ddot{h}(s) ds = -\delta h^T M \ddot{h} \quad (2.35)$$

where

$$h = \begin{bmatrix} h_1 \\ h_2 \\ h_3 \end{bmatrix}_{36 \times 1} \quad M = \frac{1}{2} \Delta s \begin{bmatrix} \frac{1}{4}M_1 + \frac{1}{12}M_2 & \frac{1}{12}M_1 + \frac{1}{12}M_2 & 0 \\ \frac{1}{12}M_1 + \frac{1}{12}M_2 & \frac{1}{12}M_1 + \frac{1}{2}M_2 + \frac{1}{12}M_3 & \frac{1}{12}M_2 + \frac{1}{12}M_3 \\ 0 & \frac{1}{12}M_2 + \frac{1}{12}M_3 & \frac{1}{12}M_2 + \frac{1}{4}M_3 \end{bmatrix}_{36 \times 36} \quad (2.36)$$

and M_i and h_i are the cross-sectional mass matrix and the nodal position vector, respectively, at node i . Note that the components of h are resolved in the frame B , relative to O_B . The time derivatives of h and the virtual displacements are resolved in frame B , relative to the fixed inertial frame, G .

Gravitational Virtual Work on Element

The virtual work done on a cross section element is derived in a similar way as that due to acceleration, where gravity is treated as a linear acceleration component,

$$\delta W = - \left[\delta p_w^T \quad \delta w_x^T \quad \delta w_y^T \quad \delta w_z^T \right] \begin{bmatrix} m \\ mr_x \\ mr_y \\ mr_z \end{bmatrix} g = -\delta h(s)^T N(s)g \quad (2.37)$$

where g is the gravity vector, resolved in the body frame and $N(s)$ is associated with the mass inertia components. The total virtual work on an element due to gravity is found by integrating Equation (2.37) over the length of the element, given by

$$\delta W = \int_{s=0}^{\Delta s} \delta h(s)^T N(s) g ds = \delta h^T N g \quad (2.38)$$

where

$$N = \frac{1}{2} L \begin{bmatrix} \frac{1}{3} N_1 + \frac{1}{6} N_2 \\ \frac{1}{6} N_1 + \frac{2}{3} N_2 + \frac{1}{6} N_3 \\ \frac{1}{6} N_2 + \frac{1}{3} N_3 \end{bmatrix}_{3 \times 3} \quad (2.39)$$

Virtual Work Due to External Distributed Forces

The total virtual work done on an element due to distributed forces are found by assuming that distributed force and virtual displacements vary linearly between the nodes,

$$\delta W = \int_{s=0}^{\Delta s} \delta p(s)^T F^{dst}(s) ds = \delta p^T B_F F^{dst} \quad (2.40)$$

where

$$\delta p = \begin{bmatrix} \delta p_1 \\ \delta p_2 \\ \delta p_3 \end{bmatrix}_{9 \times 1} \quad B_F = \frac{1}{2} \Delta s \begin{bmatrix} \frac{1}{3} & \frac{1}{6} & 0 \\ \frac{1}{6} & \frac{2}{3} & \frac{1}{6} \\ 0 & \frac{1}{6} & \frac{1}{3} \end{bmatrix}_{9 \times 9} \quad F^{dst} = \begin{bmatrix} F_1^{dst} \\ F_2^{dst} \\ F_3^{dst} \end{bmatrix}_{9 \times 1} \quad (2.41)$$

where δp_i and F_i^{dst} are the virtual displacement and force per unit length at node i , respectively, defined with respect to the body frame.

Virtual Work Due to External Distributed Moments

The virtual work due to external distributed moments are found similarly to the distributed forces

$$\delta W = \int_{s=0}^{\Delta s} \delta \theta(s)^T M^{dst}(s) ds = \delta \theta^T B_M M^{dst} \quad (2.42)$$

where

$$\delta\theta = \begin{bmatrix} \delta\theta_1 \\ \delta\theta_2 \\ \delta\theta_3 \end{bmatrix}_{9 \times 1} \quad B_M = \frac{1}{2} \Delta s \begin{bmatrix} \frac{1}{3} & \frac{1}{3} & \frac{1}{3} & 0 \\ \frac{1}{3} & \frac{2}{3} & \frac{1}{3} & \frac{1}{3} \\ \frac{1}{6} & \frac{1}{3} & \frac{1}{6} & \frac{1}{3} \\ 0 & \frac{1}{6} & \frac{1}{3} & \frac{1}{3} \end{bmatrix}_{9 \times 9} \quad M^{dst} = \begin{bmatrix} M_1^{dst} \\ M_2^{dst} \\ M_3^{dst} \end{bmatrix}_{9 \times 1} \quad (2.43)$$

Virtual Work Due to External Point Forces

The total virtual work done on an element due to external point forces is found by multiplying each force by the corresponding virtual displacement, given by

$$\delta W = \sum_{i=1}^3 \delta p_i^T F_i = \delta p^T F^{pt} \quad (2.44)$$

where

$$\delta p = \begin{bmatrix} \delta p_1 \\ \delta p_2 \\ \delta p_3 \end{bmatrix}_{9 \times 1} \quad F^{pt} = \begin{bmatrix} F_1^{pt} \\ F_2^{pt} \\ F_3^{pt} \end{bmatrix}_{9 \times 1} \quad (2.45)$$

Virtual Work Due to External Point Moments

The total virtual work done on an element due to external point moments similarly is given by

$$\delta W = \sum_{i=1}^3 \delta \theta_i^T M_i = \delta \theta^T M^{pt} \quad (2.46)$$

where

$$\delta \theta = \begin{bmatrix} \delta \theta_1 \\ \delta \theta_2 \\ \delta \theta_3 \end{bmatrix}_{9 \times 1} \quad M^{pt} = \begin{bmatrix} M_1^{pt} \\ M_2^{pt} \\ M_3^{pt} \end{bmatrix}_{9 \times 1} \quad (2.47)$$

Member Virtual Work

The virtual work done on each member is the sum of the element contributions and takes on the same form as that of an element, given by

$$\begin{aligned} \delta W = & -\delta h^T \ddot{M}h - \delta \epsilon^T K \epsilon + \delta \epsilon^T B_v v - \delta h^T N g + \delta p^T B_F F^{dst} + \delta \theta^T B_M M^{dst} \\ & + \delta p^T F^{pt} + \delta \theta^T B_M M^{pt} - \delta h_{rel}^T K_{cl} (h - h_i) - \delta h_{rel}^T C_{cl} \dot{h}_{rel} \end{aligned} \quad (2.48)$$

The matrices K_{cl} and C_{cl} are added here to impose nodal constraints, i.e, a virtual work penalty is associated with the actual position and orientation of a node not matching the initial position and orientation, h_i . The subscript $(\bullet)_{rel}$ indicates that the displacements are relative to the O_B . All of the matrices and vectors here have increased in size by a factor of n , where n is the number of elements in a member.

Member Kinematics

The kinematics for a member is the nonlinear relationship between the strain variables to the position and orientation variables. The position and orientation variables are obtained by marching the element kinematics (Equation 2.16) from the root node to the end of the last element, using the values of the strain variables in each element to march forward. For the three-node elements used in the present model, this procedure is given by

Element 1	$h_{11} = h^*$	$h_{12} = e^{G_1} h_{11}$	$h_{13} = e^{G_1} h_{12}$
Element 2	$h_{21} = D_{21} h_{13}$	$h_{22} = e^{G_2} h_{21}$	$h_{23} = e^{G_2} h_{22}$
\vdots	\vdots	\vdots	\vdots
Element n	$h_{n1} = D_{n,n-1} h_{n-1,3}$	$h_{n2} = e^{G_n} h_{n1}$	$h_{n3} = e^{G_n} h_{n2}$

(2.49)

where h_{ij} is the j th node of the i th element and the D_{ij} matrices contain elements of the direction cosines, accounting for slope discontinuities in the beam reference line at the element junction. Equation (2.49) can be written in matrix form

$$\bar{A}(\epsilon)h = h^* \quad (2.50)$$

where h is now a column matrix containing nodal position and orientation variables for all of the nodes in the member, and h^* is a column matrix containing the constant boundary condition. When the member is fixed at the first node and three node elements are used, this relation is given by

$$\left[\begin{array}{ccc|ccc|c} I & 0 & 0 & 0 & 0 & 0 & 0 \\ -e^{G_1} & I & 0 & 0 & 0 & 0 & 0 \\ 0 & -e^{G_1} & I & 0 & 0 & 0 & 0 \\ \hline 0 & 0 & D_{21} & I & 0 & 0 & 0 \\ 0 & 0 & 0 & -e^{G_2} & I & 0 & 0 \\ 0 & 0 & 0 & 0 & -e^{G_2} & I & 0 \\ \hline 0 & 0 & 0 & 0 & 0 & D_{32} & \ddots \end{array} \right] \begin{bmatrix} h_{11} \\ h_{12} \\ h_{13} \\ h_{21} \\ h_{22} \\ h_{23} \\ \vdots \end{bmatrix} = \begin{bmatrix} h^* \\ 0 \\ 0 \\ 0 \\ 0 \\ 0 \\ \vdots \end{bmatrix} \quad (2.51)$$

The D_{ij} matrices are equal to the identity matrix if the elements are aligned.

The Jacobian matrix containing derivatives of the position and orientation variables with respect to the strain variables is given by

$$dh = \left[\frac{\partial h}{\partial \epsilon} \right] d\epsilon = J_{h\epsilon} d\epsilon \quad (2.52)$$

where

$$J_{h\epsilon} = -\bar{A}^{-1} \left[\frac{\partial}{\partial \epsilon} (\bar{A}h) \right] \quad (2.53)$$

is computed through an iterative routine. The other required Jacobian matrices, which are similarly computed, are $J_{p\epsilon}$, $J_{\theta\epsilon}$, $J_{h\beta}$, $J_{p\beta}$, and $J_{\theta\beta}$, giving the instantaneous relationship between all of the dependent and independent variables. A more complete derivation of the kinematic relations and Jacobian matrices is given in Appendix D.

Rigid Bodies

Rigid bodies represent engines and other nonstructural inertias, as shown in Figure 2.10. In the present implementation, rigid bodies are associated with a node, and may be offset from the node in any direction. To simplify the implementation, the attachment point of the rigid body must be at a node, but this is not necessary in the general formulation. Since the element lengths may be variable, this does not place any restriction on the location of the rigid body.

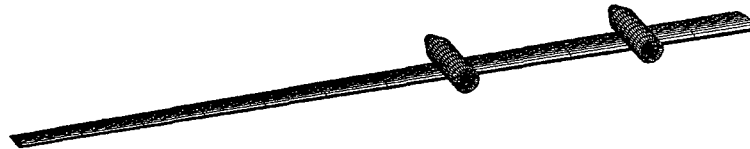


Figure 2.10: Engines and other non-structural masses are modeled as additional rigid bodies.

The virtual work done on the rigid body due to inertial forces and moments is derived similarly to the virtual work done on a beam cross section differential element, with the exception that the rigid body may be initially aligned with the body when the aircraft is unstressed. The virtual work is fundamentally written in frame b , which is initially aligned with the body frame, B , when the aircraft is undeformed. Constant matrices containing rotation variables from frame b to frame w are used to express the virtual work in terms of the dependent beam displacement variables, h . The inertial virtual work acting on the rigid body is given as

$$\delta W = -(\delta h^b)^T M \ddot{h}^b \quad (2.54)$$

where

$$h^b = \begin{bmatrix} p \\ b_x \\ b_y \\ b_z \end{bmatrix} \quad (2.55)$$

For compatibility with the present formulation, the virtual work relation must be written in terms of the coordinate system, w , for each node. The constant rotation matrix from frame b to frame w is computed at each node during vehicle initialization, and is given by

$$C^{wb} = C^{BwT} C^{Bb} \quad (2.56)$$

where C^{Bw} and C^{Bb} are the rotation matrices from frames w and b , respectively, to frame B . The rotation matrices may be written in terms of the unit direction vectors as

$$C^{Bb} = [b_x \ b_y \ b_z], \quad C^{Bw} = [w_x \ w_y \ w_z] \quad (2.57)$$

Equation (2.56) can be rewritten as

$$C^{Bb} = C^{Bw} C^{wb} \quad (2.58)$$

allowing for the relationship between the unit direction vectors of coordinate systems b and w to be written as

$$[b_x \ b_y \ b_z] = [w_x \ w_y \ w_z] C^{wb} \quad (2.59)$$

The following relations apply between b and w .

$$\begin{aligned} b_x &= C_{11}^{wb} w_x + C_{21}^{wb} w_y + C_{31}^{wb} w_z \\ b_y &= C_{12}^{wb} w_x + C_{22}^{wb} w_y + C_{32}^{wb} w_z \\ b_z &= C_{13}^{wb} w_x + C_{23}^{wb} w_y + C_{33}^{wb} w_z \end{aligned} \quad (2.60)$$

The relationship between coordinate systems b and w can now be written in column matrix form as

$$h^b = D^{bw} h \quad (2.61)$$

where

$$D^{bw} = \begin{bmatrix} I & 0 & 0 & 0 \\ 0 & C_{11}^{wb} & C_{21}^{wb} & C_{31}^{wb} \\ 0 & C_{12}^{wb} & C_{22}^{wb} & C_{32}^{wb} \\ 0 & C_{13}^{wb} & C_{23}^{wb} & C_{33}^{wb} \end{bmatrix}_{12 \times 12} \quad (2.62)$$

and each of the blocks of D^{bw} is a 3x3 diagonal matrix. In terms of the primary beam displacement variables, the virtual work is written as

$$\delta W = -\delta h^T D^{bw} M D^{wb} \ddot{h} \quad (2.63)$$

The rigid body mass matrix is then added to the wing mass matrix at the appropriate node location.

Member Fuel Mass Matrix

The mass of fuel is taken into account in the vehicle input file, and may be distributed between the fuselage and wings. Each wing is assigned a fuel distribution function and a fuel percentage value. The fuel distribution function basically specifies how much fuel is assigned to each element. The integral of this function over the length of the wing is equal to the fraction of fuel stored in that wing. When multiplied by the total fuel mass in the vehicle, the wing fuel mass distribution is determined. Rotational inertia of the fuel is also taken into account using local chord length information. Fuel swash is beyond the scope of this thesis, therefore the fuel is treated in the same way as flexible structural mass.

The fuel mass matrix for member i is then formed in the same way as the structure mass matrix, except that it is normalized by the total vehicle fuel mass, so that it can be stored as a constant matrix. The virtual work due to fuel mass inertia is given by

$$\delta W_i = -\delta h_i^T M_{f_i} \ddot{h}_i \quad (2.64)$$

After multiplication by the total fuel on board, this matrix is added to the structure mass matrix.

Member Fuel Gravity Influence Matrix

The influence of gravity on the wing fuel mass is identical to the influence of gravity on the wing structure mass. The work done by gravity on the fuel mass is given by

$$\delta W_i = \delta h_i^T N_{f_i} g \quad (2.65)$$

After multiplication by the total fuel mass on board, this matrix is added to the structural gravity influence matrix.

Member Internal Damping Matrix

Internal damping forces are assumed to arise from material strain rates in the same way as internal elastic forces arise from internal strains. Therefore, stiffness proportional damping is employed in the form

$$C = \alpha K \quad (2.66)$$

where C and K are the structure damping and stiffness matrices, respectively, for a member. The proportionality constant, α , is either directly supplied by the user, or solved for numerically, such that a desired first mode structural damping coefficient is achieved.

Member Nodal Constraint Stiffness and Damping Matrices

It may be desired to constrain a node to maintain its initial absolute or relative position or orientation from the undeformed geometry. For the absolute case, an example

of this type of constraint is shown in Figure 2.11, where the middle node is pinned. Because of the strain-based finite element implementation used here, imposition of such constraints requires special attention.

To impose this absolute constraint (relative, inter-member nodal constraint is discussed next), an effective spring/damper is applied to the node, using very large stiffness and damping constants.

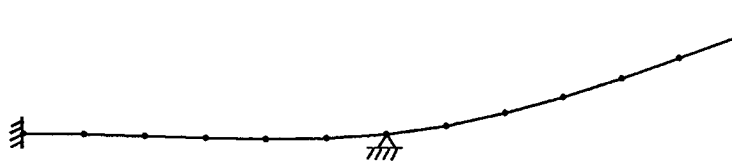


Figure 2.11: Example of a nodal constraint.

A work penalty is associated with the error in position and orientation from the initial value, as given by

$$\delta W = -\delta h^T K_{c1} (h - h_i) \quad (2.67)$$

where h_i is the position/orientation vector for the member, corresponding to the undeformed geometry. The matrix, K_{c1} , is a diagonal matrix, where the only non-zero entries correspond to the node being constrained. For numerical stability in many of the solution processes, damping is also imposed at the node. The virtual work done against these damping forces is given by

$$\delta W = -\delta h^T C_{c1} \dot{h} \quad (2.68)$$

where C_{c1} has the same form as the stiffness matrix. The virtual displacement and velocity are taken with respect to the body frame.

Inter-member Nodal Constraints

Until now, each member has been able to be treated independently of one another. Thus, most of the matrices take on a block diagonal form when all the member matrices are assembled. In the case of a joined wing configuration, a constraint must be imposed at the joint where the front and rear wings meet.

Let the i th node of member m be coincident with the j th node of member n upon initialization. Then the reference frames, b , for each node are automatically aligned on

initialization, since they are both aligned with the body frame. Then the nodal stiffness constraint can be written

$$\delta W = -(\delta h_{mi}^b - \delta h_{nj}^b)^T K (h_{mi}^b - h_{nj}^b) \quad (2.69)$$

where h^b is defined in Equation (2.55). Using Equation (2.61), the virtual work can be rewritten as

$$\delta W = -[\delta h_{mi}^T \quad \delta h_{nj}^T] \begin{bmatrix} D_{mi}^{wb} K D_{mi}^{bw} & -D_{mi}^{wb} K D_{nj}^{bw} \\ -D_{nj}^{wb} K D_{mi}^{bw} & D_{nj}^{wb} K D_{nj}^{bw} \end{bmatrix} \begin{bmatrix} h_{mi} \\ h_{nj} \end{bmatrix} = -[\delta h_{mi}^T \quad \delta h_{nj}^T] \begin{bmatrix} K_{11} & K_{12} \\ K_{21} & K_{22} \end{bmatrix} \begin{bmatrix} h_{mi} \\ h_{nj} \end{bmatrix} \quad (2.70)$$

For each inter-member nodal constraint, corresponding stiffness matrix components are added to the global inter-member stiffness matrix, K_c , and the total virtual work on the vehicle due to all inter-member stiffness constraints is given by

$$\delta W = -\delta h^T K_c h \quad (2.71)$$

where h now corresponds to the column matrix of position and orientation variables for all of the members, arranged in a suitable order. K_c is large and very sparse and has the form

$$K_c = \begin{bmatrix} 0 & K_{12} & \cdots & K_{1n} \\ K_{21} & 0 & & K_{2n} \\ \vdots & & 0 & \vdots \\ K_{n1} & K_{n2} & \cdots & 0 \end{bmatrix} \quad (2.72)$$

A damping matrix, C_c , complements the stiffness matrix, and has the same form.

As an example of the effectiveness of this constraint, the wing tips of a conventional aircraft are artificially imposed to coincide. The wings are given an initial curvature, and the wing tips are drawn together in an iterative solution process. The intermediate steps in the solution process are illustrated in Figure 2.12.

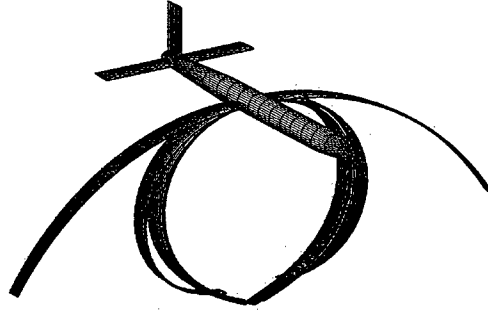


Figure 2.12: Example of inter-member constraint; eight steps to solution.

Total Virtual Work on a Member

The total virtual work on member i , with the exception of that due to inter-member constraints, can now be written in terms of the beam strain variables and rigid body variables,

$$\begin{aligned}
 \delta W = & -\delta \epsilon^T J_{he}^T M J_{he} \ddot{\epsilon} - \delta \epsilon^T J_{he}^T M J_{h\beta} \ddot{\beta} - \delta \epsilon^T C \dot{\epsilon} - \delta \epsilon^T K (\epsilon - \epsilon_i) \\
 & + \delta \epsilon^T B_v v + \delta \epsilon^T J_{he}^T N g + \delta \epsilon^T J_{pe}^T B_F F^{dst} + \delta \epsilon^T J_{pe}^T F^{pt} + \delta \epsilon^T J_{\theta e}^T B_M M^{dst} \\
 & + \delta \epsilon^T J_{\theta e}^T M^{pt} - \delta \epsilon^T J_{he}^T C_c \dot{h} - \delta \epsilon^T J_{he}^T K_c (h - h_i) - \delta \beta^T J_{h\beta}^T M \ddot{h}_{he} \ddot{\epsilon} \\
 & - \delta \beta^T J_{h\beta}^T M \ddot{h}_{h\beta} \ddot{\beta} + \delta \beta^T J_{h\beta}^T N g + \delta \beta^T J_{p\beta}^T B_F F^{dst} + \delta \beta^T J_{p\beta}^T F^{pt} \\
 & + \delta \beta^T J_{\theta\beta}^T B_M M^{dst} + \delta \beta^T J_{\theta\beta}^T M^{pt}
 \end{aligned} \quad (2.73)$$

where β is the body motion given in Equation (2.2).

The virtual work equations are arranged in a convenient form for assembly into the global structural equations of motion. For simplicity, the nodal constraints are omitted from the work equation since they represent a special case and are usually all zero. The resulting equations for the member are

$$\delta W = \begin{bmatrix} \delta \epsilon^T & \delta \beta^T \end{bmatrix} \left(- \begin{bmatrix} M_{FF} & M_{FB} \\ M_{BF} & M_{BB} \end{bmatrix} \begin{bmatrix} \ddot{\epsilon} \\ \ddot{\beta} \end{bmatrix} - \begin{bmatrix} C_{FF} & C_{FB} \\ C_{BF} & C_{BB} \end{bmatrix} \begin{bmatrix} \dot{\epsilon} \\ \dot{\beta} \end{bmatrix} - \begin{bmatrix} K_{FF} & K_{FB} \\ K_{BF} & K_{BB} \end{bmatrix} \begin{bmatrix} \epsilon \\ \beta \end{bmatrix} + R \right) \quad (2.74)$$

$$R = \begin{bmatrix} K_{FF} \\ K_{BF} \end{bmatrix} \epsilon_i + \begin{bmatrix} B_{vF} \\ B_{vB} \end{bmatrix} v + \begin{bmatrix} B_{fdF} \\ B_{fdB} \end{bmatrix} F^{dst} + \begin{bmatrix} B_{mdF} \\ B_{mdB} \end{bmatrix} M^{dst} + \begin{bmatrix} B_{fpF} \\ B_{fpB} \end{bmatrix} F^{pt} + \begin{bmatrix} B_{mpF} \\ B_{mpB} \end{bmatrix} M^{pt} + \begin{bmatrix} B_{gF} \\ B_{gB} \end{bmatrix} g \quad (2.75)$$

$M_{FF} = J_{he}^T M J_{he}$	$C_{FF} = C$	$K_{FF} = C$	$B_{fdF} = J_{pe}^T B_F$	$B_{fpF} = J_{pe}^T$	$B_{vF} = B_v$
$M_{FB} = J_{he}^T M J_{h\beta}$	$C_{FB} = 0$	$K_{FB} = 0$	$B_{fdB} = J_{p\beta}^T B_F$	$B_{fpB} = J_{p\beta}^T$	$B_{vB} = 0$
$M_{BF} = J_{h\beta}^T M J_{he}$	$C_{BF} = 0$	$K_{BF} = 0$	$B_{mdF} = J_{\theta e}^T B_M$	$B_{mpF} = J_{\theta e}^T$	$B_{gF} = J_{he}^T N$
$M_{BB} = J_{h\beta}^T M J_{h\beta}$	$C_{BB} = 0$	$K_{BB} = 0$	$B_{mdB} = J_{\theta\beta}^T B_M$	$B_{mpB} = J_{\theta\beta}^T$	$B_{gB} = J_{h\beta}^T N$

(2.76)

The subscripts F and B correspond to the flexible and the body degrees of freedom. With the exception of the Jacobian matrices, all of the matrices in these equations are constant and stored only once for a given structure.

2.2.3 Global Structural Equations of Motion

By accounting for all of the virtual work due to all of the system degrees of freedom and external loads, the instantaneous equations of motion for the system are obtained by applying the Principle of Virtual Work. The instantaneous second order matrix equations of motion for the vehicle is given by

$$M(q)\ddot{q} + C\dot{q} + Kq = R(q, \dot{q}, \ddot{q}) \quad (2.77)$$

$$R = B_{\epsilon_i} \epsilon_i + B_v v + B_{fd} F^{dst} + B_{md} M^{dst} + B_{fp} F^{pl} + B_{mp} M^{pl} + B_g g \quad (2.78)$$

where

$$q = \begin{bmatrix} \epsilon_1 \\ \epsilon_2 \\ \vdots \\ \epsilon_n \\ \beta \end{bmatrix} = \begin{bmatrix} \epsilon \\ \beta \end{bmatrix} \quad (2.79)$$

and n is the number of members attached to the body. The strain vector, ϵ , now includes all of the strain variables for all flexible members, and all of the matrices have been appropriately sized, based on vehicle configuration and member discretization.

2.2.4 Aerodynamics

The aerodynamic loads used in the present work are based on the formulation of Refs. [11] and [12]. The theory calculates loads on a thin deformable airfoil section undergoing large motion in an incompressible subsonic flow, with small deformations about that motion. The airloads used here take the large motion part of the airloads presented in Ref. [11], and rewrite them to be consistent with the present motion

variables. A Taylor expansion is used to express the aerodynamic forces in terms of an instantaneous part and a linear perturbation. The full derivation is given in appendix A, and the results are presented here. The lift, moment, and drag on a thin two-dimensional airfoil section are given by

$$\begin{aligned} L &= 2\pi\rho b A_{L,eff} - \pi\rho b^2 \ddot{z} - \pi\rho b^2 d\ddot{\alpha} \\ M &= 2\pi\rho b (dA_{L,eff} + bA_{M,eff}) - \pi\rho b^2 d\ddot{z} - \pi\rho (b^2 d^2 + \frac{1}{8}b^4)\ddot{\alpha} \\ D &= -2\pi\rho b (\dot{z}^2 + d^2\dot{\alpha}^2 + \lambda_0^2 + 2d\dot{\alpha}\dot{z} + 2\lambda_0\dot{z} + 2d\dot{\alpha}\lambda_0) \end{aligned} \quad (2.80)$$

where b is the semichord, d is the distance of the mid-chord in front of the reference axis, and λ_0 is the induced flow due to free vorticity. The motion variables are defined in Figure 2.13.

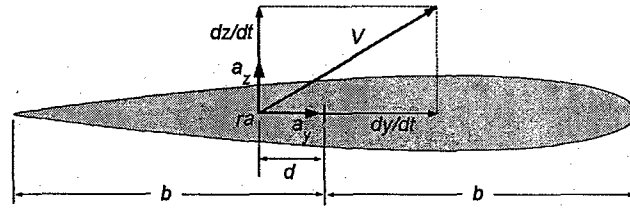


Figure 2.13: Airfoil motion definition

The terms $A_{L,eff}$ and $A_{M,eff}$ are weighted effective angle of attack terms, derived in the present formulation, given by

$$\begin{aligned} A_{L,eff} &= \dot{y}^2 \alpha_{L,eff} = \left(-\dot{y}\dot{z} + \left(\frac{1}{2}b - d\right)\dot{y}\dot{\alpha} - \dot{y}\lambda_0 \right) \\ A_{M,eff} &= \dot{y}^2 \alpha_{M,eff} = \left(-\frac{1}{2}\dot{y}\dot{z} - \frac{1}{2}d\dot{y}\dot{\alpha} - \frac{1}{2}\dot{y}\lambda_0 \right) \end{aligned} \quad (2.81)$$

where $\alpha_{L,eff}$ and $\alpha_{M,eff}$ are considered to be the effective angle of attack terms which depend on the instantaneous angle of attack as well as other velocity terms. This approach was chosen because it eliminates singularities when the flight speed is zero and allows for a simplified stall model to be implemented. When $\alpha_{L,eff}$ and $\alpha_{M,eff}$ reach their stall values, the lift and moment no longer increase for increasing angle of attack. After linearization and transformation to body coordinates, the airloads are treated as the distributed forces acting on the structure model. At time $t = t_0 + \Delta t$, the forces are given by

$$F^{aero}(t) = F^{aero}(t_0 + \Delta t) = F_0(V_{B0}, \dot{p}_0, \dot{\theta}_0, \lambda_0) + F_{\ddot{p}}\ddot{p}(t) + F_{\ddot{\theta}}\ddot{\theta}(t) + F_{\dot{p}}\Delta\dot{p} + F_{\dot{\theta}}\Delta\dot{\theta} + F_{\theta}\Delta\theta + F_{\lambda}\Delta\lambda \quad (2.82)$$

where F_0 and the derivative matrices on the right hand side are given in Appendix A.

Applying the structure linearization, the airloads can also be written in terms of the structure degrees of freedom, and the set of inflow variables,

$$F^{aero}(t) = F_0(q_0, \dot{q}_0, \lambda_0) + F_{\ddot{q}}\ddot{q} + F_{\dot{q}}\Delta\dot{q} + F_q\Delta q + F_{\lambda}\Delta\lambda \quad (2.83)$$

The size of Δt depends on the level of deformation of the structure. For a wing undergoing only small deformations, then the system may be treated as a linear system, and Equation (2.83) holds for all time. However, if large structure deformation occurs, or the flight condition is changing, then the static loads and derivative matrices in Equation (2.83) must be continuously updated.

The inflow is obtained through the finite-state inflow theory¹², and is represented in terms of N states ($\lambda_1, \lambda_2, \dots, \lambda_N$) as

$$\lambda_0 = \frac{1}{2} \sum_{n=1}^N b_n \lambda_n \quad (2.84)$$

where the b_n are found by least squares method, and the λ_n can be expressed as the solution of a set of differential equations, expressed here as

$$\dot{\lambda} = E_1\lambda + E_2\ddot{z} + E_3\ddot{\alpha} + E_4\dot{\alpha} \quad (2.85)$$

where the matrices, E_i , are based on the description given in Ref. 12. Using the kinematic relations of Section 2.2.2, the inflow rate of change, expressed in terms of the independent system degrees of freedom is given by

$$\dot{\lambda} = L_1\lambda + L_2\ddot{q} + L_3\dot{q} \quad (2.86)$$

where λ is resized here to represent all of the inflow states on all of the elements. The forces and moments due to aileron deflection also enter the airloads equation, and are included in Appendix A. Gust and turbulence wind velocities are treated as airfoil velocity components, i.e., the gust velocity is added to the airfoil velocity vector (Fig.

2.13) after transformation to local airfoil coordinates. Corrections to the spanwise aerodynamic load distribution may be applied to allow for the loads to diminish at the wing tips, as described in Appendix A.

2.2.5 Aeroelastic System Equations

The structural mass, damping, and stiffness matrices need to be modified to include the aerodynamic terms which depend on structure motion. Furthermore, the inflow states must be included in the state vector. Let the system be linearized at time, t_0 , where the state variables are given by $q_0, \dot{q}_0, \lambda_0$. Then the system matrices may be given at the time $t = t_0 + \Delta t$ by

$$M\ddot{q}(t) + C(\dot{q}(t)) + K(q(t)) = F_0(q(t_0), \dot{q}(t_0), \lambda(t_0)) + \Delta F + R, \quad (2.87)$$

where F_0 contains the instantaneous aerodynamic loads evaluated at t_0 , and ΔF contains the change in aerodynamic loads due to small changes in the state variables (from Equation 2.83), and R , contains all other time dependent loads. By moving the state dependent terms in ΔF over to the left hand side, and making the appropriate corrections to the right hand side, the aeroelastic equations of motion is given by

$$Q_1 \dot{x} = Q_2 x + Q_3 R \quad (2.88)$$

where

$$x = \begin{bmatrix} q \\ \dot{q} \\ \lambda \end{bmatrix}, \quad Q_1 = \begin{bmatrix} I & 0 & 0 \\ 0 & M & 0 \\ 0 & -L_1 & I \end{bmatrix}, \quad Q_2 = \begin{bmatrix} 0 & I & 0 \\ -K & -C & -D \\ 0 & L_3 & L_2 \end{bmatrix}, \quad Q_3 = \begin{bmatrix} 0 \\ I \\ 0 \end{bmatrix} \quad (2.89)$$

$$R = B_1 v + B_2 F_0^{aero} + B_3 M_0^{aero} + B_4 q_0 + B_5 \dot{q}_0 + B_6 \lambda_0 + B_4 h_{B_0} + B_6 \varepsilon_i \quad (2.90)$$

and ε_i is the strain vector for the undeformed geometry (wing initial twist and curvature). The user supplied distributed and point forces and moments are omitted here for simplicity, since they generally do not apply in an aeroelastic analysis, but have been implemented in the code.

Equation (2.90) can be put into state space form, and expressed as

$$\dot{x} = Ax + Bu + BF_0 + Gw \quad (2.91)$$

where

$$A = Q_1^{-1}Q_2, \quad B = Q_1^{-1}Q_3 \quad (2.92)$$

The inputs u are the control inputs, w contains the disturbance and all other right hand side inputs, and G is the assembly of influence matrices corresponding to w . The range of validity of the linearization is dependent on the amount of structural deformation over the time of integration. If large motions are involved, then the system matrices must be updated either on each time step, or after a predetermined number of time steps. If body motions are involved, then the position and orientation of the body must be updated on each time step according to Equation (2.3).

2.3 Solution of the Aeroelastic System

Several types of solution to the aeroelastic system are considered. The most basic solution is the steady state deformation of the wings under a given flight condition. The vehicle velocity vector is resolved in the body frame. Given the altitude, the air density and strength of gravity are interpolated from a look-up table. The solution provides basic structural data as well as the distribution of aerodynamic loads and the net forces and moments acting at the body origin. Stability derivatives may be obtained by applying small perturbations to the body orientation.

The trim solution is the determination of the body angle of attack such that the aerodynamic forces balance weight. Since the vehicle undergoes nonlinear deflections, the solution is obtained by iterative calculation of the steady state solution, while varying the body angle of attack. A desired load factor may be included in this solution to represent a maneuver condition.

The stability analysis is the determination of the aeroelastic system poles under a given flight condition. The system poles may be evaluated over a set of varying conditions to construct the root locus of system poles for the evaluation of instabilities. The most useful root locus evaluation uses a range of flight speeds along with the corresponding trim angle data.

The time-stepping solution is used in linearized and nonlinear simulations. In the linearized solution, the system is brought to a nonlinear steady state equilibrium, and then linearized only once. For the nonlinear solution, the system matrices are evaluated at regular time increments, depending on how fast the system parameters vary. In certain cases, the linearized flexible structure matrices may be sufficient over the whole simulation, while the integration of body motion, actuator saturation, and aerodynamic stall present the dominant nonlinearities.

2.3.1 Steady State Solution

The steady state solution determines the values of the flexible degrees of freedom under the applied external loads. User supplied point and distributed loads, and nodal constraints will be omitted for clarity. For a given member under the influence of aerodynamic loads (F^{aero} , M^{aero}), applied strain actuation voltage, v , and gravity, g , the steady state solution is

$$K\varepsilon_{ss} = R_{ss} \quad (2.93)$$

where

$$R_{ss} = K\varepsilon_i + B_v v + B_f(\varepsilon_{ss})F_{ss}^{aero}(\varepsilon_{ss}, \rho, V^B) + B_m(\varepsilon_{ss})M_{ss}^{aero}(\varepsilon_{ss}, \rho, V^B) + B_g(\varepsilon_{ss})g \quad (2.94)$$

The airspeed and orientation of the body must be given. Equation (2.93) must be solved iteratively to reach the solution. One method would be to start with an initial strain vector, compute the right hand side, R_k , and solve for the next solution

$$\varepsilon_{k+1} = K^{-1}R_k \quad (2.95)$$

After each iteration, convergence would be checked for by comparing the norm of the change in the solution with a previously established tolerance.

This approach tends to lead to numerical instability when the wings are very flexible due to geometric stiffening and large changes in the right hand side from one solution to the next, or when the dynamic pressure is very high. With numerical damping added, the incremental solution becomes

$$\epsilon_{k+1} = \alpha_N \epsilon_k + (1 - \alpha_N) K^{-1} R_k \quad (2.96)$$

where α_N is the numerical damping parameter, between 0 and 1, that determines the solution step size. When $\alpha_N = 1$, the solution is stationary. When $\alpha_N = 0$, the solution is equivalent to Equation (2.95). The typical range for good convergence is $0.2 < \alpha_N < 0.5$.

2.3.2 Trim Solution

The trim solution is computed by considering force balance in the body frame, B . Let F_z , F_y , W_z , and W_y be the components of the net aerodynamic force and vehicle weight, resolved in the body frame, as shown in Figure 2.14. The thrust vector, T , is assumed to be aligned with B_y . The trim condition is given by

$$\begin{aligned} F_z + W_z &= 0 \\ F_y + W_y + T &= 0 \end{aligned} \quad (2.97)$$

The thrust vector is assumed to balance the net force along B_y .

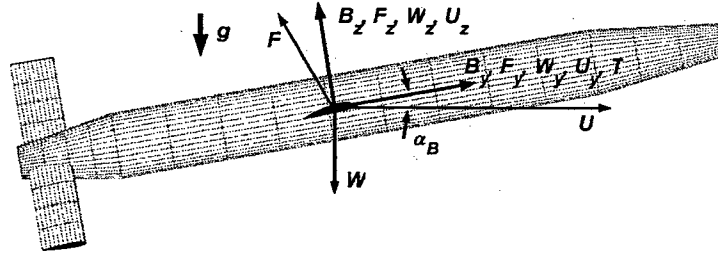


Figure 2.14: Net forces represented in the body frame.

In the solution of the trim body angle, the first relation in Equation (2.97) is used in all of the different iterative procedures. In the present implementation, the trim solution is found using the bisection method. Upper and lower bounds on the solution are first obtained to within 1° by incrementally varying the body angle and evaluating the steady state solution. Several bisection iterations are then performed until the trim condition is satisfied to within a specified tolerance.

2.3.3 Stability Analysis

Stability analyses may be carried out on several vehicle configurations. The full vehicle model is not necessary when symmetry can be exploited. The following systems may be analyzed in a stability analysis:

1. Single cantilevered wing with no body motion
2. Single cantilevered wing with vertical body motion
3. Two wings with roll motion only
4. Full vehicle model with six body degrees of freedom

In any case, the vehicle should be trimmed at each point at which the system poles are evaluated. The steady state solution is obtained and the instantaneous aeroelastic system matrices are computed. The eigenvalues of the state space A matrix determine the stability properties at the particular flight condition. Eigenvalues with positive real parts indicate instability. A root locus analysis may proceed by repeated evaluation of the aeroelastic system eigenvalues as a parameter, such as flight speed, is varied.

2.3.4 Time Stepping Solution

The time stepping solution is done using Equation (2.88). Consider the system at times t_k and $t_{k+1} = t_k + \Delta t$, where Δt is small. Let the instantaneous system matrices be computed at time t_k . Then the system equations at time step t_k are given by

$$Q_1^k \dot{x}^k = Q_2^k x^k + Q_3^k R^k \quad (2.98)$$

Assuming that the system matrices and load vector do not vary over the short interval from t_k to t_{k+1} , then the equations of motion at time t_{k+1} are given by

$$Q_1^k \dot{x}^{k+1} = Q_2^k x^{k+1} + Q_3^k R^k \quad (2.99)$$

Assuming linear variation over the short time step, the state at time t_{k+1} is given by

$$x^{k+1} = x^k + \frac{1}{2} \Delta t (\dot{x}^k + \dot{x}^{k+1}) \quad (2.100)$$

Then the following relations hold

$$Q_1^k x^{k+1} = Q_1^k x^k + \frac{1}{2} \Delta t (Q_1^k \dot{x}^k + Q_1^k \dot{x}^{k+1}) \quad (2.101)$$

$$Q_1^k x^{k+1} = Q_1^k x^k + \frac{1}{2} \Delta t (Q_2^k x^k + Q_2^k x^{k+1} + 2Q_3^k R^k) \quad (2.102)$$

$$(Q_1^k - \frac{1}{2} \Delta t Q_2^k) x^{k+1} = (Q_1^k + \frac{1}{2} \Delta t Q_2^k) x^k + \Delta t Q_3^k R^k \quad (2.103)$$

The solution at time step $k+1$ is obtained as

$$x^{k+1} = (Q_1^k - \frac{1}{2} \Delta t Q_2^k)^{-1} \left[(Q_1^k + \frac{1}{2} \Delta t Q_2^k) x^k + \Delta t Q_3^k R^k \right] \quad (2.104)$$

The system matrices are then updated based on the current state and the solution is marched forward in time.

Chapter 3

Numerical Implementation

This chapter gives a basic overview of the structure of the numerical implementation. It is intended not to be a complete description of the workings of the code. Instead, some of the more important data that is used to define the vehicle and loading conditions is presented. Several of the analysis routines are described, and some basic input/output relationships are given.

3.1 Introduction

The numerical environment for the present work was implemented entirely using the MATLAB¹⁴ software package, which is a high-level language for technical computing. Beyond the standard MATLAB environment, the Control and Optimization toolboxes are utilized. Data are stored in several basic data types which include multi-dimensional arrays, structure arrays, and cell arrays. Each of these data types have been very useful in the implementation and organization of the code.

The numerical environment was intended to be very flexible, while maintaining a standardized data structure. User input is required in defining the geometry, finite

element discretization, and some aerodynamic and structure parameters. The block diagram of the basic flow of information in the implemented code is shown in Figure 3.1. The software is initiated by supplying a vehicle input file and the name of the vehicle configuration solver to be used to process the input data.

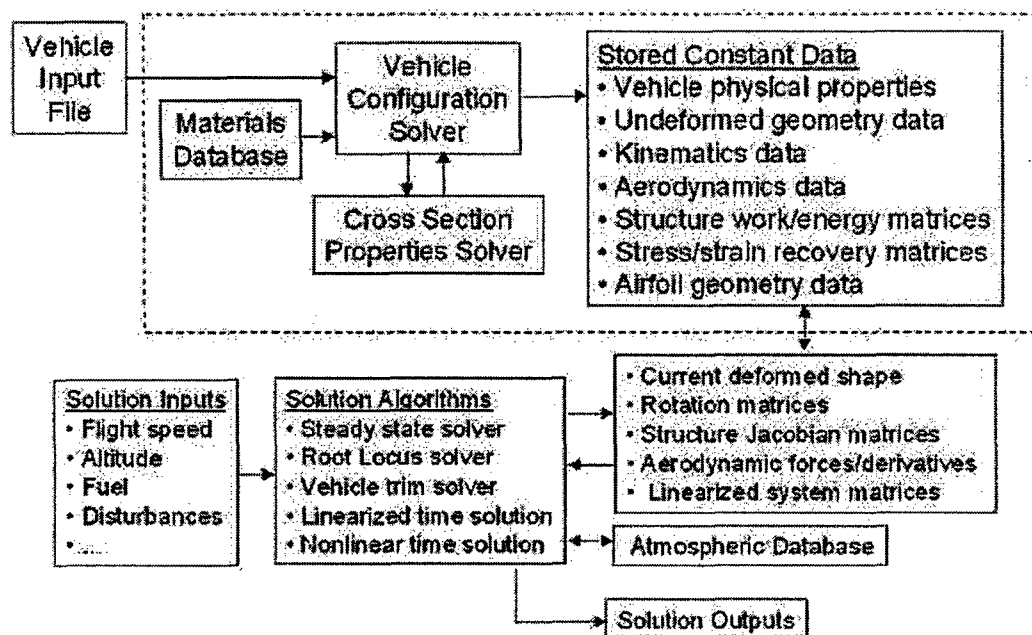


Figure 3.1: Information flow in the present representation

3.2 Processing Vehicle Configuration Data

The vehicle input file (VIF) and the vehicle configuration solver (VCS) are user-designed/modified MATLAB functions which, together, generate and format all of the data necessary to fully define the vehicle. The VIF is designed to pass any information to the VCS which may be varied during parametric studies and should not be hard coded, e.g., wing length, dihedral, airfoil, discretization, etc. The VCS is also designed by the user to take in these inputs and use them to generate the required formatted outputs. The VIF contains default inputs which may be manipulated in user routines containing loops for studying the effects of parameter variations or for design optimization. The VCS must also be directed to a user defined cross-section layup file, which returns formatted information describing the layup and location of plies within the airfoil section.

An example of some vehicle configuration parameters is shown in Figure 3.2. The basic flow of information in the VCS is shown in Figure 3.3.

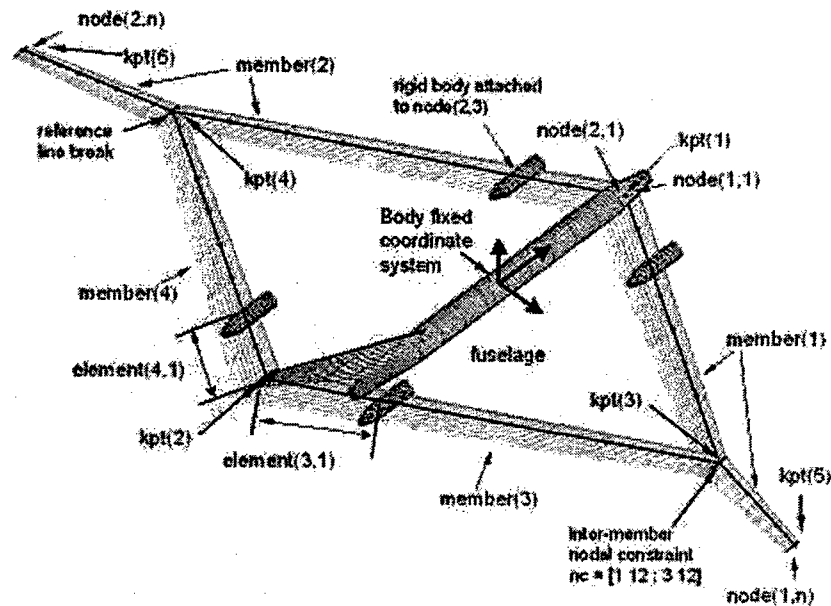


Figure 3.2: Vehicle configuration parameters

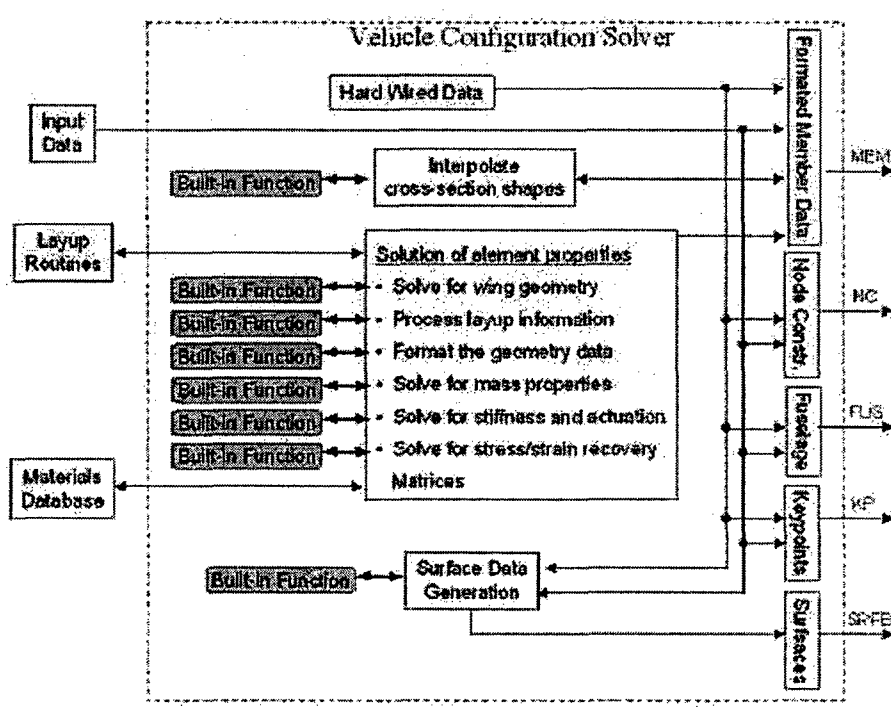


Figure 3.3: Vehicle configuration data solver block diagram

The cross section interpolation function, which is called during VCS solution allows for all of the airfoils between the root and the tip to be interpolated, giving the capability to represent wings such as the one shown in Figure 3.4. The tapered wing shown has a NACA4415 airfoil at the root and a NACA9410 airfoil at the tip, with 10° of twist from root to tip.

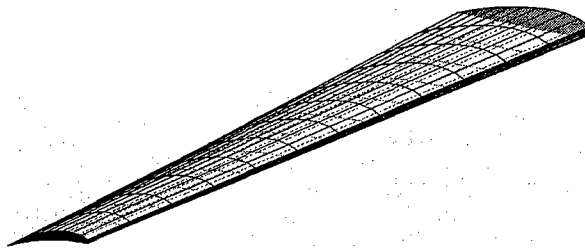


Figure 3.4: Wing model with varying airfoil from root to tip.

The data returned by the VCS are stored in the global structure arrays MEM, FUS, NC, and SRFB. The information contained in these structures is described below. MEM is a $n \times 1$ structure array, where n is the number of members attached to the body. The data it contains defines all the properties and necessary data for each member. The data contained for each member are given in table 3.1.

Table 3.1: Description of data that defines a flexible member.

MEM(i).Data - Formatted Flexible Member Data	
Data	Description
nel	total number of elements in the member
np	total number of nodes in the member
nels	number of elements in each sub-member
nps	number of nodes in each sub-member
kpts	keypoints which define the location of the beam ends and breaks in the beam reference line
nkpts	number of key points for the member
fueldst	member fuel distribution function (row array)
fuelpercent	fraction of fuel stored in each wing
direct	beam strain integration direction with respect to the beam x-axis
af	NACA 4-digit airfoil designation at each keypoint of the wing/tail
AF	structure containing airfoil contour discretization data and point

	locations
ch	chord lengths at the keypoints of the wing/tail
chord	chord lengths at each node
aoa	angle of attack at the keypoints with respect the body
zaoa	zero lift angle with respect to the airfoil reference line
Adst	span-wise aerodynamic distribution correction, at each node
NU	lift curve slope correction from assumed value of 2π
flapdims	flap dimensions for each element as a fraction of chord
xle	distance from the reference line to the leading edge for each element, x-direction
yle	distance from the reference line to the leading edge for each element, y-direction
mass	mass per unit length at the ends of each element
Ixx	xx-component of inertia per unit length matrix, at end of each element
Ixy	xy-component of inertia per unit length matrix, at end of each element
Ixz	xz-component of inertia per unit length matrix, at end of each element
Iyy	yy-component of inertia per unit length matrix, at end of each element
Iyz	yz-component of inertia per unit length matrix, at end of each element
Izz	zz-component of inertia per unit length matrix, at end of each element
cgx	location of the center of gravity for each element in the beam x-direction
cgy	location of the center of gravity for each element in the beam y-direction
cgz	location of the center of gravity for each element in the beam z-direction
K11	extensional stiffness for each element
K12	extension/twist coupling stiffness for each element
K13	extension/y-bend coupling stiffness for each element
K14	extension/z-bend coupling stiffness for each element
K22	torsional stiffness for each element
K23	torsion/y-bend coupling stiffness for each element
K24	torsion/z-bend coupling stiffness for each element
K33	bending stiffness about the beam y-axis for each element
K34	y-bend/z-bend coupling stiffness for each element
K44	bending stiffness about the beam z-axis for each element
Bv1	extension actuation array for each element
Bv2	twist actuation array for each element
Bv3	y-bending actuation array for each element
Bv4	z-bending actuation array for each element
nact	number of active plies in each element
LAY0	structure containing layup designation for each element
LAYUP	structure containing formatted layup information for each node
GEOM	structure containing formatted geometric data for cross section properties calculation
propsK	structure containing stiffness, actuation, and ply stress/strain recovery data
propsM	structure containing mass and inertia data
PLY	structure containing ply stress/strain recovery matrices and indexing

	data
nrbs	number of rigid bodies attached to member
nc	node constraints for the undeformed geometry, if any exist

If rigid bodies are attached to the member, then additional data is returned, defining the mass and inertia properties of the rigid bodies, as well as the nodes to which they are attached and surface data used in the plotting routines.

The one dimensional structure, FUS, contains the fuselage mass, inertia matrix, and center of gravity offset of the body with respect to the body-fixed coordinate system. In later processing, the finite element matrices associated with the fuselage are also stored here.

The inter-member nodal constraint structure, NC, contains data on which nodes are constrained by one another, and which degree of freedom is constrained. The array size depends upon how many constraints exist.

SRFB is a $m \times 3$ cell-array that contains the X, Y, Z mesh data for the fuselage surfaces, where m is the number of independent mesh surfaces. Several surface generation routines exist which allows the user to easily construct the fuselage based on a small amount of inputs. The mesh surfaces are initialized to be aligned with the global coordinate system.

3.2.1 Cross Section Layup Specification

The cross-section layup is defined by the following parameters, and must be supplied at each node. A layup file must be associated with each vehicle configuration file, except for when the wing stiffness and mass properties are directly supplied. The vehicle configuration solver passes input data to the layup file for each node to be processed, and receives the following formatted data in a structure array, presented in table 3.2.

Table 3.2: Data for defining the thin-wall cross-section layup

LAY0(i).Data - Formatted Layup Data	
Data	Description
x_web	location of the spar with respect to the leading edge

mat_t	material Identification numbers for each top surface ply
mat_b	material Identification numbers for each bottom surface ply
mat_w	material Identification numbers for each spar ply
xstart_t	top surface ply start locations as a fraction of chord
xstop_t	top surface ply top locations as a fraction of chord
xstart_b	bottom surface ply start locations as a fraction of chord
xstop_b	bottom surface ply stop locations as a fraction of chord
angle_t	top surface ply angles
angle_b	bottom surface ply angles
angle_w	spar ply angles
thick_t	top surface ply thicknesses
thick_b	bottom surface ply thicknesses
thick_w	spar ply thicknesses
active_t	top ply active callouts
active_b	bottom ply active callouts
active_w	spar active callouts
nact	total number of active plies
nplies_t	total number of plies on top surface
nplies_b	total number of plies on bottom surface
nplies_w	total number of plies in the spar

The formatted layup specification file along with other geometric data is processed by VCS. The airfoil contour point data is mapped onto contour coordinates. The contour discretization is adjusted and nodes are inserted for spar attachment. The contour node data are grouped according to integration paths for calculation of cross-section stiffness and actuation constants.

3.3 Initializing the Vehicle Geometric Variables

The vehicle initialization routine returns the $n \times 1$ structure array KIN0, which contains geometric and kinematic data for the undeformed vehicle. Based on keypoint, angle of attack, and other information stored in the structure MEM, the routine solves for the dihedral and sweep angles, direction vectors and rotation matrices corresponding to all relevant coordinate systems at each node, beam reference line coordinates, and the initial twist curvature of the beam reference line. At each node there are four basic coordinate systems: beam, airfoil, aerodynamic, and body aligned. The aerodynamic and airfoil coordinate systems differ due to the zero lift angle of the particular airfoil. The beam and airfoil coordinate systems differ when there is geometric sweep. The body

aligned coordinate system is aligned with the body coordinate system when the vehicle is undeformed. All four of these coordinate systems move rigidly together when a node translates and rotates, and therefore they are related to one another by constant rotation matrices which are stored in the structure array, KIN0. Some steps in the construction of the direction vectors are described below. All of the geometric variables are defined in the body frame, whose axes will be denoted $\{1,2,3\}$ here, as shown in Figure 3.5.

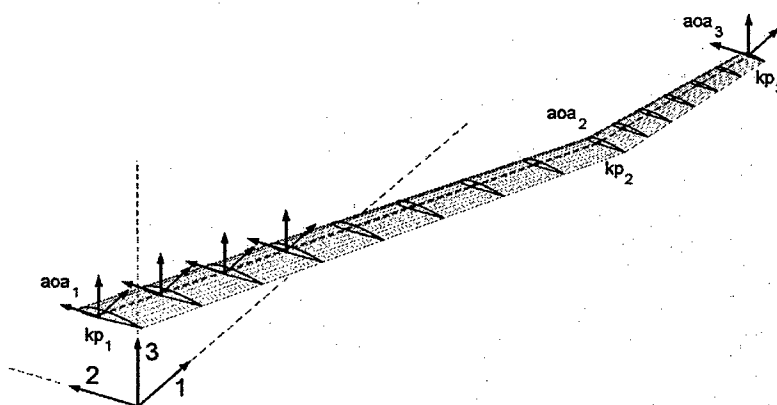


Figure 3.5: Member construction

For each member, the following operations are performed:

1. Compute and store the element lengths, ds , given the keypoint locations and number of elements on each section of the member.
2. Compute the beam reference line nodal coordinate vector, s_p .
3. Compute the sweep and dihedral angles for each sub-member. To do this, first the beam and airfoil x -axes must be determined for each sub-member. For the first sub-member shown above, the beam x -axis is aligned with the reference line, joining keypoints 1 and 2, and is given by

$$w_x = (kp_2 - kp_1) / |kp_2 - kp_1| \quad (3.1)$$

The airfoil x -axis lies in the 1 - 3 plane. The projection of w_x onto the 1 - 3 plane is co-linear with a_x ,

$$a_{x0} = \begin{bmatrix} w_x(1) \\ 0 \\ w_x(3) \end{bmatrix}, \quad a_x = a_{x0} / \|a_{x0}\| \quad (3.2)$$

The dihedral angle is the rotation of the airfoil x -axis about the 2-axis.

$$dih = \arcsin[(e_1 \times a_x) \cdot e_2] \quad (3.3)$$

The sweep angle is related to the cross product of the airfoil and beam x -axis by

$$sweep = \arcsin[\|a_x \times w_x\| \cdot \text{sign}(e_3^T \cdot (a_x \times w_x))] \quad (3.4)$$

The dihedral and sweep angles for each sub-member are computed in this way, and then stored as values at each node.

4. The rotation matrices are then constructed, using dihedral, sweep, and pre-twist information. At each node, i , the matrices are computed as follows:

$$\begin{aligned} c_i^{Ba} &= \text{rot}(2, dih_i) \cdot \text{rot}(1, \alpha_i) \\ c_i^{Ba0} &= \text{rot}(2, dih_i) \cdot \text{rot}(1, \alpha_i - \alpha_{0i}) \\ c_i^{Bw} &= \text{rot}(2, dih_i) \cdot \text{rot}(1, sweep_i) \cdot \text{rot}(2, -dih_i) \cdot c_i^{Ba} \\ c_i^{Bb} &= I_{3 \times 3} \\ c_i^{aw} &= c_i^{BaT} \cdot c_i^{Bw} \\ c_i^{a0w} &= c_i^{Ba0T} \cdot c_i^{Bw} \\ c_i^{bw} &= c_i^{BbT} \cdot c_i^{Bw} \end{aligned} \quad (3.5)$$

where the function *rot* performs a rotation about the specified axis, i.e.,

$$\text{rot}(1, \alpha) = \begin{bmatrix} 1 & 0 & 0 \\ 0 & \cos \alpha & -\sin \alpha \\ 0 & \sin \alpha & \cos \alpha \end{bmatrix} \quad (3.6)$$

5. The unit direction vectors are then extracted

$$\begin{aligned} a_{xi} &= c_i^{Ba} \cdot e_1, & a_{yi} &= c_i^{Ba} \cdot e_2, & a_{zi} &= c_i^{Ba} \cdot e_3 \\ a_{x0i} &= c_i^{Ba0} \cdot e_1, & a_{y0i} &= c_i^{Ba0} \cdot e_2, & a_{z0i} &= c_i^{Ba0} \cdot e_3 \\ w_{xi} &= c_i^{Bw} \cdot e_1, & w_{yi} &= c_i^{Bw} \cdot e_2, & w_{zi} &= c_i^{Bw} \cdot e_3 \\ b_{xi} &= c_i^{Bb} \cdot e_1, & b_{yi} &= c_i^{Bb} \cdot e_2, & b_{zi} &= c_i^{Bb} \cdot e_3 \end{aligned} \quad (3.7)$$

6. The initial twist curvature is then computed for each element, j , using the beam unit vectors at the first and third nodes of the element, given by

$$\kappa_{x_j} = \frac{1}{ds_j} \arcsin[(w_{y1_j} \times w_{y3_j}) \cdot w_{x3_j}] \quad (3.8)$$

The components of κ_x are suitably arranged into the initial strain vector, ϵ_i , for the undeformed geometry.

7. All of the nodal coordinate system data are then suitably arranged into global matrices for the entire member and stored for access by other routines.

3.4 Construction of the Finite Element Matrices

In conventional nonlinear displacement-based finite element formulations, the finite element matrices are not constant, but must be re-computed based on the current deformed geometry, involving integration over each element. In the present formulation, the finite element matrices are all constant, and need to be computed only once. However, most of these matrices involve the integration of dependent position and orientation variables over the element. The Jacobian matrices relating the independent strain variables to the dependent variables needs to be updated when the structure deforms.

The member and fuselage data are processed by the software during initialization, and used to construct the finite element matrices. The resulting flexible member matrices are stored in a the structure array MTRX, and the fuselage matrices are added to FUS. Their description are given in tables 3.3 and 3.4.

Table 3.3: Flexible member finite element data.

MTRX(i).Data - Member Finite Element Matrices		
Data	Matrix Description	Virtual Work Expression
M	structure mass (M)	$\delta W = -\delta h^T M \ddot{h} = -(\delta \epsilon^T J_{he}^T + \delta b^T J_{hb}^T) M (J_{he} \ddot{\epsilon} + J_{hb} \ddot{b})$
Mfuel	fuel mass (M_f)	$\delta W = -\delta h^T M_f \ddot{h} = -(\delta \epsilon^T J_{he}^T + \delta b^T J_{hb}^T) M_f (J_{he} \ddot{\epsilon} + J_{hb} \ddot{b})$
K	structure stiffness (K)	$\delta W = -\delta \epsilon^T K (\epsilon - \epsilon_i)$
C	structure damping (C)	$\delta W = -\delta \epsilon^T C \dot{\epsilon}$
MG	structure gravity influence (N)	$\delta W = \delta h^T N g = (\delta \epsilon^T J_{he}^T + \delta b^T J_{hb}^T) N g$
MGfuel	fuel gravity (N_f)	$\delta W = \delta h^T N_f g = (\delta \epsilon^T J_{he}^T + \delta b^T J_{hb}^T) N_f g$
Bv	actuation influence (B_v)	$\delta W = \delta \epsilon^T B_v v$
Bf	distr. force influence (B_f)	$\delta W = \delta p^T B_f F^{dst} = -(\delta \epsilon^T J_{pe}^T + \delta b^T J_{pb}^T) B_f F^{dst}$
Bm	distr. moment influence (B_m)	$\delta W = \delta p^T B_m M^{dst} = -(\delta \epsilon^T J_{\theta e}^T + \delta b^T J_{\theta b}^T) B_m M^{dst}$

KC	nodal constraint stiffness (K_c)	$\delta W = -\delta h^T K_c (h - h_i) = -\delta \epsilon^T J_{he}^T K_c (h - h_i)$
CC	nodal constraint damping (C_c)	$\delta W = -\delta h^T C_c \dot{h} = -\delta \epsilon^T J_{he}^T C_c \dot{h}$

Table 3.4: Fuselage finite element data.

FUS.Data - Fuselage Finite Element Matrices		
Data	Matrix Description	Virtual Work Expression
M	mass matrix (M_B)	$\delta W = -\delta b^T M_B \ddot{b}$
Mfuel	fuel mass matrix (M_{Bf})	$\delta W = -\delta b^T M_{Bf} \ddot{b}$
MG	gravity influence matrix (N_B)	$\delta W = -\delta b^T N_B g$
MGfuel	fuel gravity influence matrix (N_{Bf})	$\delta W = -\delta b^T N_{Bf} g$

3.5 Kinematics Solver

The kinematics solver routine is passed the current values of the strain variables for a member, and returns a structure containing the node positions and direction vectors, as well as global rotation matrices for the member. This physical information is needed for the calculation of aerodynamic loads, analysis, and plotting.

A second routine calculates the derivatives of the position and orientation variables with respect to the strain variables and body motion. The relevant data obtained are given in table 3.5.

Table 3.5: Kinematics data and derivatives, functions of the current strain values.

h	column of node positions and direction vectors
CBa	global member rotation matrix from airfoil to body frame
CBa0	global member rotation matrix from aerodynamic to body frame
CBw	global member rotation matrix from beam to body frame
CBb	global member rotation matrix from body aligned to body frame
dhdeps	Jacobian matrix relating change in beam strains to changes in the position/orientation vector relative to the body coordinate system
dpdeps	Jacobian matrix relating change in beam strains to linear displacements
dthdeps	Jacobian matrix relating change in beam strains to rotational displacements
dhdb	Jacobian matrix relating body displacements and rotations to changes in the position/orientation vector relative to the body coordinate system
dpdb	Jacobian matrix relating body displacements to nodal translations
dthdb	Jacobian matrix relating body displacements to nodal rotations

3.6 Aerodynamics Module

The aerodynamics routine returns the instantaneous aerodynamic forces and moments per unit length at each node, as well as their derivatives with respect to all of the motion variables, aileron angles, inflow states, and gust inputs. It is required to know the absolute velocity at each node with respect to still air, as well as the rotation matrices from the aerodynamic reference frames of the deformed geometry to the body reference frame. This routine may be called several times during a nonlinear steady state solution, or on every time step during a nonlinear time stepping solution. The data returned from a call to this routine are defined in table 3.6.

Table 3.6: Data returned by the aerodynamics module.

aero(i).Data - Aerodynamic Forces and Derivatives	
Data	Description
F0	static part of the aerodynamic force vector (column)
M0	static part of the aerodynamic moment vector (column)
Mh	hinge moments on flaps and ailerons (column)
F_pddot	aerodynamic forces due to linear accelerations (matrix)
F_thetaddot	aerodynamic forces due to rotational accelerations (matrix)
F_pdot	aerodynamic forces due to linear velocities (matrix)
F_thetadot	aerodynamic forces due to rotational velocities (matrix)
F_dtheta	aerodynamic forces due to small rotations (matrix)
F_gust_y	aerodynamic forces due to y-directed gust inputs (matrix)
F_gust_z	aerodynamic forces due to z-directed gust inputs (matrix)
F_dbeta	aerodynamic forces due to change in aileron angles (matrix)
F_betadot	aerodynamic forces due to aileron angle rates (matrix)
F_dbeta	aerodynamic forces due to aileron angle accelerations (matrix)
F_lambda	aerodynamic forces due to change in inflow states (matrix)
M_pddot	aerodynamic moments due to linear accelerations (matrix)
M_thetaddot	aerodynamic moments due to rotational accelerations (matrix)
M_pdot	aerodynamic moments due to linear velocities (matrix)
M_thetadot	aerodynamic moments due to rotational velocities (matrix)
M_dtheta	aerodynamic moments due to small rotations (matrix)
M_gust_y	aerodynamic moments due to y-directed gust inputs (matrix)
M_gust_z	aerodynamic moments due to z-directed gust inputs (matrix)
M_dbeta	aerodynamic moments due to change in aileron angles (matrix)
M_betadot	aerodynamic moments due to aileron angle rates (matrix)
M_dbeta	aerodynamic moments due to aileron angle accelerations (matrix)
M_lambda	aerodynamic moments due to change in inflow states (matrix)
LD_lambda	inflow rate of change due to current inflow state (matrix)

LD_pddot	inflow rate of change due to linear accelerations (matrix)
LD_thetaddot	inflow rate of change due to rotational accelerations (matrix)
LD_thetadot	inflow rate of change due to rotational velocities (matrix)
LD_betadot	inflow rate of change due to aileron angle rate (matrix)
LD_betaddot	inflow rate of change due to aileron angle acceleration (matrix)

3.7 Obtaining the Aeroelastic System Matrices

The aeroelastic system matrices correspond to the instantaneous second order plant dynamics and effects of external influences on the plant. They are functions of the strain variables and their first and second time derivatives, as well as the orientation and motion of the body, aerodynamic parameters, flight speed, and inflow states. The first order inflow dynamics matrices are also computed, since they contain terms that depend upon the current state vector as well as its derivative. The second order quasi-steady aeroelastic system dynamics matrices are combined with the inflow dynamics into a state-space representation. A schematic of the input/output relationship is shown in Figure 3.6.

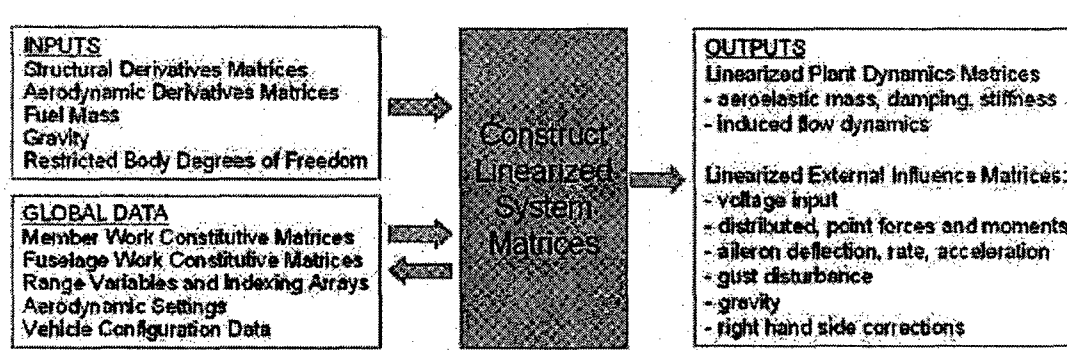


Figure 3.6: Input/output relationship for aeroelastic system update

In a linear aeroelastic analysis, these matrices would be evaluated only once, based on the undeformed vehicle geometry. In a stability analysis or a linearized transient solution, the system matrices may be solved several times in an iterative procedure to determine the steady state solution before the analysis takes place using last system update. In a fully nonlinear time stepping solution, the system matrices are updated on every time step, or after a predetermined number of time steps.

The term 'linearized' needs to be clarified here. The mass matrix and several of the influence matrices of the second-order structure equations of motion are functions of the instantaneous deformation (strain values). Furthermore, the instantaneous distributed aerodynamic forces and moments must be expanded into an instantaneous part and a perturbation, which are then written in terms of the perturbations in the structure and inflow variables, about their current values. The aerodynamic mass, damping, and stiffness matrices are then added to the structure mass, damping, and stiffness matrices. Since the integration is done in terms of the actual values of the structure and inflow variables (not perturbations), right-hand side corrections must be made. Once this process is completed, the resulting aeroelastic system dynamics are considered to be constant over either one or several time steps, assuming that they are slowly varying (which is different from a linear analysis, where these matrices would be computed only once for the undeformed structure and held constant for all time).

3.8 Steady State Solution Module

The steady state solver computes the static deformation of the flexible members due to the loading defined by the calling function or by the user. Default inputs are applied if none are given. The inputs include air speed, altitude, body orientation, fuel mass, gravity, distributed and point loads, applied voltages, gust components, and aileron angle. The convergence tolerance on the solution and the maximum number of iterations may also be changed from default values. The input data for all the external loads are in a simplified format. In order to properly size them, the solution module must use the previously stored vehicle configuration information. A block diagram of the basic solution process is shown in Figure 3.7.

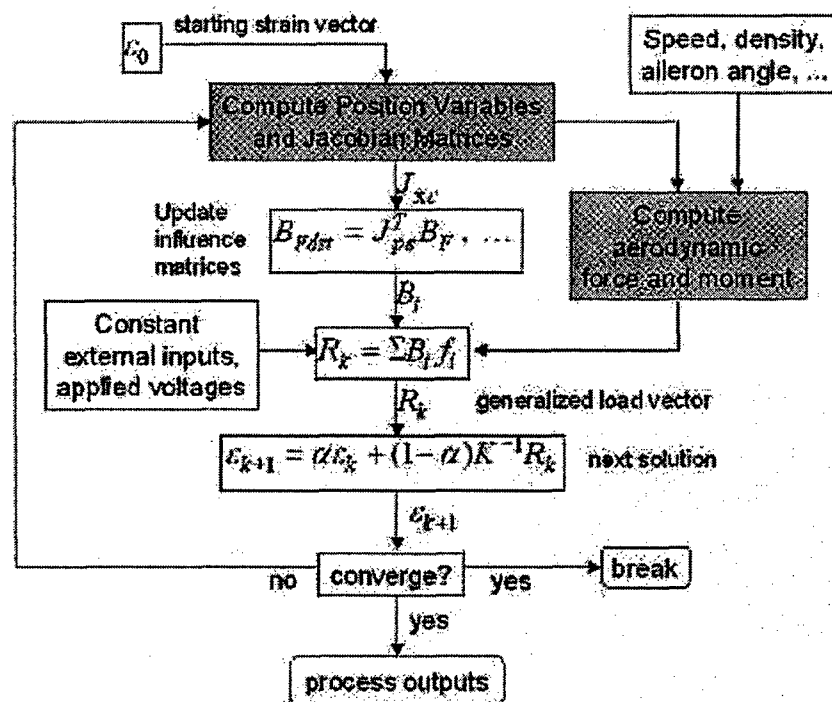


Figure 3.7: Block diagram for steady state aeroelastic solution.

The solution module outputs include

- The steady state strain vector
- Position and orientation variables
- Net lift, drag, and moment
- Distributed aerodynamic force and moment vectors
- Aerodynamic derivatives matrices
- Structure Jacobian matrices
- Ply stresses and strains

The ply stresses and strains that are included in the steady state solution output were obtained by calling a separate routine that calculates them. The inputs to this routine are the strain vector and applied voltages on a particular member. The data returned are cell arrays containing stress, strain, and strength margin data at each of the cross-section discretization points for every ply in each spanwise location along the member. The data package is large and is stored in cell arrays, since the data for each ply

differs in size. In order to obtain a time history of strain data from a transient response, the transient response outputs must be post-processed, and filtered to reduce size. Usually the filtering would search for the extreme ply strains at each wing station, and store only those. This is easily accomplished in a user defined script.

3.9 Roll Response Solver

The roll response to both aileron actuation and warping actuation may be obtained. Inputs to the solver are: flight speed, altitude, body angle of attack, fuel mass, time vector, and control inputs. The control inputs can include aileron angle, aileron rate, aileron acceleration, and applied voltage. The vehicle model which was loaded should be a symmetric one, i.e., two wings or two wings and tail surfaces, although a solution will be returned if only a single wing model is used. The control inputs are given in a simplified form, as shown below, and are formatted by the solver to have the correct size. Each input is a row vector specifying the member, the element, and a set of values corresponding to that particular input. These values have the same length as the time vector and may be any waveform. The control voltage input also specifies which mode (extension, twist, bending-y, bending-z) to excite, even though the twist mode is almost exclusively used. The solution module constructs the voltage input vector using actuation mode data stored during vehicle initialization.

Table 3.7: Control input format for roll response solver

Roll Response Control Inputs	
IN.beta(i)	= [member , element , values]
IN.betadot(i)	= [member , element , values]
IN.betaddot(i)	= [member , element , values]
IN.volt(i)	= [member , element , mode , values]

Both a linearized and a fully nonlinear solution may be obtained. In the fully nonlinear solution, the general nonlinear integrator is used with the appropriate settings. The steps for obtaining the linearized solution are as follows:

1. Unload all of the solution data from the input structure.

2. Apply default values for any solution data that does not exist.
3. Compute the steady state solution and store the strain vector.
4. Unload the aerodynamic derivatives and Structure jacobian matrices from the output of the steady state solver.
5. Compute the unsteady aeroelastic state space A with all body degrees of freedom locked except for roll.
6. Compute the influence matrices from aileron input and actuator voltage input.
7. Compute the time response of the linearized system to the applied inputs.
8. Extract the roll angle, roll rate, and strain perturbation vectors from the output.
9. Process aerodynamic loads and position data for output (for analysis).

Chapter 4

Numerical Validation of Formulation

Because of the complex, multidisciplinary nature of the implementation, the integrated code needed to be tested. Moreover, the new structural formulation and implementation developed and coded for this study had to be evaluated for accuracy. This was the case for static nonlinear deflections, large displacement nonlinear dynamic response, aeroelastic stability, structural modes, static aileron forces and moments, and solution of cross-sectional properties.

To validate the formulation, results from the present implementation are compared with previously established published results. First, basic static and dynamic numerical tests are performed on a cantilevered beam under different loading conditions, and undergoing large, nonlinear deformations. The results are compared against those of Ref. [15] and the multibody dynamics code DYMORE²¹. Ref. [15] solves the geometrically exact beam equations in mixed (generalized displacement-force) finite element method, while DYMORE solves the same beam exact representation with a displacement-based finite element formulation. These results were readily available [15] for comparison with the present formulation.

Next, validation of the structural nodal constraint formulation is performed under several loading conditions and nodal constraints. Results are compared with those generated using ANSYS²⁰. ANSYS is a widely used, general purpose finite element software package. One of its features is the capability of solving for geometrically nonlinear beam deformations. Therefore, it was determined to be a good candidate for comparison. The inter-member nodal constraints are then tested under large, nonlinear loading conditions and compared with ANSYS results.

To validate the aeroelastic implementation, the well known Goland wing flutter results are reproduced for the cases at sea level and at 20 km altitude. Flutter and natural frequency results for a highly flexible, high-aspect-ratio wing are reproduced and compared with data given in Ref. [16]. Limit cycle oscillations in the Goland wing are compared qualitatively with the results of Ref. [16]. Very good correlation is found in all of these tests.

The aileron forces and moments acting on an airfoil section were derived from the presentation of Ref. [11]. The formulation allows for the representation of aileron deflections as a special case of airfoil camber deformation. The accuracy of the predicted loads depends on the number of expansion coefficients used to represent the particular shape. For the case of static loads due to aileron deflection, the results are obtainable in closed form. Spanwise lift and moment results for a slender, tapered wing were compared with Ref. [40].

Finally, the thin-wall, active beam cross-sectional results of the present model are compared with results obtained using UM/VABS¹⁹. The cross section of the NASA/ARMY/MIT active twist rotor (ATR) blade is used to compare results of both methods.

4.1 Static and Dynamic Cantilevered Beam Tests

Several static and dynamic response tests are conducted on a 1-meter long cantilevered beam. The applied loads are sufficiently large that the effects of geometrical nonlinearities are excited. Table 4.1 presents the physical properties of the beam.

Table 4.1: Properties of the test beam.

Mass per unit span (kg/m)	0.2
Beam Length (m)	1
I_{xx} (kgm)	1.0×10^{-4}
I_{yy} (kgm)	1.0×10^{-6}
I_{zz} (kgm)	1.0×10^{-4}
K_{11} (N)	1.0×10^6
K_{22} (Nm ²)	50
K_{33} (Nm ²)	50
K_{44} (Nm ²)	1000

4.1.1 Test Case 1 - Concentrated Tip Force

The loading condition for test case 1 is shown in Figure 4.1. The concentrated tip force is varied from 0 N to 150 N. The resulting tip x and z positions are compared with those of Ref. [15] and DYMORE in Figures 4.2 and 4.3. The results show a very close correlation among all of the data.

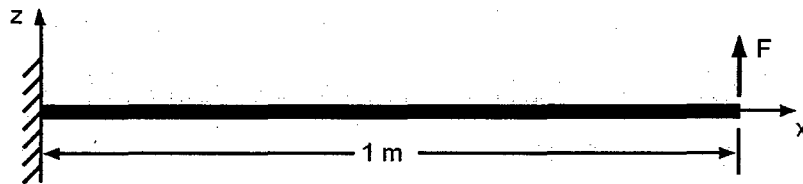


Figure 4.1: Load condition for test case 1.

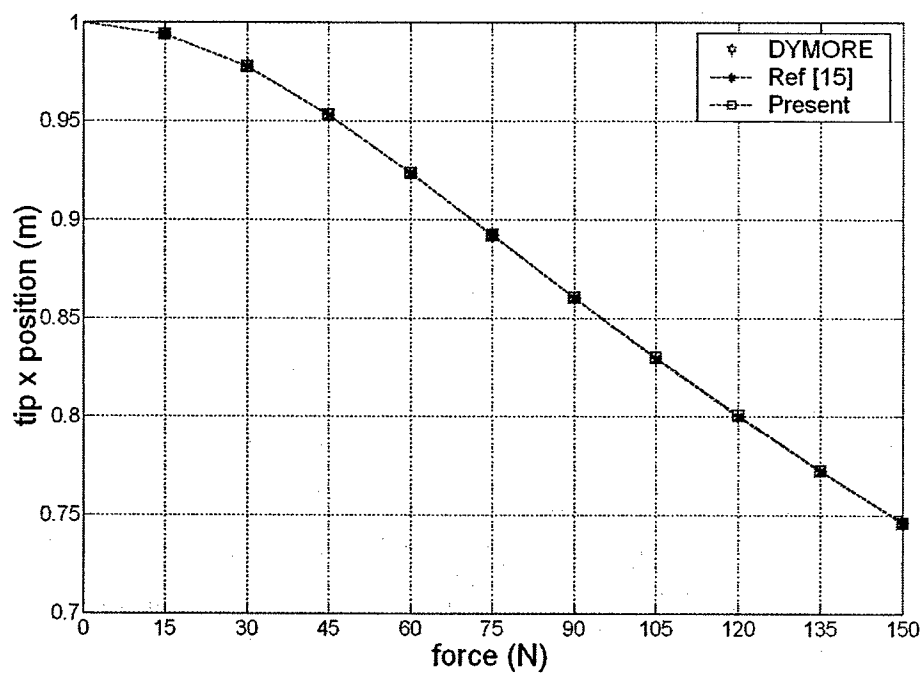


Figure 4.2: Comparison of tip position along the x axis for test case 1.

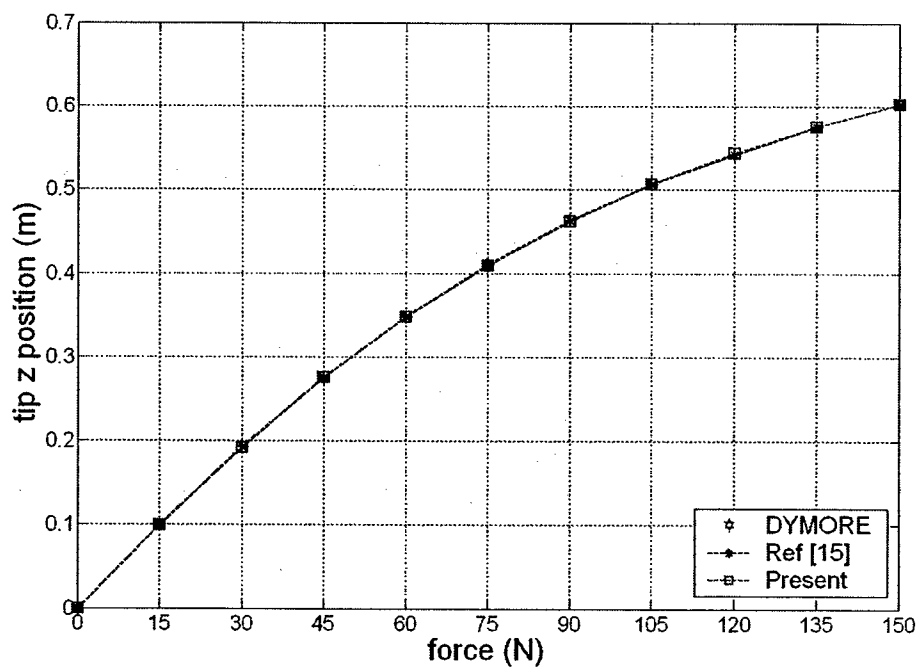


Figure 4.3: Comparison of tip position along the z axis for test case 1.

4.1.2 Test Case 2 - Concentrated Tip Moment

The loading condition for test case 2 is shown in Figure 4.4. The concentrated tip moment is varied from 0 Nm to 120 Nm. The resulting tip x and z positions are compared with those of Ref. [15] and DYMORE in Figures 4.5 and 4.6. The results show a very close correlation among all of the data.

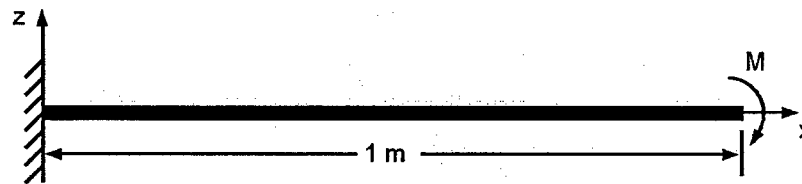


Figure 4.4: Load condition for test case 2.

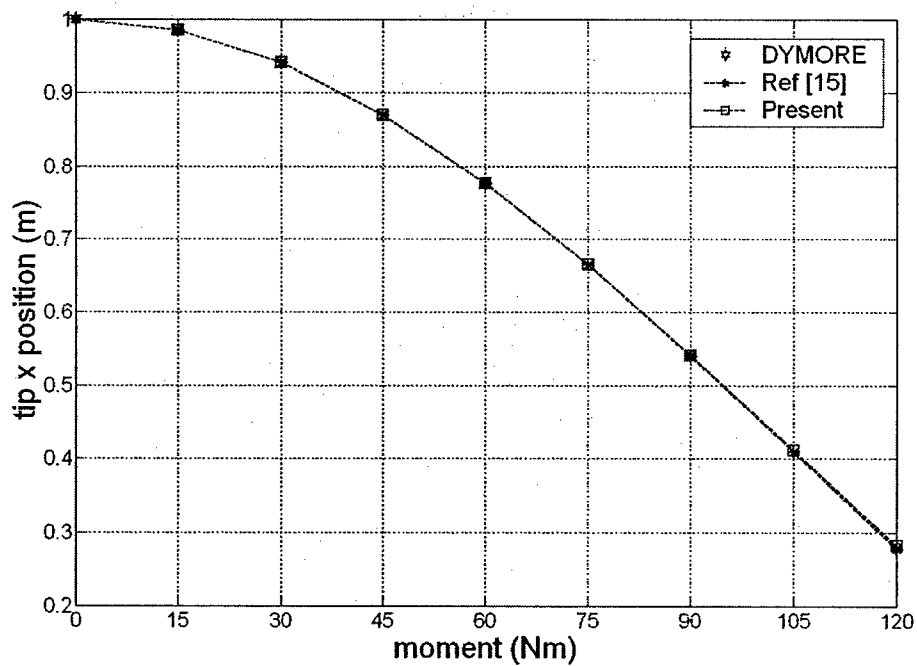


Figure 4.5: Comparison of tip position along the x axis for test case 2.

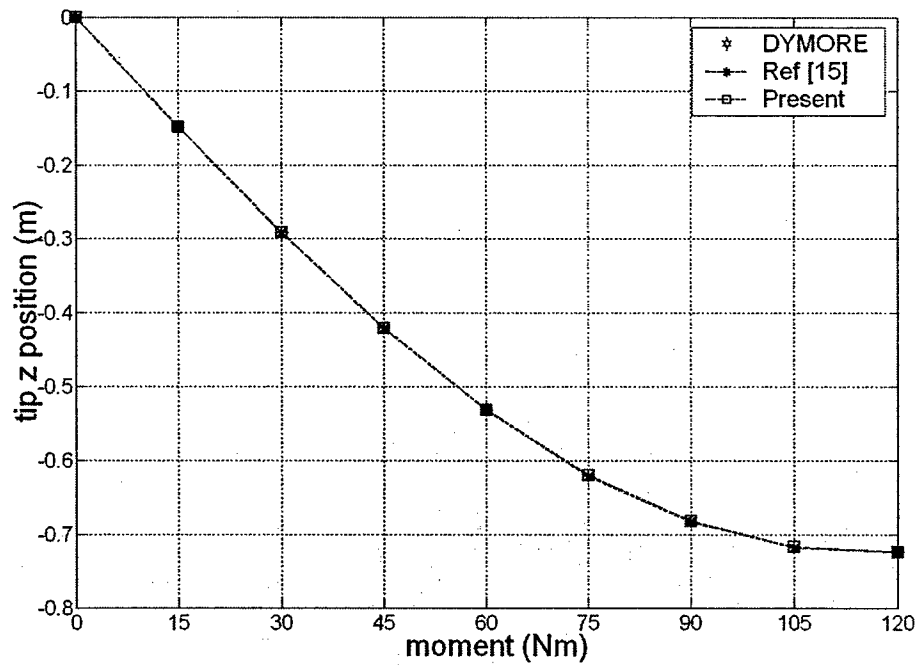


Figure 4.6: Comparison of tip position along the z axis for test case 2.

4.1.3 Test Case 3 - Multiple Point Forces

The loading condition for test case 3 is shown in Figure 4.7. The concentrated tip force is varied from 0 N to 150 N. The force in the middle of the beam has a constant value of -150 N. The resulting positions along the x and z axes are compared with those of Ref. [15] and DYMORE in Figures 4.8 and 4.9. The results show a very close correlation among all of the data.

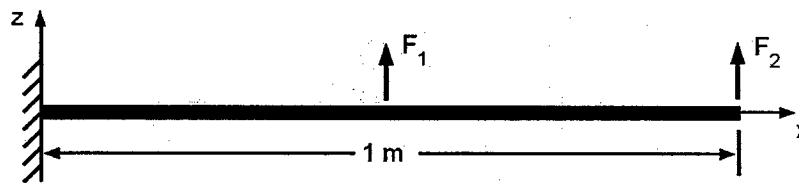


Figure 4.7: Load condition for test case 3.

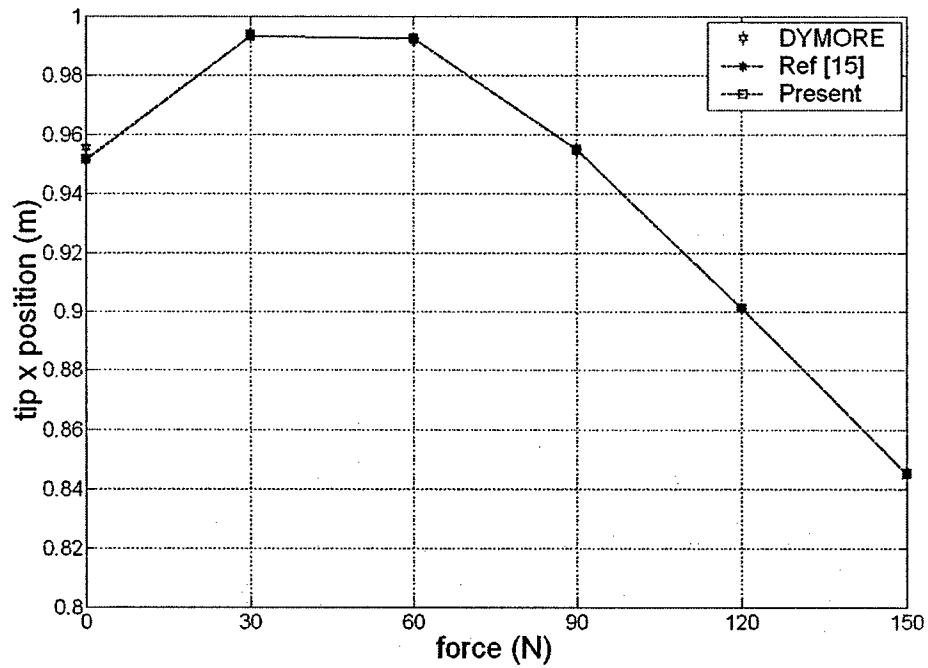


Figure 4.8: Comparison of tip position along the x axis for test case 3.

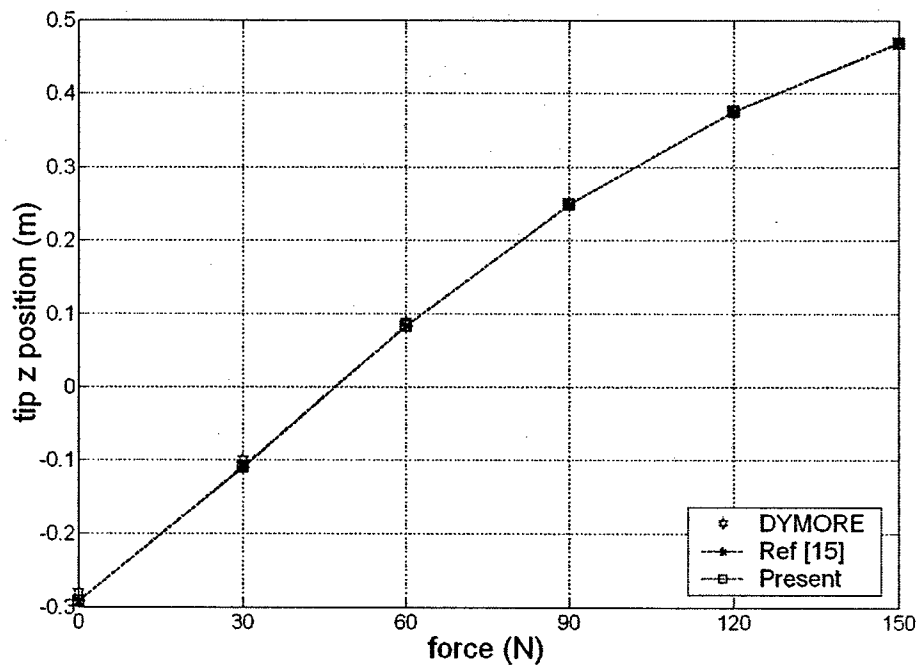


Figure 4.9: Comparison of tip position along the z axis for test case 3.

4.1.4 Test Case 4 - Dynamic Response

The same beam is used for dynamic testing as for the static testing. The loading condition is shown in Figure 4.10.

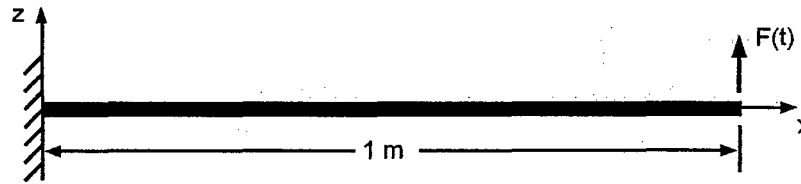


Figure 4.10: Beam model for test dynamic response test.

Three forcing functions are used, 1) $F = 10\sin 20t$; 2) $F = 10\sin 50t$; and 3) $F = 5\sin 55.6t$. The results are shown in Figures 4.11 to 4.13. The natural frequency of the beam is 55.6 rad/s. In case 2, the excitation frequency is near the natural frequency, and the beating phenomena is observed. In case 3, the beam is excited at its natural frequency, resulting in resonance. The time step used in Ref. [15] and DYMORE was 0.001 s. The present model used a time step of 0.005 s. All results are consistent.

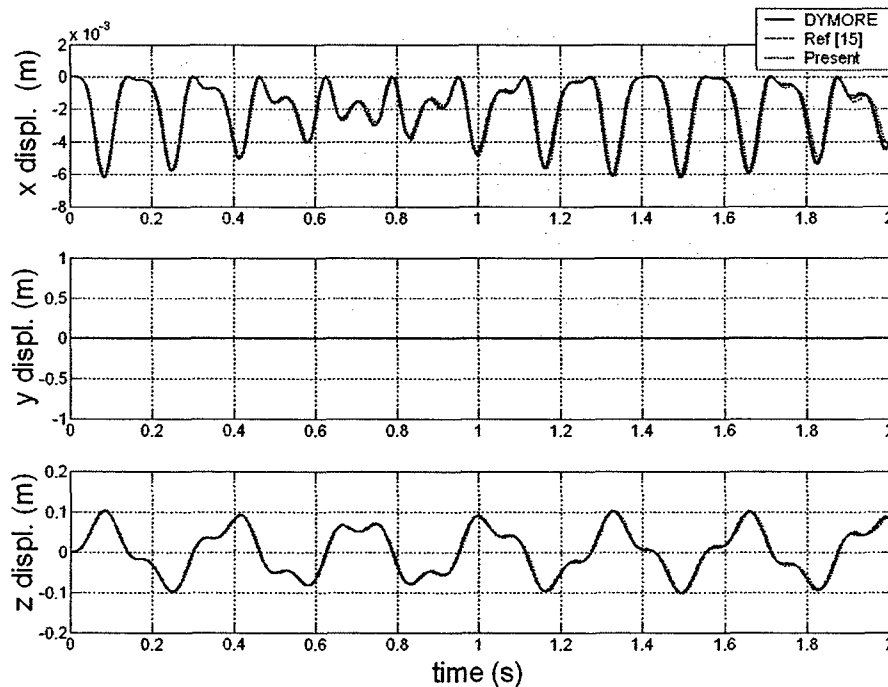


Figure 4.11: Tip displacement comparison for $F=10\sin 20t$.

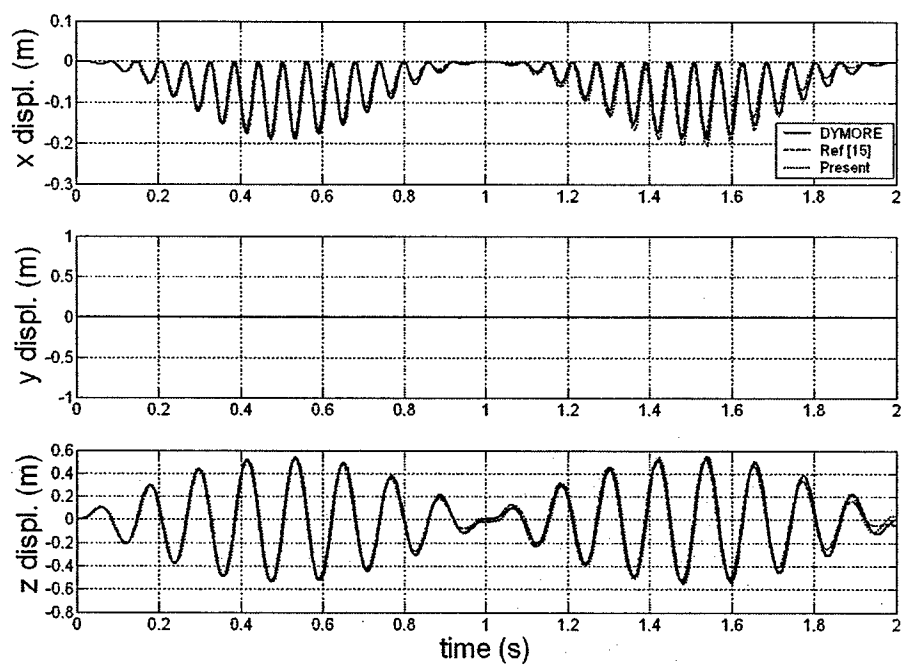


Figure 4.12: Tip displacement comparison for $F=10\sin 50t$.

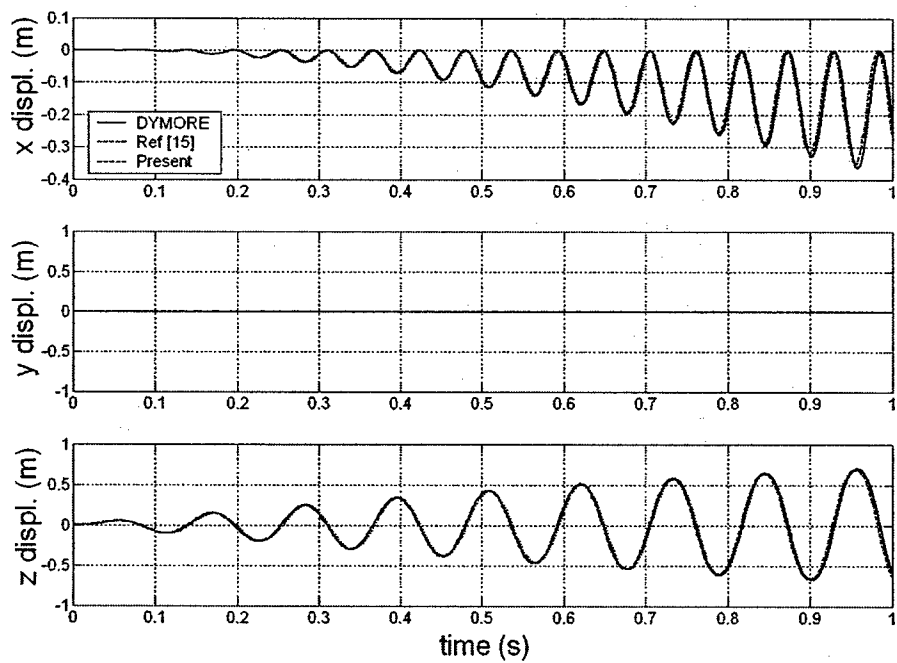


Figure 4.13: Tip displacement comparison for $F=5\sin 55.6t$.

4.2 Multiple Constraint Deflection Testing

Since the present beam model is a strain based model, only one boundary condition can be directly imposed. The other boundary constraints are enforced by applying a very large effective stiffness at the constrained node, which prevents the selected motion. In all cases, the beam is clamped at the root. The properties of the beam used in this section are given in Table 4.2.

Table 4.2: Properties of the beam for multiple constraint deflection test.

Length (m)	1.0
K_{11} (N-m)	1.6284×10^6
K_{22} (N-m ²)	37.31
K_{33} (N-m ²)	39.80
K_{44} (N-m ²)	1037.2

In all cases, the solution is compared with that obtained using ANSYS BEAM4 elements with the Large Displacement Static analysis option. Both models use a 20-element discretization.

4.2.1 Test Case 1 - Fixed-Fixed, Distributed Load

For this test, a clamped boundary condition is imposed to the tip of the beam by applying stiffness constraints to all tip degrees of freedom. The stiffness constants were set to 1×10^{12} N/m for the position constraints and 1×10^{12} Nm for the rotational constraints. A vertical distributed load of 1000 N/m is applied over the length of the beam, as shown in Figure 4.14. The resulting displacements are consistent, as shown in Figure 4.15.

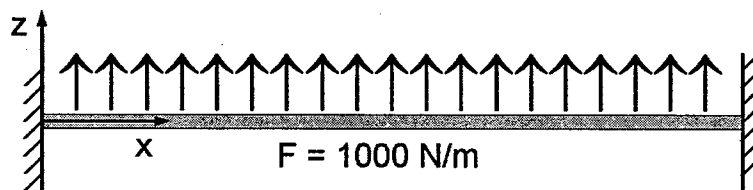


Figure 4.14: Load condition for test case 1.

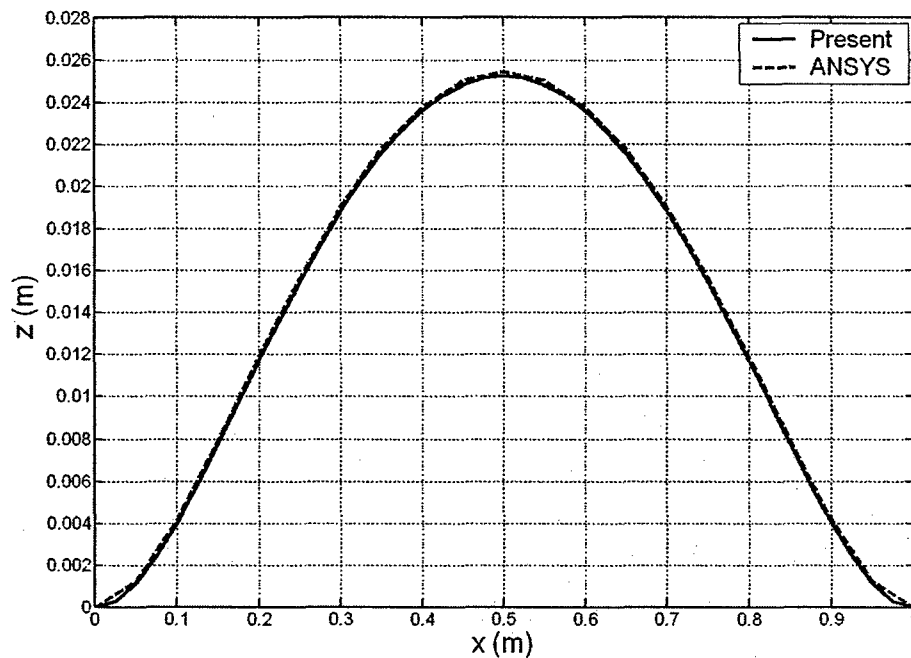


Figure 4.15: Displacement comparison for test case 1.

4.2.2 Test Case 2 - Fixed-Fixed, Point Load

For this test, the same boundary condition is imposed as in the previous case (test case 1). A vertical point load of 1000 N is applied in the middle of the beam, as shown in Figure 4.16. The resulting displacements are shown in Figure 4.17. The results show a very close correlation.

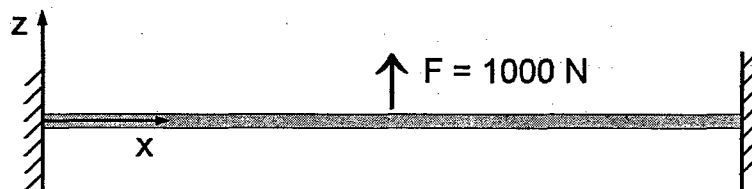


Figure 4.16: Load condition for test case 2.

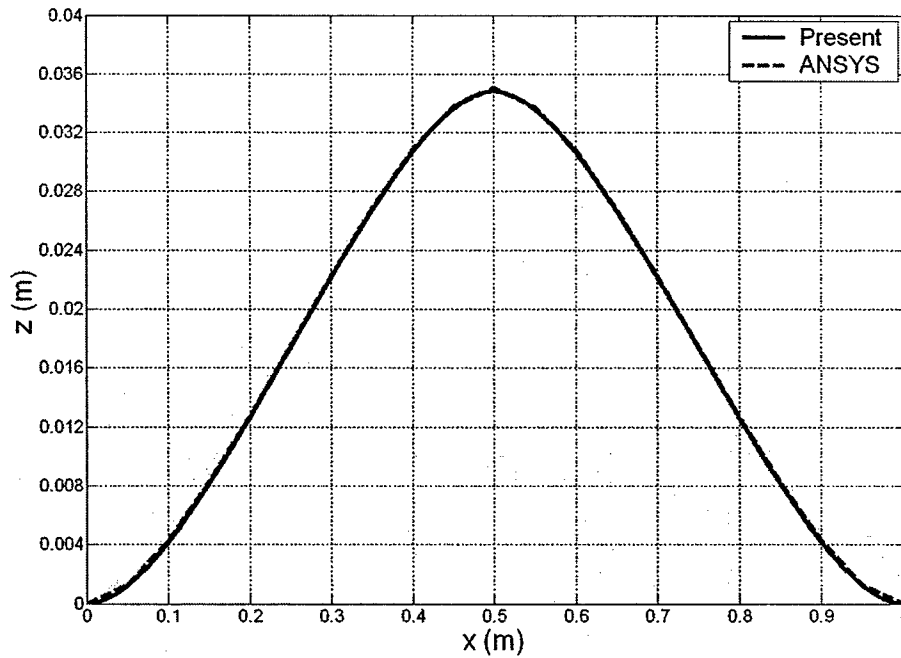


Figure 4.17: Displacement comparison for test case 2.

4.2.3 Test Case 3 - Fixed-Fixed, Axial Point Load

An axial point load of 10,000 N is applied in the middle of the beam, with the same boundary condition as the previous test cases, as shown in Figure 4.18. The results compare very closely with those obtained using ANSYS, as shown in Figure 4.19.

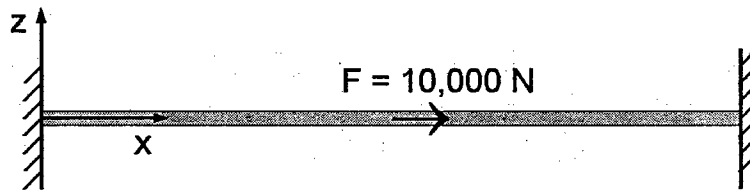


Figure 4.18: Load condition for test case 3.

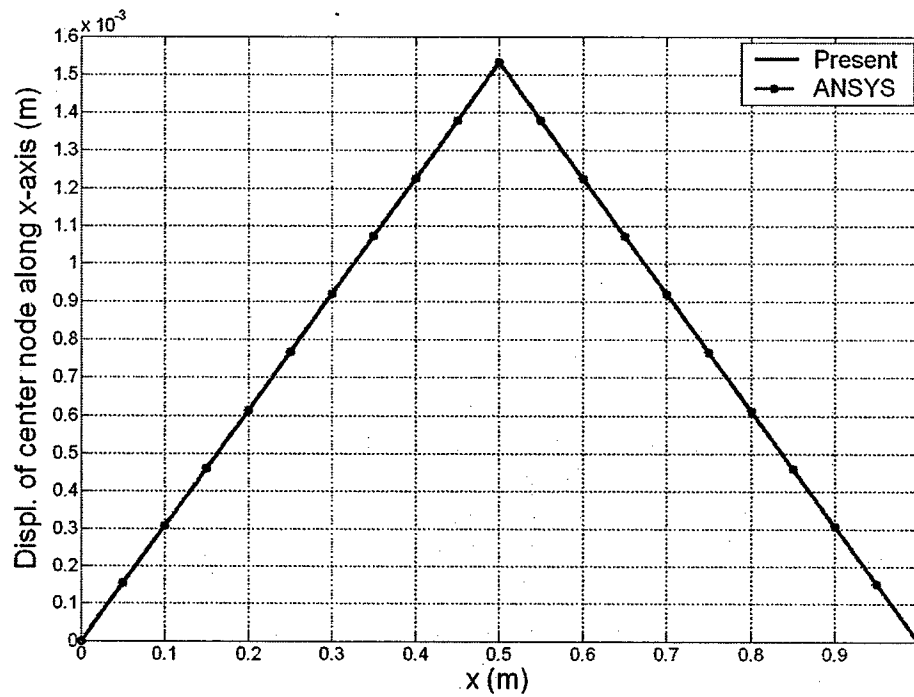


Figure 4.19: Displacement comparison for test case 3.

4.2.4 Test case 4 - Fixed-Pinned in Center, Vertical Point Tip Load

For this test, the middle node is given a pinned constraint by applying stiffness constraints to the translational degrees of freedom. The constraint stiffness constants were set to 1×10^{12} N/m. A vertical point load of 200 N is applied at the tip of the beam, as shown in Figure 4.20. The results show a very close correlation, as shown in Figure 4.21.

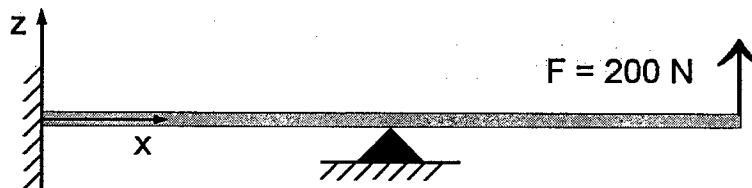


Figure 4.20: Load condition for test case 4.

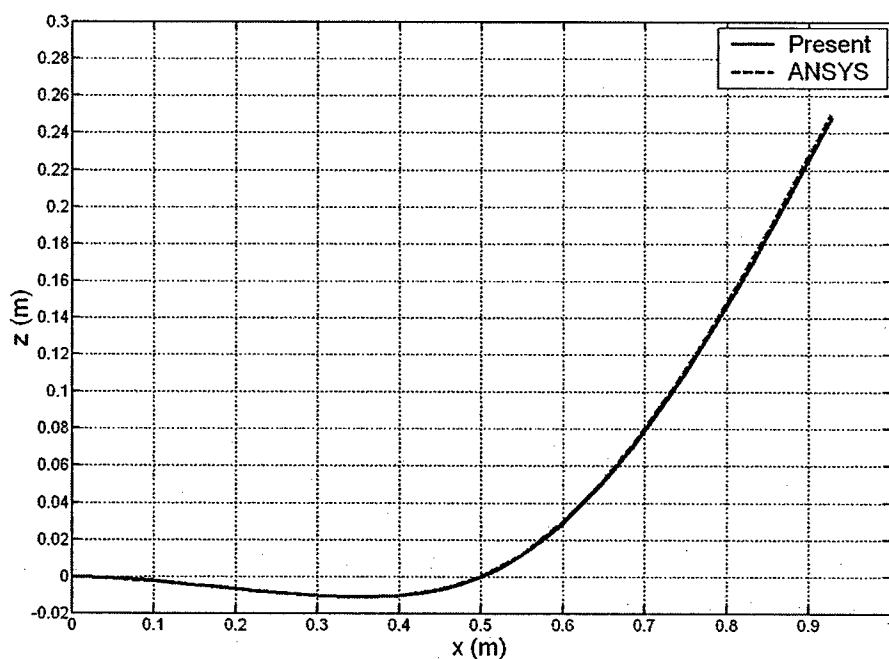


Figure 4.21: Displacement comparison for test case 4.

4.2.5 Test case 5 - Fixed-Pinned in Center, Multi-Axial Point Load

For this test, the middle node is constrained as in test case 4. A vertical point load of 200 N is applied at the tip of the beam and a horizontal point load of 1000 N is also applied at the tip (Figure 4.22). The resulting displacements are shown in Figures 4.23 and 4.24. The results show a very close correlation.

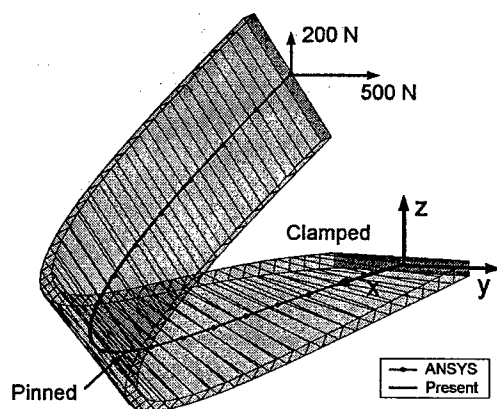


Figure 4.22: Load condition and resulting deformation for test case 5.

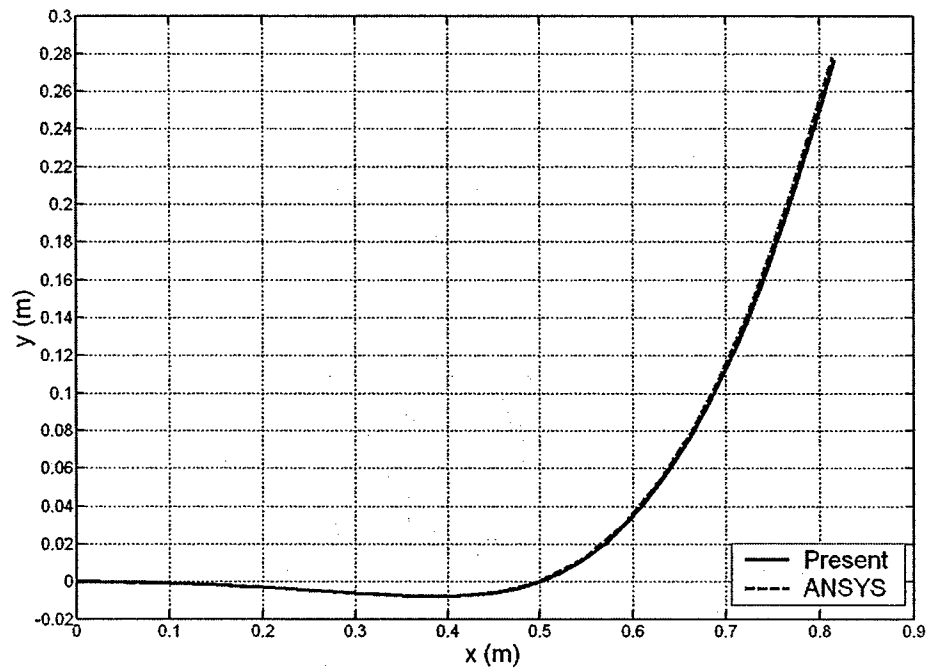


Figure 4.23: Beam deflections along the y axis for test case 5.

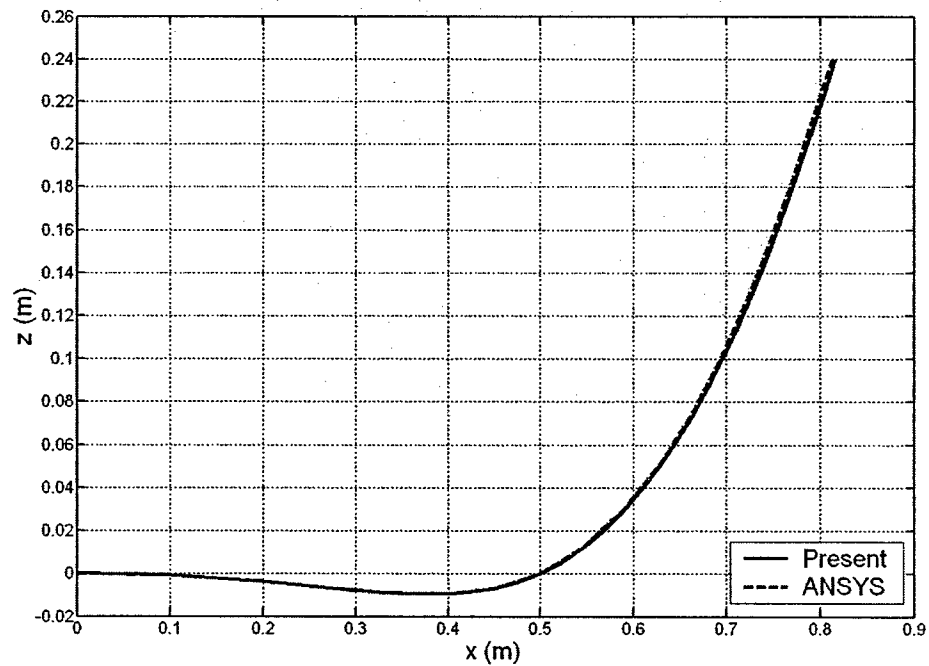


Figure 4.24: Beam deflections along the z axis for test case 5.

4.3 Joined Member Static Deflection Testing

The following test cases are to validate the inter-member constraints described in Chapter 2. This constraint generally applies to joined wing aircraft configurations. The configuration and dimensions of the test model are shown in Figure 4.25. The base of each beam is clamped at the root. At the joint, an inter-member stiffness constraint is imposed, with all the stiffness constants set to 1×10^{12} . The stiffness properties for each beam are equal and are given in Table 4.3. For each test case, the deformation is compared with a similar model constructed in ANSYS, using BEAM4 3-D elastic beam elements with three rotational and three linear displacement degrees of freedom per node. The ANSYS model used 10 elements per member, for a total of 41 degrees of freedom. The options were set for large displacement, nonlinear solution. The loading conditions result in large deformations which cannot be captured by a linear solution.

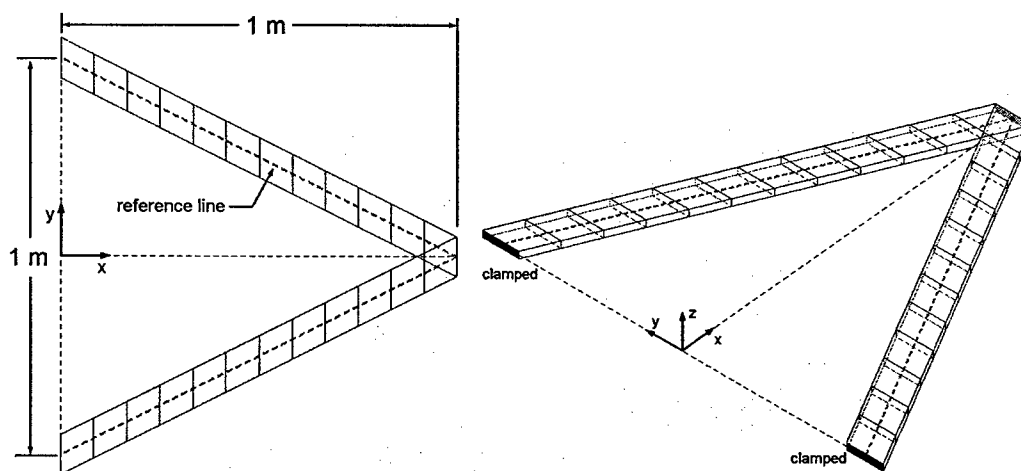


Figure 4.25: Dimensions and boundary condition for the test model.

Table 4.3: Stiffness properties of the beam for inter-member constraint test.

K_{11} (N-m)	1×10^6
K_{22} (N-m ²)	50
K_{33} (N-m ²)	50
K_{44} (N-m ²)	1000

4.3.1 Test Case 1 - Simple Point Load at Joint

In test case 1, a 100-N vertical point load is applied at the joint, as shown in Figure 4.26. The present model uses six elements per member for this test case. The resulting deflection along the z axis is shown as a function of span in Figure 4.27. The results are nearly identical between the two solution methods.

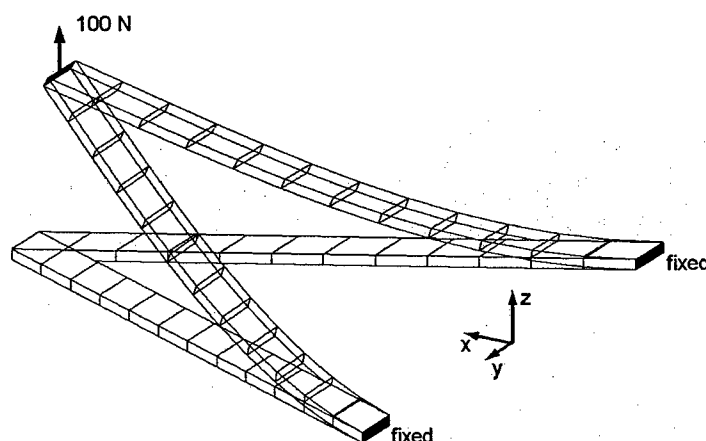


Figure 4.26: Loading condition for test case 1.

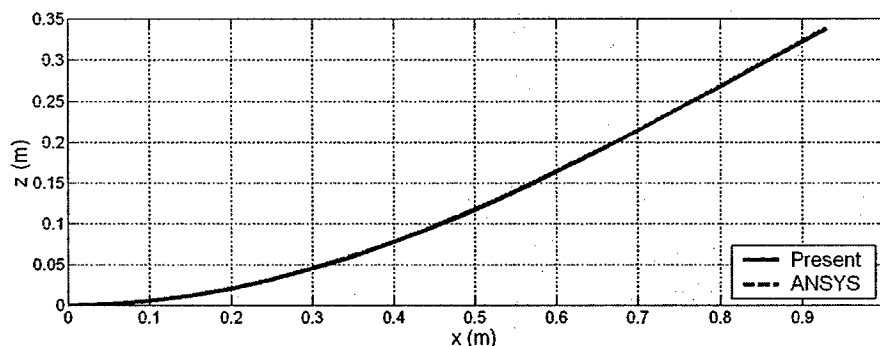


Figure 4.27: Deflection results for test case 1.

4.3.2 Test Case 2 - Multi-Axis Point Load at Joint

In this test, a point force of 10 N is applied along the z axis and a point force of 1000 N is applied along the y axis. The loading condition and deformation of the structure are shown in Figure 4.28. The present results were obtained using 10 elements per member. The position of the beam reference line along the y and z axes are presented

as a function of span (x) in Figure 4.29. The results are consistent between the two methods of solution.

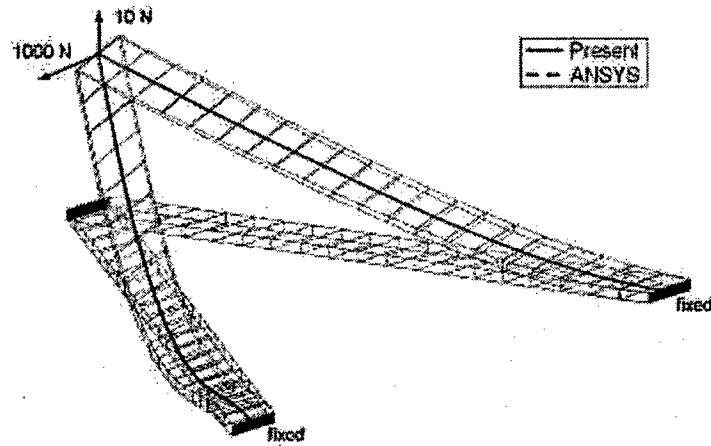


Figure 4.28: Loading condition for test case 2.

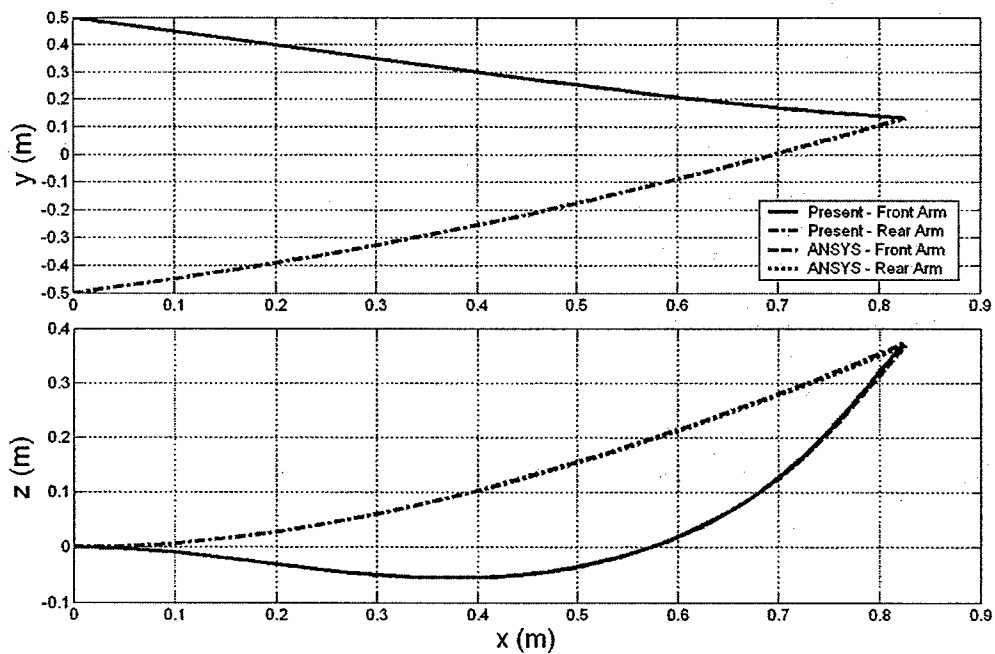


Figure 4.29: Deflection results for test case 2.

4.3.3 Test Case 3 - Complex Load Case

The loading condition for test case 3 is displayed in Figure 4.30. The 1000 N point forces are applied at the middle of each member. Each member has 10 elements

for the present model. The position of the beam reference line along the y and z axes are presented as a function of span (x) in Figure 4.31. The results are consistent between the two methods of solution.

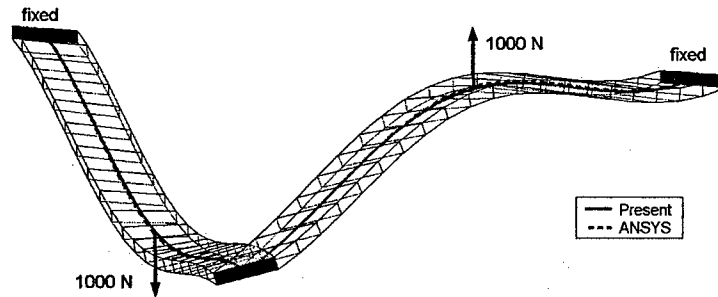


Figure 4.30: Loading condition for test case 3.

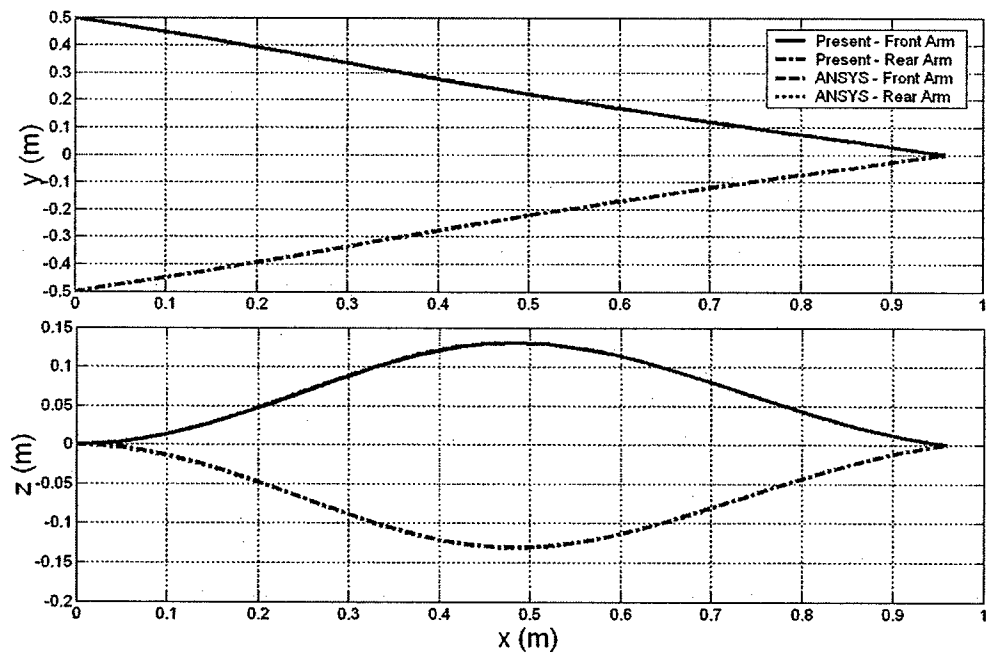


Figure 4.31: Deflection results for test case 3.

4.4 Aeroelastic Test Cases

4.4.1 Goland Wing

The Goland wing²² is a low-aspect-ratio prismatic wing studied extensively in the literature. The wing is elastically uncoupled with some inertial coupling. The properties for the wing are given in Table 4.4. Even though this wing is relatively stiff and, therefore, behaves linearly, basic aeroelastic stability capability of the present formulation can be examined.

Flutter results are obtained for the wing oriented at a 0° root angle of attack. A comparison of the flutter speed results between the present formulation and other results found in the literature [14,16] is given in Table 4.5. The results are all very close.

Table 4.4: Properties of the Goland wing.

Length	20 ft
Chord	6 ft
Mass per unit length	0.746 slug/ft
Spanwise elastic axis (from l.e.)	33% of chord
Center of gravity (from l.e.)	44% of chord
Bending rigidity, EI	23.65×10^6 lb ft ²
Torsional rigidity, GJ	2.39×10^6 lb ft ²
Rotational Inertia (about e.a.)	1.943 slug/ ft ² / ft

Table 4.5: Flutter results for the Goland wing.

	Ref. [16] incompressible	Ref. [16] compressible	Present	Ref. [14]
<u>Sea Level</u>				
Flutter Speed (ft/s)	447	446	447	445
Flutter Frequency (rad/s)	70.0	69.9	69.7	70.2
<u>20 K ft Above Sea Level</u>				
Flutter Speed (ft/s)	574	574	574	----
Flutter Frequency (rad/s)	68.9	67.0	68.1	----

Limit cycle behavior of the Goland wing is observed at a flight speed of 500 ft/s. Although the results of Ref. [14] were not available for plotting, there is a good qualitative comparison in both the frequency and amplitude of the limit cycle. The

results using the present implementation are shown in Figure 4.32. In both the present case and Ref. [14], the angle of attack goes well into the stall region. A time step of 0.002 s was used.

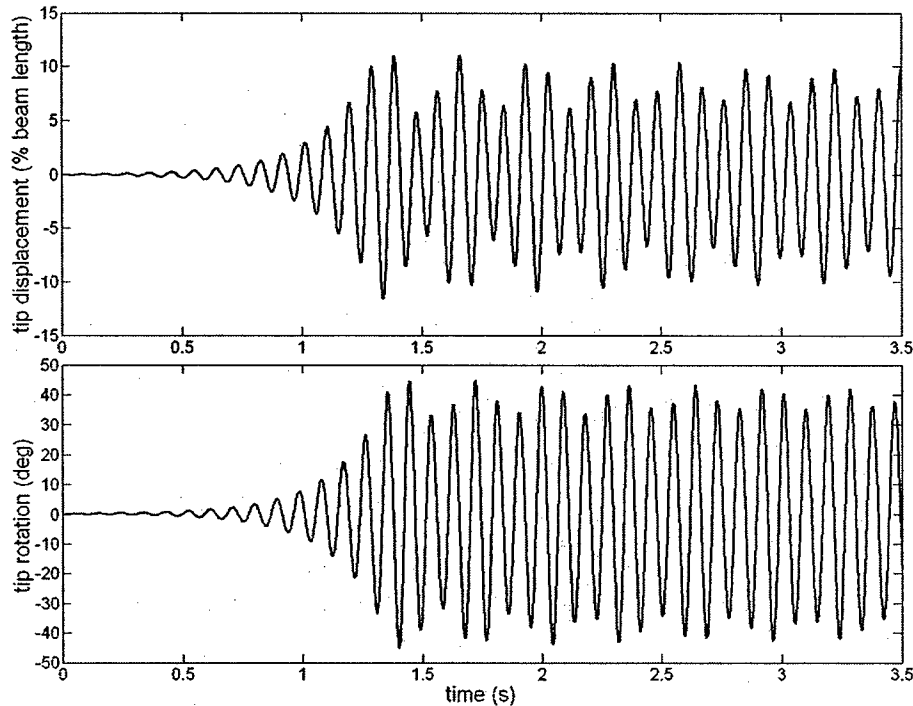


Figure 4.32: Limit cycle oscillations in the Goland wing flying at 12 % over flutter speed.

4.4.2 Highly Flexible, Slender Wing

The wing of Ref. [14] is a highly flexible, high-aspect-ratio wing. Natural frequencies and flutter results are calculated for this wing using the present formulation, and compared with those of Ref. [14], which presents both numerical and exact analytical results. The properties of the wing are given in Table 4.6. Natural frequencies are obtained for the first five structural modes of the undeformed beam, and are presented in Table 4.7. Various levels of discretization were used in the present model to detail the convergence properties. An 8-element discretization was used in Ref. [14].

The linear flutter results using the present model are compared with those presented in Ref. [14] in Table 4.8. The results are identical.

Table 4.6: Highly flexible wing properties of Ref. [14].

Length	16 m
Chord	1 m
Mass per unit length	0.75 kg/m
Spanwise elastic axis (from l.e.)	50% of chord
Center of gravity (from l.e.)	50% of chord
Bending rigidity, EI (flat bend)	$2 \times 10^4 \text{ Nm}^2$
Bending rigidity, EI (chord bend)	$4 \times 10^6 \text{ Nm}^2$
Torsional rigidity, GJ	$1 \times 10^4 \text{ Nm}^2$
Rotational Inertia per unit length	0.10 kg m

Table 4.7: Natural frequencies of the highly flexible wing (rad/s).

	Ref. [14]	Ref. [14] (exact)	Present 20 elmnt	Present 10 elmnt	Present 8 elmnt	Present 6 elmnt
First Flat Bend	2.247	2.243	2.2438	2.2468	2.2490	2.2538
Second Flat Bend	14.606	14.056	14.1129	14.2875	14.4208	14.7164
First Torsion	31.146	31.046	31.0536	31.0775	31.0955	31.1343
First Edgewise Bend	31.739	31.718	31.7323	31.7741	31.8055	31.8733
Third Flat Bend	44.012	39.356	39.7703	41.0561	42.0656	44.3967

Table 4.8: Flutter results for the highly flexible wing.

	Ref. [14]	Present
Flutter Speed (m/s)	32.2	32.2
Flutter Frequency (rad/s)	22.6	22.6

4.4.3 Aileron Lift and Moment

The static lift and moment on a slender wing due to aileron deflection are compared with an analytical solution for the lift and moment on a two-dimensional airfoil due to aileron deflection given in Ref. [40]. The wing is shown in Figure 4.33. The nodes in this figure indicate points along the wing where the forces and moments are evaluated. The relevant parameters are given in table 4.9. The results are shown in Figure 4.34. The present model used 41 expansion terms in the aerodynamic formulation for representing the airfoil shape due to aileron deflection. The results compare very well.

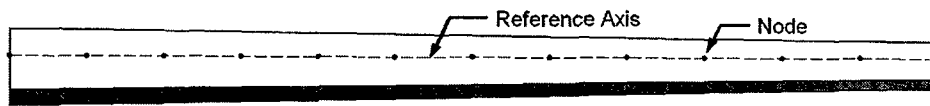


Figure 4.33: Test wing for aileron force and moment comparison.

Table 4.9: Parameters for aileron lift and moment comparison.

Length (m)	18
Root chord (m)	1.5
Tip chord (m)	0.9
Wing angle of attack (deg.)	0
Aileron dimension (% chord)	20
Reference axis location from l.e. (% chord)	35.58
Flight speed (m/s)	40
Altitude (m)	0
Aileron deflection (deg.)	15

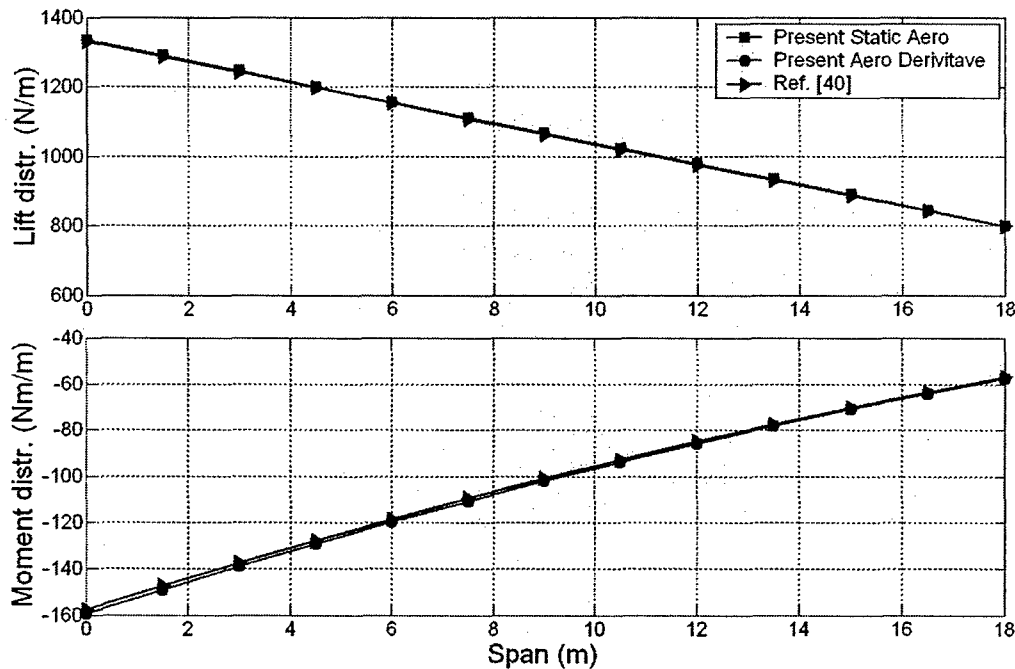


Figure 4.34: Aileron lift and moment comparison.

4.5 Cross-Sectional Properties

The active twist rotor (ATR) prototype blade was designed, built, and tested as part of a joint program between NASA Langley/Army Research Laboratory and MIT⁴².

Its cross section was analyzed using UM/VABS¹⁹ and the present thin-walled beam implementation. As shown in Figure 4.35, the cross section has a NACA0012 airfoil shape and is constructed of E-Glass, S-Glass, and piezoelectric fiber composites. The actual blade was filled with Rohacell 71 foam to facilitate manufacture, but the numerical results here neglect the effects of the foam. The relevant material properties are given in Table 4.10. The UM/VABS model had a 652 elements (881 nodes). The stiffness, inertia and actuation results are presented in tables 4.11 and 4.12. Most of the results are as expected, considering the limitations of the thin-wall approximation. In the thin-wall model, all of the material is assumed to be on the outer airfoil contour. The VABS results have a non-zero extension/torsion coupling due to the offset between the inner and outer $\pm 45^\circ$ active plies. The bending stiffness is higher for the thin-wall model since the material is located further away from the mid-chord. Overall, the thin-walled active cross-sectional formulation was implemented correctly and is able to capture the complex couplings present in a composite beam.

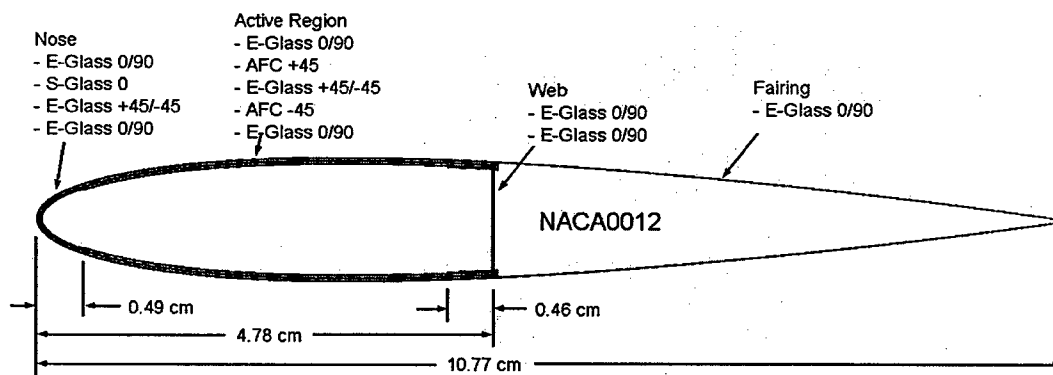


Figure 4.35: Schematic diagram of the ATR blade section.

Table 4.10: Material properties used in the ATR prototype blade cross-sectional analysis

	E-Glass	S-Glass	AFC
Q_{11} (GPa)	19.732	44.362	33.600
Q_{12} (GPa)	2.920	3.435	7.540
Q_{16} (GPa)	0	0	0
Q_{22} (GPa)	19.732	12.266	16.600
Q_{26} (GPa)	0	0	0
Q_{66} (GPa)	4.100	3.600	5.130
ν_{12}	0.1480	0.2800	0.4542
ρ (kg/m ³)	1716	1855	4060
d_{11} (pm/V)	0	0	309
d_{12} (pm/V)	0	0	-129
ply thick (mm)	0.1143	0.2286	0.2030

Table 4.11: Non-zero stiffness and inertia results for the ATR prototype blade

	Present	UM/VABS	% diff.
K_{11} (N-m)	1.6278×10^6	1.6248×10^6	-0.1846
K_{12} (N-m)	0	24.6260	---
K_{14} (N-m)	805.0030	745.6284	-7.9630
K_{22} (N-m ²)	39.9982	36.9761	-8.1731
K_{24} (N-m ²)	0	0.1767	---
K_{33} (N-m ²)	45.1332	40.3187	-11.9411
K_{44} (N-m ²)	1.0402×10^3	1.0247×10^3	-1.5126
mass (kg/m)	0.2362	0.2373	0.4635
I_{xx} (kg-m ² /m)	1.1436×10^{-4}	1.1282×10^{-4}	-1.3650
I_{yy} (kg-m ² /m)	7.4067×10^{-6}	6.6146×10^{-6}	-11.9750
I_{zz} (kg-m ² /m)	1.0696×10^{-4}	1.0620×10^{-4}	-0.7156

Table 4.12: Actuation results for the ATR prototype blade

		Present	UM/VABS	% Diff.
Bv ₁ (N/V)	patch 1	0.0229	0.0231	0.8658
	patch 2	0.0229	0.0231	0.8658
	patch 3	0.0229	0.0233	1.7167
	patch 4	0.0229	0.0233	1.7167
Bv ₂ (Nm/V)	patch 1	2.253×10^{-4}	2.607×10^{-4}	13.5788
	patch 2	2.253×10^{-4}	2.617×10^{-4}	13.9091
	patch 3	2.253×10^{-4}	2.410×10^{-4}	6.5145
	patch 4	2.253×10^{-4}	2.407×10^{-4}	6.3980
Bv ₃ (Nm/V)	patch 1	1.357×10^{-4}	1.314×10^{-4}	-3.2725
	patch 2	1.357×10^{-4}	1.316×10^{-4}	-3.1155
	patch 3	1.357×10^{-4}	1.261×10^{-4}	-7.6130
	patch 4	1.357×10^{-4}	1.260×10^{-4}	-7.6984
Bv ₄ (Nm/V)	patch 1	1.542×10^{-4}	1.543×10^{-4}	0.0648
	patch 2	1.542×10^{-4}	1.560×10^{-4}	1.1538
	patch 3	1.542×10^{-4}	1.555×10^{-4}	0.8360
	patch 4	1.542×10^{-4}	1.556×10^{-4}	0.8997

Chapter 5

Numerical Studies

This chapter numerically evaluates wing warping performance using anisotropic piezoelectric composite actuators (APC) embedded in high-aspect-ratio wings of realistic vehicles. Benchmark results are obtained for static and dynamic vehicle response, based on current actuator technology. Comparisons are made between wing warping control in active wings without ailerons and conventional control in wings with ailerons.

5.1 Introduction

A numerical test model is constructed for the study of the trends associated with the distribution of active materials in the wings and for the comparison of wing warping control and aileron control. The model is constructed such that vehicle size, planform, and cross section layup can all be varied during the study. The basic vehicle shape used for the numerical model is shown in Figure 5.1.

Several issues are addressed regarding the performance of the active wings compared with the conventional wings:

- Roll performance
- Active wing stabilization and gust load alleviation

- Maneuver load redistribution by wing twist for reducing root bend moment
- The effects of vehicle size on the performance in integral strain actuation

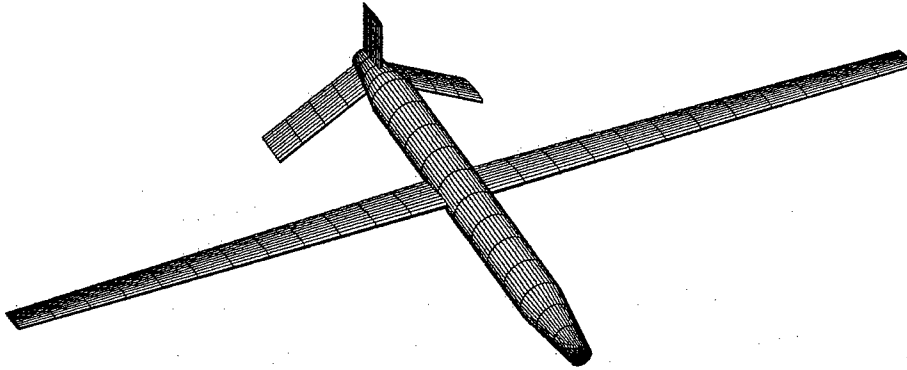


Figure 5.1: Basic vehicle geometry for numerical studies.

Because of the large number of variables involved in the study of aircraft performance and design, the effects of vehicle size are evaluated by considering three representative vehicle classes, based on existing military UAV's. For each vehicle class, a baseline wing is constructed for both an aileron design and two wing warping designs. The first wing warping model is constructed by replacing some of the passive plies from the aileron wing with standard thickness actuator plies. The second wing warping design uses reduced thickness actuator plies so that the wing weight is the same as that of the aileron wing. For consistency, geometric scaling is maintained among the three vehicle classes.

The three vehicle classes considered are denoted "small," "medium," and "large," and represent low, medium, and high altitude UAV's, respectively. The vehicles in the numerical study are based on the fielded unmanned aircraft shown in Figure 5.2. Basic data for these vehicles are given in Table 5.1. Data for the numerical comparison will vary slightly from the data presented here in order to maintain consistency among the three vehicle scales.

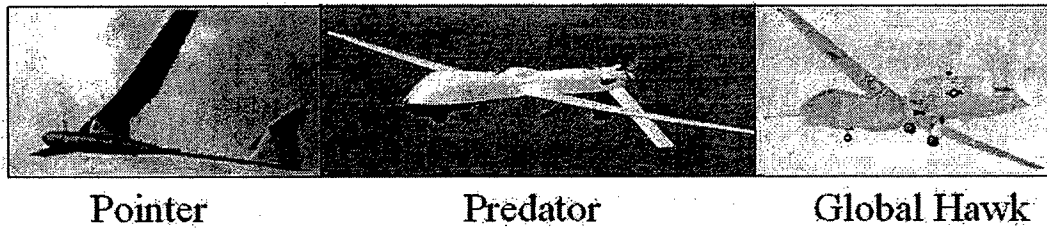


Figure 5.2: Unmanned aircraft used as baselines for creating the numerical cases studied here.

Table 5.1: Basic vehicle characteristics for numerical studies

Class	Small	Medium	Large
Based On	Pointer	Predator	Global Hawk
Altitude (m)	914	8,230	19,800
Wing Span (m)	2.44	14.84	35.42
Gross Weight (kg)	4.14	1,046	11,636
Fuel Capacity (kg)	1	295	6,590
Payload (kg)	0.91	205	864
Speed (m/s)	25	60	170

5.2 Guidelines for Creating the Numerical Models

The following guidelines apply to the comparison study between aileron control and wing warping control for the three vehicle classes. The two corresponding wings will be called "Aileron" and "ISA" (Integrated Strain Actuation), respectively. The ISA wings are denoted ISA1 for the full thickness actuators and ISA2 for the reduced thickness actuators.

5.2.1 Flight Plan Construction

The data that defines the flight plan are altitude and speed. The nominal flight speed is determined at seven representative flight index points based on a constant dynamic pressure over the mission. The body trim angle of attack is computed and stored for a range of increasing speeds at each flight index point, up to 300% of the nominal flight speed.

5.2.2 Fuselage

The fuselage mass properties are assumed to be given, and apply to both the aileron and warping designs. Payload mass is assumed to be part of the fuselage mass.

5.2.3 Fuel Storage

Since the basic wing design is inspired on the Predator UAV, which stores its fuel completely within the fuselage, the fuel will be stored in the fuselage and will be depleted over the flight plan. The Pointer UAV actually uses batteries as the power source, which will be considered as constant mass payload.

5.2.4 General Wing Properties

The wings for all three vehicle classes have a taper ratio of 0.60 and a half aspect ratio of 15. The airfoil for all cases is a NACA4415 over the entire span, which is similar to many existing UAVs. The 2D airloads approximation will apply along the entire span, i.e., there will be no correction applied for wing tip vorticity. A section lift coefficient of 2π shall be applied over the entire span. The zero-lift angle is assumed to be -4° over the entire span. The stall angle will be 16° relative to the chord line for the entire span.

5.2.5 Ailerons

For the conventional design, the aileron length will be one third of the wing length, beginning at the mid-span, as shown in Figure 5.3. No correction will be made to the stiffness matrix in the aileron region. The aileron will be assumed to extend the maximum section lift coefficient to a sufficient degree that aileron stall will not occur (the effective angle of attack due to aileron deflection will not be considered in the calculation of stall). The dynamic effects due to the weight of the ailerons and hydraulic lines and actuators are neglected.

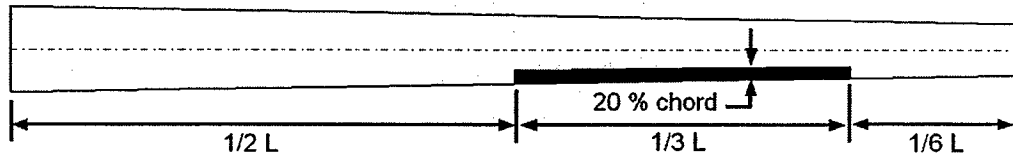


Figure 5.3: Aileron configuration for roll comparison results.

5.2.6 Passive Wing Layup and Thickness Distribution

The passive wings will be constructed completely of graphite/epoxy unidirectional layered composites. The ply angles will be a combination of 0° , $+45^\circ$, and -45° . This set of ply angles is consistent with the design of the Predator UAV. The thickness distribution along the span is determined for a minimum weight design under the following constraints:

- Ply strains do not exceed their design limits at maximum design load factor.
- The open loop flutter speed must be at least 20% above the intended flight speed for each flight index point.

5.2.7 Active Wing Layup and Thickness Distribution

For the active wings, the $\pm 45^\circ$ graphite/epoxy plies are replaced with anisotropic piezocomposite layers to provide simultaneous twist and bending authority. Two active designs are considered. For the first design, ISA1, the actuator plies use a standard thickness of 0.203 mm. For the second, ISA2, the actuator ply thickness is reduced so that the active and passive wings have the same weight.

5.2.8 Material Properties

The relevant material properties and design strain limits are given in Table 5.2. The APC represents a generic anisotropic piezocomposite material (like AFC⁸ or MFC⁴⁵).

Table 5.2: Material properties

	Graphite/Epoxy	APC
density (kg/m^3)	1545	4060
max free strain ($\mu\epsilon$)	---	± 1350
Q_{11} (GPa)	166.0	20.66
Q_{12} (GPa)	3.011	3.146
Q_{22} (GPa)	8.855	14.98
Q_{66} (GPa)	4.900	4.000
η_{12}	0.340	0.210
Design Strain Limits		
ϵ_{11} , tension	0.004	0.003
ϵ_{11} , compression	0.004	0.003
ϵ_{22} , tension	0.004	0.004
ϵ_{22} , compression	0.004	0.004
ϵ_{12}	0.0055	0.0055
Honeycomb Core		
Young's Modulus (MPa)	18	
Shear Modulus (MPa)	7	
density (kg/m^3)	15	

5.3 Baseline Vehicle Data

The same basic cross-section shape applies to all three vehicle classes. The layup for the aileron design is shown in Figure 5.4. The spar is located at 35% chord from the leading edge. The shear center location (from the leading edge) was determined using the UM/VABS cross-sectional analysis software¹⁹ to be 0.3558 chords in the horizontal direction and 0.0478 chords in the vertical direction.

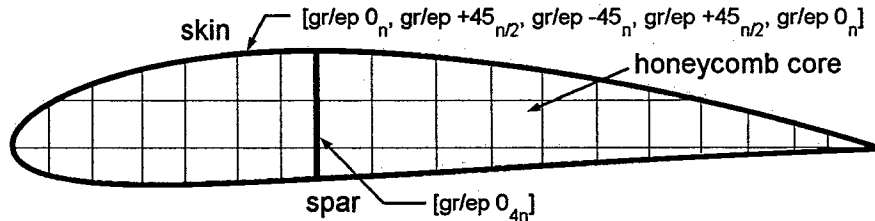


Figure 5.4: Cross section layup for the aileron design.

The baseline strain actuated wing is exactly the same as the aileron actuated wing, except that the ailerons have been removed, and the $\pm 45^\circ$ graphite/epoxy plies have been

replaced with APC. The active cross section layup is shown in Figure 5.5 for the full thickness ISA1 design.

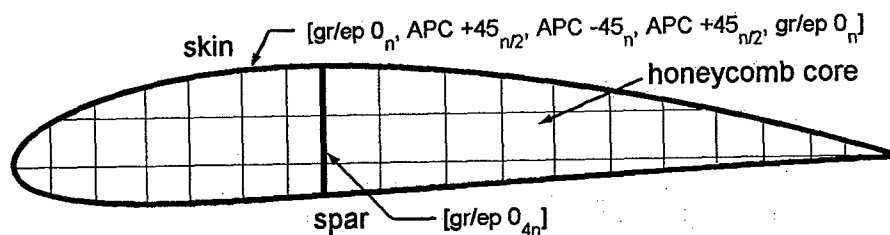


Figure 5.5: Active cross section layup.

The wing dimensions and material distribution for the three wing classes are shown in Figures 5.6 to 5.8.

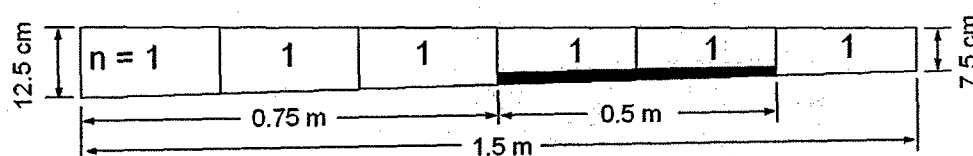


Figure 5.6: Wing geometry for the small class vehicle (n is associated with the ply layup as defined in Figs. 5.4 and 5.5).

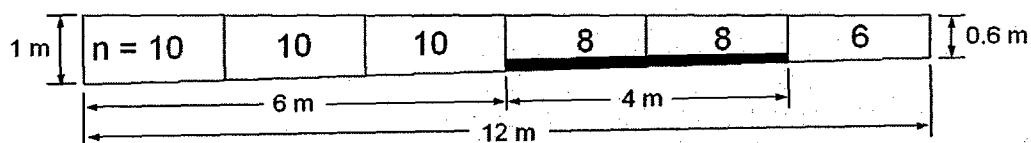


Figure 5.7: Wing geometry for the medium class vehicle (n is associated with the ply layup as defined in Figs. 5.4 and 5.5).

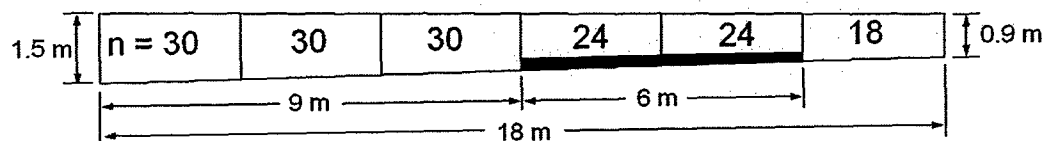


Figure 5.8: Wing geometry for the large class vehicle (n is associated with the ply layup as defined in Figs. 5.4 and 5.5).

Data for the baseline vehicles are given in tables 5.3 to 5.5 for the three vehicle classes. Wing natural frequencies are given in tables 5.6 to 5.8. Other structural properties for these wings are given in Appendix B. The nominal flight speed, altitude, and fuel burn profiles used for designing these wings are presented in Figures 5.9 to 5.11

for the three vehicle classes. The resulting trim angle of attack is also included in these figures.

Table 5.3: Physical properties of the baseline small class vehicle

	Aileron	ISA1	ISA2
Cruise Altitude (m)	1,000	1,000	1,000
Cruise Speed (m/s)	25	25	25
Fuselage Weight (kg)	10	10	10
Fuselage Roll Inertia (kg-m ²)	0.032	0.032	0.032
Fuel Weight (kg)	0	0	0
Maximum Load Factor	5.5	5.5	5.5
Total Wing Weight (kg)	0.577	1.35	0.588
Vehicle Weight (empty) (kg)	10.577	11.35	10.588
Vehicle Roll Inertia (empty) (kg-m ²)	0.4658	1.0642	0.4772
Take Off Gross Weight (kg)	10.577	11.35	10.588
Wing Weight % of Total Structural Weight	5.4	11.9	5.6

Table 5.4: Physical properties of the baseline medium class vehicle

	Aileron	ISA1	ISA2
Cruise Altitude (m)	8,000	8,000	8,000
Cruise Speed (m/s)	60	60	60
Fuselage Weight (kg)	1,000	1,000	1,000
Fuselage Roll Inertia (kg-m ²)	205.5	205.5	205.5
Fuel Weight (kg)	300	300	300
Maximum Load Factor	4	4	4
Total Wing Weight (kg)	327	765	331
Vehicle Weight (empty) (kg)	1,327	1765	1,331
Vehicle Roll Inertia (empty) (kg-m ²)	14,017	32,508	14,171
Take Off Gross Weight (kg)	1,627	2065	1,631
Wing Weight % of Total Structural Weight	24.6	43.3	24.9

Table 5.5: Physical properties of the baseline large class vehicle

	Aileron	ISA1	ISA2
Cruise Altitude (m)	18,000	18,000	18,000
Cruise Speed (m/s)	170	170	170
Fuselage Weight (kg)	6,000	6,000	6,000
Fuselage Roll Inertia (kg-m ²)	2,733	2,733	2,733
Fuel Weight (kg)	2,000	2,000	2,000
Maximum Load Factor	3	3	3
Total Wing Weight (kg)	2,125	5,082	2,150
Vehicle Weight (empty) (kg)	8,125	11,082	8,150
Vehicle Roll Inertia (empty) (kg-m ²)	204,650	485,480	206,990
Take Off Gross Weight (kg)	10,125	13,082	10,150
Wing Weight % of Total Structural Weight	26.2	45.9	26.4

Table 5.6: Wing natural frequencies for the small class vehicle (Hz)

Mode #	Aileron		ISA1		ISA2	
1	14.04	1FB	9.06	1FB	13.31	1FB
2	71.77	1CB	46.26	1CB	67.85	2CB
3	73.54	2FB	47.69	2FB	69.65	2FB
4	206.72	3FB	108.03	1T	120.13	1T
5	282.67	1T	133.89	3FB	193.33	3FB
6	375.75	2CB	242.05	2T	291.17	2T

Table 5.7: Wing natural frequencies for the medium class vehicle (Hz)

Mode #	Aileron		ISA1		ISA2	
1	2.04	1FB	1.33	1FB	1.95	1FB
2	9.64	2FB	6.26	2FB	9.15	2FB
3	10.43	1CB	6.80	1CB	9.95	1CB
4	26.53	3FB	14.70	1T	16.30	1T
5	38.55	1T	17.19	3FB	24.80	3FB
6	49.13	2CB	31.61	2T	36.88	2T

Table 5.8: Wing natural frequencies for the large class vehicle (Hz)

Mode #	Aileron		ISA1		ISA2	
1	1.39	1FB	0.89	1FB	1.33	1FB
2	6.55	2FB	4.21	2FB	6.21	2FB
3	7.09	1CB	4.57	1CB	6.76	1CB
4	18.02	3FB	9.74	1T	10.74	1T
5	25.86	1T	11.54	3FB	16.80	3FB
6	33.37	2CB	21.15	2T	24.34	2T

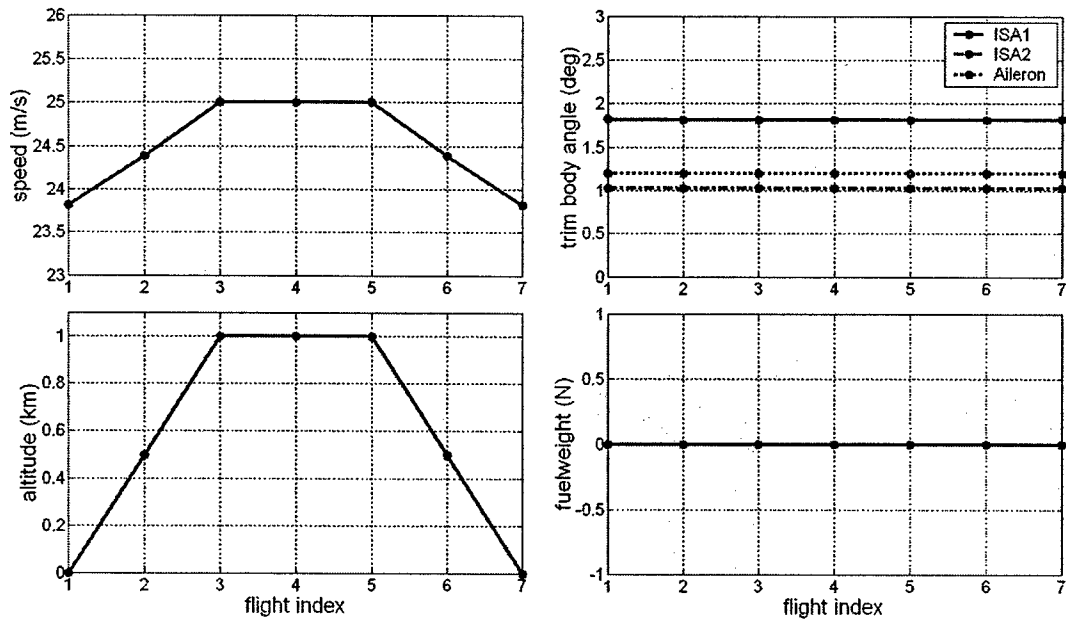


Figure 5.9: Nominal mission profile for the small class vehicle.

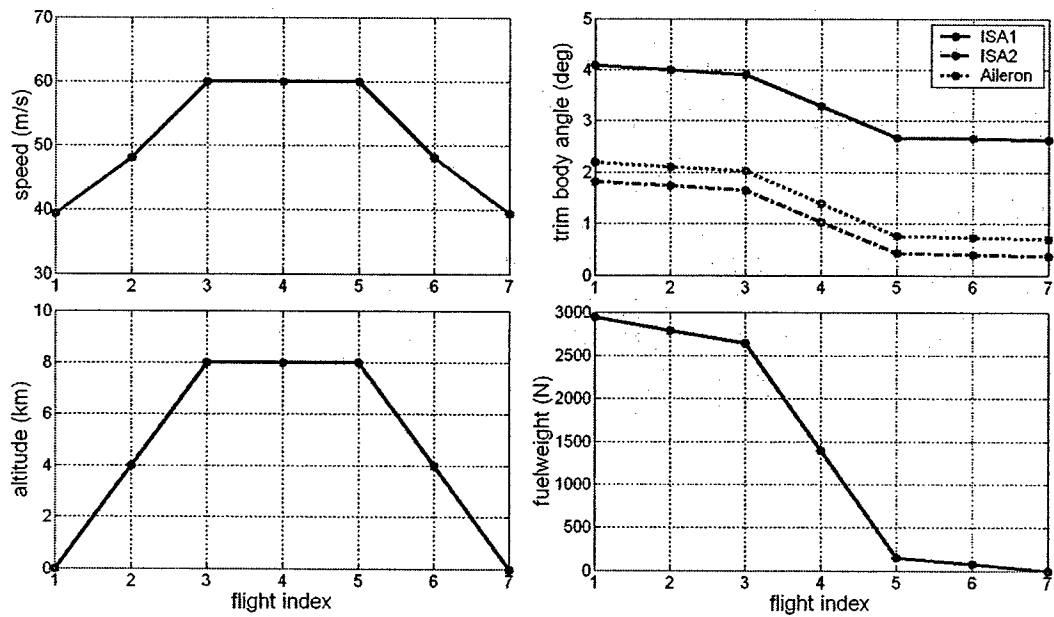


Figure 5.10: Nominal mission profile for the medium class vehicle.

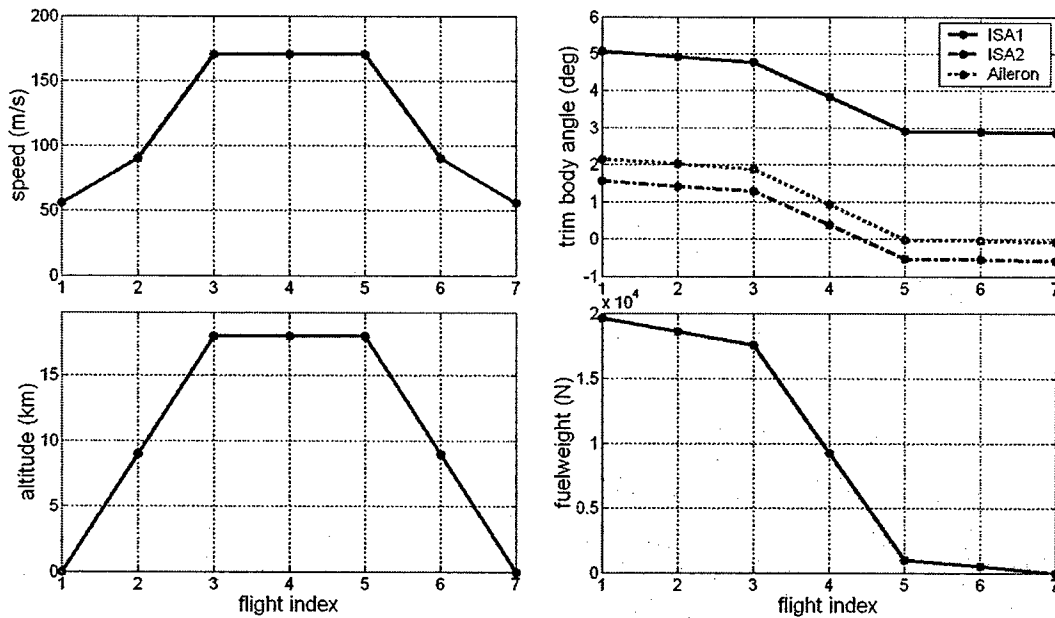


Figure 5.11: Nominal mission profile for the large class vehicle.

5.3.1 Static Twist Performance

The authority of the active wings to produce twist is determined by applying maximum twist actuation in zero gravity and vacuum. The results are presented in Figures 5.12 and 5.13. For each ISA1 wing, the peak-to-peak tip twist amplitude is approximately 24° . Each of the three ISA2 wings has a peak-to-peak tip twist amplitude of approximately 12° . The results indicate that the tip twist amplitude is roughly constant as the vehicle scales in size, when the ratio of active and passive materials is held constant.

5.3.2 Effects of Active Material Properties on Wing Twist

The properties of the APC plies play an important role in the mechanical coupling with the passive structure. Increasing the free strain or the stiffness of the active composite will increase the amount of deformation of the built-up structure. In Figure 5.14, the peak-to-peak tip twist of the ISA2 wing is plotted for increasing active ply stiffness, free strain, and thickness. In this plot, the default ISA2 design corresponds to a multiplier of 1, equivalent to 12° of tip twist.

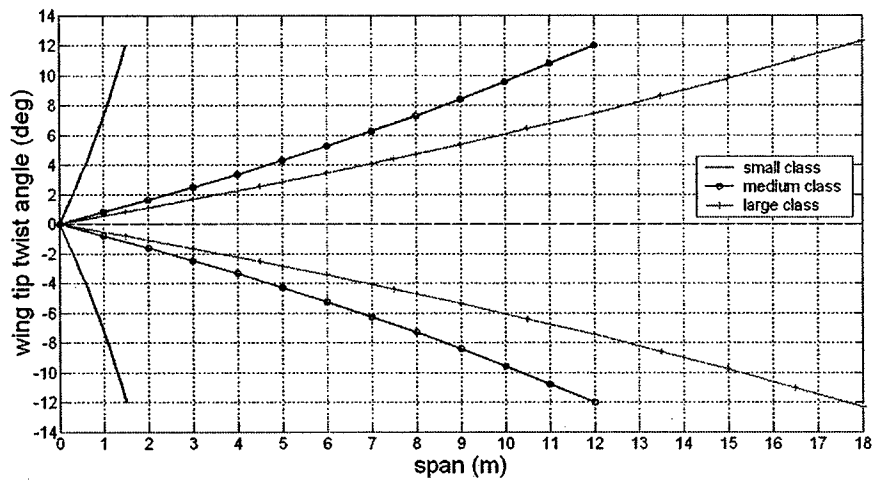


Figure 5.12: Wing tip twist due to maximum actuation for the three ISA1 wing classes.

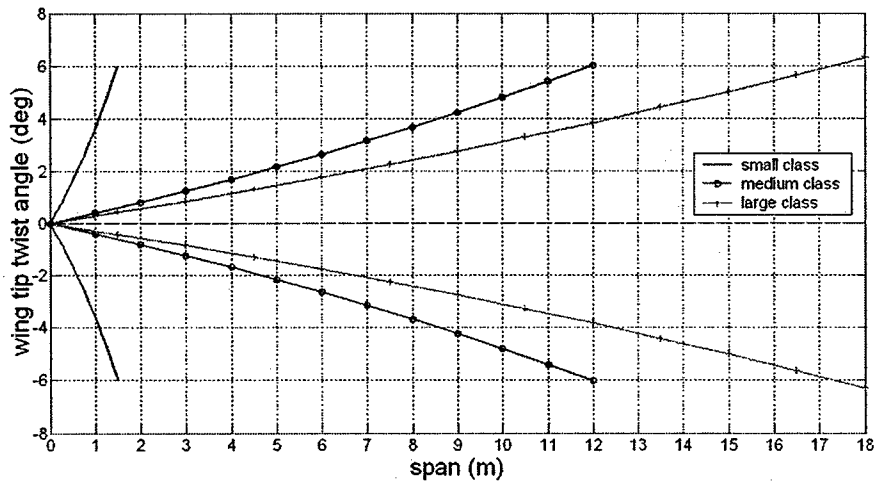


Figure 5.13: Wing tip twist due to maximum actuation for the three ISA2 wing classes.

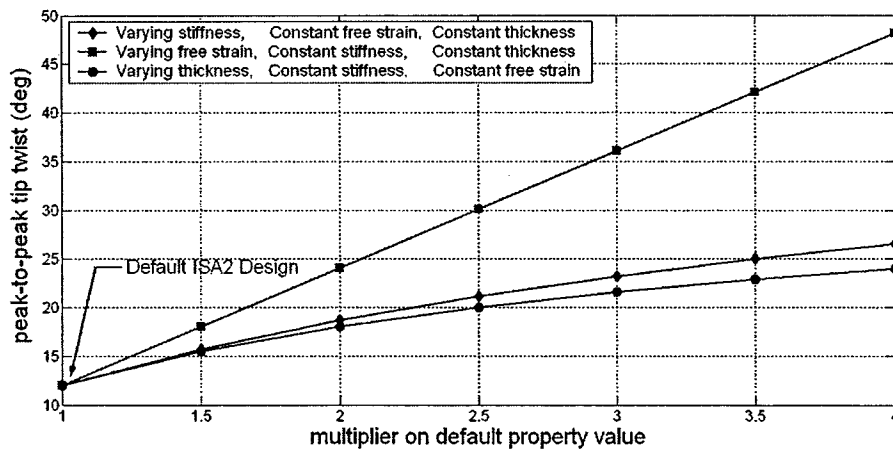


Figure 5.14: The effect of active ply properties on tip twist.

Increasing the free strain of the material has the largest effect on wing twist. When the ply thickness or stiffness is increased, a limiting value of induced twist is approached. This happens because the active plies are responsible for most of the torsional stiffness, and thus are allowed to reach the free strain limit when maximum actuation is applied.

5.4 Roll Performance - Wing Warping vs. Aileron

In this section, the open loop transient and frequency responses are obtained for roll actuation. For the transient response, each of the nine vehicles are evaluated at the first three flight index points in order to examine the effect of altitude and speed on roll angle and roll rate performance. The frequency response is then obtained at flight index 1 for each vehicle. The roll actuation inputs are maximum anti-symmetric aileron and twist actuation. The outputs are roll angle, roll rate, tip twist, and tip deflection amplitudes. In all cases, the vehicle is brought to its nonlinear steady state deformation in trimmed flight before the system is linearized. The open loop response is then obtained. The effects of aileron angle and its first and second time derivatives on the aerodynamic forces and the unsteady aerodynamic states are taken into account. Special attention is needed to obtain the frequency response. The state vector must be augmented with the aileron rate and acceleration variables, using the aileron angle as the control input.

5.4.1 Transient Roll Response

The transient roll response is obtained at the nominal (slowest) speed for flight index points 1, 2, and 3, representing the slowest roll response. The control input is shown in Figure 5.15, corresponding to both twist actuation and aileron deflection.

The roll rate and roll angle responses are shown in Figures 5.16 to 5.21. In all cases, the aileron response is slightly faster than the full thickness strain actuation design (ISA1). The ISA2 design achieves a maximum roll rate of about half that of the ISA1 design. Due to the increase in roll inertia, the ISA2 vehicle response is slower than the aileron vehicle. This effect is most apparent for the large class vehicle, which has the highest percentage increase in roll inertia.

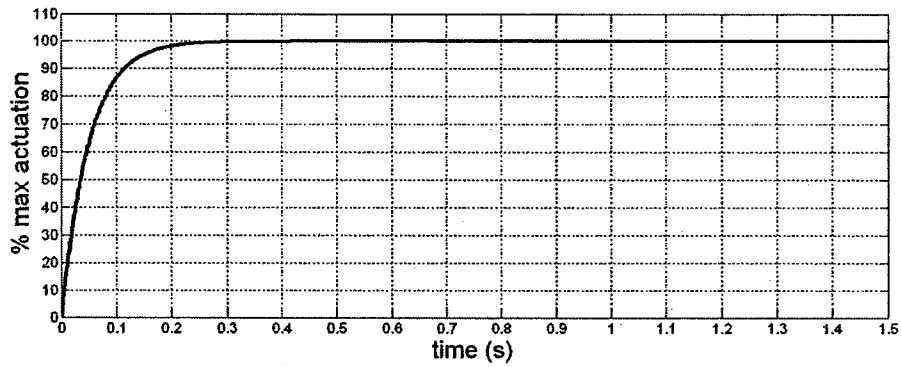


Figure 5.15: Control input for roll response.

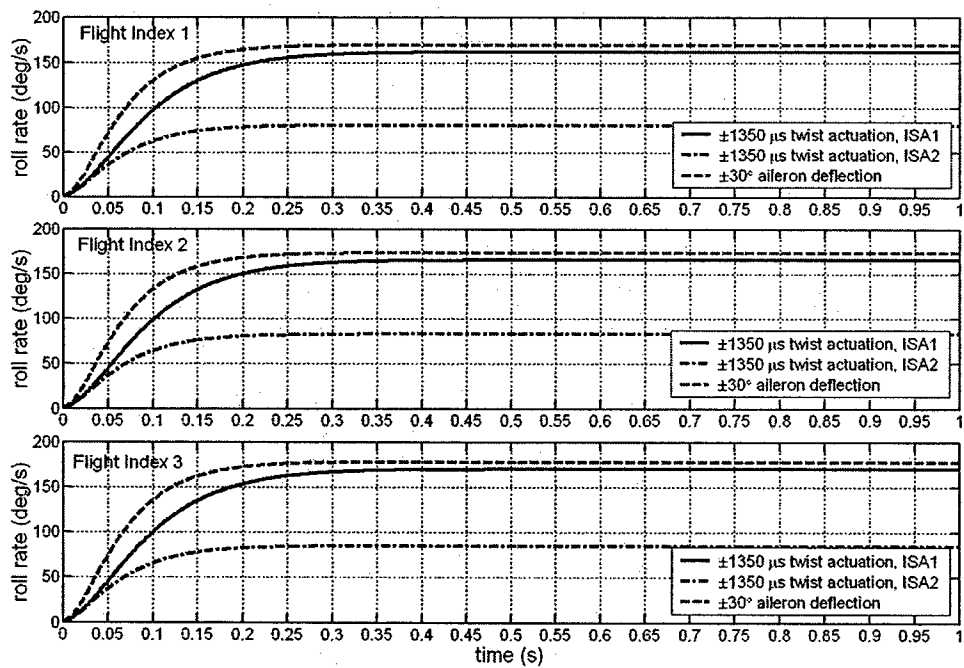


Figure 5.16: Roll rate response of the small class vehicle.

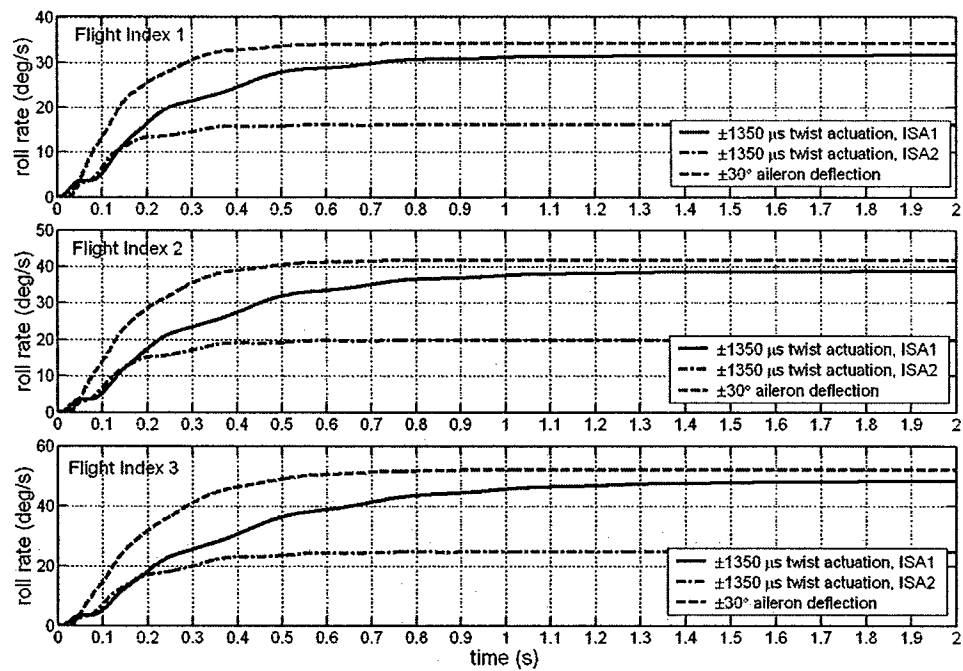


Figure 5.17: Roll rate response of the medium class vehicle.

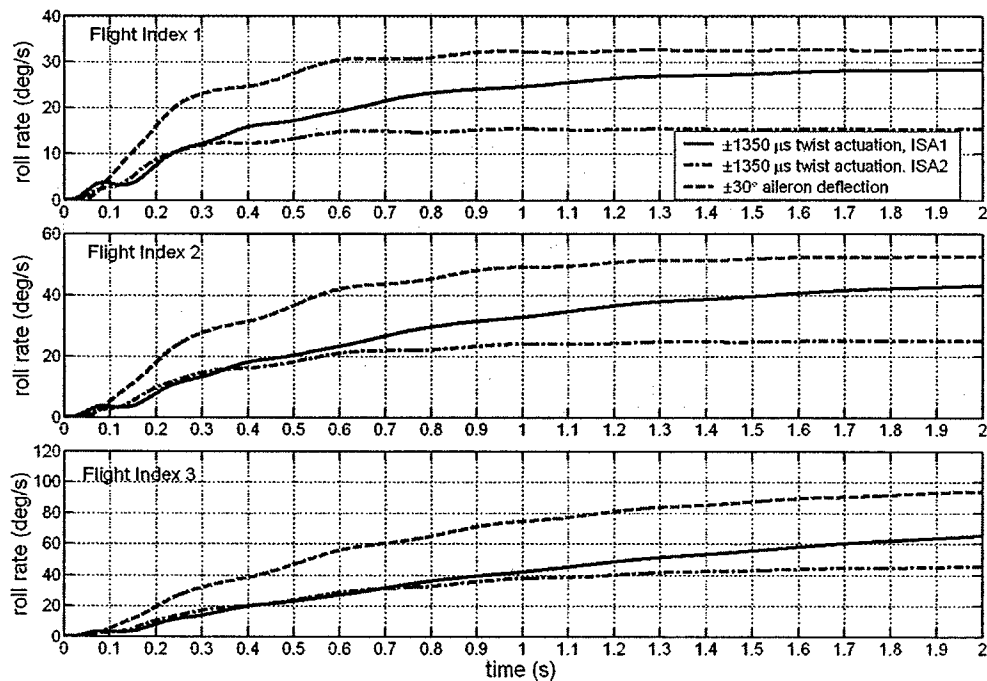


Figure 5.18: Roll rate response of the large class vehicle.

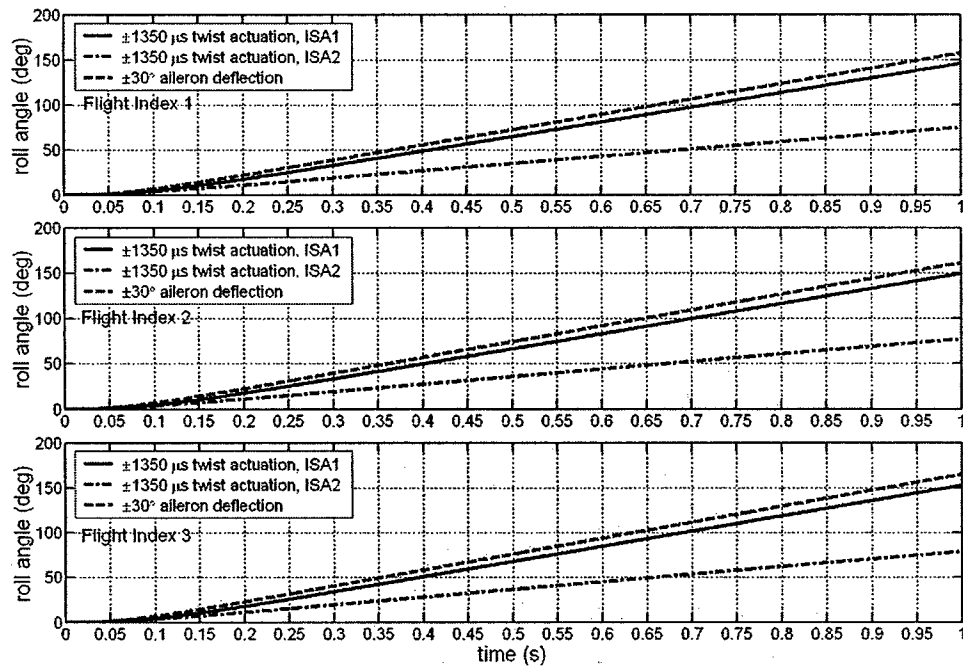


Figure 5.19: Roll angle response of the small class vehicle.

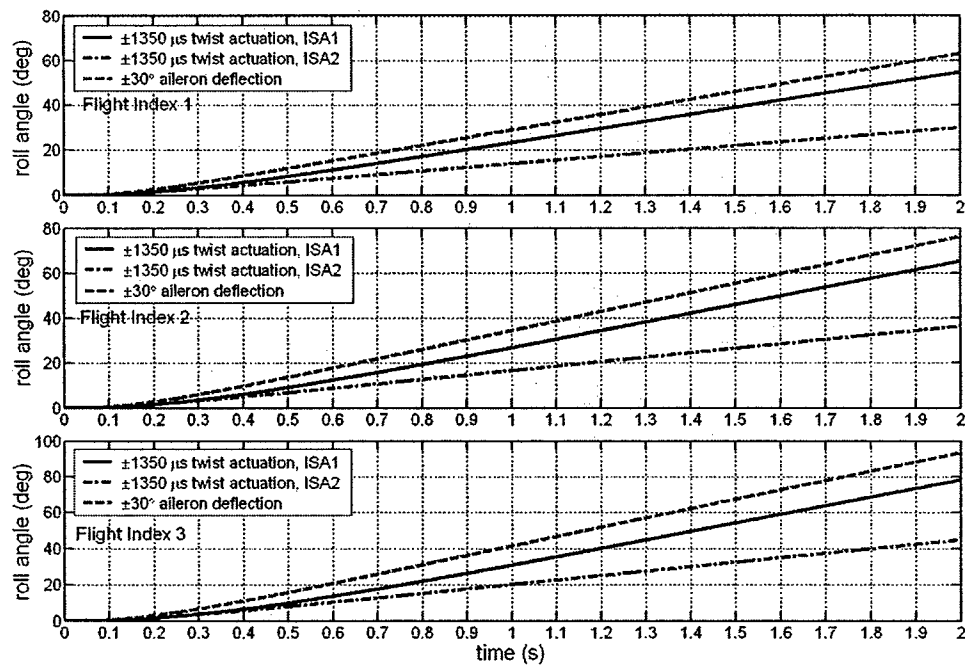


Figure 5.20: Roll angle response of the medium class vehicle.

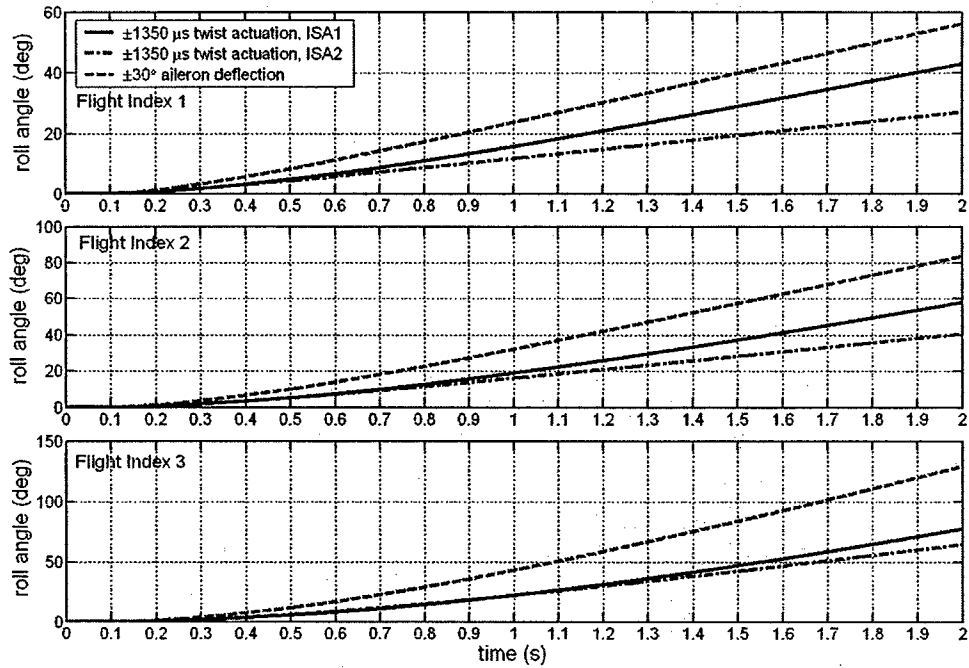


Figure 5.21: Roll angle response of the large class vehicle.

5.4.2 Roll Actuation Frequency Response

In order to obtain the frequency response from aileron angle input to system outputs, the system matrices had to be augmented with aileron states. The augmented system is given by:

$$\begin{bmatrix} I & 0 & 0 & 0 & 0 \\ 0 & M & 0 & 0 & -B_{\beta} \\ 0 & -L_1 & I & 0 & -L_4 \\ 0 & 0 & 0 & I & 0 \\ 0 & 0 & 0 & 0 & I \end{bmatrix} \begin{bmatrix} \dot{q} \\ \dot{\lambda} \\ \dot{\beta} \\ \ddot{\beta} \end{bmatrix} = \begin{bmatrix} 0 & I & 0 & 0 & 0 \\ -K & -C & -D & B_{\beta} & B_{\dot{\beta}} \\ 0 & L_2 & L_3 & 0 & -L_5 \\ 0 & 0 & 0 & 0 & I \\ 0 & 0 & 0 & 0 & 0 \end{bmatrix} \begin{bmatrix} q \\ \lambda \\ \beta \\ \dot{\beta} \end{bmatrix} + \begin{bmatrix} 0 \\ 0 \\ 0 \\ 0 \\ \Phi \end{bmatrix} \ddot{\beta}_c \quad (5.1)$$

where β is the aileron angle, B are influence matrices from aileron angle and its time derivatives, L_4 and L_5 are matrices containing the influence of aileron rate and acceleration on the inflow rate of change, and L_1 , L_2 , and L_3 are defined in Equation (2.86). The column matrix Φ is the aileron mode corresponding to anti-symmetric actuation. The scalar input, $\ddot{\beta}_c$, is the second time derivative of aileron angle amplitude. Using the aileron angle as a sinusoidal input, the relation between aileron angle and aileron angular acceleration is simply given by:

$$\beta_c = \beta_0 \sin \omega t \rightarrow \ddot{\beta}_c = -\omega^2 \beta_c \quad (5.2)$$

The frequency response from aileron angle input to the desired outputs is obtained at each frequency, ω , by scaling the input matrix by ω^2 .

The frequency response from aileron and twist actuation inputs to roll angle, roll rate, tip twist, and tip deflection outputs are obtained for each of the three vehicle classes flying at sea level at the nominal flight speed. The roll angle response is first obtained to determine the frequency range for which the roll angle amplitude is non-negligible. At higher actuation frequencies, roll actuation has little effect on controlling the roll angle, and begins to excite aeroelastic modes. Figures 5.22 to 5.24 show the roll angle frequency response of each vehicle design for the three vehicle classes.

The roll rate responses are shown in Figures 5.25 to 5.27. The low frequency amplitude for each response tends towards the static roll rate from the previous section. In each case, the roll rate amplitude of the ISA1 vehicles drops off quickly due to the larger roll inertia, when compared to the other lighter wing designs.

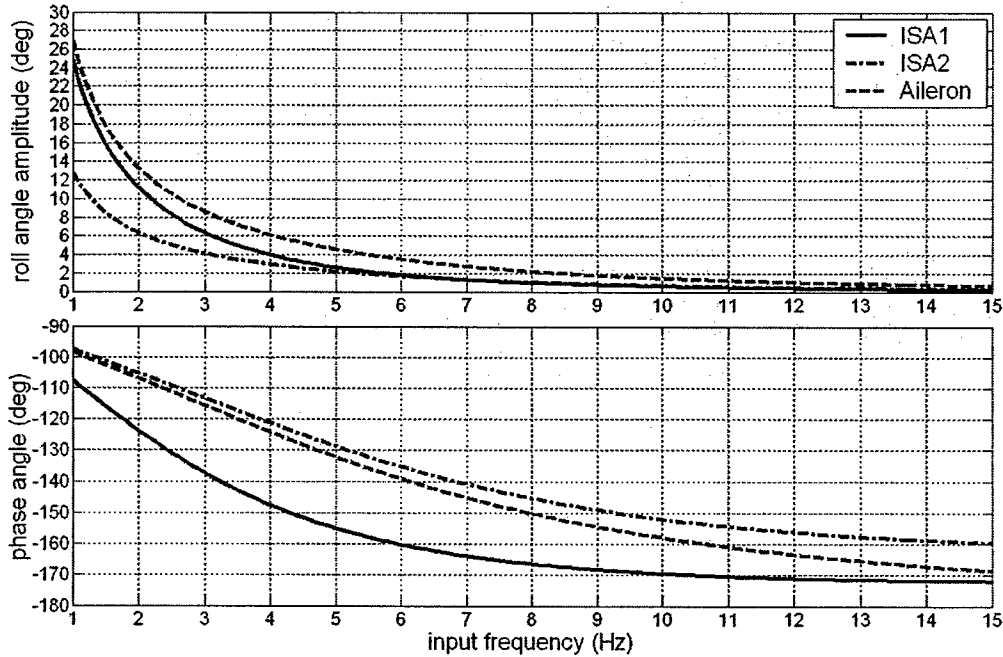


Figure 5.22: Frequency response from roll actuation input to roll angle, small vehicle.

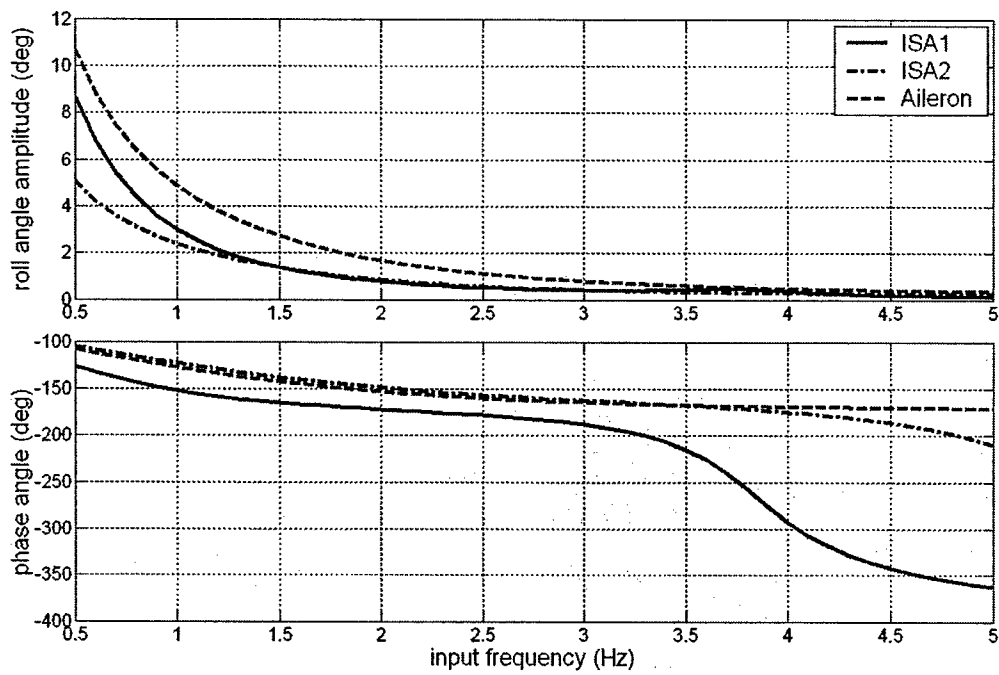


Figure 5.23: Frequency response from roll actuation input to roll angle, medium vehicle.

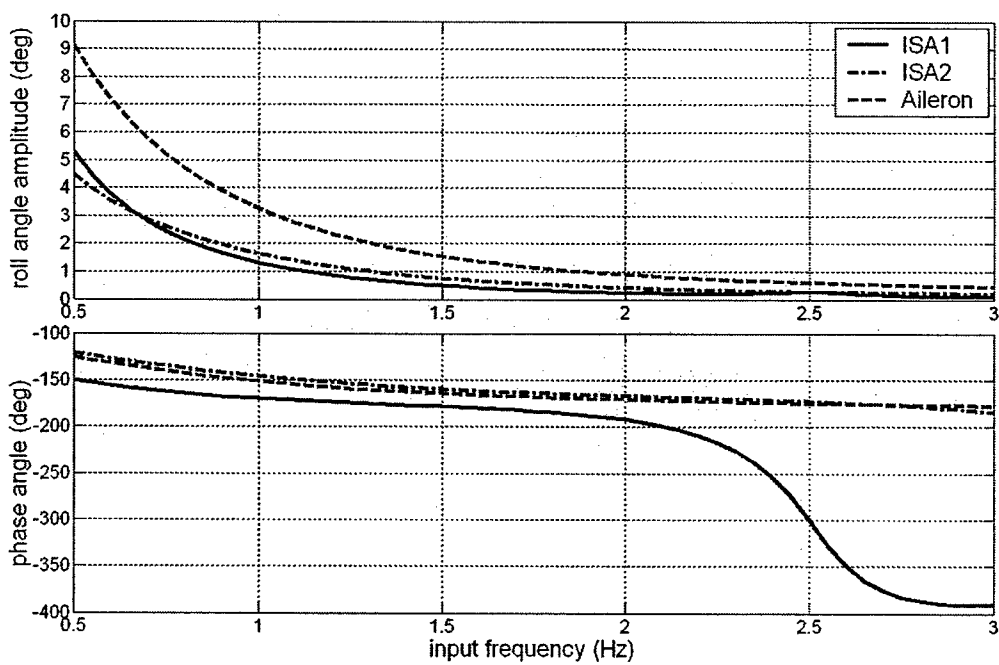


Figure 5.24: Frequency response from roll actuation input to roll angle, large vehicle.

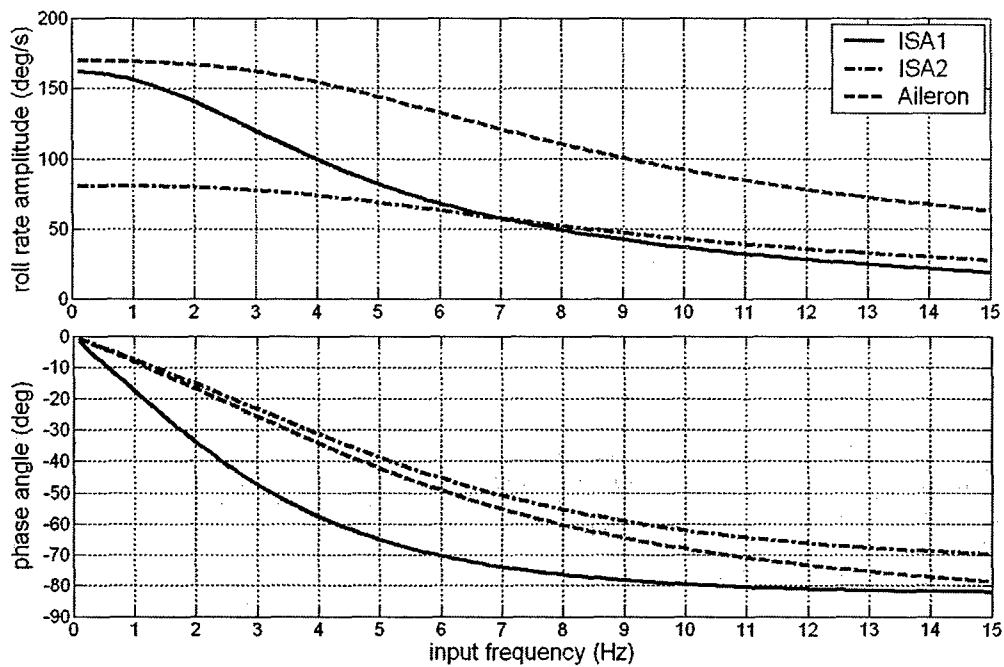


Figure 5.25: Frequency response from roll actuation input to roll rate, small vehicle.

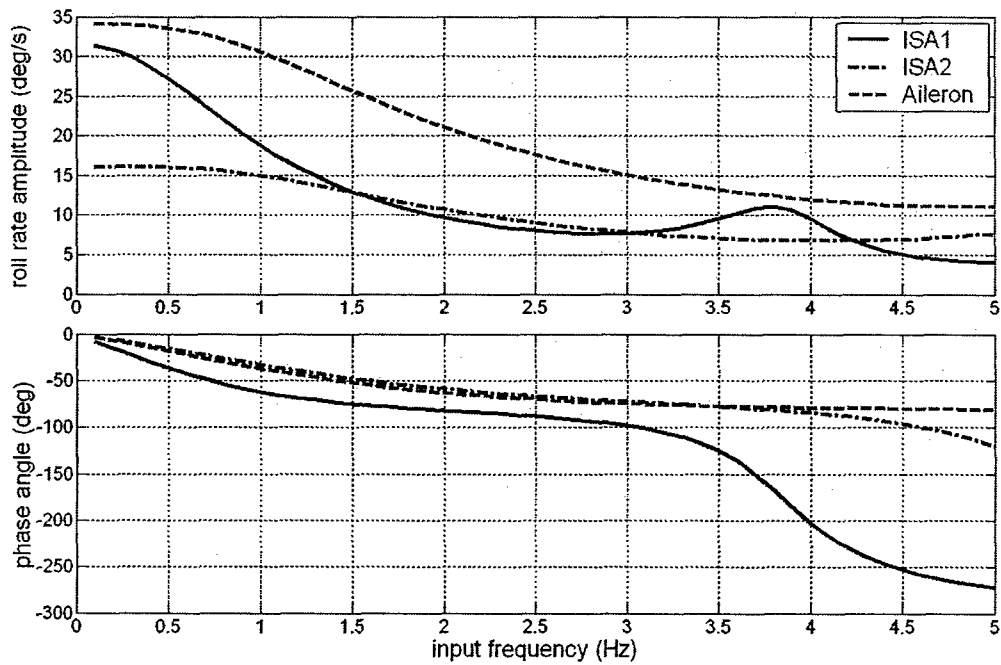


Figure 5.26: Frequency response from roll actuation input to roll rate, medium vehicle.

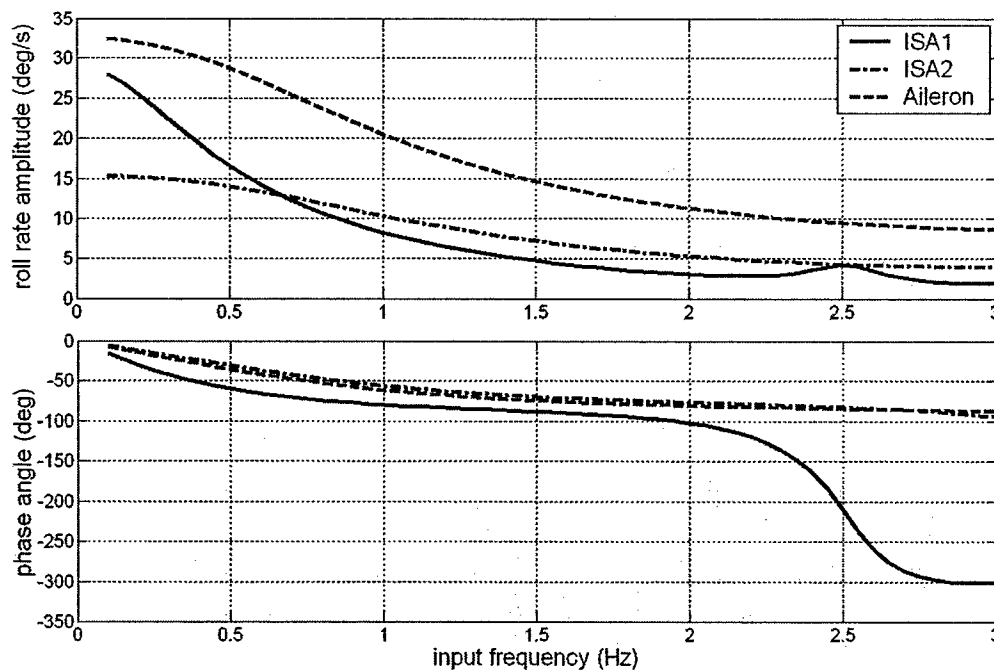


Figure 5.27: Frequency response from roll actuation input to roll rate, large vehicle.

The tip twist frequency responses are shown in Figures 5.28 to 5.30. For all of the active vehicles, the tip twist phase angle is close to 0° , indicating that there is very little lag between twist actuation input and wing twist. The twist angle amplitude remains close to the static twist angle over the frequency ranges of interest. The effects of rotational inertia of the wing about its axis have no significant effect on the twist response.

The aileron wing exhibits very little aileron induced twist at the dynamic pressure at which it is evaluated. The aileron induced wing twist is 180° out of phase with the aileron deflection, indicating the tendency to reduce the effectiveness of the aileron. The wings are evaluated at higher speeds later in this section to determine the effect of aileron induced twist on the roll response, and if any such effects are apparent on the active wings at higher dynamic pressures.

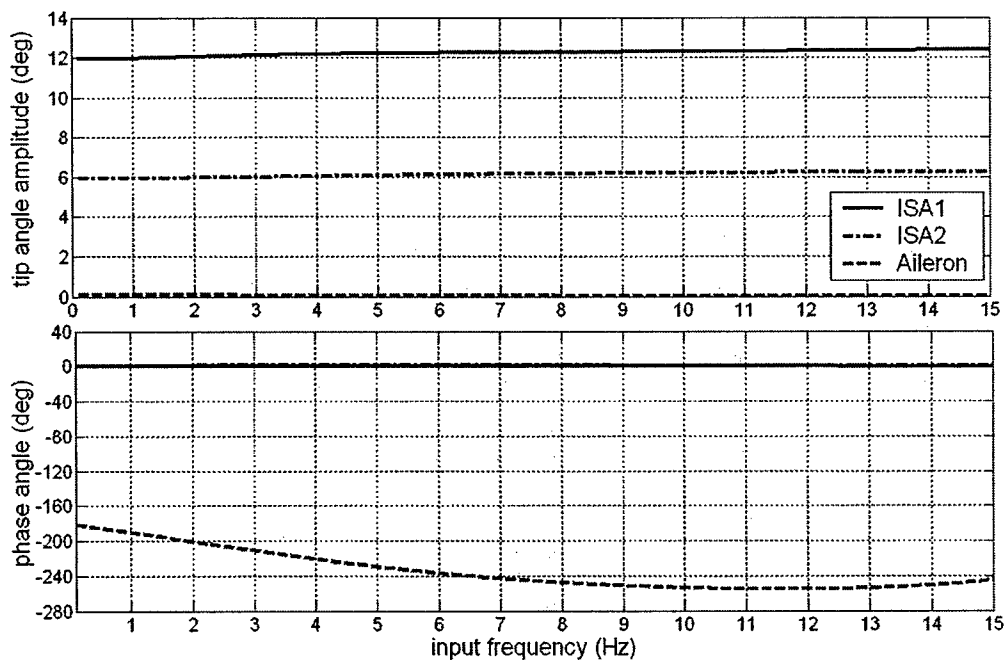


Figure 5.28: Frequency response from roll actuation input to tip twist, small vehicle.

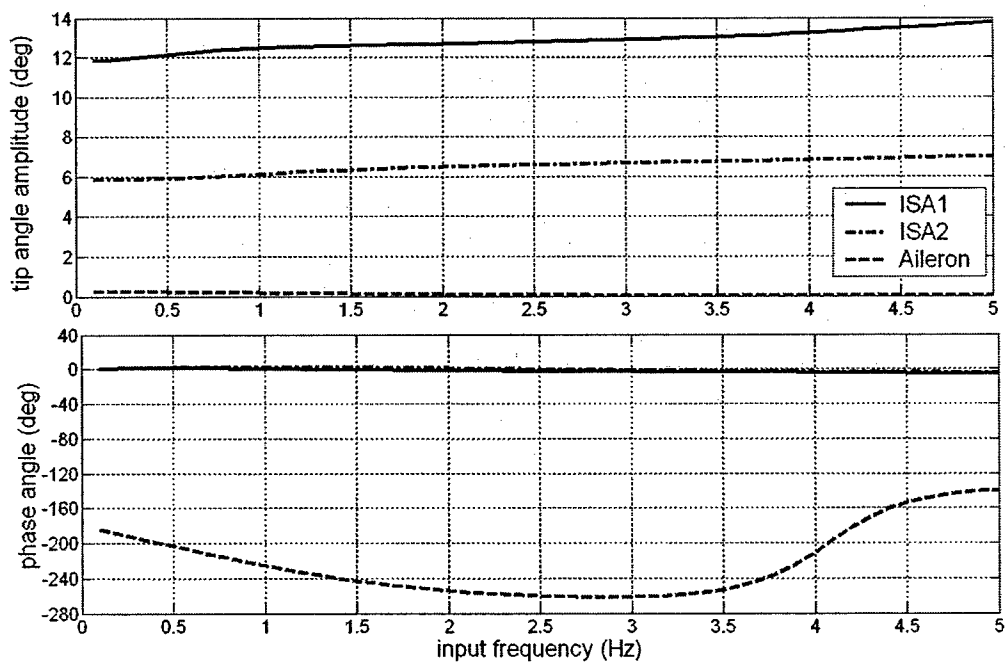


Figure 5.29: Frequency response from roll actuation input to tip twist, medium vehicle.

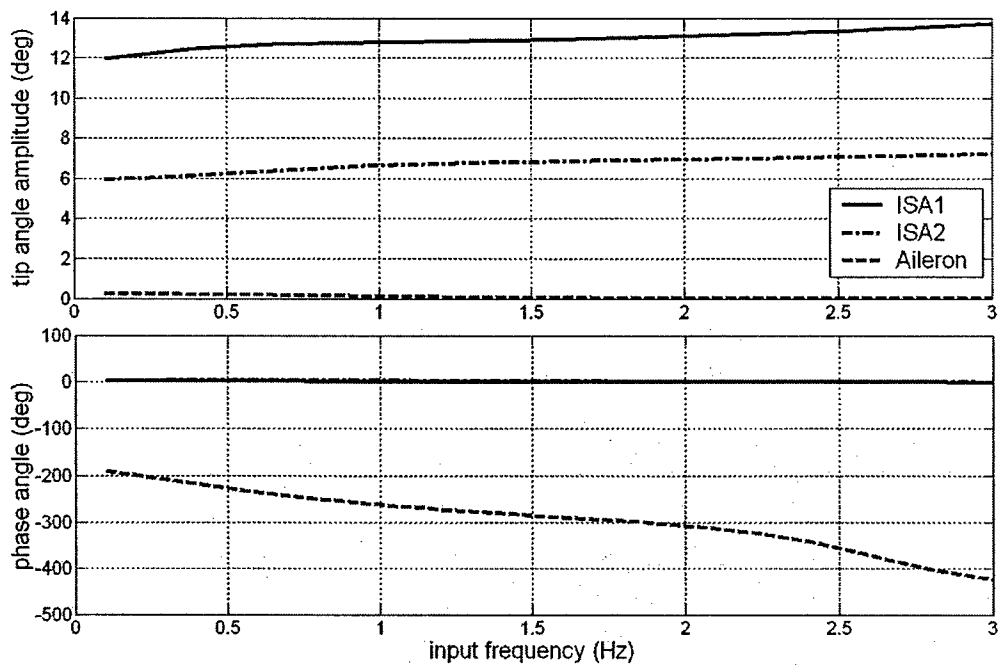


Figure 5.30: Frequency response from roll actuation input to tip twist, large vehicle.

The tip bending deflection responses are shown in Figures 5.31 to 5.33. The amplitudes are small for all cases. The peaks that occur in the medium and large vehicle responses correspond to the first anti-symmetric bending mode. For the medium ISA1 vehicle, this occurs at 3.86 Hz. The first symmetric bending mode, occurring at 1.33 Hz, is not excited by this mode of actuation.

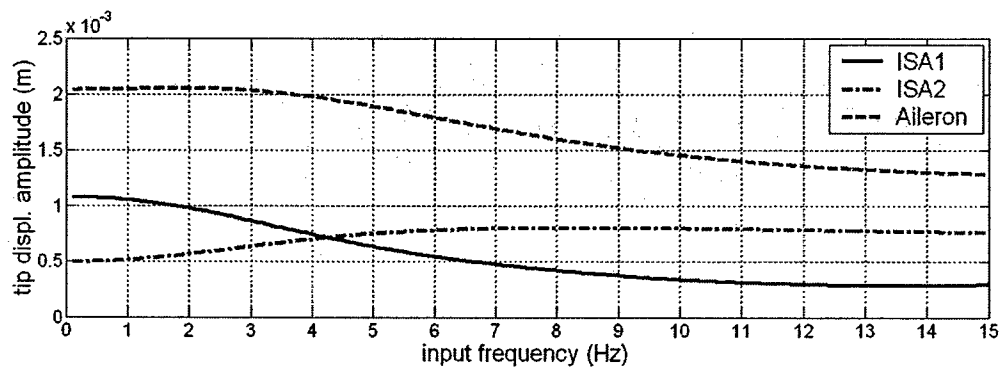


Figure 5.31: Frequency response from roll actuation input to tip deflection, small vehicle.

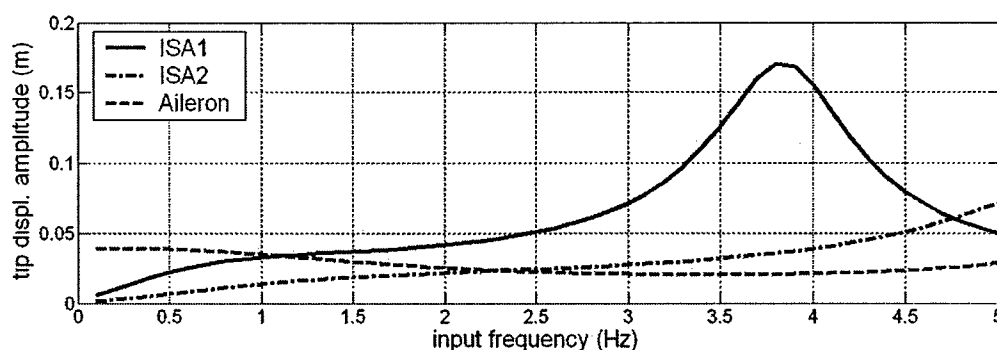


Figure 5.32: Frequency response from roll actuation input to tip deflection, medium vehicle.

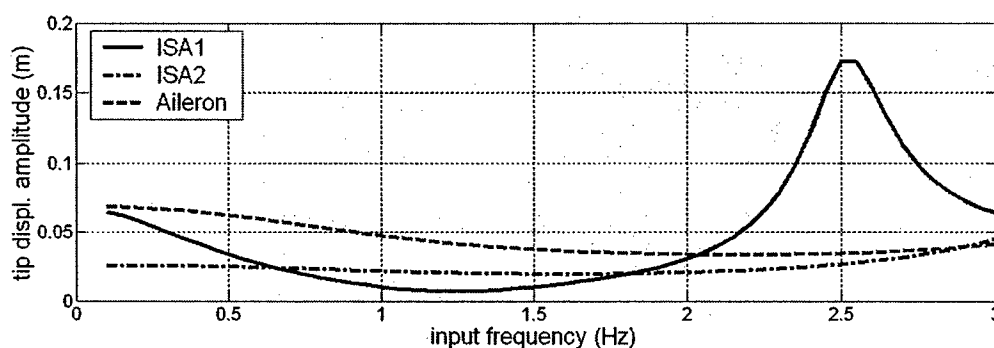


Figure 5.33: Frequency response from roll actuation input to tip deflection, large vehicle.

The frequency response for the large vehicle is investigated at Mach 0.4, sea level trimmed flight, to study the role of aileron control reversal at elevated dynamic pressure. This is relevant for the Global Hawk, since it reaches Mach 0.5+ in its operating envelope. The results are presented in Figures 5.34 to 5.37. The frequency range is increased to 6 Hz, since roll authority is higher at elevated speeds. The control input is reduced to 10% of the maximum value ($\pm 135 \mu\text{strain}$ wing warping and $\pm 3^\circ$ aileron deflection).

The roll rate for the ISA1 vehicle exceeds that of the aileron design at low input frequency, indicating that either the aileron reversal moment has slightly reduced the effectiveness of the ailerons for producing roll or that the ISA1 roll authority is slightly improved at increased dynamic pressure. The latter case is likely, since the aileron wings are stiff in torsion. When the ISA1 wings are actuated to produce positive roll, the left wing is twisted up and the right wing is twisted down. The aerodynamic twisting moment increases on the left wing and decreases on the right wing, resulting in a higher

tip twist differential between the two wings than would occur at low dynamic pressure. The effect of this is an increase in roll moment.

The low anti-symmetric bending modes of the ISA1 and ISA2 vehicles result in a roll-off of the phase angle between roll actuation input and roll angle output. The tip angle and tip displacement responses provide insight into the dynamics of the active wings at elevated dynamic pressure. Because of the reduction in aeroelastic stiffness and increase in aerodynamic twist moment, the twist-bend coupling with the air stream is increased. The tip twist angle and tip deflection become large as the input frequency is increased. Using closed-loop control to maintain the desired wing twist would overcome the degraded performance of the active wings as the roll actuation frequency is increased.

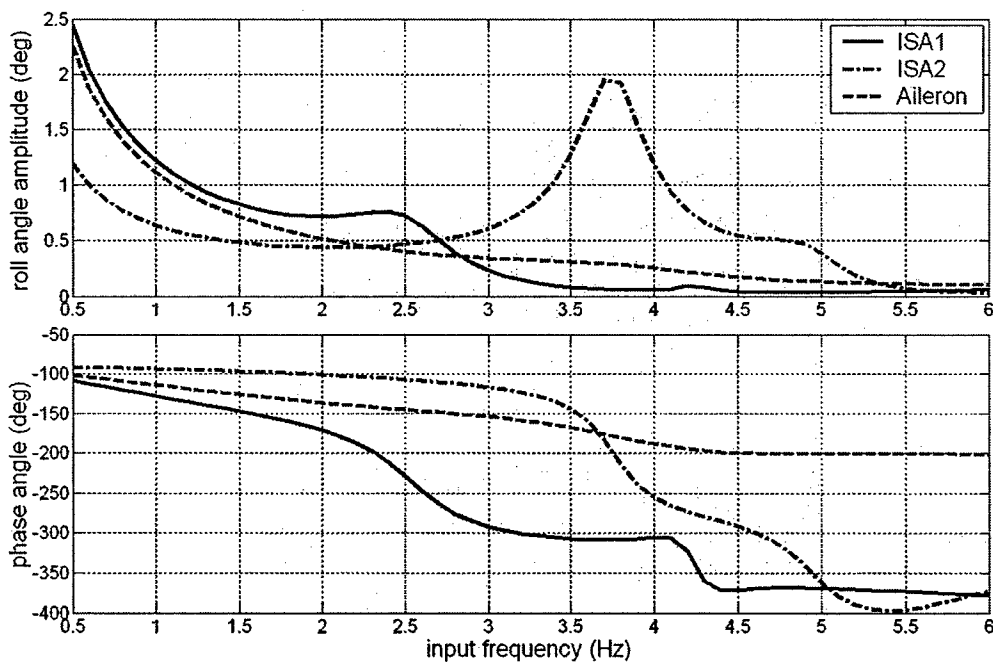


Figure 5.34: Frequency response from roll actuation input to roll angle, large vehicle (Mach 0.4, sea level).

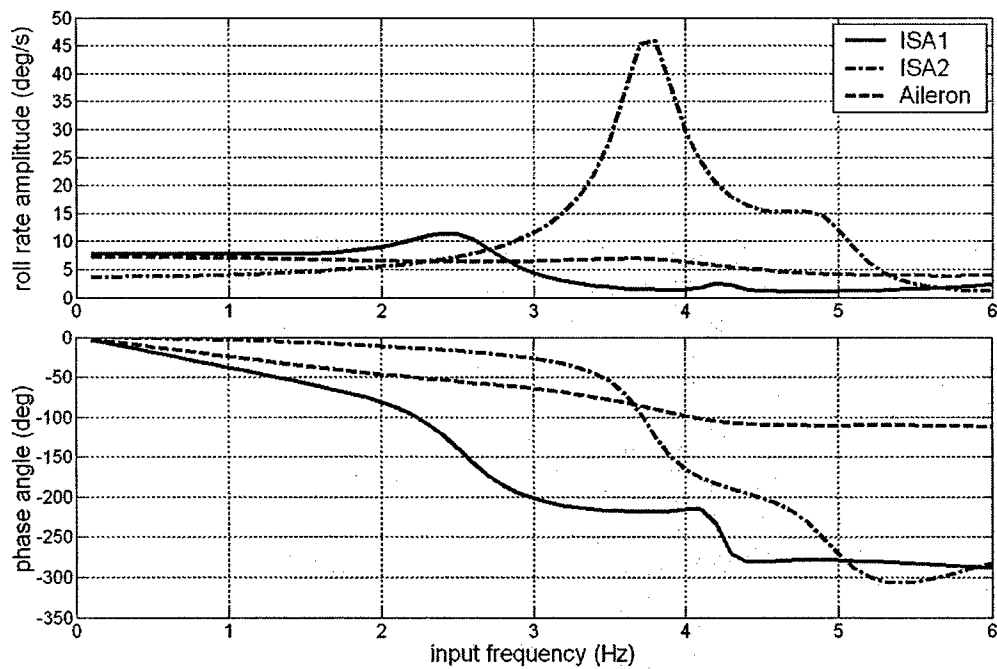


Figure 5.35: Frequency response from roll actuation input to roll rate, large vehicle (Mach 0.4, sea level).

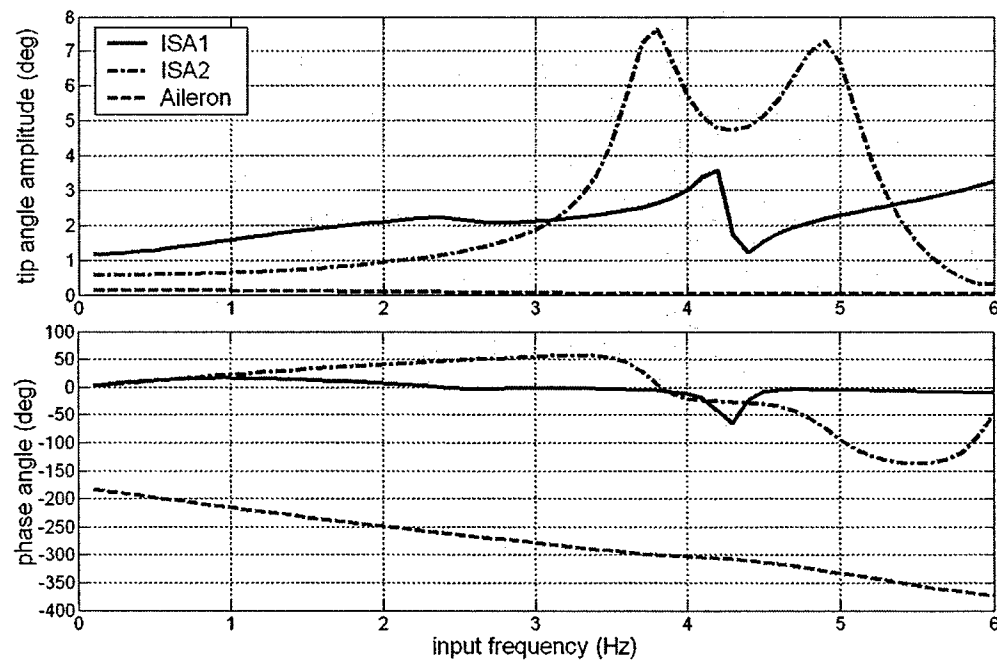


Figure 5.36: Frequency response from roll actuation input to tip twist, large vehicle (Mach 0.4, sea level).

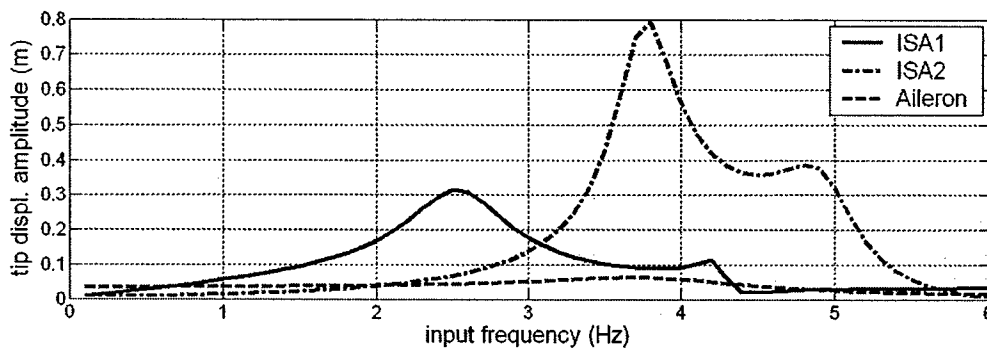


Figure 5.37: Frequency response from roll actuation input to tip deflection, large vehicle (Mach 0.4, sea level).

To further investigate the control reversal characteristics of the large class aileron wing design, the roll moment due to aileron deflection of one wing is evaluated for a range of flight speeds, varying from the nominal sea level flight speed, up to Mach 0.5. The thickness of the $\pm 45^\circ$ graphite/epoxy plies is varied from 100% to 10% of the baseline design value to observe the effects of torsional stiffness on aileron effectiveness.

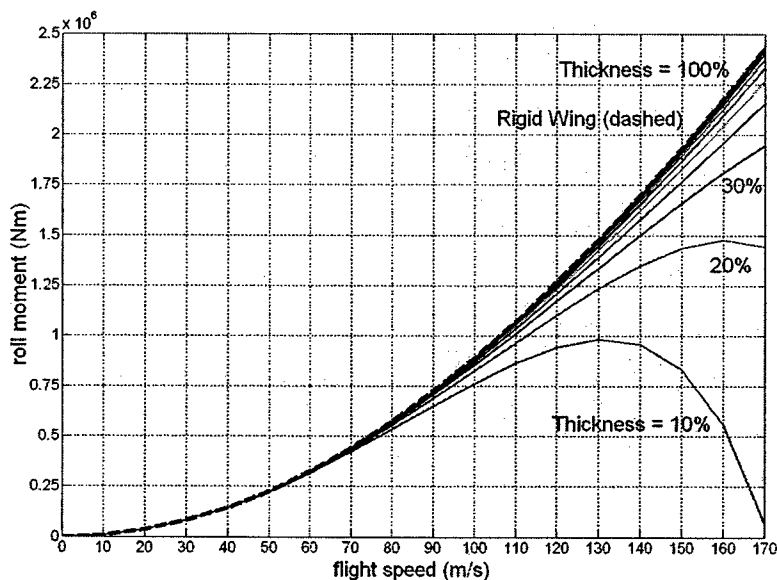


Figure 5.38: Roll moment due to aileron deflection for varying flight speed and thickness of the $\pm 45^\circ$ graphite epoxy plies (large class vehicle wing).

The results presented in Figure 5.38 indicate that the current wing design is sufficiently stiff in torsion that minimal loss of aileron effectiveness occurs. The roll moment produced by the default design is very close to that for a rigid wing, which is

represented by the dashed line. Figure 5.39 plots the roll moment at Mach 0.5 for varying thickness. From this plot it is clear that the aileron effectiveness is close to its maximum for the current aileron design.

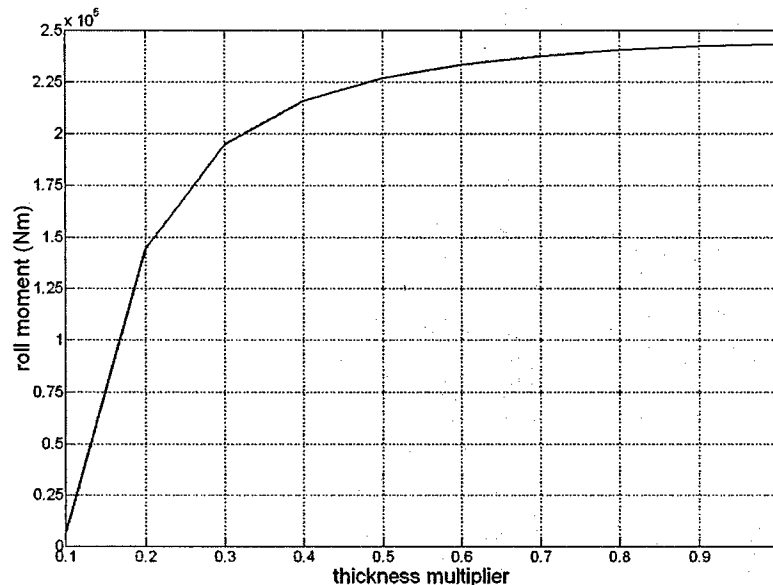


Figure 5.39: Roll moment at Mach 0.5 due to aileron deflection for varying thickness of the $\pm 45^\circ$ graphite epoxy plies (large class vehicle wing).

5.5 Wing Stabilization Using Active Control

To study stability and gust alleviation control, a reduced model is created by exploiting symmetry. The model includes the wing flexible degrees of freedom and the vertical body degrees of freedom, as shown in Figure 5.40. The present model is suited for the analysis of wing stabilization and gust load alleviation at various flight speeds and trim conditions. The vertical body degree of freedom is included since it affects the flutter speed and wing bending due to gust loading by virtue of vertical acceleration of the body.

In the analysis, the baseline wing is brought to its nonlinear steady state deformation in trimmed flight at a prescribed flight speed and altitude. The linearized aeroelastic system matrices are then computed, retaining the structural states and the unsteady aerodynamic states.

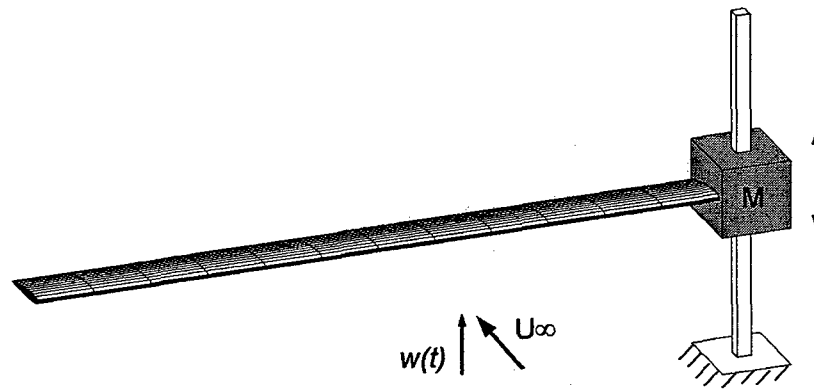


Figure 5.40: Model representation for stability and gust alleviation control.

To validate the use of the linearized plant, the open loop response of the medium scale vehicle is obtained for both the linearized model described above, and the fully nonlinear time stepping solution (in the fully nonlinear solution, the finite element matrices are recomputed on each time step, based on the current deformation). The results are shown in Figure 5.41. The tip bending displacement shown is with respect to the body, and the body displacement is in the vertical direction. The two responses are nearly identical, and the linearized solution will be employed for this particular study.

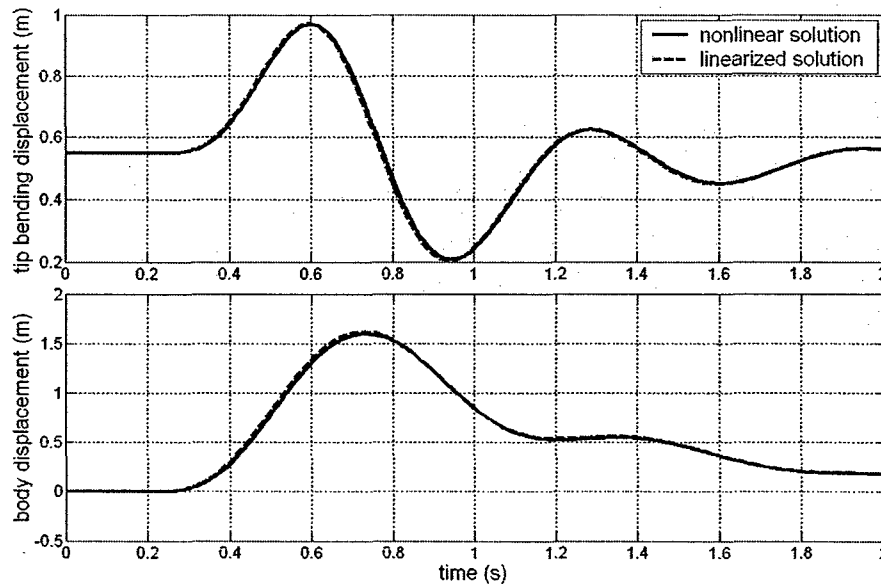


Figure 5.41: Comparison of the linearized and nonlinear responses to 5 m/s "1-cos gust" disturbance.

A feedback control law is constructed based on the system corresponding to the cantilevered wing with the inflow states suppressed. This approach allows for a simplified LQR controller to be implemented, since this system involves only the strain and strain rate variables, which are measurable. Since the finite element implementation is in terms of the beam strain variables, this approach becomes natural. The derivation of the control law is given in Appendix C. The resulting closed loop plant schematic is shown in Figure 5.42. Due to the potential for actuator saturation, a time marching solution is used. On each time step, the control input is checked for saturation and kept to its maximum allowed value if the limit is exceeded.

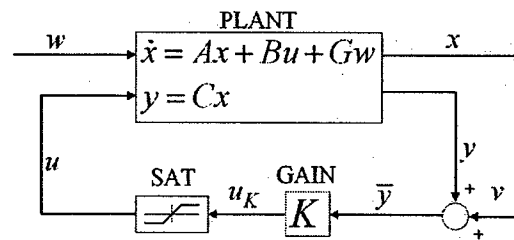


Figure 5.42: Closed loop plant representation

5.5.1 Turbulence Gust Alleviation Performance

The open and closed loop responses of the vehicle to a "moderate" vertical turbulence gust⁴⁷ encounter are recorded. The disturbance, based on the Dryden atmospheric turbulence model⁴⁷, is shown as a function of distance along the flight path in Figure 5.43, representing a stationary velocity field through which the vehicle passes.

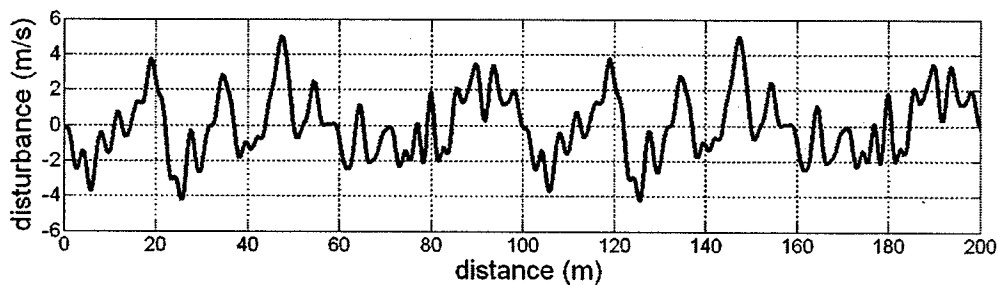


Figure 5.43: Vertical turbulence gust disturbance based on the Dryden model⁴⁷.

Three test cases are considered for each vehicle class:

- Test Case 1 - Both the simulation and the controller design take place at flight index 1 (sea level) with full fuel on board, at the nominal flight speed.
- Test Case 2 - Both the simulation and the controller design take place at flight index 3 (beginning of cruise), with 90% fuel on board for the medium and large class vehicles, at the nominal flight speed.
- Test Case 3 - The controller is designed at the nominal flight speed for flight index 3. The simulation takes place at 40% above the nominal flight speed in order to evaluate the closed-loop response when the plant dynamics have been varied. Controller measurement bias error is assumed to be zero.

Data for the simulations are summarized in Tables 5.9 to 5.11.

Table 5.9: Simulation data for Test Case 1

Vehicle Class	Small	Medium	Large
Flight Index	1	1	1
Altitude	sea level	sea level	sea level
Control Design Speed	23.8 m/s	39.3 m/s	55.6 m/s
Simulation Speed	23.8 m/s	39.3 m/s	55.6 m/s
Air Density	1.225 kg/m ³	1.225 kg/m ³	1.225 kg/m ³

Table 5.10: Simulation data for Test Case 2

Vehicle Class	Small	Medium	Large
Flight Index	3	3	3
Altitude	1 km	8 km	18 km
Control Design Speed	25 m/s	60 m/s	170 m/s
Simulation Speed	25 m/s	60 m/s	170 m/s
Air Density	1.11 kg/m ³	0.53 kg/m ³	0.13 kg/m ³

Table 5.11: Simulation data for Test Case 3

Vehicle Class	Small	Medium	Large
Flight Index	3	3	3
Altitude	1 km	8 km	18 km
Control Design Speed	25 m/s	60 m/s	170 m/s
Simulation Speed	35 m/s	84 m/s	238 m/s
Air Density	1.11 kg/m ³	0.53 kg/m ³	0.13 kg/m ³

The tip displacement responses of each vehicle passing through the turbulence field are presented in Figures 5.44 to 5.52 for the open and closed loop cases. The closed loop tip response is significantly reduced for both the aileron and strain actuated wings. Tables 5.12 to 5.14 present the root-mean-square tip bending displacement for each test case and the percentage reduction due to closed loop control. Ironically, the level of attenuation for both the aileron and the ISA1 wing designs are greater for Test Case 3, despite the plant variation. The reason for this is likely because the controller gains are computed at a lower authority region than that of the simulation. At a higher speed, the twist-bending coupling with the air stream is greater than at the control design speed, causing the restoring forces to be higher.

Table 5.12: RMS open and closed loop tip response for the small class vehicle

	Test Case	Open Loop	Closed Loop	Reduction
ISA1 RMS tip deflection (m)	1	0.0136	0.0029	78.5%
	2	0.0133	0.0027	79.7%
	3	0.0191	0.0017	91.1%
Aileron RMS tip deflection (m)	1	0.0128	0.0016	87.8%
	2	0.0121	0.0014	88.0%
	3	0.0168	0.0016	90.5%

Table 5.13: RMS open and closed loop tip response for the medium class vehicle

	Test Case	Open Loop	Closed Loop	Reduction
ISA1 RMS tip deflection (m)	1	0.1166	0.0103	91.2%
	2	0.0527	0.0049	90.7%
	3	0.0612	0.0024	96.0%
Aileron RMS tip deflection (m)	1	0.1378	0.0195	85.9%
	2	0.0843	0.0105	87.5%
	3	0.0833	0.0127	84.8%

Table 5.14: RMS open and closed loop tip response for the large class vehicle

	Test Case	Open Loop	Closed Loop	Reduction
ISA1 RMS tip deflection (m)	1	0.0448	0.0102	77.1%
	2	0.0061	0.0018	70.6%
	3	0.0062	0.0011	82.2%
Aileron RMS tip deflection (m)	1	0.0856	0.0173	79.7%
	2	0.0103	0.0027	74.0%
	3	0.0091	0.0024	73.9%

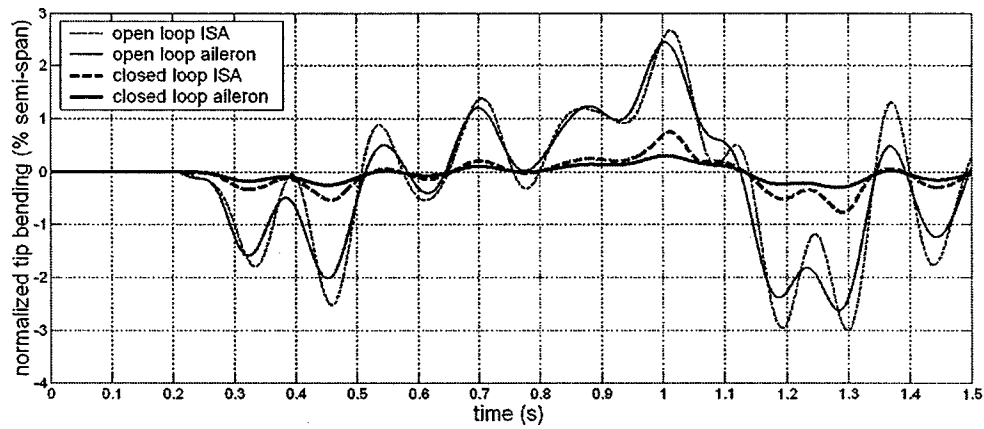


Figure 5.44: Tip bending displacement response due to turbulence, small vehicle, Test Case 1

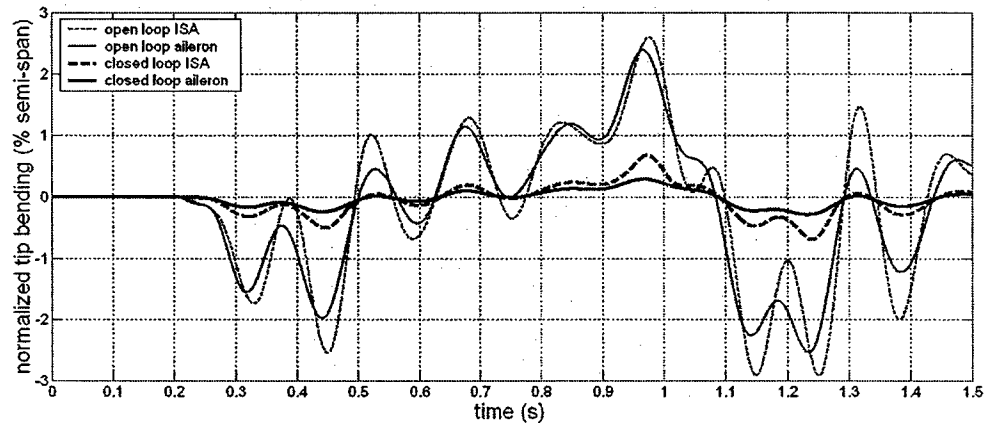


Figure 5.45: Tip bending displacement response due to turbulence, small vehicle, Test Case 2

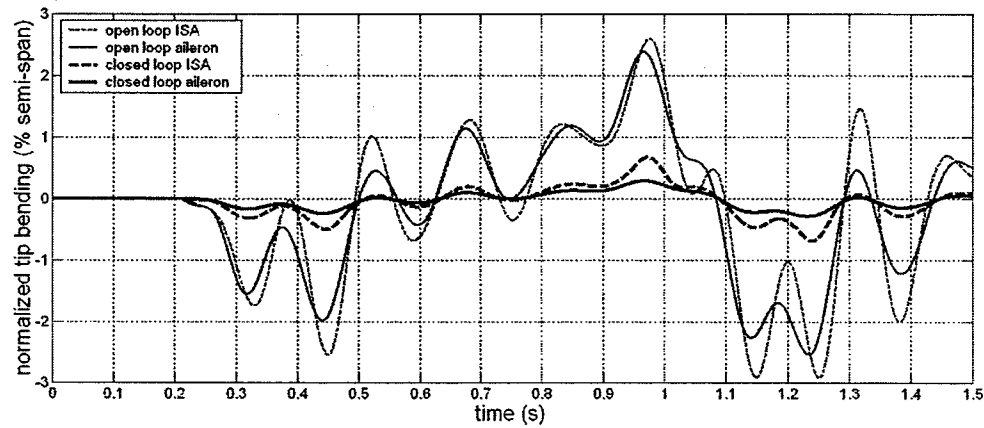


Figure 5.46: Tip bending displacement response due to turbulence, small vehicle, Test Case 3

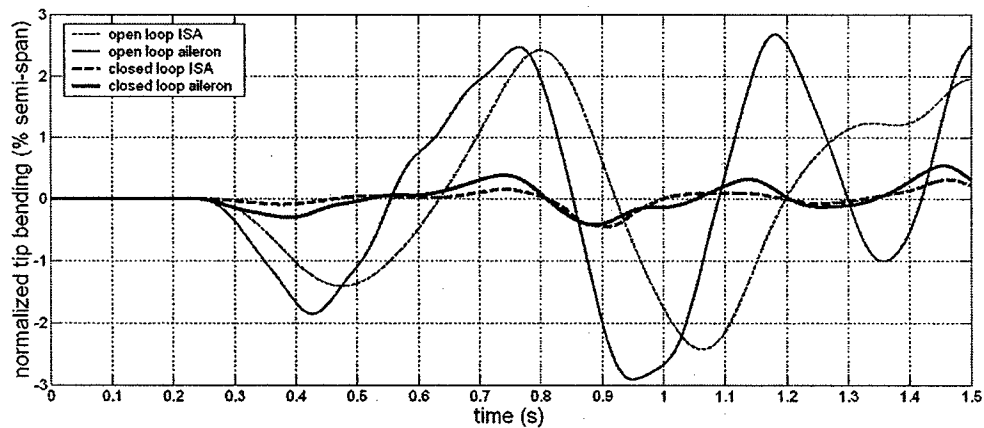


Figure 5.47: Tip bending displacement response due to turbulence, medium vehicle, Test Case 1

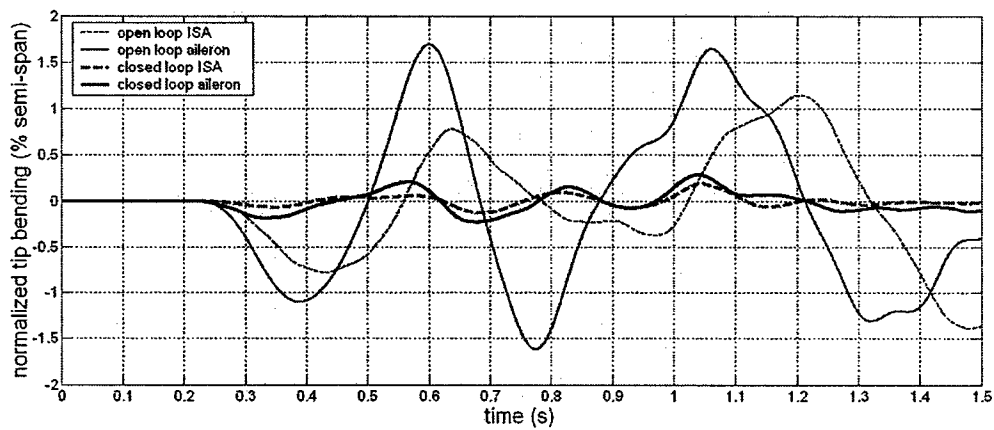


Figure 5.48: Tip bending displacement response due to turbulence, medium vehicle, Test Case 2

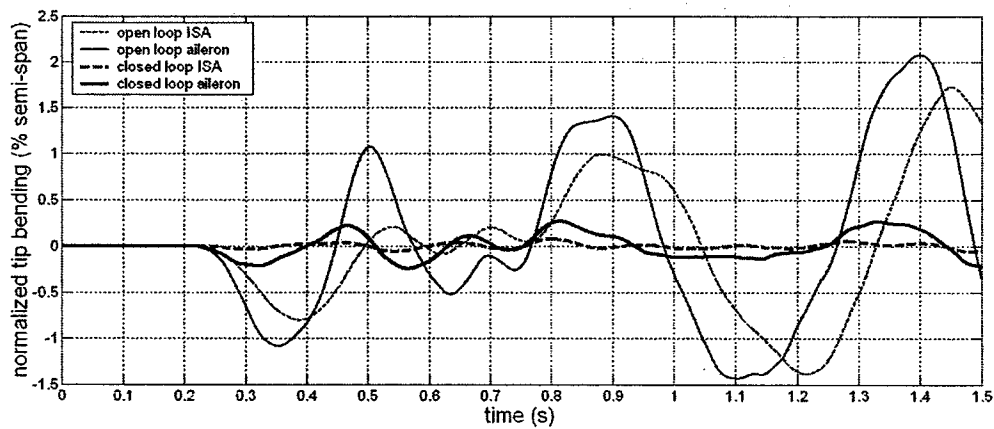


Figure 5.49: Tip bending displacement response due to turbulence, medium vehicle, Test Case 3

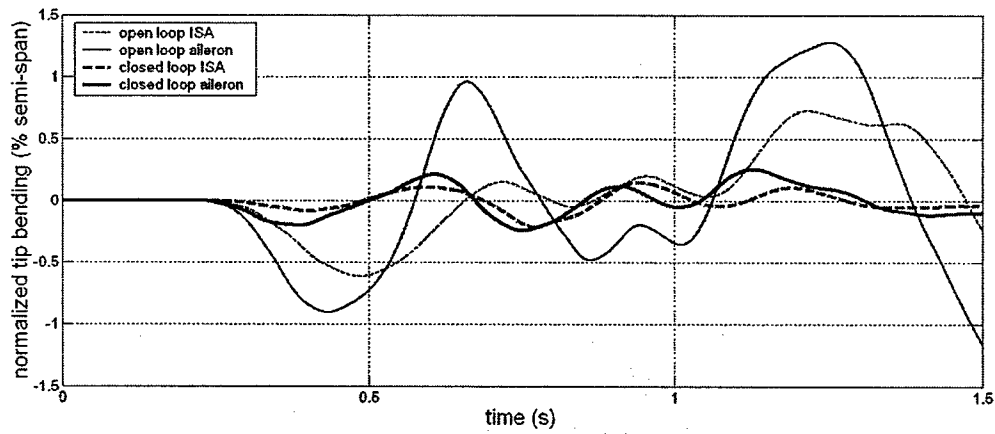


Figure 5.50: Tip bending displacement response due to turbulence, large vehicle, Test Case 1

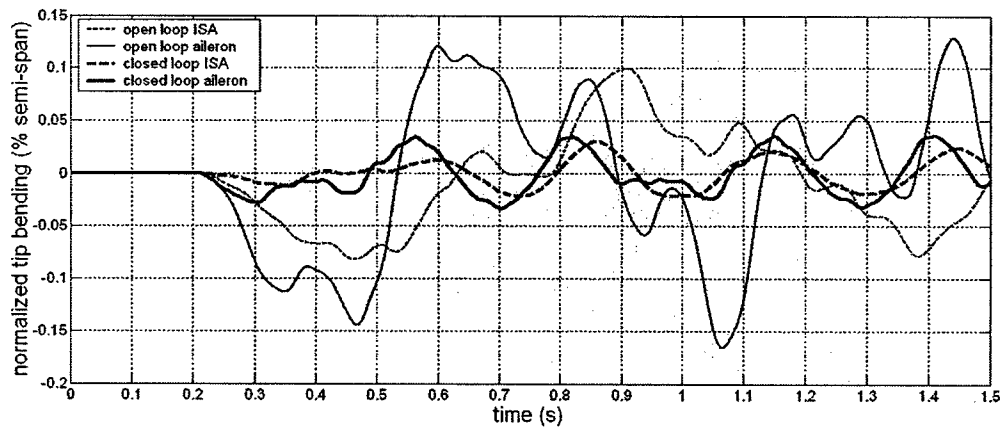


Figure 5.51: Tip bending displacement response due to turbulence, large vehicle, Test Case 2

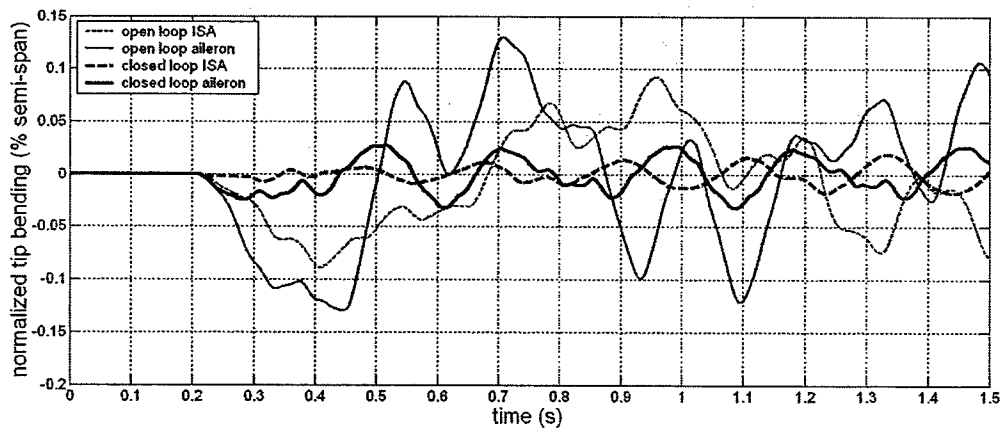


Figure 5.52: Tip bending displacement response due to turbulence, large vehicle, Test Case 3

The tip twist responses are given in Figures 5.53 to 5.61 for the three test cases for each vehicle class. Also plotted in these figures is the induced angle of attack due to the gust. It is clearly seen, in the small vehicle response, that the tip twist angle for the strain-actuated wing tends to counteract the gust-induced angle of attack. This is not the case with the medium and large vehicle class responses. The effect of the gust loading on the deformation of the small-scale wings is much faster than that of the larger vehicles, allowing for a faster control response. Furthermore, since the small vehicle is travelling slower, the frequency of excitation is much lower relative to the other vehicles. In the large vehicle class, the disturbance frequency is much higher than the tip twist response for the ISA1 design, even though the level of attenuation remains high. This implies that the frequency content of the disturbance is well above the first bending mode of the large wing. The small vehicle has relatively high structural dynamics frequencies while being excited at low frequency because of the relative lower flight speed through the turbulence. The opposite is the case for the large vehicle.

In all cases, the change in tip angle of attack of the aileron wing is small. For the large vehicle travelling at cruise altitude and nominal cruise speed and 40% above nominal cruise speed, there is some excitation of the torsion mode of the wing.

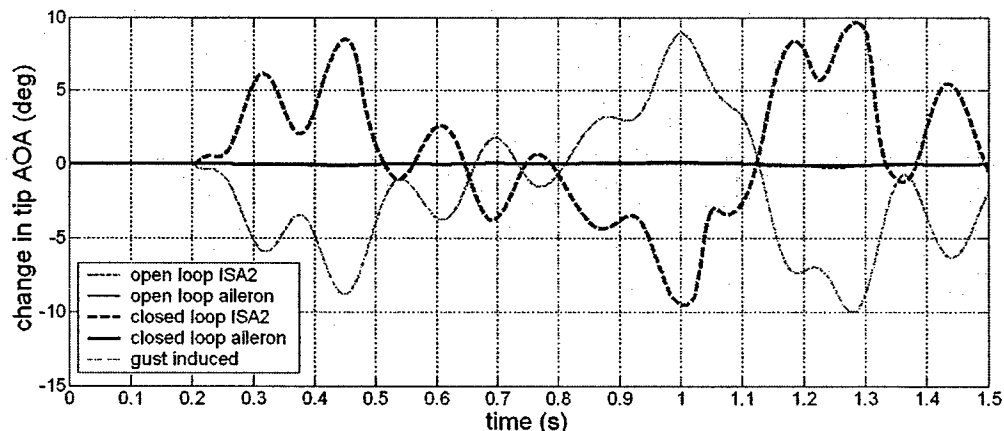


Figure 5.53: Tip rotation response due to turbulence, small vehicle, Test Case 1

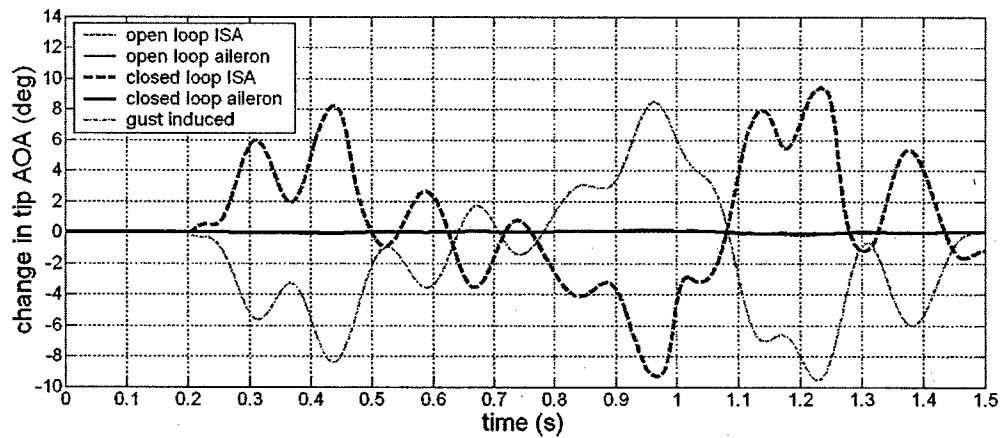


Figure 5.54: Tip rotation response due to turbulence, small vehicle, Test Case 2

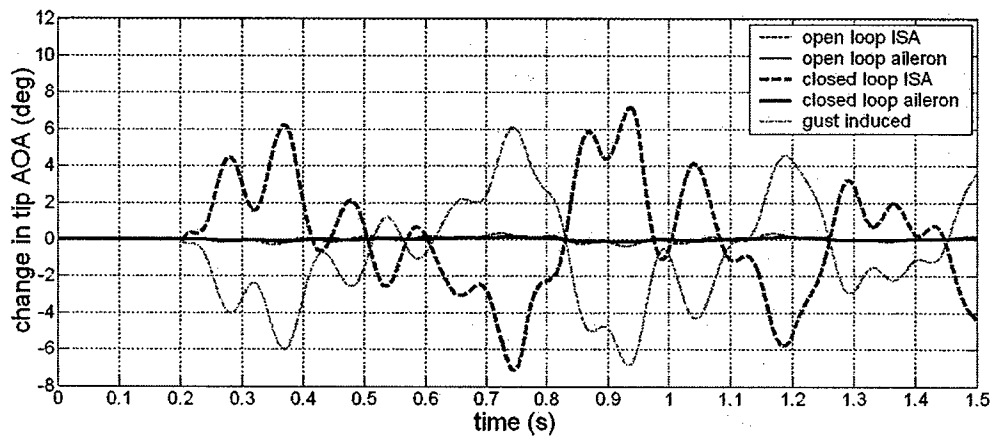


Figure 5.55: Tip rotation response due to turbulence, small vehicle, Test Case 3

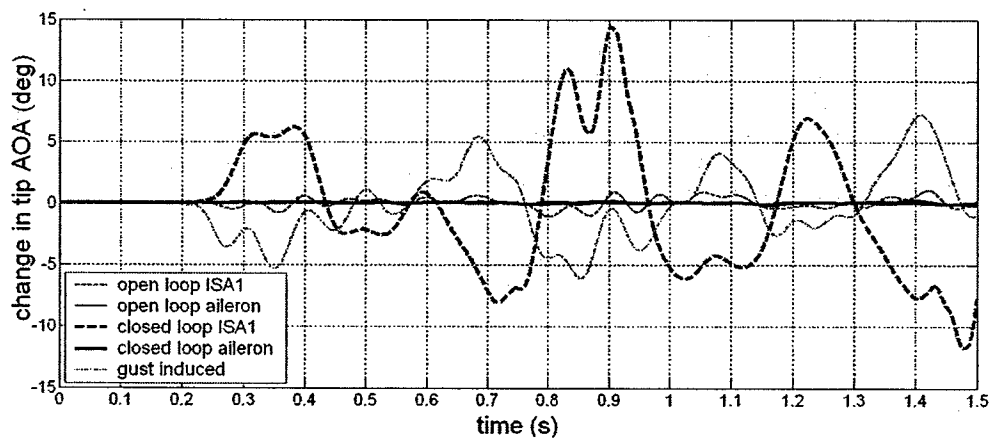


Figure 5.56: Tip rotation response due to turbulence, medium vehicle, Test Case 1

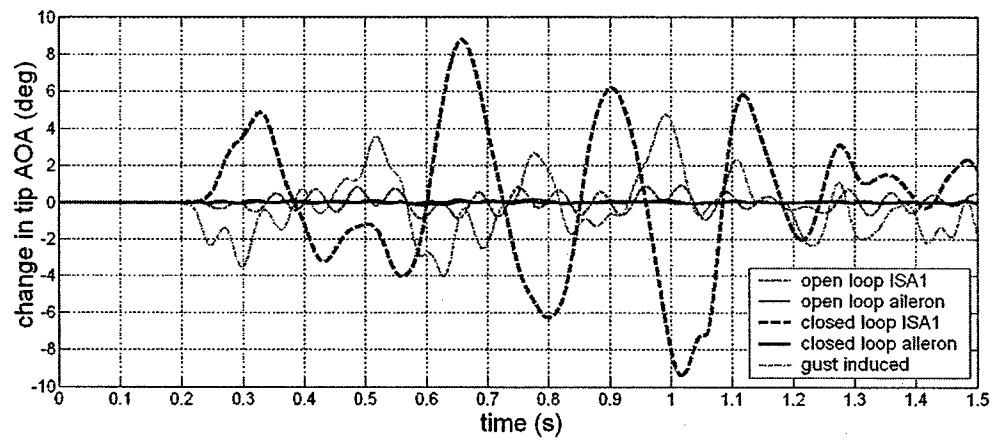


Figure 5.57: Tip rotation response due to turbulence, medium vehicle, Test Case 2

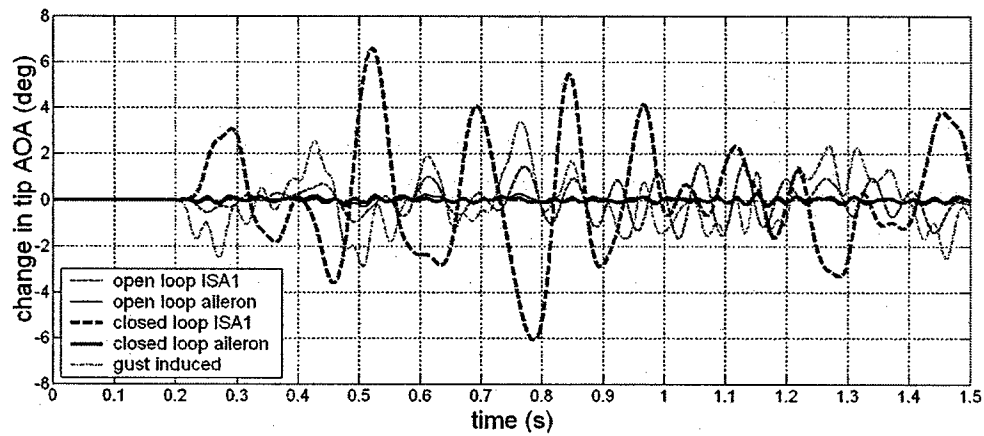


Figure 5.58: Tip rotation response due to turbulence, medium vehicle, Test Case 3

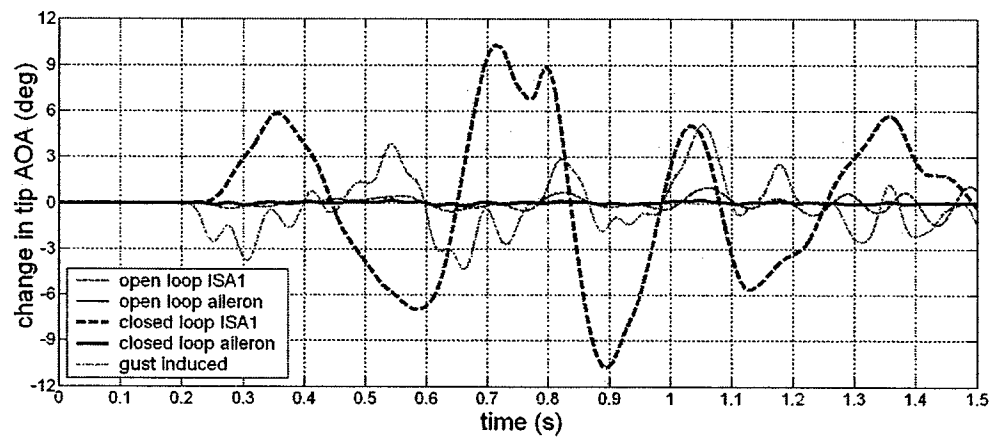


Figure 5.59: Tip rotation response due to turbulence, large vehicle, Test Case 1

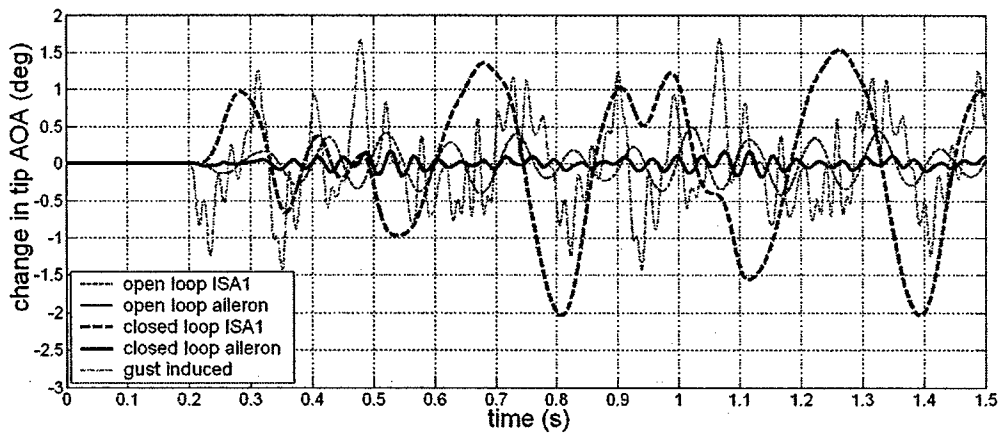


Figure 5.60: Tip rotation response due to turbulence, large vehicle, Test Case 2

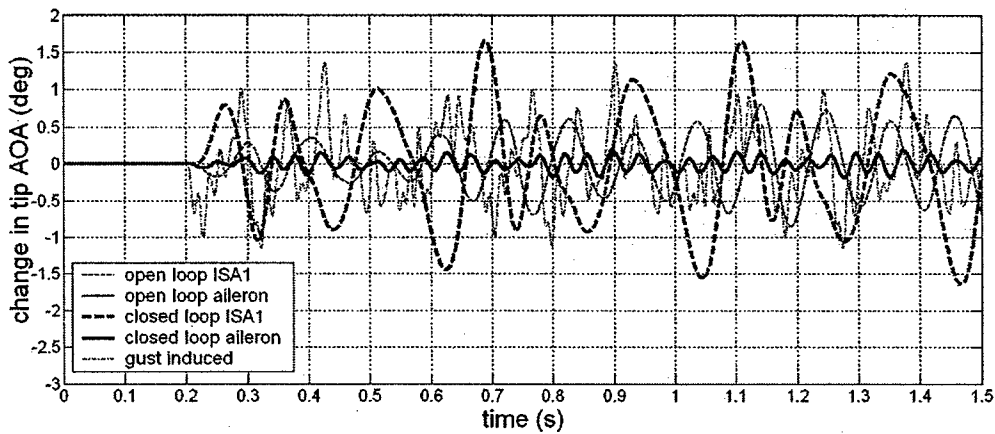


Figure 5.61: Tip rotation response due to turbulence, large vehicle, Test Case 3

In Figures 5.62 to 5.70, the aileron control deflection is compared with the control twist moment from the strain actuators in the first actuation region. For the small vehicle, the two control responses are qualitatively very similar for each test case. In Test Case 1, the ISA1 response reaches saturation at two intervals over the recorded period of time. In the same region, the aileron angle nearly reaches its limiting value. When establishing the control gains for the medium and large class aileron designs (i.e., selection of the state cost relative to the control cost), there was a limit to the amount of control deflection commanded from the ailerons. No matter how much the state cost was increased, the aileron angle response would not increase. From this it was inferred that any further improvement in the closed loop aileron response would not come from increased aileron authority, but from a higher spatial distribution of ailerons.

It is important to reinforce here that the aileron deflection is assumed to be the control input. The actuation of the ailerons is assumed to be without limit, allowing for very fast aileron deflection and ignoring the effects of aileron inertia. The control response of the large vehicle at cruise is somewhat unrealistic because the aileron control frequency is very high. However, useful information can be obtained from this. If the ailerons were truly able to deflect without lag, then this would be the optimal solution. Here, the aileron control frequency matches closely with that of the excitation.

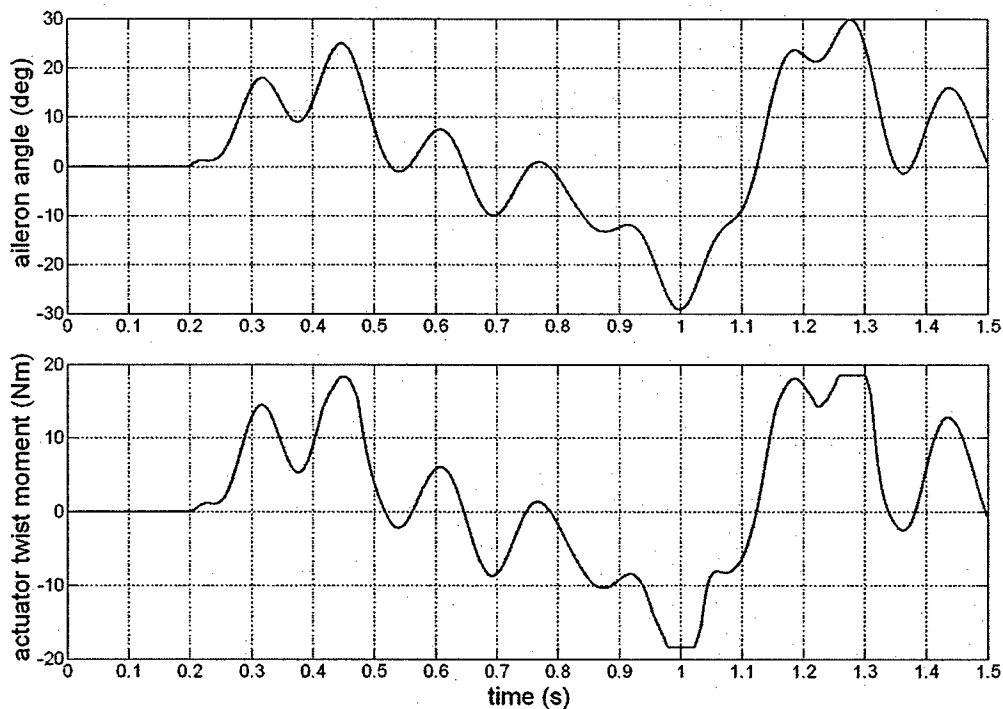


Figure 5.62: Aileron and twist moment response, small vehicle, Test Case 1

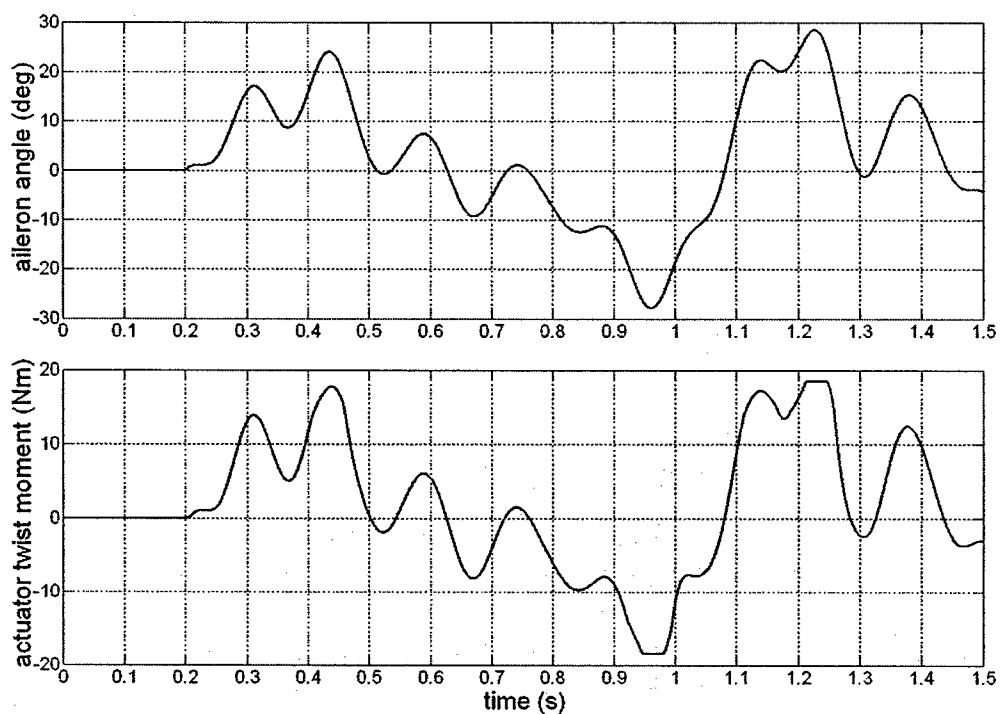


Figure 5.63: Aileron and twist moment response, small vehicle, Test Case 2

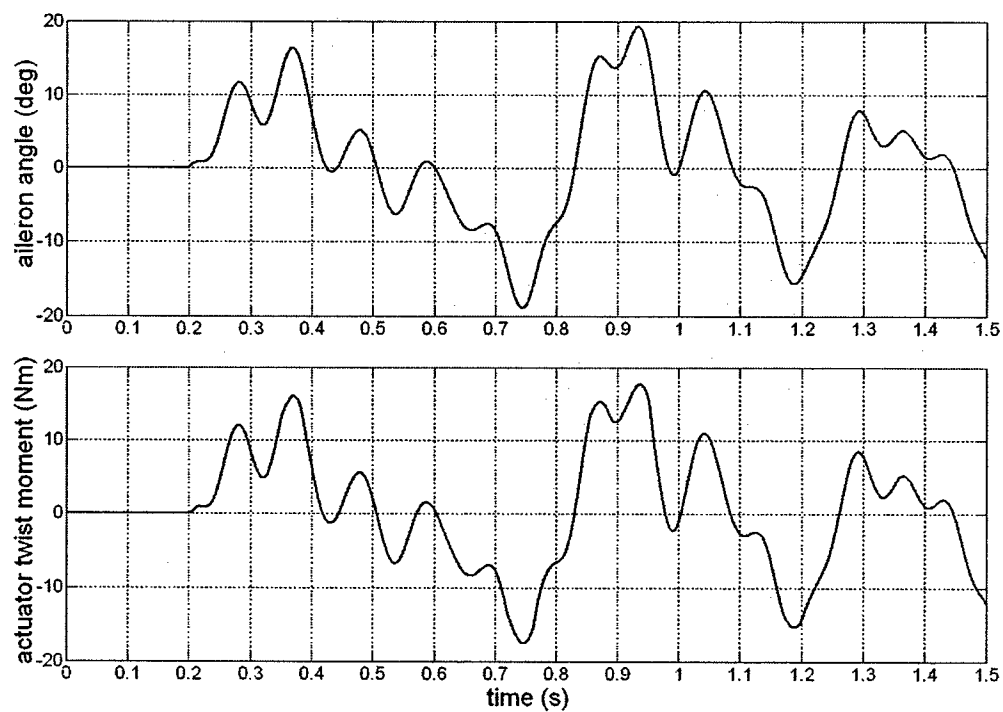


Figure 5.64: Aileron and twist moment response, small vehicle, Test Case 3

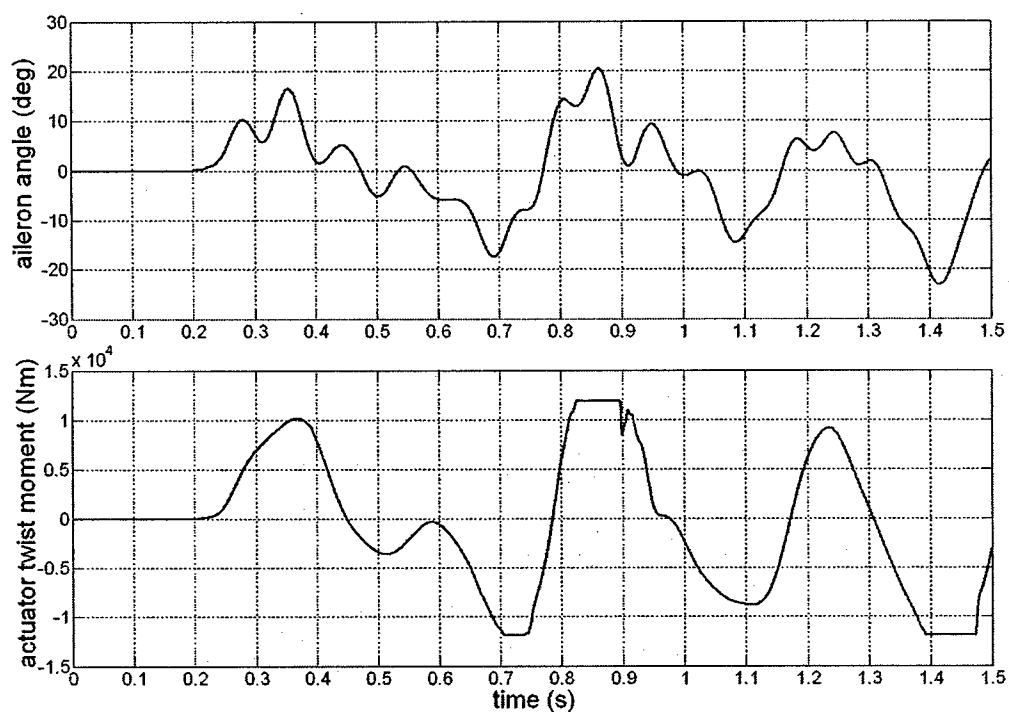


Figure 5.65: Aileron and twist moment response, medium vehicle, Test Case 1

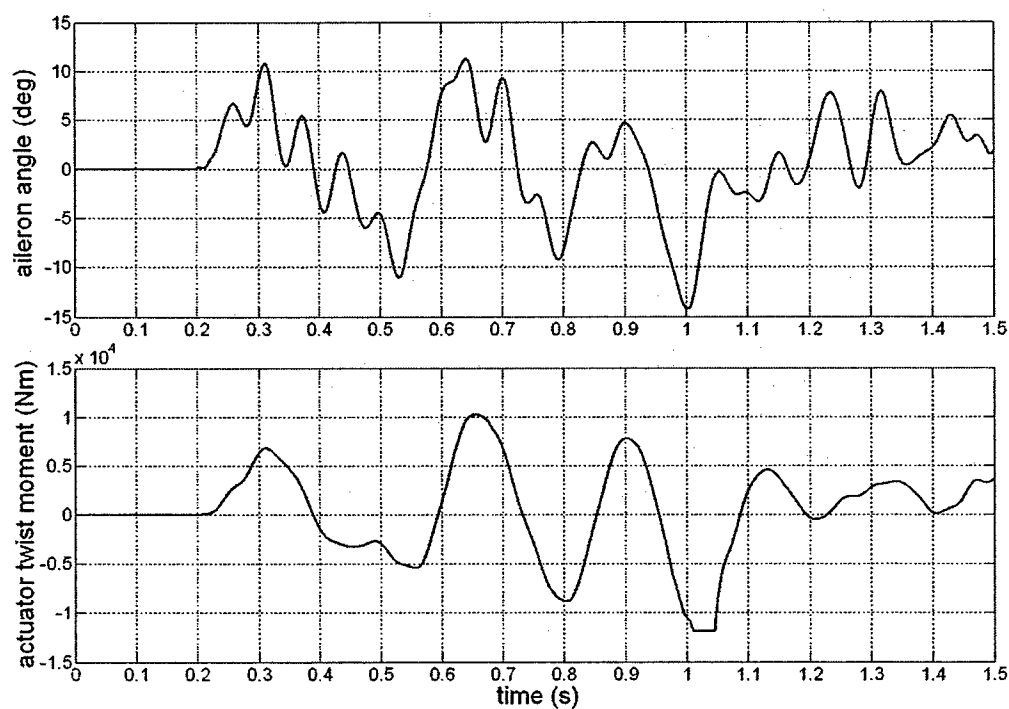


Figure 5.66: Aileron and twist moment response, medium vehicle, Test Case 2

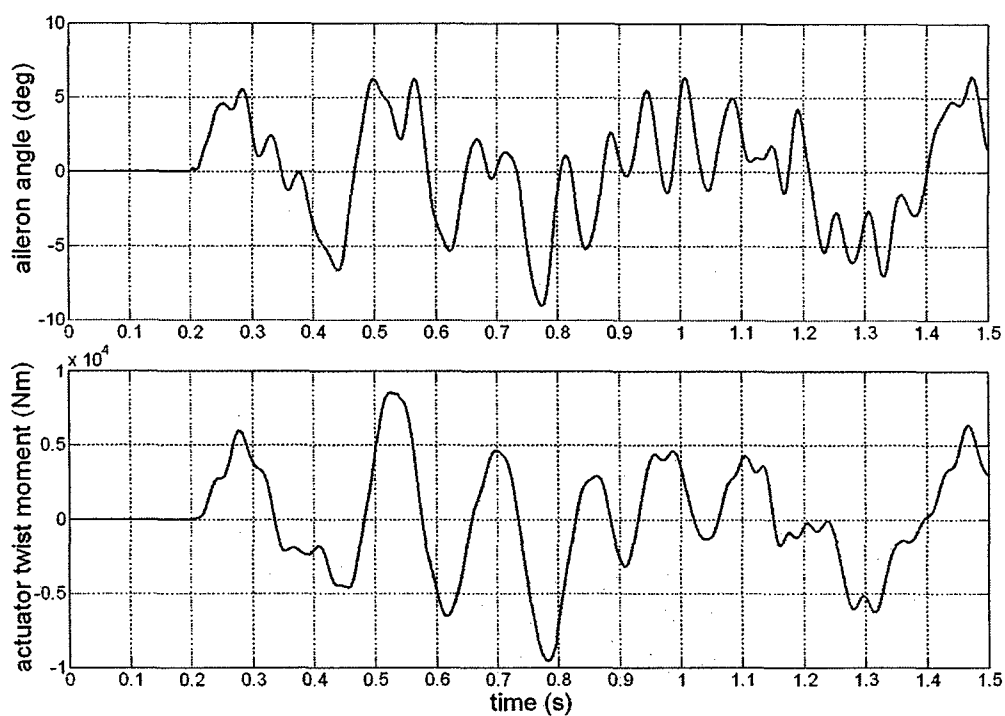


Figure 5.67: Aileron and twist moment response, medium vehicle, Test Case 3

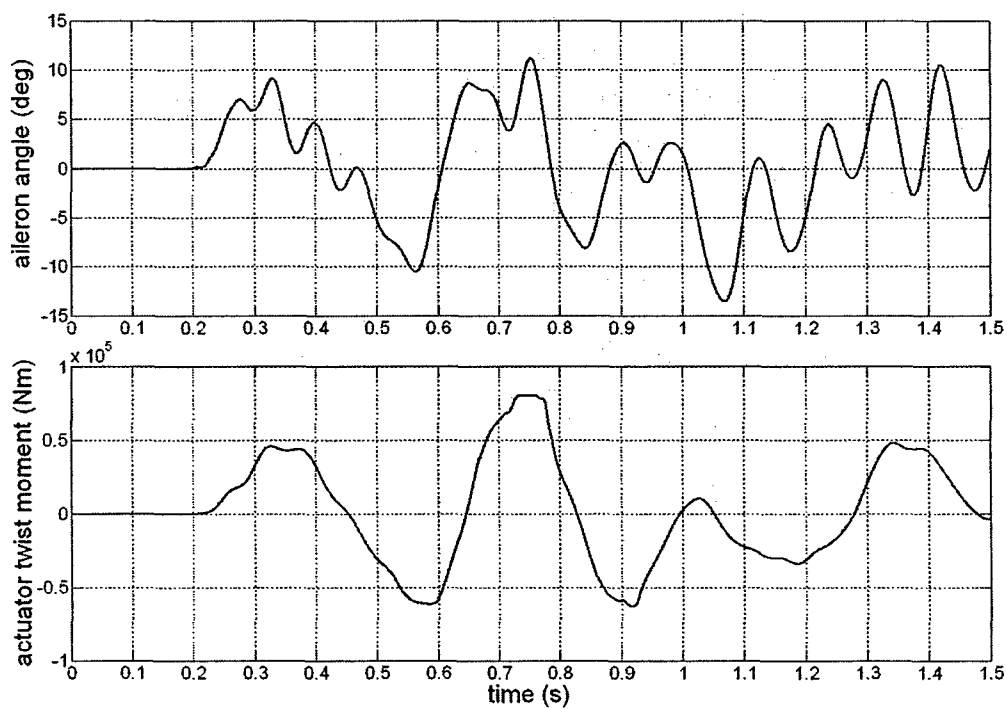


Figure 5.68: Aileron and twist moment response, large vehicle, Test Case 1

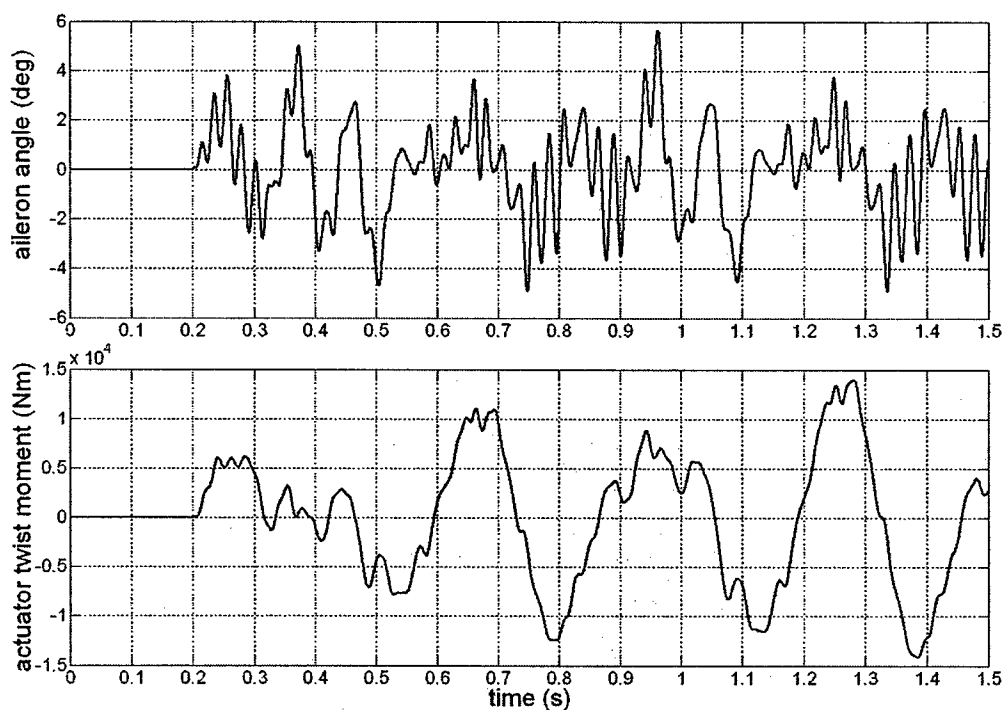


Figure 5.69: Aileron and twist moment response, large vehicle, Test Case 2

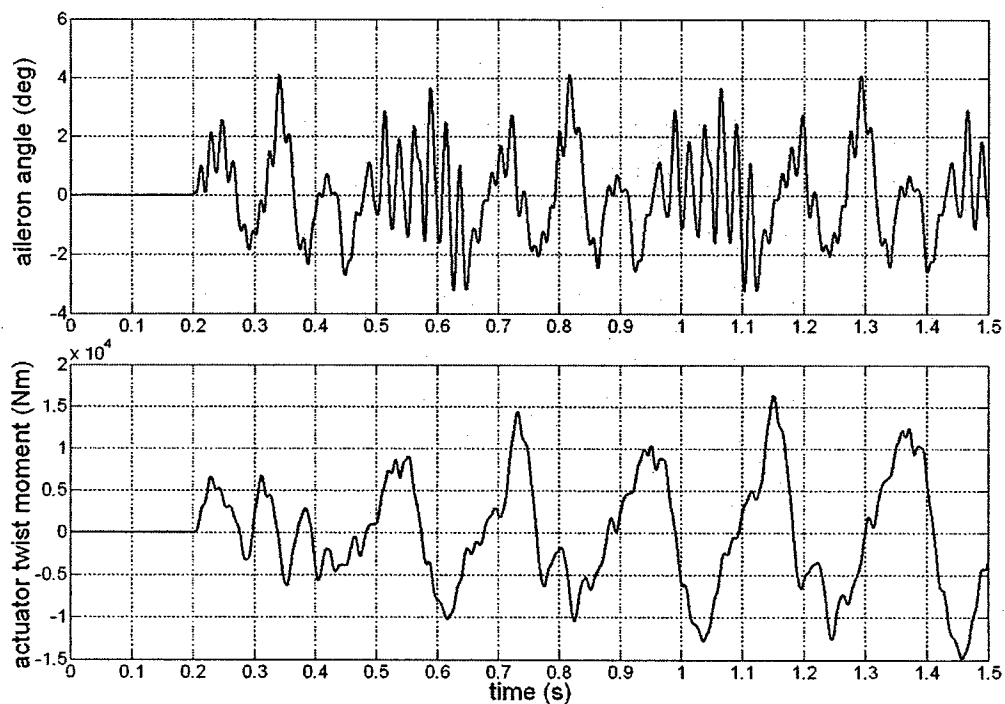


Figure 5.70: Aileron and twist moment response, large vehicle, Test Case 3

5.5.2 Flutter Suppression

In order to investigate the flutter suppression capabilities of the ISA1 model, a high-speed maneuver at low altitude is assumed. The flutter speed is computed by evaluating the stability of the vehicle over a range of closely spaced flight speeds, from the nominal speed at sea level up to 167 m/s (Mach 0.49). At each flight speed, the corresponding trim body angle of attack is used in determining the steady state wing deformation. Based on this deformation, the eigenvalues of the aeroelastic state space A matrix are obtained. The poles of the unstable aeroelastic mode are plotted in Figure 5.71 for the range of flight speeds. The flutter speed was computed to be 155 m/s (Mach 0.46) when vertical rigid body motion was allowed and 142 m/s for the cantilevered wing.

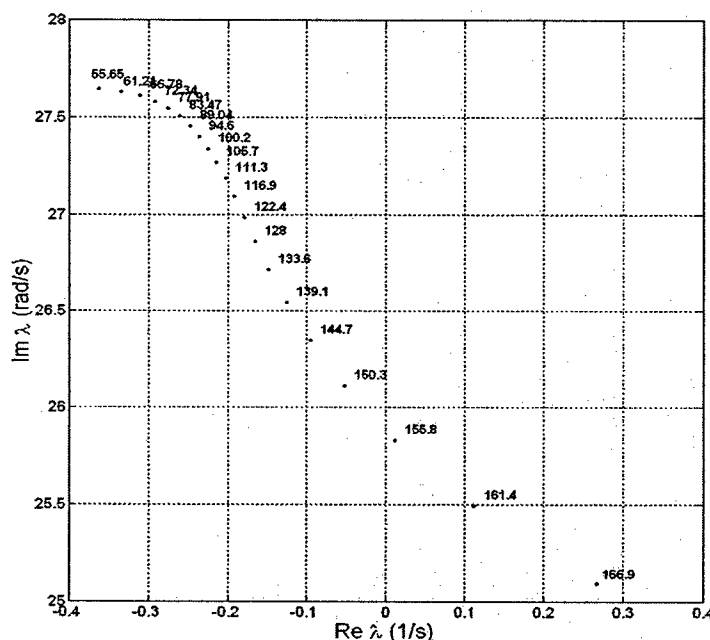


Figure 5.71: Root locus of unstable aeroelastic poles vs. flight speed, trimmed flight, with vertical rigid body motion.

The open and closed loop responses are obtained for both the linearized and fully nonlinear time stepping solutions at a flight speed of 167 m/s (Mach 0.49). The same controller used for gust alleviation is used here. The response is initiated by a small half-sine gust disturbance starting at time = 0. The results are presented in Figures 5.72 and 5.73. The open loop response of the linearized system goes unstable, as expected. The nonlinear solution shows that the wing enters a limit cycle oscillation. The closed loop

response for both the linearized and fully nonlinear solutions are very similar, since the wing displacements do not grow large with the feedback control employed.

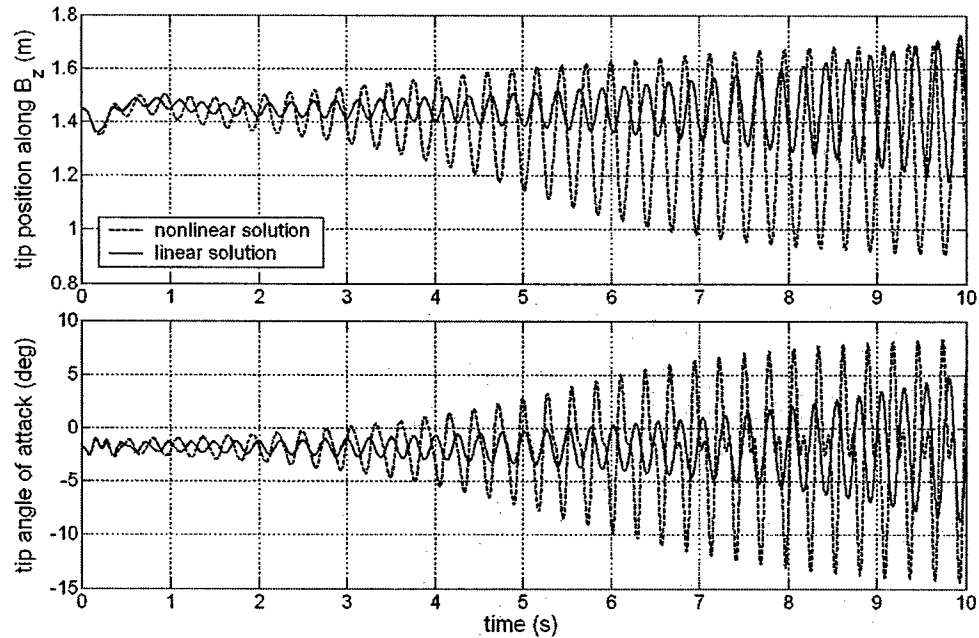


Figure 5.72: Open loop tip bending and tip angle response at 167 m/s and sea level.

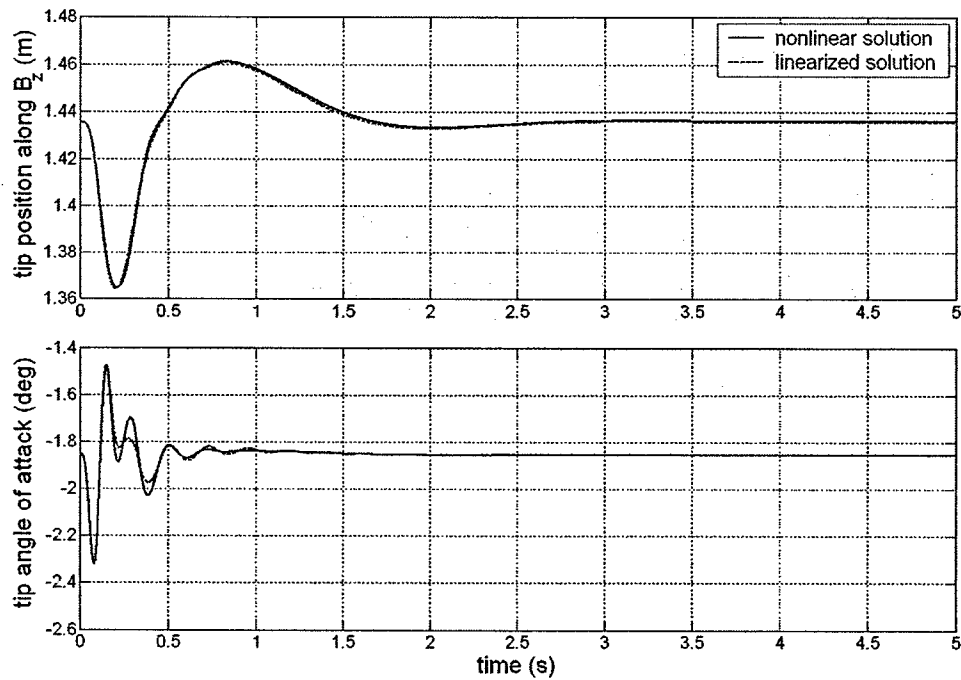


Figure 5.73: Closed loop tip bending and tip angle response at 167 m/s and sea level.

5.6 Maneuver Loads Reduction

This section explores the ability of wing warping to reduce the wing root bending moment during a high-g maneuver. This may take place when the vehicle is in the terminal phase of a dive or turn, and increases the angle of attack to reduce speed and return to trimmed flight.

For the present results, the medium scale vehicle is brought to a speed such that the load factor is equal to 4 in horizontal flight. Full twist actuation is then applied to twist the wing tips down, reducing the outboard aerodynamic loads and decreasing total lift. The body angle of attack is then increased such that the load factor is once again equal to 4. The vehicle and aerodynamic load distribution are shown in Figure 5.74 with and without load redistribution.

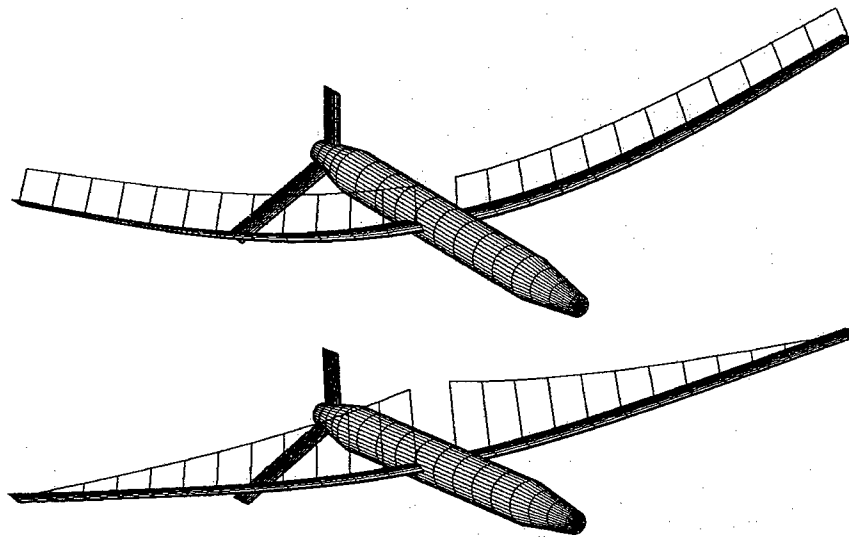


Figure 5.74: Vehicle under load factor 4 condition, with (bottom) and without (top) active load redistribution with maximum twist actuation applied.

The wing bending moment is plotted in Figure 5.75 as a function of wingspan. The bending moment is normalized by the maximum root moment with no load reduction. The results show a 30% reduction in root bending moment.

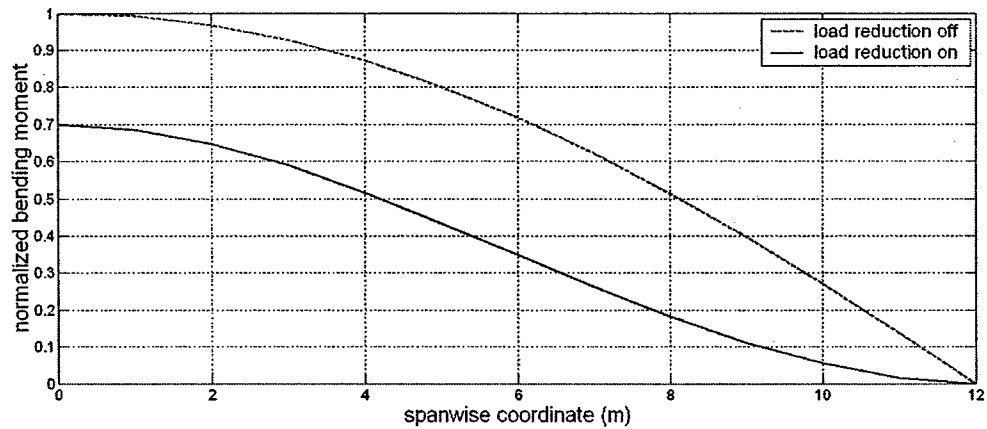


Figure 5.75: Normalized bending moment during a 4-g maneuver

The corresponding magnitude of the ply strains in the active and passive materials is shown in Figures 5.76 to 5.78. The significant results are the decrease in longitudinal strain in the 0° graphite/epoxy plies and the decrease in shear strain in the $\pm 45^\circ$ APC plies. In both cases, the strains are slightly above the design limit before load redistribution, and well below the design limit afterwards.

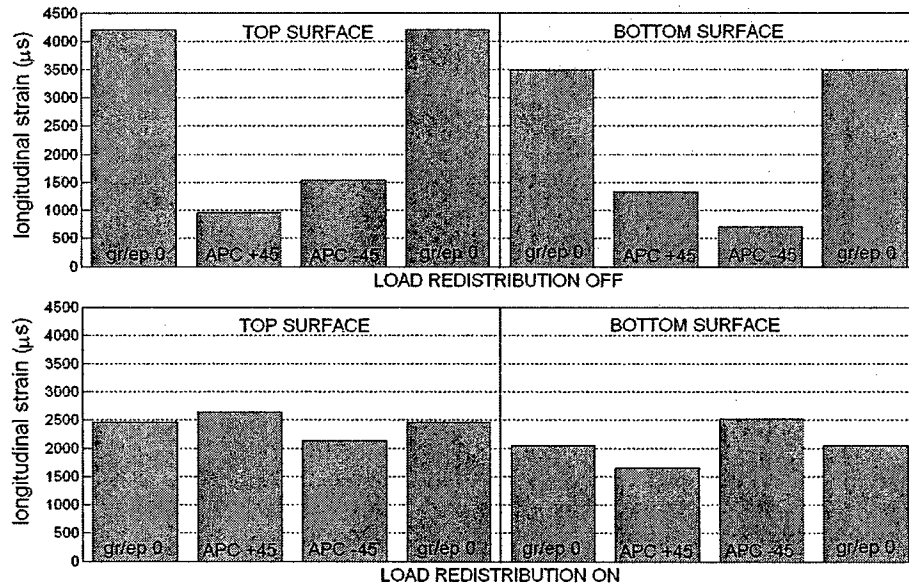


Figure 5.76: Longitudinal ply strains at the root station with and without load redistribution

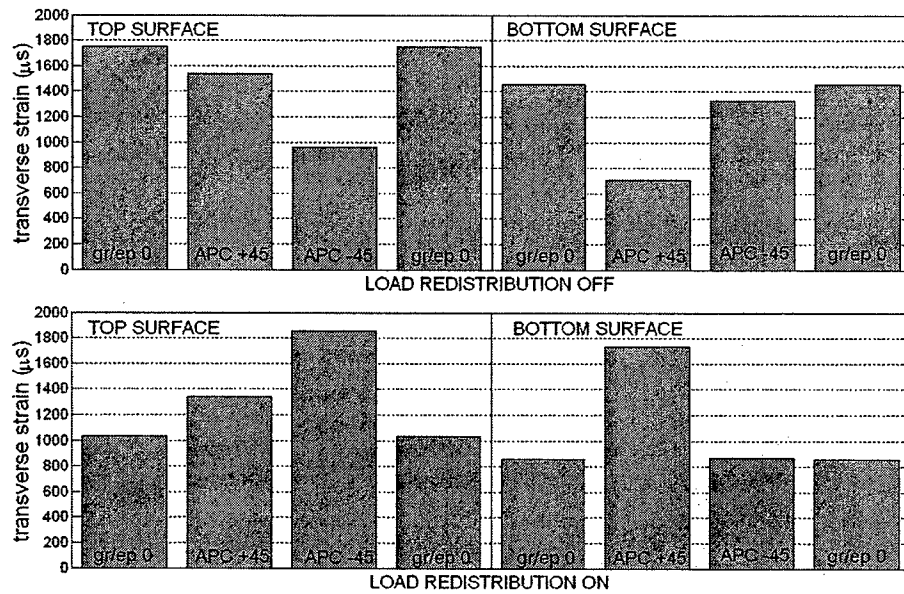


Figure 5.77: Transverse ply strains at the root station with and without load redistribution

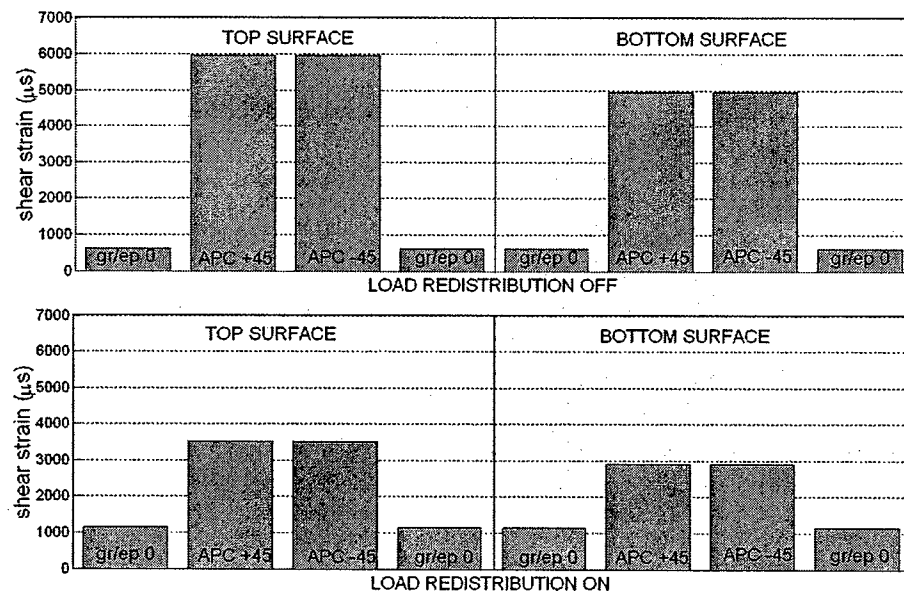


Figure 5.78: Shear ply strains at the root station with and without load redistribution

The percentage change in ply strains are presented in Table 5.15.

Table 5.15: Percentage change in ply strains due to load redistribution (root station)

TOP SURFACE				
	gr/ep 0	APC +45	APC -45	gr/ep 0
longitudinal strain	- 41%	+ 175%	+ 39%	- 41%
transverse strain	- 41%	- 13%	+ 93%	- 41%
shear strain	+ 84%	- 41%	- 41%	+ 84%
BOTTOM SURFACE				
	gr/ep 0	APC +45	APC -45	gr/ep 0
longitudinal strain	- 41%	+ 25%	+ 257%	- 41%
transverse strain	- 41%	+ 146%	- 35%	- 41%
shear strain	+ 84%	- 41%	- 41%	+ 84%

Chapter 6

Concluding Remarks

6.1 Summary

The objective of the present work was to numerically explore integrated strain actuation (ISA) as a means of enhancing aircraft stability and roll performance and potentially reducing the weight of the vehicle. To do this, a numerical framework was developed which could model the vehicle with sufficient accuracy to carry out this study. The developed framework is based upon an original theory as well as published theories found in the literature. The combined formulation was developed, from the ground up, into a design and analysis environment for the study of wing warping control of highly flexible composite wings with embedded anisotropic piezocomposite actuators.

The original theoretical formulation addresses beams undergoing arbitrarily large three-dimensional deformations. This new formulation is capable of, but not limited to, the modeling of highly flexible high-aspect-ratio wings under the influence of induced piezoelectric strains and external aerodynamic loads. The novelty of the proposed approach is in its strain-based finite element representation. This allows for a small number of independent degrees of freedom and fast numerical convergence properties.

The developed numerical environment allows for the modeling of a rigid vehicle with six rigid body degrees of freedom and highly flexible lifting surfaces. The general nature of the implementation allows for a wide variety of vehicle configurations to be constructed and analyzed. Several analysis routines were constructed to obtain aerodynamic and structural data for the vehicle in realistic flight scenarios. A procedure was developed to determine the trim equilibrium orientation of the vehicle for a given load factor maneuver. This allowed for vehicle trim data to be calculated and stored over a range of closely spaced flight speeds at various levels of load factor and altitude, thus allowing for the performance of wing warping control to be evaluated over a wide range of flight conditions (many of the aeroelastic studies in the literature analyze wing behavior without considering trim, wing stresses, or the effects of rigid body motion). The completed aeroservoelastic design and analysis environment has the following capabilities:

- A numerical environment for the representation of a variety of general aeroelastic structures, from a single wing to an aircraft of arbitrary design consisting of several flexible members
- A geometrically nonlinear, strain-based beam model for representing the wings
- Modeling of rigid bodies attached to the wings and fuel stored in the wings and fuselage
- Rigid body motion of the vehicle, with the ability to constrain degrees of freedom
- Calculation of the cross-sectional properties of thin-walled, two-cell airfoils with embedded active composites. (Modularity allows for inclusion of any other method of calculation of such properties and inclusion into the active beam model with little effort.)
- Finite-state unsteady subsonic aerodynamics with a simplified stall model
- Unsteady induced flow control surface aerodynamics
- Spanwise lift distribution correction
- Structural and aeroelastic mode shapes
- Steady-state solution under a variety of loading conditions
- Recovery of laminate stresses and strains for failure evaluation

- Evaluation of vehicle trim over a range of speeds, altitudes, and load factors
- Transient and frequency roll response
- Root locus analysis
- Nonlinear, controller-in-the-loop, time stepping simulation

6.2 Conclusions from Numerical Studies

Several numerical tests were performed to validate the structural formulation and overall implementation. The static and dynamic structural response compared very closely to the solution obtained using a commercial displacement-based finite element software package and a multibody dynamics code, as well as with published results. Aeroelastic and modal responses compared well with results from the literature.

Numerical studies were conducted on representative aircraft in three vehicle classes: Small, Medium, and Large (low, medium, high altitude). In each vehicle class, a conventional aileron wing was designed based on strength criterion during worst case maneuver loading. The vehicle weight and planform data were based, roughly, on fielded unmanned aerial vehicles, while attempting to maintain similarity among the three vehicle classes. The composite wing construction consisted of graphite/epoxy (gr/ep) plies oriented at 0° and $\pm 45^\circ$, which is consistent with data for the medium scale vehicle. For each of the aileron wing designs, two active wing designs were constructed by replacing the $\pm 45^\circ$ plies with anisotropic piezoelectric composite (APC) plies. The first active wing design, labeled ISA1, used a standard thickness for the active plies. The second active wing design, ISA2, used a reduced thickness (25% of standard) for the active plies, such that total wing weight was equal to that of the aileron design. Replacement of only the $\pm 45^\circ$ gr/ep plies with APC was done to maximize the twist authority of the active wings.

As expected, the wing tip twist due to maximum applied voltage was found to be independent of wing length, i.e., the twist per unit span is inversely proportional to wing size, when the relative amount of active to passive material is held constant. The ISA1 and ISA2 wings achieved a maximum tip twist of $\pm 12^\circ$ and $\pm 6^\circ$, respectively.

The transient response to a sudden roll actuation input was obtained for each vehicle at several points in their respective mission profiles. It was found that the ISA1 wing design was able to achieve a maximum roll rate only slightly lower than that of the aileron design. The ISA2 wing design achieved roughly half the roll rate of the ISA1 design. A significant result of these simulations was that the large vehicle with full thickness actuators suffered from a slow transient response. The density of the piezoelectric composite is higher than that of the graphite/epoxy. The effect of this on vehicle roll inertia, and thus transient response time, was found to increase with vehicle size. When designed on strength criterion, the weight of the wings tends to be a higher fraction of the total weight as the vehicle increases in size. Because of this, the response time of the small active vehicle was least affected by the increase in wing weight. The same trend applies to the roll frequency response. The roll rate amplitude of the large class ISA1 vehicle rolled off quickly as the frequency increases.

When flying at Mach 0.4, the roll rate of the large ISA1 vehicle was slightly higher than that of the aileron vehicle, but by a lower amount than expected since aeroelastic effects should degrade the aileron response. The aileron effectiveness of the baseline design was investigated over a range of flight speeds. It was determined that the aileron wing design was sufficiently stiff in torsion that very little loss of aileron effectiveness occurred. This suggests that the baseline design might not have been a minimum weight design, since it may have been possible to change the relative proportion of 0° and $\pm 45^\circ$ plies to achieve a lower weight, while satisfying design constraints.

A closed-loop controller was designed for gust alleviation and flutter suppression. A LQR controller design was assumed to be feasible, since the present formulation allows for the numerical model to be represented in such a way that all of the strain states are measurable using strain gages. This model applies to a cantilevered wing with the unsteady aerodynamic states suppressed (only quasi-steady aerodynamic forces and moments are included). The controller was then simulated on the model with all states present, including the inflow and rigid body states. The fuselage was constrained such that only the vertical degree of freedom was permitted. Allowing this degree of freedom results in a more accurate disturbance response and flutter speed calculation than the

cantilevered wing model. In selecting the state cost matrix, the best performance was found when only the wing bending strains were penalized. An alternative method would be to use the structure stiffness and mass matrices as components of the state cost matrix. This method would have the negative effect of penalizing wing twist. Since it is desired to twist the wings to generate restoring forces by interacting with the air stream, that approach is deemed incompatible. Furthermore, penalizing the extensional and chordwise bending strains seemed unnecessary. Extensional strains are induced when the wing is actuated in twist. Also, the extensional strains are not important in the aeroelastic response and may add high frequency components to the feedback loop. The chordwise bending strains are uncontrollable.

Both the active wings and the aileron wings performed very well in suppressing a moderate gust, achieving a reduction in tip response between 70% to 90%. The ailerons were idealized, however, since their inertia was not taken into account. Since the large vehicle flies faster through the turbulence field than the small vehicle, it experienced a higher frequency excitation. The commanded aileron control frequency increased in response to this. For the small vehicle, the structural frequencies are high and the excitation frequency is low. The commanded wing twist and aileron deflection responses were qualitatively very similar to the gust induced angle of attack, and nearly 180° out of phase with it. The first bending frequency of the small wing was sufficiently high that the response to disturbance was very fast.

When the controller was designed at the nominal flight speed, and simulated at a speed 40% greater, the amount of alleviation tended to be higher than the simulated response at the nominal speed. This illustrated some robustness of the controller to plant variation, since the plant dynamics change significantly when the speed is increased by 40%. The improved response at the higher speed was likely due to the stronger twist/bend coupling with the air stream.

Flutter suppression results were obtained for the large scale vehicle, which is more likely to fly at speeds approaching its flutter instability. The ISA1 design was evaluated at Mach 0.49, which was 8% above the flutter speed. The nonlinear open loop response showed that the wing enters a limit cycle oscillation. The closed loop controller was evaluated using both the linearized and fully nonlinear solvers with nearly identical

results. In both cases, flutter suppression was achieved with low levels of control actuation. It was intended to evaluate the flutter suppression capability of the active wings at a higher percentage over the passive flutter speed, but this would be above the range of valid flight speeds for the incompressible flow model.

The active wings have the unique ability to redistribute the aerodynamic load. During a high load maneuver, the ability to significantly reduce peak stress at the root was identified. Load redistribution was shown to reduce the peak strains in the 0° graphite epoxy plies from 100% of their design limit to 60% using full actuation. This may allow a weight reduction for the active wings by virtue of the increase structural failure margin.

The overall performance of the active materials on a realistic vehicle seems promising. The level of roll authority compares well with conventional wing designs. The density and stiffness of the active piezocomposite material are points of major concern. To achieve an equivalent maximum roll rate as the conventional aileron vehicle, the weight of the active wings become large, leading to a slow transient roll response. The relatively low stiffness of the piezocomposite material used in this work resulted in reduced wing torsional frequency and flutter speed than the conventional wing.

For a fair evaluation of ISA performance as compared with the aileron-based wing, an important point must be noted. The aileron-based wing was idealized. Extra weight associated with hydraulic actuators or servos, and the structural fixtures and reinforcements for the aileron attachment were not taken into account. Also, the inertia of the ailerons was neglected, allowing for unrealistic control bandwidth. Losses on the ailerons due to spanwise aerodynamic effects were also not accounted for. All of these factors cause the evaluated aileron performance to be better than it actually would be. Furthermore, typical high-aspect-ratio airplanes experience a loss of aileron effectiveness at high dynamic pressure. In the present study, the aileron-based wings were made stiff enough in torsion that there was minimal loss of effectiveness. Therefore, the ability of the wing warping control to eliminate control reversal may not given proper credit when compared with a fielded airplane.

6.3 Thesis Key Contributions

This thesis provided several key contributions to the field in the areas of modeling and analysis of flexible composite wings using integrated strain actuation as a primary means of roll and stability control. The contributions are as follows:

Modeling

- A new strain-based finite element structural formulation was developed for the modeling of three-dimensional beams undergoing arbitrarily large deformations. The structure formulation is elegant in design and easily implemented. The number of independent variables required is smaller than conventional displacement-based finite elements. This contribution is applicable to, but not limited to, the objectives of this thesis.
- A numerical framework was constructed which allows for arbitrary vehicle geometry with unlimited number of flexible lifting surfaces.
- A reduced-order unsteady aeroelastic modeling technique, utilizing the new structural formulation, was introduced. It results in a very efficient nonlinear state space form. Novel control design techniques are possible based on the strain-based representation of flexible system variables.

Analysis

- The effectiveness of state-of-the-art anisotropic piezocomposite actuators has been investigated on realistic vehicles in realistic flight conditions. Information was gained regarding the performance of these actuators relative to conventional ailerons for roll control and stability of aircraft with high aspect ratio wings.
- The effects of variation in certain piezoelectric composite properties on wing deformation was established. Some conclusions were made on how the properties should be modified to best serve the wing warping application.

6.4 Recommendations for Future Work

There are various aspects of the present formulation which were explored, but not incorporated into this thesis due to the complexity of the problem. Simple aeroservoelastic design optimization problems were performed on various wing models, and lessons were learned about the complexity of the problem. The objective function to minimize is usually weight of the wings. The design variables may consist of composite material properties, thickness distributions, actuator distribution, active and passive composite ply angles, planform dimensions, sweep and dihedral angles, and so on. Constraints may consist of strength limits, open- and closed-loop flutter margin, roll rate, closed-loop gust attenuation, etc. Although the present implementation allows for the evaluation of the objective function and constraints, as well as the variation in the design variables within an optimization loop, properly posing the optimization problem so that the capabilities of integrated strain actuation can be fully realized was found to be very difficult. Under the assumption that a model, such as the present one, is capable of representing all of the structural and aeroelastic behavior of interest, what is needed is a well defined performance criterion for wing warping designs. This is complicated by the fact that it is not yet fully known the best ways to apply wing warping for aeroelastic benefit. For instance, when evaluating peak wing stress in a high-load maneuver, is it assumed that active load redistribution is employed? If so, does that diminish the ability of the actuators to simultaneously roll the vehicle? Should wing warping be used to perform several functions simultaneously? These issues need to be well defined before an integrated design optimization technique can be employed.

In the present studies, very specific performance criteria were evaluated using a few representative wing models. More parametric studies should be done to determine the effects of such things as airfoil thickness, actuator distribution, and active/passive couplings, on the ability for wing warping to improve airplane performance. The thickness of the airfoils used in this study, along with the material design strain limits, limited the bending flexibility of the wings, so that certain nonlinear effects experienced by highly deforming wings were not present. Thinner airfoils allow for larger bending displacements since the strains at the surface are lower for a given wing bending

curvature. While large bending displacements are generally undesirable, there may be a structural benefit for using thinner airfoils because of increased twist actuation authority, which may result in reduced weight. Wing warping control may be able to enhance performance over aileron-based designs in this region of wing flexibility. This needs to be explored further.

With regard to control design, non-idealized controllers need to be evaluated. The effects of actuator bias need to be included. The typical control design attempts to regulate the wing deformation about a given shape. However, for flexible wings, their shape can change by a large amount if the vehicle enters a maneuver. This would put a bias error on the sensor readings and cause the controller to try to bring the wings to the original shape. Furthermore, roll control and gust alleviation control may be incompatible, and tend to work against one another. An overall control architecture for the lateral flight controls needs to be developed. Nonlinear and adaptive learning controllers may have a huge potential in wing warping control. A study into these issues would be invaluable in the development of this new field.

Bibliography

- [1] Jones, R. I., "The Design Challenge of High Altitude Long Endurance (Hale) Unmanned Aircraft," *The Aeronautical Journal*, June, 1999, pp. 273-280.
- [2] Jones, R. I., "Selection and Comparison of Unmanned Aircraft Configurations", In *RPVs International Conference, 12th, Bristol, United Kingdom, Sept. 9-11, 1996*, Conference Papers (A97-21501 04-01), Bristol, United Kingdom, University of Bristol, 1996.
- [3] Patil, M. J., Hodges, D. H., and Cesnik, C. E. S., "Nonlinear Aeroelasticity and Flight Dynamics of High-Altitude Long-Endurance Aircraft," *Journal of Aircraft*, Vol. 38, No. 1, January-February 2001, pp. 95-103.
- [4] Lin, C. Y. and Crawley, E. F., "Design Considerations for a Strain Actuated Adaptive Wing for Aeroelastic Control," *Journal of Intelligent Material Systems and Structures*, Vol. 6 - May 1995.
- [5] Lin, C. Y. and Crawley, E. F., "Towards Optimal Aeroelastic Control Using Elastic and Induced Strain Anisotropy," *Proceedings of the 35th AIAA/ASME/ASCE/AHS/ASC Structures, Structural Dynamics, and Materials Conference*, Hilton Head, SC, April 18-20, 1994, AIAA-94-1547-CP.
- [6] Lazarus, K. B., Lin, C. Y. and Crawley, E. F., "Fundamental Mechanisms Of Aeroelastic Control With Control Surface and Strain Actuation," *Journal of Guidance, Control, and Dynamics*, Vol. 18, No. 1, January-February 1995, pp. 10-17.
- [7] Librescu, L. and Na, S., "Vibration and Dynamic Response Control of Elastically Tailored Nonuniform Adaptive Aircraft Wings", *Proceedings of the 41st AIAA/ASME/ASCE/AHS/ASC Structures, Structural Dynamics, and Material Conference and Exhibit*, Atlanta, GA, April 3-6, 2000, AIAA-2000-1628.
- [8] Bent, A. A. and Hagood, N. W., "Piezoelectric Fiber Composites with Interdigitated Electrodes," *Journal of Intelligent Material Systems and Structures*, Vol. 8, No. 6, November 11, 1997, pp. 903-191.
- [9] Rogers, J. P. and Hagood, N. W., "Hover Testing of a 1/6TH Scale CH-47D Blade with Integral Twist Actuation," *Presented at the 9th International Conference on Adaptive Structures and Technology*, Cambridge, MA, 1998.
- [10] Pendleton, E. W., Griffin, K. E., Kehoe, M., and Perry, B., "A Flight Research Program for the Active Aeroelastic Wing Concept," *Proceedings of the 37th AIAA/ASCE/AHS/ASC Structures, Structural Dynamics and Materials Conference*, Salt Lake City, Utah, April 1996.

- [11] Peters, D. A. and Johnson, M. J., "Finite-State Airloads for Deformable Airfoils on Fixed and Rotating Wings," *Symposium on Aeroelasticity and Fluid/Structure Interaction, Proceedings of the Winter Annual Meeting*. ASME, November 6 -11, 1994.
- [12] Peters, D. A., Karunamoorthy, S., and Cao, W. M., "Finite State Induced Flow Models; Part I: Two-Dimensional Thin Airfoil," *Journal of Aircraft*, Vol. 32, No. 2, March – April 1995, pp. 313-322.
- [13] Cesnik, C. E. S. and Shin, S.-J., "On the Modeling of Active Helicopter Blades," *Int. Journal of Solids and Structures*, Vol. 38, Nos. 10-13, March 2001, pp. 1765-1789.
- [14] Patil, M. J., "Nonlinear Aeroelastic Analysis, Flight Dynamics, and Control of a Complete Aircraft," Ph.D. Thesis, Aerospace Engineering, Georgia Institute of Technology, May 1999.
- [15] Cheng, T., "Structural Dynamics Modeling of Helicopter Blades for Computational Aeroelasticity" Masters Thesis, Aeronautics and Astronautics, Massachusetts Institute of Technology, 2002.
- [16] Lin, J. and Iliff, K. W., "Aerodynamic Lift and Moment Calculations Using a Closed-Form Solution of the Possio Equation," NASA/TM-2000-209019, April 2000.
- [17] Sigmon, K., "MATLAB primer," Chapman & Hall, Boca Raton, Florida, 2002.
- [18] Cesnik, C. E. S. and Hodges, D. H., "VABS: A New Concept for Composite Rotor Blade Cross-Sectional Modeling," *Journal of the American Helicopter Society*, Vol. 42, No. 1, 1997, pp. 27-38.
- [19] Cesnik, C. E. S. and Palacios, R., "Modeling Active Materials Embedded in Slender Structures," *Proceedings of the 44th Structures, Structural Dynamics, and Material Conference*, Hampton, Virginia, April 7-10, 2003.
- [20] Lawrence, K. L., "ANSYS Tutorial," Schroff Development Corp. Publications, August 1, 2002.
- [21] Bauchau, Olivier A. and Kang, N. K., "A Multibody Formulation for Helicopter Structural Dynamic Analysis", JAHS, Vol. 32, No. 2, April 1993, pp. 3 - 14.
- [22] Goland, M., "The Flutter of a Uniform Cantilever Wing," *Journal of Applied Mechanics*, Vol. 12, No. 4, December 1945, pp. A197-A208.
- [23] Khot, N. S., "Design of an Optimum Smart Wing to Enhance Roll Performance," SPIE Proceedings, Vol. 3667, March 1999, pp. 59-67.
- [24] Khot, N. S., "Multicriteria optimization for design of structures with active control," *Journal of Aerospace Engineering* (0893-1321), Vol. 11, No. 2, Apr. 1998, pp. 45-51.

- [25] Khot, N. S., Eastep, F. E., and Kolonay, R. M., "Optimization of a composite Wing Structure for Enhancement of the Rolling Maneuver," *AIAA, NASA, and ISSMO, Symposium on Multidisciplinary Analysis and Optimization*, 6th, Bellevue, WA, Sept. 4-6, 1996 AIAA Paper 96-3998, pp. 152-161.
- [26] Khot, N. S., "Computational Method for the Simultaneous Design of Structural and Control Systems," *SPIE Proceedings*, Vol. 2442, February 1995, pp. 268-279.
- [27] Drela, M., "Integrated Simulation Model For Preliminary Aerodynamic, Structural, and Control-Law Design of Aircraft", AIAA-99-1394.
- [28] Karpel, M. "Multidisciplinary optimization of aeroservoelastic systems using reduced-size models", *Journal of Aircraft*, Vol. 29, No. 5, Sept. 1992, pp. 939-946.
- [29] Karpel, M. and Brainin, L., "Stress considerations in reduced-size aeroelastic optimization", *AIAA Journal*, Vol. 33, No. 4, 1995, pp. 716-722.
- [30] Karpel, M. and Strul, E., "Minimum-state unsteady aerodynamic approximations with flexible constraints", *Journal of Aircraft*, Vol. 33, No. 6, 1996, pp. 1190-1196.
- [31] Idan, M., Karpel, M. and Moulin, B., "Aeroservoelastic Interaction Between Aircraft Structural and Control Design Schemes", *Journal of Guidance and Control*, Vol. 22, No. 4, July-August 1999, pp. 513-519.
- [32] Ortega-Morales, M. and Cesnik, C. E. S., "Modeling and Control of the Aeroelastic Response of Highly Flexible Active Wings," AMSL Report #2000-2, 2000.
- [33] Cesnik, C. E. S. and Ortega-Morales, M., "Active Aeroelastic Tailoring of Slender Flexible Wings," *International Forum on Aeroelasticity and Structural Dynamics*, Madrid, Spain, June 5-7, 2001.
- [34] Rogers, R. M., "Reduced Sensitivity Nonlinear Control of an Aeroelastic Wing with Torsional Nonlinearity," *AIAA Guidance, Navigation, and Control Conference and Exhibit*, Boston, MA, Aug. 10-12, 1998, AIAA-98-4324.
- [35] McGowan, A. R., Heeg, J., and Lake, R., "Results of Wind-Tunnel Testing from the Piezoelectric Aeroelastic Tailoring Investigation," In *Proceedings of the 37th AIAA/ASCE/AHS/ASC Structures, Structural Dynamics and Materials Conference*, Salt Lake City, Utah, April 1996.
- [36] Khot, N. S. and Zweber, J. V., "Lift Efficient Composite Flexible Wing for Rolling Maneuver Without Ailerons," In *Proceedings of the 41st AIAA/ASME/ASCE/ AHS/ASC Structures, Structural Dynamics, and Material Conference and Exhibit*, Atlanta, GA, April 3-6, 2000, AIAA-2000-1333.

- [37] Khot, N. S., Bhungallia, A. A., and Hartog, A. R., "Deformation of a flexible structure using an actuating system for enhancing performance," *The 7th International Conference and Exposition on Engineering, Construction, Operations, and Business in Space*, Albuquerque, NM, Feb. 27-Mar. 2, 2000 (A00-30101 07-12), pp. 384-390.
- [38] Khot, N. S., Appa, A., and Eastep, F. E., "Actuating system for enhancement of rolling maneuver of a wing with ailerons," *AIAA/ASME/ASCE/AHS/ASC Structures, Structural Dynamics, and Materials Conference and Exhibit*, St. Louis, MO, Apr. 12-15, 1999.
- [39] Pendleton, E., Bessette, D., Field, P., Miller, G., and Griffin, B., "The Active Aeroelastic Wing Flight Research Program, AIAA-98-1972.
- [40] Fung, Y. C., "An Introduction to the Theory of Aeroelasticity," Dover, Reprint Edition, January 1994.
- [41] Cesnik, C. E. S., Shin, S.-J., Wilkie, W. K., Wilbur, M. L., and Mirick, P. H., "Modeling, Design and Testing of the NASA/ARMY/MIT Active Twist Rotor Prototype Blade," in *Proceedings of the American Helicopter Society 55th Annual Forum*, Montreal, Canada, May 25-27, 1999.
- [42] Cesnik, C. E. S. and Shin, S.-J., "Structural Analysis for Designing Rotor Blades With Integral Actuators," in *Proceedings of the 39th Structures, Structural Dynamics, and Materials Conference*, Long Beach, California, 370 L'Enfant Promenade, S. W., Washington, D.C. 20024, April 20-23 1998, American Institute of Aeronautics and Astronautics, AIAA Paper No. 98-2107.
- [43] Friedmann, P. P., "Renaissance of Aeroelasticity and Its Future," *Journal of Aircraft*, Vol. 36, no. 1, Jan. - Feb. 1999, pp. 105-121.
- [44] Giurgiutiu, V., "Review of Smart-Materials Actuation Solutions for Aeroelastic and Vibration Control," *Journal of Intelligent Materials Systems and Structures*, Vol. 11, July 2000, pp. 525-544.
- [45] Wilkie, W. K., Bryant, R. G., High, J. W., Fox, R. L., Hellbaum, R. F., Jalink, A., Little, B. D., and Mirick, P. H., "Low-Cost Piezocomposite Actuator for Structural Control Applications," In *Proceedings of the SPIE 7th Annual International Symposium on Smart Structures and Materials*, Newport Beach, CA, March 5-9, 2000.
- [46] Pendaries, C., "From the HALE Gnat to the Ornithopter- Or How to Take Advantage of Aircraft Flexibility," In *21st ICAS Congress*, Melbourne, Australia, September 13-18, 1998.
- [47] Hoblit, F. M., "Gust Loads on Aircraft: Concepts and Applications," AIAA Education Series, American Institute of Aeronautics and Astronautics Inc., Washington D.C., 1988.

[48] Shin, S.-J., Cesnik, C. E. S., and Hall, S. R., "Closed Loop Testing of the NASA/Army/MIT Active Twist Rotor for Vibration Reduction," in *Proceedings of the American Helicopter Society 59th Annual Forum*, Pheonix, Arizona, May 6-8, 2003.

[49] Sahoo, D. and Cesnik, C. E. S., "Roll Maneuver Control of UCAV Wing Using Anisotropic Piezoelectric Actuators," in *Proceedings of the 43rd Structures, Structural Dynamics, and Materials Conference*, Denver, Colorado, April 22-25, 2002, AIAA Paper 2002-1720.

APPENDIX A - Aerodynamic Loads Derivation

The aerodynamic forces and moments used here are based on the formulation of [11]. The theory allows for a thin, deformable airfoil performing small arbitrary motions with respect to a reference frame that can undergo arbitrarily large translations and rotations in two dimensions. Trailing edge flap deflection is treated as a special case of general airfoil deformation. Some modifications were made to the formulation for compatibility with the geometric variables used in this thesis. It was determined that the aerodynamic loads could be initially written in terms of the large motion of the airfoil. The small perturbations about this motion could later be reproduced using Taylor expansion, retaining the first order terms.

Lift and Moment per Unit Span

The relevant generalized aerodynamic forces are given by

$$\frac{1}{2\pi\rho} \underline{L}_n = -b^2[M](\ddot{\underline{h}}_n + \dot{\underline{v}}_n) - bu_0[C](\dot{\underline{h}}_n + \underline{v}_n - \underline{\lambda}_0) - u_0^2[K]\underline{h}_n + bu_0[G](\underline{v}_n - \underline{\lambda}_0) \quad A.1$$

where the $\underline{L}_n = [L_0, L_1, L_2, \dots]^T$ are generalized aerodynamic forces. Only L_0 and L_1 contribute to the lift and moment on the airfoil. The corresponding variables in Equation A.1 are given by

$$\underline{L}_n = \begin{bmatrix} L_0 \\ L_1 \end{bmatrix}, \quad \underline{v}_n = \begin{bmatrix} v_0 \\ v_1 \\ 0 \\ 0 \\ \vdots \end{bmatrix} = \begin{bmatrix} -\dot{z} - d\dot{\alpha} \\ b\dot{\alpha} \\ 0 \\ 0 \\ \vdots \end{bmatrix}, \quad \underline{h}_n = \begin{bmatrix} bg_0\beta \\ bg_1\beta \\ bg_2\beta \\ bg_3\beta \\ \vdots \end{bmatrix}, \quad \underline{\lambda}_0 = \begin{bmatrix} \lambda_0 \\ 0 \\ 0 \\ 0 \\ \vdots \end{bmatrix}, \quad u_0 = \dot{y} \quad A.2$$

$$M = \begin{bmatrix} \frac{1}{2} & 0 & -\frac{1}{4} & 0 & 0 & 0 & \dots \\ 0 & \frac{1}{16} & 0 & -\frac{1}{16} & 0 & 0 & \dots \end{bmatrix}, \quad C = \begin{bmatrix} 1 & 1 & 0 & 0 & 0 & \dots \\ -\frac{1}{2} & 0 & \frac{1}{2} & 0 & 0 & \dots \end{bmatrix}, \quad K = \begin{bmatrix} 0 & 1 & 2 & 3 & 4 & \dots \\ 0 & -\frac{1}{2} & 0 & 0 & 0 & \dots \end{bmatrix} \quad A.3$$

$$G = \begin{bmatrix} 0 & \frac{1}{2} & 0 & 0 & 0 & \dots \\ 0 & 0 & \frac{1}{4} & 0 & 0 & \dots \end{bmatrix}$$

where λ_0 is the inflow, β is the aileron angle (not to be confused with the definition for body motion in Chapter 2), g_n are expansion coefficients used in defining airfoil camber, and they can be found in [11]. The other motion variables are shown in Figure A.1, which is reproduced here from Chapter 2.

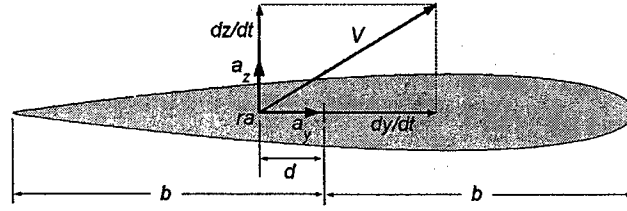


Figure A.1: Airfoil motion definition.

The lift and moment per unit span acting on the reference point (labeled ra in Figure A.1) are given by

$$\begin{aligned} L &= -L_0 \\ M_x &= dL + bL_1 \end{aligned} \quad A.4$$

After algebraic manipulations, the lift per unit span acting at the reference point is given by

$$L = 2\pi\rho b[-\dot{y}\dot{z} + (b-d)\dot{y}\dot{\alpha} - \dot{y}\lambda_0 - \frac{1}{2}b\ddot{z} - \frac{1}{2}bd\ddot{\alpha} + c_1\dot{y}^2\beta + c_2\dot{y}\dot{\beta} + c_3\ddot{\beta}] \quad A.5$$

where

$$\begin{aligned} c_1 &= (g_1 + 2g_2 + 3g_3 + 4g_4 + \dots) \\ c_2 &= b(g_0 + g_1) \\ c_3 &= b^2(\frac{1}{2}g_0 - \frac{1}{4}g_2) \end{aligned} \quad A.6$$

Note that the first term is similar to the familiar static term found in 2-D airloads approximations on thin airfoils,

$$L_{static} = 2\pi\rho bV^2\alpha \approx 2\pi\rho b\dot{y}^2\alpha \approx -2\pi\rho b\dot{y}^2(\dot{z}/\dot{y}) = -2\pi\rho b\dot{y}\dot{z} \quad A.7$$

The first three terms of Equation A.5 contribute to an effective angle of attack, given by

$$A_{Leff} = \dot{y}^2\alpha_{Leff} = -\dot{y}\dot{z} + (b-d)\dot{y}\dot{\alpha} - \dot{y}\lambda_0 \quad A.8$$

where α_{Leff} is the effective angle of attack, and A_{Leff} is the weighted effective angle of attack. In determining stall, A_{Leff} is used instead of α_{Leff} in order to avoid dividing by zero when the flight speed is zero. Stall occurs when the following condition applies

$$|A_{Leff}| \geq |A_{Lstall}|, \quad A_{Lstall} = \dot{y}^2\alpha_{Lstall} \quad A.9$$

where α_{Lstall} is the stall angle (input by user or default value), above which the lift no longer increases. The lift is now given by

$$L = 2\pi\rho b A_{Leff} - \pi\rho b^2 \ddot{z} - \frac{1}{2} 2\pi\rho b^2 d\ddot{\alpha} + 2\pi\rho b c_1 \dot{y}^2 \beta + 2\pi\rho b c_2 \dot{y} \dot{\beta} + 2\pi\rho b c_3 \ddot{\beta} \quad A.10$$

The moment per unit span (about the axis perpendicular to the airfoil) acting on the airfoil section is similarly found after algebraic manipulation, and is given by

$$M_x = dL + 2\pi\rho b^2 \left(-\frac{1}{2} \dot{y} \ddot{z} - \frac{1}{2} d\dot{y} \ddot{\alpha} - \frac{1}{2} \dot{y} \lambda_0 - \frac{1}{16} b^2 \ddot{\alpha} + c_4 \dot{y}^2 \beta + c_5 \dot{y} \dot{\beta} + c_6 \ddot{\beta} \right) \quad A.11$$

where

$$\begin{aligned} c_4 &= \frac{1}{2} g_1 \\ c_5 &= -b \left(-\frac{1}{2} g_0 + \frac{1}{2} g_2 \right) \\ c_6 &= b^2 \left(-\frac{1}{16} g_1 + \frac{1}{16} g_3 \right) \end{aligned} \quad A.12$$

The moment can be rewritten as

$$M_x = 2\pi\rho b \left(dA_{Leff} + bA_{Meff} - \frac{1}{2} b d\ddot{z} - \left(\frac{1}{2} b d^2 + \frac{1}{16} b^3 \right) \ddot{\alpha} + (dc_1 + bc_4) \dot{y}^2 \beta + (dc_2 + bc_5) \dot{y} \dot{\beta} + (dc_3 + bc_6) \ddot{\beta} \right) \quad A.13$$

where

$$A_{Meff} = \left(-\frac{1}{2} \dot{y} \ddot{z} - \frac{1}{2} d\dot{y} \ddot{\alpha} - \frac{1}{2} \dot{y} \lambda_0 \right) = \dot{y}^2 \alpha_{Meff} \quad A.14$$

A_{Meff} is used to calculate the effect of stall on the aerodynamic moment in a similar way as A_{Leff} .

The drag per unit span is found using the relations given in [11], and is given by

$$\begin{aligned} D = -2\pi\rho b \left(\dot{z}^2 + d^2 \dot{\alpha}^2 + \lambda_0^2 + 2d\dot{\alpha}\dot{z} + 2\lambda_0\dot{z} + 2d\dot{\alpha}\lambda_0 \right. \\ \left. + c_1 \beta \dot{y} \dot{z} + (dc_1 + bg_2) \beta \dot{y} \ddot{\alpha} + c_1 \beta \dot{y} \lambda_0 + \frac{1}{2} bg_2 \beta \ddot{z} + \left(\frac{1}{2} bdg_2 - \frac{1}{4} b^2 g_3 \right) \beta \ddot{\alpha} \right) \end{aligned} \quad A.15$$

Here, the direct effect of aileron deflection time derivatives is neglected. However, the aileron motion affects the induced flow, which has a secondary effect on the drag forces.

The lift, moment and drag forces must be put into a form compatible with the present formulation. Derivatives of the lift and moment taken with respect to the local motion variables are given by

$$\begin{aligned}
\frac{\partial L}{\partial z} &= -\pi\rho b^2 \\
\frac{\partial L}{\partial \alpha} &= -\pi\rho b^2 d \\
\frac{\partial L}{\partial y} &= 2\pi\rho b \left(-\dot{z} + (b-d)\dot{\alpha} - \lambda_0 + 2c_1\dot{y}\beta + c_2\dot{\beta} \right) \\
\frac{\partial L}{\partial z} &= -2\pi\rho b\dot{y} \\
\frac{\partial L}{\partial \alpha} &= 2\pi\rho b(b-d)\dot{y} \\
\frac{\partial L}{\partial \alpha} &= 2\pi\rho b\dot{y}^2 \\
\frac{\partial L}{\partial \lambda_0} &= -2\pi\rho b\dot{y} \\
\frac{\partial L}{\partial \beta} &= 2\pi\rho b c_1 \dot{y}^2 \\
\frac{\partial L}{\partial \beta} &= 2\pi\rho b c_2 \dot{y} \\
\frac{\partial L}{\partial \beta} &= 2\pi\rho b c_1 \dot{y}^2 \\
\frac{\partial M_z}{\partial z} &= d \frac{\partial L}{\partial z} \\
\frac{\partial M_z}{\partial \alpha} &= -\pi\rho b^2 d - \frac{1}{8}\pi\rho b^4 \\
\frac{\partial M_z}{\partial y} &= d \frac{\partial L}{\partial y} + 2\pi\rho b^2 \left(-\frac{1}{2}\dot{z} - \frac{1}{2}d\dot{\alpha} - \frac{1}{2}\lambda_0 + 2c_4\dot{y}\beta + c_5\dot{\beta} \right) \\
\frac{\partial M_z}{\partial z} &= d \frac{\partial L}{\partial z} - \pi\rho b^2 \dot{y} \\
\frac{\partial M_z}{\partial \alpha} &= d \frac{\partial L}{\partial \alpha} - \pi\rho b^2 d\dot{y} \\
\frac{\partial M_z}{\partial \alpha} &= d \frac{\partial L}{\partial \alpha} + \pi\rho b^2 \dot{y}^2 \\
\frac{\partial M_z}{\partial \lambda_0} &= d \frac{\partial L}{\partial \lambda_0} - \pi\rho b^2 \dot{y} \\
\frac{\partial M_z}{\partial \beta} &= d \frac{\partial L}{\partial \beta} 2\pi\rho b^2 c_4 \dot{y}^2 \\
\frac{\partial M_z}{\partial \beta} &= d \frac{\partial L}{\partial \beta} 2\pi\rho b^2 c_5 \dot{y} \\
\frac{\partial M_z}{\partial \beta} &= d \frac{\partial L}{\partial \beta} 2\pi\rho b^2 c_6
\end{aligned}
\tag{A.16}$$

The drag derivatives are given by

$$\begin{aligned}
\frac{\partial D}{\partial z} &= -\pi\rho b^2 g_2 \beta \\
\frac{\partial D}{\partial \alpha} &= -\pi\rho b^2 \left(dg_2 - \frac{1}{2}bg_3 \right) \beta \\
\frac{\partial D}{\partial y} &= -2\pi\rho b \left(c_1\beta\dot{z} + (dc_1 + bg_2)\beta\dot{\alpha} + c_1\beta\lambda_0 \right) \\
\frac{\partial D}{\partial z} &= -2\pi\rho b \left(2\dot{z} + 2d\dot{\alpha} + 2\lambda_0 + c_1\beta\dot{y} \right) \\
\frac{\partial D}{\partial \alpha} &= -2\pi\rho b \left(2d^2\dot{\alpha} + 2d\dot{z} + 2d\lambda_0 + (dc_1 + bg_2)\beta\dot{y} \right) \\
\frac{\partial D}{\partial \alpha} &= -2\pi\rho b \left(2\dot{y}\dot{z} + 2d\dot{y}\dot{\alpha} + 2\dot{y}\lambda_0 - c_1\beta\dot{y}^2 \right) \\
\frac{\partial D}{\partial \lambda_0} &= -2\pi\rho b \left(2\dot{z} + 2d\dot{\alpha} + 2\lambda_0 + c_1\beta\dot{y} \right)
\end{aligned}
\tag{A.17}$$

The 3x1 cross-sectional aerodynamic force and moment vectors, resolved in the body frame, are then given by

$$F = C^{BA} \begin{bmatrix} 0 \\ D \\ L \end{bmatrix}, \quad M = C^{BA} \begin{bmatrix} M_x \\ 0 \\ 0 \end{bmatrix} \quad \text{A.18}$$

where C^{BA} is the rotation matrix from frame A to the body frame, B . Axis A_y is aligned with the velocity vector. A_x is normal to the airfoil section, and A_z is normal to A_x and A_y .

Relating Local Variables to the Wing Variables

The local motion variables must be related to the beam variables. Let the forces and moments described above apply to an airfoil section at a node of the beam reference line. The kinematics relating the rigid body motion of the vehicle and the flexible motion to the local linear and angular velocities are given by

$$\begin{aligned} \dot{y} &= e_2^T C^{a_0 B} (v_B + \dot{p} + w) \\ \dot{z} &= e_3^T C^{a_0 B} (v_B + \dot{p} + w) \\ \dot{\alpha} &= e_1^T C^{a_0 B} \dot{\theta} \end{aligned} \quad \text{A.19}$$

where $e_1 = [1 \ 0 \ 0]^T$, $e_2 = [0 \ 1 \ 0]^T$, $e_3 = [0 \ 0 \ 1]^T$, v_B is the velocity of coordinate system B , \dot{p} and $\dot{\theta}$ are the flexible linear and rotational velocities at the node, and w is the gust velocity (gust is incorporated here as an extra component of airfoil velocity). $C^{a_0 B}$ is the rotation matrix from frame B to frame a_0 , as defined in Chapter 2. The velocity components are resolved in frame B .

Aerodynamic force and moment derivatives with respect to the beam displacement and rotation variables are required, and are given by

$$\begin{aligned} F_{\dot{p}} &= C^{BA} \left(e_3 \frac{\partial L}{\partial \dot{z}} + e_2 \frac{\partial D}{\partial \dot{z}} \right) e_3^T C^{a_0 B} & M_{\dot{p}} &= C^{BA} e_1 \frac{\partial M}{\partial \dot{z}} e_3^T C^{a_0 B} \\ F_{\dot{\theta}} &= C^{BA} \left(e_3 \frac{\partial L}{\partial \dot{\alpha}} + e_2 \frac{\partial D}{\partial \dot{\alpha}} \right) e_1^T C^{a_0 B} & M_{\dot{\theta}} &= C^{BA} e_1 \frac{\partial M}{\partial \dot{\alpha}} e_1^T C^{a_0 B} \\ F_{\dot{p}} &= C^{BA} \left(\left(e_3 \frac{\partial L}{\partial \dot{z}} + e_2 \frac{\partial D}{\partial \dot{z}} \right) e_3^T + \left(e_3 \frac{\partial L}{\partial \dot{y}} + e_2 \frac{\partial D}{\partial \dot{y}} \right) e_2^T \right) C^{a_0 B} & M_{\dot{p}} &= C^{BA} e_1 \frac{\partial M}{\partial \dot{z}} e_3^T C^{a_0 B} \\ F_{\dot{\theta}} &= C^{BA} \left(e_3 \frac{\partial L}{\partial \dot{\alpha}} + e_2 \frac{\partial D}{\partial \dot{\alpha}} \right) e_1^T C^{a_0 B} & M_{\dot{\theta}} &= C^{BA} e_1 \frac{\partial M}{\partial \dot{\alpha}} e_1^T C^{a_0 B} \\ F_{\theta} &= C^{BA} \left(e_3 \frac{\partial L}{\partial \alpha} + e_2 \frac{\partial D}{\partial \alpha} \right) e_1^T C^{a_0 B} & M_{\theta} &= C^{BA} e_1 \frac{\partial M}{\partial \alpha} e_1^T C^{a_0 B} \\ F_{\beta} &= C^{BA} \left(e_3 \frac{\partial L}{\partial \beta} + e_2 \frac{\partial D}{\partial \beta} \right) & M_{\beta} &= C^{BA} e_1 \frac{\partial M}{\partial \beta} \\ F_{\dot{\beta}} &= C^{BA} e_3 \frac{\partial L}{\partial \dot{\beta}} & M_{\dot{\beta}} &= C^{BA} e_1 \frac{\partial M}{\partial \dot{\beta}} \\ F_{\beta} &= C^{BA} e_3 \frac{\partial L}{\partial \beta} & M_{\beta} &= C^{BA} e_1 \frac{\partial M}{\partial \beta} \\ F_{\lambda_0} &= C^{BA} \left(e_3 \frac{\partial L}{\partial \lambda_0} + e_2 \frac{\partial D}{\partial \lambda_0} \right) & M_{\lambda_0} &= C^{BA} e_1 \frac{\partial M}{\partial \lambda_0} \end{aligned} \quad \text{A.20}$$

The forces, moments, and their derivatives as presented above apply to a two-dimensional airfoil section at a node on the beam reference line. Without loss of generality, these relations are applied to each node of the beam reference line using the same notation. The force and moment vectors are increased in size to $3n \times 1$, where n is the number of nodes in the beam discretization. The derivatives are arranged into matrices of size $3n \times 3n$.

Spanwise Aerodynamic Corrections

Corrections may be applied to the aerodynamic load distribution to account for the effects of finite span. The value of the lift-slope has been assumed to equal 2π (thin airfoil) throughout the derivation, but adjustments may be made by using the spanwise correction option. The nodal distributed aerodynamic forces and moments can be modified based on a user defined correction function, as shown in Figure A.2. The straight line on top in the figure represents the two-dimensional lift distribution with no correction applied. The bottom straight line represents a uniform reduction in the lift-curve slope in order to account for finite-thick airfoils. The middle curve allows for the lift to go to zero at the wing tip to approximate the true lift distribution on a finite wing.

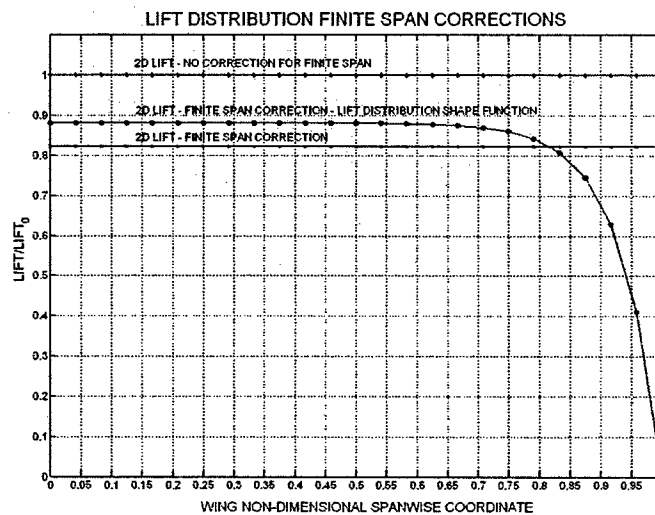


Figure A.2: Example of finite span correction distribution.

APPENDIX B - Properties of the Test Wings

This appendix contains the basic wing properties used for each of the three vehicles studied in this thesis. The numerical value of a given property is presented for each wing element (from root to tip). The nomenclature used, as well as the units corresponding to the numerical values, are defined as follows:

K11	- Nm	- extensional stiffness
K12	- Nm	- extension-twist coupling stiffness
K13	- Nm	- extension-flatwise bending coupling stiffness
K14	- Nm	- extension-chordwise bending coupling stiffness
K22	- Nm ²	- torsional stiffness
K23	- Nm ²	- twist-flatwise bending coupling stiffness
K24	- Nm ²	- twist-chordwise bending coupling stiffness
K33	- Nm ²	- flatwise bending stiffness
K34	- Nm ²	- flatwise bending-chordwise bending coupling stiffness
K44	- Nm ²	- chordwise bending stiffness
mass	- kg/m	- mass per unit length
Ixx	- kgm ² /m	- x-axis rotational inertia per unit length
Ixy	- kgm ² /m	- x-axis to y-axis coupling rotational inertia per unit length
Ixz	- kgm ² /m	- x-axis to z-axis coupling rotational inertia per unit length
Iyy	- kgm ² /m	- y-axis rotational inertia per unit length
Iyz	- kgm ² /m	- y-axis to z-axis coupling rotational inertia per unit length
Izz	- kgm ² /m	- z-axis rotational inertia per unit length
chord	- m	- chord lengths
xle	- m	- distance of airfoil tip from reference axis, local x direction
yle	- m	- distance of airfoil tip from reference axis, local y direction
Bv1	- N/μs	- normalized APC extensional actuation
Bv2	- Nm/μs	- normalized APC twist actuation
Bv3	- Nm/μs	- normalized APC flatwise bending actuation
Bv4	- Nm/μs	- normalized APC chordwise bending actuation

% -----
 SMALL VEHICLE AILERON
 % -----

K11 = 1.0e+007 *

1.3530
 1.2595
 1.1660
 1.0481
 0.9569
 0.8454

K12 =

0
 0
 0
 0
 0
 0

K13 = 1.0e+004 *

-3.1401
 -2.7219
 -2.3336
 -1.9553
 -1.6300
 -1.3207

K14 = 1.0e+005 *

1.9312
 1.6740
 1.4352
 1.2161
 1.0138
 0.8308

K22 =

457.2059
 368.4621
 292.0817
 226.9168
 172.4731
 127.4225

K23 =

0
 0
 0
 0
 0
 0

K24 =

0
 0
 0
 0
 0
 0

K33 =

672.6978
 542.8599
 430.9103
 331.2420
 252.1099
 184.2952

K34 =

-602.2668
 -486.0559
 -385.8468
 -300.5649
 -228.7771
 -169.5022

K44 = 1.0e+004 *

1.8390
 1.4840
 1.1780
 0.9172
 0.6980
 0.5169

mass =

0.2465	0.2376	0.2286
0.2286	0.2197	0.2109
0.2109	0.2021	0.1934
0.1910	0.1824	0.1739
0.1739	0.1654	0.1570
0.1550	0.1468	0.1385

Ixx = 1.0e-003 *

0.3761	0.3403	0.3045
0.3045	0.2737	0.2428
0.2428	0.2165	0.1902
0.1901	0.1680	0.1459
0.1459	0.1275	0.1091
0.1091	0.0941	0.0792

Ixy =

```

0 0 0
0 0 0
0 0 0
0 0 0
0 0 0
0 0 0

```

Ixz =

```

0 0 0
0 0 0
0 0 0
0 0 0
0 0 0
0 0 0

```

Iyy = 1.0e-004 *

```

0.1276 0.1155 0.1034
0.1034 0.0929 0.0825
0.0825 0.0736 0.0647
0.0642 0.0567 0.0493
0.0493 0.0431 0.0369
0.0366 0.0316 0.0266

```

Iyz = 1.0e-004 *

```

-0.1119 -0.1014 -0.0910
-0.0910 -0.0819 -0.0728
-0.0728 -0.0651 -0.0573
-0.0573 -0.0507 -0.0441
-0.0441 -0.0386 -0.0332
-0.0332 -0.0287 -0.0242

```

Izz = 1.0e-003 *

```

0.3634 0.3288 0.2942
0.2942 0.2644 0.2346
0.2346 0.2092 0.1837
0.1837 0.1623 0.1409
0.1409 0.1232 0.1054
0.1054 0.0910 0.0765

```

chord =

```

0.1250 0.1208 0.1167
0.1167 0.1125 0.1083
0.1083 0.1042 0.1000
0.1000 0.0958 0.0917
0.0917 0.0875 0.0833
0.0833 0.0792 0.0750

```

xle =

```

0.0445 0.0430 0.0415
0.0415 0.0400 0.0385
0.0385 0.0371 0.0356

```

```

0.0356 0.0341 0.0326
0.0326 0.0311 0.0297
0.0297 0.0282 0.0267

```

yle =

```

0.0060 0.0058 0.0056
0.0056 0.0054 0.0052
0.0052 0.0050 0.0048
0.0048 0.0046 0.0044
0.0044 0.0042 0.0040
0.0040 0.0038 0.0036

```

Bv1 = []

Bv1 = []

Bv1 = []

Bv1 = []

Bv1 = []

Bv1 = []

Bv2 = []

Bv2 = []

Bv2 = []

Bv2 = []

Bv2 = []

Bv2 = []

Bv3 = []

Bv3 = []

Bv3 = []

Bv3 = []

Bv3 = []

Bv3 = []

Bv4 = []

Bv4 = []

Bv4 = []

Bv4 = []

Bv4 = []

Bv4 = []

% -----

SMALL VEHICLE ISA1

% -----

K11 = 1.0e+007 *

1.3455

1.2525

1.1596

1.0667

0.9738

0.8809

K12 =

0

0
0
0
0
0

K13 = 1.0e+004 *

-3.1215
-2.7058
-2.3198
-1.9635
-1.6368
-1.3399

K14 = 1.0e+005 *

1.9191
1.6635
1.4262
1.2071
1.0063
0.8238

K22 =

165.5589
133.0901
105.2358
81.6223
61.8812
45.6489

K23 =

0
0
0
0
0
0
0

K24 =

0
0
0
0
0
0
0

K33 =

668.7729
539.6923
428.3958
333.5639

253.8772
188.0169

K34 =

-598.5027
-483.0181
-383.4353
-298.5765
-227.2636
-168.3189

K44 = 1.0e+004 *

1.8275
1.4748
1.1706
0.9115
0.6937
0.5137

mass =

0.5684	0.5487	0.5290
0.5290	0.5094	0.4899
0.4899	0.4704	0.4509
0.4509	0.4315	0.4121
0.4121	0.3929	0.3736
0.3736	0.3544	0.3353

Ixx = 1.0e-003 *

0.9232	0.8362	0.7493
0.7493	0.6741	0.5989
0.5989	0.5346	0.4703
0.4703	0.4160	0.3616
0.3616	0.3164	0.2712
0.2712	0.2343	0.1974

Ixy =

0	0	0
0	0	0
0	0	0
0	0	0
0	0	0
0	0	0

Ixz =

0	0	0
0	0	0
0	0	0
0	0	0
0	0	0
0	0	0

Iyy = 1.0e-004 *

0.3088	0.2797	0.2507
0.2507	0.2256	0.2004
0.2004	0.1789	0.1574
0.1574	0.1393	0.1211
0.1211	0.1060	0.0909
0.0909	0.0785	0.0661

Iyz = 1.0e-004 *

-0.2857	-0.2590	-0.2322
-0.2322	-0.2091	-0.1860
-0.1860	-0.1661	-0.1463
-0.1463	-0.1295	-0.1127
-0.1127	-0.0986	-0.0846
-0.0846	-0.0732	-0.0617

Izz = 1.0e-003 *

0.8923	0.8083	0.7243
0.7243	0.6516	0.5789
0.5789	0.5167	0.4546
0.4546	0.4020	0.3495
0.3495	0.3059	0.2622
0.2622	0.2265	0.1908

chord =

0.1250	0.1208	0.1167
0.1167	0.1125	0.1083
0.1083	0.1042	0.1000
0.1000	0.0958	0.0917
0.0917	0.0875	0.0833
0.0833	0.0792	0.0750

xle =

0.0445	0.0430	0.0415
0.0415	0.0400	0.0385
0.0385	0.0371	0.0356
0.0356	0.0341	0.0326
0.0326	0.0311	0.0297
0.0297	0.0282	0.0267

yle =

0.0060	0.0058	0.0056
0.0056	0.0054	0.0052
0.0052	0.0050	0.0048
0.0048	0.0046	0.0044
0.0044	0.0042	0.0040
0.0040	0.0038	0.0036

Bv1 = 1.0e-001 *

[1.2198 1.2198 1.1777 1.1777]

[1.1357	1.1357	1.0965	1.0965]
[1.0516	1.0516	1.0153	1.0153]
[.9674	.9674	.9340	.9340]
[.8833	.8833	.8528	.8528]
[.7992	.7992	.7716	.7716]

Bv2 = 1.0e-003 *

[-3.4938	3.4938	-3.3663	3.3663]
[-3.0285	3.0285	-2.9180	2.9180]
[-2.5965	2.5965	-2.5017	2.5017]
[-2.1976	2.1976	-2.1175	2.1175]
[-1.8321	1.8321	-1.7652	1.7652]
[-1.4997	1.4997	-1.4450	1.4450]

Bv3 = 1.0e-003 *

[0.4261	0.4261	-1.0239	-1.0239]
[0.3694	0.3694	-0.8875	-0.8875]
[0.3167	0.3167	-0.7609	-0.7609]
[0.2680	0.2680	-0.6440	-0.6440]
[0.2234	0.2234	-0.5369	-0.5369]
[0.1829	0.1829	-0.4395	-0.4395]

Bv4 = 1.0e-003 *

[1.9291	1.9291	1.9639	1.9639]
[1.6722	1.6722	1.7024	1.7024]
[1.4336	1.4336	1.4595	1.4595]
[1.2134	1.2134	1.2353	1.2353]
[1.0116	1.0116	1.0298	1.0298]
[0.8281	0.8281	0.8430	0.8430]

% -----

SMALL VEHICLE ISA2

% -----

K11 = 1.0e+007 *

1.2573
1.1704
1.0835
0.9967
0.9099
0.8231

K12 =

0
0
0
0
0
0

K13 = 1.0e+004 *

-2.9015
 -2.5151
 -2.1563
 -1.8251
 -1.5215
 -1.2455

K14 = 1.0e+005 *

1.7758
 1.5393
 1.3197
 1.1170
 0.9312
 0.7623

K22 =

83.7084
 67.0331
 52.7976
 40.7894
 30.8009
 22.6298

K23 =

0
 0
 0
 0
 0
 0

K24 =

0
 0
 0
 0
 0
 0

K33 =

622.3592
 502.2344
 398.6605
 310.4093
 236.2529
 174.9638

K34 =

-553.9896
 -447.0941
 -354.9177

-276.3701
 -210.3611
 -155.8003

K44 = 1.0e+004 *

1.6920
 1.3654
 1.0838
 0.8439
 0.6423
 0.4756

mass =

0.2492	0.2402	0.2311
0.2311	0.2222	0.2132
0.2132	0.2044	0.1955
0.1955	0.1868	0.1780
0.1780	0.1694	0.1608
0.1608	0.1523	0.1437

Ixx = 1.0e-003 *

0.3806	0.3444	0.3082
0.3082	0.2770	0.2458
0.2458	0.2192	0.1925
0.1925	0.1701	0.1477
0.1477	0.1291	0.1105
0.1105	0.0954	0.0802

Ixy =

0	0	0
0	0	0
0	0	0
0	0	0
0	0	0
0	0	0

Ixz =

0	0	0
0	0	0
0	0	0
0	0	0
0	0	0
0	0	0

Iyy = 1.0e-004 *

0.1291	0.1168	0.1046
0.1046	0.0940	0.0835
0.0835	0.0744	0.0654
0.0654	0.0578	0.0502
0.0502	0.0439	0.0376
0.0376	0.0325	0.0273

Iyz= 1.0e-004 *

-0.1133	-0.1027	-0.0921
-0.0921	-0.0830	-0.0738
-0.0738	-0.0659	-0.0580
-0.0580	-0.0514	-0.0447
-0.0447	-0.0391	-0.0336
-0.0336	-0.0290	-0.0245

Izz = 1.0e-003 *

0.3678	0.3328	0.2978
0.2978	0.2676	0.2374
0.2374	0.2117	0.1860
0.1860	0.1643	0.1427
0.1427	0.1247	0.1067
0.1067	0.0921	0.0775

chord =

0.1250	0.1208	0.1167
0.1167	0.1125	0.1083
0.1083	0.1042	0.1000
0.1000	0.0958	0.0917
0.0917	0.0875	0.0833
0.0833	0.0792	0.0750

xle =

0.0445	0.0430	0.0415
0.0415	0.0400	0.0385
0.0385	0.0371	0.0356
0.0356	0.0341	0.0326
0.0326	0.0311	0.0297
0.0297	0.0282	0.0267

yle =

0.0060	0.0058	0.0056
0.0056	0.0054	0.0052
0.0052	0.0050	0.0048
0.0048	0.0046	0.0044
0.0044	0.0042	0.0040
0.0040	0.0038	0.0036

Bv1 = 1.0e-002 *

[3.2349	3.2349	3.1233	3.1233]
[3.0118	3.0118	2.9079	2.9079]
[2.7887	2.7887	2.6925	2.6925]
[2.5656	2.5656	2.4771	2.4771]
[2.3425	2.3425	2.2617	2.2617]
[2.1194	2.1194	2.0463	2.0463]

Bv2 = 1.0e-003 *

[-0.8736	0.8736	-0.8414	0.8414]
[-0.7573	0.7573	-0.7293	0.7293]
[-0.6493	0.6493	-0.6253	0.6253]
[-0.5495	0.5495	-0.5292	0.5292]
[-0.4581	0.4581	-0.4412	0.4412]
[-0.3750	0.3750	-0.3612	0.3612]

Bv3 = 1.0e-003 *

[0.1130	0.1130	-0.2715	-0.2715]
[0.0979	0.0979	-0.2354	-0.2354]
[0.0840	0.0840	-0.2018	-0.2018]
[0.0711	0.0711	-0.1708	-0.1708]
[0.0593	0.0593	-0.1424	-0.1424]
[0.0485	0.0485	-0.1166	-0.1166]

Bv4 = 1.0e-003 *

[0.5116	0.5116	0.5208	0.5208]
[0.4434	0.4434	0.4514	0.4514]
[0.3802	0.3802	0.3870	0.3870]
[0.3218	0.3218	0.3276	0.3276]
[0.2683	0.2683	0.2731	0.2731]
[0.2196	0.2196	0.2236	0.2236]

% -----
MEDIUM VEHICLE AILERON
% -----

K11 = 1.0e+009 *

1.0819
1.0072
0.9325
0.6865
0.6267
0.4254

K12 =

0
0
0
0
0
0

K13 = 1.0e+007 *

-2.0097
-1.7420
-1.4935
-1.0113
-0.8431
-0.5176

K14 = 1.0e+008 *

1.2360
1.0714
0.9185
0.6219
0.5185
0.3183

K22 = 1.0e+006 *

2.3313
1.8793
1.4901
0.9303
0.7071
0.3940

K23 =

0
0
0
0
0
0

K24 =

0
0
0
0
0
0

K33 = 1.0e+006 *

3.4435
2.7789
2.2059
1.3743
1.0460
0.5811

K34 = 1.0e+006 *

-3.0836
-2.4886
-1.9755
-1.2307
-0.9367
-0.5203

K44 = 1.0e+007 *

9.4132
7.5963
6.0298
3.7568
2.8592
1.5885

mass =

19.3368	18.6441	17.9515
17.9515	17.2657	16.5799
16.5799	15.9009	15.2220
12.3755	11.8221	11.2687
11.2687	10.7221	10.1755
7.8034	7.3823	6.9612

Ixx =

1.9019	1.7216	1.5412
1.5412	1.3855	1.2299
1.2299	1.0970	0.9641
0.7790	0.6883	0.5976
0.5976	0.5223	0.4471
0.3400	0.2932	0.2465

Ixy =

```

0      0      0
0      0      0
0      0      0
0      0      0
0      0      0
0      0      0

Ixz =

0      0      0
0      0      0
0      0      0
0      0      0
0      0      0
0      0      0

Iyy =

0.0647    0.0585    0.0524
0.0524    0.0471    0.0419
0.0419    0.0374    0.0328
0.0265    0.0234    0.0203
0.0203    0.0178    0.0152
0.0115    0.0100    0.0084

Iyz =

-0.0573   -0.0519   -0.0466
-0.0466   -0.0419   -0.0373
-0.0373   -0.0333   -0.0293
-0.0235   -0.0208   -0.0181
-0.0181   -0.0158   -0.0136
-0.0102   -0.0088   -0.0074

Izz =

1.8374    1.6631    1.4889
1.4889    1.3385    1.1881
1.1881    1.0597    0.9313
0.7526    0.6649    0.5773
0.5773    0.5046    0.4319
0.3285    0.2833    0.2381

chord =

1.0000    0.9667    0.9333
0.9333    0.9000    0.8667
0.8667    0.8333    0.8000
0.8000    0.7667    0.7333
0.7333    0.7000    0.6667
0.6667    0.6333    0.6000

xle =

0.3558    0.3439    0.3321
0.3321    0.3202    0.3084
0.3084    0.2965    0.2846

```

```

0.2846    0.2728    0.2609
0.2609    0.2491    0.2372
0.2372    0.2253    0.2135

```

yle =

```

0.0478    0.0462    0.0446
0.0446    0.0430    0.0414
0.0414    0.0398    0.0382
0.0382    0.0366    0.0351
0.0351    0.0335    0.0319
0.0319    0.0303    0.0287

```

Bv1 = []

Bv1 = []

Bv1 = []

Bv1 = []

Bv1 = []

Bv1 = []

Bv2 = []

Bv2 = []

Bv2 = []

Bv2 = []

Bv2 = []

Bv2 = []

Bv3 = []

Bv3 = []

Bv3 = []

Bv3 = []

Bv3 = []

Bv3 = []

Bv4 = []

Bv4 = []

Bv4 = []

Bv4 = []

Bv4 = []

Bv4 = []

% -----

MEDIUM VEHICLE ISA1

% -----

K11 = 1.0e+009 *

1.0760

1.0017

0.9274

0.6827

0.6232

0.4230

K12 =

```

0
0
0
0
0
0
0
K13 = 1.0e+007 *
-1.9977
-1.7317
-1.4847
-1.0053
-0.8381
-0.5145
K14 = 1.0e+008 *
1.2282
1.0646
0.9128
0.6180
0.5152
0.3163
K22 = 1.0e+005 *
8.3803
6.7419
5.3349
3.3433
2.5347
1.4201
K23 =
0
0
0
0
0
0
0
K24 =
0
0
0
0
0
0
0
K33 = 1.0e+006 *
3.4234
2.7627

```

```

2.1930
1.3663
1.0399
0.5777
K34 = 1.0e+006 *
-3.0643
-2.4731
-1.9632
-1.2230
-0.9309
-0.5171
K44 = 1.0e+007 *
9.3546
7.5490
5.9922
3.7334
2.8414
1.5786
mass =
45.0884 43.5373 41.9863
41.9863 40.4421 38.8979
38.8979 37.3606 35.8233
28.8566 27.6164 26.3762
26.3762 25.1430 23.9097
18.1041 17.1679 16.2318
Ixx =
4.7029 4.2607 3.8185
3.8185 3.4359 3.0532
3.0532 2.7257 2.3982
1.9263 1.7038 1.4813
1.4813 1.2961 1.1110
0.8379 0.7237 0.6095
Ixy =
0 0 0
0 0 0
0 0 0
0 0 0
0 0 0
0 0 0
Ixz =
0 0 0
0 0 0
0 0 0
0 0 0
0 0 0

```

```

0      0      0
Iyy =
0.1574  0.1426  0.1279
0.1279  0.1151  0.1023
0.1023  0.0913  0.0803
0.0645  0.0570  0.0496
0.0496  0.0434  0.0372
0.0280  0.0242  0.0204

Iyz =
-0.1463 -0.1326 -0.1189
-0.1189 -0.1071 -0.0952
-0.0952 -0.0850 -0.0749
-0.0599 -0.0530 -0.0461
-0.0461 -0.0404 -0.0347
-0.0260 -0.0225 -0.0190

Izz =
4.5456  4.1182  3.6907
3.6907  3.3209  2.9510
2.9510  2.6345  2.3179
1.8619  1.6468  1.4317
1.4317  1.2528  1.0738
0.8099  0.6995  0.5891

chord =
1.0000  0.9667  0.9333
0.9333  0.9000  0.8667
0.8667  0.8333  0.8000
0.8000  0.7667  0.7333
0.7333  0.7000  0.6667
0.6667  0.6333  0.6000

xle =
0.3558  0.3439  0.3321
0.3321  0.3202  0.3084
0.3084  0.2965  0.2846
0.2846  0.2728  0.2609
0.2609  0.2491  0.2372
0.2372  0.2253  0.2135

yle =
0.0478  0.0462  0.0446
0.0446  0.0430  0.0414
0.0414  0.0398  0.0382
0.0382  0.0366  0.0351
0.0351  0.0335  0.0319
0.0319  0.0303  0.0287

Bv1 =

```

```

9.7590  9.7590  9.4222  9.4222
9.0860  9.0860  8.7724  8.7724
8.4130  8.4130  8.1226  8.1226
6.1919  6.1919  5.9782  5.9782
5.6535  5.6535  5.4584  5.4584
3.8363  3.8363  3.7039  3.7039

Bv2 =
-2.2360  2.2360 -2.1544  2.1544
-1.9383  1.9383 -1.8675  1.8675
-1.6617  1.6617 -1.6011  1.6011
-1.1252  1.1252 -1.0841  1.0841
-0.9380  0.9380 -0.9038  0.9038
-0.5759  0.5759 -0.5549  0.5549

Bv3 =
0.2727  0.2727 -0.6553 -0.6553
0.2364  0.2364 -0.5680 -0.5680
0.2027  0.2027 -0.4870 -0.4870
0.1372  0.1372 -0.3297 -0.3297
0.1144  0.1144 -0.2749 -0.2749
0.0702  0.0702 -0.1688 -0.1688

Bv4 =
1.2346  1.2346  1.2569  1.2569
1.0702  1.0702  1.0895  1.0895
0.9175  0.9175  0.9341  0.9341
0.6213  0.6213  0.6325  0.6325
0.5179  0.5179  0.5273  0.5273
0.3180  0.3180  0.3237  0.3237

% -----
MEDIUM VEHICLE ISA2
% -----

K11 = 1.0e+009 *
1.0054
0.9359
0.8665
0.6379
0.5823
0.3953

K12 =
0
0
0
0
0
0
0

```

K13 = 1.0e+007 *

-1.8570
-1.6097
-1.3800
-0.9344
-0.7790
-0.4783

K14 = 1.0e+008 *

1.1365
0.9852
0.8446
0.5719
0.4768
0.2927

K22 = 1.0e+005 *

4.1896
3.3598
2.6501
1.6707
1.2616
0.7129

K23 =

0
0
0
0
0
0

K24 =

0
0
0
0
0
0

K33 = 1.0e+006 *

3.1858
2.5709
2.0408
1.2714
0.9677
0.5376

K34 = 1.0e+006 *

-2.8364
-2.2891
-1.8172
-1.1320
-0.8616
-0.4786

K44 = 1.0e+007 *

8.6609
6.9892
5.5478
3.4565
2.6307
1.4616

mass =

19.5514	18.8516	18.1518
18.1518	17.4588	16.7659
16.7659	16.0798	15.3937
12.5129	11.9537	11.3946
11.3946	10.8423	10.2900
7.8893	7.4639	7.0385

Ixx =

1.9253	1.7427	1.5602
1.5602	1.4026	1.2451
1.2451	1.1106	0.9761
0.7886	0.6968	0.6049
0.6049	0.5288	0.4526
0.3441	0.2968	0.2495

Ixy =

0	0	0
0	0	0
0	0	0
0	0	0
0	0	0
0	0	0

Ixz =

0	0	0
0	0	0
0	0	0
0	0	0
0	0	0
0	0	0

Iyy =

0.0654	0.0592	0.0531
0.0531	0.0477	0.0424
0.0424	0.0378	0.0332

0.0268	0.0237	0.0206
0.0206	0.0180	0.0154
0.0117	0.0101	0.0085

Iyz =

-0.0580	-0.0526	-0.0472
-0.0472	-0.0425	-0.0378
-0.0378	-0.0337	-0.0297
-0.0238	-0.0210	-0.0183
-0.0183	-0.0160	-0.0138
-0.0103	-0.0089	-0.0075

Izz =

1.8599	1.6836	1.5072
1.5072	1.3550	1.2028
1.2028	1.0728	0.9429
0.7618	0.6731	0.5844
0.5844	0.5108	0.4372
0.3325	0.2868	0.2410

chord =

1.0000	0.9667	0.9333
0.9333	0.9000	0.8667
0.8667	0.8333	0.8000
0.8000	0.7667	0.7333
0.7333	0.7000	0.6667
0.6667	0.6333	0.6000

xle =

0.3558	0.3439	0.3321
0.3321	0.3202	0.3084
0.3084	0.2965	0.2846
0.2846	0.2728	0.2609
0.2609	0.2491	0.2372
0.2372	0.2253	0.2135

yle =

0.0478	0.0462	0.0446
0.0446	0.0430	0.0414
0.0414	0.0398	0.0382
0.0382	0.0366	0.0351
0.0351	0.0335	0.0319
0.0319	0.0303	0.0287

Bv1 =

2.5880	2.5880	2.4986	2.4986
2.4095	2.4095	2.3263	2.3263
2.2310	2.2310	2.1540	2.1540
1.6420	1.6420	1.5853	1.5853
1.4992	1.4992	1.4475	1.4475
1.0173	1.0173	0.9822	0.9822

Bv2 =

-0.5591	0.5591	-0.5385	0.5385
-0.4847	0.4847	-0.4668	0.4668
-0.4155	0.4155	-0.4002	0.4002
-0.2814	0.2814	-0.2710	0.2710
-0.2346	0.2346	-0.2259	0.2259
-0.1440	0.1440	-0.1387	0.1387

Bv3 =

0.0723	0.0723	-0.1738	-0.1738
0.0627	0.0627	-0.1506	-0.1506
0.0537	0.0537	-0.1291	-0.1291
0.0364	0.0364	-0.0874	-0.0874
0.0303	0.0303	-0.0729	-0.0729
0.0186	0.0186	-0.0448	-0.0448

Bv4

0.3274	0.3274	0.3333	0.3333
0.2838	0.2838	0.2889	0.2889
0.2433	0.2433	0.2477	0.2477
0.1648	0.1648	0.1677	0.1677
0.1373	0.1373	0.1398	0.1398
0.0843	0.0843	0.0858	0.0858

% -----
 LARGE VEHICLE AILERON
 % -----

K11 = 1.0e+009 *

4.8649
 4.5291
 4.1934
 3.0867
 2.8181
 1.9125

K12 =

0
 0
 0
 0
 0
 0

K13 = 1.0e+008 *

-1.3565
 -1.1759
 -1.0081
 -0.6826
 -0.5691
 -0.3494

K14 = 1.0e+008 *

8.3427
 7.2317
 6.2000
 4.1982
 3.4998
 2.1487

K22 = 1.0e+007 *

2.3409
 1.8881
 1.4980
 0.9342
 0.7106
 0.3953

K23 =

0
 0
 0
 0
 0
 0

K24 =

0
 0
 0
 0
 0
 0

K33 = 1.0e+007 *

3.4852
 2.8126
 2.2327
 1.3909
 1.0587
 0.5881

K34 = 1.0e+007 *

-3.1222
 -2.5197
 -2.0002
 -1.2460
 -0.9484
 -0.5268

K44 = 1.0e+008 *

9.5260
 7.6876
 6.1025
 3.8018
 2.8936
 1.6075

mass =

83.5364	80.6436	77.7508
77.7508	74.8735	71.9961
71.9961	69.1343	66.2724
53.4633	51.1506	48.8379
48.8379	46.5407	44.2435
33.5692	31.8211	30.0731

Ixx =

18.7784	17.0100	15.2416
15.2416	13.7120	12.1825
12.1825	10.8740	9.5655
7.6916	6.8018	5.9119
5.9119	5.1721	4.4323
3.3478	2.8908	2.4337

Ixy =

```

0      0      0
0      0      0
0      0      0
0      0      0
0      0      0
0      0      0

Ixz =

0      0      0
0      0      0
0      0      0
0      0      0
0      0      0
0      0      0

Iyy =

0.6415    0.5812    0.5209
0.5209    0.4687    0.4165
0.4165    0.3718    0.3271
0.2628    0.2324    0.2021
0.2021    0.1768    0.1515
0.1143    0.0987    0.0831

Iyz =

-0.5800   -0.5257   -0.4715
-0.4715   -0.4245   -0.3775
-0.3775   -0.3372   -0.2969
-0.2376   -0.2103   -0.1830
-0.1830   -0.1602   -0.1375
-0.1031   -0.0891   -0.0752

Izz =

18.1374   16.4292   14.7211
14.7211   13.2437   11.7663
11.7663   10.5025    9.2386
7.4291    6.5696    5.7100
5.7100    4.9954    4.2808
3.2336    2.7921    2.3506

chord =

1.5000    1.4500    1.4000
1.4000    1.3500    1.3000
1.3000    1.2500    1.2000
1.2000    1.1500    1.1000
1.1000    1.0500    1.0000
1.0000    0.9500    0.9000

xle =

0.5337    0.5159    0.4981
0.4981    0.4803    0.4625
0.4625    0.4447    0.4270

```

```

0.4270    0.4092    0.3914
0.3914    0.3736    0.3558
0.3558    0.3380    0.3202

yle =

0.0717    0.0693    0.0669
0.0669    0.0645    0.0621
0.0621    0.0598    0.0574
0.0574    0.0550    0.0526
0.0526    0.0502    0.0478
0.0478    0.0454    0.0430

Bv1 = []
Bv1 = []
Bv1 = []
Bv1 = []
Bv1 = []
Bv1 = []

Bv2 = []
Bv2 = []
Bv2 = []
Bv2 = []
Bv2 = []
Bv2 = []

Bv3 = []
Bv3 = []
Bv3 = []
Bv3 = []
Bv3 = []
Bv3 = []

Bv4 = []
Bv4 = []
Bv4 = []
Bv4 = []
Bv4 = []
Bv4 = []

% -----
LARGE VEHICLE ISA1
% -----

K11 = 1.0e+009 *

4.8380
4.5041
4.1702
3.0696
2.8025
1.9020

K12 =

```

```

0
0
0
0
0
0
0
K13 = 1.0e+008 *
-1.3485
-1.1689
-1.0021
-0.6786
-0.5657
-0.3473
K14 = 1.0e+008 *
8.2904
7.1863
6.1611
4.1718
3.4778
2.1352
K22 = 1.0e+006 *
8.2901
6.6796
5.2939
3.3079
2.5127
1.4019
K23 =
0
0
0
0
0
0
0
K24
0
0
0
0
0
0
0
K33 = 1.0e+007 *
3.4649
2.7962
2.2197

```

```

1.3828
1.0525
0.5847
K34 = 1.0e+007 *
-3.1026
-2.5040
-1.9877
-1.2383
-0.9425
-0.5235
K44 = 1.0e+008 *
9.4666
7.6397
6.0644
3.7781
2.8756
1.5975
mass =
199.4185 192.6629 185.9074
185.9074 179.1674 172.4273
172.4273 165.7027 158.9781
127.6278 122.2249 116.8221
116.8221 111.4347 106.0473
79.9220 75.8563 71.7906
Ixx =
47.1385 42.7190 38.2994
38.2994 34.4717 30.6439
30.6439 27.3649 24.0859
19.3079 17.0837 14.8594
14.8594 13.0071 11.1547
8.3896 7.2494 6.1092
Ixy =
0 0 0
0 0 0
0 0 0
0 0 0
0 0 0
0 0 0
Ixz =
0 0 0
0 0 0
0 0 0
0 0 0
0 0 0
0 0 0

```

Iyy =

1.5809	1.4327	1.2846
1.2846	1.1563	1.0279
1.0279	0.9180	0.8081
0.6475	0.5730	0.4984
0.4984	0.4363	0.3742
0.2813	0.2431	0.2049

Iyz =

-1.4808	-1.3424	-1.2040
-1.2040	-1.0840	-0.9640
-0.9640	-0.8611	-0.7582
-0.6065	-0.5369	-0.4672
-0.4672	-0.4091	-0.3510
-0.2633	-0.2276	-0.1919

Izz =

45.5582	41.2867	37.0152
37.0152	33.3158	29.6163
29.6163	26.4472	23.2781
18.6606	16.5109	14.3612
14.3612	12.5709	10.7806
8.1084	7.0064	5.9043

chord =

1.5000	1.4500	1.4000
1.4000	1.3500	1.3000
1.3000	1.2500	1.2000
1.2000	1.1500	1.1000
1.1000	1.0500	1.0000
1.0000	0.9500	0.9000

xle =

0.5337	0.5159	0.4981
0.4981	0.4803	0.4625
0.4625	0.4447	0.4270
0.4270	0.4092	0.3914
0.3914	0.3736	0.3558
0.3558	0.3380	0.3202

yle =

0.0717	0.0693	0.0669
0.0669	0.0645	0.0621
0.0621	0.0598	0.0574
0.0574	0.0550	0.0526
0.0526	0.0502	0.0478
0.0478	0.0454	0.0430

Bv1 =

43.916	43.916	42.400	42.400
40.887	40.887	39.476	39.476
37.858	37.858	36.552	36.552
27.864	27.864	26.902	26.902
25.441	25.441	24.563	24.563
17.263	17.263	16.668	16.668

Bv2 =

-15.093	15.093	-14.543	14.543
-13.083	13.083	-12.606	12.606
-11.217	11.217	-10.807	10.807
-7.595	7.595	-7.318	7.318
-6.332	6.332	-6.101	6.101
-3.887	3.887	-3.745	3.745

Bv3 =

1.841	1.841	-4.423	-4.423
1.596	1.596	-3.834	-3.834
1.368	1.368	-3.287	-3.287
0.926	0.926	-2.226	-2.226
0.772	0.772	-1.856	-1.856
0.474	0.474	-1.139	-1.139

Bv4 =

8.334	8.334	8.484	8.484
7.224	7.224	7.354	7.354
6.193	6.193	6.305	6.305
4.194	4.194	4.269	4.269
3.496	3.496	3.559	3.559
2.146	2.146	2.185	2.185

% -----

LARGE VEHICLE ISA2

% -----

K11 = 1.0e+009 *

4.5204
4.2084
3.8964
2.8681
2.6185
1.7771

K12 =

0
0
0
0
0
0

K13 = 1.0e+008 *

-1.2534
-1.0865
-0.9315
-0.6307
-0.5258
-0.3228

K14 = 1.0e+008 *

7.6715
6.6498
5.7012
3.8604
3.2182
1.9758

K22 = 1.0e+006 *

4.0470
3.2553
2.5755
1.6145
1.2238
0.6859

K23 =

0
0
0
0
0
0

K24 =

0
0
0
0
0
0

K33 = 1.0e+007 *

3.2242
2.6020
2.0655
1.2868
0.9794
0.5441

K34 = 1.0e+007 *

-2.8719
-2.3177
-1.8399
-1.1462
-0.8724
-0.4846

K44 = 1.0e+008 *

8.7642
7.0728
5.6144
3.4978
2.6622
1.4790

mass =

84.5022	81.5772	78.6522
78.6522	75.7427	72.8332
72.8332	69.9391	67.0451
54.0814	51.7429	49.4045
49.4045	47.0815	44.7586
33.9555	32.1881	30.4208

Ixx =

19.0147	17.2242	15.4338
15.4338	13.8851	12.3364
12.3364	11.0115	9.6866
7.7884	6.8875	5.9865
5.9865	5.2374	4.4883
3.3898	2.9271	2.4643

Ixy =

0	0	0
0	0	0
0	0	0
0	0	0
0	0	0
0	0	0

Ixz =

0	0	0
0	0	0
0	0	0
0	0	0
0	0	0
0	0	0

Iyy =

0.6494	0.5883	0.5272
0.5272	0.4744	0.4216
0.4216	0.3763	0.3311

0.2660	0.2353	0.2045
0.2045	0.1790	0.1534
0.1157	0.0999	0.0842

Iyz =

-0.5875	-0.5326	-0.4776
-0.4776	-0.4300	-0.3824
-0.3824	-0.3416	-0.3008
-0.2406	-0.2130	-0.1853
-0.1853	-0.1623	-0.1393
-0.1044	-0.0903	-0.0761

Izz =

18.3659	16.6364	14.9069
14.9069	13.4110	11.9151
11.9151	10.6354	9.3556
7.5227	6.6524	5.7821
5.7821	5.0586	4.3350
3.2743	2.8272	2.3802

chord =

1.5000	1.4500	1.4000
1.4000	1.3500	1.3000
1.3000	1.2500	1.2000
1.2000	1.1500	1.1000
1.1000	1.0500	1.0000
1.0000	0.9500	0.9000

xle =

0.5337	0.5159	0.4981
0.4981	0.4803	0.4625
0.4625	0.4447	0.4270
0.4270	0.4092	0.3914
0.3914	0.3736	0.3558
0.3558	0.3380	0.3202

yle =

0.0717	0.0693	0.0669
--------	--------	--------

0.0669	0.0645	0.0621
0.0621	0.0598	0.0574
0.0574	0.0550	0.0526
0.0526	0.0502	0.0478
0.0478	0.0454	0.0430

Bv1 =

11.6459	11.6459	11.2439	11.2439
10.8427	10.8427	10.4685	10.4685
10.0395	10.0395	9.6930	9.6930
7.3891	7.3891	7.1341	7.1341
6.7466	6.7466	6.5137	6.5137
4.5780	4.5780	4.4200	4.4200

Bv2 =

-3.7741	3.7741	-3.6348	3.6348
-3.2715	3.2715	-3.1507	3.1507
-2.8048	2.8048	-2.7012	2.7012
-1.8992	1.8992	-1.8291	1.8291
-1.5833	1.5833	-1.5248	1.5248
-0.9720	0.9720	-0.9361	0.9361

Bv3 =

0.4882	0.4882	-1.1730	-1.1730
0.4231	0.4231	-1.0168	-1.0168
0.3628	0.3628	-0.8717	-0.8717
0.2456	0.2456	-0.5903	-0.5903
0.2048	0.2048	-0.4921	-0.4921
0.1257	0.1257	-0.3021	-0.3021

Bv4 =

2.2100	2.2100	2.2499	2.2499
1.9157	1.9157	1.9502	1.9502
1.6424	1.6424	1.6720	1.6720
1.1121	1.1121	1.1322	1.1322
0.9271	0.9271	0.9438	0.9438
0.5692	0.5692	0.5795	0.5795

APPENDIX C - Controller Design

It is assumed that the deformation of the beam reference line can be inferred from strain gages placed on the wing surface and that beam strain rates can be calculated by differentiating the strain signals, and passing them through a low pass filter to minimize signal noise. Therefore, all the state variables associated with the flexible degrees of freedom are measurable. An LQR design method based on the quasi-steady aeroelastic plant with the wing fixed at the root is employed here. This approach is appropriate for finding the feedback gain matrix, since the state variables for that system include only the flexible degrees of freedom. The computed feedback gains are then used on the fully unsteady plant described above. The state space equations for the linearized unsteady system are given by

$$\begin{aligned} \dot{x} &= Ax + Bu + Gw \\ y &= Cx + v \end{aligned} \quad \begin{matrix} \dot{x} \\ y \end{matrix} = \begin{pmatrix} q \\ \tilde{q} \\ \lambda \end{pmatrix}, \quad q = \begin{pmatrix} \tilde{\epsilon} \\ \tilde{b} \end{pmatrix}, \quad y = \tilde{\epsilon} \quad (\text{C.1})$$

where x contains the flexible and rigid body variables, u is a vector of voltages, and w is the external gust disturbance. The column matrix, b , contains the six rigid-body degrees of freedom. The system matrices are constructed with all rigid-body degrees of freedom locked, except for the vertical degree of freedom. Signal noise, v , can then be added in the simulation. The closed loop plant schematic is shown in Fig. C.1.

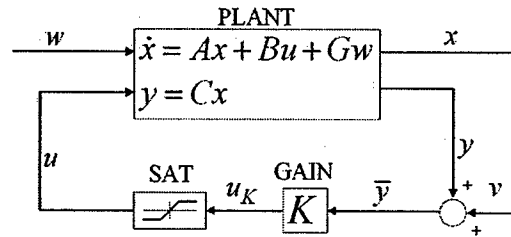


Figure C.1: Closed loop plant representation

The optimal feedback, K , is found by minimizing the cost function

$$J = \int_0^{\infty} (x^T Q x + u^T R u + 2 \dot{x}^T N u) d\tau \quad (\text{C.2})$$

where Q is the state cost matrix and R is the control cost matrix. The cost matrix N is usually set to zero, but for this particular case, it could be used as a measure of how much work is done on the structure by the actuators and how much power is used by the amplifiers. The state, x , corresponds to the quasi-steady plant with only flexible degrees of freedom.

Selection of the State Cost Matrix

Several methods were investigated to construct the state cost matrix, Q . If it contains the components of the stiffness and mass matrices, then the state cost is a measure of the total change in mechanical energy of the wing from the steady value. However, this method has a negative effect on the controller solution. If all of the beam strains are penalized, then there is a cost associated with wing twisting, which is just what the controller wants to do to stabilize the wing. The feedback gain solution to this problem would not exploit aerodynamic couplings, but would directly try to counteract deformation.

The best method found for constructing the Q matrix in this study was determined by penalizing only the flatwise bending strains (perturbations from the steady state value). This frees the controller to use twist actuation for control.

This method also allows for a procedure to find the proper scaling between the Q and R matrices. An estimate of the maximum surface ply strains can be made using the beam bending strains. This information can be used to find the scaling between the Q and R matrices. For instance, both the ply strain limits and the actuator saturation limits are known. The Q and R matrices can be chosen such that the state and control cost are equal when the state and control variables are at some fraction of their limits.

Comparison of the Present Controller and a Full State Feedback Controller

To justify the use of the present LQR controller over an LQG controller (which would combine a Kalman filter with the full state LQR feedback gains), a second LQR controller is designed using full state feedback, i.e., measuring flexible, body, and unsteady aerodynamic states. This controller represents the upper bound on the performance of the LQG controller, since it assumes that the Kalman filter would be able

to perfectly estimate the state vector based on the limited measurements. For both controllers, the same penalties are applied to bending strains and actuator voltages to determine the feedback gains. The response of the system to a vertical gust turbulence loading is shown in Figs. C.2 - C.5. The vehicle is flown at 80 m/s and 5 km altitude, in trimmed flight. The peak amplitude of the turbulence is 2 m/s, which may be considered a "moderate turbulence." The results show that the realizable LQR system performs as well as the system based on full state feedback.

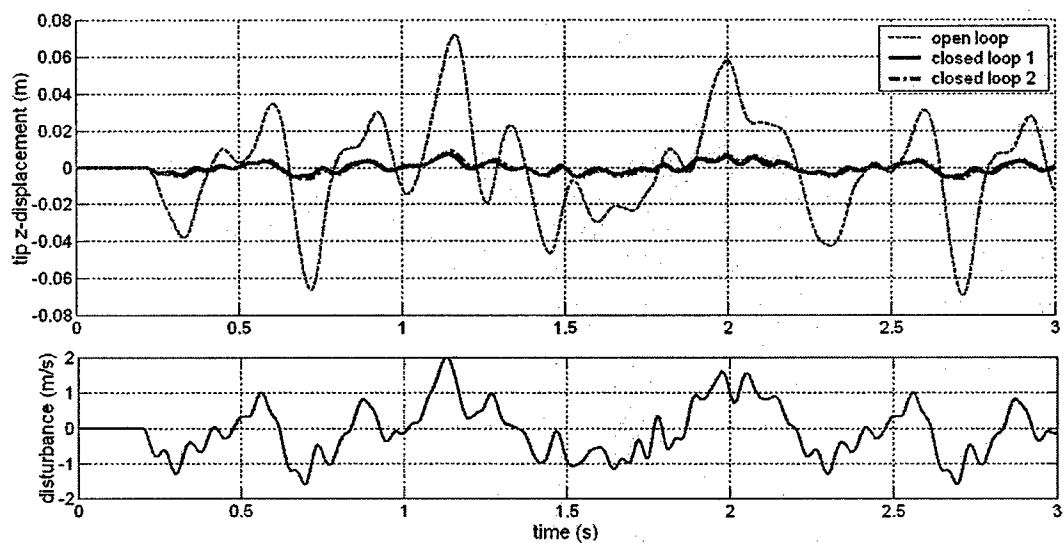


Figure C.2: Tip response of the analytical model to a random gust disturbance, ('closed loop 1' refers to the realizable LQR gains and 'closed loop 2' refers to the full state LQR gains).

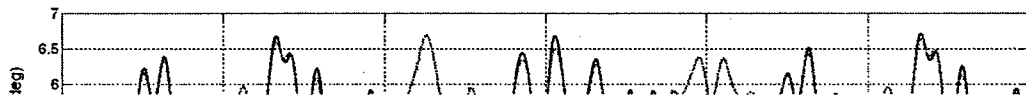


Figure C.3: Tip angle of attack response of the open and closed loop system to a random gust disturbance.

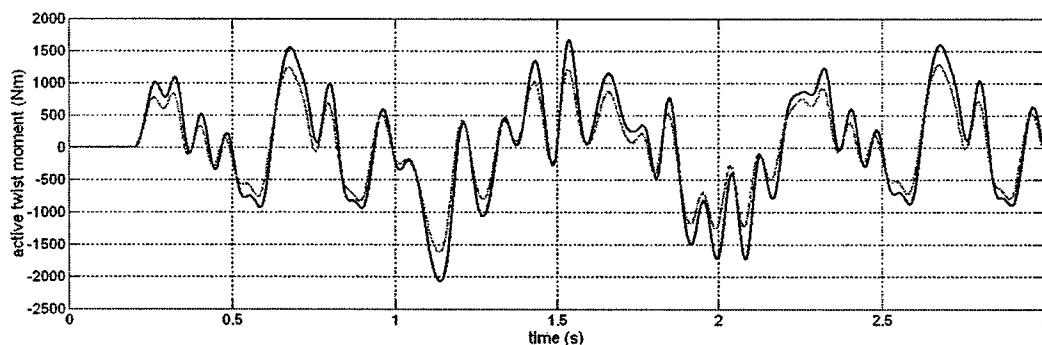


Figure C.4: Twist moment response of the closed loop system to a random gust disturbance.

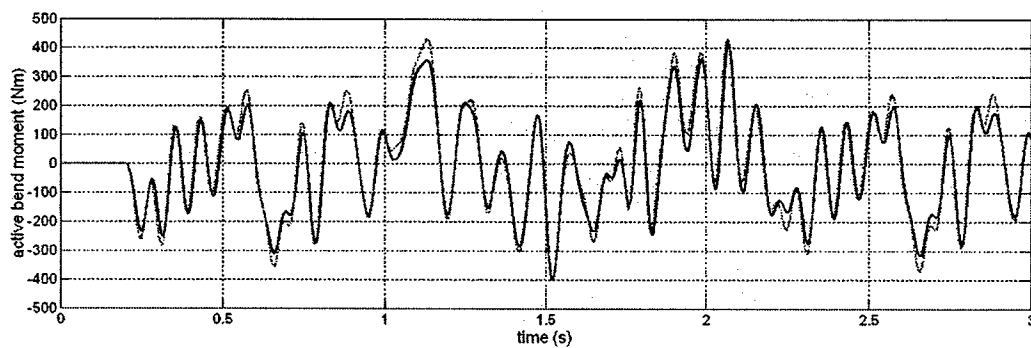


Figure C.5: Bending moment response of the closed loop system to a random gust disturbance.

From Fig. C.3, it is clear that the control voltages cause the wing to twist in response to a change in the gust-induced angle of attack, i.e., the controller uses the coupling between wing twist and aerodynamic lift to counteract bending.

Several LQG controllers were designed, and the performance was not nearly as good as that shown in the present example, probably due to the difficulty in estimating the unsteady aerodynamic states.

APPENDIX D - Member Kinematics

The instantaneous relationship between the beam strain variables and the nodal translation and rotation variables is described here. Derivatives with respect to both strain and body displacement variables are then obtained. A schematic for a member attached to the body is given in Figure D.1.

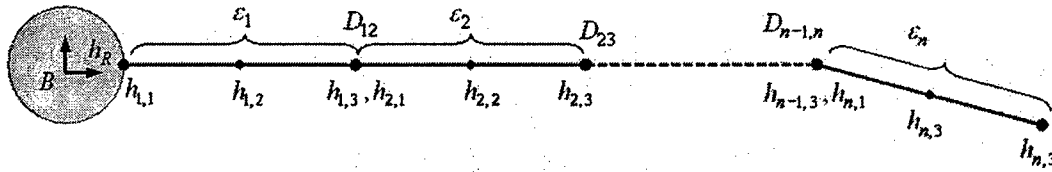


Figure D.1: Independent and dependent beam variables

The dependent position/orientation variables, h , are a function of the independent variables, ϵ . For each member, the variables are assembled into column matrices, given by

$$\epsilon_i = \begin{bmatrix} \epsilon_x \\ \kappa_x \\ \kappa_y \\ \kappa_z \end{bmatrix}_i \quad h_{ij} = \begin{bmatrix} p \\ w_x \\ w_y \\ w_z \end{bmatrix}_{ij} \quad \epsilon = \begin{bmatrix} \epsilon_1 \\ \epsilon_2 \\ \epsilon_3 \\ \vdots \\ \epsilon_n \end{bmatrix}_{4n \times 1} \quad h = \begin{bmatrix} h_{11} \\ h_{12} \\ h_{13} \\ h_{21} \\ h_{22} \\ h_{23} \\ \vdots \\ h_{n1} \\ h_{n2} \\ h_{n3} \end{bmatrix}_{36n \times 1} \quad h^* = \begin{bmatrix} h_R \\ 0 \\ 0 \\ 0 \\ 0 \\ 0 \\ \vdots \\ 0 \\ 0 \\ 0 \end{bmatrix}_{36n \times 1} \quad (D.1)$$

where h_R is the fixed root boundary condition. The column matrix, h , which contains nodal position and orientation variables, is called the position vector for the member. All position variables are resolved in frame B .

The governing differential equation for the continuous beam reference line is given by

$$\frac{\partial}{\partial s} h(s) = A(s)h(s) \quad (D.2)$$

where, for left to right integration

$$A(s) = \begin{bmatrix} 0 & 1 + \varepsilon_x(s) & 0 & 0 \\ 0 & 0 & \kappa_z(s) & -\kappa_y(s) \\ 0 & -\kappa_z(s) & 0 & \kappa_x(s) \\ 0 & \kappa_y(s) & -\kappa_x(s) & 0 \end{bmatrix}_{12 \times 12} \quad (D.3)$$

Assuming constant strain on each element and marching from the root boundary condition, the solution for the dependent variables is obtained as

element 1	element 3	element 3	element n
$h_{1,1} = h_R$	$h_{2,1} = D_{2,1} h_{1,3}$	$h_{3,1} = D_{3,2} h_{2,3}$		$h_{n,1} = D_{n,n-1} h_{n-1,3}$
$h_{1,2} = e^{G_1} h_{1,1}$	$h_{2,2} = e^{G_2} h_{2,1}$	$h_{3,2} = e^{G_3} h_{3,1}$	$h_{n,2} = e^{G_n} h_{n,1}$
$h_{1,3} = e^{G_1} h_{1,2}$	$h_{2,3} = e^{G_2} h_{2,2}$	$h_{3,3} = e^{G_3} h_{3,2}$		$h_{n,3} = e^{G_n} h_{n,2}$

(D.4)

where

$$G_i = \frac{1}{2} A_i(\varepsilon_i) \Delta s_i \quad (D.5)$$

and Δs_i is the length of element i . The relations in equation D.4 can be written in matrix-vector form as

$$A(\varepsilon)h(\varepsilon) = h^* \quad (D.6)$$

where, for simplicity, $A(\varepsilon)$ is given for a three element member as

$$A(\varepsilon) = \begin{bmatrix} I & 0 & 0 & 0 & 0 & 0 & 0 & 0 & 0 \\ -e^{G_1} & I & 0 & 0 & 0 & 0 & 0 & 0 & 0 \\ 0 & -e^{G_1} & I & 0 & 0 & 0 & 0 & 0 & 0 \\ 0 & 0 & -D_{21} & I & 0 & 0 & 0 & 0 & 0 \\ 0 & 0 & 0 & -e^{G_2} & I & 0 & 0 & 0 & 0 \\ 0 & 0 & 0 & 0 & -e^{G_2} & I & 0 & 0 & 0 \\ 0 & 0 & 0 & 0 & 0 & -D_{32} & I & 0 & 0 \\ 0 & 0 & 0 & 0 & 0 & 0 & -e^{G_3} & I & 0 \\ 0 & 0 & 0 & 0 & 0 & 0 & 0 & -e^{G_3} & I \end{bmatrix}_{36n \times 36n}, \quad n=3 \quad (D.7)$$

Derivatives of the position variables with respect to the strain variables

The Jacobian matrix, $J_{h\varepsilon}(\varepsilon)$, relates the change in the strain vector to the change in the position vector, and satisfies the relation

$$dh = J_{h\varepsilon}(\varepsilon) \cdot d\varepsilon \quad (D.8)$$

The elements of $J_{h\epsilon}$ are the partial derivatives of the individual position vectors to each scalar strain variable, as given by

$$J_{h\epsilon} = \begin{bmatrix} \frac{\partial h_{11}}{\partial \epsilon_{x_1}} & \frac{\partial h_{11}}{\partial \kappa_{x_1}} & \frac{\partial h_{11}}{\partial \kappa_{y_1}} & \frac{\partial h_{11}}{\partial \kappa_{z_1}} & \frac{\partial h_{11}}{\partial \epsilon_{x_2}} & \frac{\partial h_{11}}{\partial \kappa_{x_2}} & \frac{\partial h_{11}}{\partial \kappa_{y_2}} & \frac{\partial h_{11}}{\partial \kappa_{z_2}} & \dots & \frac{\partial h_{11}}{\partial \epsilon_{x_n}} & \frac{\partial h_{11}}{\partial \kappa_{x_n}} & \frac{\partial h_{11}}{\partial \kappa_{y_n}} & \frac{\partial h_{11}}{\partial \kappa_{z_n}} \\ \frac{\partial h_{12}}{\partial \epsilon_{x_1}} & \frac{\partial h_{12}}{\partial \kappa_{x_1}} & \frac{\partial h_{12}}{\partial \kappa_{y_1}} & \frac{\partial h_{12}}{\partial \kappa_{z_1}} & \frac{\partial h_{12}}{\partial \epsilon_{x_2}} & \frac{\partial h_{12}}{\partial \kappa_{x_2}} & \frac{\partial h_{12}}{\partial \kappa_{y_2}} & \frac{\partial h_{12}}{\partial \kappa_{z_2}} & \dots & \frac{\partial h_{12}}{\partial \epsilon_{x_n}} & \frac{\partial h_{12}}{\partial \kappa_{x_n}} & \frac{\partial h_{12}}{\partial \kappa_{y_n}} & \frac{\partial h_{12}}{\partial \kappa_{z_n}} \\ \frac{\partial h_{13}}{\partial \epsilon_{x_1}} & \frac{\partial h_{13}}{\partial \kappa_{x_1}} & \frac{\partial h_{13}}{\partial \kappa_{y_1}} & \frac{\partial h_{13}}{\partial \kappa_{z_1}} & \frac{\partial h_{13}}{\partial \epsilon_{x_2}} & \frac{\partial h_{13}}{\partial \kappa_{x_2}} & \frac{\partial h_{13}}{\partial \kappa_{y_2}} & \frac{\partial h_{13}}{\partial \kappa_{z_2}} & \dots & \frac{\partial h_{13}}{\partial \epsilon_{x_n}} & \frac{\partial h_{13}}{\partial \kappa_{x_n}} & \frac{\partial h_{13}}{\partial \kappa_{y_n}} & \frac{\partial h_{13}}{\partial \kappa_{z_n}} \\ \frac{\partial h_{21}}{\partial \epsilon_{x_1}} & \frac{\partial h_{21}}{\partial \kappa_{x_1}} & \frac{\partial h_{21}}{\partial \kappa_{y_1}} & \frac{\partial h_{21}}{\partial \kappa_{z_1}} & \frac{\partial h_{21}}{\partial \epsilon_{x_2}} & \frac{\partial h_{21}}{\partial \kappa_{x_2}} & \frac{\partial h_{21}}{\partial \kappa_{y_2}} & \frac{\partial h_{21}}{\partial \kappa_{z_2}} & \dots & \frac{\partial h_{21}}{\partial \epsilon_{x_n}} & \frac{\partial h_{21}}{\partial \kappa_{x_n}} & \frac{\partial h_{21}}{\partial \kappa_{y_n}} & \frac{\partial h_{21}}{\partial \kappa_{z_n}} \\ \frac{\partial h_{22}}{\partial \epsilon_{x_1}} & \frac{\partial h_{22}}{\partial \kappa_{x_1}} & \frac{\partial h_{22}}{\partial \kappa_{y_1}} & \frac{\partial h_{22}}{\partial \kappa_{z_1}} & \frac{\partial h_{22}}{\partial \epsilon_{x_2}} & \frac{\partial h_{22}}{\partial \kappa_{x_2}} & \frac{\partial h_{22}}{\partial \kappa_{y_2}} & \frac{\partial h_{22}}{\partial \kappa_{z_2}} & \dots & \frac{\partial h_{22}}{\partial \epsilon_{x_n}} & \frac{\partial h_{22}}{\partial \kappa_{x_n}} & \frac{\partial h_{22}}{\partial \kappa_{y_n}} & \frac{\partial h_{22}}{\partial \kappa_{z_n}} \\ \frac{\partial h_{23}}{\partial \epsilon_{x_1}} & \frac{\partial h_{23}}{\partial \kappa_{x_1}} & \frac{\partial h_{23}}{\partial \kappa_{y_1}} & \frac{\partial h_{23}}{\partial \kappa_{z_1}} & \frac{\partial h_{23}}{\partial \epsilon_{x_2}} & \frac{\partial h_{23}}{\partial \kappa_{x_2}} & \frac{\partial h_{23}}{\partial \kappa_{y_2}} & \frac{\partial h_{23}}{\partial \kappa_{z_2}} & \dots & \frac{\partial h_{23}}{\partial \epsilon_{x_n}} & \frac{\partial h_{23}}{\partial \kappa_{x_n}} & \frac{\partial h_{23}}{\partial \kappa_{y_n}} & \frac{\partial h_{23}}{\partial \kappa_{z_n}} \\ \vdots & \vdots & \vdots & \vdots & \vdots & \vdots & \vdots & \vdots & \vdots & \vdots & \vdots & \vdots & \vdots \\ \frac{\partial h_{n1}}{\partial \epsilon_{x_1}} & \frac{\partial h_{n1}}{\partial \kappa_{x_1}} & \frac{\partial h_{n1}}{\partial \kappa_{y_1}} & \frac{\partial h_{n1}}{\partial \kappa_{z_1}} & \frac{\partial h_{n1}}{\partial \epsilon_{x_2}} & \frac{\partial h_{n1}}{\partial \kappa_{x_2}} & \frac{\partial h_{n1}}{\partial \kappa_{y_2}} & \frac{\partial h_{n1}}{\partial \kappa_{z_2}} & \dots & \frac{\partial h_{n1}}{\partial \epsilon_{x_n}} & \frac{\partial h_{n1}}{\partial \kappa_{x_n}} & \frac{\partial h_{n1}}{\partial \kappa_{y_n}} & \frac{\partial h_{n1}}{\partial \kappa_{z_n}} \\ \frac{\partial h_{n2}}{\partial \epsilon_{x_1}} & \frac{\partial h_{n2}}{\partial \kappa_{x_1}} & \frac{\partial h_{n2}}{\partial \kappa_{y_1}} & \frac{\partial h_{n2}}{\partial \kappa_{z_1}} & \frac{\partial h_{n2}}{\partial \epsilon_{x_2}} & \frac{\partial h_{n2}}{\partial \kappa_{x_2}} & \frac{\partial h_{n2}}{\partial \kappa_{y_2}} & \frac{\partial h_{n2}}{\partial \kappa_{z_2}} & \dots & \frac{\partial h_{n2}}{\partial \epsilon_{x_n}} & \frac{\partial h_{n2}}{\partial \kappa_{x_n}} & \frac{\partial h_{n2}}{\partial \kappa_{y_n}} & \frac{\partial h_{n2}}{\partial \kappa_{z_n}} \\ \frac{\partial h_{n3}}{\partial \epsilon_{x_1}} & \frac{\partial h_{n3}}{\partial \kappa_{x_1}} & \frac{\partial h_{n3}}{\partial \kappa_{y_1}} & \frac{\partial h_{n3}}{\partial \kappa_{z_1}} & \frac{\partial h_{n3}}{\partial \epsilon_{x_2}} & \frac{\partial h_{n3}}{\partial \kappa_{x_2}} & \frac{\partial h_{n3}}{\partial \kappa_{y_2}} & \frac{\partial h_{n3}}{\partial \kappa_{z_2}} & \dots & \frac{\partial h_{n3}}{\partial \epsilon_{x_n}} & \frac{\partial h_{n3}}{\partial \kappa_{x_n}} & \frac{\partial h_{n3}}{\partial \kappa_{y_n}} & \frac{\partial h_{n3}}{\partial \kappa_{z_n}} \end{bmatrix} \quad (D.9)$$

The governing relation for absolute motion will be discussed later, and is given here by

$$dh = J_{h\epsilon} \cdot d\epsilon + J_{hb} \cdot db \quad (D.10)$$

where db contains infinitesimal body motions (Note that b here is the same as β in Chapter 2). The matrix, $J_{h\epsilon}$, is found as follows. The derivative of equation D.6, with respect to the strain variables, is given by

$$\left. \frac{d}{d\epsilon} (A(\epsilon)h(\epsilon)) \right|_{\epsilon_0} = A_0 \frac{d}{d\epsilon} h(\epsilon) + \frac{d}{d\epsilon} (A(\epsilon)h_0) = 0 \quad (D.11)$$

where ϵ_0 is the instantaneous value of the strain vector about which the linearization takes place. This leads to

$$J_{h\epsilon} = \frac{d}{d\epsilon} h(\epsilon) = -A_0^{-1} \left[\frac{d}{d\epsilon} (A(\epsilon)h_0) \right] \quad (D.12)$$

The derivatives on the right hand side must be evaluated in terms of the individual components of the strain vector. The matrix vector product, $A \cdot h$, is given by

$$Ah = \begin{bmatrix} h_{11} \\ h_{12} - e^{G_1} h_{11} \\ h_{13} - e^{G_1} h_{12} \\ h_{21} - D_{21} h_{13} \\ h_{22} - e^{G_2} h_{21} \\ h_{23} - e^{G_2} h_{22} \\ \vdots \\ h_{n1} - D_{n,n-1} h_{n-1,3} \\ h_{n2} - e^{G_n} h_{n1} \\ h_{n3} - e^{G_n} h_{n2} \end{bmatrix} \quad (D.13)$$

The right hand side derivatives of Equation D.12 are computed numerically, one column at a time. Columns 1 and 6 are shown here, and are given by

$$\frac{\partial(Ah_0)}{\partial \varepsilon_{x1}} = \begin{bmatrix} 0 \\ -\frac{1}{2} \left(\frac{dG_1}{d\varepsilon_{x1}} e^{G_1} + e^{G_1} \frac{dG_1}{d\varepsilon_{x1}} \right) \cdot h_{11}(\varepsilon_0) \\ -\frac{1}{2} \left(\frac{dG_1}{d\varepsilon_{x1}} e^{G_1} + e^{G_1} \frac{dG_1}{d\varepsilon_{x1}} \right) \cdot h_{12}(\varepsilon_0) \\ 0 \\ 0 \\ \vdots \\ 0 \\ 0 \\ 0 \end{bmatrix}, \quad \frac{\partial(Ah_0)}{\partial \kappa_{x2}} = \begin{bmatrix} 0 \\ 0 \\ 0 \\ -\frac{1}{2} \left(\frac{dG_2}{d\kappa_{x2}} e^{G_2} + e^{G_2} \frac{dG_2}{d\kappa_{x2}} \right) \cdot h_{21}(\varepsilon_0) \\ -\frac{1}{2} \left(\frac{dG_2}{d\kappa_{x2}} e^{G_2} + e^{G_2} \frac{dG_2}{d\kappa_{x2}} \right) \cdot h_{22}(\varepsilon_0) \\ \vdots \\ 0 \\ 0 \\ 0 \end{bmatrix} \quad (D.14)$$

In order to obtain the absolute motion at each node, derivatives must be taken with respect to body motion. Let the vector of infinitesimal body displacements and rotations, db , be given by

$$db = \begin{bmatrix} dp_B \\ d\theta_B \end{bmatrix}_{6 \times 1} \quad (D.15)$$

where the displacements and rotations are resolved in frame B . The (absolute) change in the position vector due to body motion is given by

$$dh = J_{hb} \cdot db \quad (D.16)$$

where J_{hb} is constructed numerically, one node at a time. The derivative of the nodal position vector, h_{ij} , with respect to body motion is given by

$$\frac{\partial h_{ij}}{\partial b} = \begin{bmatrix} 1 & 0 & 0 & 0 & p(3) & -p(2) & 0 & 0 & 0 & 0 & 0 & 0 & 0 \\ 0 & 1 & 0 & -p(3) & 0 & p(1) & 0 & 0 & 0 & 0 & 0 & 0 & 0 \\ 0 & 0 & 1 & p(2) & -p(1) & 0 & 0 & 0 & 0 & 0 & 0 & 0 & 0 \\ 0 & 0 & 0 & 0 & w_x(3) & -w_x(2) & 0 & 0 & 0 & 0 & 0 & 0 & 0 \\ 0 & 0 & 0 & -w_x(3) & 0 & w_x(1) & 0 & 0 & 0 & 0 & 0 & 0 & 0 \\ 0 & 0 & 0 & w_x(2) & -w_x(1) & 0 & 0 & 0 & 0 & 0 & 0 & 0 & 0 \\ 0 & 0 & 0 & 0 & 0 & 0 & 0 & w_y(3) & -w_y(2) & 0 & 0 & 0 & 0 \\ 0 & 0 & 0 & 0 & 0 & 0 & -w_y(3) & 0 & w_y(1) & 0 & 0 & 0 & 0 \\ 0 & 0 & 0 & 0 & 0 & 0 & w_y(2) & -w_y(1) & 0 & 0 & 0 & 0 & 0 \\ 0 & 0 & 0 & 0 & 0 & 0 & 0 & 0 & 0 & 0 & w_z(3) & -w_z(2) & 0 \\ 0 & 0 & 0 & 0 & 0 & 0 & 0 & 0 & 0 & -w_z(3) & 0 & w_z(1) & 0 \\ 0 & 0 & 0 & 0 & 0 & 0 & 0 & 0 & 0 & w_z(2) & -w_z(1) & 0 & 0 \end{bmatrix}_{ij} \quad (D.17)$$

The exogenous Jacobian matrices, J_{pe} and J_{pb} , are subsets of J_{he} and J_{hb} , and relate the nodal translations to small changes in the strain and body variables. They are constructed selecting the appropriate rows of the larger matrices.

The matrices $J_{\theta e}$ and $J_{\theta b}$ relate nodal rotations to small changes in the strain and body variables. Their components are found using subsets of J_{he} and J_{hb} as well as the current value of the unit direction vectors. The relationship between an infinitesimal rotation at a node and an infinitesimal change in the direction vectors is given, in frame w , by

$$\begin{bmatrix} d\theta_x \\ d\theta_y \\ d\theta_z \end{bmatrix} = \begin{bmatrix} dw_y^T \cdot w_z \\ dw_z^T \cdot w_x \\ dw_x^T \cdot w_y \end{bmatrix} \quad (D.18)$$

Since the nodal rotations are resolved in the body frame, they are simply related to the body rotations by the identity matrix. From the above derivation, the following absolute relations are thus obtained

$$\begin{aligned} dh &= J_{he} \cdot d\epsilon + J_{hb} \cdot db \\ dp &= J_{pe} \cdot d\epsilon + J_{pb} \cdot db \\ d\theta &= J_{\theta e} \cdot d\epsilon + J_{\theta b} \cdot db \end{aligned} \quad (D.19)$$

Appendix B:

Cesnik, C. E. S. and Brown, E. L., "Active Warping Control of a Joined Wing Airplane Configuration," *Proceedings of the 44th Structures, Structural Dynamics, and Material Conference*, Hampton, Virginia, April 7—10, 2003.

ACTIVE WARPING CONTROL OF A JOINED-WING AIRPLANE CONFIGURATION

Carlos E. S. Cesnik*

University of Michigan, Ann Arbor, Michigan
and

Eric L. Brown†

Massachusetts Institute of Technology, Cambridge, Massachusetts

Abstract

This paper assesses the use of existing piezoelectric material technology for induced strain and producing wing-warping control on joined-wing aircraft configurations. Anisotropic piezocomposite actuators integrated into the wing structure are the method of actuation. Comparisons are made with traditional aileron control surface. This study is conducted based on a proposed framework in which the developed formulation captures the nonlinear (large) deflection behavior of the wings, the effects of anisotropic piezoelectric composites embedded in the skin, and the unsteady subsonic aerodynamic forces acting on the wing. Because the wing is long and slender, it can be modeled as a beam undergoing three dimensional displacements and rotations. The cross sectional stiffness, inertia, and actuation properties of the wing are calculated along the span, and then incorporated into the 1-D nonlinear beam model derived in this paper. Finite-state unsteady subsonic airloads are incorporated to complete the state space aeroelastic model. Some of the capabilities of the formulation are exemplified within the numerical studies. Two baseline vehicles are designed: one with APA incorporated in the outer wing so to generate wing warping, and the second based on a 50%-span aileron. Different results include static and dynamic instabilities associated with the joined-wing configuration, roll rate and roll angle performance, and the overall ability of the different concept to produce maneuver loads. Finally, discussion on required material technology improvements to make the wing-warping authority par with the aileron for a joined-wing configuration is presented.

* Associate Professor of Aerospace Engineering. Associate Fellow, AIAA. Member, AHS.

† Graduate Research Assistant. Mechanical Engineering. Currently Research Engineer, C.S. Draper Labs., Cambridge, Massachusetts.

Copyright©2003 by Carlos E. S. Cesnik and Eric L. Brown.
Published by the American Institute of Aeronautics and Astronautics, Inc., with permission.

Introduction

The first successful heavier-than-air flight took place 100 years ago. The Wright Flier used the motion of the pilot's hips to control the warping of the wing and, therefore, the vehicle roll. The relatively soft-in-torsion wings were replaced by stiffer designs with the increase on vehicle flying speeds. The lack of authority to twist the stiffer wings resulted in replacing wing warping with discrete aileron control. Within this concept, maneuver loads are generated at discrete movable parts of the wings in contrast to the reshaping of the wing.

Two decades ago, the concept of active aeroelastic wing (AAW) was introduced. There, instead of generating maneuver loads from a set of control surfaces and fight the flexibility of the wing, the control surfaces are used to induce deformation on the wing so that the reshape of the wing is responsible for generating such loads. Different numerical studies have been pursued, showing promises of achieving different objectives while reducing overall systems weight¹. A modified F/A-18A with a relatively flexible wing was constructed as a testbed for this concept and just recently has started flight tests at NASA Dryden.

More recently, with the advancement of active materials and the development of anisotropic piezocomposite actuators (APA)^{2,3}, one may be able to once again implement wing warping for maneuver load generation. Through APA embedded as an integral load-bearing component of the wing structure, local strains can be induced at certain areas of the wing structure and in certain directions. Those strains are controlled externally by applied electric field to the actuators. By properly designing the active structure, a single physical structural realization can achieve several different aeroservoelastic objectives, presenting itself as a truly active aeroelastic tailoring mechanism. Moreover, this could bring the AAW concept to its fulfillment, and represents a fundamental step towards the development of a more generic morphing aircraft.

Among the types of aircraft that could take advantage of such concept, high-altitude long-endurance ones are the most likely candidates. Due to mission requirements, those vehicles present high-aspect-ratio wings that result in relatively flexible structures. If the conventional design paradigm is to be used, the wing flexibility has to be counteracted by additional structural reinforcements that will result in extra mass penalty. Some basic studies exploring APA for active aeroelastic tailoring of such vehicles⁴ show that multiple objectives can be achieved by the same wing realization. Studies were conducted for flutter boundary enhancement and gust load response. It is worthwhile mentioning here that the wing's high flexibility result in nonlinear structural motions. This adds another degree of complexity to this already reach domain in which the structural dynamics of the flexible vehicle must be modeled accordingly.

A recent work⁵ by the authors investigates in-depth the effects of using APA in three classes of Uninhabited Aerial Vehicles (UAV): small (e.g., Pointer), medium (e.g., Predator), and large (e.g., Global Hawk). For that study, a framework was created for analyzing and designing different high-aspect-ratio wing vehicles. A new strain-based active structural formulation was created and implemented in the framework. The three classes of UAVs were studied for both wing warping and aileron controls. Different objectives included: roll controllability, flutter enhancement, and gust load alleviation and response. Also, an assessment of the structural weight penalty incurred for using current technology APA was conducted. Although the final decision has to be made at the system's level (including mission effectiveness, survivability, etc.) and a formal numerical optimization study is still needed, results from Ref. 5 show that wing warping is possible today by employing APA as part of the composite wing construction. Basic performance results of the active wing are comparable with the ones from a wing with ailerons.

The intent of the present paper is to perform similar investigations as in Ref. 5 on a joined-wing Sensorcraft configuration. This is a new high-altitude long-endurance ISR platform that carries a variety of sensors.

Due to the unusual shapes of joined-wing airplane configurations, the effects of structural deformation on the static aerodynamic and aeroelastic behavior are difficult to intuit and predict. Deformation of the structure at a certain location may produce large changes in angle of attack in the lifting surfaces at other locations. Efforts to minimize structural weight may create aeroelastic instabilities that are not encountered

in conventional aircraft design. For joined-wing aircraft, the first sign of failure may be in the buckling of the aft members as the structure is softened. Flutter and divergence may also become a problem in these members due to the reduction in structural frequency as they go into compression. As the aircraft becomes more flexible, the nature of the geometric structural nonlinearities become more important and the lift distribution on the aircraft may be adversely affected. Livne⁶ presented a thought provoking survey on the design challenges of joined-wing aircraft configurations. Therein, he presents a review of past works in joined-wing aeroelasticity and gives a qualitative discussion of their behavior in a multidisciplinary context. Much of the discussion in the paper deals with structural and aeroelastic issues relating to the aft wing/tail. The in-plane loads due to structure deformation and changes in geometric stiffness give rise to non-intuitive aeroelastic behavior. Bending and twisting couplings of the entire structure cause natural frequencies and mode shapes to shift. The tendency for buckling and divergence in the aft member is of major concern when trying to reduce weight. The finding of rear wing divergence to be more critical than flutter is counterintuitive, since the aft wing is supported at the joint. This phenomenon seems associated with a reduction in structural stiffness due to the in-plane compressive loads in the rear members. The geometry of the joint between forward and aft wings is also of importance because it influences how in-plane, bending, and torsion loads are transferred. For instance, a pinned joint may allow upward buckling of the aft wing, while a fixed rigid joint may allow the aft wing to buckle downward, since bending moments are transferred across the joint.

While no firm design of a joined-wing Sensorcraft exists in public literature, Refs. 7 and 8 present a systematic design optimization study for the basic vehicle with regular control mechanisms. The authors proposed an integrated design method that brings together different software packages like NASTRAN and PanAir, and integrate then through the Air Vehicles Technology Integration Environment (AVTIE). Their most recent work⁸ addresses some of the nonlinear structural issues present in the joined-wing configuration and discuss the impact of different constraints on a fully stressed design. Ref. 9 employs multiple control surfaces on the different wing segments to implement the AAW concept on the joined-wing Sensorcraft. There, the authors employ a linear aeroelastic representation of the lifting surfaces to optimize trim so that to minimize the overall structural deformation (that may affect antenna performance). It was numerically shown that the vehicle could be trimmed for 1-g flight using six

independent control surfaces and simultaneously minimizing structural deformation.

Active distributed control using embedded piezocomposites in the wing structure may be able to improve the performance in several ways, and also may allow for lighter designs by actively offsetting critical instabilities. Warping the structure in order to change the aerodynamic force distribution across the vehicle may be a means of eliminating or reducing unwanted structural couplings due to deformation. The degrading effects of in-plane loads on the aft members may be dealt with through the use of active/passive internal structural couplings. Passive structure design may be incapable of dealing with the global structural load transfers at all flight conditions. By embedding active materials in large areas of the vehicle, the global behavior of the structure may be enhanced. Actuators embedded in the forward wings will be able to respond to stresses measured in the aft wings. Actuators anywhere in the structure can respond to measurements taken everywhere over the structure. This may allow for global modal behavior to be adjusted by timing and shaping the internal stresses in the structure.

The state of the art in passive composite structure design exploits structural couplings to prevent aeroelastic instabilities. While this may work for certain instabilities at certain flight conditions, it may have a negative effect on other aeroelastic characteristics at other flight conditions. The ability to actively adjust the structural couplings would have obvious benefits. Before any claims can be made, however, it is necessary to determine the scale of the problem and the relative amount of active material to passive material required to accomplish this goal.

The potential for new ideas in this area seems limitless. For now, however, this paper concentrates in two key issues:

1. New proposed formulation for highly flexible active vehicle analyses and the importance of geometrically nonlinear structural modeling;
2. Assessment of wing warping as a means of roll control of a joined-wing configuration based on state-of-the-art anisotropic piezocomposite actuator technology.

Formulation

For the present study, the vehicle is allowed six rigid body degrees of freedom as well as flexible degrees of freedom. The wings are allowed fully coupled three-dimensional bending, twisting, and extensional deformation. Flaps and ailerons may be included for

comparison purposes and for the study of hybrid vehicle control. A finite-state unsteady airloads model based on the work of Peters² is integrated into the system equations. The model allows for a low order set of nonlinear equations that can be put into state-space form to facilitate control design.

Element Description: Specialized nonlinear beam elements were created for the ongoing work, each having four strain degrees of freedom, representing extension, twist, and two bending strains. Deformations of this element are exemplified in Fig. 1. With a constant strain distribution over the element, a wide range of geometrically nonlinear shapes can be obtained. A single element, for example, can be deformed into a circle or spiral shape.

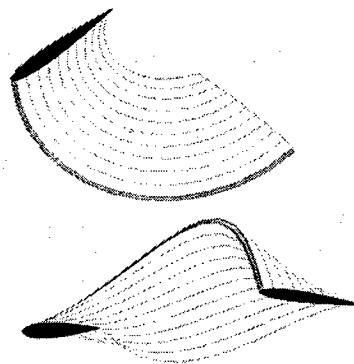


Figure 1: Deformations represented by a single element with constant strain distribution

The kinematics of the element are described as follows. The beam reference frame is denoted w , and is a function of the beam coordinate, s . The position and orientation of a point on the reference line can be described by the 12×1 vector h as

$$h(s) = [p_w(s)^T, w_x(s)^T, w_y(s)^T, w_z(s)^T]^T \quad (1)$$

where p_w is the position of frame w in the body coordinate system and w_x , w_y , and w_z are the direction vectors pointing along the beam axis, toward the leading edge, and normal to the airfoil, respectively, defined in the body frame. The partial differential equation governing how h moves through space involves the strain variables,

$$\frac{\partial h(s)}{\partial s} = A(s)h(s) \quad (2)$$

with

$$A(s) = \begin{bmatrix} 0 & 1 + \varepsilon_x(s) & 0 & 0 \\ 0 & 0 & \kappa_z(s) & -\kappa_y(s) \\ 0 & -\kappa_z(s) & 0 & \kappa_x(s) \\ 0 & \kappa_y(s) & -\kappa_x(s) & 0 \end{bmatrix} \quad (3)$$

where the blocks are all 3x3 diagonal matrices. When the element is assumed to have a constant strain vector, the solution can be obtained

$$h(s) = e^{As} h_0 = e^{G(s)} h_0 \quad (4)$$

where h_0 is the element boundary condition. The total virtual work done on an element due to all internal and external forces and moments can be written as

$$\begin{aligned} \delta W = & -\delta h^T M \ddot{h} - \delta \varepsilon^T K \varepsilon + \delta \varepsilon^T B_v v + \\ & -\delta h^T N g + \delta p^T B_F F^{dst} + \delta \theta^T B_M M^{dst} + \\ & + \delta p^T F^{PI} + \delta \theta^T B_M M^{PI} \end{aligned} \quad (5)$$

where the terms involved include the effects of inertial, gravitational, internal strain, piezoelectric, distributed, and point forces and moments.

Member Equations: Each member is an assemblage of elements and may include breaks in the beam reference line at the joint between elements and variation in the level of discretization.

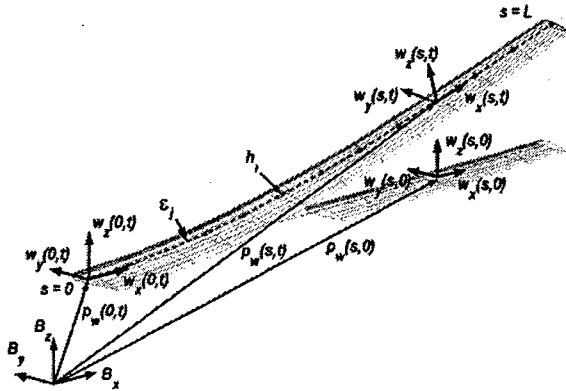


Figure 2: Illustration of a single undeformed and deformed member with different reference frames.

The kinematics for a member is obtained by marching the element kinematics from the boundary node to the end of the last element, using the values of the strain variables in each element to march forward. This procedure is given for the three node elements used in the present model,

	Element 1	Element 2	...	Element n
Node 1	$h_{11} = h^*$	$h_{21} = D_{21} h_{11}$...	$h_{n1} = D_{n,n-1} h_{n-1,1}$
Node 2	$h_{12} = e^{G_1} h_{11}$	$h_{22} = e^{G_2} h_{21}$...	$h_{n2} = e^{G_n} h_{n1}$
Node 3	$h_{13} = e^{G_1} h_{12}$	$h_{23} = e^{G_2} h_{22}$...	$h_{n3} = e^{G_n} h_{n2}$

(6)

where h_{ij} is the j th node of the i th element and the D_{ij} matrices contain elements of the direction cosines, accounting for the break at the element junction. Eq. (6) can be put into matrix form

$$\bar{A} h = h^* \quad (7)$$

where h is now a column matrix containing nodal position and orientation variables for all of the nodes in the member, and h^* is a column matrix containing the boundary condition. When the member is fixed at the first node and the element has three nodes, this relation is given by

$$\begin{bmatrix} I & 0 & 0 & 0 & 0 & 0 & 0 \\ -e^{G_1} & I & 0 & 0 & 0 & 0 & 0 \\ 0 & -e^{G_1} & I & 0 & 0 & 0 & 0 \\ 0 & 0 & D_{21} & I & 0 & 0 & 0 \\ 0 & 0 & 0 & -e^{G_2} & I & 0 & 0 \\ 0 & 0 & 0 & 0 & -e^{G_2} & I & 0 \\ 0 & 0 & 0 & 0 & 0 & D_{32} & \ddots \end{bmatrix} \begin{bmatrix} h_{11} \\ h_{12} \\ h_{13} \\ h_{21} \\ h_{22} \\ h_{23} \\ \vdots \end{bmatrix} = \begin{bmatrix} h^* \\ 0 \\ 0 \\ 0 \\ 0 \\ 0 \\ \vdots \end{bmatrix} \quad (8)$$

The D_{ij} matrices are equal to the identity matrix if the elements are aligned, and contain rotation variables if the beam reference line makes a break at an element intersection.

The Jacobian matrix relating changes in the element strain variables to changes in the position and direction vectors, taken about the current strain vector ε_0 , is given by

$$dh = \left[\frac{\partial h}{\partial \varepsilon} \right] d\varepsilon = J_{he} d\varepsilon \quad (9)$$

where

$$J_{he} = -\bar{A}_0^{-1} \left[\frac{d}{d\varepsilon} (\bar{A}(\varepsilon) h_0) \right] \quad (10)$$

is found though an iterative routine. The total virtual work done on a member due to all internal and external loads has the same form as Eq. (5), except that the size has increased by a factor of n , where n is the number of elements in the member.

Global Finite Element Matrices: At this point, each wing member represents an independent entity, for

which equations of motion may be constructed. However, because inter-member constraints will be imposed, it is more convenient to assemble the individual member matrices into a global equation for the virtual work. Before applying the inter-member constraints, the expression for work takes on the same form, where the matrices are in an uncoupled block diagonal form, and can be written as

$$\delta W = -\delta h^T (\dot{M}\ddot{h} - \delta h^T Ng) - \delta \varepsilon^T (K\varepsilon - B_v v) + \delta p^T (B_F F^{dst} + F^{pt}) + \delta \theta^T (B_M M^{dst} + M^{pt}) \quad (11)$$

Inter-member constraints are used to enforce that a node position, which is coincident to two members, remains coincident and that the relative orientation of the member coordinate systems at those nodes remains fixed. Let two members be initialized such that in their undeformed state they share a common node location. Each node has three coordinate frames associated with it. Frame w is the beam frame and is aligned with the beam axes as described above. Frame b is aligned with the body frame, B , when the member is undeformed. Frame a is aligned with the airfoil local coordinate system. In the case of a wing with zero root angle of attack and zero sweep and dihedral, frames w , b , and a are in alignment, but in general this is not the case.

The nodal position and orientation vector, h , can be defined for three corresponding frames, e.g.,

$$\begin{aligned} h^w &= [p_x^T, w_x^T, w_y^T, w_z^T]^T \\ h^b &= [p_b^T, b_x^T, b_y^T, b_z^T]^T \\ h^a &= [p_a^T, a_x^T, a_y^T, a_z^T]^T \end{aligned} \quad (12)$$

where the following constant relations hold

$$\begin{aligned} h^b &= D^{bw} h^w, \quad h^a = D^{aw} h^w \\ D^{bw} &= \begin{bmatrix} 1 & 0 & 0 & 0 \\ 0 & C_{11}^{wb} & C_{21}^{wb} & C_{31}^{wb} \\ 0 & C_{12}^{wb} & C_{22}^{wb} & C_{32}^{wb} \\ 0 & C_{13}^{wb} & C_{23}^{wb} & C_{33}^{wb} \end{bmatrix} \\ D^{aw} &= \begin{bmatrix} 1 & 0 & 0 & 0 \\ 0 & C_{11}^{wa} & C_{21}^{wa} & C_{31}^{wa} \\ 0 & C_{12}^{wa} & C_{22}^{wa} & C_{32}^{wa} \\ 0 & C_{13}^{wa} & C_{23}^{wa} & C_{33}^{wa} \end{bmatrix} \end{aligned} \quad (13)$$

The D matrices here are 12x12 matrices where each block is a 3x3 diagonal matrix and C^{wb} and C^{wa} are components of the rotation matrices from frames b and a , respectively, to frame w . It should be clear now that the vector h is simply a way to express the position and

orientation of a coordinate system in a single vector format, and that the D matrices are a rearrangement of the standard direction cosines matrices.

If node m of member i is initially coincident with node n of member j , then coordinate systems b_m^i and b_n^j are equivalent for the undeformed geometry. To enforce the inter-member constraint, it is required that

$$h_{i,m}^b = h_{j,n}^b \rightarrow D_{i,m}^{bw} h_{i,m}^w = D_{j,n}^{bw} h_{j,n}^w \quad (14)$$

This can be done by associating a large virtual work penalty term if the equality in Eq. (14) is violated, that is,

$$\delta W = - (D_{i,m}^{bw} \delta h_{i,m}^w - D_{j,n}^{bw} \delta h_{j,n}^w)^T \hat{K} (D_{i,m}^{bw} h_{i,m}^w - D_{j,n}^{bw} h_{j,n}^w) \quad (15)$$

which can be rearranged into the matrix form

$$\begin{aligned} \delta W &= -[\delta h_{i,m}^T, \delta h_{j,n}^T] \begin{bmatrix} D_{i,m}^{wb} \hat{K} D_{i,m}^{bw} & -D_{i,m}^{wb} \hat{K} D_{j,n}^{bw} \\ -D_{j,n}^{wb} \hat{K} D_{i,m}^{bw} & D_{j,n}^{wb} \hat{K} D_{j,n}^{bw} \end{bmatrix} \begin{bmatrix} h_{i,m} \\ h_{j,n} \end{bmatrix} \\ &= -[\delta h_{i,m}^T, \delta h_{j,n}^T] \begin{bmatrix} K_{11} & K_{12} \\ K_{21} & K_{22} \end{bmatrix} \begin{bmatrix} h_{i,m} \\ h_{j,n} \end{bmatrix} \end{aligned} \quad (16)$$

To impose the inter-member constraint, Eq. (11) is augmented with a stiffness matrix acting on the nodal position vector, becoming

$$\delta W = -\delta h^T (\dot{M}\ddot{h} + C_c \dot{h} + K_c h - \delta h^T Ng) - \delta \varepsilon^T (K\varepsilon - B_v v) + \delta p^T (B_F F^{dst} + F^{pt}) + \delta \theta^T (B_M M^{dst} + M^{pt}) \quad (17)$$

where K_c is a matrix of zeros except in the rows and columns corresponding to the entries in Eq. (16). For numerical stability, a constraint damping matrix C_c is also added to Eq. (17) in the same way. Some care is required in selecting the constraint damping and stiffness constants.

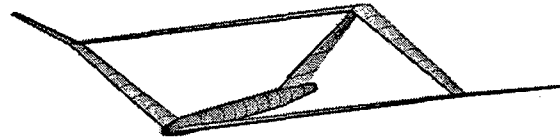


Figure 3: Illustration of a built up joined-wing structure with inter-member constraints imposed

Equations of Motion: With the six rigid body degrees of freedom, the system structural degrees of freedom are represented by the column matrix q , where

$$\dot{q} = [\dot{\varepsilon}_1^T, \dot{\varepsilon}_2^T, \dots, \dot{\varepsilon}_n^T, V_B^T, \omega_B^T]^T \quad (18)$$

and ε_i contains the strain variables for wing member i , V_B and ω_B are the linear velocity and angular velocity of the vehicle, respectively, represented in the body frame, B . The dependent variables for the entire vehicle are put into the column matrix H ,

$$\dot{H} = [\dot{h}_1^T, \dot{h}_2^T, \dots, \dot{h}_n^T, V_B^T, \omega_B^T]^T \quad (19)$$

The dependent degrees of freedom are related to the independent degrees of freedom through a Jacobian matrix relation

$$H = f(q), \quad dH = \left[\frac{\partial H}{\partial q} \right] dq = [J_H(q)] dq \quad (20)$$

The expression for virtual work on the vehicle is now given by

$$\begin{aligned} \delta W = \delta q^T & (-\bar{M}\ddot{q} - \bar{C}\dot{q} - \bar{K}q + \bar{N}g + \bar{B}_v V + \bar{B}_{F1} F^{dst} + \\ & + \bar{B}_{F2} F^{pt} + \bar{B}_{M1} M^{dst} + \bar{B}_{M2} M^{pt} + \\ & + B_{q0} q_0 + B_H H) \end{aligned} \quad (21)$$

The principle of virtual work requires that the total virtual work done on the system be equal to zero, leading to the equations of motion,

$$\begin{aligned} \bar{M}\ddot{q} + \bar{C}\dot{q} + \bar{K}q = \\ B_v V + B_{F1} F^{dst} + B_{F2} F^{pt} + B_{M1} M^{dst} + \\ + B_{M2} M^{pt} + \bar{N}g + B_{q0} q_0 + B_H H \end{aligned} \quad (22)$$

The distributed loads are divided into aerodynamic loads and user supplied loads. The aerodynamic loads evaluated at the current state have the incremental form

$$\begin{aligned} F^{aero}(t) &= F^{aero}(t_0 + \Delta t) \\ &\approx F_0(q_0, \dot{q}_0, \lambda_0) + F_{\dot{q}} \ddot{q} + F_{\dot{q}} \Delta \dot{q} + F_q \Delta q + F_{\lambda} \Delta \lambda \\ M^{aero}(t) &= M^{aero}(t_0 + \Delta t) \\ &\approx M_0(q_0, \dot{q}_0, \lambda_0) + M_{\dot{q}} \ddot{q} + M_{\dot{q}} \Delta \dot{q} + M_q \Delta q + M_{\lambda} \Delta \lambda \end{aligned} \quad (23)$$

where λ is column matrix of induced flow states as described in Ref. [10]. The induced flow states are governed by a differential equation of the form

$$\dot{\lambda} = L_1 \lambda + L_2 \ddot{q} + L_3 \dot{q} \quad (24)$$

The aeroelastic equations of motion are obtained by moving the state dependent aerodynamic loads over to

the left hand side of Eq. (22) and augmenting the structure states with the induced flow states, which can be represented in state space form as

$$\dot{x} = A(x)x + B(x)u(x, t) \quad (25)$$

where the state vector is now given by

$$x = [\dot{q}^T, q^T, \lambda^T]^T \quad (26)$$

Numerical Results

For the numerical study, baseline vehicles are created for the wing warping (active) and for the aileron (passive) concepts. For both cases, controllable changes in aerodynamic loads only occur in the outer wing. The active wing contains APAs that can produce 1350 μ strain of free strain amplitude and are distributed along the entire span. The passive wing contains a 50%-span/20%-chord aileron that is allowed 30° of amplitude deflection.

Once the baselines are designed, different sensitivity studies are presented to exemplify further capabilities of the proposed framework and the relative performance of wing-warping controlled configuration with respect to an aileron-controlled one

Baseline Vehicles

Two distinct designs are needed to study the effects of wing warping and its relative performance with respect to an aileron-controlled vehicle. First, a design that represents an active wing with embedded APA. Second, a passive wing designed to have an aileron. Three sets of constraints were defined to help guide the baseline designs: laminate strength (based on first-ply failure) at 2.5-g load, laminate strength based on gust loads, and minimum linearized flutter margin. For all the cases, the fuselage and tail are assumed rigid (Fig. 4).

Vehicle Model Description: From top view, the vehicle shape is symmetric (although one may want to vary the forward/aft location of the joint). The wings are denoted right forward inboard, left forward inboard, right rear inboard, left rear inboard, right outboard, and left outboard. Right and left are determined as in Fig. 5 (as viewed from top with nose pointing up). Dimensions are given in Table 1. Each of the six wing members is divided into four regions for definition of cross-section layup and ply thickness distribution. The forward and rear members are identical in construction, and the material distribution will follow the numbering convention as indicated in Fig. 5.

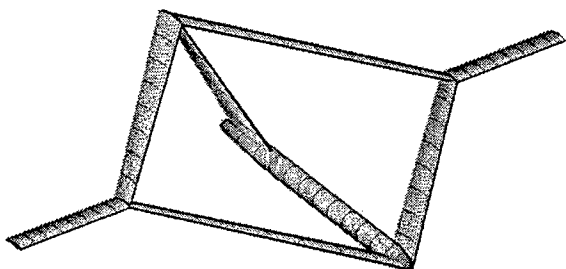


Figure 4: Baseline joined-wing Sensorcraft vehicle with unswept outer wings (where APA actuators or ailerons are present).

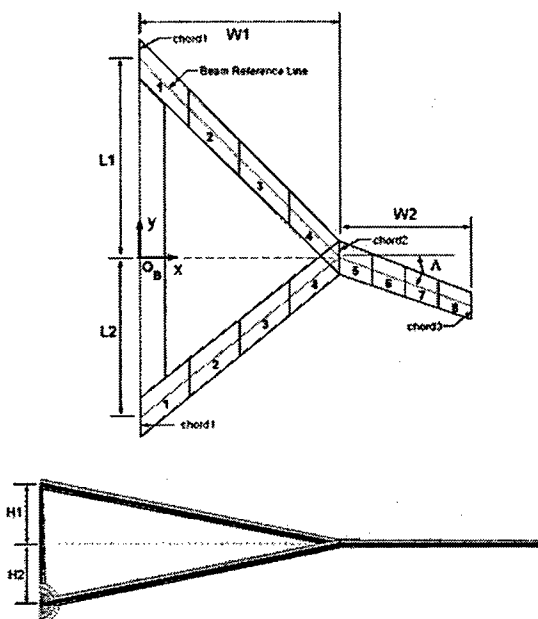


Figure 5: Baseline joined-wing Sensorcraft vehicle geometry.

Mission Profile: Seven flight index points represent the nominal mission profile, as indicated in Fig. 6. At each index point, the altitude, fuel mass, and nominal flight velocity are specified. The index points represent: (1) takeoff, (2) climb, (3) cruise ingress, (4) cruise/loiter/cruise, (5) cruise egress, (6) decent, and (7) landing. The fuel burn determines the duration of each flight segment. The nominal flight speed at each index point is based on the cruise speed (input parameter), and is computed such that the dynamic pressure is constant (constant indicated air speed). The trim body angle is also obtained at each index point for a set of equally spaced increasing flight speeds, up to 200% of the nominal speed at that flight index.

Table 1: Baseline joined-wing Sensorcraft vehicle planform data.

$L1 = L2$	15 m
$W1 = W2$	20 m
$H1 = H2$	4 m
chord1	3.5 m
chord2	2 m
chord3	1.5 m
Sweep angle (Λ)	0°

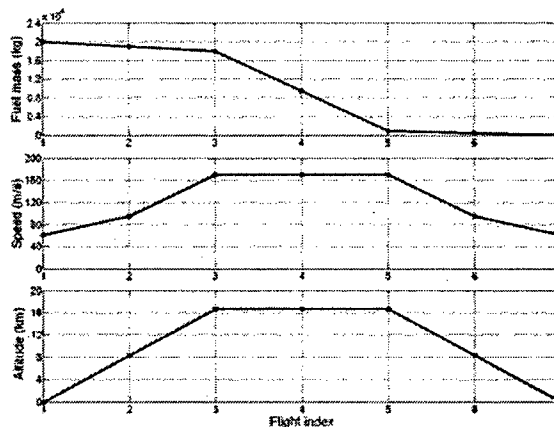


Figure 6: Nominal mission profile.

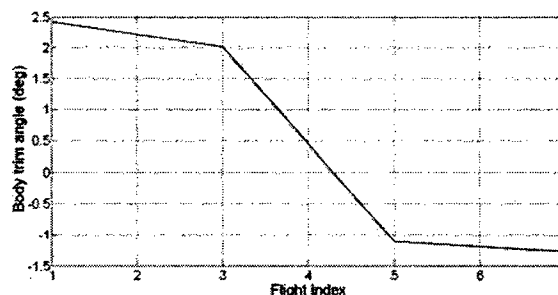


Figure 7: Active vehicle body trim angle as a function of flight index (nominal flight speed at each index point)—similarly for aileron concept.

Vehicle Trim: At each flight index point, the vehicle is trimmed for equilibrium in horizontal flight at a given flight speed. The trim angle is shown in Fig. 7 for the nominal flight speeds.

Vehicle Mass Breakdown: The vehicle mass breakdown is given in Table 2. The fuel is assumed to be distributed evenly throughout the inner and outer wings, independent of the total amount of fuel on board. The fuselage contains no fuel.

Table 2: Vehicle Mass Distribution.

Cruise altitude	16,700 m
Cruise speed	170 m/s
Fuselage structure + payload + engine mass	4,000 kg
Fuel mass	20,000 kg
Active vehicle total wing structure mass	11,191 kg
Passive vehicle total wing structure mass	10,459 kg
Added mass for aileron mounts/wing	58.9 kg

Wing Cross Section: For simplicity, NACA 4415 was chosen as the airfoil and it is kept constant throughout the wing members (see Fig. 8). A single spar is used at 45% chord. (This could be easily replaced with a two-spar configuration, particularly for the inner wings. This, however, reduces the computational time for each design iteration and does not qualitatively affect the results.) The wing reference axis is indicated in Fig. 8. For the final wing layup, the top and bottom skins have ply groups composed of $[0/45/-45/0]$ and the web with ply groups of $[0_4]$. For the active outer wing, the “45” and “-45” ply groups are APA. Everything else is S-glass. Material properties are given in Table 3. The thickness distribution for each element within a wing member (according to the numbering scheme defined in Fig. 5) is given in Figs. 9 and 10 for the active and passive wings, respectively. The web thickness is four times the thickness of a 0° ply group at a given span member. The maximum induced twist angle distribution along the span generated by the APA is shown in Fig. 11.

Table 3: Material properties (1—fiber direction; 2—transverse to fiber; 6—shear)

	S-glass/epoxy	APA
Mass (kg/m^3)	1855	4100
Q_{11} (GPa)	48.0	34
Q_{12} (GPa)	3.5	7.5
Q_{22} (GPa)	12.2	17
Q_{66} (GPa)	3.6	5.1
Max. free strain ($\mu\epsilon$)	N/A	2700

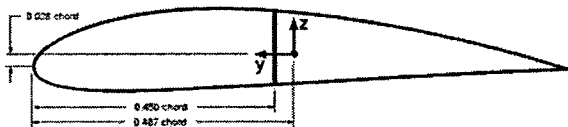


Figure 8: NACA 4415 cross-section geometry.

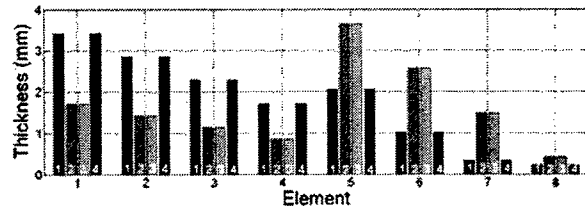


Figure 9: Ply group thickness for each element (see Fig. 5), active wing. The bar numbers indicate the ply number in the wing skin.

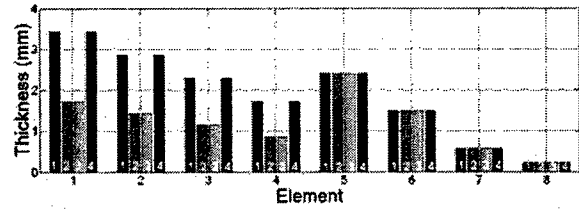


Figure 10: Ply group thickness for each element (see Fig. 5), passive wing. The bar numbers indicate the ply number in the wing skin.

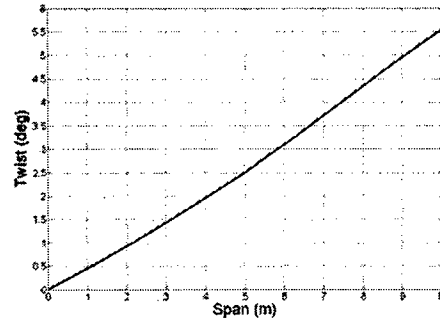


Figure 11: Twist distribution along the outer wing due to 1350 μstrain actuation.

Design Constraint 1 (2.5 g load condition): To evaluate DC1, the vehicle is flown in level flight at sea level. The speed is increased until the lift equals 2.5 times the weight. The vehicle is fully fueled to represent the worst-case scenario. Fig. 12 shows the vehicle deformation and distribution of aerodynamic forces under these conditions. The wing vertical bending displacements are plotted in Figs. 13 and 14 for the active and passive configurations, respectively. The deflection at the wing tip is approximately 12% of the semi-span. Similarly, the (absolute value of the) maximum ply strains are plotted in Figs. 15 and 16. The strains are with respect to the fiber direction (11—along fiber, 22—transverse to fiber, 12—shear). The constraint imposed here is that the maximum strain does not surpass 3,000 microstrain in any of the components. The ply thicknesses in each wing region were minimized until the design strain limits were

approached. DC1 is now considered the active constraint, and will remain so unless DC2 (gust load structure failure) or DC3 (flutter failure) becomes active.

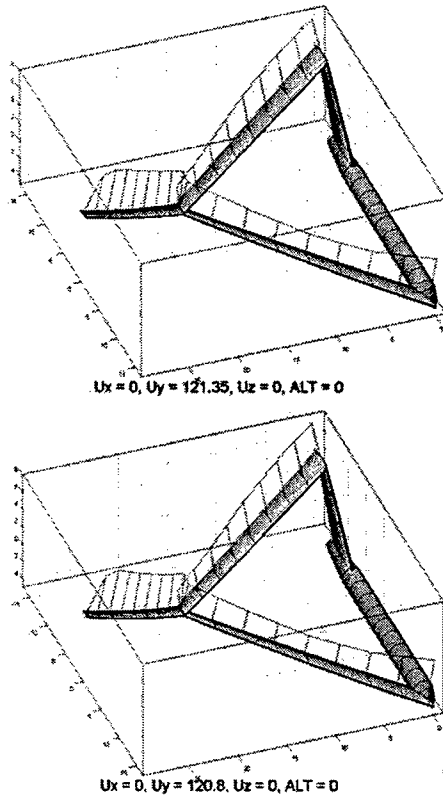


Figure 12: Active (top) and passive (bottom) vehicles at 2.5 g loading condition (note lift loss at the wing tip).

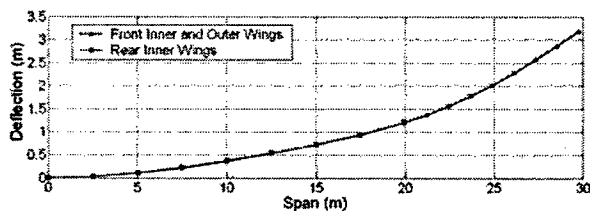


Figure 13: Wing deflections for active vehicle (lift/weight = 2.5, sea level, fully fueled, $U = 121.3\text{m/s}$).

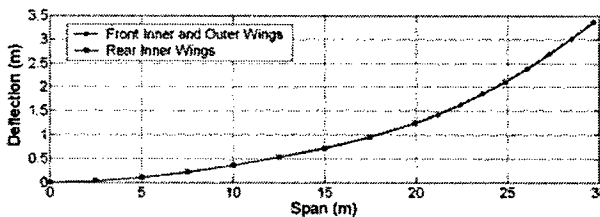


Figure 14: Wing deflections for passive vehicle (lift/weight = 2.5, sea level, fully fueled, $U = 120.8\text{m/s}$).

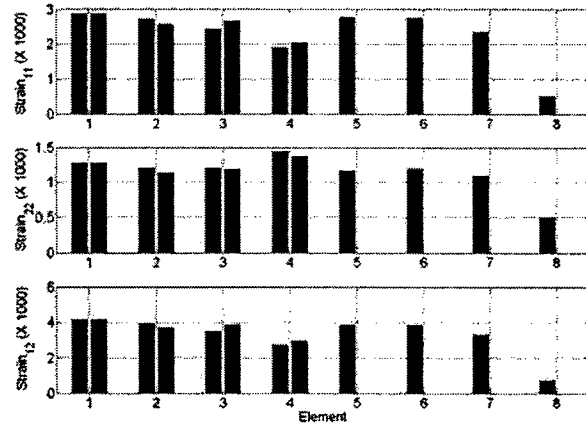


Figure 15: Maximum ply strains in each element during 2.5 g loading condition, active vehicle.

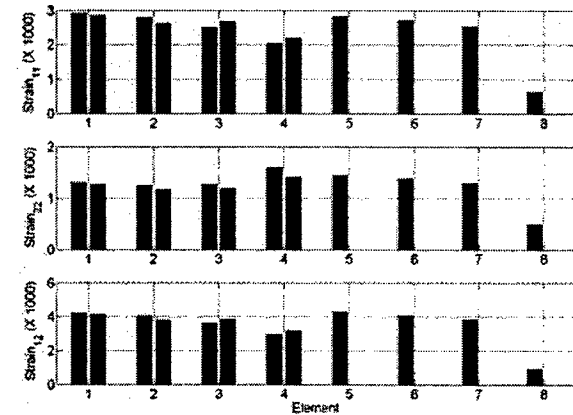


Figure 16: Maximum ply strains in each element during 2.5 g loading condition, passive vehicle.

Design Constraint 2 (gust load failure): The worst-case gust loading occurs when the wings are depleted of fuel (no inertia relief) and the vehicle is traveling at sea-level and nominal speed. The slowest flight speed maximizes the vertical gust-induced angle of attack ($\alpha_{\text{gust}} = \tan^{-1}(w/U)$). Even though the framework implements the Dryden gust model, for this design exercise, the "1-cosine" gust model is used for simplicity. The amplitude of the 1-cosine vertical gust is 10 m/s (22.4 mph). The response is shown in Fig. 17. The maximum ply strains as function of time are shown in Fig. 18. As one can see, the maximum values are still well below the imposed limit on the maximum ply strains.

Design Constraint 3 (flutter speed): The flutter speed is approximated at each flight index point by determining the stability characteristics of the linearized system about its nonlinear equilibrium condition. The minimum linearized flutter margin along the mission profile is imposed to be 25% above the corresponding

nominal flight speed. As it can be seen from Table 4, both designs satisfy that limit without much difficulty. This could be relaxed in the future by allowing actively enhancement of the flutter boundary.

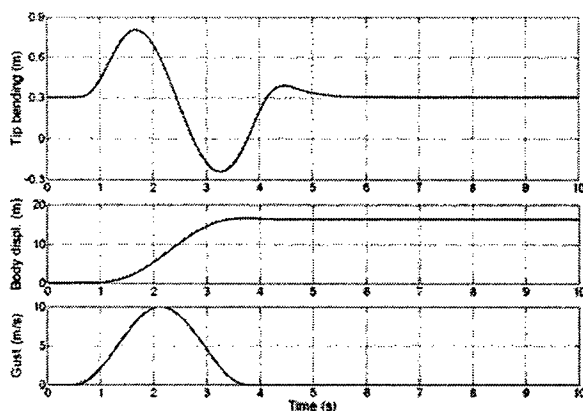


Figure 17: Response to gust input, sea-level, flight index 7, active wings (similar for passive wings).

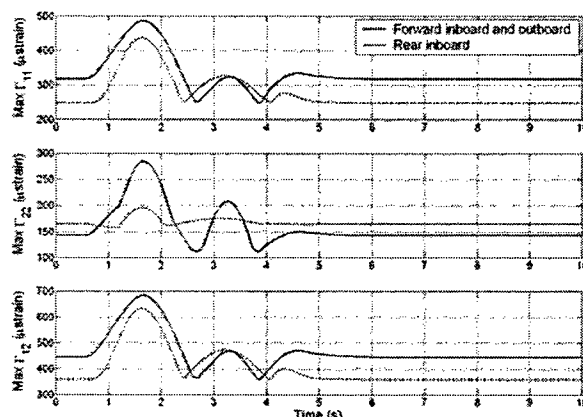


Figure 18: Maximum ply strains (absolute value) during gust encounter, active wings (similar for passive wings).

Table 3: Flutter speed margins for the active and passive (aileron) vehicles at each flight index.

Flight index	Nominal speed m/s	Margin/Active %	Margin/Aileron %
1	61.21	33.97	36.45
2	95.30	32.23	33.78
3	170.0	34.09	34.31
4	170.0	34.53	35.13
5	170.0	28.89	26.34
6	95.30	34.29	39.67
7	61.21	46.45	66.74

Characteristics of the Two Vehicle Concepts

Once the baselines have been established, different studies on the vehicles can be conducted. The ones chosen to be presented here illustrate some of the capabilities of the formulation, the unique behavior of joined-wing configurations, and the relative performance of wing warping and aileron control schemes for vehicle primary roll control.

Effects of Load Factor on the Stability of the Rear Wing: Since the aft wings are primarily under compression, their buckling response can be a sizing limitation for the vehicle. For the particular baseline designs considered here, deformation of the rear inboard wing increases dramatically when the load factor reaches about 2.7, bring the whole wing system close to a collapse (see Fig. 19). This condition is naturally modeled in the presented framework through the nonlinear structural analysis.

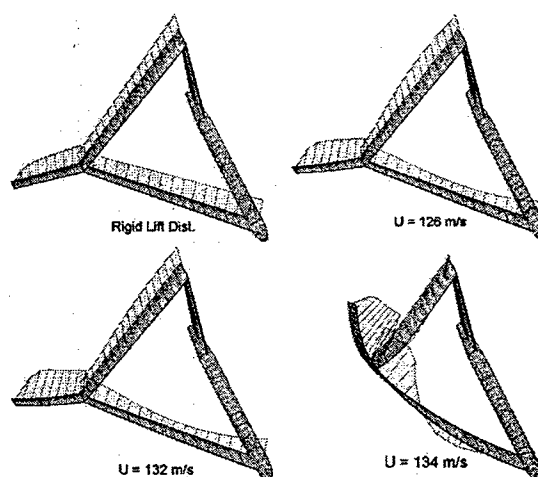


Figure 19: Lift distribution on the vehicle as the buckling speed is approached (sea level, fully fueled, no rigid body degrees of freedom, zero body angle of attack)

To exemplify this, a half-vehicle model is brought to steady state at level flight (at sea level). Then, its flight speed is varied from 70 m/s to 130 m/s, with a resulting load factor ranging from 0.83 to 2.66. The wing shape and deflections are plotted for varying load factor in Figs. 20 thru 24. As may be seen from Figs. 22 and 23, the passive wing configuration is more susceptible to the increase in speed due to a softer outboard wing (higher lift outboard due to aeroelastic effects). The suddenly reduction of the rear wing stiffness results in large bending deflection of the overall wing structure and, consequently, drop in the overall lift (represented by the reduction in load factor as shown in Fig. 24).

This level of wing displacement causes high composite ply strains (stresses), to the point of ply failure. A typical strain component dependence on the load factor is shown in Fig. 25

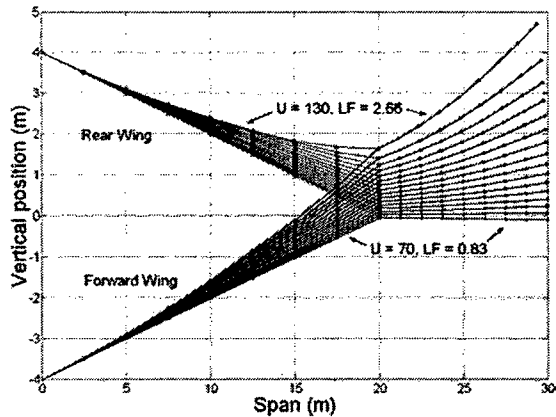


Figure 20: Active wing shape for varying flight speed (level flight at sea level).

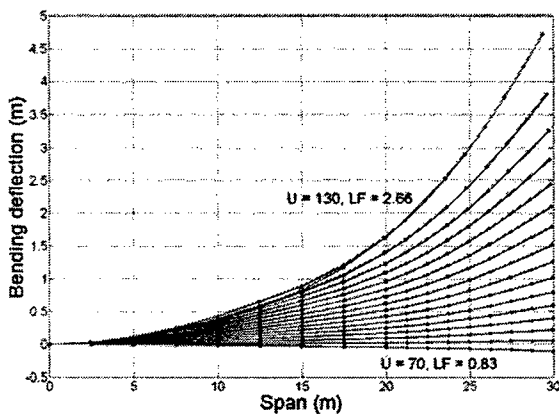


Figure 21: Active wing bending deflections for varying flight speed (level flight at sea level).

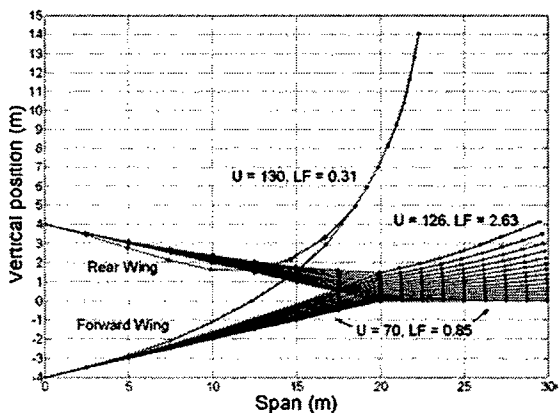


Figure 22: Passive wing shape for varying flight speed (level flight at sea level).

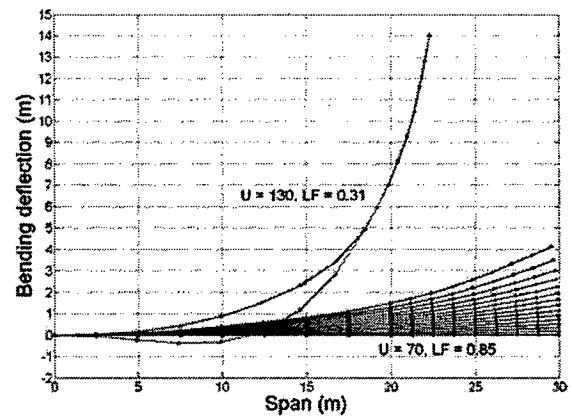


Figure 23: Passive wing bending deflections for varying flight speed (level flight at sea level).

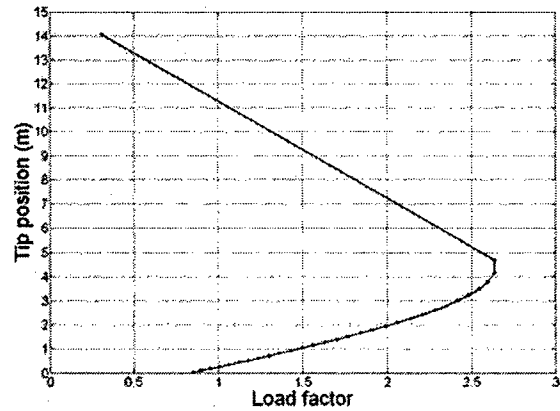


Figure 24: Changes in tip deflection as function of the lift generation capability of the passive wing vehicle at level flight (sea level).

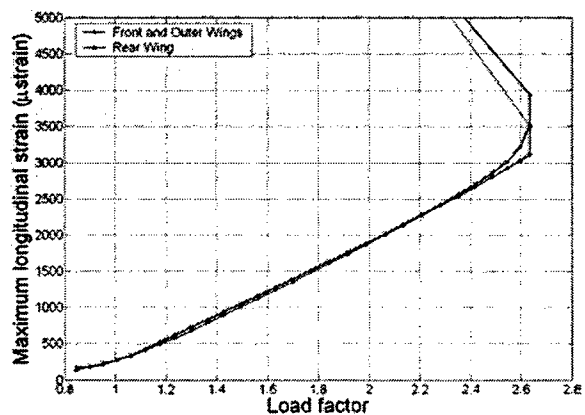


Figure 25: Sample of maximum strain component nonlinear growth due to loss of stiffness on the rear wing with increase load factor (passive wing vehicle at level flight, sea level).

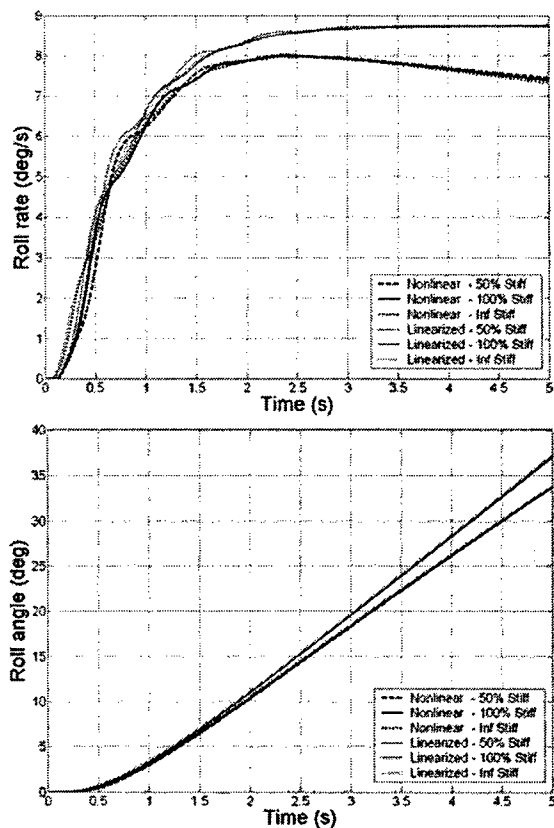


Figure 26: Active concept roll rate and roll angle responses with varying inner wing stiffness (flight index 5, maximum actuation; 100% stiffness is nominal)

Roll Response: To study roll response, two approaches have been implemented: a linearized approach and a nonlinear one. In the linearized approach, the vehicle is first brought to its nonlinear steady state with roll motion locked, and under the influence of applied actuation. Both the static aerodynamic roll moment and roll rate damping moment are computed based on the deformed structure. A representative fuselage roll inertia is used, although the major contributors to roll inertia are the wings. The roll rate response is then solved based on these quantities. This approach has the main advantage of being computationally very efficient. In the nonlinear approach, the vehicle is first brought to its nonlinear steady state with no actuation applied. Then a nonlinear time stepping roll simulation is performed. The input (ply voltage and aileron deflection) is ramped from zero to its maximum value in 0.5 s. Moreover, to assess the impact of the inner wing flexibility to the roll response of the vehicle, two other cases were created: one (denoted as “50% Stiff”) where the inner wings have half of the stiffness (extension, bending, and

torsion) of the baseline (denoted as “100% Stiff”), and the other one (denoted by “Inf Stiff”) with 100 times the baseline stiffnesses, representing an almost rigid case. The roll rate and roll angle responses to applied twist actuation and aileron deflection are shown in Figs. 26 and 27, respectively, for both linear and nonlinear roll calculations during 1-g level flight.

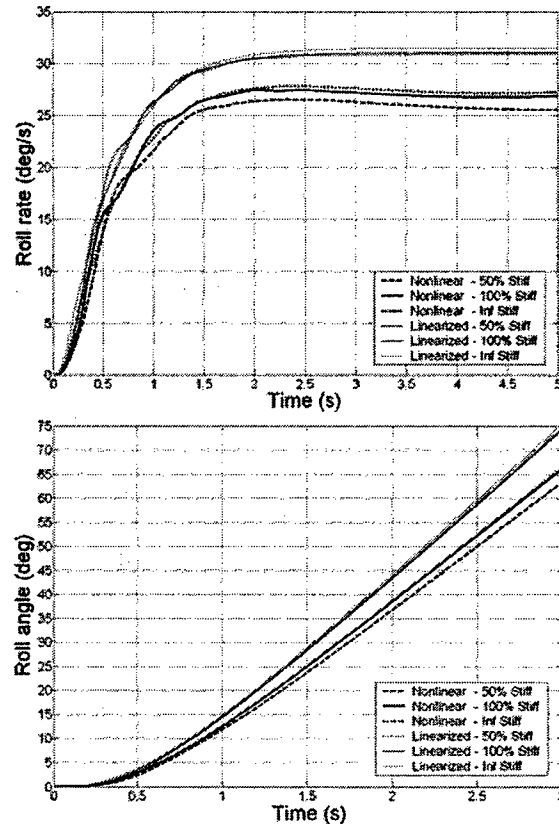


Figure 27: Aileron concept roll rate and roll angle responses with varying inner wing stiffness (flight index 5, maximum deflection; 100% stiffness is nominal)

The very first observation that can be made from Figs. 28 and 29 is that the roll performance level of the wing warping actuation with APA is about three fold lower than the aileron concept. While roll angles of over 50° can be reached by the latter in 2.5 s, for the same time period only 15° is reachable with the active wing. This was expected based on the fact that the quasi-linear twist distribution generated by the active concept reaches 5.5° at the wing tip (where aerodynamic losses are imposed) while the aileron imposes 30° deflection of 25% wing chord between 1/3 and 2/3 of the outer wing span.

For the ways the analysis may be conducted, there is a significant difference between the linearized and fully nonlinear approaches for roll analysis, particularly for the terminal roll rate. In fact, the overshoot that happens due to wing flexibility is not captured at all in the linearized approach. On the other hand, the roll angle response is less sensitivity to the full nonlinear effects, presenting differences between the two analyses predictions of 10% for the active and 15% for the aileron actuations after 3 s into the roll bank.

Regarding the effects on the flexibility of the inner wings, the primary impact is on the dynamics of the response to reach maximum roll rate. For the active concept, due to low roll rates, the effects of the flexibility of the inner wings does not become a factor. However, for the levels of response presented by the ailerons, a significant difference can be seen from Fig. 27. As the inner wings become less stiff, there is a loss on the terminal roll rate due to the deformation of the inner wings. This is only capture by the fully nonlinear analysis.

Outer Wing Sweep Effect on Roll Response: As an indication of the effects of outer wing sweep on roll response, a 25° backward sweep case is compared with the 0° sweep baseline cases. Figs. 28 and 29 show the roll rate results for the active and aileron cases, respectively. Note that the effects of moving the vehicle's aerodynamic center with the outer wing sweep⁷ is beyond the scope of this paper even though modeled in the framework. As can be observed from the plots, a decrease in roll rate is observed from both linearized and nonlinear analyses. When the wing is swept, there is a reduction in angle of attack as the wing bends. Since the twist axis of the wing is no longer perpendicular to the airfoil, the effectiveness of twisting the wing to change the angle of attack is decreased. Furthermore, the lift per unit span of the swept wing decreases with the cosine of the sweep angle. Since the roll rate damping of the inner wings is constant as the outer wings are swept, there is an overall reduction in effectiveness of the outer wings to produce roll rate for the same spanwise angle of attack distribution.

APA Technology Impact on Roll Performance: All the studies presented so far were based on representative APA material properties from current existing polycrystalline piezocomposite materials. There have been efforts within the materials research community for the development of different material systems with improved piezoelectric properties. Among them, the single-crystal program¹² for AFC could lead to a significant increase in actuation authority. To estimate the required actuation needed for the joined-wing Sensorcraft-like application, consider the same

APA material properties and wing design as previously discussed, but allow for the maximum free strain of the APA be increased. Fig. 30 shows the impact on wing twist distribution along the outer wingspan for different levels of APA's free strain. Considering the case of 3.75-fold increase in free strain (and keeping the passive material properties of the APA the same), Fig. 31 show the impact on roll rate and roll angle responses. As indicated in these plots, this is the level of material improvement required so the wing-warping concept may achieve similar levels of performance as the aileron concept discussed before. These levels were improvements may be theoretically achievable¹² but only time can tell the viability of the concept.

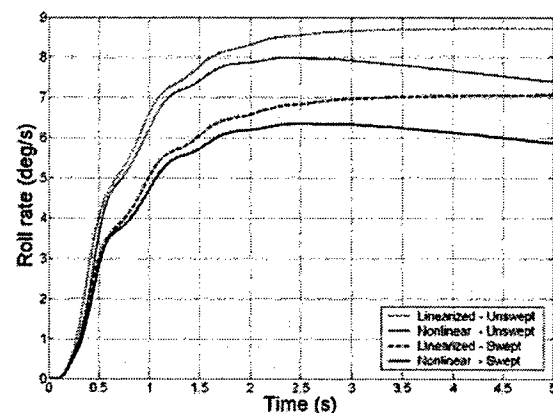


Figure 28: Active concept roll response for different outer wing sweep angles (25° sweep indicated by "Swept"; flight index 5, maximum actuation).

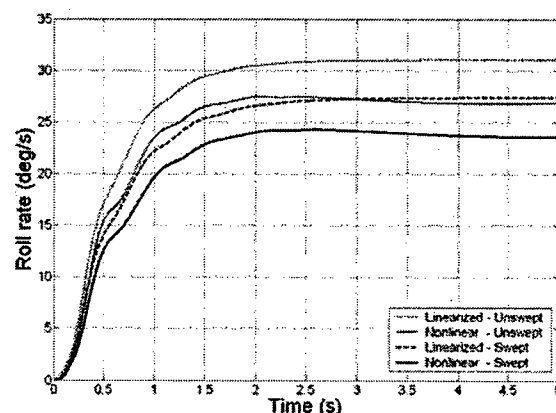


Figure 29: Aileron concept roll response for different outer wing sweep angles (25° sweep indicated by "Swept"; flight index 5, maximum actuation).

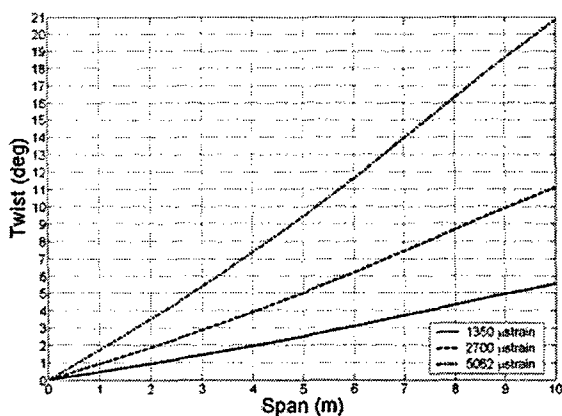


Figure 30: Spanwise twist distribution on the active outer wing considering different APA free strain levels (1350 μ strain represents available technology)

General Remarks

Even though numerical design optimization will improve the baseline vehicle designs and should be employed support navigating such reach design space, the relative results obtained here represent the order of response expected from each concept for the joined-wing Sensorcraft configuration. Again, the concepts are based on current technology material properties and construction practices. The active concept uses APA properties that are achievable with today's technology and the model includes all the fundamental static and dynamic effects on the aeroelastic responses. The aileron design contains significant idealizations, and represents the performance upper bound for the concept. No surface control inertia or aerodynamic losses with high deflection angles have been included in the model, or any control flexibility that comes with very large control surfaces. In fact, the chosen size of the aileron was based on the maximum practical size surface that can be fitted within such wing¹¹ without being concerned with mechanical fixtures and actuator systems.

Another important aspect of the vehicles' designs presented here is that they are driven by strength consideration, which penalized the wing-warping concept and favored the aileron-actuated one. Stiffness constraints got automatically satisfied once the layups were thickened enough to sustain the high loads. If a reduced maximum load factor is chosen, other constraints may become active, particularly related to aileron reversal and gust loads (as was seen for the latter in some of the design studies conducted in Ref. 5). In fact, the overall system/mission requirements, including performance and survivability considerations, will certainly impact the design solution, potentially changing the importance of roll performance as assumed here.

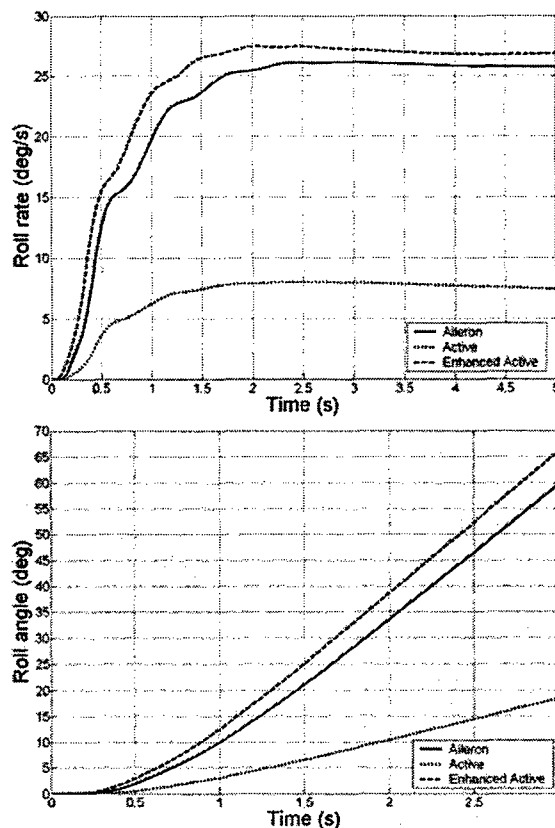


Figure 31: Roll response considering a mechanically equivalent APA but with 3.75-fold increase in its free strain properties (flight index 5; vehicles are trimmed prior to roll maneuver)

Conclusions

This paper discussed some of the unique aeroelastic characteristics of the joined-wing Sensorcraft, with emphasis on the concept of wing warping actuation for maneuver load generation. The study employs a newly developed framework for the analysis, design, and simulation of high-flexible multi-segmented wing vehicles, also described in this paper.

To study the effectiveness of wing warping to generate aircraft roll control, two baseline vehicles were designed. The first one has anisotropic piezocomposite actuators embedded in the composite construction of the outer wing, inducing strain and twist deformation. The second baseline vehicle has an aileron spanning 50% of the outer wing. Both designs satisfy the same set of constraints. Strength of the laminates at 2.5-g load factor became the sizing constraint for both designs.

When analyzing the joined-wing concepts, the importance of wing flexibility and the availability of a

geometrically nonlinear structural dynamics solver were demonstrated. Of particular interest for the joined-wing configuration is the criticality of the sudden rear wing loss of stiffness (buckling) that compromises the vehicle integrity. For the roll response, it was shown that the wing-warping design based on currently APA technology presents a terminal roll rate which is over three-times smaller than the aileron concept due to limited twist authority. This could be overcome with an APA of similar mechanical properties as used in this study but with 3.75-times greater maximum free strain. This is within range of the promises of single-crystal fiber composites.

Acknowledgements

The authors gratefully acknowledge the technical interactions with Dr. Roy Ikegami, Mr. Christopher L. Davis, and Mr. Gerald F. Herndon from the Boeing Co., Phantom Works, Kent, Washington, and Drs. Brian P. Sanders and Gregory W. Reich from AFRL/WPAFB, Dayton, Ohio. The second author gratefully acknowledges C.S. Draper Laboratory for providing his fellowship for graduate studies. This work is sponsored by AFOSR under grant F49620-01-1-0133. The technical monitor is Dr. Dean Mook.

References

- [1] Pendleton, E. W., Griffin, K. E., Kehoe, M., and Perry, B., "A Flight Research Program for the Active Aeroelastic Wing Concept," In *Proceedings of the 37th AIAA/ASME/AHS/ASC Structures, Structural Dynamics and Materials Conference*, Salt Lake City, Utah, April 1996.
- [2] Bent, A. A., "Active Fiber Composite Material Systems for Structural Control Applications," In *Proceedings of the SPIE's 6th International Symposium on Smart Structures and Materials*, Newport Beach, California, March 1999.
- [3] Wilkie, W.K., Bryant, R.G., High, J.W., Fox, R.L., Hellbaum, R.F., Jalink, A., Little, B.D., and Mirick, P.H., "Low-cost piezocomposite actuator for structural control applications," In *Proceedings of the SPIE 7th Symposium on Smart Structures and Materials*, Newport Beach, California, March 2000. pp. 323-334.
- [4] Cesnik, C. E. S. and Ortega-Morales, M., "Active Aeroelastic Tailoring of Slender Flexible Wings," *International Forum on Aeroelasticity and Structural Dynamics*, Madrid, Spain, June 5-7, 2001.
- [5] Brown, E. L., "Integrated Strain Actuation in Aircraft with Highly Flexible Composite Wings," Ph.D. Thesis, Massachusetts Institute of Technology, Cambridge, Massachusetts, June 2003.
- [6] Livne, E., "Aeroelasticity of Joined-Wing Airplane Configurations: Past Work and Future Challenges - A Survey," In *Proceedings of the 42nd AIAA/ASME/AHS/ASC Structures, Structural Dynamics, and Materials Conference*, Seattle, WA, April 16-19, 2001, AIAA-2001-1370.
- [7] Blair, M. and Canfield, R. A., "A Joined-Wing Structural Weight Modeling Study," In *Proceedings of the 43rd AIAA/ASME/AHS/ASC Structures, Structural Dynamics and Materials Conference*, Denver, Colorado, April 2002, AIAA-2002-1337.
- [8] Roberts, R. W., Canfield, R. A., and Blair, M., "Sensor-craft Structural Optimization and Analytical Certification," In *Proceedings of the 44th AIAA/ASME/AHS/ASC Structures, Structural Dynamics and Materials Conference*, Denver, Colorado, April 2003.
- [9] Reich, G. W., Raveh, D., and Zink, P. S., "Application of Active Aeroelastic Wing Technology to a Joined-Wing Sensorcraft," In *Proceedings of the 43rd AIAA/ASME/AHS/ASC Structures, Structural Dynamics and Materials Conference*, Denver, Colorado, April 2002, AIAA-2002-1633.
- [10] Peters, D. A. and Johnson, M. J., "Finite-State Airloads for Deformable Airfoils on Fixed and Rotating Wings," In *Symposium on Aeroelasticity and Fluid/Structure Interaction, Proceedings of the Winter Annual Meeting*. ASME, November 6-11, 1994.
- [11] Ikegami, R., Private communication, The Boeing Co., Phantom Works, Seattle, Washington, 2002.
- [12] Rossetti Jr., G. A., Pizzochero, A., and Bent, A. A., "Recent Advances in Active Fiber Composites Technology," In *Proceedings of the 12th IEEE International Symposium on Applications of Ferroelectrics*, Honolulu, Hawaii, 2000, pp. 753-756.

Appendix C:

Cesnik, C. E. S. and Brown, E., "Modeling of High Aspect Ratio Active Flexible Wings for Roll Control," *Proceedings of the 43rd Structures, Structural Dynamics, and Material Conference*, Denver, Colorado, April 22—25, 2002, AIAA Paper 2002-1719.

MODELING OF HIGH ASPECT RATIO ACTIVE FLEXIBLE WINGS FOR ROLL CONTROL

Carlos E. S. Cesnik*

University of Michigan, Ann Arbor, Michigan
and

Eric L. Brown†

Massachusetts Institute of Technology, Cambridge, Massachusetts

Abstract

The study of wing-warping roll control for high-altitude long-endurance vehicle wings is the primary objective of this paper. For that, a formulation is developed for the preliminary design of high aspect ratio active flexible wings. The formulation captures the nonlinear (large) deflection behavior of the wings, the effects of anisotropic piezoelectric composites embedded in the skin, and the unsteady subsonic aerodynamic forces acting on the wing. Because the wing is long and slender, it can be modeled as a beam undergoing three dimensional displacements and rotations. The cross sectional stiffness, inertia, and actuation properties of the wing are calculated along the span, and then incorporated into the 1-D nonlinear beam model derived in this paper. Finite-state unsteady subsonic airloads are incorporated to complete the state space aeroelastic model. The result is a low order model, capable of representing the important aeroelastic behavior, suitable for preliminary structural design and control synthesis. The capabilities of the formulation are exemplified at the end. Among other things it is shown that the wing-warping control with embedded anisotropic piezocomposite actuators can be more effective than conventional aileron for roll control.

Introduction

In the design of aircraft wings, the goal is usually to minimize the weight of the aircraft structure for a given payload weight. In the optimal design process, the structural material of the wings is reduced until design constraints become active. Reducing the weight of the structure tends to produce wings that are more flexible,

making them prone to aeroelastic instability. At the optimal design point, it is possible that one or more of the constraints associated with strength and aeroelastic stability are active. Furthermore, flexible wings will undergo large deflections, making their aeroelastic response difficult to analyze and control using linear methods. Replacing the conventional flaps and ailerons with conformable surfaces with embedded anisotropic piezoelectric materials in the skin may lead to lighter designs. Two main reasons for that are:

1. The actuators are integral to the structure, and contribute to its overall stiffness; it eliminates the extra weight associated with hydraulic lines and mechanical linkages.
2. The active wings will be able to extend the flutter and divergence boundaries through active control, allowing for a new optimal design point to be reached, increasing the feasible design space.

Structural design of aircraft wings is an inherently iterative process. With flexible wings, this is complicated by the fact that the lift characteristics depend on the deformed shape of the wing, which cannot be accurately computed without simulation. Knowledge of how the active and passive composite constructions affect the overall aeroelastic behavior is critical for a successful design. In order for the active skin plies to have the mechanical coupling authority for producing the desired deformation, the active plies must contribute to the overall stiffness of the wings. Varying the active composite ply orientations in order to produce higher twist authority may make the wings less stiff in bending and lead to higher static deflections and aeroelastic instability. The design of the active part of the structure should be considered within the overall context of aeroelastic design.

The active wing may be able to exploit aeroelastic tailoring concepts to the limit, using wing flexibility to

* Associate Professor of Aerospace Engineering. Associate Fellow, AIAA. Member, AHS.

† Graduate Research Assistant. Mechanical Engineering.

Copyright©2002 by the authors. Published by the American Institute of Aeronautics and Astronautics, Inc., with permission.

improve performance rather than degrade it. At high dynamic pressure, flaps and ailerons may experience control reversal, due to the aerodynamic twisting moment experienced by the wing when the flaps are deflected. High frequency control surface actuation may excite structural or aeroelastic modes of the complete aircraft, or may produce no effect at all. Active induced-strain actuated wings may have the ability to overcome some of these problems.

There are different studies found in the literature that address some of the issues associated with highly-flexible active wings as discussed in this paper. One of the first active aeroelastic wing studies was conducted by Crawley and co-workers (e.g., Ref. [1]). They examined dominant issues in the preliminary design of a strain actuated aeroelastic wing. Scaling parameters were used to characterize the authority and effectiveness of the piezoelectric actuation. They studied the effects of composite fiber angle and sweep and used isotropic piezoelectric wafers to exploit bend-twist couplings for producing wing twist. The resulting active wing hardware was studied at NASA Langley under the PARTI wing program².

Librescu and co-workers have studied the use of adaptive materials to control the effects of pressure pulse loading on wings³. In this study, the wings were modeled as doubly tapered thin walled beams, taking into account the effects of transverse shear, warping inhibition, material anisotropy, and the effects of piezoactuators spread over the surface. The results detail the effects of wing parameters, such as ply angles, tapering, and actuator size, on the response due to various excitations.

Khot and co-workers have explored the active aeroelastic wing concept⁴ by using elastic twist and camber deformation in a fighter-type wing (e.g., Ref. [5]). The goal was to enhance roll maneuver performance at high dynamic pressures. Therein, a full-scale conventional wing construction was considered for the assessment of the strain energy required to produce the antisymmetric twist and camber deformation needed for a given roll performance. The actuators that would generate the deformation were not defined in the study and therefore their effects on the aeroelastic characteristics of the wing could not be accounted.

Jones and co-workers have worked on high-altitude long-endurance (HALE) vehicle design during the last decade (e.g., Ref. [6]). They describe some of the design challenges associated with these vehicles. Among other things, they show that standard initial aircraft design techniques such as EDSU data sheets are

not applicable for these wings as the altitude and aspect ratio increase.

Patil and co-workers have studied the nonlinear behavior of flexible wings undergoing large deflections. In Ref. [7], the necessity for including higher-order nonlinear effects to accurately model the aeroelastic behavior is detailed. In particular, a linear aeroelastic analysis based on the undeformed geometry will lead to erroneous results when the wings are highly flexible. To accurately model the behavior, the wings must be brought to their nonlinear equilibrium condition before the analysis can proceed. From there, a stability analysis can be performed on the linearized model. It was found that the flutter speed tends to decrease when the wing tip displacements increase. This effect can only be obtained if the wings are first brought to the nonlinear static equilibrium through an iterative process. The main reasons for the changes in aeroelastic behavior as the wings deform are that both the structural modes and the influence of aerodynamic forces onto the structure change considerably as the deformation increases. The first chord-wise bending mode of the straight wing, for instance, will tend towards a rocking mode as the tip deflection increases, and may coalesce with the first torsion mode. Another important result of Ref. [7] is that the total lift predicted from a linear model will generally be higher than the actual lift. As the wing deforms, the direction of the lift forces rotate with the wing, and do not remain parallel.

In Ref. [8], Drela modeled the complete flexible aircraft as an assemblage of joined nonlinear beams and applied aerodynamic strip theory. The resulting nonlinear equation set is solved by a full Newton method. Through simplifications of the model, the computational size is made small enough for interactive preliminary design.

Cesnik and Ortega-Morales present a framework for studying the effects of combined bending and twisting actuation on the aeroelastic performance of highly-flexible active composite wings^{9,10}. Therein, the nonlinear active aeroelastic analysis consists of an asymptotically correct active cross section formulation, geometrically-exact mixed formulation for dynamics of moving beams, and a finite-state unsteady aerodynamics model. LQG controllers were designed to alleviate gust loads and to extend the flutter boundary.

To navigate the rich structural design space of active flexible wings requires a large degree of iteration. The ongoing work intends to develop a framework for the integrated active structure and control design for

studying the behavior of these wings. The derivation of the equations of motion for the two-wing active roll model is discussed in this paper. First a nonlinear beam model is derived in which the effects of embedded anisotropic piezoelectric strain actuation are taken into account. Then the principle of virtual work is employed to arrive at the equations of motion for the rigid roll/flexible wing structure. A finite-state unsteady airloads model^{11,12} is incorporated to complete the aeroelastic model. Finally, the equations are developed in state-space form to facilitate control synthesis.

Formulation

For the present study, the vehicle is treated as a rigid body free to roll. The wings are allowed fully coupled three-dimensional bending and twisting deformation. It is assumed that extensional and shear deformations play a negligible role in the overall wing deformation.

Kinematics

Three reference frames are used in this study. The global frame is represented by a , with gravity pointing in the negative z direction. The body frame, b , is fixed to the fuselage, and is initially aligned with frame a before being taken through two rotations. First, as shown in Fig. 1, the body is rotated about the x axis by α_b , the body angle of attack. Then the body is rotated about its y -axis by ϕ , the roll angle. The orientation of the body with respect to the global frame is given by

$$C^{ab} = \begin{bmatrix} 1 & 0 & 0 \\ 0 & \cos \alpha_b & -\sin \alpha_b \\ 0 & \sin \alpha_b & \cos \alpha_b \end{bmatrix} \begin{bmatrix} \cos \phi & 0 & \sin \phi \\ 0 & 1 & 0 \\ -\sin \phi & 0 & \cos \phi \end{bmatrix} \quad (1)$$

Angle α_b is fixed and is not considered a motion variable in this study.

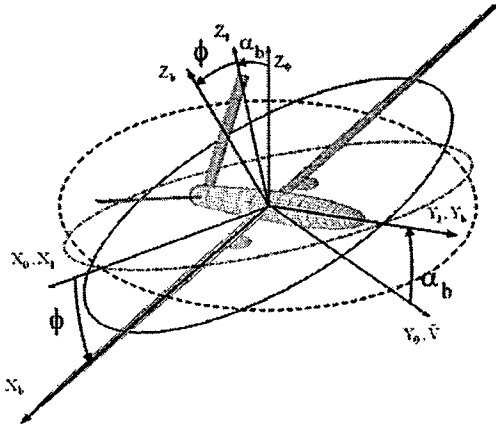


Figure 1: Global and Body Coordinate Systems

The local beam (wing) coordinate system, w , is constructed from the local unit direction vectors, u_x , u_y , and u_z , attached to the deformed beam reference line as shown in Fig. 2. The direction vectors are defined with respect to frame b unless otherwise subscripted.

The vehicle velocity with respect to the body frame is given by

$$V_b = C^{ba} V_a \quad (2)$$

where V_a is the velocity in the global frame.

Since the wings are long and slender, they can be well modeled as beams undergoing fully coupled three-dimensional deformation. Because of the large deformation due to wing flexibility, a nonlinear formulation is derived that describes the motion of the reference line. The beam reference line is treated as a three dimensional line of constant length, with bending and torsion deformation. The shape of the line is determined by the distribution of curvature, $\kappa_x(s)$, $\kappa_y(s)$, $\kappa_z(s)$.

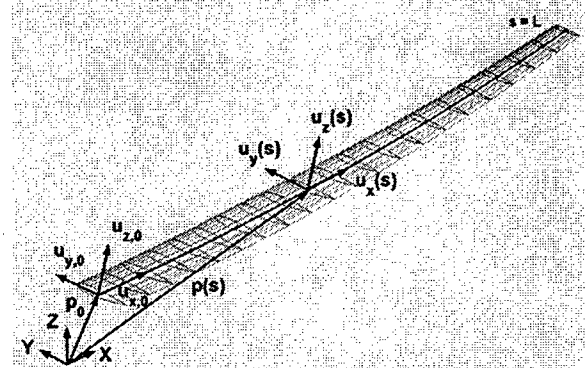


Figure 2: Wing Coordinate System

Assuming that the wing deformation is dominated by bending and twisting deformation, i.e., the extensional and shear strains play a negligible role in the gross deformation, the beam direction vectors can be obtained from the differential equations

$$\begin{aligned} \frac{d}{ds} u_x(s) &= \kappa_z(s) u_y(s) - \kappa_y(s) u_z(s) \\ \frac{d}{ds} u_y(s) &= \kappa_x(s) u_z(s) - \kappa_z(s) u_x(s) \\ \frac{d}{ds} u_z(s) &= \kappa_y(s) u_x(s) - \kappa_x(s) u_y(s) \end{aligned} \quad (3)$$

The above equation is expressed in a more compact form as

$$\frac{d}{ds} u(s) = K(s) u(s) \quad (4)$$

where

$$u = \begin{Bmatrix} u_x \\ u_y \\ u_z \end{Bmatrix}, K = \begin{bmatrix} 0 & I\kappa_z & -I\kappa_y \\ -I\kappa_z & 0 & I\kappa_x \\ I\kappa_y & -I\kappa_x & 0 \end{bmatrix} \quad (5)$$

and I is the 3×3 identity matrix. The transformation matrix from the local deformed wing frame to the body frame is constructed from the local direction vectors

$$C^{wb}(s) = \begin{bmatrix} : & : & : \\ u_x(s) & u_y(s) & u_z(s) \\ : & : & : \end{bmatrix} \quad (6)$$

A vector expressed in frame w , can be expressed in frame b by the transformation

$$v_b = C^{wb} v_w = v_{w_x} u_x + v_{w_y} u_y + v_{w_z} u_z \quad (7)$$

The position, $p(s)$, of a point on the reference line can be found from the relation

$$\frac{d}{ds} p(s) = u_x(s) \quad (8)$$

Given the initial condition at the wing root, the shape of the wing is completely defined by the distribution of curvature along the beam coordinate, s .

Using curvature as the primary kinematic variables has several advantages. First, the shape of the reference line is completely defined by three variables along the coordinate, s , instead of six to twelve required when displacements and rotations are used as the independent variables. Since no extra variables are used to define the shape of the reference line, the need for constraint equations is eliminated. Second, when solving for the motion of the reference line, no singularities exist in the solution. Furthermore, it is generally more difficult to solve for the strain variables from the displacement variables than vice-versa.

Virtual Work Formulation

The total virtual work done on the vehicle is found by integrating over the volume all internal and external forces times their corresponding displacements, and is given in a general form by

$$\delta W = \int_V (f(x, y, z) \delta \zeta'(x, y, z)) dV \quad (9)$$

where f represents all generalized forces acting on a differential volume element, including the inertial forces distributed over the element, pressure forces applied to any free surfaces, and internal elastic and

piezoelectric stresses, and $\delta \zeta'$ is the corresponding virtual displacement.

This equation can be simplified through the assumed kinematical and constitutive relations of the present problem. The fuselage is treated as a rigid body with only roll degree of freedom and center of gravity on the roll axis, and the wings as beams (lines with mass, inertia, and stiffness) with three dimensional curvature, so the virtual work done on the vehicle is written as

$$\begin{aligned} \delta W = & -\delta \phi I_{fus} \ddot{\phi} \\ & + \int_{s=0}^L (\delta p^T F + \delta \theta^T M + \delta \kappa^T M^{int}) ds \Big|_{\text{right wing}} \\ & + \int_{s=0}^L (\delta p^T F + \delta \theta^T M + \delta \kappa^T M^{int}) ds \Big|_{\text{left wing}} \end{aligned} \quad (10)$$

The kinematic variables that describe the rigid and flexible motion of the vehicle are

$$q = \{\kappa(s_R), \kappa(s_L), \phi\} \quad (11)$$

where the subscripts R and L correspond to quantities associated with the right and left wing, respectively. Furthermore, it is assumed that the curvature variables can be interpolated from discrete values at linearly spaced coordinates along the beam reference line. So that the complete set of discrete kinematic variables is given by

$$\underline{q} = \begin{Bmatrix} \underline{\kappa}_R \\ \underline{\kappa}_L \\ \phi \end{Bmatrix} \quad (12)$$

where $\underline{\kappa}_R$ and $\underline{\kappa}_L$ are columns containing the $\{x, y, z\}$ curvature variables at the node locations, and ϕ is the roll angle. For the rest of this paper, the notation (\bullet) will be used to denote a column vector of nodal quantities.

The position and orientation of the local coordinate system fixed to the beam reference line are dependent variables given by

$$\begin{aligned} \underline{P}_R &= \underline{P}(\underline{\kappa}_R) & \underline{P}_L &= \underline{P}(\underline{\kappa}_L) \\ \underline{u}_{x,R} &= \underline{u}_{x,R}(\underline{\kappa}_R) & \underline{u}_{x,L} &= \underline{u}_{x,L}(\underline{\kappa}_L) \\ \underline{u}_{y,R} &= \underline{u}_{y,R}(\underline{\kappa}_R) & \underline{u}_{y,L} &= \underline{u}_{y,L}(\underline{\kappa}_L) \\ \underline{u}_{z,R} &= \underline{u}_{z,R}(\underline{\kappa}_R) & \underline{u}_{z,L} &= \underline{u}_{z,L}(\underline{\kappa}_L) \end{aligned} \quad (13)$$

where P_i is the position of the i th node with respect to the body coordinate system, fixed at the fuselage centerline and $u_{x,i}$, $u_{y,i}$, and $u_{z,i}$ are the orthogonal unit

direction vectors that define the local coordinate system at the i th node.

The specific terms in the integration of Eq. (10) will be described later and the result is given by

$$\delta W = \delta \underline{q}^T (-M_q \ddot{\underline{q}} - C_q \dot{\underline{q}} - K_q \underline{q} + \underline{R}_q) \quad (14)$$

where M_q , C_q , and K_q are the mass, damping, and stiffness matrices, respectively, and \underline{R}_q contains the effects of external loads and applied voltage to the piezoelectric plies within the wing construction. In Eq. (14), the total virtual work contributed by each virtual displacement must be zero, since the virtual displacements are arbitrary. Then, the term in parentheses must vanish, giving the second order structure equations of motion

$$M_q \ddot{\underline{q}} + C_q \dot{\underline{q}} + K_q \underline{q} = \underline{R}_q \quad (15)$$

The system matrices and load vector are described next.

Beam Discretization

The reference axis is discretized at n_k equally spaced coordinates, \underline{s}_k , between which the curvature is assumed to vary linearly (Fig. 3). The $3n_k \times 1$ column matrix of nodal curvatures, given by

$$\underline{\kappa} = \begin{Bmatrix} \kappa_x \\ \kappa_y \\ \kappa_z \end{Bmatrix} \quad (16)$$

which are the curvature variables that define the beam geometry with respect to the body.



Figure 3: Discretization of the beam reference line

Mid-nodes are used to represent displacement variables so that a second set of coordinates, \underline{s}_p , will be used frequently. For the purpose of numerical integration, a fine spacing coordinate set, \underline{s}_f , is also used. An array of distributed beam properties, $\underline{m}(\underline{s}_p)$, defined at \underline{s}_p , can be interpolated onto the fine spacing using an interpolating matrix

$$\underline{m}_f = [a_p^f] \underline{m}_p \quad (17)$$

The integral of the product of two or more functions of the beam coordinate may be performed using the following relation

$$\int_{s=0}^L h(s)g(s)ds \equiv \underline{h}^T [a_p^f]^T [a_p^f] \underline{g} \Delta s_f \quad (18)$$

where Δs_f is the fine coordinate spacing. Similarly, a column matrix of nodal x , y , and z vector components is denoted

$$\underline{F} = \begin{Bmatrix} F_x \\ F_y \\ F_z \end{Bmatrix} \quad (19)$$

and may be integrated using the matrix relation

$$\int_{s=0}^L F(s)G(s)ds \equiv \underline{F}^T [A_p^f]^T [A_p^f] \underline{G} \Delta s_f \quad (20)$$

where

$$[A_p^f] = \begin{bmatrix} a_p^f & 0 & 0 \\ 0 & a_p^f & 0 \\ 0 & 0 & a_p^f \end{bmatrix} \quad (21)$$

Starting with the position and orientation of the beam root attachment point, and using the assumption that curvature varies linearly between the nodes, an approximate solution to Eq. (4) is obtained by marching the solution forward from the wing root,

$$\begin{aligned} u_{i+1} &= e^{G_i} u_i \\ p_{i+1} &= p_i + \frac{1}{2} \Delta s (\dot{u}_{x,i} + \dot{u}_{x,i+1}) \end{aligned} \quad (22)$$

where

$$G_i = \frac{1}{2} \Delta s (K_i + K_{i+1}) \quad (23)$$

Nodal velocities, accelerations, and partial derivatives can be obtained by differentiation of Eq. (22)

$$\begin{aligned} \dot{u}_{i+1} &= \dot{G}_i e^{G_i} u_i + e^{G_i} \dot{u}_i \\ \dot{p}_{i+1} &= \dot{p}_i + \frac{1}{2} \Delta s (\ddot{u}_{x,i} + \ddot{u}_{x,i+1}) \end{aligned} \quad (24)$$

$$\begin{aligned} \ddot{u}_{i+1} &= \ddot{G}_i e^{G_i} u_i + \dot{G}_i \dot{u}_{i+1} + e^{G_i} \ddot{u}_i \\ \ddot{p}_{i+1} &= \ddot{p}_i + \frac{1}{2} \Delta s (\ddot{u}_{x,i} + \ddot{u}_{x,i+1}) \end{aligned} \quad (25)$$

$$\frac{\partial u_{i+1}}{\partial \kappa_{x,j}} = \frac{\partial G_i}{\partial \kappa_{x,j}} e^{G_i} u_i + e^{G_i} \frac{\partial u_i}{\partial \kappa_{x,j}} \quad (26)$$

and the velocities at the root are given by

$$\begin{aligned} \dot{u}_{s=0} &= \omega_f \times u_{s=0} \\ \dot{p}_{s=0} &= V + \omega_f \times p_{s=0} \end{aligned} \quad (27)$$

where ω_j is the fuselage angular velocity. The angular velocity at a node, and the derivative of the i th rotation variable with respect to the j th curvature variable can be expressed in frame b using the motion of the direction vectors

$$\dot{\theta} = C^{wb} \begin{Bmatrix} \dot{u}_y \cdot u_z \\ \dot{u}_z \cdot u_x \\ \dot{u}_x \cdot u_y \end{Bmatrix}, \quad \frac{\partial \theta_i}{\partial \kappa_j} = C_i^{wb} \begin{Bmatrix} \frac{\partial u_{y,i}}{\partial \kappa_j} \cdot u_{z,i} \\ \frac{\partial u_{z,i}}{\partial \kappa_j} \cdot u_{x,i} \\ \frac{\partial u_{x,i}}{\partial \kappa_j} \cdot u_{y,i} \end{Bmatrix} \quad (28)$$

where κ_j is a nodal curvature variable, as in Eq. (16). The nodal displacement and rotation variables for a wing are related to the curvature and roll variables through a set of kinematic relations,

$$\begin{Bmatrix} \delta P \\ \delta u_i \end{Bmatrix} = \begin{bmatrix} J_\kappa^P & J_\phi^P \\ J_\kappa^{u_i} & J_\phi^{u_i} \end{bmatrix} \begin{Bmatrix} \delta \kappa \\ \delta \phi \end{Bmatrix} \quad (29)$$

$$\begin{Bmatrix} \dot{P} \\ \dot{u}_i \end{Bmatrix} = \begin{bmatrix} J_\kappa^P & J_\phi^P \\ J_\kappa^{u_i} & J_\phi^{u_i} \end{bmatrix} \begin{Bmatrix} \dot{\kappa} \\ \dot{\phi} \end{Bmatrix} \quad (30)$$

$$\begin{Bmatrix} \ddot{P} \\ \ddot{u}_i \end{Bmatrix} = \begin{bmatrix} J_\kappa^P & J_\phi^P \\ J_\kappa^{u_i} & J_\phi^{u_i} \end{bmatrix} \begin{Bmatrix} \ddot{\kappa} \\ \ddot{\phi} \end{Bmatrix} + \begin{bmatrix} \dot{J}_\kappa^P & \dot{J}_\phi^P \\ \dot{J}_\kappa^{u_i} & \dot{J}_\phi^{u_i} \end{bmatrix} \begin{Bmatrix} \dot{\kappa} \\ \dot{\phi} \end{Bmatrix} \quad (31)$$

where $i = x, y, z$ and the elements of the Jacobian matrices in these equations are constructed by applying the relationships in Eqs. (22)–(26). The nodal angular velocity and accelerations are determined by applying the relations in Eq. (28).

Coriolis and centrifugal accelerations are accounted for in the velocity terms. Note that in these relations the nodal position and direction vectors, P and u , do not depend on the orientation of the body since they are defined with respect to the body frame. The virtual displacements, velocities, and accelerations, however, are absolute quantities represented in the body frame, and therefore depend on body motion.

Inertia and Gravity Loads

The inertial and gravitational forces acting on each volume element of the wings and wing stores are considered. The total virtual work is derived in a form which is compatible with the beam motion variables. The position and acceleration of a point, a , in a body A can be given by

$$\begin{aligned} p_a &= p_A + xu_x + yu_y + zu_z \\ &= R_a h_A \end{aligned} \quad (32)$$

$$R_a = [1 \ x \ y \ z] \quad (33)$$

$$h_A^T = [p_A^T \ u_x^T \ u_y^T \ u_z^T] \quad (34)$$

where p_A is the position of the origin of a coordinate system fixed in A with respect to an inertial frame, and $\{x, y, z\}$ is the position of point a in the body, with respect to that local coordinate system.

The inertial and gravitational forces acting on a differential volume element are given by

$$F_a = \rho(-\ddot{p}_a + g)dV = \rho(-R_a \ddot{h}_A + g)dV \quad (35)$$

where ρ is the density and g is the gravity vector. The virtual work done on a volume element in the body due to the inertial and gravitational forces acting on it is given by

$$\delta W_a = \delta p_a^T F_a = \delta h_A^T \rho (R_a^T g - R_a^T R_a \ddot{h}_A) dV \quad (36)$$

The total virtual work acting on body A is found by integrating Eq. (36) over the volume,

$$\delta W_A = \delta h_A^T (N_A g_A - M_A \ddot{h}_A) \quad (37)$$

where

$$N_A = \begin{bmatrix} m \\ mr_x \\ mr_y \\ mr_z \end{bmatrix}, \quad M_A = \begin{bmatrix} m & mr_x & mr_y & mr_z \\ mr_x & A_{xx} & A_{xy} & A_{xz} \\ mr_y & A_{yx} & A_{yy} & A_{yz} \\ mr_z & A_{zx} & A_{zy} & A_{zz} \end{bmatrix} \quad (38)$$

m is the mass of the body, or mass per length for a cross section, $\{r_x, r_y, r_z\}$ are the center of gravity offsets in the local coordinate system, and the constants A_{ij} are closely related to the elements of the rigid body inertia matrix, I_{ij} ,

$$\begin{aligned} A_{xx} &= \int_V \rho x^2 dV = mr_x^2 + \frac{1}{2}(I_{yy} + I_{zz} - I_{xx}) \\ A_{yy} &= \int_V \rho y^2 dV = mr_y^2 + \frac{1}{2}(I_{xx} + I_{zz} - I_{yy}) \\ A_{zz} &= \int_V \rho z^2 dV = mr_z^2 + \frac{1}{2}(I_{xx} + I_{yy} - I_{zz}) \\ A_{xy} &= A_{yx} = \int_V \rho xy dV = mr_x r_y + I_{xy} \\ A_{xz} &= A_{zx} = \int_V \rho xz dV = mr_x r_z + I_{xz} \\ A_{yz} &= A_{zy} = \int_V \rho yz dV = mr_y r_z + I_{yz} \end{aligned} \quad (39)$$

where I_{ij} are taken about the center of gravity. Eq. (37) represents the total inertial and gravitational virtual work acting on a rigid body, such as an engine, or the virtual work per length acting on a wing cross section. The total virtual work done on the flexible part of the wing structure is found by integrating along the beam reference line, yielding

$$\delta W = \int_{s=0}^L \delta W_A(s) ds = \delta \underline{h}^T (N_h \underline{g} - M_h \ddot{\underline{h}}) \quad (40a)$$

where

$$M_h = \begin{bmatrix} M_{11} & M_{12} & M_{13} & M_{14} \\ M_{21} & M_{22} & M_{23} & M_{24} \\ M_{31} & M_{32} & M_{33} & M_{34} \\ M_{41} & M_{42} & M_{43} & M_{44} \end{bmatrix} \quad N_h = \begin{bmatrix} M_{11} \\ M_{21} \\ M_{31} \\ M_{41} \end{bmatrix} \quad (40b)$$

and \underline{h} is a column matrix of nodal displacement variables. The M_{ij} contain mass properties and performs the integration of Eq. (40), i.e.,

$$\begin{aligned} \delta \underline{P}^T M_{11} \ddot{\underline{P}} &= \int_{s=0}^L \delta \underline{p}(s)^T m(s) \ddot{\underline{p}}(s) ds \\ \delta \underline{u}_x^T M_{23} \ddot{\underline{u}}_y &= \int_{s=0}^L \delta \underline{u}_x(s)^T A_{xy}(s) \ddot{\underline{u}}_y(s) ds \end{aligned} \quad (41)$$

and so on, and are constructed using the relations given by Eqs. (17)-(21).

Considering all of the vehicle motion, the total virtual work due to inertial forces acting on the vehicle is established

$$\delta W^{acc} = \delta \underline{H}^T (N_H \underline{g} - M_H \ddot{\underline{H}}) \quad (42)$$

where

$$\underline{H}^T = \{\underline{h}_R^T, \underline{h}_L^T, \phi\} \quad (43)$$

$$M_H = \begin{bmatrix} M_h & 0 & 0 \\ 0 & M_h & 0 \\ 0 & 0 & I_f \end{bmatrix} \quad N_H = \begin{bmatrix} N_h \\ N_h \\ 0 \end{bmatrix} \quad (44)$$

and I_f is the fuselage roll inertia. Eq. (42) can be written in terms of the curvature and roll variables by applying Eqs. (29) and (31), and constructing the Jacobian matrix,

$$\delta \underline{H} = J \delta \underline{q} \quad , \quad \ddot{\underline{H}} = J \ddot{\underline{q}} + \dot{J} \dot{\underline{q}} \quad (45)$$

with

$$J = \begin{bmatrix} J_{\kappa_R}^P & 0 & J_{\phi_R}^P \\ J_{\kappa_R}^{ux} & 0 & J_{\phi_R}^{ux} \\ J_{\kappa_R}^{uy} & 0 & J_{\phi_R}^{uy} \\ J_{\kappa_R}^{uz} & 0 & J_{\phi_R}^{uz} \\ 0 & J_{\kappa_L}^P & J_{\phi_L}^P \\ 0 & J_{\kappa_L}^{ux} & J_{\phi_L}^{ux} \\ 0 & J_{\kappa_L}^{uy} & J_{\phi_L}^{uy} \\ 0 & J_{\kappa_L}^{uz} & J_{\phi_L}^{uz} \\ 0 & 0 & 1 \end{bmatrix} \quad , \quad \dot{J} = \begin{bmatrix} j_{\kappa_R}^P & 0 & j_{\phi_R}^P \\ j_{\kappa_R}^{ux} & 0 & j_{\phi_R}^{ux} \\ j_{\kappa_R}^{uy} & 0 & j_{\phi_R}^{uy} \\ j_{\kappa_R}^{uz} & 0 & j_{\phi_R}^{uz} \\ 0 & j_{\kappa_L}^P & j_{\phi_L}^P \\ 0 & j_{\kappa_L}^{ux} & j_{\phi_L}^{ux} \\ 0 & j_{\kappa_L}^{uy} & j_{\phi_L}^{uy} \\ 0 & j_{\kappa_L}^{uz} & j_{\phi_L}^{uz} \\ 0 & 0 & 0 \end{bmatrix} \quad (46)$$

The total virtual work becomes

$$\delta W^{acc} = \delta \underline{q}^T J^T (-M_H J \ddot{\underline{q}} - M_H \dot{J} \dot{\underline{q}} + N_H \underline{g}) \quad (47)$$

In this equation, the coriolis and centrifugal effects are contained in the second term in parentheses.

Aerodynamic Loads

The aerodynamic loads used in the present work are based on the formulation of Refs. [11] and [12]. The theory calculates loads on a thin deformable airfoil undergoing large motion in a subsonic flow, with small deformations about that motion. In the present approach, the airloads are written in terms of the total instantaneous motion of the airfoil, and then a Taylor expansion is used. The lift, moment, and drag are given by

$$\begin{aligned} L &= 2\pi\rho b \left(\dot{y} \left[\left(\frac{1}{2}b - d \right) \dot{\alpha} - \dot{z} - \lambda_0 \right] - \frac{1}{2}b\ddot{z} - \frac{1}{2}b d \ddot{\alpha} \right) \\ M &= 2\pi\rho b \left(\dot{y} \left[- \left(d + \frac{1}{2}b \right) \dot{z} - \left(d + \frac{1}{2}b \right) \lambda_0 - d^2 \dot{\alpha} \right] \right. \\ &\quad \left. - \frac{1}{2}b d \ddot{z} - \frac{1}{2}b (d^2 + \frac{1}{8}b^2) \ddot{\alpha} \right) \\ D &= -2\pi\rho b (\dot{z}^2 + d^2 \dot{\alpha}^2 + \lambda_0^2 + 2d\dot{\alpha}\dot{z} + 2\lambda_0\dot{z} + 2d\dot{\alpha}\lambda_0) \end{aligned} \quad (48)$$

where b is the semichord, d is the distance of the mid-chord in front of the reference axis, and λ_0 is the induced flow due to free vorticity. The motion variables are defined in Fig. 4.

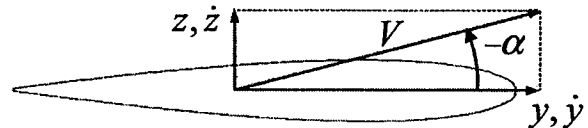


Figure 4: Airfoil motion definition

The inflow is obtained through the finite-state inflow theory¹¹, and is represented in terms of N states ($\lambda_1, \lambda_2, \dots, \lambda_N$) as

$$\lambda_0 = \frac{1}{2} \sum_{n=1}^N b_n \lambda_n \quad (49)$$

where the b_n are found by least squares method, and the λ_n can be expressed as a set of differential equations, expressed here as

$$\dot{\lambda} = E_1 \lambda + E_2 \ddot{z} + E_3 \ddot{\alpha} + E_4 \dot{\alpha} \quad (50)$$

where the matrices, E_i , are based on the description given in Ref. [12]. The airloads are linearized about time t_a by making the substitutions,

$$\begin{aligned} \dot{y} &= (\dot{y}_a + \Delta \dot{y}) \\ \dot{z} &= (\dot{z}_a + \Delta \dot{z} - \dot{y}_a \Delta \alpha) \\ \dot{\alpha} &= (\dot{\alpha}_a + \Delta \dot{\alpha}) \\ \lambda_0 &= (\lambda_{0,a} + \Delta \lambda_0) \end{aligned} \quad (51)$$

which to first order gives the linearized lift, moment, and drag as

$$\begin{aligned} L &= L_a + L_{\dot{\alpha}} \Delta \dot{\alpha} + L_{\dot{y}} \Delta \dot{y} + L_{\dot{z}} \Delta \dot{z} \\ &\quad + L_{\alpha} \Delta \alpha + L_{\lambda_0} \Delta \lambda_0 + L_{\ddot{z}} \ddot{z} + L_{\ddot{\alpha}} \ddot{\alpha} \\ M &= M_a + M_{\dot{\alpha}} \Delta \dot{\alpha} + M_{\dot{y}} \Delta \dot{y} + M_{\dot{z}} \Delta \dot{z} \\ &\quad + M_{\alpha} \Delta \alpha + M_{\lambda_0} \Delta \lambda_0 + M_{\ddot{z}} \ddot{z} + M_{\ddot{\alpha}} \ddot{\alpha} \\ D &= D_a + D_{\dot{\alpha}} \Delta \dot{\alpha} + D_{\dot{y}} \Delta \dot{y} + D_{\dot{z}} \Delta \dot{z} \\ &\quad + D_{\alpha} \Delta \alpha + D_{\lambda_0} \Delta \lambda_0 + D_{\ddot{z}} \ddot{z} + D_{\ddot{\alpha}} \ddot{\alpha} \end{aligned} \quad (52)$$

where the lift terms are given here as

$$\begin{aligned} L_a &= 2\pi\rho b \left(\left(\frac{1}{2}b - d \right) \dot{y}_a \dot{\alpha}_a - \dot{y}_a \dot{z}_a - \dot{y}_a \lambda_{0,a} \right) \\ L_{\dot{\alpha}} &= 2\pi\rho b \left(\frac{1}{2}b - d \right) \dot{y}_a \\ L_{\dot{y}} &= 2\pi\rho b \left[\left(\frac{1}{2}b - d \right) \dot{\alpha}_a - \dot{z}_a \right] \\ L_{\dot{z}} &= -2\pi\rho b \dot{y}_a \\ L_{\alpha} &= 2\pi\rho b \dot{y}_a^2 \\ L_{\lambda_0} &= -2\pi\rho b \dot{y}_a \\ L_{\ddot{z}} &= -\pi\rho b^2 \\ L_{\ddot{\alpha}} &= -\pi\rho b^2 d \end{aligned} \quad (53)$$

and similarly for the drag and moment terms.

The virtual work done by these forces acting over the wing is given by

$$\delta W = \int_{s=0}^L (L \delta x + D \delta y + M \delta \alpha) ds \quad (54)$$

The integration is performed by evaluating the aerodynamic forces and moments at the nodes, and using the interpolation functions so that Eq. (54) can be expressed as

$$\delta W^{aero} = \delta \underline{p}^T B_F \underline{F}^{aero} + \delta \underline{\theta}^T B_M \underline{M}^{aero} \quad (55a)$$

where

$$\underline{F}^{aero} = \begin{Bmatrix} 0 \\ D \\ L \end{Bmatrix}, \quad \underline{M}^{aero} = \begin{Bmatrix} M_x \\ 0 \\ 0 \end{Bmatrix} \quad (55b)$$

After some manipulation, the virtual work can be written in terms of the vehicle degrees of freedom as

$$\delta W^{aero} = \delta \underline{q}^T \left(B_2 \begin{Bmatrix} \underline{F}_R^{aero} \\ \underline{F}_L^{aero} \end{Bmatrix} + B_3 \begin{Bmatrix} \underline{M}_R^{aero} \\ \underline{M}_L^{aero} \end{Bmatrix} \right) \quad (56)$$

where the nodal aerodynamic forces and moments can be linearized about the instantaneous state, $\{q_0, \dot{q}_0\}^T$, as

$$\begin{Bmatrix} \underline{F} \\ \underline{M} \end{Bmatrix} = \begin{Bmatrix} \underline{F}_0 \\ \underline{M}_0 \end{Bmatrix} + \begin{bmatrix} F_{\dot{q}} & F_{\ddot{q}} & F_q \\ M_{\dot{q}} & M_{\ddot{q}} & M_q \end{bmatrix} \begin{Bmatrix} \ddot{q} \\ \Delta \dot{q} \\ \Delta q \end{Bmatrix} + \begin{bmatrix} F_{\lambda} & F_w \\ M_{\lambda} & M_w \end{bmatrix} \begin{Bmatrix} \lambda \\ w \end{Bmatrix} \quad (57)$$

where $\Delta q = q - q_0$, and q_0 is the system state where the instantaneous loads are evaluated. Here, gust input, w , was introduced, which enters the equations in the same way as the airfoil velocity terms.

Internal Elastic and Piezoelectric Forces and Moments

The internal elastic and piezoelectric forces and moments constitutive relation may be obtained from a thin-walled model, such as given in Ref. [13], or from a more general finite element program such as VABS-A¹⁴, and are symbolic represented by

$$\begin{Bmatrix} F_1 \\ M_1 \\ M_2 \\ M_3 \end{Bmatrix} = \begin{Bmatrix} F_1 \\ M_1 \\ M_2 \\ M_3 \end{Bmatrix}^e - \begin{Bmatrix} F_1 \\ M_1 \\ M_2 \\ M_3 \end{Bmatrix}^a \quad (58)$$

where F_1 is the extensional force, M_1 , M_2 , and M_3 , are the moments about the local x , y , and z axes. The total internal forces and moments are based on the 4x4 stiffness constitutive relation,

$$\begin{Bmatrix} F_1 \\ M_1 \\ M_2 \\ M_3 \end{Bmatrix}^e = \begin{bmatrix} K_{11} & K_{12} & K_{13} & K_{14} \\ K_{21} & K_{22} & K_{23} & K_{24} \\ K_{31} & K_{32} & K_{33} & K_{34} \\ K_{41} & K_{42} & K_{43} & K_{44} \end{bmatrix} \begin{Bmatrix} \epsilon_x \\ \kappa_x \\ \kappa_y \\ \kappa_z \end{Bmatrix} \quad (59)$$

and the piezoelectric forcing is given by

$$\begin{Bmatrix} F_1 \\ M_1 \\ M_2 \\ M_3 \end{Bmatrix}^a = \begin{bmatrix} B_{11} & B_{12} & \cdots & B_{1,m} \\ B_{21} & B_{22} & \cdots & B_{2,m} \\ B_{31} & B_{32} & \cdots & B_{3,m} \\ B_{41} & B_{42} & \cdots & B_{4,m} \end{bmatrix} \begin{Bmatrix} v_1 \\ v_2 \\ \vdots \\ v_m \end{Bmatrix} \quad (60)$$

where v_i is the voltage applied to the i th active ply in the cross section. Each active region along the span has m voltage degrees of freedom, where m is the number of active plies in the cross section.

Since the external forces in the span-wise direction are small, the internal extensional elastic and piezoelectric force are assumed to be in balance. Then by setting F_1 equal to zero, the first equation can be condensed out by a suitable matrix manipulation.

$$\begin{Bmatrix} F \\ M \end{Bmatrix} = \begin{Bmatrix} 0 \\ M \end{Bmatrix} = \begin{bmatrix} K_{aa} & K_{ab} \\ K_{ba} & K_{bb} \end{bmatrix} \begin{Bmatrix} \epsilon_x \\ \kappa \end{Bmatrix} - \begin{bmatrix} B_a \\ B_b \end{bmatrix} \{v\}$$

$$\epsilon_x = [K_{aa}]^{-1}([B_a]\{v\} - [K_{ab}]\{\kappa\}) \quad (61)$$

$$[K] = [K_{bb}] - [K_{ba}][K_{aa}]^{-1}[K_{ab}]$$

$$[B] = [B_b] - [K_{ba}][K_{aa}]^{-1}[B_a]$$

$$\{M\} = [B]\{v\} - [K]\{\kappa\}$$

This allows for the extensional strains to be eliminated from the wing dynamics while retaining the effects of extension/twist and extension/bend couplings, and the ability to recover extensional stresses and strains for ply failure analysis.

The virtual work done on a wing against the internal elastic and piezoelectric forces by a variation in each of the curvature variables is given by

$$\delta W^{\text{internal}} = \int_{s=0}^L \delta \bar{\kappa}^T \{B \bar{v} - K(\bar{\kappa} - \bar{\kappa}_i)\} ds \quad (62)$$

$$= \delta \underline{\kappa}^T \{B_v \underline{v} - K_\kappa (\underline{\kappa} - \underline{\kappa}_i)\}$$

Equations of Motion

After gathering terms from the previous section, the total virtual work done on the vehicle becomes

$$\delta W = \delta \underline{q}^T (-M_q \ddot{\underline{q}} - C_q \dot{\underline{q}} - K_q \underline{q} + B_1 \underline{v} + B_2 \underline{F}^{\text{aero}} + B_3 \underline{M}^{\text{aero}} + B_4 \underline{G}_b + B_5 \underline{\kappa}_i) \quad (63)$$

where all the coefficient matrices except for the stiffness and voltage influence matrices depend on the current wing position.

The structure equations of motion are obtained by requiring that the net virtual work due to each virtual displacement is zero,

$$\frac{\partial \delta W}{\partial \delta q_i} = 0 \quad (64)$$

from which the second order equations of motion arise,

$$M_q \ddot{\underline{q}} + C_q \dot{\underline{q}} + K_q \underline{q} = B_1 \underline{v} + B_2 \underline{F}^{\text{aero}} + B_3 \underline{M}^{\text{aero}} + B_4 \underline{G}_b + B_5 \underline{\kappa}_i \quad (65)$$

The equations of motion for the single wing fixed at the root are obtained by retaining only the curvature degrees of freedom for that wing and has the form

$$M_{RR} \ddot{\underline{\kappa}} + C_{RR} \dot{\underline{\kappa}} + K_{RR} \underline{\kappa} = B_{1R} \underline{v}_R + B_{2R} \underline{F}_R^{\text{aero}} + B_{3R} \underline{M}_R^{\text{aero}} + B_{4R} \underline{G}_b + K_{RR} \underline{\kappa}_i \quad (66)$$

Aeroelastic Equations of Motion

As described above, the aerodynamic forces and moments can be written in terms of the vehicle motion variables, the induced flow, and gust velocity. The mass, stiffness, and damping matrices are modified to include the corresponding unsteady aerodynamic terms, yielding the aeroelastic equations of motion,

$$M \ddot{\underline{q}} + C \dot{\underline{q}} + K \underline{q} + D \underline{\lambda} = \underline{F} \quad (67a)$$

$$\dot{\underline{\lambda}} = F_1 \ddot{\underline{q}} + F_2 \dot{\underline{q}} + F_3 \underline{\lambda} \quad (67b)$$

$$\underline{F} = C_q \dot{\underline{q}}_0 + K_q \underline{q}_0 + D \underline{\lambda}_0 + B_1 \underline{v} + B_2 \underline{F}_0^{\text{aero}} + B_3 \underline{M}_0^{\text{aero}} + B_4 \underline{G}_b + B_5 \underline{\kappa}_i + B_6 \underline{w} \quad (67c)$$

where

$$\dot{M} = M_q - B_2 F_{\dot{q}} - B_3 M_{\dot{q}} \quad (68a)$$

$$\dot{C} = C_q - B_2 F_{\dot{q}} - B_3 M_{\dot{q}} \quad (68b)$$

$$\dot{K} = K - B_2 F_q - B_3 M_q \quad (68c)$$

$$D = -B_2 F_{\lambda} - B_3 M_{\lambda} \quad (68d)$$

$$B_5 = B_2 F_w + B_3 M_w \quad (68e)$$

and the single wing aeroelastic model is similarly derived.

State Space Representation

By adopting a state space format, the structure states can be augmented with the inflow states. Then Eq. (67) becomes

$$\begin{bmatrix} I & 0 & 0 \\ 0 & \dot{M} & 0 \\ 0 & -F_1 & I \end{bmatrix} \begin{bmatrix} \dot{q} \\ \dot{\dot{q}} \\ \dot{\lambda} \end{bmatrix} = \begin{bmatrix} 0 & I & 0 \\ -\dot{K} & -\dot{C} & -D \\ 0 & F_2 & F_3 \end{bmatrix} \begin{bmatrix} q \\ \dot{q} \\ \lambda \end{bmatrix} + \begin{bmatrix} 0 \\ I \\ 0 \end{bmatrix} F \quad (69)$$

Using the full state vector in Eq. (69), instead of perturbation of the state vector about the instantaneous linearization facilitates a nonlinear time stepping solution effectively since the perturbation equations do not have to be constructed on each time step.

The state space system can be represented in the form

$$\begin{aligned} \dot{x} &= A(x)x + B(x)u + G(x)w + F(x) \\ y &= C(x)x + Du \end{aligned} \quad (70)$$

where u is the control input, y is a vector of outputs, which may correspond to strain gages, accelerometers, and rate gyros, w is the gust loading, and F contains all other external loads and disturbance. The state vector is given by

$$x^T = \{\kappa_R^T \quad \kappa_L^T \quad \phi^T \quad \dot{\kappa}_R^T \quad \dot{\kappa}_L^T \quad \dot{\phi}^T \quad \lambda_R^T \quad \lambda_L^T\}^T \quad (71)$$

for the roll model and

$$x^T = \{\kappa^T \quad \phi^T \quad \dot{\kappa}^T \quad \dot{\phi}^T \quad \lambda^T\}^T \quad (72)$$

for the single wing model.

Steady State Deformation

The steady deformed shape of the wing under the influence of aerodynamic loads, gravity, and applied electric field is given by the nonlinear equation

$$K(\underline{\kappa} - \underline{\kappa}_i) = B_1 \underline{v} + B_2 \underline{F}^{aero} + B_3 \underline{M}^{aero} + B_4 \underline{G} \quad (73)$$

which must be solved in an iterative manner since the right hand side matrices and static aerodynamic loads vectors depend on the current deformed geometry. This can be done by successively applying the load vector based on the current geometry and allowing the solution to converge to a final value. Numerical damping may be added for numerical stability. For a stiff wing, the solution is usually obtained within 5 to 7 iterations. As the wings become more flexible, the number of iterations generally increases because of the greater changes in B_2 , B_3 , and B_4 as the structure deforms.

Flutter Analysis

Stability analysis can be conducted by bringing the wing to its steady state nonlinear deflection at various flight conditions and computing the eigenvalues of the linearized system. At the critical flutter speed the real part of the eigenvalues corresponding to the unstable aeroelastic mode become positive, indicating that the mode has negative damping. While the linearized analysis is capable of determining the point of instability, a nonlinear time stepping analysis is needed to identify the presence of a limit cycle if one exists.

Damping

Internal damping may be added to the model to approximate the true behavior of the wings and to reduce the effects of high frequency structural modes, which may not be well modeled. This can be done in many ways. In the present formulation, the internal damping forces are assumed to enter the structure equations in a similar way as internal elastic forces, i.e., a constitutive equation relating internal forces to strain rates. This enters the discrete model as stiffness proportional damping,

$$C = \alpha K \quad (74)$$

where α is solved for which results in the desired first mode damping. Typically, the first mode damping is set to a very small non-zero value ($< .001$). This has the effect of damping out high frequency structural modes, which do not play an important role in the aeroelastic behavior of the wing.

Numerical Results

A numerical test model was representing a high-altitude long-endurance vehicle. A graphical representation is shown in Figure 5. These aircraft are designed to fly above 50,000 ft and have half-aspect ratio of around 10:1. In the present study, each wing is 30 m in length, as shown in Figure 6, and has a single spar running the entire length. The airfoil profile is a NACA 0014 (Figure 7). The active/passive composite layup is

constant along the span, and is summarized in the appendix. The spanwise stiffness and actuation distributions are shown in Figures 8 and 9, respectively.

A total of four anisotropic piezoelectric actuator (APA) layers are embedded in the airfoil skins; two layers on top and two on bottom, and are arranged to produce both twisting and bending deformation. Two more APA layers are incorporated in the spar.

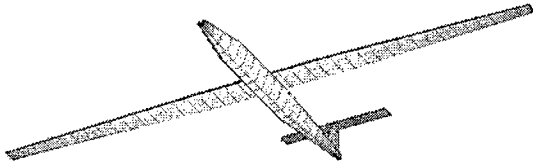


Figure 5: HALE Test Vehicle

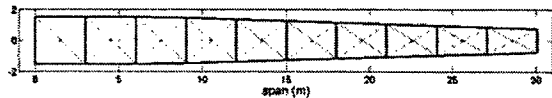


Figure 6: Planform geometry

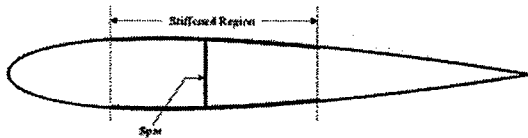


Figure 7: Cross section geometry (NACA0014 airfoil)

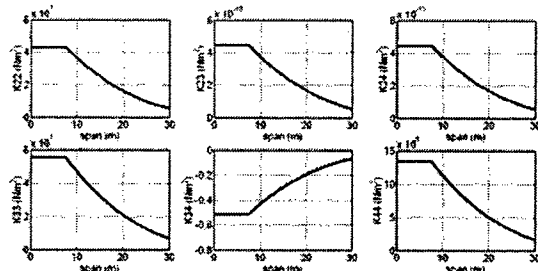


Figure 8: Spanwise Stiffness Distribution

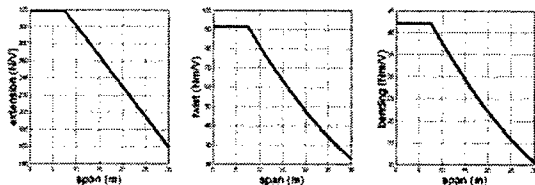


Figure 9: Spanwise actuation distribution

Flight Plan

A simple flight plan was constructed based on the desired altitude profile (Figure 10). The wings are

assumed to carry 40% of the total fuel, distributed over the inboard 60% of each wing. The fuel mass is assumed to be depleted linearly from the beginning to the end of the flight. A cruise speed of 195 m/s and cruise altitude of 19,800 m are selected. The flight speed profile is constructed such that the dynamic pressure is constant for the duration of the flight. The body trim angle of attack is then solved for at each point along the flight plan (based on the linearized model). Certain points along the flight profile are selected for analysis.

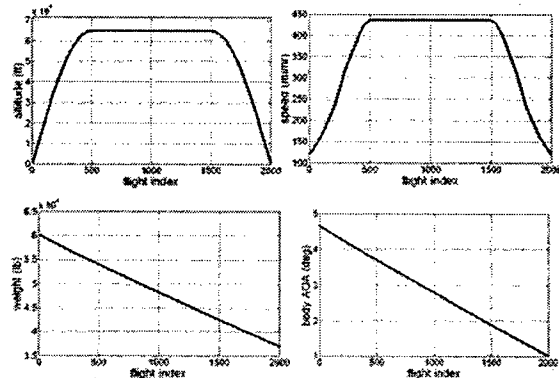


Figure 10: Flight profile definition

Twist Actuation vs. Skin Active Ply Angle

Twist is achieved by adjusting the polarity of the electric field applied to the four active layers on the airfoil surface. Figure 11 shows the twist response of the wing as the active ply angle is varied from 0 to 90 deg. Normally, the maximum twist response would occur at 45 degrees with respect to the spanwise direction. However, since there is coupling with the +/- 45-degree spar plies, the maximum twist response occurs when the active plies are oriented at approximately 39 degrees.

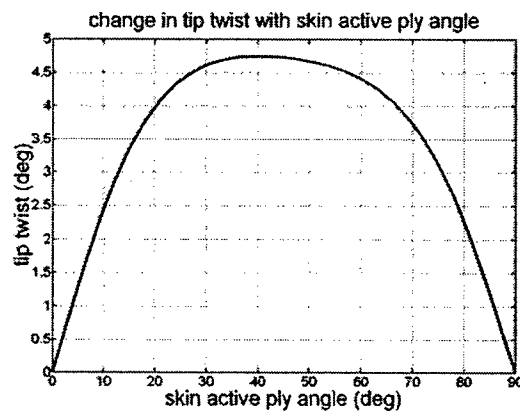


Figure 11: Twist response of the active wing with variation in the orientation of the APA layer angle

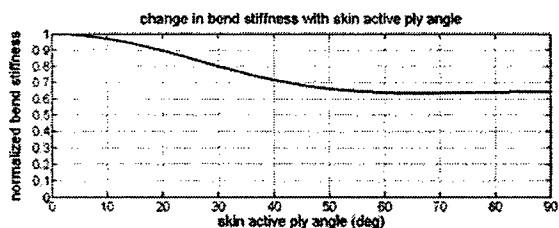


Figure 12: Change in bend stiffness with actuator angle

As seen in Figure 12, changing the fiber direction of the active plies also affects the bending stiffness. The maximum bending stiffness occurs when the active plies are oriented at 0 degrees with respect to the span direction. Rotating the active ply angle by 39 deg. corresponds to a 28% reduction in the bending stiffness.

Stress Distribution in the Deformed Wing

The steady state solution was obtained for the vehicle at a point in the middle of the flight plan as given in Table 1. The deformed vehicle is shown in Figure 13. Based on the deformed shape of the wing, the stresses on the outer surface were evaluated. Figure 14 shows the spanwise lift distribution and bending moment. Ply stresses were evaluated at several spanwise stations in various plies and are exemplified in Figures 14 and 15.

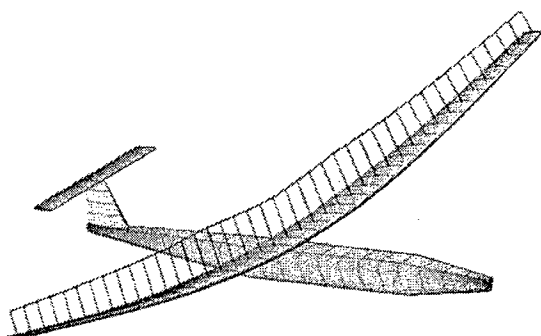


Figure 13: Vehicle at steady state

Table 1: Hale flight data

Cruise flight speed	195 m/s
Cruise altitude	19,800 m
body trim angle	2.8 deg
Max. fuel mass	5250 kg
Root attachment angle	5 deg

In Figure 17, the maximum stress in selected plies are plotted as a function of span. As expected, the highest longitudinal stresses occur in the stiffener plies, which its fibers oriented in the spanwise direction. The 30 deg. graphite composite plies are also highly stressed. The maximum transverse stresses occur in the 4th ply, which is oriented at 39 deg.

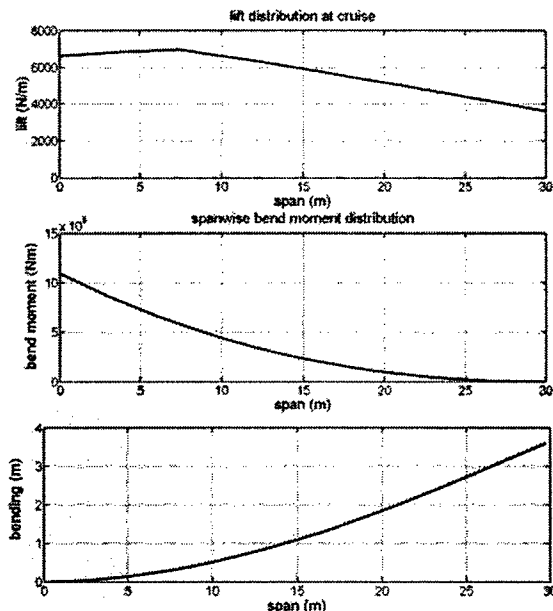


Figure 14: Lift, bending moment, and bending deflection distributions along the wing span

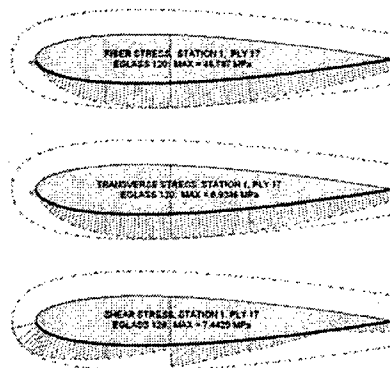


Figure 15: Stress distribution in ply 17 of station 1

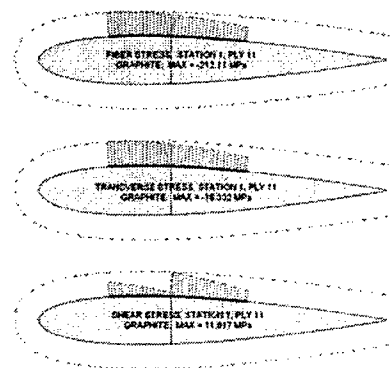


Figure 16: Stress distribution in ply 1 of station 10

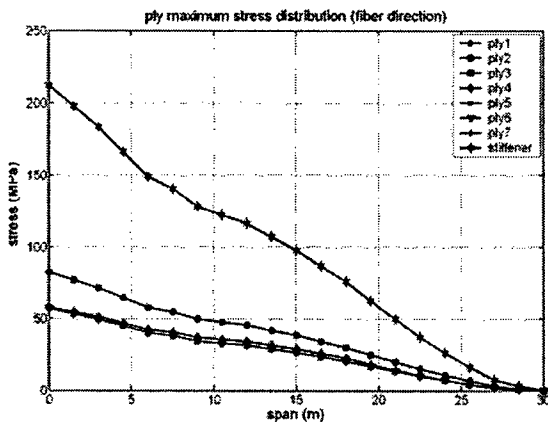


Figure 17: Maximum ply stresses vs. span

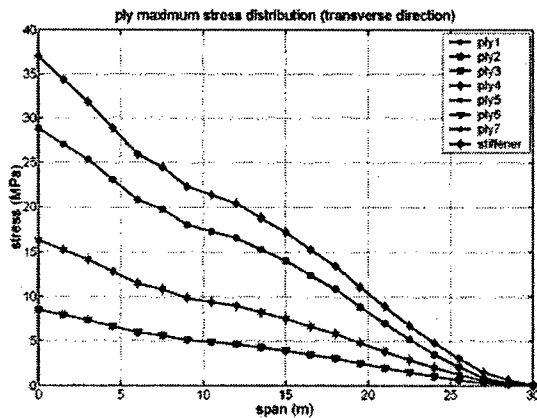


Figure 18: Maximum transverse ply stresses vs. span

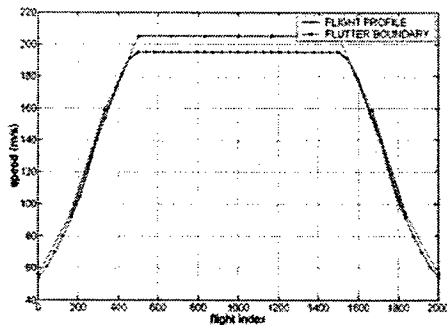


Figure 19: Flutter boundary vs. flight speed profile

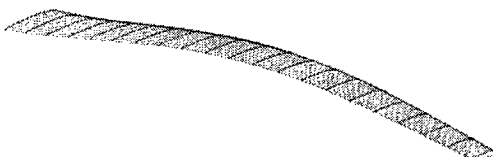


Figure 20: Unstable aeroelastic mode shape

Aeroelastic Stability

The flutter boundary was obtained at several points along the flight profile. At each point, a nonlinear equilibrium solution was obtained and the wing was linearized about that to evaluate the flutter speed. The result is plotted along with the design speed profile in Figure 19. The result shows that the vehicle has approximately 7% flutter margin in the cruise segment of the flight and it is at the flutter boundary for the other points. This leads either to the need for structural redesign, or the continuous use of active controls (not treated here). Figure 20 shows the flutter mode at middle of the cruise segment.

Roll Rate Response

A comparison between twist actuation and conventional aileron actuation for producing roll is exemplified here. Figure 21 shows the maximum achievable roll rate over the flight plan, based on static calculations. Because the flight speed is lower at the beginning and end of the mission, the roll rate is correspondingly slower. These results show that for this wing, the warping control for roll can provide about 60% more authority than the aileron control. Figures 22 and 23 show the roll rate time response at three characteristic points along the flight plan for the wing warping and aileron control inputs, respectively. The response to 20 deg. flap deflection is shown for comparison. As would be expected, the response in the landing phase is the fastest, since the fuel in the wings has been used up, reducing the roll inertia. The maximum roll rate at takeoff and landing are about the same since the flight speed and altitude are the same.

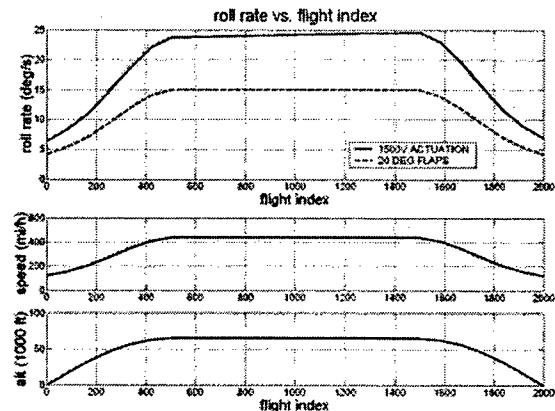


Figure 21: Maximum roll rate vs. flight index

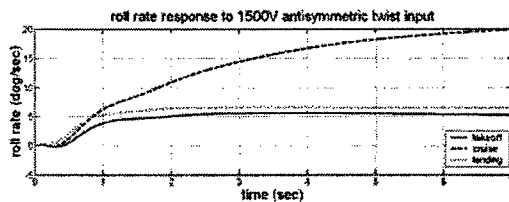


Figure 22: Roll rate response due to wing warping control input at different flight conditions

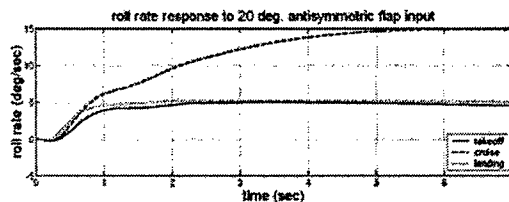


Figure 23: Roll rate response due to 20-deg. aileron control input at different flight conditions

Due to the wing flexibility, the application of sudden aileron or actuator input tends to couple into the first anti-symmetric roll mode of the vehicle, shown in figure 24, delaying the roll angle response slightly.



Figure 24: First antisymmetric roll mode (2.21 Hz)

Conclusions

This paper presented a method for modeling the effects of internal anisotropic strain actuation on the behavior of highly flexible high-aspect ratio wings. The numerical studied presented in this paper showed some of the capabilities of the active aeroelastic formulation in dealing with a HALE-class aircraft. For the proposed design, twisting the wing with embedded anisotropic piezocomposite actuators provides an improvement in performance when compared with traditional ailerons and shows the potential for primary wing control without discrete control surfaces. A nonlinear beam model was developed in order to represent large (coupled) bending and twisting deformations. By dealing with strain variables instead of displacements, the formulations allows for the exact solution of the elastica problem in a very efficient manner. To study the effectiveness of active wings to generate aircraft roll control, a two-wing formulation with freedom to roll was developed based on the strain-based beam formulation. Both wing warping and aileron roll controls are included in the present study. The resulting framework is capable of representing the large

deformations associated with the flexible wing with the aeroelastic equations in state-space form. The low-order resulting model allows for control synthesis and simulation. The present implementation provides the capability for integrated structure and control preliminary design for active flexible wings and the exploration of active aeroelastic tailoring concepts.

Acknowledgements

The second author gratefully acknowledges C.S. Draper Laboratory for providing his fellowship for graduate studies. This work is sponsored by AFOSR under grant F49620-01-1-0133 and by AFOSR-DARPA's Single Crystal Program through Boeing contract No. KH2679. The AFOSR technical monitors are Drs. Daniel Segalman and Dean Mook. The AFOSR-DARPA program managers are Drs. Spencer Wu and Wallace Smith.

Appendix

The properties of the HALE wing model used in example presented in this paper is summarized below.

WING				
Length		30 m		
Length to start tapering		7.5		
Root chord		3		
Tip chord		1.5		
Airfoil		NACA 0014		
Top and Bottom Surfaces				
Material	Thick (mm)	Angle (deg)	Start (chords)	Stop (chords)
E-glass	1.143	0/90	0	1
APA	4.360	-39	0	1
E-glass	1.143	0/90	0	1
APA	4.360	39	0	1
E-glass	4.932	0/90	0	1
APA	0	-39	0	1
Graphite	2.286	0	0.2	0.6
Spar				
Location		38% from LE		
Material	Thick (mm)	Angle (deg)		
APA	2.180	45		
Graphite	2.286	-45		
Graphite	2.286	45		
APA	2.180	-45		

The material properties of the composite layers used in HALE wing model are summarized below.

	E-glass	Graphite	APA
Mass (kg/m ³)	1700	1500	4100
Q ₁₁ (GPa)	20	73	34
Q ₁₂ (GPa)	2.9	5.6	7.5
Q ₂₂ (GPa)	20	73	17
Q ₃₃ (GPa)	4.1	6.6	5.1
Free strain (μ ϵ)	-	-	2700

References

- [1] Lin, C. Y. and Crawley, E. F., "Design Considerations for a Strain Actuated Adaptive Wing for Aeroelastic Control," Journal of Intelligent Material Systems and Structures, Vol. 6 - May 1995
- [2] McGowan, A. R., Heeg, J., and Lake, R., "Results of Wind-Tunnel Testing from the Piezoelectric Aeroelastic Tailoring Investigation," In *Proceedings of the 37th AIAA/ASCE/AHS/ASC Structures, Structural Dynamics and Materials Conference*, Salt Lake City, Utah, April 1996.
- [3] Librescu, L. and Na, S., "Vibration and Dynamic Response Control of Elastically Tailored Nonuniform Adaptive Aircraft Wings," In *Proceedings of the 41st AIAA/ASME/ASCE/ AHS/ASC Structures, Structural Dynamics, and Material Conference and Exhibit*, Atlanta, GA, April 3-6, 2000, AIAA-2000-1628.
- [4] Pendleton, E. W., Griffin, K. E., Kehoe, M., and Perry, B., "A Flight Research Program for the Active Aeroelastic Wing Concept," In *Proceedings of the 37th AIAA/ASCE/AHS/ASC Structures, Structural Dynamics and Materials Conference*, Salt Lake City, Utah, April 1996.
- [5] Khot, N. S. and Zweber, J. V., "Lift Efficient Composite Flexible Wing for Rolling Maneuver Without Ailerons," In *Proceedings of the 41st AIAA/ASME/ASCE/ AHS/ASC Structures, Structural Dynamics, and Material Conference and Exhibit*, Atlanta, GA, April 3-6, 2000, AIAA-2000-1333.
- [6] Jones, R. I., "The Design Challenge of High Altitude Long Endurance (Hale) Unmanned Aircraft," The Aeronautical Journal, June, 1999, pp. 273-280.
- [7] Patil, M. J., Hodges, D. H., and Cesnik, C. E. S., "Nonlinear Aeroelasticity and Flight Dynamics of High-Altitude Long-Endurance Aircraft," J. of Aircraft, Vol. 38, No. 1, January-February 2001, pp. 95-103.
- [8] Drela, M., "Integrated Simulation Model For Preliminary Aerodynamic, Structural, and Control-Law Design of Aircraft", AIAA-99-1394.
- [9] Ortega-Morales, M. and Cesnik, C. E. S., "Modeling and Control of the Aeroelastic Response of Highly Flexible Active Wings," AMSL Report #2000-2, 2000.
- [10] Cesnik, C. E. S. and Ortega-Morales, M., "Active Aeroelastic Tailoring of Slender Flexible Wings," *International Forum on Aeroelasticity and Structural Dynamics*, Madrid, Spain, June 5-7, 2001
- [11] Peters, D. A. and Johnson, M. J., "Finite-State Airloads for Deformable Airfoils on Fixed and Rotating Wings", In *Symposium on Aeroelasticity and Fluid/Structure Interaction, Proceedings of the Winter Annual Meeting*. ASME, November 6-11, 1994.
- [12] Peters, D. A., Karunamoorthy, S., and Cao, W. M., "Finite State Induced Flow Models; Part I: Two-Dimensional Thin Airfoil", *Journal of Aircraft*, Vol. 32, No. 2, March - April 1995, pp. 313-322.
- [13] Cesnik, C. E. S. and Shin, S.-J., "On the Modeling of Active Helicopter Blades," *Int. Journal of Solids and Structures*, Vol. 38, Nos. 10-13, March 2001, pp. 1765-1789.
- [14] Cesnik, C. E. S. and Ortega-Morales, M., "Active Beam Cross-Sectional Modeling" *J. of Intelligent Material Systems & Structures*, 2002 (to appear).

Appendix D:

Cesnik, C. E. S. and Brown, E., "Active Warping Control of a Joined Wing Aircraft," *International Forum on Aeroelasticity and Structural Dynamics*, Amsterdam, The Netherlands, June 4—6, 2003.

Active Warping Control of Joined Wing Aircraft

Carlos E. S. Cesnik¹ and Eric L. Brown²

¹Department of Aerospace Engineering, University of Michigan
1320 Beal Avenue, Ann Arbor, Michigan 48109-2140 USA
e-mail: cesnik@umich.edu

²Department of Mechanical Engineering, Massachusetts Institute of Technology
77 Massachusetts Avenue, Cambridge, Massachusetts 02139 USA
e-mail: ebrown@draper.com

Key words: wing warping, active aeroelasticity, joined wing aircraft, sensorcraft.

Abstract. This paper assesses the use of existing piezoelectric material technology for induced strain and producing wing-warping control on joined-wing aircraft configurations. Anisotropic piezocomposite actuators integrated into the wing structure are the method of actuation. Comparisons are made with traditional aileron control surface. This study is conducted based on a proposed framework in which the developed formulation captures the nonlinear (large) deflection behavior of the wings, the effects of anisotropic piezoelectric composites embedded in the skin, and the unsteady subsonic aerodynamic forces acting on the wing. Because the wing is long and slender, it can be modeled as a beam undergoing three dimensional displacements and rotations. The cross sectional stiffness, inertia, and actuation properties of the wing are calculated along the span, and then incorporated into the 1-D nonlinear beam model derived in this paper. Finite-state unsteady subsonic airloads are incorporated to complete the state space aeroelastic model. Some of the capabilities of the formulation are exemplified within the numerical studies. Two baseline vehicles are designed: one with APA incorporated in the outer wing so to generate wing warping, and the second based on a 50%-span aileron. Different results include static and dynamic instabilities associated with the joined-wing configuration, roll rate and roll angle performance, and the overall ability of the different concepts to produce maneuver loads. Finally, discussion on required material technology improvements to make the wing-warping authority par with the aileron for a joined-wing configuration is presented.

1 INTRODUCTION

The first successful heavier-than-air flight took place 100 years ago. The Wright Flier used the motion of the pilot's hips to control the warping of the wing and, therefore, the vehicle roll. The relatively soft-in-torsion wings were replaced by stiffer designs with the increase in vehicle flying speeds. The lack of authority to twist the stiffer wings resulted in replacing wing warping with discrete aileron control. Within this concept, maneuver loads are generated at discrete movable parts of the wings in contrast to the reshaping of the wing.

Two decades ago, the concept of active aeroelastic wing (AAW) was introduced. There, instead of generating maneuver loads from a set of control surfaces and fight the flexibility of the wing, the control surfaces are used to induce deformation on the wing so that the reshape of the wing is responsible for generating such loads. Different numerical studies have been pursued, showing promises of achieving different objectives while reducing overall systems weight¹. A modified F/A-18A with a relatively flexible wing was constructed as a testbed for this concept and just recently has started flight tests at NASA Dryden.

More recently, with the advancement of active materials and the development of anisotropic piezocomposite actuators (APA)^{2,3}, one may be able to once again implement wing warping for maneuver

load generation. Through APA embedded as an integral load-bearing component of the wing structure, local strains can be induced at certain areas of the wing structure and in certain directions. Those strains are controlled externally by applied electric field to the actuators. By properly designing the active structure, a single physical structural realization can achieve several different aeroservoelastic objectives, presenting itself as a truly active aeroelastic tailoring mechanism. Moreover, this could bring the AAW concept to its fulfillment, and represents a fundamental step towards the development of a more generic morphing aircraft.

Among the types of aircraft that could take advantage of such concept, high-altitude long-endurance ones are the most likely candidates. Due to mission requirements, those vehicles present high-aspect-ratio wings that result in relatively flexible structures. If the conventional design paradigm is to be used, the wing flexibility has to be counteracted by additional structural reinforcements that will result in extra mass penalty. Some basic studies exploring APA for active aeroelastic tailoring of such vehicles⁴ show that multiple objectives can be achieved by the same wing realization. Studies were conducted for flutter boundary enhancement and gust load response. It is worthwhile mentioning here that the wing's high flexibility results in nonlinear structural motions. This adds another degree of complexity to this already reach domain in which the structural dynamics of the flexible vehicle must be modeled accordingly.

A recent work⁵ by the authors investigates in-depth the effects of using APA in three classes of Uninhabited Aerial Vehicles (UAV): small (e.g., Pointer), medium (e.g., Predator), and large (e.g., Global Hawk). For that study, a framework was created for analyzing and designing different high-aspect-ratio wing vehicles. A new strain-based active structural formulation was created and implemented in the framework. The three classes of UAVs were studied for both wing warping and aileron controls. Different objectives included: roll controllability, flutter enhancement, and gust load alleviation and response. Also, an assessment of the structural weight penalty incurred for using current technology APA was conducted. Although the final decision has to be made at the system's level (including mission effectiveness, survivability, etc.) and a formal numerical optimization study is still needed, results from [5] show that wing warping is possible today by employing APA as part of the composite wing construction. Basic performance results of the active wing are comparable with the ones from a wing with ailerons.

The intent of the present paper is to perform similar investigations as in [5] on a joined-wing Sensorcraft configuration. This is a new high-altitude long-endurance ISR platform that carries a variety of sensors.

Due to the unusual shapes of joined-wing airplane configurations, the effects of structural deformation on the static aerodynamic and aeroelastic behavior are difficult to intuit and predict. Deformation of the structure at a certain location may produce large changes in angle of attack in the lifting surfaces at other locations. Efforts to minimize structural weight may create aeroelastic instabilities that are not encountered in conventional aircraft design. For joined-wing aircraft, the first sign of failure may be in the buckling of the aft members as the structure is softened. Flutter and divergence may also become a problem in these members due to the reduction in structural frequency as they go into compression. As the aircraft becomes more flexible, the nature of the geometric structural nonlinearities become more important and the lift distribution on the aircraft may be adversely affected.

Livne⁶ presented a thought provoking survey on the design challenges of joined-wing aircraft configurations. Therein, he presents a review of past works in joined-wing aeroelasticity and gives a qualitative discussion of their behavior in a multidisciplinary context. Much of the discussion in the paper deals with structural and aeroelastic issues relating to the aft wing/tail. The in-plane loads due to structure deformation and changes in geometric stiffness give rise to non-intuitive aeroelastic behavior. Bending and twisting couplings of the entire structure cause natural frequencies and mode shapes to shift. The tendency for buckling and divergence in the aft member is of major concern when trying to reduce weight. The finding of aft wing divergence to be more critical than flutter is

counterintuitive, since the aft wing is supported at the joint. This phenomenon seems associated with a reduction in structural stiffness due to the in-plane compressive loads in the rear members. The geometry of the joint between forward and aft wings is also of importance because it influences how in-plane, bending, and torsion loads are transferred. For instance, a pinned joint may allow upward buckling of the aft wing, while a fixed rigid joint may allow the aft wing to buckle downward, since bending moments are transferred across the joint.

While no firm design of a joined-wing Sensorcraft exists in public literature, [7] and [8] present a systematic design optimization study for the basic vehicle with regular control mechanisms. The authors proposed an integrated design method that brings together different software packages like NASTRAN and PanAir, and integrate then through the Air Vehicles Technology Integration Environment (AVTIE). Their most recent work⁸ addresses some of the nonlinear structural issues present in the joined-wing configuration and discuss the impact of different constraints on a fully stressed design. Ref. [9] employs multiple control surfaces on the different wing segments to implement the AAW concept on the joined-wing Sensorcraft. There, the authors employ a linear aeroelastic representation of the lifting surfaces to optimize trim so that to minimize the overall structural deformation (that may affect antenna performance). It was numerically shown that the vehicle could be trimmed for 1-g flight using six independent control surfaces and simultaneously minimizing structural deformation.

Active distributed control using embedded piezocomposites in the wing structure may be able to improve the performance in several ways, and also may allow for lighter designs by actively offsetting critical instabilities. Warping the structure in order to change the aerodynamic force distribution across the vehicle may be a means of eliminating or reducing unwanted structural couplings due to deformation. The degrading effects of in-plane loads on the aft members may be dealt with through the use of active/passive internal structural couplings. Passive structure design may be incapable of dealing with the global structural load transfers at all flight conditions. By embedding active materials in large areas of the vehicle, the global behavior of the structure may be enhanced. Actuators embedded in the forward wings will be able to respond to stresses measured in the aft wings. Actuators anywhere in the structure can respond to measurements taken everywhere over the structure. This may allow for global modal behavior to be adjusted by timing and shaping the internal stresses in the structure.

Passive composite structural design can exploit structural couplings to prevent aeroelastic instabilities. While this may work for certain instabilities at certain flight conditions, it may have a negative effect on other aeroelastic characteristics at other flight conditions. The ability to actively adjust the structural couplings would have obvious benefits. Before any claims can be made, however, it is necessary to determine the scale of the problem and the relative amount of active material to passive material required to accomplish goals such as this. The potential for new ideas in this area seems limitless. For now, however, this paper concentrates in two key issues:

- New proposed formulation for highly flexible active vehicle analyses and the importance of geometrically nonlinear structural modeling;
- Assessment of wing warping as a means of roll control of a joined-wing configuration based on state-of-the-art anisotropic piezocomposite actuator technology.

2. FORMULATION

For the present study, the vehicle is allowed six rigid body degrees of freedom as well as flexible degrees of freedom. The wings are allowed fully coupled three-dimensional bending, twisting, and extensional deformation. Flaps and ailerons may be included for comparison purposes and for the study of hybrid vehicle control. A finite-state unsteady airloads model based on the work of Peters¹⁰ is integrated into the system equations. The model allows for a low order set of nonlinear equations that can be put into state-space form to facilitate control design.

2.1. Element Description

Specialized nonlinear beam elements were created for the ongoing work, each having four strain degrees of freedom, representing extension (ϵ_x), twist (κ_x), and two bending strains (κ_y and κ_z). Deformations of this element are exemplified in Fig. 1. With a constant strain distribution over the element, a wide range of geometrically nonlinear shapes can be obtained. A single element, for example, can be deformed into a circle or spiral shape.



Figure 1: Deformations represented by a single element with constant strain distribution

The kinematics of the element are described as follows. The beam reference frame is denoted w , and is a function of the beam coordinate, s . The position and orientation of a point on the reference line can be described by the 12×1 vector h as

$$h(s) = [p_w(s)^T, w_x(s)^T, w_y(s)^T, w_z(s)^T]^T \quad (1)$$

where p_w is the position of frame w in the body coordinate system and w_x , w_y , and w_z are the direction vectors pointing along the beam axis, toward the leading edge, and normal to the airfoil, respectively, defined in the body frame. The partial differential equation governing how h moves through space involves the strain variables,

$$\frac{\partial h(s)}{\partial s} = A(s)h(s) \quad (2)$$

with

$$A(s) = \begin{bmatrix} 0 & 1 + \epsilon_x(s) & 0 & 0 \\ 0 & 0 & \kappa_z(s) & -\kappa_y(s) \\ 0 & -\kappa_z(s) & 0 & \kappa_x(s) \\ 0 & \kappa_y(s) & -\kappa_x(s) & 0 \end{bmatrix} \quad (3)$$

where the blocks are all 3×3 diagonal matrices. When the element is assumed to have a constant strain vector, the solution can be obtained

$$h(s) = e^{As} h_0 = e^{G(s)} h_0 \quad (4)$$

where h_0 is the element boundary condition. The total virtual work done on an element due to all internal and external forces and moments can be written as

$$\delta W = -\delta h^T M \ddot{h} - \delta \epsilon^T K \epsilon + \delta \epsilon^T B_v v - \delta h^T N g + \delta p^T B_F F^{dst} + \delta \theta^T B_M M^{dst} + \delta p^T F^{pt} + \delta \theta^T B_M M^{pt} \quad (5)$$

where the terms involved include the effects of inertial, gravitational, internal strain, piezoelectric, distributed, and point forces and moments.

2.2. Member Equations

Each member is an assemblage of elements and may include breaks in the beam reference line at the joint between elements and variation in the level of discretization.

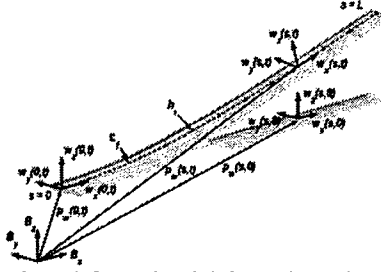


Figure 2: Illustration of a single undeformed and deformed member with different reference frames.

The kinematics for a member is obtained by marching the element kinematics from the boundary node to the end of the last element, using the values of the strain variables in each element to march forward. This procedure is given for the three node elements used in the present model,

Element 1			Element 2			...	Element n		
Node 1	Node 2	Node 3	Node 1	Node 2	Node 3	...	Node 1	Node 2	Node 3
$h_{11} = h^*$	$h_{12} = e^{G_1} h_{11}$	$h_{13} = e^{G_1} h_{12}$	$h_{21} = D_{21} h_{13}$	$h_{22} = e^{G_2} h_{21}$	$h_{23} = e^{G_2} h_{22}$...	$h_{n1} = D_{n,n-1} h_{n-1,3}$	$h_{n2} = e^{G_n} h_{n1}$	$h_{n3} = e^{G_n} h_{n2}$

(6)

where h_{ij} is the j th node of the i th element and the D_{ij} matrices contain elements of the direction cosines, accounting for the break at the element junction. Eq. (6) can be put into matrix form

$$\bar{A}h = h^* \quad (7)$$

where h is now a column matrix containing nodal position and orientation variables for all of the nodes in the member, and h^* is a column matrix containing the boundary condition. When the member is fixed at the first node and the element has three nodes, this relation is given by

$$\begin{bmatrix} I & 0 & 0 & 0 & 0 & 0 & 0 \\ -e^{G_1} & I & 0 & 0 & 0 & 0 & 0 \\ 0 & -e^{G_1} & I & 0 & 0 & 0 & 0 \\ 0 & 0 & D_{21} & I & 0 & 0 & 0 \\ 0 & 0 & 0 & -e^{G_2} & I & 0 & 0 \\ 0 & 0 & 0 & 0 & -e^{G_2} & I & 0 \\ 0 & 0 & 0 & 0 & 0 & D_{32} & \ddots \end{bmatrix} \begin{bmatrix} h_{11} \\ h_{12} \\ h_{13} \\ h_{21} \\ h_{22} \\ h_{23} \\ \vdots \end{bmatrix} = \begin{bmatrix} h^* \\ 0 \\ 0 \\ 0 \\ 0 \\ 0 \\ \vdots \end{bmatrix} \quad (8)$$

The D_{ij} matrices are equal to the identity matrix if the elements are aligned, and contain rotation variables if the beam reference line makes a break at an element intersection.

The Jacobian matrix relating changes in the element strain variables to changes in the position and direction vectors, taken about the current strain vector ϵ_0 , is given by

$$dh = \left[\frac{\partial h}{\partial \epsilon} \right] d\epsilon = J_{he} d\epsilon \quad (9)$$

where

$$J_{he} = -\bar{A}_0^{-1} \left[\frac{d}{d\epsilon} \left(\bar{A}(\epsilon) h_0 \right) \right] \quad (10)$$

is found though an iterative routine. The total virtual work done on a member due to all internal and external loads has the same form as Eq. (5), except that the size has increased by a factor of n , where n is the number of elements in the member.

2.3. Global Finite Element Matrices

At this point, each wing member represents an independent entity, for which equations of motion may be constructed. However, because inter-member constraints will be imposed, it is more convenient to

assemble the individual member matrices into a global equation for the virtual work. Before applying the inter-member constraints, the expression for the virtual work takes on the same form, where the matrices are in an uncoupled block diagonal form, and can be written as

$$\delta W = -\delta h^T (M\ddot{h} - \delta h^T Ng) - \delta \varepsilon^T (K\varepsilon - B_v v) + \delta p^T (B_F F^{dst} + F^{pt}) + \delta \theta^T (B_M M^{dst} + M^{pt}) \quad (11)$$

Inter-member constraints are used to enforce that a node position, which is coincident to two members, remains coincident and that the relative orientation of the member coordinate systems at those nodes remains fixed. Let two members be initialized such that in their undeformed state they share a common node location. Each node has three coordinate frames associated with it. Frame w is the beam frame and is aligned with the beam axes as described above. Frame b is aligned with the body frame, B , when the member is undeformed. Frame a is aligned with the airfoil local coordinate system. In the case of a wing with zero root angle of attack and zero sweep and dihedral, frames w , b , and a are in alignment, but in general this is not the case.

The nodal position and orientation vector, h , can be defined for three corresponding frames, e.g.,

$$h^w = [p_w^T, w_x^T, w_y^T, w_z^T]^T, \quad h^b = [p_b^T, b_x^T, b_y^T, b_z^T]^T, \quad h^a = [p_a^T, a_x^T, a_y^T, a_z^T]^T \quad (12)$$

where the following constant relations hold

$$h^b = D^{bw} h^w, \quad h^a = D^{aw} h^w, \quad D^{bw} = \begin{bmatrix} 1 & 0 & 0 & 0 \\ 0 & C_{11}^{wb} & C_{21}^{wb} & C_{31}^{wb} \\ 0 & C_{12}^{wb} & C_{22}^{wb} & C_{32}^{wb} \\ 0 & C_{13}^{wb} & C_{23}^{wb} & C_{33}^{wb} \end{bmatrix}, \quad D^{aw} = \begin{bmatrix} 1 & 0 & 0 & 0 \\ 0 & C_{11}^{wa} & C_{21}^{wa} & C_{31}^{wa} \\ 0 & C_{12}^{wa} & C_{22}^{wa} & C_{32}^{wa} \\ 0 & C_{13}^{wa} & C_{23}^{wa} & C_{33}^{wa} \end{bmatrix} \quad (13)$$

The D matrices here are 12x12 matrices where each block is a 3x3 diagonal matrix and C^{wb} and C^{wa} are components of the rotation matrices from frames b and a , respectively, to frame w . It should be clear now that the vector h is simply a way to express the position and orientation of a coordinate system in a single vector format, and that the D matrices are a rearrangement of the standard direction cosines matrices.

If node m of member i is initially coincident with node n of member j , then coordinate systems b_m^i and b_n^j are equivalent for the undeformed geometry. To enforce the inter-member constraint, it is required that

$$h_{i,m}^b = h_{j,n}^b \rightarrow D_{i,m}^{bw} h_{i,m}^w = D_{j,n}^{bw} h_{j,n}^w \quad (14)$$

This can be done by associating a large virtual work penalty term if the equality in Eq. (14) is violated, that is,

$$\delta W = -(D_{i,m}^{bw} \delta h_{i,m}^w - D_{j,n}^{bw} \delta h_{j,n}^w)^T \hat{K} (D_{i,m}^{bw} h_{i,m}^w - D_{j,n}^{bw} h_{j,n}^w) \quad (15)$$

which can be rearranged into the matrix form

$$\delta W = -[\delta h_{i,m}^T, \delta h_{j,n}^T] \begin{bmatrix} D_{i,m}^{wb} \hat{K} D_{i,m}^{bw} & -D_{i,m}^{wb} \hat{K} D_{j,n}^{bw} \\ -D_{j,n}^{wb} \hat{K} D_{i,m}^{bw} & D_{j,n}^{wb} \hat{K} D_{j,n}^{bw} \end{bmatrix} \begin{bmatrix} h_{i,m} \\ h_{j,n} \end{bmatrix} = -[\delta h_{i,m}^T, \delta h_{j,n}^T] \begin{bmatrix} K_{11} & K_{12} \\ K_{21} & K_{22} \end{bmatrix} \begin{bmatrix} h_{i,m} \\ h_{j,n} \end{bmatrix} \quad (16)$$

To impose the inter-member constraint, Eq. (11) is augmented with a stiffness matrix acting on the nodal position vector, becoming

$$\delta W = -\delta h^T (M\ddot{h} + C_c \dot{h} + K_c h - \delta h^T Ng) - \delta \varepsilon^T (K\varepsilon - B_v v) + \delta p^T (B_F F^{dst} + F^{pt}) + \delta \theta^T (B_M M^{dst} + M^{pt}) \quad (17)$$

where K_c is a matrix of zeros except in the rows and columns corresponding to the entries in Eq. (16). For numerical stability, a constraint damping matrix C_c is also added to Eq. (17) in the same way. Some care is required in selecting the constraint damping and stiffness constants.

2.4. Equations of Motion

With the six rigid body degrees of freedom, the system structural degrees of freedom are represented by the column matrix q , where

$$\dot{q} = [\dot{\varepsilon}_1^T, \dot{\varepsilon}_2^T, \dots, \dot{\varepsilon}_n^T, V_B^T, \omega_B^T]^T \quad (18)$$

and ε_i contains the strain variables for wing member i , V_B and ω_B are the linear velocity and angular velocity of the vehicle, respectively, represented in the body frame, B . The dependent variables for the entire vehicle are put into the column matrix H ,

$$\dot{H} = [\dot{h}_1^T, \dot{h}_2^T, \dots, \dot{h}_n^T, V_B^T, \omega_B^T]^T \quad (19)$$

The dependent degrees of freedom are related to the independent degrees of freedom through a Jacobian matrix relation

$$H = f(q), \quad dH = \left[\frac{\partial H}{\partial q} \right] dq = [J_H(q)] dq \quad (20)$$

The expression for virtual work on the vehicle is now given by

$$\delta W = \delta q^T (-\bar{M}\ddot{q} - \bar{C}\dot{q} - \bar{K}q + \bar{N}g + \bar{B}_v V + \bar{B}_{F1} F^{dst} + \bar{B}_{F2} F^{pt} + \bar{B}_{M1} M^{dst} + \bar{B}_{M2} M^{pt} + B_{q0} q_0 + B_H H) \quad (21)$$

The principle of virtual work requires that the total virtual work done on the system be equal to zero, leading to the equations of motion,

$$\bar{M}\ddot{q} + \bar{C}\dot{q} + \bar{K}q = B_v V + B_{F1} F^{dst} + B_{F2} F^{pt} + B_{M1} M^{dst} + B_{M2} M^{pt} + \bar{N}g + B_{q0} q_0 + B_H H \quad (22)$$

The distributed loads are divided into aerodynamic loads and user supplied loads. The aerodynamic loads evaluated at the current state have the incremental form

$$\begin{aligned} F^{aero}(t) &= F^{aero}(t_0 + \Delta t) \approx F_0(q_0, \dot{q}_0, \lambda_0) + F_{\dot{q}} \dot{q} + F_q \Delta q + F_{\lambda} \Delta \lambda \\ M^{aero}(t) &= M^{aero}(t_0 + \Delta t) \approx M_0(q_0, \dot{q}_0, \lambda_0) + M_{\dot{q}} \dot{q} + M_q \Delta q + M_{\lambda} \Delta \lambda \end{aligned} \quad (23)$$

here λ is column matrix of induced flow states as described in [10]. The induced flow states are governed by a differential equation of the form

$$\dot{\lambda} = L_1 \lambda + L_2 \ddot{q} + L_3 \dot{q} \quad (24)$$

The aeroelastic equations of motion are obtained by moving the state dependent aerodynamic loads over to the left hand side of Eq. (22) and augmenting the structure states with the induced flow states, which can be represented in state space form as

$$\dot{x} = A(x)x + B(x)u(x, t) \quad (25)$$

where the state vector is now given by

$$x = [\dot{q}^T, q^T, \lambda^T]^T \quad (26)$$

Further details of the formulation can be found in [5].

3. NUMERICAL RESULTS

For the numerical study, baseline vehicles were created for the wing warping (active) and for the aileron (passive) concepts. For both cases, controllable changes in aerodynamic loads only occur in the outer wing. Exception to this is a special case of the wing warping concept in which actuation is allowed in the inner forward wing. The active wing contains APAs that can produce 1350 μ strain of free strain amplitude and are distributed along the entire outer span. The passive wing contains a 50%-span/20%-chord aileron that is allowed 30° of amplitude deflection. For all the cases, the fuselage and tail are assumed rigid (Fig. 3).

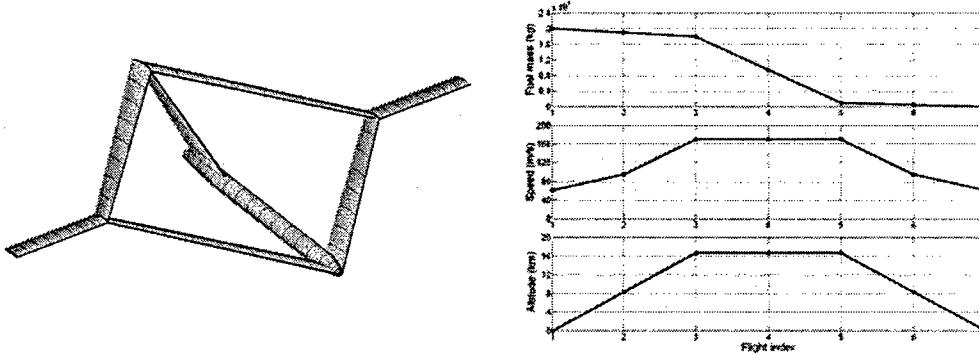


Figure 3: Baseline joined-wing Sensorcraft vehicle with unswept outer wings (where APA actuators or ailerons are present) and its basic mission profile.

Using these baseline vehicles, different sensitivity studies are presented to exemplify further capabilities of the proposed framework and the relative performance of wing-warping controlled configuration with respect to an aileron-controlled one.

3.1. Baseline Vehicles

Two distinct designs are needed to study the effects of wing warping and its relative performance with respect to an aileron-controlled vehicle. First, a design that represents an active wing with embedded APA. Second, a passive wing designed to have an aileron. Three sets of constraints were defined to help guide the baseline designs: laminate strength (based on first-ply failure) at 2.5-g load, laminate strength based on gust loads, and minimum linearized flutter margin. For both vehicles, the 2.5-g load factor was shown to be the critical constraint and the wing structural thickness distribution were sized so that maximum strain was reached along the span. All the results related to the baseline designs can be found in [13].

Seven flight index points represent the nominal mission profile, as also indicated in Fig. 3. At each index point, the altitude, fuel mass, and nominal flight velocity are specified. The index points represent: (1) takeoff, (2) climb, (3) cruise ingress, (4) cruise/loiter/cruise, (5) cruise egress, (6) decent, and (7) landing. The fuel burn determines the duration of each flight segment. The nominal flight speed at each index point is based on the cruise speed (input parameter), and is computed such that the dynamic pressure is constant (constant indicated air speed). The trim body angle is also obtained at each index point for a set of equally spaced increasing flight speeds, up to 200% of the nominal speed at that flight index. At each flight index point, the vehicle is trimmed for equilibrium in horizontal flight at a given flight speed.

From top view, the vehicle shape is symmetric (although one may want to vary the forward/aft location of the joint). The wings are denoted right forward inboard, left forward inboard, right rear inboard, left rear inboard, right outboard, and left outboard. Right and left are determined as in Fig. 4 (as viewed from top with nose pointing up). Each of the six wing members is divided into four regions for definition of cross-section layup and ply thickness distribution. The forward and rear members are

identical in construction, and the material distribution will follow the numbering convention as indicated in Fig. 4.

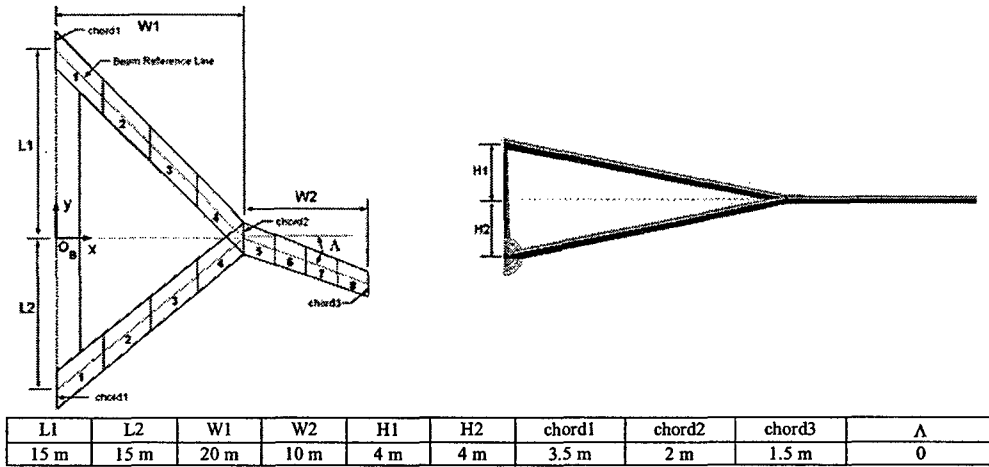


Figure 4: Baseline joined-wing Sensorcraft vehicle geometry.

Vehicle Mass Breakdown. The vehicle mass breakdown is given in Table 1. The fuel is assumed to be distributed evenly throughout the inner and outer wings, independent of the total amount of fuel on board. The fuselage contains no fuel.

Table 1: Vehicle Mass Distribution.

Cruise altitude	16,700 m
Cruise speed	170 m/s
Fuselage structure + payload + engine mass	4,000 kg
Fuel mass	20,000 kg
Active vehicle total wing structure mass	11,191 kg
Passive vehicle total wing structure mass	10,459 kg
Added mass for aileron mounts/wing	58.9 kg

Wing Cross Section. For simplicity, NACA 4415 was chosen as the airfoil and it is kept constant throughout the wing members. A single spar is used at 45% chord. For the final wing layup, the top and bottom skins have ply groups composed of [0/45/-45/0] and the web with ply groups of [0₄]. For the active outer wing, the “45” and “-45” ply groups are APA. Everything else is S-glass. Material properties and thickness distributions can be found in [13]. The maximum induced tip twist angle generated by the APA is 5.5°.

3.2. Characteristics of the Two Vehicle Concepts

Different studies on the baseline vehicles can be conducted. The ones selected here illustrate some of the capabilities of the formulation, the unique behavior of joined-wing configurations, and the relative performance of wing warping and aileron control schemes for vehicle primary roll control.

Effects of Load Factor on the Stability of the Rear Wing. Since the aft wings are primarily under compression, their buckling response can be a sizing limitation for the vehicle. For the particular baseline designs considered here, deformation of the rear inboard wing increases dramatically when the load factor reaches about 2.7, bringing the whole wing system close to a collapse (see Fig. 5). This condition is naturally modeled in the presented framework through the nonlinear structural analysis.

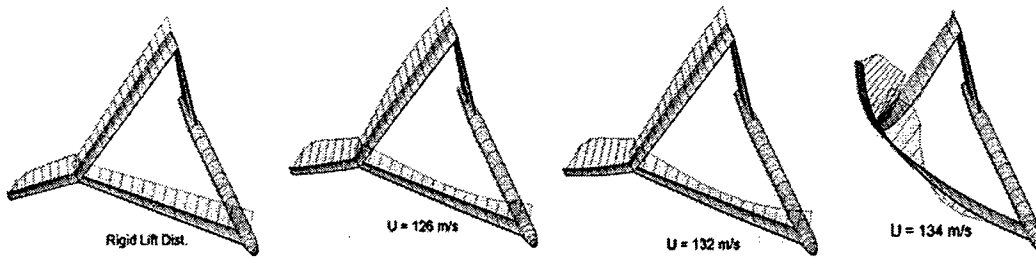


Figure 5: Lift distribution on the vehicle as the buckling speed is approached (sea level, fully fueled, no rigid body degrees of freedom, zero body angle of attack)

To exemplify this, a half-vehicle model is brought to steady state at level flight (at sea level). Then, its flight speed is varied from 70 m/s to 130 m/s, with a resulting load factor ranging from 0.83 to 2.66. The wing shape and deflections are plotted for varying load factor in Figs. 6 thru 8. As may be seen from Fig. 6, the passive wing configuration is more susceptible to the increase in speed due to a softer outboard wing (higher lift outboard due to aeroelastic effects). The sudden reduction of the rear wing stiffness results in large bending deflection of the overall wing structure and, consequently, drop in the overall lift (represented by the reduction in load factor as shown in Fig. 7). This level of wing displacement causes high composite ply strains (stresses), to the point of ply failure. A typical strain component dependence on the load factor is shown in Fig. 8.

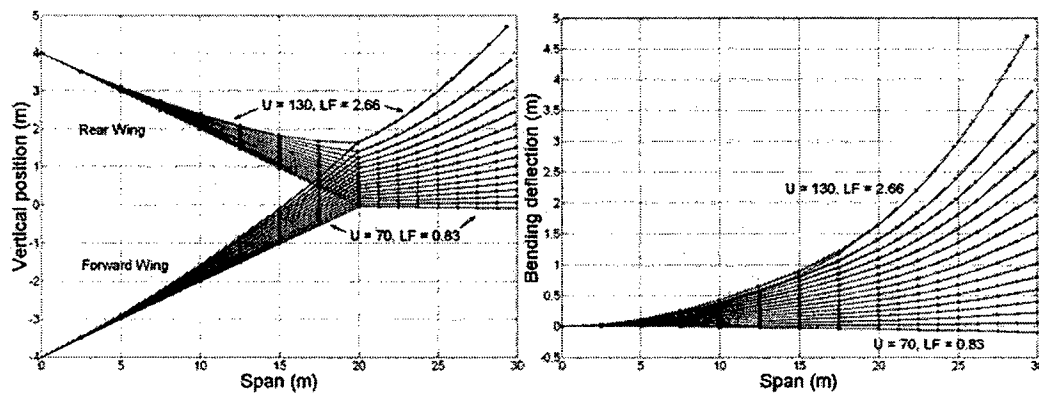


Figure 6: Active wing shape (left) and bending deflections (right) for varying flight speed (level flight at sea level).

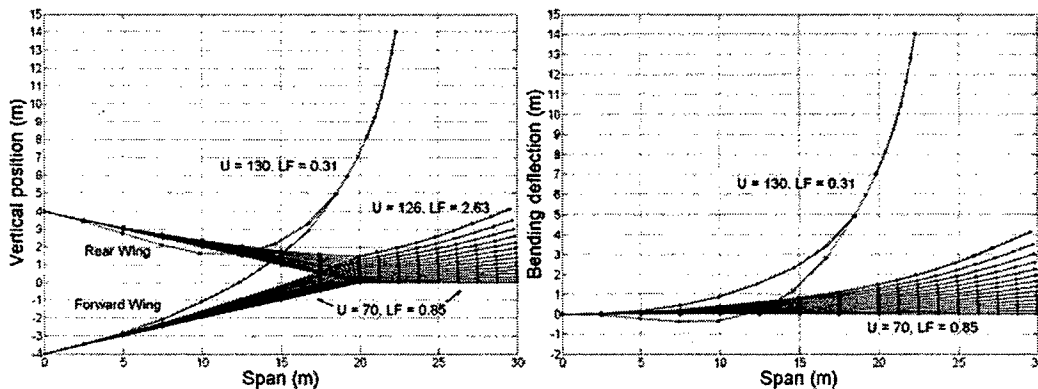


Figure 7: Passive wing shape (left) and bending deflections (right) for varying flight speed (level flight at sea level).

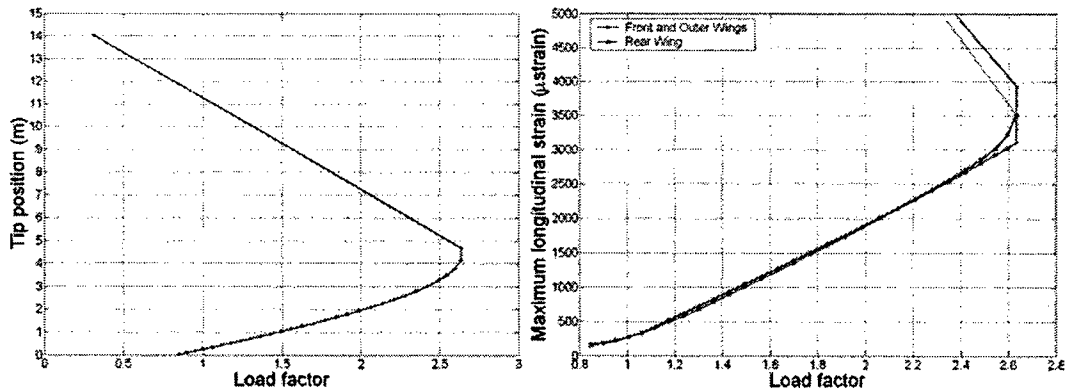


Figure 8: Nonlinear growth in tip deflection (left) and maximum longitudinal strain component (right) as function of the lift generation capability of the passive wing vehicle at level flight (sea level).

Effects of Wing Warping from the Forward Inboard Wing on the Stability of the Rear Wing: For studying the effect of the forward inboard wing on the stability of the rear inboard wing, consider a modified active vehicle case in which all the $\pm 45^\circ$ passive plies of the forward inboard wing are replaced with corresponding APA. The number of plies everywhere else is kept the same. The standard ply thickness for the APA plies is used. Similarly to what was done in the previous section, the modified vehicle is brought to steady state and the speed is increased. Due to stiffness changes in the forward inboard wing, the speed (136 m/s) in which loss of rear wing structural stability occurs varies slightly from the results presented previously (see Fig. 9).

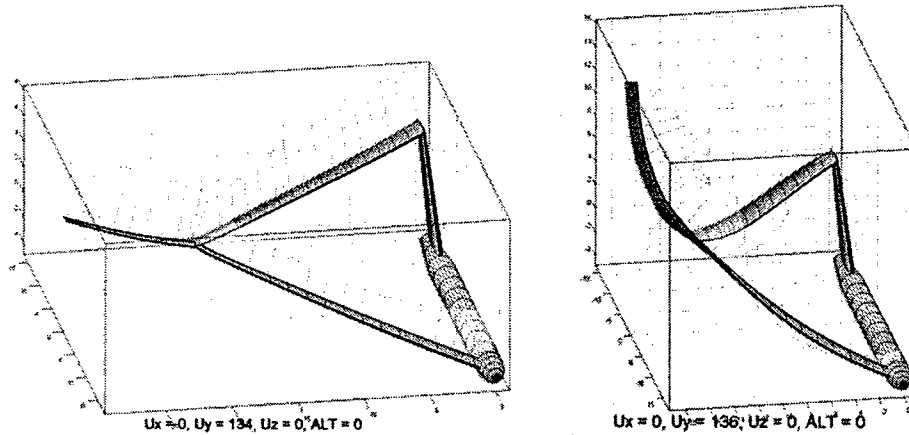


Figure 9: Modified active vehicle just below and above critical buckling speed (no actuation of the forward inboard wing).

The forward inboard wing can be actuated in a combination of bending and twist modes. Numerically, the bending actuation has no effect on the buckling speed. However, applying maximum nose-down twist actuation on the forward inboard wing improves the un-actuated buckling speed by 20%. The results are shown in Fig. 10 for different levels above the un-actuated buckling speed. Note that the lift distribution on the rear wing remains with its original concave shape. There are two main reasons for the increased resistance to buckling: a) the downward twist of the front wing causes the outboard wing to lower its angle of attack, resulting in a lower overall bending moment on the inner wings; and b) the moment at the joint due to front wing actuation opposes the rotation required for the rear wing to buckle downward. Similar effect should be possible with the actuation of an aileron in the forward inboard wing. Studies considering a trimmed vehicle in pitch as it undergoes increase in speed must

be conducted to fully quantify the effects of the forward inboard wing on the static stability of the rear one.

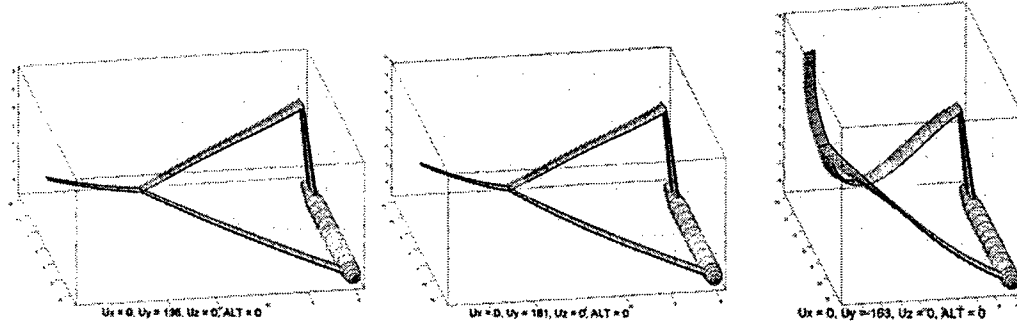


Figure 10: Modified active vehicle flying above the un-actuated buckling speed (nose-down twist actuation of the forward inboard wing).

Roll Response: To study roll response, two approaches have been implemented: a linearized approach and a nonlinear one. In both approaches, the vehicle is first brought to its nonlinear steady state equilibrium with roll motion locked. The roll degree of freedom is then unlocked. In the linearized approach, the system matrices are computed only once based on the steady state deformed geometry. The equations of motion are then integrated in a linear solution process. This approach has the advantage of being computationally efficient. In contrast, in the nonlinear approach, the system matrices are updated on every time step, capturing the change in aeroelastic behavior more accurately as the vehicle deforms. In each case, the input (ply voltage or aileron deflection) is ramped from zero to its maximum value in 0.5 s. Moreover, to assess the impact of the inner wing flexibility to the roll response of the vehicle, two other cases were created: one (denoted as “50% Stiff”) where the inner wings have half of the stiffness (extension, bending, and torsion) of the baseline (denoted as “100% Stiff”), and the other one (denoted by “Inf Stiff”) with 100 times the baseline stiffness, representing an almost rigid case. The roll rate and roll angle responses to applied twist actuation and aileron deflection are shown in Figs. 11 and 12, respectively, for both linear and nonlinear roll calculations during 1-g level flight.

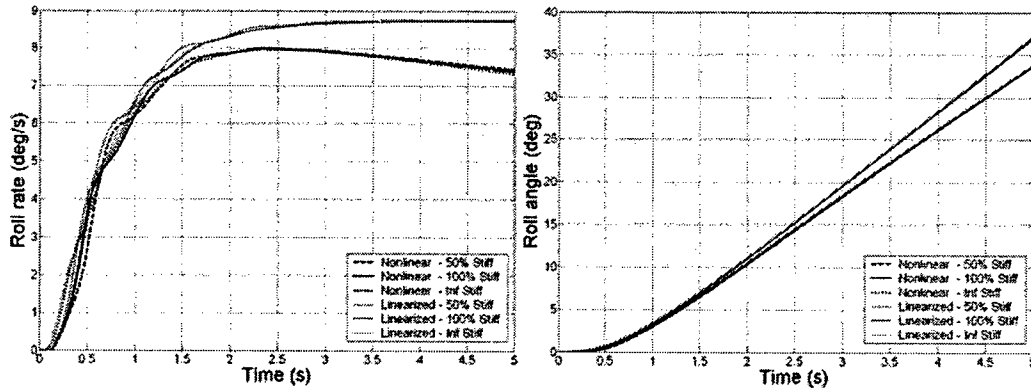


Figure 11: Active concept roll rate and roll angle responses with varying inner wing stiffness (flight index 5, maximum actuation; 100% stiffness is nominal)

The very first observation that can be made from Figs. 11 and 12 is that the roll performance level of the wing warping actuation with APA is about three fold lower than the aileron concept. While roll angles of over 50° can be reached by the latter in 2.5 s, for the same time period only 15° is reachable with the active wing. This was expected based on the fact that the quasi-linear twist distribution generated by the active concept reaches 5.5° at the wing tip (where aerodynamic losses are imposed)

while the aileron imposes 30° deflection of 25% wing chord between 1/3 and 2/3 of the outer wing span.

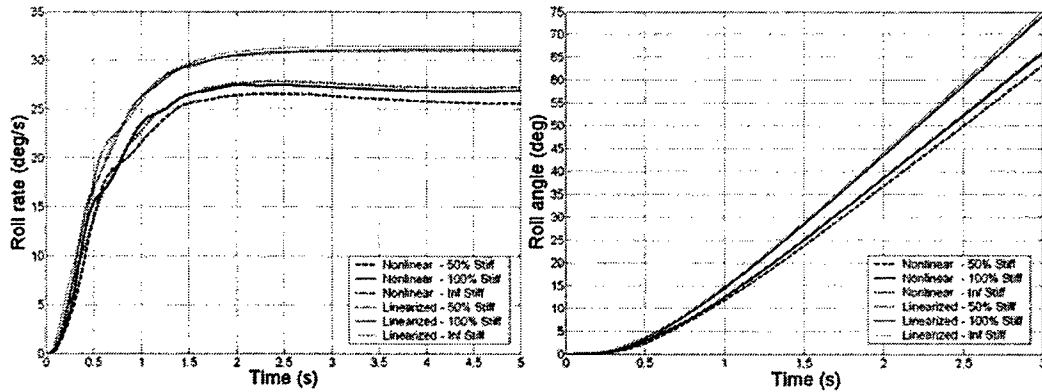


Figure 12: Aileron concept roll rate and roll angle responses with varying inner wing stiffness (flight index 5, maximum deflection; 100% stiffness is nominal)

For the ways the analysis may be conducted, there is a significant difference between the linearized and fully nonlinear approaches for roll analysis, particularly for the terminal roll rate. In fact, the overshoot that happens due to wing flexibility and relative position of vehicle c.g. and roll axis is not captured in the linearized approach. On the other hand, the roll angle response is less sensitivity to the full nonlinear effects, presenting differences between the two analyses predictions of 10% for the active and 15% for the aileron actuations after 3 s into the roll bank.

Regarding the effects on the flexibility of the inner wings, the primary impact is on the dynamics of the response to reach maximum roll rate. For the active concept, due to low roll rates, the effects of the flexibility of the inner wings does not become a factor. However, for the levels of response presented by the ailerons, a significant difference can be seen from Fig. 12. As the inner wings become less stiff, there is a loss on the terminal roll rate due to the deformation of the inner wings. This is only capture by the fully nonlinear analysis.

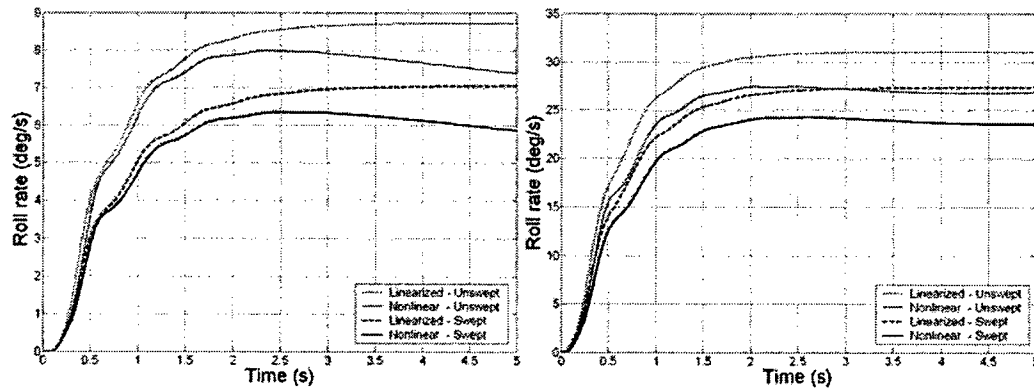


Figure 13: Active concept (left) and aileron concept (right) roll responses for different outer wing sweep angles (25° sweep indicated by "Swept"; flight index 5, maximum actuation).

Outer Wing Sweep Effect on Roll Response: As an indication of the effects of outer wing sweep on roll response, a 25° backward sweep case is compared with the 0° sweep baseline cases. Fig. 13 shows the roll rate results for the active and aileron cases. Note that the effects of moving the vehicle's aerodynamic center with the outer wing sweep⁷ is beyond the scope of this paper even though

modeled in the framework. As can be observed from the plots, a decrease in roll rate is observed from both linearized and nonlinear analyses. When the wing is swept, there is a reduction in angle of attack as the wing bends. Since the twist axis of the wing is no longer perpendicular to the airfoil, the effectiveness of twisting the wing to change the angle of attack is decreased. Furthermore, the lift per unit span of the swept wing decreases with the cosine of the sweep angle. Since the roll rate damping of the inner wings is constant as the outer wings are swept, there is an overall reduction in effectiveness of the outer wings to produce roll rate for the same spanwise angle of attack distribution.

APA Technology Impact on Roll Performance: All the studies presented so far were based on representative APA material properties from current existing polycrystalline piezocomposite materials. There have been efforts within the materials research community for the development of different material systems with improved piezoelectric properties. Among them, the single-crystal program¹² for AFC could lead to a significant increase in actuation authority. To estimate the required actuation needed for the joined-wing Sensorcraft-like application, consider the same APA material properties and wing design as previously discussed, but allow for the maximum free strain of the APA be increased. Fig. 14 shows the impact on wing twist distribution along the outer wingspan for different levels of APA's free strain. Considering the case of 3.75-fold increase in free strain (and keeping the passive material properties of the APA the same), Fig. 15 show the impact on roll rate and roll angle responses. As indicated in these plots, this is the level of material improvement required so the wing-warping concept may achieve similar levels of performance as the aileron concept discussed before. These levels of improvements may be theoretically achievable¹² but only time can tell the viability of the concept.

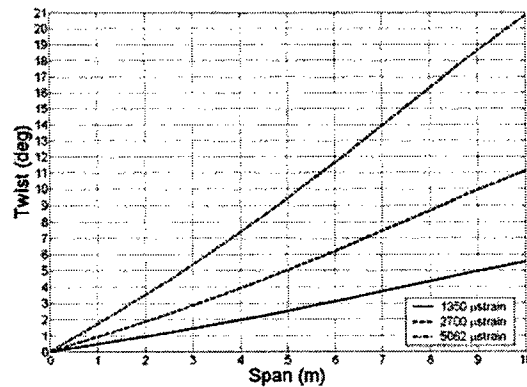


Figure 14: Spanwise twist distribution on the active outer wing considering different APA free strain levels (1350 µstrain represents available technology)

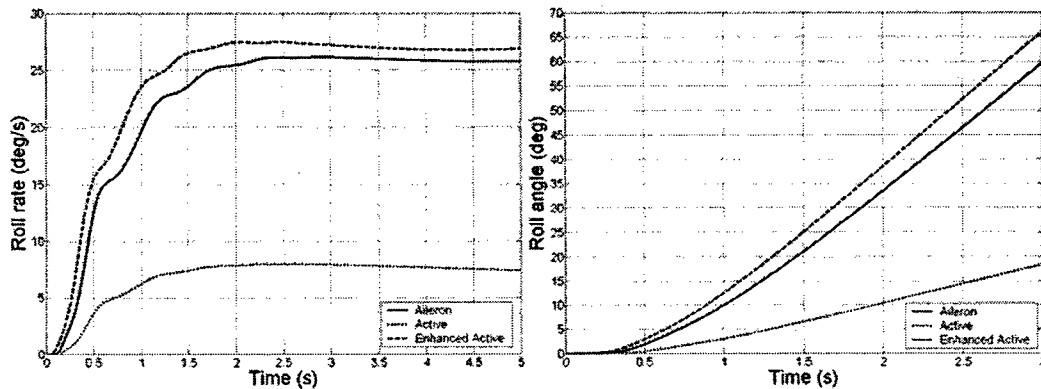


Figure 15: Roll response considering a mechanically equivalent APA but with 3.75-fold increase in its free strain properties (flight index 5; vehicles are trimmed prior to roll maneuver)

3.3. General Remarks

Even though numerical design optimization will improve the baseline vehicle designs and should be employed to support navigating such reach design space, the relative results obtained here represent the order of response expected from each concept for the joined-wing Sensorcraft configuration. Again, the concepts are based on current technology material properties and construction practices. The active concept uses APA properties that are achievable with today's technology and the model includes all the fundamental static and dynamic effects on the aeroelastic responses. The aileron design contains significant idealizations, and represents the performance upper bound for the concept. No surface control inertia or aerodynamic losses with high deflection angles have been included in the model, or any control flexibility that comes with very large control surfaces. In fact, the chosen size of the aileron was based on the maximum practical size surface that can be fitted within such wing¹¹ without being concerned with mechanical fixtures and actuator systems.

Another important aspect of the vehicles' designs presented here is that they are driven by strength consideration, which penalized the wing-warping concept and favored the aileron-actuated one. Stiffness constraints got automatically satisfied once the layups were thickened enough to sustain the high loads. If a reduced maximum load factor is chosen, other constraints may become active, particularly related to aileron reversal and gust loads (as was seen for the latter in some of the design studies conducted in [5]). In fact, the overall system/mission requirements, including performance and survivability considerations, will certainly impact the design solution, potentially changing the importance of roll performance as assumed here.

4. CONCLUSIONS

This paper discussed some of the unique aeroelastic characteristics of the joined-wing Sensorcraft, with emphasis on the concept of wing warping actuation for maneuver load generation. The study employs a newly developed framework for the analysis, design, and simulation of high-flexible multi-segmented wing vehicles, also described in this paper.

Two baseline vehicles were used in this study. The first one has anisotropic piezocomposite actuators embedded in the composite construction of the outer wing, inducing strain and twist deformation (later it was modified to have an active forward inboard wing as well). The second baseline vehicle has an aileron spanning 50% of the outer wing. Both designs satisfy the same set of constraints. Strength of the laminates at 2.5-g load factor became the sizing constraint for both designs.

When analyzing the joined-wing concepts, the importance of wing flexibility and the availability of a geometrically nonlinear structural dynamics solver were demonstrated. Of particular interest for the joined-wing configuration is the criticality of the sudden rear wing loss of stiffness (buckling) that compromises the vehicle integrity. This can be alleviated by proper twist control of the forward inboard wing. While in this paper this was demonstrated using wing warping induced by APA, in principle similar effect could be achieved using ailerons in the forward inboard wing. For the roll response, it was shown that the wing-warping design based on current APA technology presents a terminal roll rate which is over three-times smaller than the aileron concept due to limited twist authority. This could be overcome with an APA of similar mechanical properties as used in this study but with 3.75-times greater maximum free strain. This is within range of the promises of single-crystal fiber composites.

5. ACKNOWLEDGEMENTS

The authors gratefully acknowledge the technical interactions with Dr. Roy Ikegami, Mr. Christopher L. Davis, and Mr. Gerald F. Herndon from the Boeing Co., Phantom Works, Kent, Washington, and Drs. Brian P. Sanders and Gregory W. Reich from AFRL/WPAFB, Dayton, Ohio. The second author gratefully acknowledges C.S. Draper Laboratory for providing his fellowship for graduate studies.

This work is sponsored by AFOSR under grant F49620-01-1-0133. The technical monitor is Dr. Dean Mook.

6. REFERENCES

- [1] Pendleton, E. W., Griffin, K. E., Kehoe, M., and Perry, B., "A Flight Research Program for the Active Aeroelastic Wing Concept," In *Proceedings of the 37th AIAA/ASME/AHS/ASC Structures, Structural Dynamics and Materials Conference*, Salt Lake City, Utah, April 1996.
- [2] Bent, A. A., "Active Fiber Composite Material Systems for Structural Control Applications," In *Proceedings of the SPIE's 6th International Symposium on Smart Structures and Materials*, Newport Beach, California, March 1999.
- [3] Wilkie, W.K., Bryant, R.G., High, J.W., Fox, R.L., Hellbaum, R.F., Jalink, A., Little, B.D., and Mirick, P.H., "Low-cost piezocomposite actuator for structural control applications," In *Proceedings of the SPIE 7th Symposium on Smart Structures and Materials*, Newport Beach, California, March 2000. pp. 323-334.
- [4] Cesnik, C. E. S. and Ortega-Morales, M., "Active Aeroelastic Tailoring of Slender Flexible Wings," *International Forum on Aeroelasticity and Structural Dynamics*, Madrid, Spain, June 5—7, 2001.
- [5] Brown, E. L., "Integrated Strain Actuation in Aircraft with Highly Flexible Composite Wings," Ph.D. Thesis, Massachusetts Institute of Technology, Cambridge, Massachusetts, June 2003.
- [6] Livne, E., "Aeroelasticity of Joined-Wing Airplane Configurations: Past Work and Future Challenges - A Survey," In *Proceedings of the 42nd AIAA/ASME/AHS/ ASC Structures, Structural Dynamics, and Materials Conference*, Seattle, WA, April 16-19, 2001, AIAA-2001-1370.
- [7] Blair, M. and Canfield, R. A., "A Joined-Wing Structural Weight Modeling Study," In *Proceedings of the 43rd AIAA/ASME/AHS/ASC Structures, Structural Dynamics and Materials Conference*, Denver, Colorado, April 2002, AIAA-2002-1337.
- [8] Roberts, R. W., Canfield, R. A., and Blair, M., "Sensor-craft Structural Optimization and Analytical Certification," In *Proceedings of the 44th AIAA/ASME/AHS/ASC Structures, Structural Dynamics and Materials Conference*, Denver, Colorado, April 2003.
- [9] Reich, G. W., Raveh, D., and Zink, P. S., "Application of Active Aeroelastic Wing Technology to a Joined-Wing Sensorcraft," In *Proceedings of the 43rd AIAA/ASME/AHS/ASC Structures, Structural Dynamics and Materials Conference*, Denver, Colorado, April 2002, AIAA-2002-1633.
- [10] Peters, D. A. and Johnson, M. J., "Finite-State Airloads for Deformable Airfoils on Fixed and Rotating Wings," In *Symposium on Aeroelasticity and Fluid/Structure Interaction, Proceedings of the Winter Annual Meeting*. ASME, November 6 -11, 1994.
- [11] Ikegami, R., Private communication, The Boeing Co., Phantom Works, Seattle, Washington, 2002.
- [12] Rossetti Jr., G. A., Pizzochero, A., and Bent, A. A., "Recent Advances in Active Fiber Composites Technology," In *Proceedings of the 12th IEEE International Symposium on Applications of Ferroelectrics*, Honolulu, Hawaii, 2000, pp. 753-756.
- [13] Cesnik, C. E. S. and Brown, E. L., "Active Warping Control of a Joined Wing Airplane Configuration," *Proceedings of the 44th Structures, Structural Dynamics, and Material Conference*, Hampton, Virginia, April 7—10, 2003.

Appendix E:

Cesnik, C. E. S. and Su, W., "Nonlinear Aeroelastic Modeling and Analysis of Fully Flexible Aircraft," Proceedings of the 46th AIAA/ASME/ASCE/AHS/ASC Structural, Structural Dynamics and Materials Conference, Austin, Texas, April 18—21, 2005, AIAA-2005-2169.

Nonlinear Aeroelastic Modeling and Analysis of Fully Flexible Aircraft

Carlos E. S. Cesnik* and Weihua Su†
The University of Michigan, Ann Arbor, MI, 48109-2140

This paper introduces an approach to effectively model the nonlinear aeroelastic behavior of fully flexible aircraft. The study is conducted based on a nonlinear strained-based finite element framework in which the developed low-order formulation captures the nonlinear (large) deflection behavior of the wings, and the unsteady subsonic aerodynamic forces acting on them. Instead of merely considering the nonlinearity of the wings, the paper will allow all members of the vehicle to be flexible. Due to their characteristics of being long and slender structures, the wings, tail, and fuselage of highly flexible aircraft can be modeled as beams undergoing three dimensional displacements and rotations. The cross-sectional stiffness and inertia properties of the beams are calculated along the span, and then incorporated into the 1-D nonlinear beam model. Finite-state unsteady subsonic aerodynamic loads are incorporated to be coupled with all lifting surfaces, so as to complete the state space aeroelastic model. Different Sensorcraft concepts are modeled and studied, including conventional single-wing and joined-wing aircraft configurations with flexible fuselage and tail. Based on the proposed models, roll responses and stabilities are studied and compared with linearized and rigidized models. At last, effects of the flexibility of the fuselage and tail on the roll maneuver and stability of the aircraft are presented.

I. Introduction

HIGH-ALTITUDE Long-Endurance (HALE) vehicles are being developed for multiple applications, including environmental sensing, telecom relay, and military reconnaissance. These HALE concepts feature light wings with a high aspect ratio. These long and slender wings, by their inherent nature, can maximize lift to drag ratio. On the other hand, these wings may undergo large deformations during normal operating loads, exhibiting geometrically nonlinear behavior. Patil, Hodges, and Cesnik¹ studied the aeroelasticity and flight dynamics of HALE aircraft. The results indicate the aeroelastic behavior and flight dynamics characteristic of the aircraft can be significantly changed due to the large deflection of the flexible wings. Van Schoor, Zerweckh and von Flotow² studied aeroelastic characteristics and control of highly flexible aircraft. They used linearized modes including rigid-body modes to predict the stability of the aircraft under different flight conditions. Their results indicate that unsteady aerodynamics and flexibility of the aircraft should be considered so as to correctly model the dynamic system. This leads to the conclusion that the coupled effects between these large deflection and vehicle flexibility and flight dynamics (e.g., roll controllability) as well as other aeroelastic effects (e.g., gust response, flutter instability) must be properly accounted for in a nonlinear aeroelastic formulation. Drela³ modeled a complete flexible aircraft as an assemblage of joined nonlinear beams. In his work, the aerodynamic model was a compressible vortex/source-lattice with wind-aligned trailing vorticity. The nonlinear equation was solved by using a full Newton method. Through simplifications of the model, the computational size was reduced for iterative preliminary design.

In the last several years, the Air Force has been working on a new generation Intelligence, Surveillance, and Reconnaissance (ISR) platform, which is called "Sensorcraft." These are large HALE aircraft, with wing span of approximately 60m. At this moment, three basic platform shapes are being considered: wing-body-tail, single-wing and joined-wing configurations⁴.

* Associate Professor (cesnik@umich.edu), Department of Aerospace Engineering, Associate Fellow, AIAA.

† Graduate Research Assistant (suw@umich.edu), Department of Aerospace Engineering.

Copyright©2005 by Carlos E. S. Cesnik and Weihua Su. Published by the American Institute of Aeronautics and Astronautics, Inc., with permission.

Among the Sensorcraft concepts, the joined-wing configuration is the most unusual one. It was first proposed by Wolkovitch⁵, who suggested that this new design would lead to possible weight savings and some aeroelastic benefits. However, the effects of structural deformation on the aerodynamic and aeroelastic responses are difficult to intuit and predict.

Livne⁶ presented a comprehensive survey on the design challenges of joined-wing aircraft configurations. Therein, he presented a review of past works in joined-wing aeroelasticity and gave a qualitative discussion of their behavior in a multidisciplinary context. Much of the discussion in the paper dealt with structural and aeroelastic issues relating to the aft wing/tail. The in-plane loads due to structure deformation and changes in geometric stiffness give rise to non-intuitive aeroelastic behavior. Bending and twisting couplings of the entire structure cause natural frequencies and mode shapes to shift. The tendency for buckling and divergence in the aft member is of major concern when trying to reduce weight. The finding of rear wing divergence to be more critical than flutter is counterintuitive, since the aft wing is supported at the joint. This phenomenon seems associated with a reduction in structural stiffness due to the in-plane compressive loads in the rear members. The geometry of the joint between forward and aft wings is also of importance because it plays a major role in how in-plane, bending, and torsion loads are transferred. For instance, a pinned joint may allow upward buckling of the aft wing, while a fixed rigid joint may allow the aft wing to buckle downward, since bending moments are transferred across the joint. Lin, Zhou and Stearman⁷ studied the influence of joint fixity on the aeroelastic characteristics of the joined-wing. They suggested that the fixed joint provide the best characteristic.

Weight estimation of joined-wing has been studied before. The structural weight of a joined-wing and that of a Boeing 727 were compared by Samuels⁸. His conclusion is the joined-wing's structural weight is 12-22% lighter than that of a conventional configuration, while in Ref. 9, Gallman and Kroo concluded that the structural weight was increased by 13% when including the buckling constraint of the aft wing. Therefore, joined-wing configurations are not guaranteed to be lighter than conventional ones. Miural, Shyu, and Wolkovitch¹⁰ found that the structural weight of a joined-wing strongly depend on geometry and structural arrangement of the wing. Blair and Canfield¹¹ described an integrated design process for generating high fidelity analytical weight estimations of joined-wing configurations. They suggested an integrated design process that can bring together different software package, such as NASTRAN, PanAir, and integrate them through the Air Vehicles Technology Integration Environment (AVTIE), so that structures, aerodynamics and aeroelastic analysis are incorporated.

Structural optimization for joined-wing was done by Kroo, Gallman and Smith^{9,12,13}. The wings were modeled as boxed-beams to study for the effects of several parameters on the trimmed performance of joined-wing aircraft. In Ref. 12, the results show that the wings with similar aspect ratio joining at 60-75% of the front wing span are optimal for the given condition. Asymmetric material distribution leads to more drag reduction than symmetric distribution. They also suggest using fully stressed design method since it is computationally cheaper even though it produced a result that is a little bit heavier and with more direct operation cost (DOC). Roberts, Canfield and Blair¹⁴ performed the structural optimization for a joined-wing Sensorcraft. They identified some critical points in a flight index and optimized the Sensorcraft with respect to these critical points. Their results suggest the necessity of nonlinear structural analysis. More recently, Rasmussen, Canfield and Blair¹⁵ performed an optimum design for joined-wing aircraft that utilizes both structural and aerodynamic analysis. Response surface method was employed within their scheme of design optimization.

Different technologies, in addition to the traditional ailerons, have been included in structural design of joined-wing Sensorcraft, in order to improve their performance. Active aeroelastic wing (AAW)¹⁶ technology was applied in a joined-wing Sensorcraft for his purpose of minimum deformations of the antenna embedded in the wing skins, in addition to generate maneuver loads for the Sensorcraft.

Meanwhile, Cesnik and Brown¹⁷ studied some of aeroelastic characteristics of the joined-wing aircraft with the concept of active warping actuation for maneuver load generation. The active piezoelectric concepts have their advantage over traditional ailerons in terms of structural integration. However, according to the studies of Ref. 17, the wing-warping design based on current anisotropic piezoelectric actuators (APA) technology presents a terminal roll rate which is three times smaller than the aileron concept due to limited actuator authority.

From the elicitation of previous researches, deformation of the structure of joined-wing Sensorcraft at a certain location may produce large changes in angle of attack in the lifting surfaces at other locations, due to their complex structure. Efforts to minimize structural weight may create aeroelastic instabilities that are not encountered in conventional aircraft design. For joined-wing aircraft, the first sign of failure may be associated with the buckling of the aft members as the structure is softened. Flutter and divergence may also become a problem in these members due to the reduction in structural frequency as they go into compression. As the aircraft becomes more flexible, the nature of the geometric structural nonlinearities become more important and the lift distribution on the aircraft may be adversely affected.

Not being limited within the scope of joined-wing configurations, the large overall vehicle size associated with the different Sensorcraft configurations being studied may lead to a very flexible aircraft overall. In fact, long and slender fuselage and tail surfaces result in elastic coupling with the lifting surfaces. This directly impacts the trimming of the vehicle, and the couplings among roll, yaw, and pitch require the use of nonlinear aeroelastic and flight dynamics analyses to predict vehicle response, design of control laws, and its overall guidance. These flexibility effects may make the response of the vehicle very different than its rigid or linearized models. The current study is an extension of the work of Ref. 18, allowing all members of the vehicle to be flexible. There are limitless aspects of fully flexible aircraft that are necessary to be studied, however, this paper focuses on two key points:

- 1) New approach for the modeling of the complex nonlinear structural system of fully flexible aircraft;
- 2) Assessment of the effects of induced flexibility of fuselage and tail on roll performances and stabilities of fully flexible Sensorcraft, particularly applied to a single-wing and joined-wing configurations.

II. Theoretical Formulation

In the proposed formulation, the vehicle is allowed six rigid-body and multiple flexible degrees of freedom. The structures are allowed fully coupled three-dimensional bending, twisting, and extensional deformations. Control surfaces may be included for maneuver studies. Inclusion of flexible fuselage and vertical tail are new to the formulation. A finite-state unsteady airloads model is integrated into the system equations, with the exception of the fuselage (at this stage). The model allows for a low-order set of nonlinear equations that can be put into state-space form to facilitate control design.

A. Element Description

Consider a typical slender structural component (e.g. wing) being represented as shown in Fig. 1. In the work of Ref. 17, specialized beam elements were developed that have four local strain degrees-of-freedom: extension, twist, and two bending ones. Fig. 2 exemplifies the deformations of constant-strain elements.

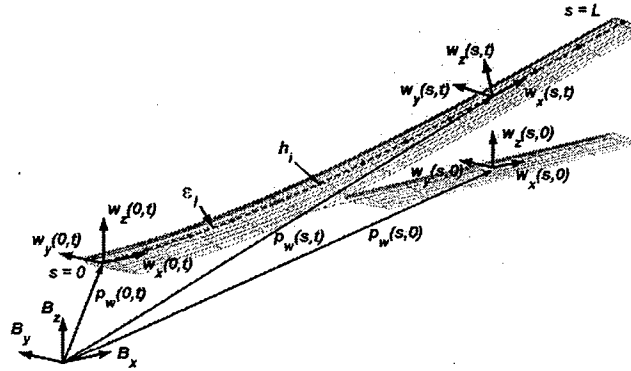


Figure 1. Wing coordinates

Each node along the beam is determined by a vector consisting of 12 components. Suppose the beam reference frame is w , which is a function of the natural beam coordinate s , the 12-component vector is denoted as,

$$h(s)^T = [p_w(s)^T, w_x(s)^T, w_y(s)^T, w_z(s)^T] \quad (1)$$

where, p_w is the position of frame w in the body coordinate, w_x , w_y , and w_z are the direction vectors pointing along the beam axis, toward the leading edge, and normal to the airfoil, respectively (see Fig. 1). As discussed in Ref. 17, the governing equation, which relates the dependent displacements to the independent strains, is,

$$\frac{\partial h(s)}{\partial s} = A(s)h(s) \quad (2)$$

where, A is a matrix function of the strains.

$$A(s) = \begin{bmatrix} 0 & 1 + \varepsilon_x(s) & 0 & 0 \\ 0 & 0 & \kappa_z(s) & -\kappa_y(s) \\ 0 & -\kappa_z(s) & 0 & \kappa_x(s) \\ 0 & \kappa_y(s) & -\kappa_x(s) & 0 \end{bmatrix} \quad (3)$$

where the blocks are all 3x3 diagonal matrices. The solution of Eq. (2) can be given by Eq. (4), with the assumption that the element has a constant strain vector

$$h(s) = e^{As} h_0 = e^{G(s)} h_0 \quad (4)$$

where, h_0 is the beam boundary conditions.



Figure 2. Deformations of a typical constant-strain element.

The total virtual work done on an element due to all internal and external forces and moments can be written as,

$$\delta W = -\delta h^T M \ddot{h} - \delta \varepsilon^T K \varepsilon + \delta \varepsilon^T B_v \nu - \delta h^T N g + \delta p^T B_F F^{ds} + \delta \theta^T B_M M^{ds} + \delta p^T F^p + \delta \theta^T M^p \quad (5)$$

where the terms involved include the effects of inertia ($M \ddot{h}$), gravity field ($N g$), internal strain (ε), piezoelectric actuation (ν), distributed forces (F^{ds}) and moments (M^{ds}), and point forces (F^p) and moments (M^p).

B. Member and Inter-Member Equations

In the model of fully flexible aircraft, the fuselage and the vertical tail are both modeled as slender beams, similarly to the wings. Therefore, it is necessary to model a split beam system as illustrated in Fig. 3. For simplicity, consider three members in this beam system. Member 1 consists of two elements and Members 2 and 3 each consist of one element only. Every element has three nodes, each with the degrees of freedom given by Eq. (1). The proposed approach here is to modify the original kinematics of Ref. 17 to allow the analysis of split beams.

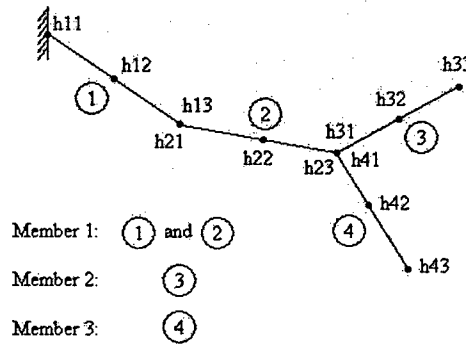


Figure 3. A split (or bifurcated) beam system.

The kinematics for these members is obtained by marching the element kinematics from the boundary node to the end nodes at each branch, which can be written as follows:

C. Equations of Motion

The equations of motion of the system are obtained by following the Principle of Virtual Work. With the six rigid-body degrees of freedom, the system structural degrees of freedom are represented by the column matrix q , where

$$\dot{q} = [\dot{\epsilon}_1^T, \dot{\epsilon}_2^T, \dots, \dot{\epsilon}_n^T, V_B^T, \omega_B^T]^T \quad (7)$$

and ϵ_i contains the strain variables for wing member i , V_B and ω_B are the linear velocity and angular velocity of the vehicle reference point (original of the B frame), respectively, represented in the body frame, B . The dependent variables for the entire vehicle are collected into the column matrix H ,

$$\dot{H} = [\dot{h}_1^T, \dot{h}_2^T, \dots, \dot{h}_n^T, V_B^T, \omega_B^T]^T \quad (8)$$

The dependent degrees of freedom are related to the independent degrees of freedom through a Jacobian matrix relation

$$H = f(q), \quad dH = \left[\frac{\partial H}{\partial q} \right] dq = [J_{Hq}(q)] dq \quad (9)$$

The expression for virtual work on the vehicle is now given by

$$\delta W = \delta q^T (-\bar{M}\ddot{q} - \bar{C}\dot{q} - \bar{K}q + \bar{N}g + \bar{B}_V V + \bar{B}_{F1} F^{dst} + \bar{B}_{F2} F^{pt} + \bar{B}_{M1} M^{dst} + \bar{B}_{M2} M^{pt} + B_{q0} q_0 + B_H H) \quad (10)$$

where \bar{M} , \bar{C} , and \bar{K} are generalized mass, damping, and stiffness matrices corresponding to the independent degrees of freedom of the total system. Note that the matrices above are all assembled ones with respect to global degrees of freedom. The principle of virtual work requires that the total virtual work done on the system be equal to zero, leading to the equations of motion,

$$\bar{M}\ddot{q} + \bar{C}\dot{q} + \bar{K}q = B_V V + B_{F1} F^{dst} + B_{F2} F^{pt} + B_{M1} M^{dst} + B_{M2} M^{pt} + \bar{N}g + B_{q0} q_0 + B_H H \quad (11)$$

The distributed loads, F^{dst} and M^{dst} , are divided into aerodynamic loads and user supplied loads. The aerodynamic loads evaluated at the current state have the incremental form

$$\begin{aligned} F^{aero}(t) &= F^{aero}(t_0 + \Delta t) \approx F_0(q_0, \dot{q}_0, \lambda_0) + F_{\ddot{q}} \ddot{q} + F_{\dot{q}} \Delta \dot{q} + F_q \Delta q + F_{\lambda} \Delta \lambda \\ M^{aero}(t) &= M^{aero}(t_0 + \Delta t) \approx M_0(q_0, \dot{q}_0, \lambda_0) + M_{\ddot{q}} \ddot{q} + M_{\dot{q}} \Delta \dot{q} + M_q \Delta q + M_{\lambda} \Delta \lambda \end{aligned} \quad (12)$$

here λ is column matrix of induced flow states as described in Ref. 19. The induced flow states are governed by a differential equation of the form

$$\dot{\lambda} = L_1 \lambda + L_2 \ddot{q} + L_3 \dot{q} \quad (13)$$

The aeroelastic equations of motion are obtained by moving the state dependent aerodynamic loads over to the left hand side of Eq. (11) and augmenting the structure states with the induced flow states, which can be represented in state space form as

$$\dot{x} = A(x)x + B(x)u(x, t) \quad (14)$$

where the state vector is now given by

$$x = [q^T, \dot{q}^T, \lambda^T]^T \quad (15)$$

III. Numerical Studies

To exemplify the capability of the new formulation and study the impact of overall vehicle flexibility, two different baseline vehicles were created. They represent two different configurations: a single-wing and a joined-wing configuration. Seven flight index points represent the nominal mission profile, as indicated in Fig. 5. At each index point, the altitude, fuel mass, and nominal flight velocity are specified. The index points represent: (1) takeoff, (2) climb, (3) cruise ingress, (4) cruise/loiter/cruise, (5) cruise egress, (6) decent, and (7) landing. The fuel burn determines the duration of each flight segment. The nominal flight speed at each index point is based on the cruise speed (input parameter), and is computed such that the dynamic pressure is constant (constant indicated air speed). At each flight index point, the vehicle is trimmed for equilibrium in horizontal flight at given flight speed.

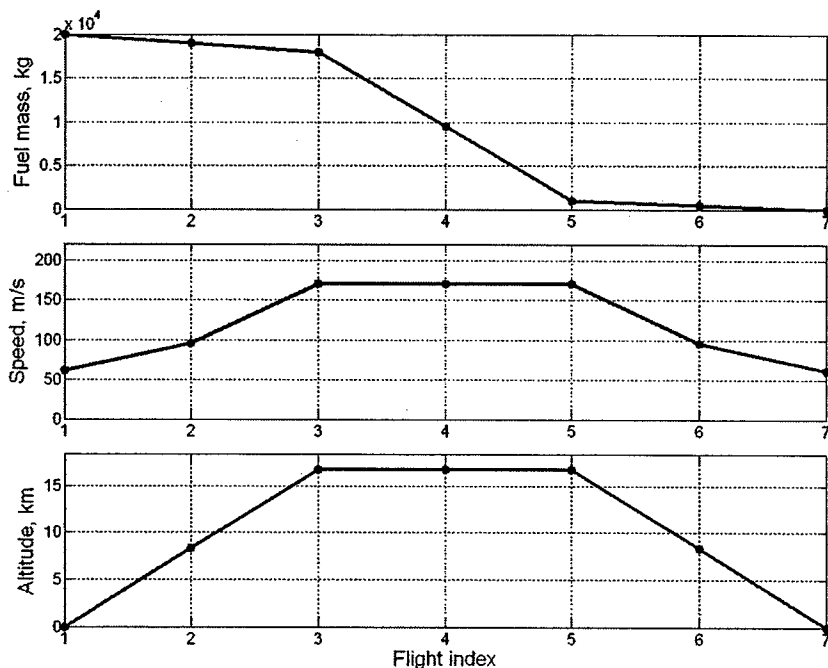


Figure 5. Basic mission profile.

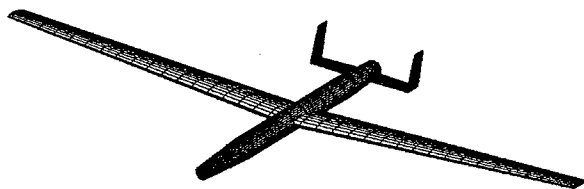


Figure 6. Baseline single-wing vehicle and trimmed body angle of attack.

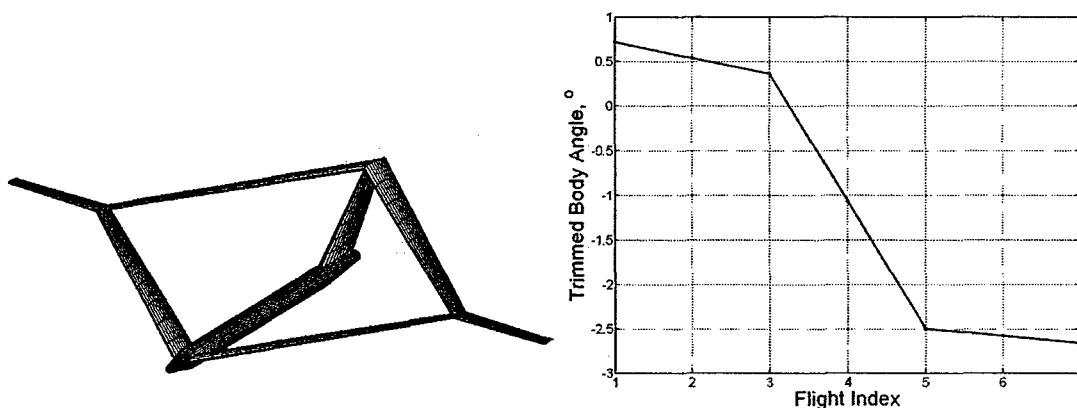


Figure 7. Baseline joined-wing vehicle with unswept outer wings (where ailerons are present).

A. Baseline Vehicles

Three sets of constraints were defined to help sizing the baseline designs: strength (based on first-ply failure) at 1.5-g load, strength based on gust loads, and minimum linearized flutter margin. For both vehicles, the 1.5-g load factor was shown to be the critical constraint and the wing structural thickness distribution was sized for fully-strained design along span. A description of the design process can be found in Ref. 17.

1. Single-wing Configuration

Geometry. From top view, the vehicle shape is symmetric. As indicated in Fig. 8, the wings are divided into nine regions, and the horizontal and vertical tail surfaces are both divided into two regions for definition of cross-sectional property distribution. For simplicity, NACA 4415 is chosen as the airfoil and it is kept constant throughout the wing members. The wing contains three independent ailerons, which present in regions 3 and 4, 5 to 7, and 8 and 9, as indicated in Fig. 8. These ailerons occupy 20% of the chord from 22% span to the tip of the wing, which are allowed to deflect $\pm 30^\circ$.

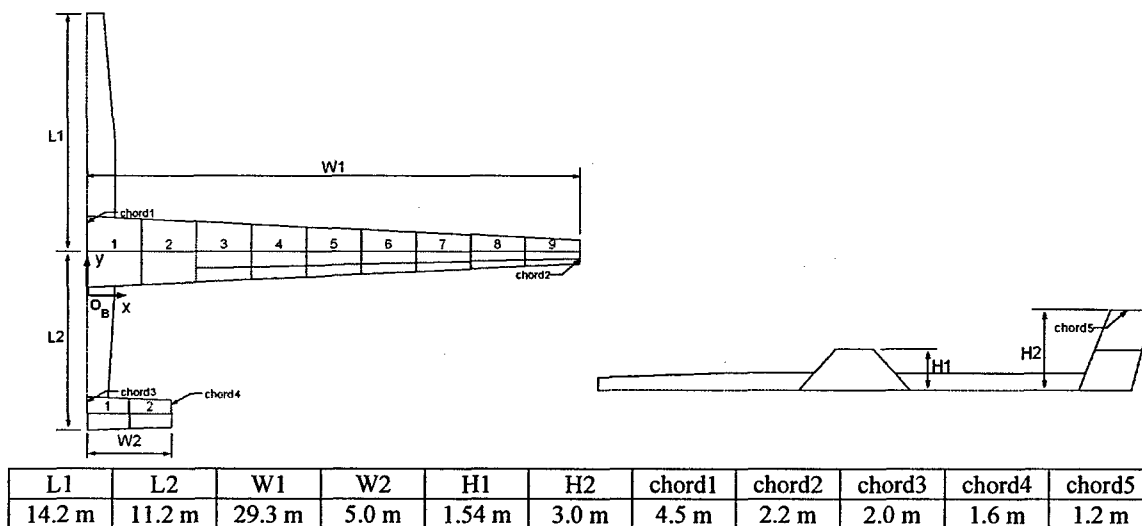


Figure 8. Baseline single-wing configuration sensorcraft vehicle geometry.

Vehicle Mass Breakdown. The vehicle mass breakdown is given in Table 1. The fuel is assumed to be distributed up to half span of the wings, independent of the total amount of fuel on board. The fuselage contains no fuel.

Table 1. Vehicle mass distribution for single-wing configuration.

Fuselage structure + payload + engine mass	4,000 kg
Fuel mass	20,000 kg
Tails structure mass	420 kg
Vehicle total wing structure mass	4,230 kg
Vehicle gross take-off mass	28,650 kg

Cross-sectional Inertia and Stiffness Distributions. The stiffness and inertia properties of each cross-section of the wing, tail and fuselage can be found in the Appendix (Figs. A1 to A21). Note that nonstructural masses of 155 kg each is used for the modeling of aircraft payload, which are assigned at each node of the fuselage for simplicity.

2. Joined-wing Configuration

Geometry. From top view, the vehicle shape is symmetric (although one may want to vary the forward/aft location of the joint). The wings are denoted right front wing (with inner and outer wings), left front wing, right aft wing (with inner-wing only), and left aft wing. Right and left are determined as in Fig. 9 (as viewed from top with nose pointing up). The front wings are divided into eight regions while the aft wings are divided into four regions for definition of cross-sectional properties distribution. The members of all inner wings are identical in construction, and the material distribution follows the numbering convention indicated in Fig. 9. For simplicity, NACA 4415 is chosen as the airfoil and it is kept constant throughout the wing members. The outer wing contains a 50%-span/20%-chord aileron that is allowed 30° of amplitude deflection.

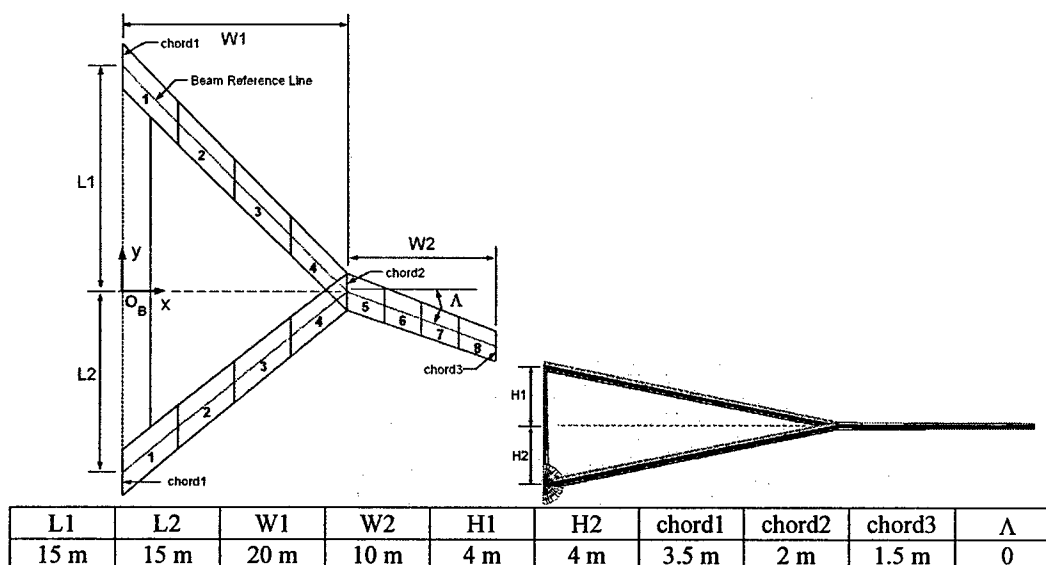


Figure 9. Baseline joined-wing sensorcraft vehicle geometry.

Vehicle Mass Breakdown. The vehicle mass breakdown is given in Table 2. The fuel is assumed to be distributed evenly throughout the inner and outer wings, independent of the total amount of fuel on board. The fuselage contains no fuel.

Table 2. Vehicle mass distribution for joined-wing configuration.

Fuselage structure + payload + engine mass	4,000 kg
Fuel mass	20,000 kg
Vertical tail structure mass	550 kg
Vehicle total wing structure mass	3,440 kg
Vehicle gross take-off mass	27,990 kg

Cross-sectional Inertia and Stiffness Distributions. The stiffness and inertia properties of the wing, vertical tail and fuselage can be found in the Appendix (Figs. A22 to A42). Note that nonstructural masses of 100 kg each is used for the modeling of aircraft payloads, which are attached at each node of the fuselage for simplicity.

B. Models for Different Degrees of Flexibility

To assess the effects of the flexibility of different parts of the vehicles on their roll response and stability, five different models are considered for both single-wing and joined-wing configurations. They are summarized in Tables 3 and 4.

Table 3. Different levels of flexibility to be considered for single-wing configuration.

	Fuselage	Tails	Wings
Model 1	Rigid	Rigid	Flexible
Model 2	Rigid	Flexible	Flexible
Model 3	Rigid	4 * Flexible	Flexible
Model 4	Flexible	Rigid	Flexible
Model 5	Flexible	Flexible	Flexible

Table 4. Different levels of flexibility to be considered for joined-wing configuration.

	Fuselage	Vertical Tail	Inner Wings	Outer Wings
Model 1	Rigid	Rigid	Rigid	Flexible
Model 2	Rigid	Rigid	Flexible	Flexible
Model 3	Rigid	Flexible	Flexible	Flexible
Model 4	Flexible	Rigid	Flexible	Flexible
Model 5	Flexible	Flexible	Flexible	Flexible

In the above tables, the "rigid" members are modeled with 100 times the nominal stiffnesses, representing almost rigid cases, whereas the "4 * Flexible" members are modeled to have 25% of the nominal stiffness, representing an extra flexible case.

C. Roll Responses

In the study of roll response, the analysis takes place at flight index 5 (see Fig. 5), where the flight condition is 16.7 km altitude, and 170 m/s. The trimmed body angle of attack is -2.40° for single-wing and -2.50° for joined-wing configuration, respectively. These angles, however, may vary for the models with different level of flexibility. To achieve the roll motion, anti-symmetric aileron deflection is employed. As a comparison, both linearized and non-linear approaches are implemented¹⁷ here. In the linearized approach, the aircraft is first brought to its nonlinear steady state with roll motion locked. Both the roll moment and roll damping are calculated based on this deformed structure. The roll responses are then calculated based on these quantities. This approach has the advantage of being computationally efficient, which is very desirable for preliminary studies. On the other hand in the non-linear approach, the deformed shape of the aircraft is updated at each time step, and all the aerodynamic loads are calculated according to the updated deformed shapes. Although more time consuming, this presents the most accurate representation of the maneuver.

Figs. 10 and 11 show the comparison of the roll results from linearized and nonlinear approach for the fully flexible model (model 5) of the single-wing configuration. From the plots, one can see that there is over-15% difference in the steady state roll rate. This reflect at the different roll angle values at given instant of time. However, this may not be an issue for shallow angle roll maneuvers, where the difference between the two models is very small.

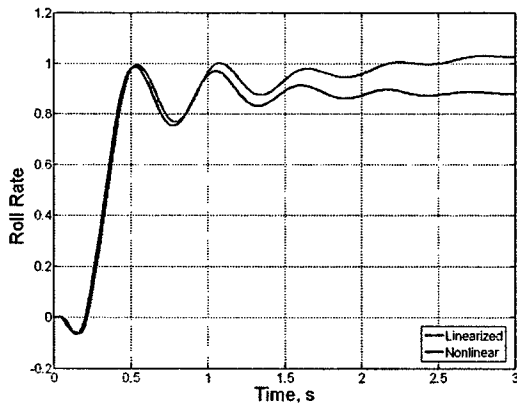


Figure 10. Comparison of roll rate results from linearized and nonlinear approaches (Normalized wrt $42.59^\circ/\text{s}$).

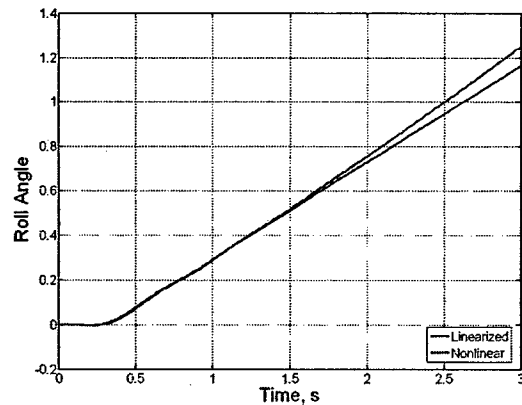


Figure 11. Comparison of roll angle results from linearized and nonlinear approaches (Normalized wrt 86.29°).

Figs. 12 to 15 show the roll response of different models of the single-wing configuration. As it can be seen from the pictures, the flexibility of the fuselage and the tails does not play an important role in the roll response of this aircraft configuration.

Figs. 16 to 19 show the roll response of different models of the joined-wing configuration. For this configuration, there is a significant difference between the linearized and fully nonlinear approaches for roll analysis, particularly for the terminal roll rate. Moreover, as it can be seen from Figs. 16 and 18, the additional vehicle flexibility brings more complexity to the roll response as it starts developing. Also the maximum roll rate that the vehicle can reach is actually lower than what the semi-rigid model can predict (see Figs. 17 and 19). As it can also be seen from the figures, even though the flexibility of the fuselage brings oscillations to the roll rate responses, the overall roll angle does not show a significant reduction. On the other hand, the induced flexibility of the vertical tail brings both the oscillations of the roll response and reductions to the overall roll angle.

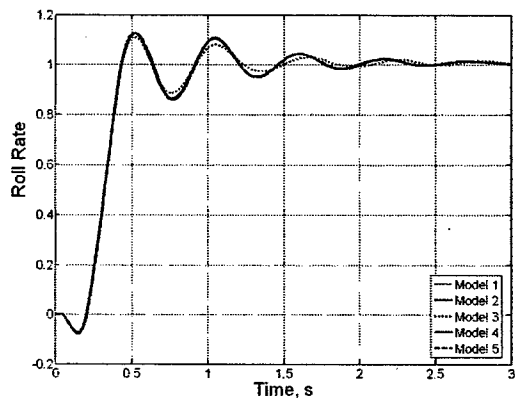


Figure 12. Linearized roll rate for single-wing configuration (Normalized wrt $37.32^\circ/\text{s}$).

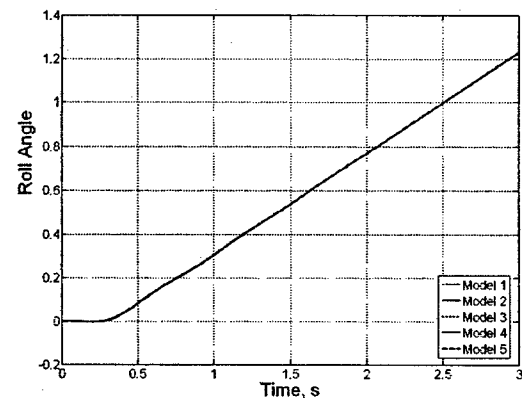


Figure 13. Linearized roll angle for single-wing configuration (Normalized wrt 81.67°).

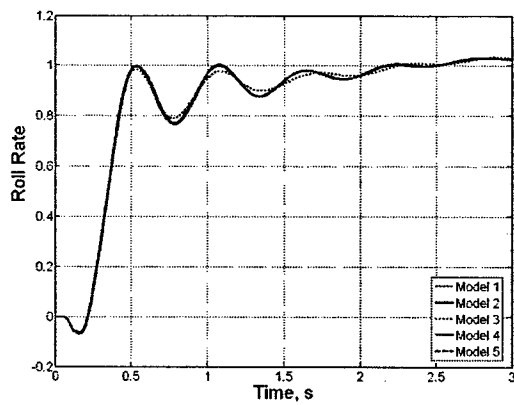


Figure 14. Nonlinear roll rate for single-wing configuration (Normalized wrt $42.59^\circ/\text{s}$).

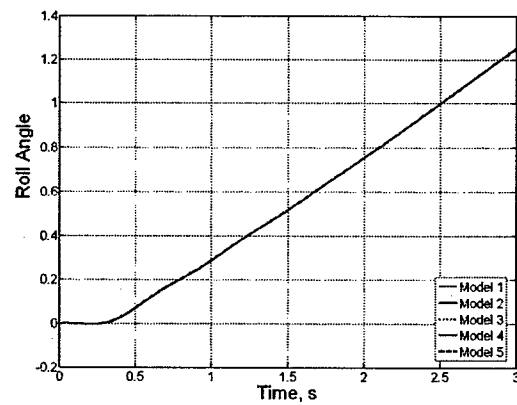


Figure 15. Nonlinear roll angle for single-wing configuration (Normalized wrt 86.29°).

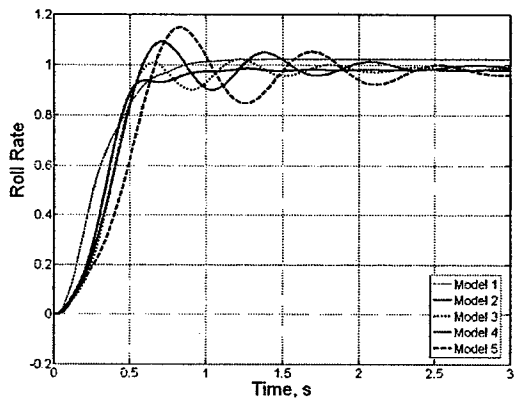


Figure 16. Linearized roll rate for joined-wing configuration (Normalized wrt $29.98^\circ/\text{s}$).

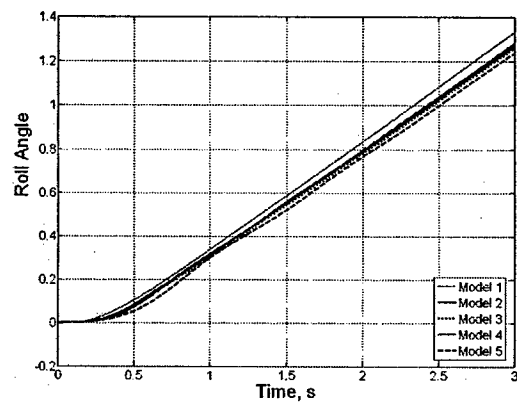


Figure 17. Linearized roll angle for joined-wing configuration (Normalized wrt 61.56°).

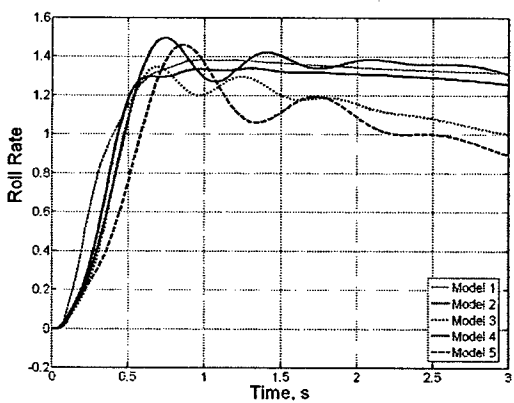


Figure 18. Nonlinear roll rate for joined-wing configuration (Normalized wrt $21.46^\circ/\text{s}$).

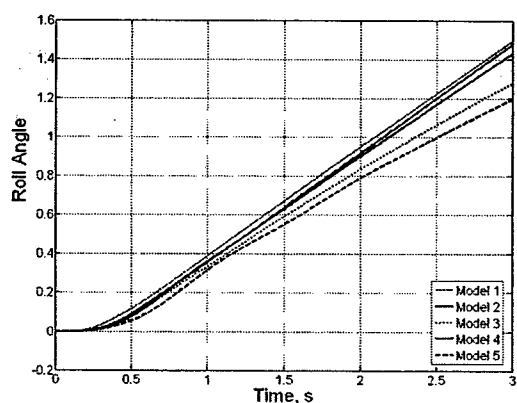


Figure 19. Nonlinear roll angle for joined-wing configuration (Normalized wrt 52.16°).

D. Dynamic Stability

For both the single-wing and joined-wing configurations, the flutter speed is approximated at each flight index point by determining the stability characteristics of the linearized system about its nonlinear equilibrium condition. The calculated flutter speeds are plotted in Figs. 20 and 25 for single-wing and joined-wing configurations, respectively.

For the single-wing configuration, the induced flexibility of the fuselage reduces the flutter speed slightly. However, this effect is very small, almost negligible. The reduction of the flutter speed due to the induced flexibility of the tail should be considered carefully. In the studies, overall system stabilities are calculated and analyzed, which includes both the wings and the tails. Since the relative elastic coupling between the wing and tail is weak (i.e., relatively rigid fuselage), one would not expect any significant influence of the tail on the flutter characteristics of the wing. This explains why there is nearly no change in the flutter speed when the tail is set from rigid to flexible. However, if the stiffness of the tail is further reduced (say, 25% of the nominal stiffness), there will be a significant decrease of the tail flutter speed, which ended up lower than that of the wing. This is shown in shown in Fig. 20 (Model 3). This can also be observed from the flutter modes. Figs. 21 and 22 show the flutter modes of the Model 3, which has fluttering tail. But in Model 5, the flutter comes from the wings as indicated in Figs. 23 and 24.

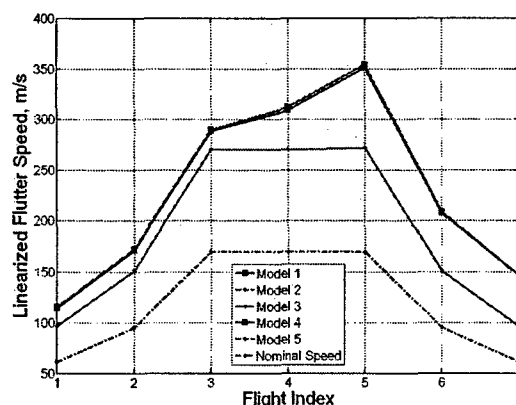
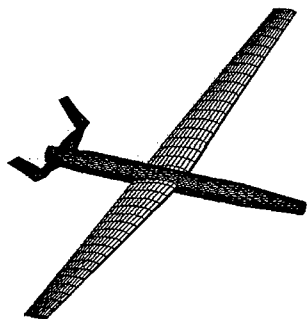
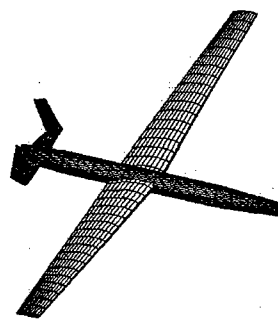


Figure 20. Flutter (unstable) speed at each flight index for different models of single-wing configuration.



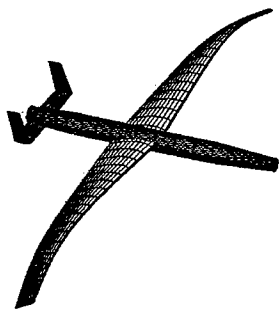
Flutter Speed: 270.31 m/s; Frequency: 2.91 HZ

Figure 21. Symmetric flutter (unstable) mode of single-wing configuration (Model 3, Index 3).



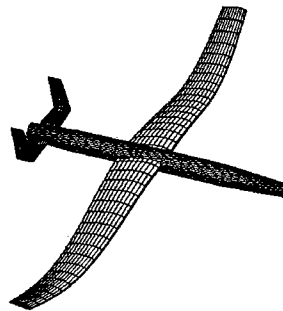
Flutter Speed: 271.63 m/s; Frequency: 2.91 HZ

Figure 22. Anti-symmetric flutter (unstable) mode of single-wing configuration (Model 3, Index 5).



Flutter Speed: 288.48 m/s; Frequency: 3.14 HZ

Figure 23. Symmetric flutter (unstable) mode of single-wing configuration (Model 5, Index 3).



Flutter Speed: 351.29 m/s; Frequency: 4.00 HZ

Figure 24. Symmetric flutter (unstable) mode of single-wing configuration (Model 5, Index 5).

For the joined-wing configuration, the induced flexibility of the fuselage and vertical tail on the flutter speed is prominent as indicated in Fig. 25. Sample of the flutter modes are depicted in Figs. 26 to 33. Models 2, 3 and 4 seem to keep the same corresponding flutter mode throughout the different flight indices. Model 2 is purely wing flutter (anti-symmetric mode). Model 4 presents a symmetric flutter mode with vertical bending contribution of the fuselage, which reduces the flutter speed in comparison with Model 2. Model 3 presents an anti-symmetric flutter mode enabled by the lateral bending of the tail. Model 5 (fully flexible vehicle), however, shows a change in the flutter mode shape with flight index. At flight index 3, it presents an anti-symmetric flutter mode with contribution of both lateral bending of the vertical tail and lateral bending of the fuselage. At index 5, the flutter mode switches to be a symmetric one, similar to Model 4.

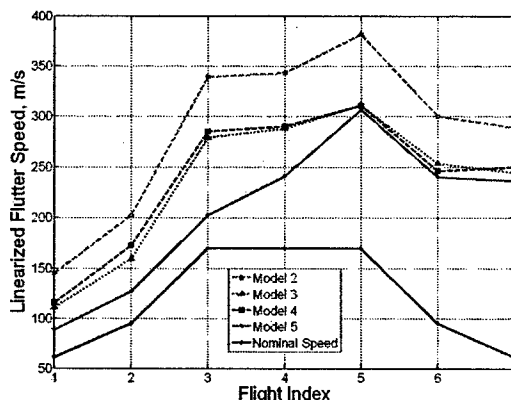
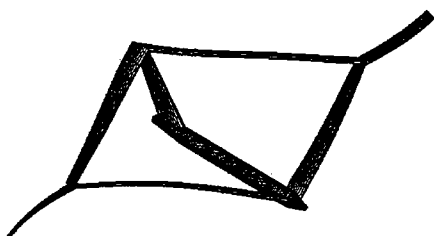
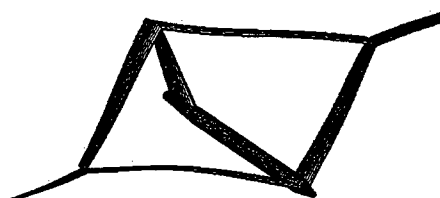


Figure 25. Flutter (unstable) speed at each flight index for different models of joined-wing configuration.



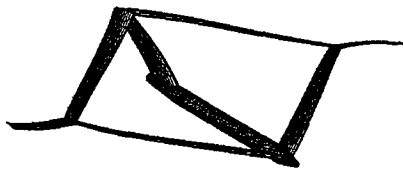
Flutter Speed: 339.34 m/s; Frequency: 0.94 HZ

Figure 26. Anti-symmetric flutter (unstable) mode of joined-wing configuration (Model 2, Index 3).



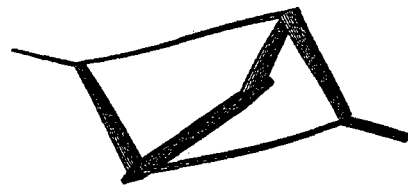
Flutter Speed: 381.66 m/s; Frequency: 2.29 HZ

Figure 27. Anti-symmetric flutter (unstable) mode of joined-wing configuration (Model 2, Index 5).



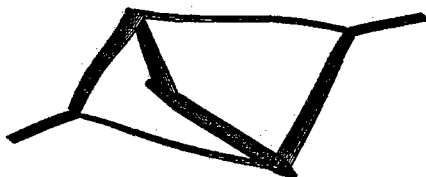
Flutter Speed: 279.20 m/s; Frequency: 0.97 HZ

Figure 28. Anti-symmetric flutter (unstable) mode of joined-wing configuration (Model 3, Index 3).



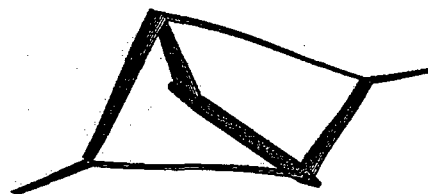
Flutter Speed: 310.82 m/s; Frequency: 2.32 HZ

Figure 29. Anti-symmetric flutter (unstable) mode of joined-wing configuration (Model 3, Index 5).



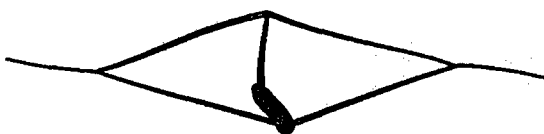
Flutter Speed: 285.36 m/s; Frequency: 0.96 HZ

Figure 30. Symmetric flutter (unstable) mode of joined-wing configuration (Model 4, Index 3).



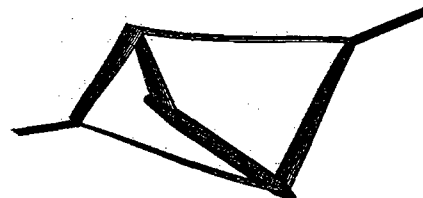
Flutter Speed: 311.05 m/s; Frequency: 2.11 HZ

Figure 31. Symmetric flutter (unstable) mode of joined-wing configuration (Model 4, Index 5).



Flutter Speed: 202.54 m/s; Frequency: 0.63 HZ

Figure 32. Anti-symmetric flutter (unstable) mode of joined-wing configuration (Model 5, Index 3).



Flutter Speed: 306.58 m/s; Frequency: 2.08 HZ

Figure 33. Symmetric flutter (unstable) mode of joined-wing configuration (Model 5, Index 5).

E. Static Stability

Since the aft wings of a joined-wing aircraft are subject to compressive loads, their buckling response can be a sizing limitation for the vehicle. For the particular baseline designs considered here, deformation of the aft wing increases dramatically when the load factor reaches about 1.60, bringing the whole wing system close to a collapse. This is illustrated in Fig. 34 as the flight speed is increased at level flight (no retrimming). Note that this condition is naturally modeled in the presented framework through the nonlinear structural analysis.

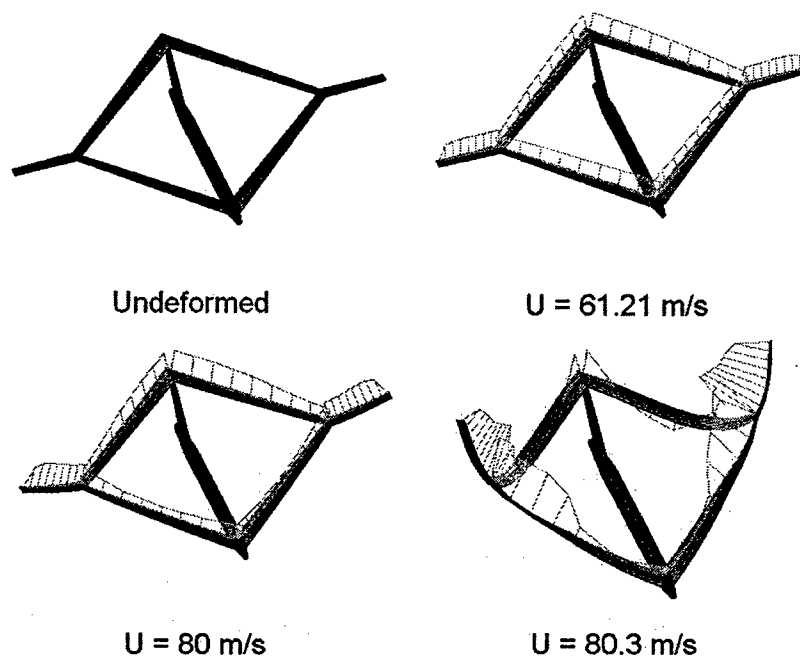


Figure 34. Lift distribution on the vehicle as the buckling speed is approached (sea level, fully fueled, no rigid body degrees of freedom, zero body angle of attack).

To study the effects of the flexibility from different members of the aircraft on the loss of static stability of the wings, Models 2 to 5 are brought to steady state at level flight (at sea level). Then, their flight speeds are varied from the nominal flight speed, which is 61.21 m/s, until there is a sudden drop in the lift generation capacity. This results in load factors ranging from 1.00 to approximately 1.60, depending on the model. The wing shape and deflections of the fully flexible model (Model 5) are plotted for varying load factor in Figs. 35 and 36. The corresponding tip positions versus flight speed and load factor are shown in Fig. 37. The sudden reduction of the aft wing stiffness results in large bending deflection of the overall wing structure and, consequently, drop in the overall lift (represented by the reduction in load factor as shown in Fig. 37). This level of wing displacement causes high composite ply strains (stresses), to the point of ply failure. Strain components dependence on the load factor is shown in Figs. 38 to 40.

This static instability speed may vary because of different levels of flexibility of the vehicle (Table 4). The load factors, whose sudden reduction indicates the onset of instability, are plotted as function of flight speed for different models, as shown in Fig 41. The model with a flexible vertical tail has the highest buckling speed, whereas the one with flexible fuselage has the lowest buckling speed. If one looks closer to the modes of deformation ("buckling mode"), they show a complex interaction between the vertical bending of the fuselage (particularly at the front wing connecting region) and the in-plane bending of the tail. These induced a change in the overall aerodynamic loading of the different wing segments, influencing the compressive load applied to the aft wing. Since the different models were only trimmed at the point corresponding to load factor 1 in Fig. 41, the other load factor points may represent a very different solution in terms of vehicle c.g. forces and moments. Further studies are needed to better understand the implications of the flexibility of the fuselage and vertical tail on the static instability of the vehicle.

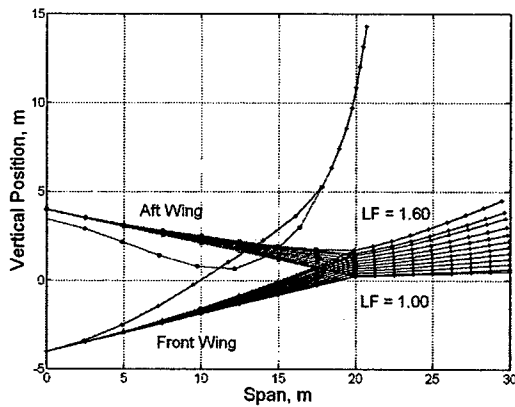


Figure 35. Wing shape for varying flight speed (level flight at sea level).

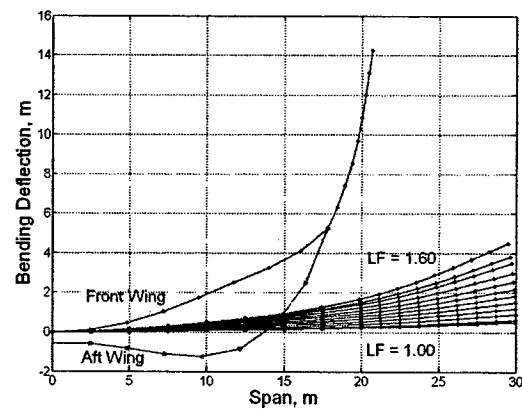


Figure 36. Wing bending deflections for varying flight speed (level flight at sea level).

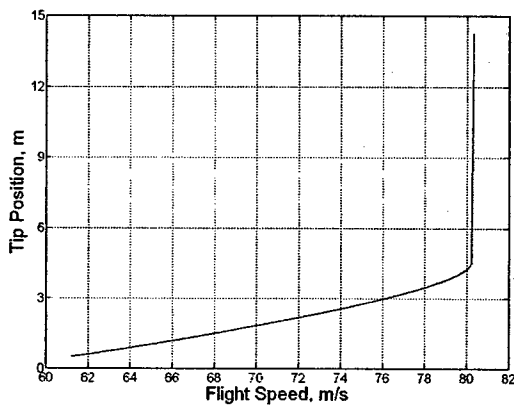


Figure 37. Changes in tip deflection as function of the lift generation capability of the vehicle at level flight (sea level).

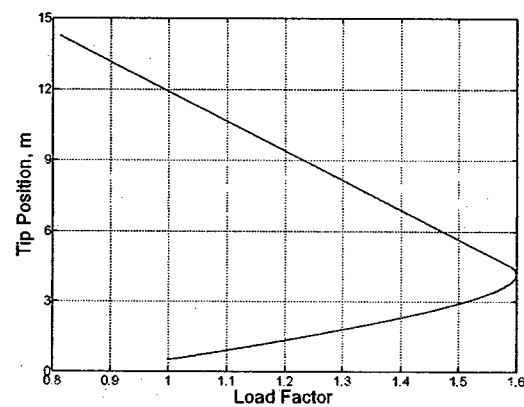


Figure 38. Maximum longitudinal strain component nonlinear growth due to loss of stiffness on the aft wing with increase load factor (level flight, sea level).

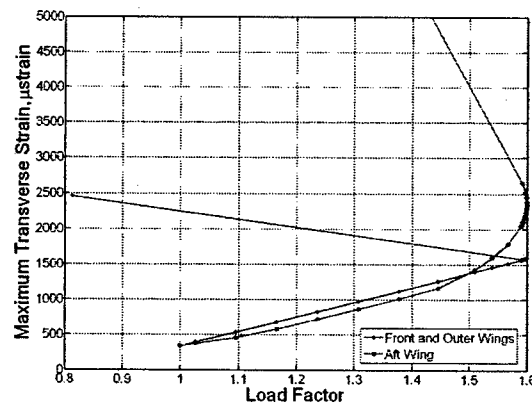


Figure 39. Maximum transverse strain component nonlinear growth due to loss of stiffness on the aft wing with increase load factor (level flight, sea level).

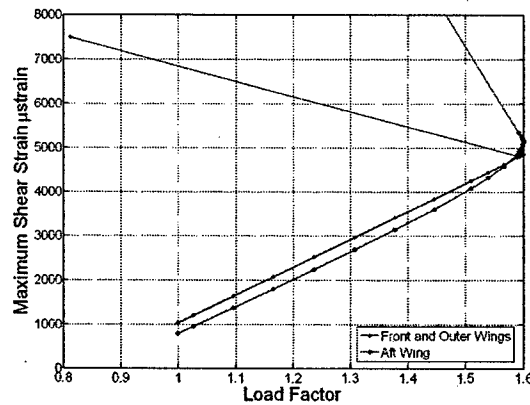


Figure 40. Maximum shear strain component nonlinear growth due to loss of stiffness on the aft wing with increase load factor (level flight, sea level).

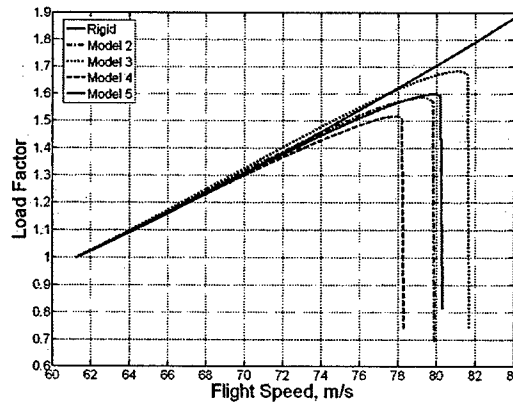


Figure 41. Load fact with respect to flight speeds for different models of joined-wing configuration (level flight, sea level).

IV. Concluding Remarks

This paper presented a nonlinear aeroelastic formulation for the modeling and analysis not only of the very flexible wings but also their coupling with flexible fuselage and tail. The geometrically-nonlinear structural model is a strain-based formulation able to capture the large deformations in slender composite structures. The unsteady aerodynamics is incompressible, and written in space-state form. The low-order aeroelastic framework is intended for preliminary design and assessment of aeroelastic response and its coupling with flight dynamics of very flexible aircraft. The low-order representation of the fully flexible vehicle is to be used for control design.

Based on the new approach, two of the three aircraft configurations being considered for the Sensorcraft program were studied: single-wing and joined-wing configurations. Specifically, the paper presented the effects of the added flexibility of the fuselage and tail to the very flexible wings in the roll response, onset of flutter, and static ("buckling-like") instability (for joined-wing only).

From the results of the numerical studies, it is clear that joined-wing configurations present much richer and complex aeroelastic characteristics than single-wing ones. The modeled joined-wing vehicle is more susceptible to the induced flexibility of the fuselage and tail in terms of roll performance, where there can be a significant reduction in roll angle as function of time due to the added flexibility. As for the linearized flutter speed, flexible fuselage and vertical tail both reduces the flutter speed of joined-wing configuration, whereas the flexibility of the fuselage and tail of the single-wing configuration does not significantly impacts the wing flutter (unless the wing flutters first). Regarding the unique problem of loss of stiffness in the aft wing in the joined-wing configuration, preliminary results indicated that the added flexible fuselage decreases "buckling" speed, while adding the flexibility of the vertical tail increases it. More studies are needed to better understand those relative effects.

While the proposed framework has been created to handle any structural configuration made of slender (active) composite components (wings, tails, fuselages), in its current form it cannot properly handle the flexibility of the body in a wing-body configuration (third Sensorcraft concept being considered). Current work is under way to extend the framework to bring non-slender flexible bodies to be coupled with the present nonlinear aeroelastic formulation.

Acknowledgment

This work has been sponsored by AFOSR grant F49620-02-1-0425. The technical monitor is Dr. Clark Allred, Capt. USAF.

References

- ¹Patil, M. J., Hodges, D. H., and Cesnik, C. E. S., "Nonlinear Aeroelasticity and Flight Dynamics of High-Altitude Long Endurance Aircraft," *Journal of Aircraft*. Vol. 38, No. 1 Jan. - Feb. 2001.
- ²Van Shoor, M. C., Zerweckh, S. H. and von Flotow, A. H., "Aeroelastic Stability and Control of a Highly Flexible Aircraft", AIAA Paper, AIAA-89-1187-CP, 1989.
- ³Drela, M., "Integrated Simulation Model for Preliminary Aerodynamic, Structural, and Control-Law Design of Aircraft", AIAA Paper, AIAA-99-1394, 1999.
- ⁴Tilman, C. P., Flick, P. M., Martin, C. A., and Love, M. H., "High-Altitude Long Endurance Technologies for Sensorcraft," *RTO AVT Symposium on Novel and Emerging Vehicle and Vehicle Technology Concepts*. Brussels, Belgium, April 2003. RTO Paper MP-104-P-26.
- ⁵Wolkovitch, J., "The Joined Wing: An Overview", *Journal of Aircraft*. Vol. 23, No. 3, 1996, pp. 161-178.
- ⁶Livne, E., "Aeroelasticity of Joined-Wing Airplane configurations: Past Work and Future Challenges – a Survey", AIAA Paper AIAA-2001-1370, *AIAA/ASME/ASCE/AHS 42nd Structures, Structural Dynamics, and Materials Conference*, Seattle, WA, 16-19 April 2001.
- ⁷Lin, H.-H., Zhou, J., and Stearman, R., "Influence of Joint Fixity on the Aeroelastic Characteristics of a Joined Wing Structure," AIAA-90-0980-CP, pp. 1442-1454, 1990
- ⁸Samuels, M. F., "Structural Weight Comparison of a Joined Wing and a Conventional Wing", *Journal of Aircraft*. June 1982, pp. 485-491.
- ⁹Gallman, J.W. and Kroo, I.M., "Structural Optimization for Joined-Wing Synthesis", *Journal of Aircraft*. Vol. 33, No. 1, Jan-Feb 1996, pp. 214-223.
- ¹⁰Miural, H., Shyu, A. T., and Wolkovitch, J., "Parameter Weight Evaluation of Joined Wing by Structural Optimization", AIAA Paper 85-0642, *AIAA/ASME/ASCE/AHS 26th Structures, Structural Dynamics, and Materials Conference*, Orlando, FL, April 1985.
- ¹¹Blair, M. and Canfield, R. A., "A Joined-Wing Structural Weight Modeling Study", AIAA Paper, AIAA-2002-1337, 2002.
- ¹²Kroo, I.M., Gallman, J.W. and Smith, S.C., "Aerodynamic and Structural Studies of Joined-Wing Aircraft" *Journal of Aircraft*. Vol. 28, No. 1, 1991, pp. 74-81.
- ¹³Gallman, J.W. and Smith, S.C., "Optimization of Joined Wing Aircraft", *Journal of Aircraft*. Vol. 30, No. 6, Nov-Dec 1993, pp. 897-965.
- ¹⁴Roberts, R.W. Jr., Canfield, R.A. and Blair, M., "Sensor-Craft Structural Optimization and Analytical Certification", AIAA Paper AIAA-2003-1458, *AIAA/ASME/ASCE/AHS 44th Structures, Structural Dynamics, and Materials Conference*. Norfolk, VA, 7-10 April 2003.
- ¹⁵Rasmussen, C. C., Canfield, R. A. and Blair, M., "Optimization Process for Configuration of Flexible Joined-wing", AIAA Paper AIAA-2004-4330, *10th AIAA/ISSMO Multidisciplinary Analysis and Optimization Conference*, August 30 - September 1, 2004, Albany, NY
- ¹⁶Reich, G.W., Raveh, D. and Zink, P.S., "Application of Active Aeroelastic Wing Technology to a Joined-Wing Sensorcraft", AIAA Paper AIAA-2002-1633, 2002.
- ¹⁷Cesnik, C. E. S. and Brown, E. L., "Active Warping Control of a Joined Wing Airplane Configuration," *Proceedings of the 44th Structures, Structural Dynamics, and Material Conference*, Hampton, Virginia, April 7 - 10, 2003.
- ¹⁸Brown, E. L., "Integrated Strain Actuation in Aircraft with Highly Flexible Composite Wings," Ph.D. Thesis, Mechanical Engineering, Massachusetts Institute of Technology, Cambridge, Massachusetts, June 2003.
- ¹⁹Peters, D. A. and Johnson, M. J., "Finite-State Airloads for Deformable Airfoils on Fixed and Rotating Wings", *Symposium on Aeroelasticity and Fluid/Structure Interaction Proceedings of the Winter Annual Meeting*, AD Vol. 44, American Society of Mechanical Engineers, Fairfield, NJ, 1994, pp.1-28.

Appendix

Single-wing Configuration Cross-sectional Property Distributions. The stiffness and inertia properties of each cross-section of the wing, tail and fuselage are shown in Figs A1 to A21.

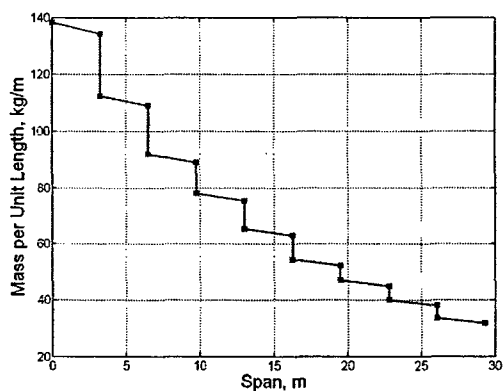


Figure A1. Wing spanwise mass distribution for single-wing configuration.

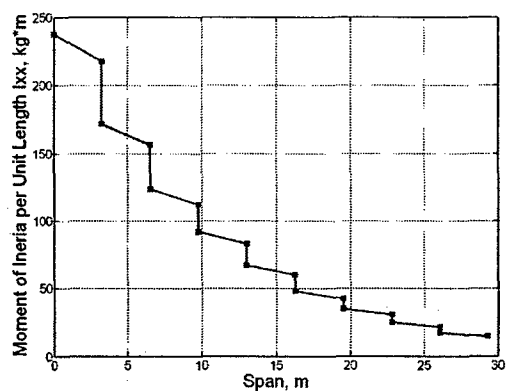


Figure A2. Wing spanwise torsional moment of inertia distribution (Ixx) for single-wing configuration.

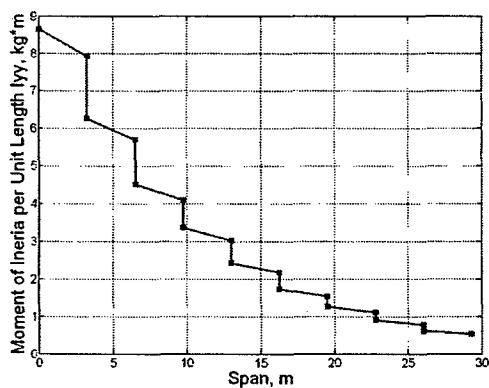


Figure A3. wing spanwise bending moment of inertia distribution (Iyy) for single-wing configuration.

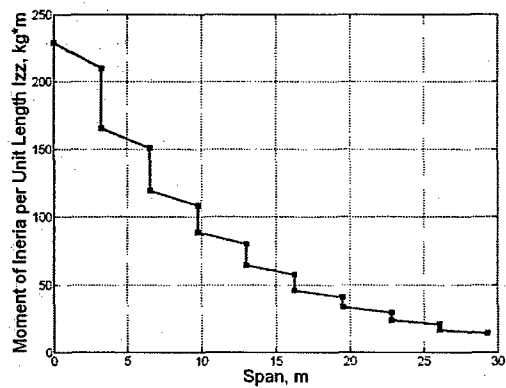


Figure A4. Wing spanwise chordwise bending moment of inertia distribution (Izz) for single-wing configuration.

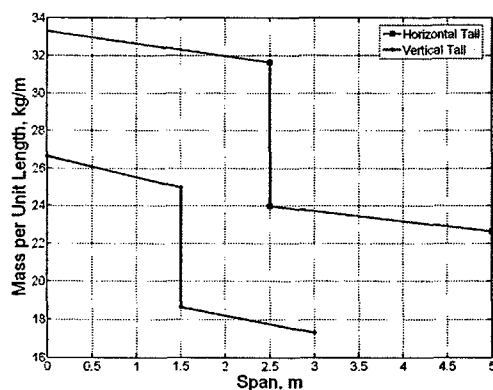


Figure A5. Tail spanwise mass distribution for single-wing configuration.

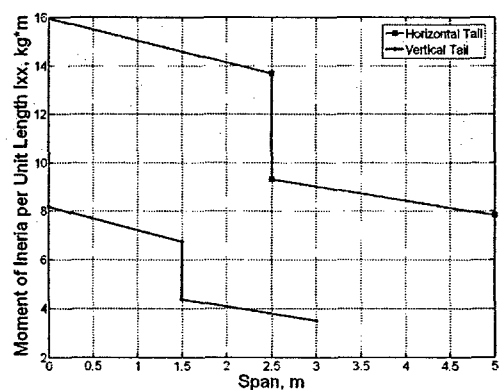


Figure A6. Tail spanwise torsional moment of inertia distribution (Ixx) for single-wing configuration.

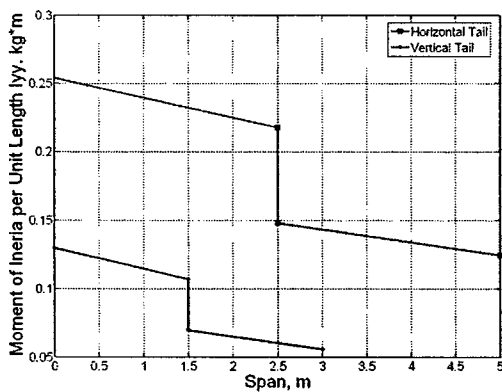


Figure A7. Tail spanwise bending moment of inertia distribution (I_{yy}) for single-wing configuration.

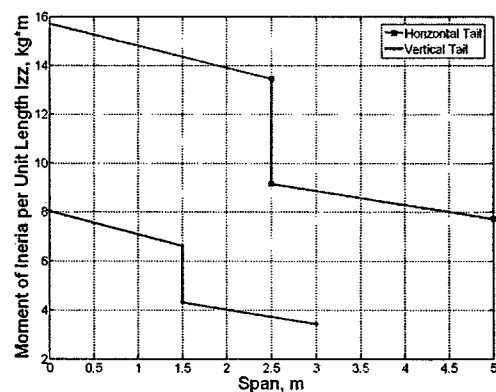


Figure A8. Tail spanwise chordwise bending moment of inertia distribution (I_{zz}) for single-wing configuration.

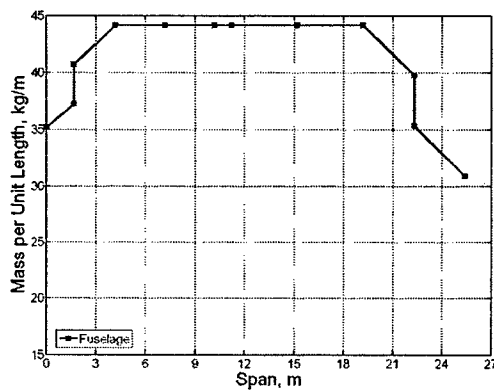


Figure A9. Fuselage spanwise mass distribution for single-wing configuration.

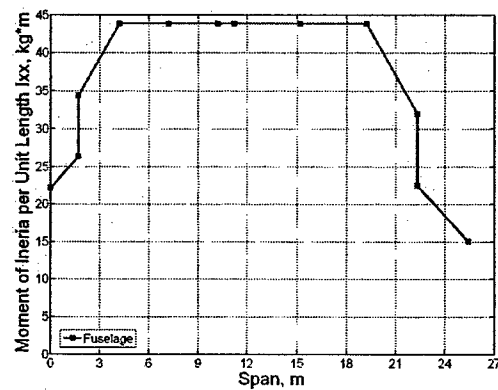


Figure A10. Fuselage spanwise torsional moment of inertia distribution (I_{xx}) for single-wing configuration.

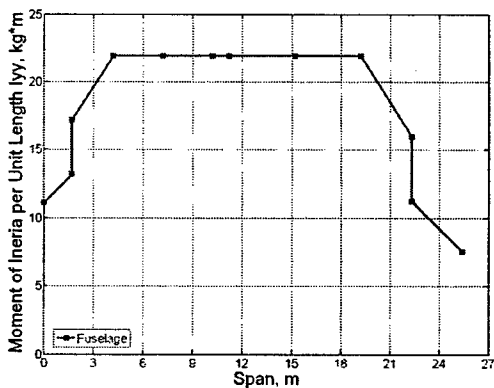


Figure A11. Fuselage spanwise bending moment of inertia distribution (I_{yy}) for single-wing configuration.

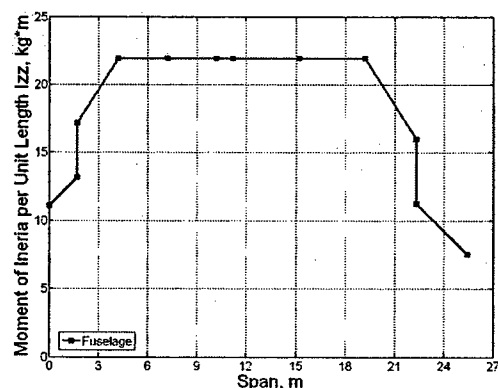


Figure A12. Fuselage spanwise chordwise bending moment of inertia distribution (I_{zz}) for single-wing configuration.

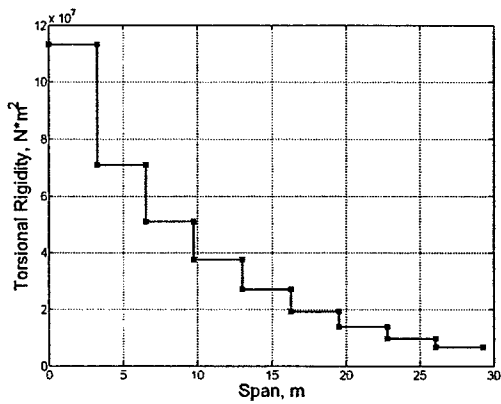


Figure A13. Wing spanwise torsional rigidity distribution for single-wing configuration.

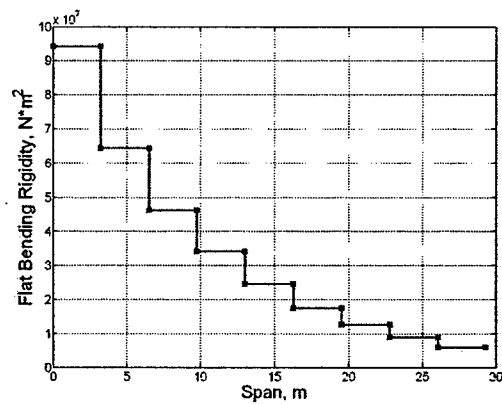


Figure A14. Wing spanwise flatbending rigidity distribution for single-wing configuration.

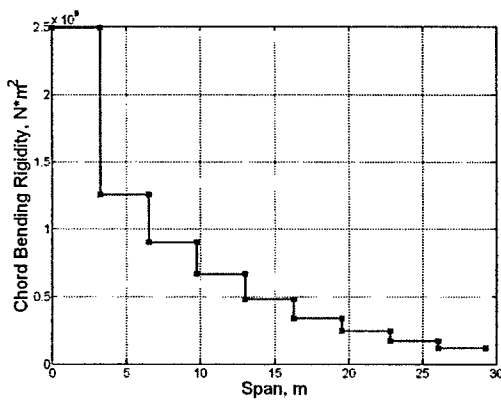


Figure A15. Wing spanwise chordbending rigidity distribution for single-wing configuration.

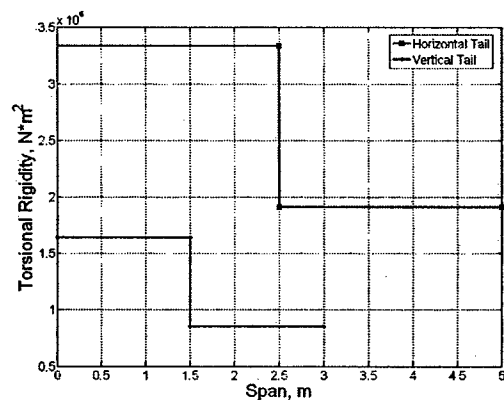


Figure A16. Tail spanwise torsional rigidity distribution for single-wing configuration.

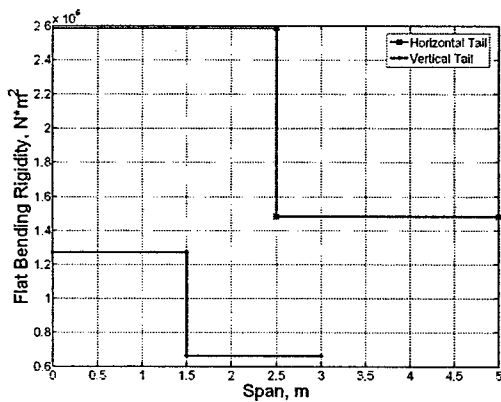


Figure A17. Tail spanwise flatbending rigidity distribution for single-wing configuration.

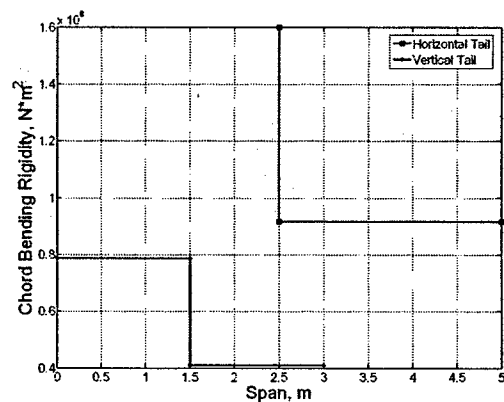


Figure A18. Tail spanwise chordbending rigidity distribution for single-wing configuration.

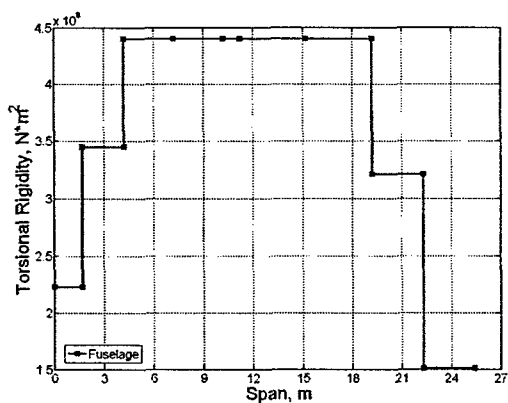


Figure A19. Fuselage spanwise torsional rigidity distribution for single-wing configuration.

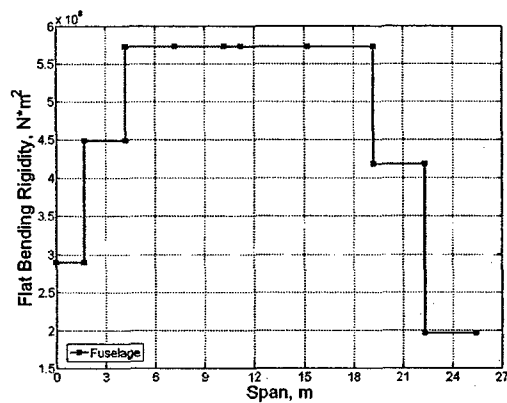


Figure A20. Fuselage spanwise flatbending rigidity distribution for single-wing configuration.

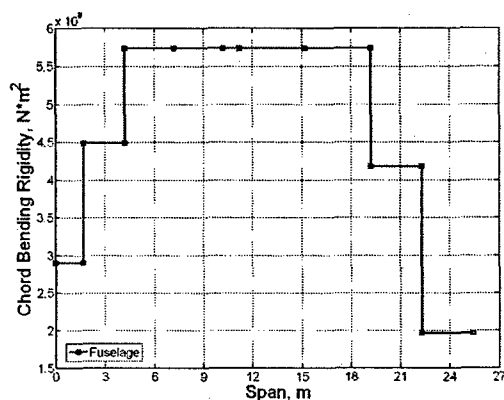


Figure A21. Fuselage spanwise chorbending rigidity distribution for single-wing configuration.

Joined-wing Configuration Cross-sectional Property Distributions. The stiffness and inertia properties of the wing, vertical tail and fuselage are shown in Figs. A22 to A42.

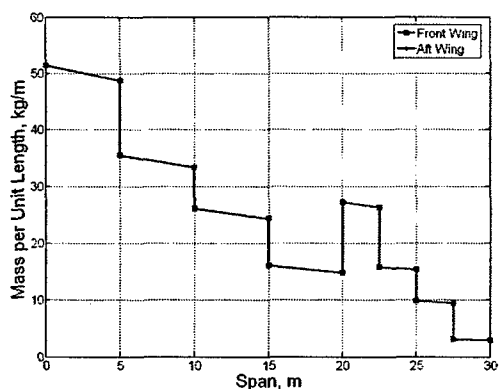


Figure A22. Wing spanwise mass distribution for joined-wing configuration.

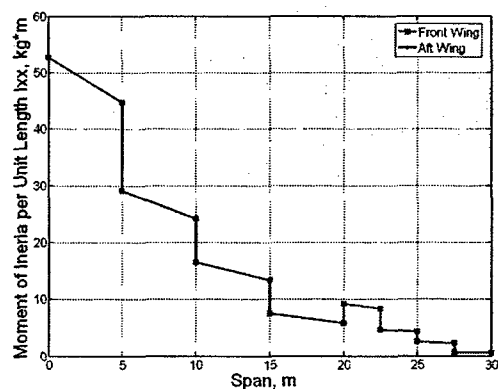


Figure A23. Wing spanwise torsional moment of inertia distribution (Ixx) for joined-wing configuration.

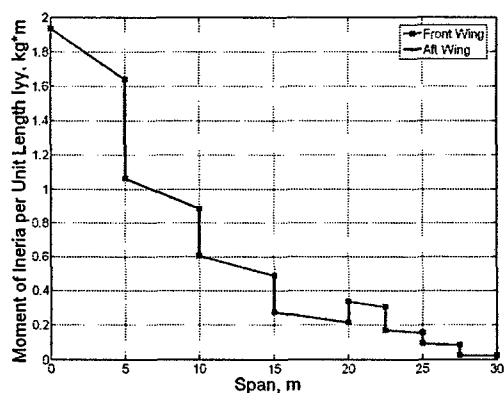


Figure A24. Wing spanwise bending moment of inertia distribution (I_{yy}) for joined-wing configuration.

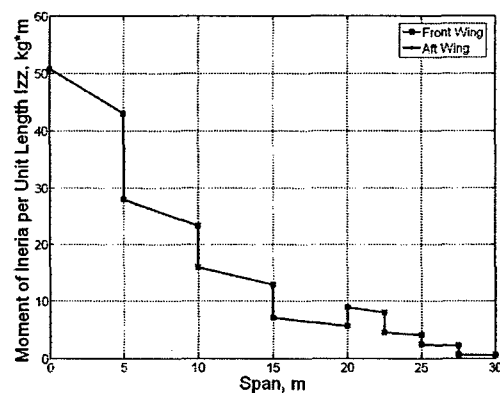


Figure A25. Wing spanwise chordwise bending moment of inertia distribution (I_{zz}) for joined-wing configuration.

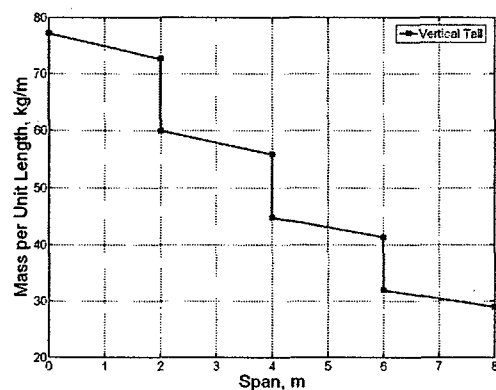


Figure A26. Vertical tail spanwise mass distribution for joined-wing configuration.

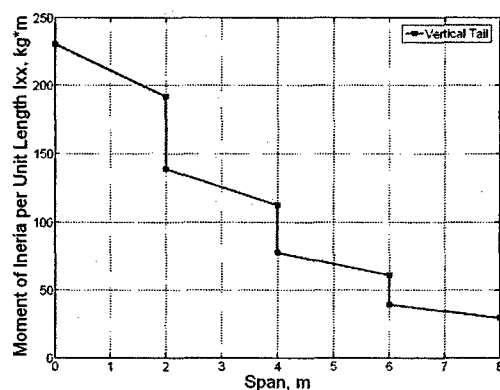


Figure A27. Vertical tail spanwise torsional moment of inertia distribution (I_{xx}) for joined-wing configuration.

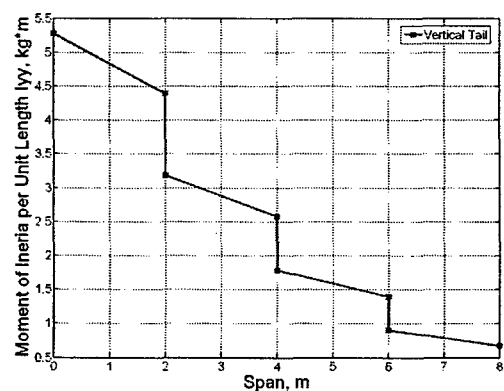


Figure A28. Vertical tail spanwise bending moment of inertia distribution (I_{yy}) for joined-wing configuration.

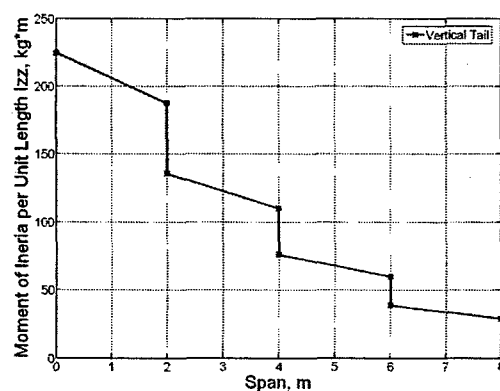


Figure A29. Vertical tail spanwise chordwise bending moment of inertia distribution (I_{zz}) for joined-wing configuration.

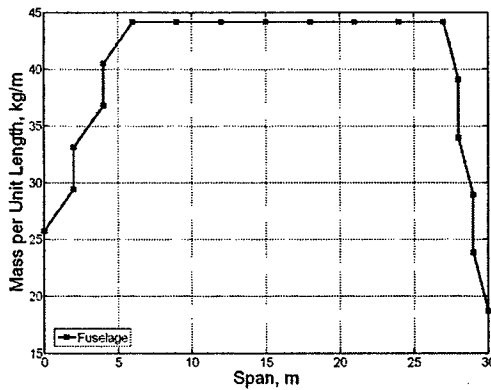


Figure A30. Fuselage spanwise mass distribution for joined-wing configuration.

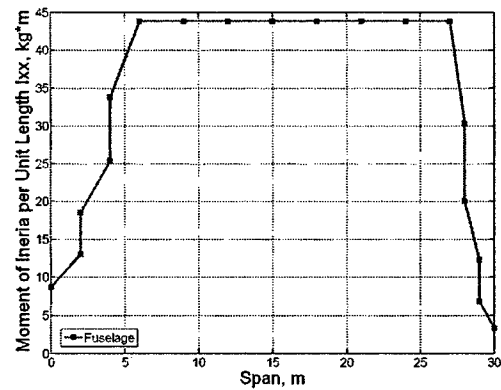


Figure A31. Fuselage spanwise torsional moment of inertia distribution (Ixx) for joined-wing configuration.

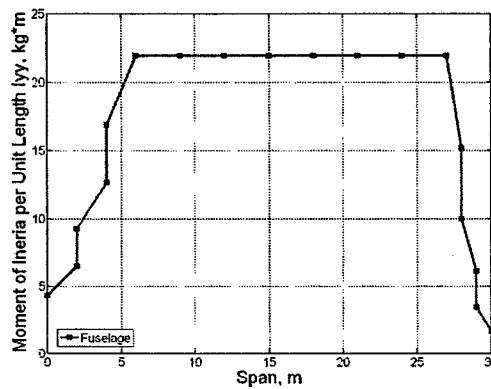


Figure A32. Fuselage spanwise bending moment of inertia distribution (Iyy) for joined-wing configuration.

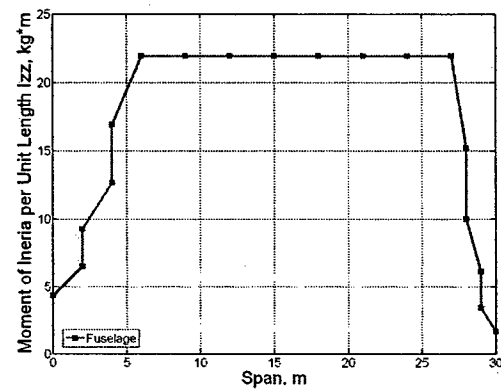


Figure A33. Fuselage spanwise chordwise bending moment of inertia distribution (Izz) for joined-wing configuration.

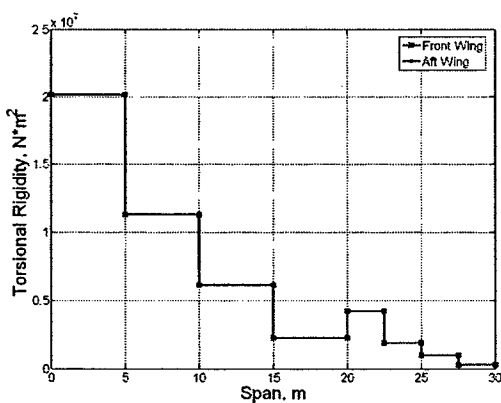


Figure A34. Wing spanwise torsional rigidity distribution for joined-wing configuration.

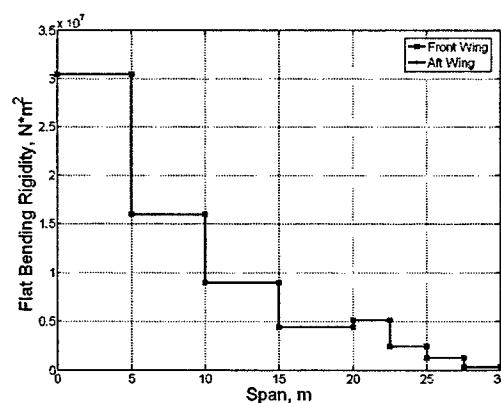


Figure A35. Wing spanwise flatbending rigidity distribution for joined-wing configuration.

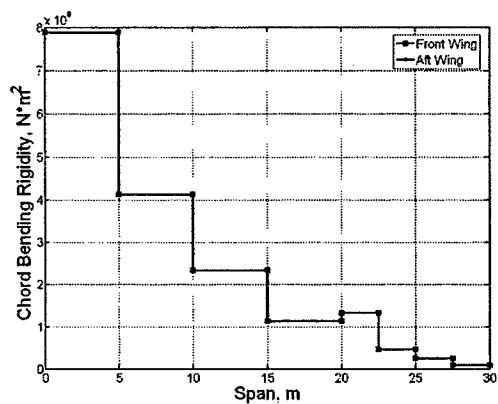


Figure A36. Wing spanwise chordbending rigidity distribution for joined-wing configuration.

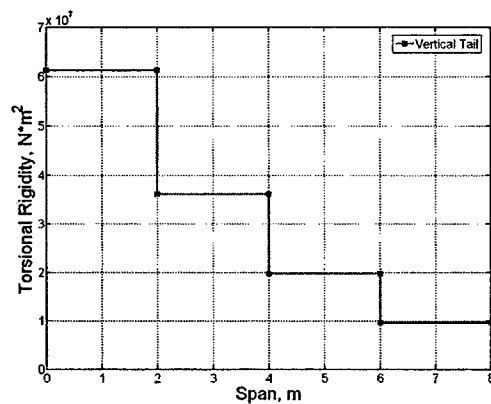


Figure A37. Vertical tail spanwise torsional rigidity distribution for joined-wing configuration.

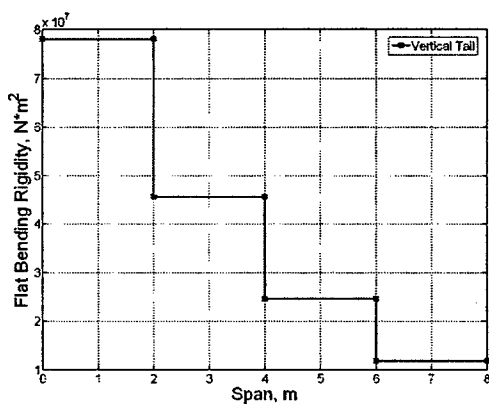


Figure A38. Vertical tail spanwise flatbending rigidity distribution for joined-wing configuration.

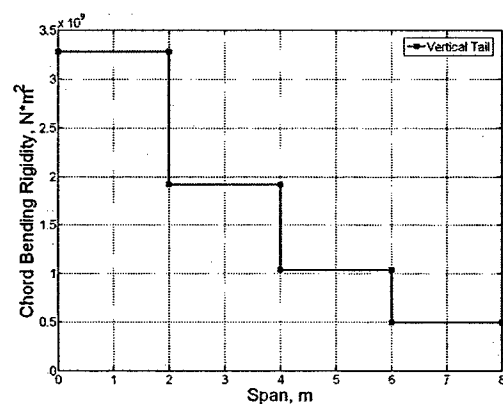


Figure A39. Vertical tail spanwise chordbending rigidity distribution for joined-wing configuration.

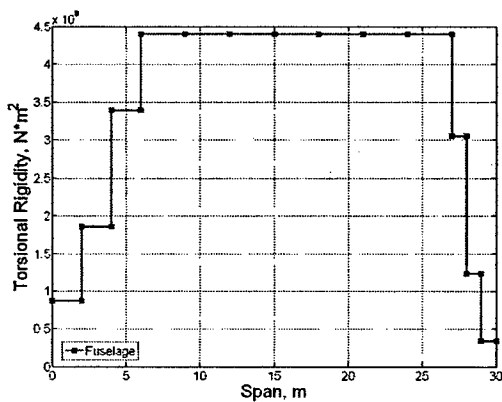


Figure A40. Fuselage spanwise torsional rigidity distribution for joined-wing configuration.

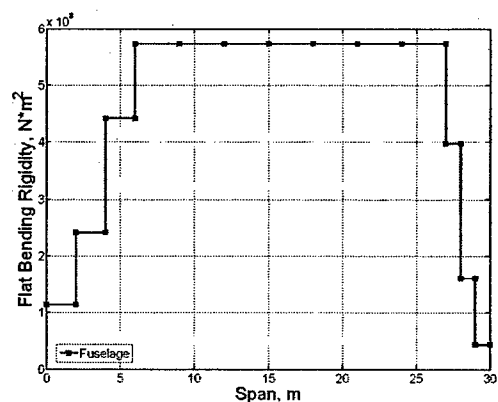


Figure A41. Fuselage spanwise flatbending rigidity distribution for joined-wing configuration.

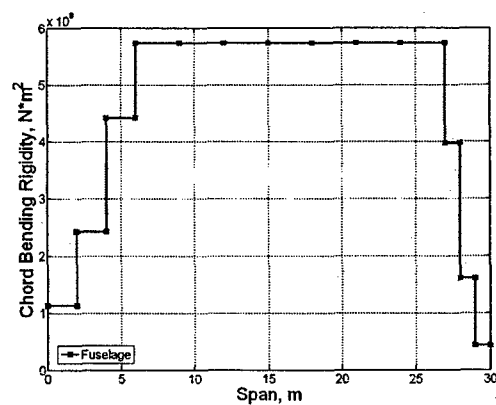


Figure A42. Fuselage spanwise chordbending rigidity distribution for joined-wing configuration.

Appendix F:

Cesnik, C. E. S. and Su, W., "Nonlinear Aeroelastic Behavior of Fully Flexible Slender Vehicles," *International Forum on Aeroelasticity and Structural Dynamics*, Munich, Germany, June 28—July 1, 2005.

NONLINEAR AEROELASTIC BEHAVIOR OF FULLY FLEXIBLE SLENDER VEHICLES

Carlos E. S. Cesnik¹ and Weihua Su²

Department of Aerospace Engineering
The University of Michigan, Ann Arbor, Michigan, 48109-2140, USA

¹e-mail: cesnik@umich.edu

²e-mail: suw@umich.edu

Key words: Nonlinear Aeroelasticity, HALE Aircraft, Fully Flexible Aircraft

Abstract. This paper focuses on effectively modeling the nonlinear aeroelastic behavior of fully flexible aircraft for preliminary design. The study is conducted based on a nonlinear strained-based finite element framework in which the developed low-order formulation captures the nonlinear (large) deflection behavior of the wings, and the unsteady subsonic aerodynamic forces acting on them. Instead of merely considering the nonlinearity of the wings, the paper will allow all members of the vehicle to be flexible. Due to their characteristics of being long and slender structures, the wings, tail, and fuselage of the fully flexible aircraft can be modeled as beams undergoing three dimensional displacements and rotations. The cross-sectional stiffness and inertia properties of the beams are calculated along the span, and then incorporated into the 1-D nonlinear beam model. Finite-state unsteady subsonic aerodynamic loads are coupled with all lifting surfaces, so as to complete the state space aeroelastic model. Two different vehicle configurations are modeled and studied, that is, a conventional single-wing and a joined-wing aircraft with flexible fuselage and tail. Based on the proposed models, static and dynamic stabilities are studied and compared with rigidized, linearized, and/or nonlinear models.

1 INTRODUCTION

High-Altitude Long-Endurance (HALE) vehicles are being developed for multiple applications, including environmental sensing, telecom relay, and military reconnaissance. These HALE concepts feature light wings with a high aspect ratio. These long and slender wings, by their inherent nature, can maximize lift to drag ratio. On the other hand, these wings may undergo large deformations during normal operating loads, exhibiting geometrically nonlinear behavior. Patil, Hodges, and Cesnik¹ studied the aeroelasticity and flight dynamics of HALE aircraft. The results indicate their behavior can be significantly changed due to the large deflection of the flexible wings. Moreover, a linear aeroelastic analysis based on the undeformed geometry may lead to errors when the wings are highly flexible. Van Schoor, Zerweckh and von Flotow² studied aeroelastic characteristics and control of highly flexible aircraft. They used linearized modes including rigid-body modes to predict the stability of the aircraft under different flight conditions. Their results indicate that unsteady aerodynamics and flexibility of the aircraft should be considered so as to correctly model the dynamic system. This leads to the conclusion that the coupled effects between these large deflection and vehicle flexibility and flight dynamics (e.g., roll controllability) as well as other aeroelastic effects (e.g., gust response, flutter instability) must be properly accounted for in a nonlinear aeroelastic formulation. Drela³ modeled a complete flexible aircraft as an assemblage of joined nonlinear beams. In his work, the aerodynamic model was a compressible vortex/source-lattice with wind-aligned trailing vorticity. The nonlinear equation was solved by using a full Newton method. Through simplifications of the model, the computational size was reduced for iterative preliminary design.

Jones and his co-workers have also worked on the design of HALE^{4,5}. In their work, they described some design challenges associated with these vehicles. From their conclusion, it is shown that standard aircraft design techniques are no longer applicable for these high-aspect-ratio wings.

In the last several years, the US Air Force has been working on a new generation Intelligence, Surveillance, and Reconnaissance (ISR) platform called "Sensorcraft." These are large HALE aircraft, with wing span of approximately 60m. At this stage, three basic platform shapes are being considered further: wing-body-tail, single-wing and joined-wing configurations⁶.

Among the Sensorcraft concepts, the joined-wing configuration is the most unusual one. It was first proposed by Wolkovitch⁷, who suggested that this new design would lead to possible weight savings and some aeroelastic benefits. However, the effects of structural deformation on the aerodynamic and aeroelastic responses are difficult to intuit and predict.

Livne⁸ presented a comprehensive survey on the design challenges of joined-wing aircraft configurations. Therein, he presented a review of past works in joined-wing aeroelasticity and gave a qualitative discussion of their behavior in a multidisciplinary context. Much of the discussion in the paper dealt with structural and aeroelastic issues relating to the aft wing/tail. The in-plane loads due to structure deformation and changes in geometric stiffness give rise to non-intuitive aeroelastic behavior. Bending and twisting couplings of the entire structure cause natural frequencies and mode shapes to shift. The tendency for buckling and divergence in the aft member is of major concern when trying to reduce weight. The finding of rear wing divergence to be more critical than flutter is counterintuitive, since the aft wing is supported at the joint. This phenomenon seems associated with a reduction in structural stiffness due to the in-plane compressive loads in the rear members. The geometry of the joint between forward and aft wings is also of importance because it plays a major role in how in-plane, bending, and torsion loads are transferred. For instance, a pinned joint may allow upward buckling of the aft wing, while a fixed rigid joint may allow the aft wing to buckle downward, since bending moments are transferred across the joint. Lin, Jhou and Stearman⁹ studied the influence of joint fixity on the aeroelastic characteristics of the joined-wing. They suggested that the fixed joint provide the best characteristic. Blair and Canfield¹⁰ described an integrated design process for generating high fidelity analytical weight estimations of joined-wing configurations. They suggested an integrated design process that can bring together different software package, such as NASTRAN, PanAir, and integrate them through the Air Vehicles Technology Integration Environment (AVTIE), so that structures, aerodynamics and aeroelastic analysis are incorporated. Roberts, Canfield and Blair¹¹ performed the structural optimization for a joined-wing Sensorcraft. They identified some critical points in a flight index and optimized the Sensorcraft with respect to those. Their results suggest the necessity of nonlinear structural analysis.

Different technologies, in addition to the traditional ailerons, have been included in structural design of joined-wing Sensorcraft, in order to improve their performance. Active aeroelastic wing (AAW)¹² technology was applied in a joined-wing Sensorcraft for minimum deformations of the antenna embedded in the wing skins, in addition to generate aircraft maneuver loads. Meanwhile, Cesnik and Brown¹³ studied the aeroelastic characteristics of the joined-wing aircraft including active warping actuation for maneuver load generation. The active piezoelectric concepts have their advantage over traditional ailerons in terms of structural integration. However, according to the studies of Ref. 13, the wing-warping design

based on current anisotropic piezoelectric actuators (APA) technology presents a terminal roll rate which is two to three times smaller than the aileron concept due to limited actuator authority. As seen in the studies, the first sign of failure may be associated with the static instability (buckling) of the aft members as the structure is softened. Flutter and divergence may also become a problem in these members due to the reduction in structural frequency as they go into compression. As the aircraft becomes more flexible, the nature of the geometric structural nonlinearities become more important and the lift distribution on the aircraft may be adversely affected.

Not being limited within the scope of joined-wing configurations, the large overall vehicle size associated with the different Sensorcraft configurations being studied will lead to generally very flexible aircraft. In fact, long and slender fuselage and tail surfaces result in elastic coupling with the lifting surfaces. This directly impacts the trimming of the vehicle, and the couplings among roll, yaw, and pitch require the use of nonlinear aeroelastic and flight dynamics analyses to predict vehicle response, design of control laws, and its overall guidance. These flexibility effects may make the response of the vehicle very different than its rigid or linearized models. The current study is an extension of the work of Ref. 14, allowing all members of the vehicle to be flexible. Among different aspects of fully flexible aircraft that must be studied, this paper focuses on two key points:

- 1) The new modeling approach of the complex nonlinear structural system of fully flexible aircraft;
- 2) Assessment of the effects of induced flexibility of fuselage and tail on the static and dynamic stabilities of a single-wing and a joined-wing configuration.

2 THEORETICAL FORMULATION

In the proposed formulation, the vehicle is allowed six rigid-body and multiple flexible degrees of freedom. The structures are allowed fully coupled three-dimensional bending, twisting, and extensional deformations. Control surfaces may be included for maneuver studies. Inclusion of flexible fuselage and vertical tail are new to the formulation. A finite-state unsteady airloads model is integrated into the system equations, with the exception of the fuselage (at this stage). The model allows for a low-order set of nonlinear equations that can be put into state-space form to facilitate aeroelastic studies.

2.1 Element description

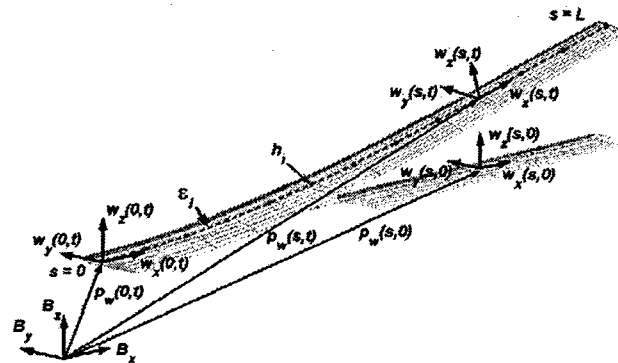


Figure 1: Wing coordinates

Consider a typical slender structural component (e.g. wing) being represented as shown in Fig. 1. In the work of Ref. 13, specialized beam elements were developed that have four local

strain degrees-of-freedom: extension, twist, and two bending ones. Fig. 2 exemplifies the deformations of constant-strain elements.

Each node along the beam is determined by a vector consisting of 12 components. Suppose the beam reference frame is w , which is a function of the natural beam coordinate s , the 12-component vector is denoted as,

$$h(s)^T = [p_w(s)^T, w_x(s)^T, w_y(s)^T, w_z(s)^T] \quad (1)$$

where, p_w is the position of frame w in the body coordinate, w_x, w_y , and w_z are the direction vectors pointing along the beam axis, toward the leading edge, and normal to the airfoil, respectively (see Fig. 1). As discussed in Ref. 13, the governing equation, which relates the dependent displacements to the independent strains, is,

$$\frac{\partial h(s)}{\partial s} = A(s)h(s) \quad (2)$$

where, A is a matrix function of the strains.

$$A(s) = \begin{bmatrix} 0 & 1 + \varepsilon_x(s) & 0 & 0 \\ 0 & 0 & \kappa_z(s) & -\kappa_y(s) \\ 0 & -\kappa_z(s) & 0 & \kappa_x(s) \\ 0 & \kappa_y(s) & -\kappa_x(s) & 0 \end{bmatrix} \quad (3)$$

where the blocks are all 3x3 diagonal matrices. The solution of Eq. (2) can be given by Eq. (4), with the assumption that the element has a constant strain vector

$$h(s) = e^{As} h_0 = e^{G(s)} h_0 \quad (4)$$

where, h_0 is the beam boundary conditions.



Figure 2: Deformations of a typical constant-strain element

The total virtual work done on an element due to all internal and external forces and moments can be written as,

$$\delta W = -\delta h^T M \ddot{h} - \delta \varepsilon^T K \varepsilon + \delta \varepsilon^T B_v \nu - \delta h^T N g + \delta p^T B_F F^{dst} + \delta \theta^T B_M M^{dst} + \delta p^T F^{pt} + \delta \theta^T M^{pt} \quad (5)$$

where the terms involved include the effects of inertia ($M\ddot{h}$), gravity field (Ng), internal strain (ε), piezoelectric actuation (ν), distributed forces (F^{dst}) and moments (M^{dst}), and point forces (F^{pt}) and moments (M^{pt}).

2.2 Member and inter-member equations

In the model of fully flexible aircraft, the fuselage and the vertical tail are both modeled as slender beams, similarly to the wings. Therefore, it is necessary to model a split beam system as illustrated in Fig. 3. For simplicity, consider three members in this beam system. Member 1 consists of two elements and Members 2 and 3 each consist of one element only. Every element has three nodes, each with the degrees of freedom given by Eq. (1). The proposed

approach here is to modify the original kinematics of Ref. 13 to allow the analysis of split beams.

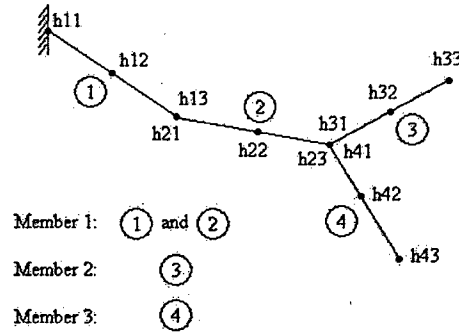


Figure 3: A split (or bifurcated) beam system

The kinematics for these members is obtained by marching the element kinematics from the boundary node to the end nodes at each branch, which can be written as follows:

Element 1			Element 2		
Node 1	Node 2	Node 3	Node 1	Node 2	Node 3
$h_{11} = h_0$	$h_{12} = e^{G_1} h_{11}$	$h_{13} = e^{G_1} h_{12}$	$h_{21} = D_{21} h_{13}$	$h_{22} = e^{G_2} h_{21}$	$h_{23} = e^{G_2} h_{22}$
Element 3			Element 4		
Node 1	Node 2	Node 3	Node 1	Node 2	Node 3
$h_{31} = D_{32} h_{23}$	$h_{32} = e^{G_3} h_{31}$	$h_{33} = e^{G_3} h_{32}$	$h_{41} = D_{42} h_{23}$	$h_{42} = e^{G_4} h_{41}$	$h_{43} = e^{G_4} h_{42}$

where h_{ij} is the displacement of the j th node of the i th element. D_{ij} contains the direction cosines, accounting for the different directions of different elements at the connection. These equations can be written into a matrix form as

$$\begin{bmatrix}
 I & & & & & & & & & & \\
 -e^{G_1} & I & & & & & & & & & \\
 & -e^{G_1} & I & & & & & & & & \\
 & & -D_{21} & I & & & & & & & \\
 & & & -e^{G_2} & I & & & & & & \\
 & & & & -e^{G_2} & I & & & & & \\
 & & & & & -D_{32} & I & & & & \\
 & & & & & & -e^{G_3} & I & & & \\
 & & & & & & & -e^{G_3} & I & & \\
 & & & & & & & & -D_{42} & I & \\
 & & & & & & & & & -e^{G_4} & I \\
 & & & & & & & & & & -e^{G_4} & I
 \end{bmatrix}
 \begin{bmatrix}
 h_{11} \\
 h_{12} \\
 h_{13} \\
 h_{21} \\
 h_{22} \\
 h_{23} \\
 h_{31} \\
 h_{32} \\
 h_{33} \\
 h_{41} \\
 h_{42} \\
 h_{43}
 \end{bmatrix}
 =
 \begin{bmatrix}
 h_0 \\
 0 \\
 0 \\
 0 \\
 0 \\
 0 \\
 0 \\
 0 \\
 0 \\
 0 \\
 0 \\
 0
 \end{bmatrix} \quad (6)$$

Note that the location of D_{42} reflects the relation between members 2 and 4.

The other parts of the current framework, such as the construction of stiffness matrix, mass matrix, equation of motion, and the solution procedure are basically left unchanged, except for some modifications to make them compatible with the new kinematics relation added into the existing framework. This framework is now enhanced with the ability to model the highly flexible aircraft with flexible fuselage and vertical tail. Fig. 4 shows a built-up model.

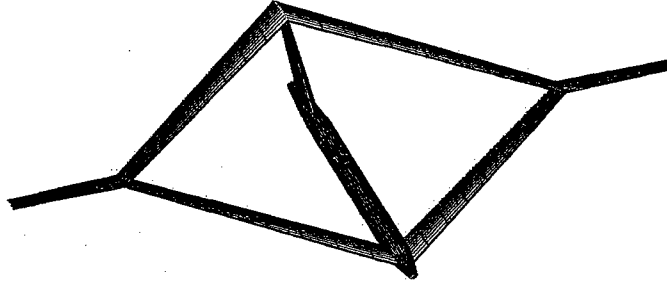


Figure 4: Illustration of a built-up joined wing aircraft with flexible fuselage and vertical tail

2.3 System equations

The equations of motion of the system are obtained by following the Principle of Virtual Work. With the six rigid-body degrees of freedom, the system structural degrees of freedom are represented by the column matrix q , where

$$\dot{q} = [\dot{\varepsilon}_1^T, \dot{\varepsilon}_2^T, \dots, \dot{\varepsilon}_n^T, V_B^T, \omega_B^T]^T \quad (7)$$

and ε_i contains the strain variables for wing member i , V_B and ω_B are the linear velocity and angular velocity of the vehicle reference point (original of the B frame), respectively, represented in the body frame, B . The dependent variables for the entire vehicle are collected into the column matrix H ,

$$\dot{H} = [\dot{h}_1^T, \dot{h}_2^T, \dots, \dot{h}_n^T, V_B^T, \omega_B^T]^T \quad (8)$$

The dependent degrees of freedom are related to the independent degrees of freedom through a Jacobian matrix relation

$$H = f(q), \quad dH = \left[\frac{\partial H}{\partial q} \right] dq = [J_{Hq}(q)] dq \quad (9)$$

The expression for virtual work on the vehicle is now given by

$$\delta W = \delta q^T (-\bar{M}\ddot{q} - \bar{C}\dot{q} - \bar{K}q + \bar{N}g + \bar{B}_v V + \bar{B}_{F1} F^{dst} + \bar{B}_{F2} F^{pt} + \bar{B}_{M1} M^{dst} + \bar{B}_{M2} M^{pt} + B_{q0} q_0 + B_H H) \quad (10)$$

where \bar{M} , \bar{C} , and \bar{K} are generalized mass, damping, and stiffness matrices corresponding to the independent degrees of freedom of the total system. Note that the matrices above are all assembled ones with respect to global degrees of freedom. The principle of virtual work requires that the total virtual work done on the system be equal to zero, leading to the equations of motion,

$$\bar{M}\ddot{q} + \bar{C}\dot{q} + \bar{K}q = B_v V + B_{F1} F^{dst} + B_{F2} F^{pt} + B_{M1} M^{dst} + B_{M2} M^{pt} + \bar{N}g + B_{q0} q_0 + B_H H \quad (11)$$

The distributed loads, F^{dst} and M^{dst} , are divided into aerodynamic loads and user supplied loads. The aerodynamic loads evaluated at the current state have the incremental form

$$\begin{aligned} F^{aero}(t) &= F^{aero}(t_0 + \Delta t) \approx F_0(q_0, \dot{q}_0, \lambda_0) + F_{\dot{q}} \dot{q} + F_{\dot{\lambda}} \dot{\lambda} + F_q \Delta q + F_{\lambda} \Delta \lambda \\ M^{aero}(t) &= M^{aero}(t_0 + \Delta t) \approx M_0(q_0, \dot{q}_0, \lambda_0) + M_{\dot{q}} \dot{q} + M_{\dot{\lambda}} \dot{\lambda} + M_q \Delta q + M_{\lambda} \Delta \lambda \end{aligned} \quad (12)$$

here λ is column matrix of induced flow states as described in Ref. 15. The induced flow states are governed by a differential equation of the form

$$\dot{\lambda} = L_1 \lambda + L_2 \ddot{q} + L_3 \dot{q} \quad (13)$$

The aeroelastic equations of motion are obtained by moving the state dependent aerodynamic loads over to the left hand side of Eq. (11) and augmenting the structure states with the induced flow states, which can be represented in state space form as

$$\dot{x} = A(x)x + B(x)u(x,t) \quad (14)$$

where the state vector is now given by

$$x = [q^T, \dot{q}^T, \lambda^T]^T \quad (15)$$

3 NUMERICAL STUDIES

To exemplify the capability of the new formulation and study the impact of overall vehicle flexibility on its stability, two different baseline vehicles were created. They represent two different configurations: a single-wing and a joined-wing configuration. Seven flight index points represent the nominal mission profile, as indicated in Fig. 5. At each index point, the altitude, fuel mass, and nominal flight velocity are specified. The index points represent: (1) takeoff, (2) climb, (3) cruise ingress, (4) cruise/loiter/cruise, (5) cruise egress, (6) decent, and (7) landing. The fuel burn determines the duration of each flight segment. The nominal flight speed at each index point is based on the cruise speed (input parameter), and is computed such that the dynamic pressure is constant (constant indicated air speed). At each flight index point, the vehicle is trimmed for equilibrium in horizontal flight at given flight speed. The trimmed body angles of attack can be found in Ref. 16.

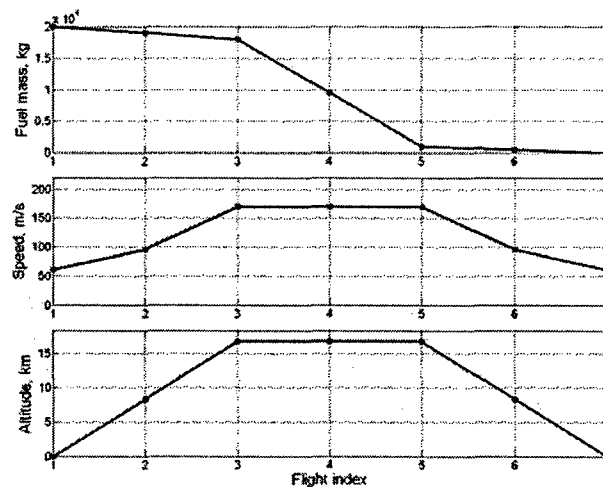


Figure 5: Basic mission profile

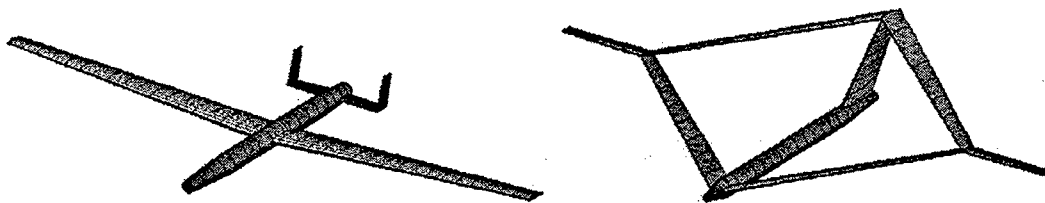


Figure 6: Baseline single-wing and joined-wing vehicles

3.1 Baseline vehicles

Three sets of constraints were defined to help sizing the baseline designs: strength (based on first-ply failure) at 1.5-g load, strength based on gust loads, and minimum linearized flutter margin. For both vehicles, the 1.5-g load factor was shown to be the critical constraint and the wing structural thickness distribution was sized for fully-strained design along span. A description of the design process can be found in Ref. 13.

3.1.1 Single-wing configuration

Geometry. From top view, the vehicle shape is symmetric. As indicated in Fig. 7, the wings are divided into nine regions, and the horizontal and vertical tail surfaces are both divided into two regions for definition of cross-sectional property distribution. For simplicity, NACA 4415 is chosen as the airfoil and it is kept constant throughout the wing members. The wing contains three independent ailerons, which present in regions 3 and 4, 5 to 7, and 8 and 9, as indicated in Fig. 7. These ailerons occupy 20% of the chord from 22% span to the tip of the wing, which are allowed to deflect $\pm 30^\circ$.

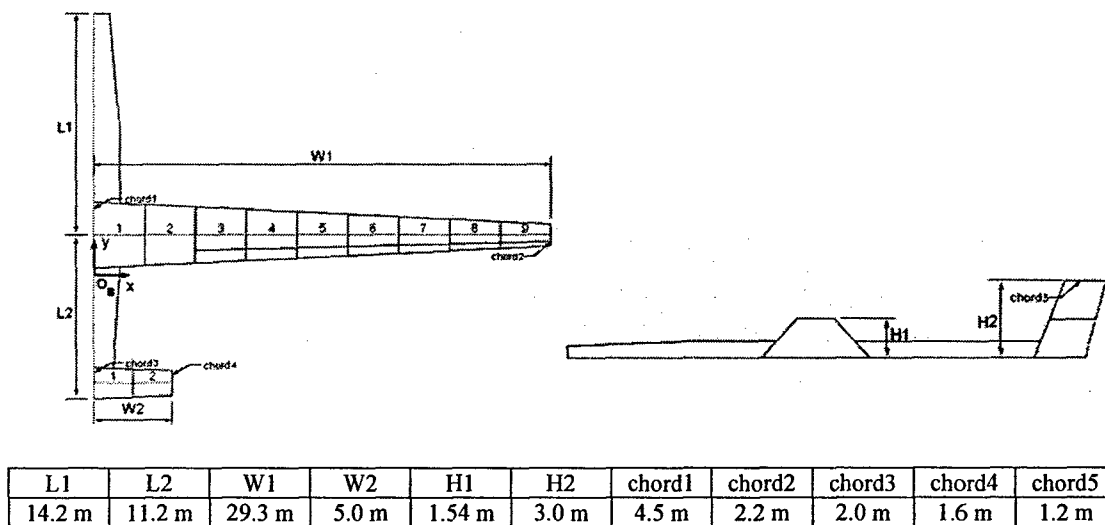


Figure 7: Baseline single-wing configuration vehicle geometry

Vehicle Mass Breakdown. The vehicle mass breakdown is given in Table 1. The fuel is assumed to be distributed up to half span of the wings, independent of the total amount of fuel on board. The fuselage contains no fuel.

Fuselage structure + payload + engine mass	4,000 kg
Fuel mass	20,000 kg

Tails structure mass	420 kg
Vehicle total wing structure mass	4,230 kg
Vehicle gross take-off mass	28,650 kg

Table 1: Vehicle mass distribution for single-wing configuration

Cross-sectional Inertia and Stiffness Distributions. The stiffness and inertia properties of each cross-section of the wing, tail and fuselage can be found in Ref. 16. Note that nonstructural masses of 155 kg each is used for the modeling of aircraft payload, which are assigned at each node of the fuselage for simplicity.

3.1.2 Joined-wing configuration

Geometry. From top view, the vehicle shape is symmetric (although one may want to vary the forward/aft location of the joint). The wings are denoted right front wing (with inner and outer wings), left front wing, right aft wing (with inner-wing only), and left aft wing. Right and left are determined as in Fig. 8 (as viewed from top with nose pointing up). The front wings are divided into eight regions while the aft wings are divided into four regions for definition of cross-sectional properties distribution. The members of all inner wings are identical in construction, and the material distribution follows the numbering convention indicated in Fig. 8. For simplicity, NACA 4415 is chosen as the airfoil and it is kept constant throughout the wing members. The outer wing contains a 50%-span/20%-chord aileron that is allowed 30° of amplitude deflection.

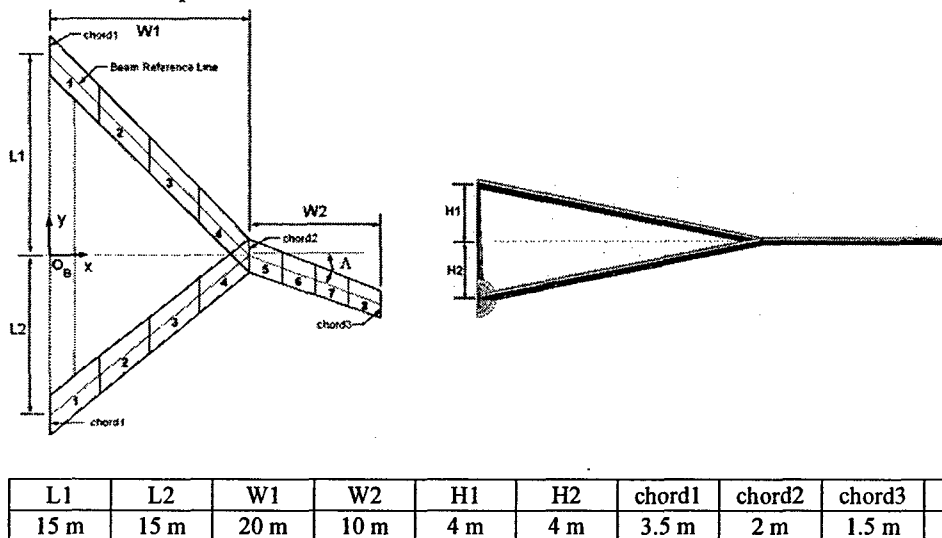


Figure 8: Baseline joined-wing vehicle geometry

Vehicle Mass Breakdown. The vehicle mass breakdown is given in Table 2. The fuel is assumed to be distributed evenly throughout the inner and outer wings, independent of the total amount of fuel on board. The fuselage contains no fuel.

Fuselage structure + payload + engine mass	4,000 kg
Fuel mass	20,000 kg
Vertical tail structure mass	550 kg
Vehicle total wing structure mass	3,440 kg
Vehicle gross take-off mass	27,990 kg

Table 2: Vehicle mass distribution for joined-wing configuration

Cross-sectional Inertia and Stiffness Distributions. The stiffness and inertia properties of the wing, vertical tail and fuselage can be found in Ref. 16. Note that nonstructural masses of 100 kg each is used for the modeling of aircraft payloads, which are attached at each node of the fuselage for simplicity.

3.2 Models for different degrees of flexibility

To assess the effects of the flexibility of different parts of the vehicles on their stability, five different models are considered for both single-wing and joined-wing configurations. They are summarized in Tables 3 and 4.

	Fuselage	Tails	Wings
Model 1	Rigid	Rigid	Flexible
Model 2	Rigid	Flexible	Flexible
Model 3	Rigid	4 * Flexible	Flexible
Model 4	Flexible	Rigid	Flexible
Model 5	Flexible	Flexible	Flexible

Table 3: Different levels of flexibility to be considered for single-wing configuration

	Fuselage	Vertical Tail	Inner Wings	Outer Wings
Model 1	Rigid	Rigid	Rigid	Flexible
Model 2	Rigid	Rigid	Flexible	Flexible
Model 3	Rigid	Flexible	Flexible	Flexible
Model 4	Flexible	Rigid	Flexible	Flexible
Model 5	Flexible	Flexible	Flexible	Flexible

Table 4: Different levels of flexibility to be considered for joined-wing configuration.

In the above tables, the “rigid” members are modeled with 100 times the nominal stiffnesses, representing almost rigid cases, whereas the “4 * Flexible” members are modeled to have 25% of the nominal stiffness, representing an extra flexible case.

3.3 Dynamic stability

3.3.1 Linearized flutter speed (unstable speed)

For both the single-wing and joined-wing configurations, the flutter speed is approximated at each flight index point by determining the stability characteristics of the linearized system about its nonlinear equilibrium condition. The calculated flutter speeds normalized by the corresponding nominal flight speed are plotted in Figs. 9 and 14 for single-wing and joined-wing configurations, respectively.

For the single-wing configuration, the induced flexibility of the fuselage reduces the flutter speed slightly. However, this effect is very small, almost negligible. The reduction of the flutter speed due to the induced flexibility of the tail should be considered carefully. In the studies, overall system stabilities are calculated and analyzed, which includes both the wings and the tails. Since the relative elastic coupling between the wing and tail is weak (i.e., relatively rigid fuselage), one would not expect any significant influence of the tail on the flutter characteristics of the wing. This explains why there is nearly no change in the flutter speed when the tail is set from rigid to flexible. However, if the stiffness of the tail is further reduced (say, 25% of the nominal stiffness), there will be a significant decrease of the tail

flutter speed, which ended up lower than that of the wing. This is shown in shown in Fig. 9 (Model 3). This can also be observed from the flutter modes. Figs. 10 and 11 show the flutter modes of the Model 3, which has fluttering tail. But in Model 5, the flutter comes from the wings as indicated in Figs. 12 and 13.

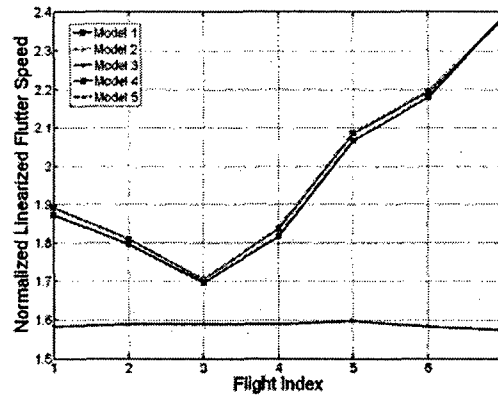


Figure 9: Flutter (unstable) speed at each flight index for different models of single-wing configuration

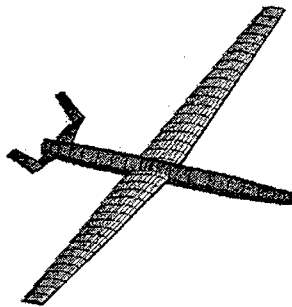


Figure 10: Symmetric flutter (unstable) mode of single-wing configuration (Model 3, Index 3, frequency, 2.91 Hz)

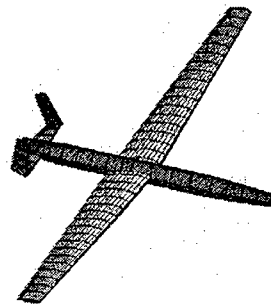


Figure 11: Anti-symmetric flutter (unstable) mode of single-wing configuration (Model 3, Index 5, frequency, 2.91 Hz)

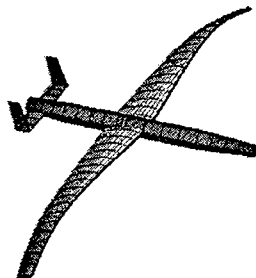


Figure 12: Symmetric flutter (unstable) mode of single-wing configuration (Model 5, Index 3, frequency, 3.14 Hz)

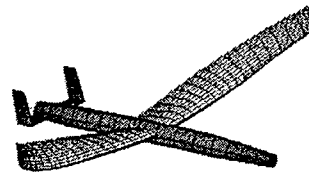


Figure 13: Symmetric flutter (unstable) mode of single-wing configuration (Model 5, Index 5, frequency, 4.00 Hz)

For the joined-wing configuration, the induced flexibility of the fuselage and vertical tail on the flutter speed is prominent as indicated in Fig. 14. Sample of the flutter modes are depicted in Figs. 15 to 22. Models 2, 3 and 4 seem to keep the same corresponding flutter mode throughout the different flight indices. Model 2 is purely wing flutter (anti-symmetric mode). Model 4 presents a symmetric flutter mode with vertical bending contribution of the fuselage, which reduces the flutter speed in comparison with Model 2. Model 3 presents an anti-symmetric flutter mode enabled by the lateral bending of the tail. Model 5 (fully flexible vehicle), however, shows a change in the flutter mode shape with flight index. At flight index 3, it presents an anti-symmetric flutter mode with contribution of both lateral bending of the vertical tail and lateral bending of the fuselage. At index 5, the flutter mode switches to be a symmetric one, similar to Model 4.

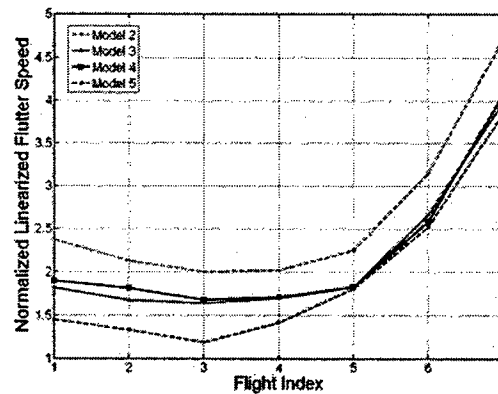


Figure 14: Flutter (unstable) speed at each flight index for different models of joined-wing configuration

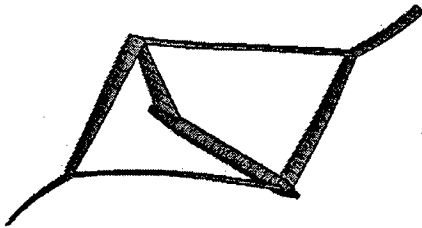


Figure 15: Anti-symmetric flutter (unstable) mode of joined-wing configuration (Model 2, Index 3, frequency, 0.94 Hz)

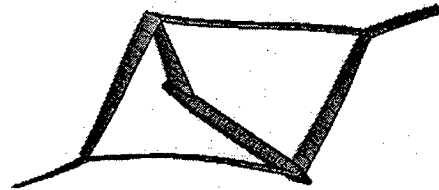


Figure 15: Anti-symmetric flutter (unstable) mode of joined-wing configuration (Model 2, Index 5, frequency, 2.29 Hz)

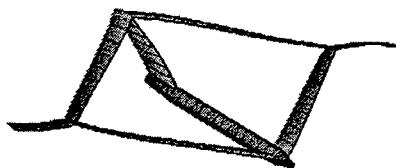


Figure 17: Anti-symmetric flutter (unstable) mode of joined-wing configuration (Model 3, Index 3, frequency, 0.97 Hz)

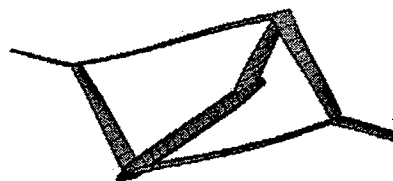


Figure 18: Anti-symmetric flutter (unstable) mode of joined-wing configuration (Model 3, Index 5, frequency, 2.32 Hz)

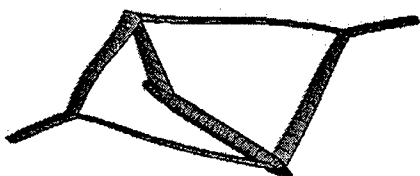


Figure 19: Symmetric flutter (unstable) mode of joined-wing configuration (Model 4, Index 3, frequency, 0.96 Hz)

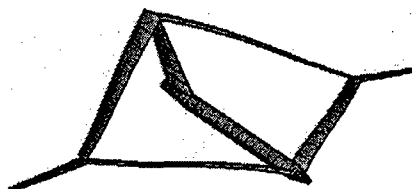


Figure 20: Symmetric flutter (unstable) mode of joined-wing configuration (Model 4, Index 5, frequency, 2.11 Hz)



Figure 21: Anti-symmetric flutter (unstable) mode of joined-wing configuration (Model 5, Index 3, frequency, 0.63 Hz)

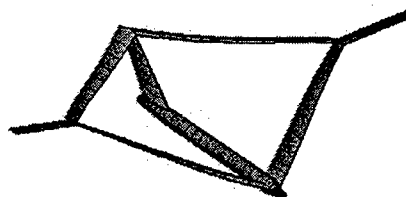


Figure 22: Symmetric flutter (unstable) mode of joined-wing configuration (Model 5, Index 5, frequency, 2.08 Hz)

3.3.2 Nonlinear flutter speed

For the single-wing configurations, the nonlinear flutter speed is approximated at each index point by determining the stability characteristics of the system linearized at each flight speed increment, in addition to its nominal flight condition. It is, therefore, a matching problem between the instability speed and the uniform flow speed. Flutter speeds can be affected by many parameters, such as geometry and flight conditions of the vehicle.

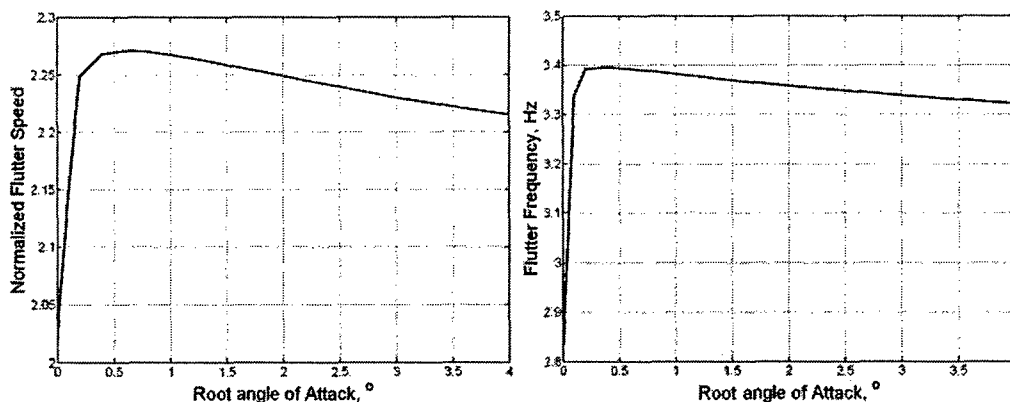


Figure 23: Normalized nonlinear flutter speeds and frequencies at different wing root angle of attack

Fig. 23 shows the nonlinear flutter speed with the variation of the wing root angle of attack of the vehicle (no change in altitude is considered). The flight index 4 is selected for this study. The vehicle is flying with a speed of 170 m/s, at 16.7 km altitude. The nominal (trim) root angle of attack is approximately 3° , and this angle is now varied from 0° to 4° , to generate different lift distributions. It can be seen from the figure that the flutter speed changes rapidly at very small root angles of attack. At around 0.6° , flutter speed and frequency reach their maximum values, after which, the flutter speed and frequency decrease monotonically. The results here agree with those in Ref. 1, in which this effect was originally presented.

For the seven flight indices, some of them can be considered *heavy* configurations (1, 2, 3, and 4), where the vehicle carries significant fuel, and *light* configurations (5, 6, and 7), where the fuel is almost depleted. Now, the c.g. (center of gravity) position is allowed to vary, so that its effect on the flutter speed of corresponding heavy and light vehicles can be compared. The c.g. is moved from 15% chord to 55% chord. Note that the aerodynamic center is located at 25% of the chord. From Fig. 24, one may notice that the position of c.g. has more effect on heavy configurations (Index 1) than on light ones (Index 7). For the heavy configurations, the nonlinear flutter speed increased at first and then starts decreasing. However, for the light configurations, nonlinear flutter speed is always monotonically decreasing. This also holds for high altitude cases (see Fig. 25).

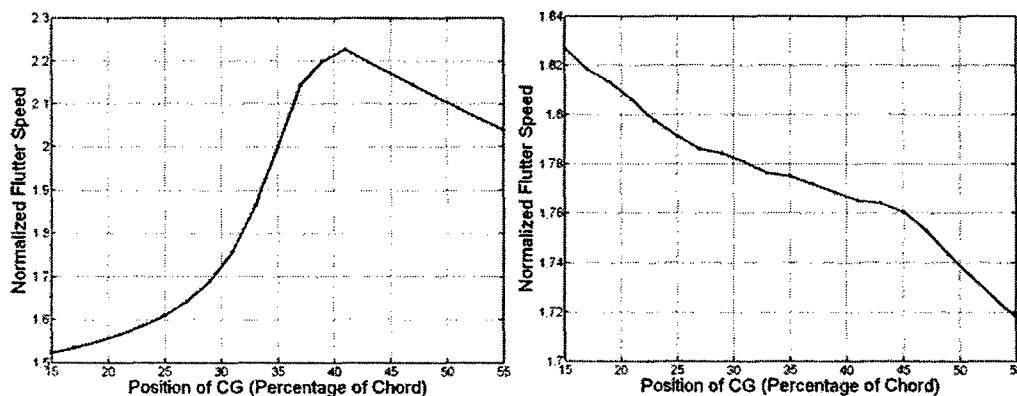


Figure 24: Normalized flutter speeds with moving c.g. (left: heavy configuration, right: light configuration; low altitude)

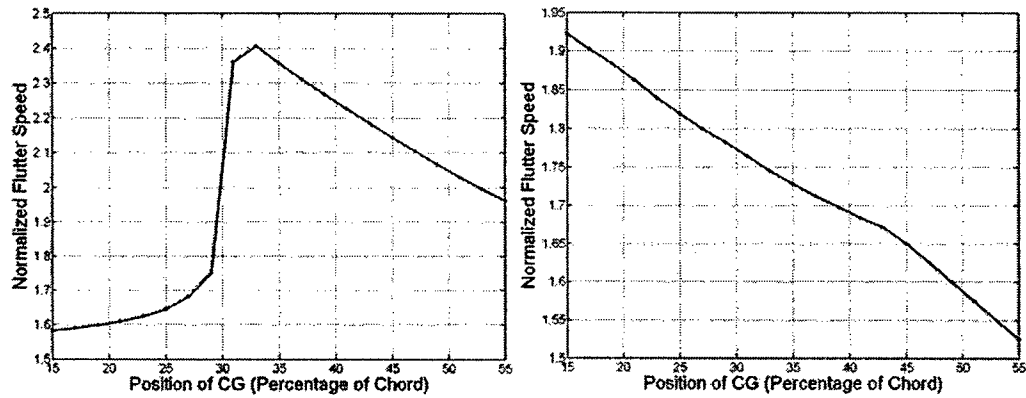


Figure 25: Normalized flutter speeds with moving c.g. (left: heavy configuration, right: light configuration; high altitude)

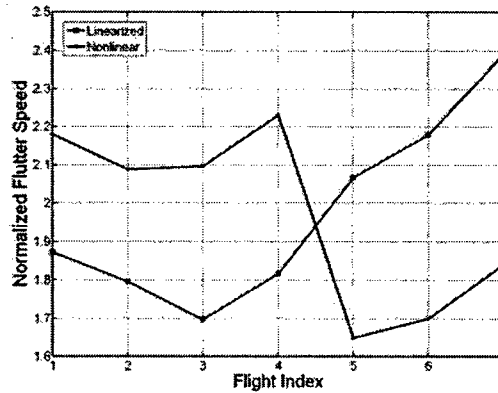


Figure 26: Nonlinear flutter speed at each flight index for fully flexible model of single-wing configuration

The calculated flutter speeds are plotted in Figs. 26. From that, it can be seen that for Indices 1 to 4, the nonlinear solution predicts higher flutter speeds than the linearized one. This trend reverses for the last three flight indices.

If one looks at the flutter modes of Index 1, one will see a mode which is a combination of a coupled bending-twist (for inner half) and bending (for outer half) of the wings. For the linearized solution, the mode is symmetric, while it is non-symmetric for the nonlinear one (Fig. 27). The non-symmetric mode comes with a large deformation of the fuselage (although the fuselage flexibility is not responsible for the flutter instability as one can see in Fig. 28). For Index 5 (Fig. 29), things are somewhat different. The linearized flutter mode shape is similar to the linearized one at Index 1, which is also symmetric. The frequency is 4.00 Hz. The nonlinear flutter mode at Index 5 is switched to a purely second bending mode, whose frequency is reduced to 2.78 Hz.



Figure 27: Linearized (left, frequency 3.36 Hz) and nonlinear (right, frequency 3.14 Hz) flutter modes of single-wing configuration (Model 5, Index 1)

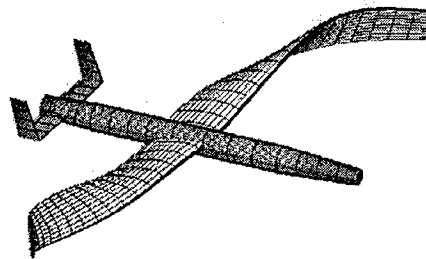


Figure 28: Nonlinear flutter mode of single-wing configuration with rigid fuselage and tails (Model 1, Index 1, frequency 4.08 Hz)

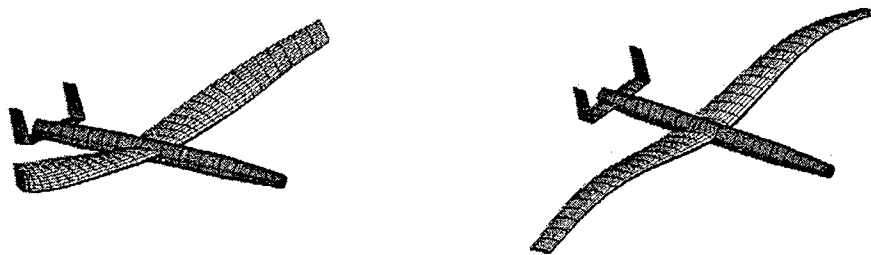


Figure 29: Linearized (left, frequency, 4.00 Hz) and nonlinear (right, frequency, 2.78 Hz) flutter modes of single-wing configuration (Model 5, Index 5)

The linearized and nonlinear flutter results of Model 5, joined-wing configuration are summarized in Table 5. Unfortunately, as indicated in the table by the notation “BBF,” the nonlinear solution leads to “buckling” before flutter happens for most of the flight indices. This is the case for this particular design, since the aft wing is always subject to the compressive loads due to the lift on the front wing. Details on the study of the “buckling” will be provided in the next section.

Index	Normalized linearized Flutter Speed	Normalized nonlinear Flutter Speed
1	1.45	BBF* (1.31)
2	1.33	BBF (1.32)
3	1.19	BBF (1.33)
4	1.42	BBF (1.41)
5	1.80	1.81
6	2.52	BBF (2.28)
7	3.86	BBF (2.28)
* Buckle before flutter		

Table 5: comparison of flutter speed results from different calculation schemes (Model 5, joined-wing configuration)

3.4 Static stability

Since the aft wings of a joined-wing aircraft may be subject to compressive loads, their buckling response can be a sizing limitation for the vehicle. For the particular baseline design considered here, deformation of the aft wing increases dramatically when the load factor reaches about 1.60, bringing the whole wing system close to a collapse. This is illustrated in Fig. 30 as the flight speed is increased at level flight (no retrimming). Note that this condition is naturally modeled in the presented framework through the nonlinear structural analysis.

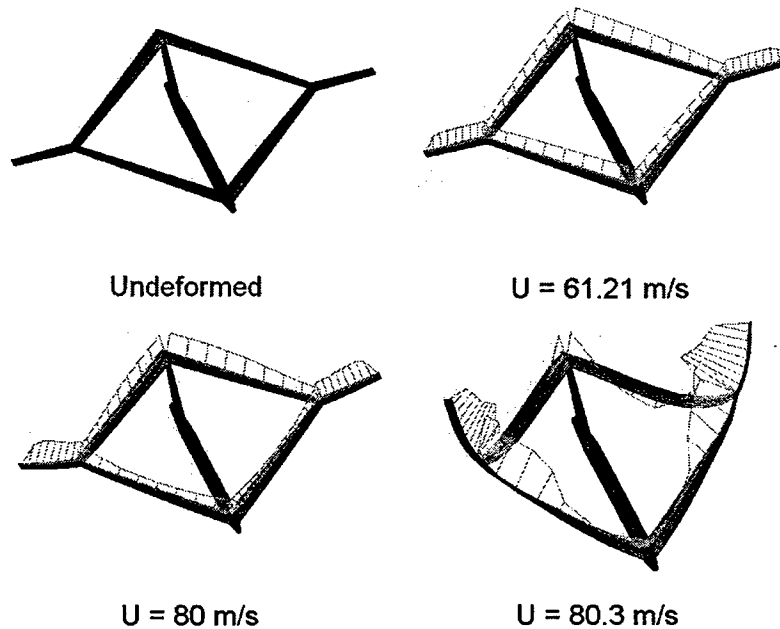


Figure 30: Lift distribution on the vehicle as the buckling speed is approached (sea level, fully fueled, no rigid body degrees of freedom, zero body angle of attack)

To study the effects of the flexibility from different members of the aircraft on the loss of static stability of the wings, Models 2 to 5 are brought to steady state at level flight (at sea level). Then, their flight speeds are varied from the nominal flight speed, which is 61.21 m/s, until there is a sudden drop in the lift generation capacity. This results in load factors ranging

from 1.00 to approximately 1.60, depending on the model. The wing shape and deflections of the fully flexible model (Model 5) are plotted for varying load factor in Figs. 31 and 32. The corresponding tip positions versus flight speed and load factor are shown in Fig. 33. The sudden reduction of the aft wing stiffness results in large bending deflection of the overall wing structure and, consequently, drop in the overall lift (represented by the reduction in load factor) as shown in Fig. 33. This level of wing displacement causes high composite ply strains (stresses), to the point of ply failure. Strain components dependence on the load factor is shown in Figs. 34 to 36.

This static instability speed may vary because of different levels of flexibility of the vehicle (Table 4). The load factors, whose sudden reduction indicates the onset of instability, are plotted as function of flight speed for different models, as shown in Fig. 37. The model with a flexible vertical tail has the highest buckling speed, whereas the one with flexible fuselage has the lowest buckling speed. If one looks closer to the modes of deformation ("buckling mode"), they show a complex interaction between the vertical bending of the fuselage (particularly at the front wing connecting region) and the in-plane bending of the tail. These induced a change in the overall aerodynamic loading of the different wing segments, influencing the compressive load applied to the aft wing. Since the different models were only trimmed at the point corresponding to load factor 1 in Fig. 37, the other load factor points may represent a very different solution in terms of vehicle c.g. forces and moments. Further studies are needed to better understand the implications of the flexibility of the fuselage and vertical tail on the static instability of the vehicle.

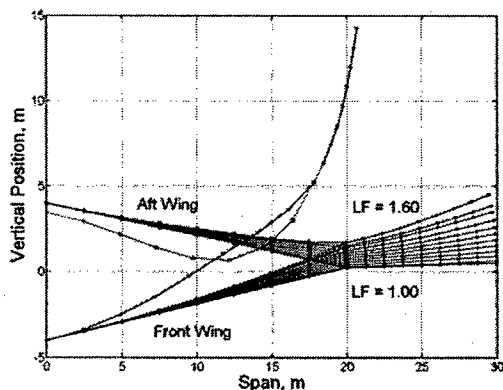


Figure 31: Wing shape for varying flight speed (level flight at sea level)

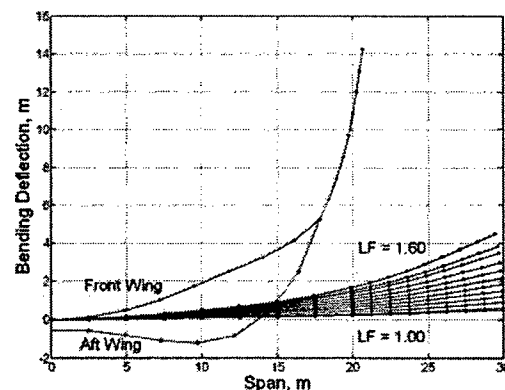


Figure 32: Wing bending deflections for varying flight speed (level flight at sea level)

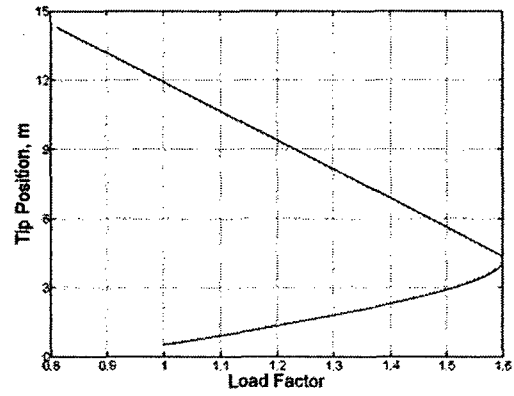
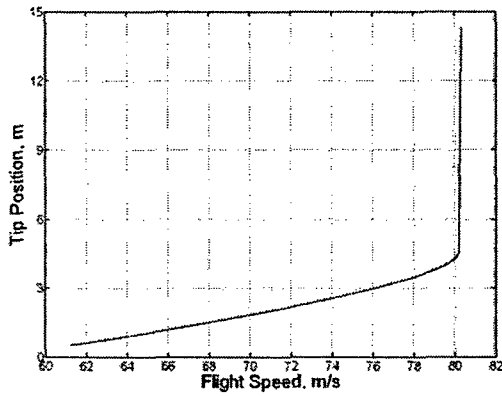


Figure 33: Changes in tip deflection as function of the lift generation capability of the vehicle at level flight (sea level)

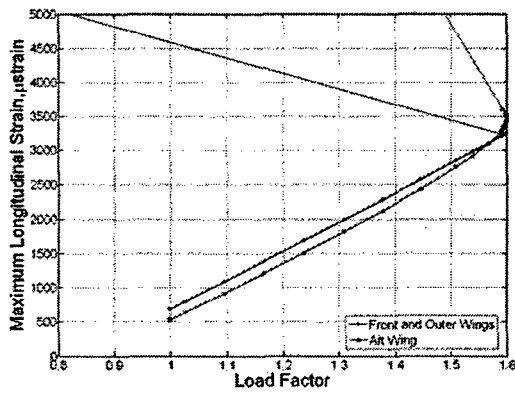


Figure 34: Maximum longitudinal strain component nonlinear growth due to loss of stiffness on the aft wing with increase load factor (level flight, sea level)

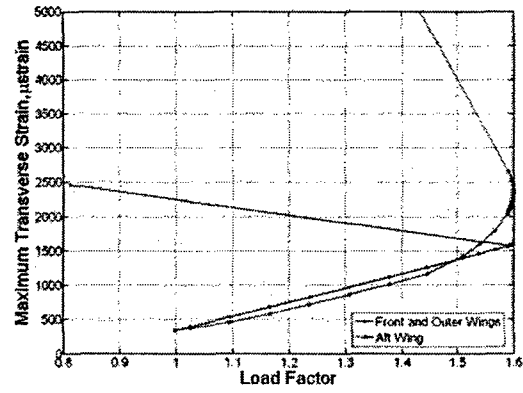


Figure 35: Maximum transverse strain component nonlinear growth due to loss of stiffness on the aft wing with increase load factor (level flight, sea level)

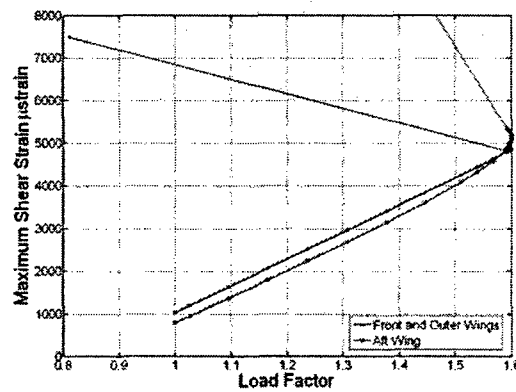


Figure 36: Maximum shear strain component nonlinear growth due to loss of stiffness on the aft wing with increase load factor (level flight, sea level)

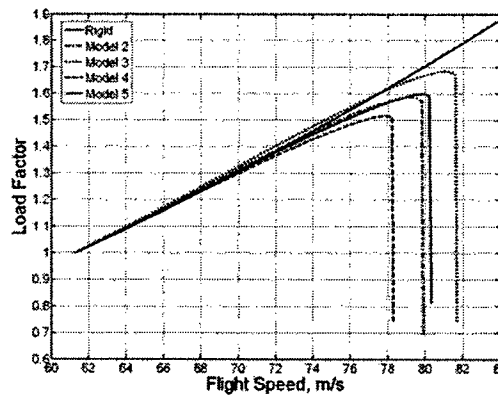


Figure 37: Load fact with respect to flight speeds for different models of joined-wing configuration (level flight, sea level)

4 CONCLUDING REMARKS

This paper presented a nonlinear aeroelastic formulation for the modeling and analysis not only of the very flexible wings but also their coupling with flexible fuselage and tail. The geometrically-nonlinear structural model is a strain-based formulation able to capture the large deformations in slender composite structures. The unsteady aerodynamics is incompressible, and written in space-state form. The low-order aeroelastic framework is intended for preliminary design and assessment of aeroelastic response and its coupling with flight dynamics of very flexible aircraft. The low-order representation of the fully flexible vehicle is to be used for control design.

Based on the new approach, two of the three aircraft configurations being considered for the Sensorcraft program were studied: single-wing and joined-wing configurations. Specifically, the paper presented the effects of the added flexibility of the fuselage and tail to the very flexible wings in the onset of flutter and static ("buckling-like") instability (for joined-wing only).

From the results of the numerical studies, it is clear that joined-wing configurations present much richer and complex aeroelastic characteristics than single-wing ones. As for the linearized flutter speed, flexible fuselage and vertical tail both reduces the flutter speed of joined-wing configuration, whereas the flexibility of the fuselage and tail of the single-wing configuration does not significantly impacts the wing flutter (unless the wing flutters first). Although the linearized flutter speed can be easily obtained, the actual (nonlinear) flutter speed can be higher or lower than that, depending on a series of parameters. Therefore, it is recommended that one uses the nonlinear flutter speed calculation to determine the stability boundary of flexible vehicles like the ones studied here. Regarding the unique problem of loss of stiffness in the aft wing in the joined-wing configuration, preliminary results indicated that the added flexible fuselage decreases "buckling" speed, while adding the flexibility of the vertical tail increases it. More studies are needed to better understand those relative effects.

While the proposed framework has been created to handle any structural configuration made of slender (active) composite components (wing, tail, fuselage), in its current form it cannot naturally handle the flexibility of the body in a wing-body (flying wing) configuration (third Sensorcraft concept being considered). Current work is under way to extend the framework to bring non-slender flexible bodies to be coupled with the present nonlinear aeroelastic formulation.

REFERENCES

- [1] Patil, M. J., Hodges, D. H., and Cesnik, C. E. S., "Nonlinear Aeroelasticity and Flight Dynamics of High-Altitude Long Endurance Aircraft," *Journal of Aircraft*. Vol. 38, No. 1 Jan. - Feb. 2001.
- [2] Van Shoor, M. C., Zerweckh, S. H. and von Flotow, A. H., "Aeroelastic Stability and Control of a Highly Flexible Aircraft", AIAA Paper, AIAA-89-1187-CP, 1989.
- [3] Drela, M., "Integrated Simulation Model for Preliminary Aerodynamic, Structural, and Control-Law Design of Aircraft", AIAA Paper, AIAA-99-1394, 1999.
- [4] Jones, R. I., "The Design Challenge of High Altitude Long Endurance (Hale) Unmanned Aircraft," *The Aeronautical Journal*, June, 1999, pp. 273-280.
- [5] Jones, R. I., "Selection and Comparison of Unmanned Aircraft Configurations," In *RPVs International Conference, 12th, Bristol, United Kingdom, Sept. 9-11, 1996*, Conference Papers (A97-21501 04-01), Bristol, United Kingdom, University of Bristol, 1996.
- [6] Tilmann, C. P., Flick, P. M., Martin, C. A., and Love, M. H., "High-Altitude Long Endurance Technologies for SensorCraft," *RTO AVT Symposium on Novel and Emerging Vehicle and Vehicle Technology Concepts*. Brussels, Belgium, April 2003. RTO Paper MP-104-P-26.
- [7] Wolkovitch, J., "The Joined Wing: An Overview", *Journal of Aircraft*. Vol. 23, No. 3, 1996, pp. 161-178.
- [8] Livne, E., "Aeroelasticity of Joined-Wing Airplane configurations: Past Work and Future Challenges – a Survey", AIAA Paper AIAA-2001-1370, *AIAA/ASME/ASCE/AHS 42nd Structures, Structural Dynamics, and Materials Conference*, Seattle, WA, 16-19 April 2001.
- [9] Lin, H.-H., Jhou, J., and Stearman, R., "Influence of Joint Fixity on the Aeroelastic Characteristics of a Joined Wing Structure," AIAA-90-0980-CP, pp. 1442-1454, 1990.
- [10] Blair, M. and Canfield, R. A., "A Joined-Wing Structural Weight Modeling Study", AIAA Paper, AIAA-2002-1337, 2002.
- [11] Roberts, R.W. Jr., Canfield, R.A. and Blair, M., "Sensor-Craft Structural Optimization and Analytical Certification", AIAA Paper AIAA-2003-1458, *AIAA/ASME/ASCE/AHS 44th Structures, Structural Dynamics, and Materials Conference*. Norfolk, VA, 7-10 April 2003.
- [12] Reich, G.W., Raveh, D. and Zink, P.S., "Application of Active Aeroelastic Wing Technology to a Joined-Wing Sensorcraft", AIAA Paper AIAA-2002-1633, 2002.
- [13] Cesnik, C. E. S. and Brown, E. L., "Active Warping Control of a Joined Wing Airplane Configuration," *Proceedings of the 44th Structures, Structural Dynamics, and Material Conference*, Hampton, Virginia, April 7 - 10, 2003.
- [14] Brown, E. L., "Integrated Strain Actuation in Aircraft with Highly Flexible Composite Wings," Ph.D. Thesis, Mechanical Engineering, Massachusetts Institute of Technology, Cambridge, Massachusetts, June 2003.

[15] Peters, D. A. and Johnson, M. J., "Finite-State Airloads for Deformable Airfoils on Fixed and Rotating Wings", *Symposium on Aeroelasticity and Fluid/Structure Interaction Proceedings of the Winter Annual Meeting*, AD Vol. 44, American Society of Mechanical Engineers, Fairfield, NJ, 1994, pp.1-28.

[16] Cesnik, C. E. S. and Su, W., "Nonlinear Aeroelastic Modeling and Analysis of Fully Flexible Aircraft," AIAA Paper AIAA-2005-2169, *AIAA/ASME/ASCE/AHS 46th Structures, Structural Dynamics, and Materials Conference*. Austin, Texas, April 18-21, 2005.